Transactions of the ASME®

Journal of Fluids Engineering

Published Quarterly by The American Society of Mechanical Engineers

VOLUME 115 • NUMBER 4 • DECEMBER 1993

(Contents continued on page 709)

FLUIDS ENGINEERING DIVISION
Technical Editor
DEMETRI P. TELIONIS (1995)
Executive Secretary
PAT WHITE (1995)
Technical Editor's Office
SAAD A. RAGAB
Calendar Editor
M. F. ACKERSON

Associate Technical Editors
R. K. AGARWAL (1994)
R. E. A. ARNDT (1996)
O. BAYSAL (1995)
DENNIS M. BUSHNELL (1993)
N. A. CUMPSTY (1995)
M. GHARIB (1995)
A. F. GHONIEM (1995)
CHIH-MING HO (1993)
THOMAS T. HUANG (1993)
J. A. C. HUMPHREY (1994)
O. C. JONES (1995)
G. KARNIADAKIS (1995)
R. W. METCALFE (1995)
L. NELIK (1995)
WING-FAI NG (1996)
R. L. PANTON (1995)
ANDREA PROSPERETTI (1993)
M. W. REEKS (1995)
W. S. SARIC (1996)

BOARD ON COMMUNICATIONS
Chairman and Vice-President
R. D. ROCKE

Members-at-Large
T. BARLOW, T. DEAR, L. KEER,
J. KITTO, W. MORGAN, E. M. PATTON,
S. PATULSKI, R. E. REDER, R. SHAH,
A. VAN DER SLUYS, F. M. WHITE,
J. WHITEHEAD

OFFICERS OF THE ASME
President, **J. H. FERNANDES**
Exec. Dir.
D. L. BELDEN
Treasurer,
R. A. BENNETT

PUBLISHING STAFF
Mng. Dir., Publ.,
CHARLES W. BEARDSLEY
Managing Editor,
CORNELIA MONAHAN
Production Asstistant, **MARISOL ANDINO**

Transactions of the ASME, Journal of Fluids Engineering (ISSN 0098-2202) is published quarterly (Mar., June, Sept., Dec.) for $130.00 per year by The American Society of Mechanical Engineers, 345 East 47th Street, New York, NY 10017. Second class postage paid at New York, NY and additional mailing offices. POSTMASTER: Send address changes to Transactions of the ASME, Journal of Fluids Engineering, c/o THE AMERICAN SOCIETY OF MECHANICAL ENGINEERS, 22 Law Drive, Box 2300, Fairfield, NJ 07007-2300. **CHANGES OF ADDRESS** must be received at Society headquarters seven weeks before they are to be effective. Please send old label and new address. **PRICES:** To members, $40.00, annually: to nonmembers, $130.00. Add $24.00 for postage to countries outside the United States and Canada.

STATEMENT from By-Laws. The Society shall not be responsible for statements or opinions advanced in papers or . . . printed in its publications (B7.1, Par. 3). **COPYRIGHT** © **1993** by The American Society of Mechanical Engineers. Authorization to photocopy material for internal or personal use under circumstances not falling within the fair use provisions of the Copyright Act is granted by ASME to libraries and other users registered with the Copyright Clearance Center (CCC) Transactional Reporting Service provided that the base fee of $3.00 per article is paid directly to CCC, 27 Congress St., Salem, MA 01970. Request for special permission or bulk copying should be addressed to Reprints/Permission Department.

INDEXED by Applied Mechanics Reviews and Engineering Information, Inc.
Canadian Goods & Services Tax Registration #126148048

Downloaded 03 Jun 2010 to 171.66.16.159. Redistribution subject to ASME license or copyright; see http://www.asme.org/terms/Terms_Use.cfm

Technical Briefs

Announcements and Special Notices

Journal of
Fluids
Engineering

Editorial

This issue of the *Journal of Fluids Engineering* is dedicated to Professor William R. Sears on the occasion of his 80th birthday. Over the past fifty years, Bill Sears has made a great many significant contributions to fluid mechanics and fluids engineering. He has also provided impetus in several areas of fluid mechanics through his own pioneering works, which since then have been referenced hundreds of times. But to all of us who have known him, Bill Sears is appreciated even more for his ability to motivate and inspire others, students and colleagues alike. With his unassuming and warm personality, he has attracted and guided many students who later themselves excelled. Over the years, he has freely handed out, both to colleagues and students, excellent ideas which later matured into significant contributions and for which he often refrained from having his name listed as a co-author.

Bill obtained his B. Aero. E. from the University of Minnesota, and then, in 1934, moved on to where he was eventually to become one of the most famous students of Theodore von Kármán. At Caltech, he started out with a wind tunnel assistantship, became an instructor in 1937, and an assistant professor in 1940. Bill has always loved the challenge of wind tunnel measurements and their importance to aerodynamics, and does so to this day. But, as fate would have it, he would not return to the wind tunnel work until many decades later. Von Kármán had his eye on the young man for even greater things.

In those days, in the period 1936–1938, controversy was brewing in the scientific community regarding vital issues in unsteady aerodynamics, and especially the interpretation of measurements taken in certain laboratory modeling schemes if they were to be applied to practical flight. Kármán, returning to Caltech from an earlier trip to Europe in 1937, proposed to his young assistant and doctoral student, Bill Sears, that they set out to clarify the issue. Kármán's idea was to apply a unifying concept of fluid mechanics, Lord Kelvin's widely accepted notion of impulse in potential flows, to the problem. To do this, he turned to Bill, proposed a doctoral dissertation to his young student, and thereby started a collaboration between the two that endured for the rest of Kármán's lifetime.

Sears completed his thesis at Caltech in 1938 under Kármán's tutelage and received his Ph.D. there that year. He and Kármán also published that same year a landmark paper on unsteady wing theory arising from Bill's dissertation, which not only clarified existing confusion, but set new standards for the whole field. Even now, more than a half century later, that paper is still a subject of, or principal reference for, at least one of the articles in this special issue of the *Journal of Fluids Engineering*. It was also during this period at Caltech that Bill developed both the experience and extraordinary skills of clear thought and exposition that have made him, many of us believe, one of the great teachers of our time.

Following immediately upon his Caltech experiences, and partly because of the onset of World War II, Bill entered industry as a practical engineer and aerodynamicist. In 1941, he became Chief of Aerodynamics and Flight Testing at Northrop, and spent five years of the Allied effort there. During these years, he participated in the design of the P-61 series (Black Widow) and led the effort in designing the Northrop experimental tail-less flying-wing aircraft, as long-range, highly efficient bomber aircraft. This effort culminated in the development of the YB-49, a beautiful, jet-powered, high-performance airplane meeting or exceeding all its original design specifications. Only the end of the war seems to have precluded the YB-49 from going into extensive production, and the aircraft was later superseded by the Air Force's order of the B-52. A version of the "49" can still be viewed at the Air Force museum at Wright-Patterson AFB in Ohio.

Once the war was over, a unique opportunity was offered to Bill by Cornell University to come to Ithaca and found a new school of aeronautical engineering. For many people of vision, it was now clear that the era of flight was coming into its own and needed to be developed into a mature science and field of excellence in engineering practice. Kármán was becoming recognized worldwide as one of this country's great pioneers in engineering science and proponents of advanced technology. His students, including Sears, were sought out by people of vision in the country's great universities. Dean S. C. Hollister at Cornell believed in this view of the future of technology and invited Bill to come to Cornell to help prove that he was right.

Bill Sears, with his young wife Mabel—the former Mabel Rhodes, who, as von Kármán's secretary in 1937–1938, actually typed Bill's Ph.D. thesis, and has since emerged as his "wisest advisor and lifetime companion" (Bill's own words)—moved to Ithaca, New York from southern California to be in this great adventure. What was to follow was remarkable by any measure.

Founding a new graduate school in 1946, at the age of 33, Bill assembled an impressive faculty of young enthusiasts of science, all imbued with the same sense of commitment and skill that he himself treasured. Over the next two decades, under his leadership, he and his colleagues' students have emerged from Cornell not only dedicated to the school and its ideas (as personified by Bill Sears himself), but also ready to contribute to their chosen fields. Today, one can find an extraordinary number of Bill Sears' former students, and their students, as leaders in industry, advisors and consultants in science and engineering, and teachers on a wide range of university faculties worldwide.

Returning to Bill's research efforts and pioneering contributions in science and engineering, we have space here only to concentrate on a few highlights. During the early part of his Cornell years, among other topics, Bill worked on three-dimensional boundary layers, internal flow in turbomachinery, and slender-body theory. He and his associates extended the Busemann biplane study to one with identical rectangular planform. A few years before the method of matched asymptotic expansions was formalized, Bill employed an asymptotic method to attack the problem of not-so-slender wings and to carry the classical theory of Munk, Jones, and Ward to the next higher order.

Bill served as the editor of the *Journal of Aeronautical Sciences* from 1955 to 1963 and, at about this time, he developed great interest in magnetofluid or magneto-aerodynamics. A large number of his papers which appeared during this time have widened the scientific interest in this area.

Bill Sears' early interest in unsteady flows led him to recognize the significance of the concept of unsteady boundary-layer separation. He pointed this out clearly, as early as during the fifties, but it was a decade later before he had the opportunity to work on this problem. This idea, like so many others, was pursued by his students and by many other investigators, with immediate applications to engineering problems such as unsteady stall.

At about the same time Bill became interested in the problem of rotating blade noise. He and his associates recognized that a method proposed by Ffowcs Williams and Hawkins to calculate noise generated by turbulence or surfaces in arbitrary motion could be applied directly to the problem of rotating blade noise, and indeed to its control or diminution. Until then, intuitive and physical reasoning were used to find the acoustic source strengths via methods which, however, sometimes turned out to violate the conservation laws of continuity and momentum. Bill and his associates introduced additional mathematical and physical rigor in their method of establishing acoustical source strengths. A look at the current literature of helicopter rotor and propeller acoustics shows how farsighted Sears had been.

On the lighter side, Sears and his associates recognized that the noise of two billiard balls hitting each other is not from the vibration of the balls themselves, but rather has aerodynamic origin. It was easy to show that the lowest frequency of vibration of a billiard ball was ultrasonic, and thus could not be heard. The noise is actually generated in the surrounding fluid by the sudden deceleration and acceleration of the ball. They predicted the acoustic waveform and then verified it by a simple experiment using colliding steel balls. They were, of course, correct.

While Bill was working on acoustics and unsteady separation, he became very interested in the problem of tunnel wall interference in wind tunnel testing at transonic speeds. At about this time (1973) he moved to The University of Arizona, where he has continued working on aerodynamics and has devoted much of his time to the development of his ''smart tunnels,'' tunnels which ''know'' how to minimize wall interference. Such facilities reduce or eliminate interference effects by a clever choice of adaptive adjustment of the wall properties themselves. For example, this is accomplished by controlling the flow, so as to ensure that two independent flow-disturbance quantities measured at an interface surface near the wind-tunnel walls are compatible with the same quantities as computed for interference-free outer flow beyond the interface. During the course of his work, he and his associates also developed a method for adjusting the effective free-stream vector in the wind tunnel so that the powered-lift vortex wake generated in testing vertical/short takeoff and landing aircraft (V/STOL) would lie entirely within the wind tunnel test section. Current wind tunnel testing procedures have been influenced by the adaptive wall concept in many ways. The synergism of experiment and theory that is inherent in the adaptive wall concept was a forerunner of the integration of simultaneous experiment and analysis that is being pursued today.

With his hundreds of intellectual offspring, one can say that Bill Sears has actually established a new way of approaching engineering problems. No doubt, he started at the right place and at the right time, yet it has been his unique dual strengths in abstract mathematical thinking and natural engineering intuition that have allowed him to show us the way in employing both elegant theory and insight to the solution of so many practical problems. His philosophy and approach, shared by his own mentor von Kármán, are seen to be strikingly justified today, when engineers actually design by methods including solutions of complex nonlinear differential equations. Surely, at the time when Bill started his career, many practicing engineers might have scoffed at such a suggestion.

Bill's papers are self-contained in the sense that we can always begin with him at the beginning, pay attention to his steps, logical, or mathematical, and come out with him just where he wanted us to go. If we or our successors should want to begin a study of, say, unsteady wing theory, aeroacoustics, magneto-hydrodynamics, or cascade interactions, we have Bill Sears' papers to read, so that we not only understand in which way to go, but also are ready to set out in a cheerful frame of mind.

Bill Sears' contributions have been recognized formally by a wide group of societies and associations who honored him with many invitations to deliver lectures, such as the Lanchester Memorial Lecture, Royal Aeronautical Society, London, 1973, and international awards, such as the Prandtl Ring, 1974, and the Von Kármán Medal of AGARD, 1977. He was named a Distinguished Alumnus of both The University of Minnesota and The California Institute of Technology. Bill is a Fellow of the American Academy of Arts and Sciences and was elected to the National Academy of Engineering in 1968, to the National Academy of Sciences in 1974, and to the Academia Nacional de Ingenieria de Mexico in 1977. He is a Fellow of the International Academy of Astronautics and an Honorary Fellow of both the American Institute of Aeronautics and Astronautics and The American Society of Mechanical Engineers.

Demetri Telionis and James McCune

This short editorial biography of Professor W. R. Sears was composed with the help of passages contributed by H. K. Cheng, John Erickson, Feri Farassat, Frank Moore, Ed Ressler, and S.-F. Shen. An earlier and more detailed biography, written by the late Nelson Kemp, which appeared in W. R. Sears's *Collected Works through 1973*, has also been an important added source of information.

Journal of Fluids Engineering Technical Forum

Aerospace Propulsion Technology— A Fertile Source of Issues in Basic Fluid Mechanics

by Frank E. Marble [1]

It is a defensible proposition that the advance of aerospace propulsion technology underlies the striking improvement in both performance and economy of commercial and military aerospace operations over the past fifty years. It is less well recognized that propulsion, as a result of the innovation that led to these advances, has introduced a large number of new, stimulating areas of inquiry in each of the basic disciplines of engineering science that form the basis of this technology. Of these, I believe that fluid mechanics and materials are the greatest benefactors. Here our interest is in the former and a few examples will clarify fluid mechanics indebtedness to the stimulation of propulsion technology.

Mixing Processes. The laminar or turbulent mixing between two streams of gas is an essential process of most propulsion systems; mixing of fuel injected into a combustor, mixing of core and fan air in a gas turbine and mixing of rocket exhaust with the ambient air are typical examples. These issues have not only provided powerful incentives in the fundamental studies of mixing layers, wakes, and other classical problems, but have stimulated the extension of these investigations to mixing between gases of different densities and to mixing between streams at high relative Mach numbers. Equally important, propulsion challenges have stimulated the investigation of innovative means to accelerate, or more generally to control, mixing processes with low loss.

Chemically Reacting Flows. Before the prominence of combustion problems in gas turbine and rocket motors, combustion research had little presence in the domain of fluid mechanics. The recognition, in the mid 1940's, that gas dynamic processes were dominant, or at least of great importance, in most of the technological combustion processes, revolutionized the studies of combustion and profoundly enriched the field of fluid mechanics.

The chemical reaction between two or more gases requires that these gases be mixed on the molecular scale, inasmuch as molecular interaction is essential to changes in molecular structure that constitute the combustion process. In many cases of technological interest, the diffusion processes leading to molecular mixing, rather than the chemical reaction rates, controlled by progress of combustion. As a consequence, the investigation of exothermic reactions in boundary layer-like regions became a "classical" problem in fluid mechanics. As usual, turbulent flows presented its unique difficulties. In gases the molecular mixing occurs only in the small wave-length of the spectrum where viscosity is dominant and hence the diffusion processes necessary for combustion are active. This feature has provided novel incentives for turbulence research and powerful challenges in the development of rational turbulence models and their computational implementation.

Aerodynamic Noise. It is fair to say that the technological issue of noise generated by propulsion systems transformed acoustics research from the comfortable realm of architectural acoustics into an exciting branch of contemporary fluid dynamics. Jet noise, fan and propeller noise, noise associated with the motion of nonuniform gases, each drew upon skills acquired in the disciplines of compressible flow and thereby immensely enriched fluid mechanics. The basic mechanisms and descriptions of turbulence generated noise, noise from rotating blade row interference, and combustion generated noise and other propulsion sources occupy important places in the spectrum of gas dynamic research.

Instrumentation and Computation. Immense advances in computational power and techniques and equally striking innovation in optical and non-invasive instrumentation have added new dimensions to research in fluid mechanics. To a considerable extent, propulsion technology is responsible for the urgency of non-invasive measurements and for setting the most exacting goals for computational fluid dynamics. As CFD and computer capacity continue to develop, we shall be able to cope rationally with flow fields in gas turbine engines—blade wake interaction, unsteady interaction of blade rows, blade tip leakage—for which detailed measurement is out of the question. In fact, without computational exploration we should not even be sure what to measure.

In combustion systems, reliable optical measuring techniques are gradually allowing resolution of questions that for generations were inaccessible due to poor time resolution and probe interference. Of equal importance they encourage experiments of very short time duration—shock tubes, pulsed combustion systems, blowdown turbomachinery experiments—thereby making these fields accessible to the modest budgets we associate with research in fluid mechanics.

Numerous other issues—particulate and droplet laden gases, resolution of nonequilibrium effects in hypersonic flow, ultra-

---

[1] Richard L. and Dorothy M. Hayman Professor Emeritus, Mechanical Engineering and Jet Propulsion, California Institute of Technology, Pasadena, CA.

rapid mixing for low-NOX combustors—raise issues that are both vital to propulsion technology and stimulating to basic fluid mechanics. A final and most significant general problem should be mentioned: fluid mechanics problems related to active control of propulsion systems. While most current efforts involve the control of stall and surge of compression systems and the control of combustion oscillations, a host of other areas of "Smart Engine" applications are on the horizon. The issue here is that most of these instability problems have a fluid mechanical origin and unless this mechanism is recognized and quantitatively understood, the control of its consequences becomes a more complicated, more energy consuming, and possibly an impossible task.

It is very appropriate for this contribution to appear in the issue commemorating Professor William Sears' 80th birthday because he is one of the researchers who first employed rational fluid mechanical modeling to practical problems in turbomachinery flows and in aeroacoustics.

Questions in Fluid Mechanics:

Flow Near Thermodynamic Critical Points

by M. M. Kilgo,[1] R. Greif,[1] and R. E. Russo[1]

In typical analyses of compressible flow, the fluid involved is assumed to be an ideal gas, possibly with variable properties. While this is generally acceptable for the external flows encountered in aerodynamic problems, in several processes of practical interest the fluid's behavior is decidedly non ideal. In particular, unusual behavior is seen for a fluid near a thermodynamic critical point. Flows of such fluids raise many problems of engineering interest for the process industries.

The description of the equilibrium behavior of systems very near a critical point has been the focus of much elegant work over the past several decades. Although critical points are found in many types of systems, this column focuses on the liquid-vapor critical point. This type of critical point has attracted significant attention since it was first reported by Andrews in 1869.

Many of the thermodynamic properties of a fluid near its liquid-vapor critical point either diverge or disappear as the critical point is approached. Of particular interest for flow situations, are the facts that such a fluid exhibits liquid-like densities, gas-like viscosities, and has vanishingly small surface tension and enthalpy of vaporization. Furthermore, the strength of solvents is dramatically increased near the critical point. The open questions in these flows involve the coupling of property variations with the flow conditions. These questions fall into three general categories: physicochemical, mechanical, and thermodynamic.

The physicochemical problems associated with the flow of supercritical fluids center around the manipulation of energy and mass transfer processes. For example, supercritical fluids (SCF) are widely used in extraction and chromatography systems because they show significantly enhanced performance as solvents. This effect is explained by a tendency of the solvent to cluster around solute molecules. As a saturated supercritical solvent expands, it rapidly precipitates the solute. In a flow system, such behavior would obviously be of interest. Consider the fact that quartz is soluble in water near its critical point: control of the precipitation could be important in any application where supercritical water is rapidly expanded. Recent work has shown an empirical ability to control particle size by varying the expansion conditions. Is the precipitation a homogeneous nucleation process? If precipitation is rapid, how is the flow field altered?

Even in the absence of solutes, interesting critical behavior can be observed. If the solvent is a mixture, the formation of a condensed phase will alter component concentrations in the fluid and thus change its critical point. What is the impact of this change on physical property variation?

The specific heat and the thermal conductivity follow a power law growth as the critical point is approached, and many of the more interesting applications of SCF take advantage of this fact. Supercritical water has been used as a reactor coolant, and supercritical hydrogen has been proposed as a coolant in aerospace applications. Very close to the critical point, however, the thermal diffusivity decreases, leading to a phenomenon known as "critical slowing down." Physically this is due to the growth of the correlation length scale, and the relatively small energy changes associated with large fluctuations. This phenomenon might be expected to reduce the impact of conduction, but recent observations indicate that an acoustic "piston effect" can lead to dramatically enhanced transport in a closed constant volume system. This effect is due to the expansion of the fluid in the thermal boundary layer. This expansion allows the rapid transport of energy across the volume. Can similar effects be observed in flow systems?

Equally interesting are the mechanical questions raised by the flow of SCF. It is possible to imagine a highly compressible, relatively slow flow. Density fluctuations of all length scales occur even for closed equilibrium SCF systems. If the system is open, how and where do shocks develop? Furthermore, the compressibility of supercritical fluids is so great that hydrostatic density changes on the order of ten percent over a height of 5 mm have been observed near the critical density. Since the density is a strong function of pressure, the pressure gradient driving an isothermal flow can cause significant density fluctuations. An almost limitless number of interesting design questions can be raised regarding thermal cycling and pressure recovery techniques. Is it possible to formulate a consistent design strategy, or will design of supercritical extraction and cooling systems remain largely phenomenological?

The thermodynamic problems associated with flowing supercritical fluids are extensions of the problems addressed for equilibrium fluids. Among the more interesting is determining the range of applicability of equations of state for the fluid. For example, the van der Waals (VDW) equation is known to be qualitatively and quantitatively incorrect very near the critical point. Several recent studies, however, have adopted the VDW equation of state with reasonable results. What is the magnitude of error associated with the use of various alternatives? Is the difficulty of working with a qualitatively "better" EOS justified?

Other thermodynamic questions arise because of the enhanced compressibility of supercritical fluids. For example, carbon dioxide—the most commonly used SCF—has a bulk viscosity which is three orders of magnitude greater than its

---

[1] Department of Mechanical Engineering and Lawrence Berkeley Laboratory, University of California, Berkeley, CA.

rapid mixing for low-NOX combustors—raise issues that are both vital to propulsion technology and stimulating to basic fluid mechanics. A final and most significant general problem should be mentioned: fluid mechanics problems related to active control of propulsion systems. While most current efforts involve the control of stall and surge of compression systems and the control of combustion oscillations, a host of other areas of "Smart Engine" applications are on the horizon. The issue here is that most of these instability problems have a fluid mechanical origin and unless this mechanism is recognized and quantitatively understood, the control of its consequences becomes a more complicated, more energy consuming, and possibly an impossible task.

It is very appropriate for this contribution to appear in the issue commemorating Professor William Sears' 80th birthday because he is one of the researchers who first employed rational fluid mechanical modeling to practical problems in turbomachinery flows and in aeroacoustics.

Questions in Fluid Mechanics:

Flow Near Thermodynamic Critical Points

by M. M. Kilgo,[1] R. Greif,[1] and R. E. Russo[1]

In typical analyses of compressible flow, the fluid involved is assumed to be an ideal gas, possibly with variable properties. While this is generally acceptable for the external flows encountered in aerodynamic problems, in several processes of practical interest the fluid's behavior is decidedly non ideal. In particular, unusual behavior is seen for a fluid near a thermodynamic critical point. Flows of such fluids raise many problems of engineering interest for the process industries.

The description of the equilibrium behavior of systems very near a critical point has been the focus of much elegant work over the past several decades. Although critical points are found in many types of systems, this column focuses on the liquid-vapor critical point. This type of critical point has attracted significant attention since it was first reported by Andrews in 1869.

Many of the thermodynamic properties of a fluid near its liquid-vapor critical point either diverge or disappear as the critical point is approached. Of particular interest for flow situations, are the facts that such a fluid exhibits liquid-like densities, gas-like viscosities, and has vanishingly small surface tension and enthalpy of vaporization. Furthermore, the strength of solvents is dramatically increased near the critical point. The open questions in these flows involve the coupling of property variations with the flow conditions. These questions fall into three general categories: physicochemical, mechanical, and thermodynamic.

The physicochemical problems associated with the flow of supercritical fluids center around the manipulation of energy and mass transfer processes. For example, supercritical fluids (SCF) are widely used in extraction and chromatography systems because they show significantly enhanced performance as solvents. This effect is explained by a tendency of the solvent to cluster around solute molecules. As a saturated supercritical solvent expands, it rapidly precipitates the solute. In a flow system, such behavior would obviously be of interest. Consider the fact that quartz is soluble in water near its critical point: control of the precipitation could be important in any application where supercritical water is rapidly expanded. Recent work has shown an empirical ability to control particle size by varying the expansion conditions. Is the precipitation a homogeneous nucleation process? If precipitation is rapid, how is the flow field altered?

Even in the absence of solutes, interesting critical behavior can be observed. If the solvent is a mixture, the formation of a condensed phase will alter component concentrations in the fluid and thus change its critical point. What is the impact of this change on physical property variation?

The specific heat and the thermal conductivity follow a power law growth as the critical point is approached, and many of the more interesting applications of SCF take advantage of this fact. Supercritical water has been used as a reactor coolant, and supercritical hydrogen has been proposed as a coolant in aerospace applications. Very close to the critical point, however, the thermal diffusivity decreases, leading to a phenomenon known as "critical slowing down." Physically this is due to the growth of the correlation length scale, and the relatively small energy changes associated with large fluctuations. This phenomenon might be expected to reduce the impact of conduction, but recent observations indicate that an acoustic "piston effect" can lead to dramatically enhanced transport in a closed constant volume system. This effect is due to the expansion of the fluid in the thermal boundary layer. This expansion allows the rapid transport of energy across the volume. Can similar effects be observed in flow systems?

Equally interesting are the mechanical questions raised by the flow of SCF. It is possible to imagine a highly compressible, relatively slow flow. Density fluctuations of all length scales occur even for closed equilibrium SCF systems. If the system is open, how and where do shocks develop? Furthermore, the compressibility of supercritical fluids is so great that hydrostatic density changes on the order of ten percent over a height of 5 mm have been observed near the critical density. Since the density is a strong function of pressure, the pressure gradient driving an isothermal flow can cause significant density fluctuations. An almost limitless number of interesting design questions can be raised regarding thermal cycling and pressure recovery techniques. Is it possible to formulate a consistent design strategy, or will design of supercritical extraction and cooling systems remain largely phenomenological?

The thermodynamic problems associated with flowing supercritical fluids are extensions of the problems addressed for equilibrium fluids. Among the more interesting is determining the range of applicability of equations of state for the fluid. For example, the van der Waals (VDW) equation is known to be qualitatively and quantitatively incorrect very near the critical point. Several recent studies, however, have adopted the VDW equation of state with reasonable results. What is the magnitude of error associated with the use of various alternatives? Is the difficulty of working with a qualitatively "better" EOS justified?

Other thermodynamic questions arise because of the enhanced compressibility of supercritical fluids. For example, carbon dioxide—the most commonly used SCF—has a bulk viscosity which is three orders of magnitude greater than its

---

[1] Department of Mechanical Engineering and Lawrence Berkeley Laboratory, University of California, Berkeley, CA.

dynamic viscosity. When CO_2 is flowing near its critical point, the dilatation may be large, and bulk viscosity terms can not automatically be dropped from the governing equations. Such a system may provide an experimentally feasible alternative to hypersonic boundary layers for observing the influence of bulk viscosity.

Significant progress has been made recently in describing the physics of systems near a critical point, but many questions of engineering interest remain unresolved. Because such systems can exhibit counterintuitive behavior, the resolution of these problems provides both intellectual challenges and the opportunity to develop systems of great practical value.

U.S. Technological Competitiveness: A Fluids Engineers' Viewpoint

Column 5—In Recapitulation of our Previous Editorials

by J. L. Dussoura[1]

The general topic of Competitiveness and what we as Fluids Engineers may contribute to restore the luster it seems to have lost in the U.S., have been examined by several concerned authors, through the editorial columns of the most recent issues of the *Journal of Fluids Engineering*.

The problem was addressed by first identifying certain perceived obstacles that seem to stand in the way of an effective transfer of technology from research or from analytically oriented groups to those more directly responsible for engineering our commercial products. The perceived obstacles assume various forms, but seem to have their roots equally firmly embedded in the individual cultures of the major sectors dedicated to engineering pursuits, be they of academic, industrial or government provenance. They often have to do with practices so long established that they have come to be assumed as having some sort of perpetual sanctity that cannot be questioned.

In an effort to get around these real or imagined obstacles, a number of suggestions and recommendations were advanced.

The suggestions that were advanced by the authors (chosen to represent all main engineering working sectors) did not by any means address all of the areas where disjoints or bottlenecks were felt to interfere with the transfer of technologies. But they addressed some important ones with ideas which have the portend to cut across some existing bureaucratic practices and in so doing lubricate the transfer processes considerably.

In particular, a cost-effective model based on simple, direct interactions between engineering faculty specialists and their counterparts from industry was proposed. It shows great promise for opening communication channels in a fashion that is time- and cost-effective as well as capable of providing the financial support for continuing academic research. It creates a setting in which an improved understanding of one another's technical challenges by practitioners from different cultures, yet having complementary skills. And it can break through the stereotype and the barriers of suspicions which were bred heretofore from a perception of mutually divergent motivations.

It was also suggested that technical societies like ASME assume a new function, that of serving as an intermediary between academe and industry for the purpose of brokering engineering transactions mutually beneficial to both parties. By necessity, these efforts would address only classes of technologies identified as "Basic" or as "Emerging", such as the needed conversion of some existing but obscure scientific principle into a more readily assimilated form or such as the breaking open of new fields of research. Consortia, workshops and technical exchange markets may thus well be set up, brokered by regional ASME chapters or at the national level. Such a role may well entail surveys and polls for technical needs and the maintenance of skills banks, the catalogue contents of which are set by industry and the products of which are delivered by research groups, consultants, educational institutions and even through sharing of industrial know-how.

Furthermore, the notion that our competitiveness may be improved through the creation of industry/government consortia having the object of developing products and processes right down to the commercial stage was also advanced. For this and other purposes, much can be found overseas, notwithstanding that much of this overseas technology originated in the U.S. A special point was made of the need for greater reciprocity of access, in effect calling for increased efforts on the part of the U.S. government and of U.S. industry and of educational institutions to disseminate as well as assimilate the information and publications generated offshore.

These and other ideas are to be reviewed and discussed with the membership in the context of a second panel on the subject of U.S. competitiveness during the 1993 WAM in New Orleans. This panel will also seek to give a voice to senior members of the Division as well as to selected individuals with experience, who have long been faced with this issue and who will serve as responders to the premises proposed by the editorial writers. Finally, as an epilogue, the overall interaction with the membership, written and verbal, will be summarized in the March issue of the *Journal of Fluids Engineering*.

It goes without saying that if sufficiently well-developed ideas can be generated, an ultimate objective of this entire initiative would be to submit an entry to the ASME National Agenda with the object of preparing a white paper on this subject. It should be seen as expressing not jut the views of the Fluids Engineers but equally well those of the entire mechanical engineering community. The participation from the readership of the *JFE* and the benefits of all the valued opinions from the membership are hereby solicited.

---

[1] Fluids Engineering Associates, 14 Clevelant Rod West R.D. 2, Princeton, N.J. 08540.

dynamic viscosity. When CO_2 is flowing near its critical point, the dilatation may be large, and bulk viscosity terms can not automatically be dropped from the governing equations. Such a system may provide an experimentally feasible alternative to hypersonic boundary layers for observing the influence of bulk viscosity.

Significant progress has been made recently in describing the physics of systems near a critical point, but many questions of engineering interest remain unresolved. Because such systems can exhibit counterintuitive behavior, the resolution of these problems provides both intellectual challenges and the opportunity to develop systems of great practical value.

U.S. Technological Competitiveness: A Fluids Engineers' Viewpoint

Column 5—In Recapitulation of our Previous Editorials

by J. L. Dussoura[1]

The general topic of Competitiveness and what we as Fluids Engineers may contribute to restore the luster it seems to have lost in the U.S., have been examined by several concerned authors, through the editorial columns of the most recent issues of the *Journal of Fluids Engineering*.

The problem was addressed by first identifying certain perceived obstacles that seem to stand in the way of an effective transfer of technology from research or from analytically oriented groups to those more directly responsible for engineering our commercial products. The perceived obstacles assume various forms, but seem to have their roots equally firmly embedded in the individual cultures of the major sectors dedicated to engineering pursuits, be they of academic, industrial or government provenance. They often have to do with practices so long established that they have come to be assumed as having some sort of perpetual sanctity that cannot be questioned.

In an effort to get around these real or imagined obstacles, a number of suggestions and recommendations were advanced.

The suggestions that were advanced by the authors (chosen to represent all main engineering working sectors) did not by any means address all of the areas where disjoints or bottlenecks were felt to interfere with the transfer of technologies. But they addressed some important ones with ideas which have the portend to cut across some existing bureaucratic practices and in so doing lubricate the transfer processes considerably.

In particular, a cost-effective model based on simple, direct interactions between engineering faculty specialists and their counterparts from industry was proposed. It shows great promise for opening communication channels in a fashion that is time- and cost-effective as well as capable of providing the financial support for continuing academic research. It creates a setting in which an improved understanding of one another's technical challenges by practitioners from different cultures, yet having complementary skills. And it can break through the stereotype and the barriers of suspicions which were bred heretofore from a perception of mutually divergent motivations.

It was also suggested that technical societies like ASME assume a new function, that of serving as an intermediary between academe and industry for the purpose of brokering engineering transactions mutually beneficial to both parties. By necessity, these efforts would address only classes of technologies identified as "Basic" or as "Emerging", such as the needed conversion of some existing but obscure scientific principle into a more readily assimilated form or such as the breaking open of new fields of research. Consortia, workshops and technical exchange markets may thus well be set up, brokered by regional ASME chapters or at the national level. Such a role may well entail surveys and polls for technical needs and the maintenance of skills banks, the catalogue contents of which are set by industry and the products of which are delivered by research groups, consultants, educational institutions and even through sharing of industrial know-how.

Furthermore, the notion that our competitiveness may be improved through the creation of industry/government consortia having the object of developing products and processes right down to the commercial stage was also advanced. For this and other purposes, much can be found overseas, notwithstanding that much of this overseas technology originated in the U.S. A special point was made of the need for greater reciprocity of access, in effect calling for increased efforts on the part of the U.S. government and of U.S. industry and of educational institutions to disseminate as well as assimilate the information and publications generated offshore.

These and other ideas are to be reviewed and discussed with the membership in the context of a second panel on the subject of U.S. competitiveness during the 1993 WAM in New Orleans. This panel will also seek to give a voice to senior members of the Division as well as to selected individuals with experience, who have long been faced with this issue and who will serve as responders to the premises proposed by the editorial writers. Finally, as an epilogue, the overall interaction with the membership, written and verbal, will be summarized in the March issue of the *Journal of Fluids Engineering*.

It goes without saying that if sufficiently well-developed ideas can be generated, an ultimate objective of this entire initiative would be to submit an entry to the ASME National Agenda with the object of preparing a white paper on this subject. It should be seen as expressing not jut the views of the Fluids Engineers but equally well those of the entire mechanical engineering community. The participation from the readership of the *JFE* and the benefits of all the valued opinions from the membership are hereby solicited.

---

[1] Fluids Engineering Associates, 14 Clevelant Rod West R.D. 2, Princeton, N.J. 08540.

J. E. McCune
Professor,
Department of Aeronautics and Astronautics,
Massachusetts Institute of Technology,
Cambridge, MA 02139

T. S. Tavares
NRC Air Force Materiel
Command Research Associate,
United States Air Force Wright Laboratory,
Wright-Patterson Air Force Base, OH

Perspective: Unsteady Wing Theory—The Kármán/Sears Legacy[1,2]

The aerodynamic analysis of wings and their vortex wakes is discussed from a perspective of its relation to the 1938 work of Kármán and Sears. The key concepts from this early paper on the analysis of airfoils in small amplitude unsteady motion are reviewed. These concepts are then used as a point of departure for developing techniques for calculating and interpreting the aerodynamic characteristics of both airfoils in large amplitude motion with deforming vortex wakes, and maneuvering low-aspect-ratio wings with leading-edge separation. Calculated examples are presented for this extended set of applications, and are compared to related analyses and experiments.

Introduction

This paper focuses on an important part of the heritage of Professor William R. Sears to the scientific and engineering community, a legacy to which even at this writing, on the occasion of his 80th birthday, he continues to contribute. Because this heritage is so far reaching, we are able to touch here only on a comparatively small slice of Bill's contributions; for that reason, we have chosen the area with which he began his extraordinary career—the theory of the unsteady aerodynamics of lifting wings. This happens also to be an area in which he shared his contributions particularly strongly with his own mentor, Professor Theodor von Kármán. This legacy, bequeathed not only to Sears' own students, but also to their students, and, over the fifty or more intervening years, to so many of his colleagues and friends, can only be briefly sketched in this paper, nor can we do it complete justice in one short article.

An earlier version of our present article was delivered in Cincinnati, Ohio in 1988, at the First National Fluid Dynamics Congress; it was dedicated at the time to Professor Sears in celebration of his (then) 75th birthday. That earlier version also appeared in the Proceedings of the Congress. Our current paper, although of the same title, has been extended and updated significantly, to include new results and more modern applications. These new results have been obtained not only for airfoils but also for slender wings (low aspect ratio deltas and the like) at high angles of attack and at high rates of maneuver. Nevertheless they rely heavily on the basic method introduced by Sears and von Kármán—i.e., on the "legacy" referred to in our title.

It is not our intention to attempt a more complete review of the subject of unsteady aerodynamics here; excellent review papers on unsteady wing theory and associated topics are already available (see, for example, Hitzel and Schmidt, (1984), Hoeijmakers (1988), McCroskey (1982), Sarpkaya (1979)). Rather, in this article, we attempt to portray, with examples, something of the flavor of Bill's creative influence, and to provide a perspective as to how it is that his original works continue to influence modern efforts.

In the late spring of 1988, during the year of the celebration of his 75th birthday, Prof. Sears was invited to give a seminar on unsteady wing theory at M.I.T. His lecture was attended by a standing-room only audience of several hundred colleagues and M.I.T. students. Sears' opening remarks for that seminar provide an excellent introduction to the topic: "The theory of wings in unsteady flow is a particularly fascinating area of fluid mechanics. It originated in Prandtl's school. In [this talk] we will recount some of its brighter aspects and also some of the remarkable confusion that grew up among people then working in the field. This part of aerodynamics is still an active one today and profits greatly nowadays from the advent of the high-speed computer."

As a student of Sears many years earlier, one of us (JEM) caught the sense of Bill's fascination with the subject and took furious notes in the wing theory course (in india ink, of all things). Perhaps the india ink was the right decision, though, because Bill never did publish those lectures, and as a result, the "indelible" notes have been passed along over the years to many a student and to many a colleague.

In discussing Sears' legacy to modern wing theory, we also

---

[1] The authors wish to dedicate this paper to Professor W. R. Sears, on the occasion of his 80th birthday, in gratitude for the inspiration, wisdom, and friendship he has offered both of us over two different generations. As students within the lineage of Prandtl, von Kármán, and Sears we feel especially privileged also to have known Bill Sears the man. We take this opportunity to renew our dedication to the practice and teaching of engineering and science in the manner Bill himself has loved so much and shared with so many over a remarkable lifetime.

[2] This work was supported in part by AFOSR Grant No. 86-157 and by AFOSR Grant No. 87-NA-249.

Contributed by the Fluids Engineering Division for publication in the JOURNAL OF FLUIDS ENGINEERING. Manuscript received by the Fluids Engineering Division May 7, 1993; revised manuscript received September 13, 1993. Associate Technical Editor: D. P. Telionis.

have the opportunity to touch on a part of that of Sears' teacher, Theodor von Kármán. A central event was the publication of a paper Kármán and Sears wrote together and published in 1938 (Kármán and Sears, 1938). Looking back now, the Kármán-Sears paper seems to have capped a great worldwide burst of effort, spanning more than a decade, by the aerodynamic community. But the obvious harmony of this paper is also symbolic of the close relationship that existed between these two men, student and teacher, over several decades of their professional and personal lives.

The principal subject of the original Kármán-Sears paper was, of course, unsteady airfoil theory; its importance at the time—in the burgeoning era of flight—seemed to be matched only by the difficulty of the task. Kármán and Sears themselves quoted a British author on the subject: "The general formulae we have now obtained are rather too complex to convey directly any idea of their physical significance." If this was indeed the case, Kármán and his student took it upon themselves to try to remedy the situation: They declared that in their treatment they wished "to use only the basic conceptions of the vortex theory familiar to the modern aeronautical engineer." (Kármán and Sears, 1938).

It can be said that their paper "capped" a great effort because if it was among the best and most helpful it was also among the latest chronologically in a substantial list of contributions. By that time, such pioneering efforts as those of Birnbaum, Wagner, Glauert, Küssner, Theodorsen, Jones, and others were also available in the literature. Wagner had laid the foundation of the eventual gust-response theory. Glauert and Theodorsen had provided extensive numerical tables determining oscillating airfoil response and the dreaded flutter phenomenon was beginning to be understood and mastered at last.

But, in the midst of all this, there was apparent controversy amongst the experts. Glauert was dead, the victim of a tragic accident, Wagner was doing other things, and Küssner had excellent and compelling experimental results and a theoretical interpretation of them which, however, seemed unconvincing.

So, in choosing to emphasize the physical interpretation of their results and to offer an alternative and innovative formulation of the basic theory, Kármán and Sears provided a major service and a lasting contribution. That legacy has endured these 55 years, and is the real subject of this paper.

The "Dissertation"—How it Began

We've heard this story so many times, we have to believe it's true. Professor Theodore von Kármán of Caltech called his Ph.D. candidate William R. Sears into his office one day in the mid-30's and said:

> ..."So! Bill! You want a dissertation? Here is a dissertation."...

Kármán had an idea, and he proceeded to entrust his young student with it. He also described to Bill his reasons for becoming more deeply involved in unsteady wing theory. As the story is told, one can sense the frustration that Kármán felt in not being able to reach a complete consensus on the subject with the "experts" in the field, including some of his former colleagues in Göttingen.

And so, a great project was launched. Through his thesis, through his subsequent joint paper with Kármán (Kármán and Sears, 1938) and through his later papers on the subject (for example, Sears, 1941), Sears himself became one of the experts and, as in so many other cases later on in his distinguished career, one of the true leaders in the field. In the process, Bill both criticized and profited from—and provided insight into—the works of Glauert (1929), Küssner (1936a and b), Theodorsen (1935), and Wagner (1925), among others. Later, he entrusted many of these same insights to his own students, much in the way Kármán had done.

1 Kelvin Impulse and the Wake Integrals. Virtually all of the material in this section is excerpted directly from the initial and fundamental contribution to the field by Kármán and Sears (1938). Despite their continued close association and friendship over a lifetime, this was to be the only paper these two authors were to publish together.

According to Sears, Kármán suggested at the same time he proposed the dissertation topic to Bill that they try to settle once and for all the confusion that seemed to exist regarding the lift and moment formulations for airfoils in unsteady motion. Sears tells us that it was Kármán who proposed the use of the concept of the impulse of vortex pairs, having recognized that the combination of the airfoil and its wake, with zero net time-dependent circulation, must comprise a system of such pairs.

A few years ago one of us commented to Professor Sears that perhaps he had "always been a teacher at heart," since in the Abstract of their famous paper he and Kármán describe part of their motivation as: "to make the airfoil theory of non-uniform motion more accessible to engineers by showing the physical significance . . . of the mathematical deductions, [of airfoil theory]."

In any case, Sears replied to that comment that he thought "it was probably more Kármán" than he. He recounts, for example, an exchange between Kármán and Theodorsen at a seminar they both attended. Theodorsen reportedly inquired of Kármán why he had thought it necessary to publish a paper on the same subject as that of Theodorsen's own NACA Report (Theodorsen, 1935). Kármán is said to have replied that "your (Theodorsen's) report was mostly about flutter," and he (Kármán) thought that some people might have difficulty in appreciating the other aerodynamic aspects of the problem. Theodorsen apparently retorted wryly: "And you think they will understand Kelvin impulse better?"

However that may be, the lift and moment formulations in these terms have turned out over the years to be vitally useful. In fact, as we show in the next sections, we have had to relearn that lesson once more in carrying out our corresponding nonlinear calculations and modern applications of unsteady wing theory.

In reviewing here the Kármán-Sears formulations of airfoil lift and moment per unit span, let us adopt, as they did, the linearizing approximation of a thin airfoil with a flat wake extending along the x-axis, thus ignoring wake deformation and roll-up, to that approximation. The y-component of impulse for the vortex-pair system is then[3]

$$I_y = -\rho_\infty \sum_i \Gamma_i x_i \tag{1.1}$$

on taking due care not to count pairs twice and recalling $\Sigma_i \Gamma_i = 0$ for a paired system. Here, Γ_i is the circulation of a given vortex located at x_i along x-axis. The corresponding lift acting on the system is $-dI_y/dt$ per unit span, or

$$L = +\rho_\infty \frac{d}{dt} \sum_i \Gamma_i x_i. \tag{1.2}$$

Correspondingly, and in the same approximation, Kármán and Sears show that the pitching moment about the origin is

$$M = +\frac{\rho_\infty}{2} \frac{d}{dt} \sum_i \Gamma_i x_i^2 \tag{1.3}$$

per unit span. By convention the moment is positive nose-down, i.e., counterclockwise.

Referring to Fig. 1 the sum in Eq. (1.1) can be recast in terms of integrals over the airfoil chord and the wake

---

[3] Here and throughout this paper we adjust the notation wherever necessary to include the right-hand rule convention for both the vorticity and the circulation. Kármán and Sears did not use this convention.

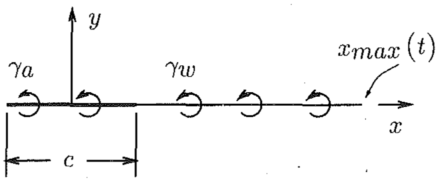

Fig. 1 Thin airfoil and flat wake system for linear theory

$$I_y = -\rho_\infty \int_{-\frac{c}{2}}^{\frac{c}{2}} x\gamma_a(x, t)dx - \rho_\infty \int_{+\frac{c}{2}}^{x_{\max}(t)} x\gamma_w(x, t)dx \quad (1.4)$$

whereas the net bound circulation on the airfoil is

$$\Gamma_a(t) = \int_{-\frac{c}{2}}^{\frac{c}{2}} \gamma_a(x, t)dx \quad (1.5)$$

and the net wake circulation is

$$\Gamma_w(t) = \int_{\frac{c}{2}}^{x_{\max}(t)} \gamma_w(x, t)dx. \quad (1.6)$$

In these expressions $\gamma_a(x, t)$ is the distributed bound vorticity on the airfoil while $\gamma_w(x, t)$ is the free vorticity in the wake and $x_{\max}(t)$ is the furthest downstream extent of the linear wake. Also, "c" is the airfoil chord and the origin of the coordinate system is at midchord.

Two key features of the dynamics of vorticity are then used. First, Kármán and Sears note that in the wake the free vorticity is convected by the surrounding stream; in the linearized limit this reduces to the statement

$$\gamma_w(x, t) \doteq \gamma_w\left(t - \frac{x}{U_\infty}\right) \quad (1.7)$$

so that

$$\frac{\partial \gamma_w}{\partial t} \doteq -U_\infty \frac{\partial \gamma_w}{\partial x}.$$

Further, by Kelvin's theorem for the conservation of circulation, one has

$$\Gamma_a(t) + \Gamma_w(t) = \Gamma(0) \quad (1.8)$$

where $\Gamma(0)$ is the initial stationary circulation, if any, existing before unsteady motion begins. Correspondingly,

$$\frac{d\Gamma_a}{dt} = -\frac{d\Gamma_w}{dt}. \quad (1.9)$$

The Kármán-Sears paper then demonstrates that it is useful to divide the airfoil bound vorticity, γ_a, and its circulation, Γ_a, into two parts with different physical meanings. The first part, denoted by γ_0 and Γ_0, comprises the response of the airfoil to the boundary conditions associated with the imposed motion that would arise *if there were no wake*. γ_0 is obtained from the theory of steady airfoil motion as if, absent the wake, the instantaneous boundary conditions were to persist forever; Γ_0 is specified by the Kutta condition at the trailing edge under the same circumstances. Kármán and Sears refer to this response as "quasi-steady"; for specified airfoil motion $\gamma_0(x, t)$ and $\Gamma_0(t)$ can both be regarded as known.

The second part of the response, denoted by γ_1 and Γ_1, is unknown in advance and is associated with the effect of the wake: For example, additional bound vorticity is necessary at the airfoil to cancel the normal component of wake-induced velocity there. Kármán and Sears show how to determine γ_1 and demonstrate in particular that, whereas

$$\Gamma_1(t) \equiv \int_{-\frac{c}{2}}^{\frac{c}{2}} dx\gamma_1(x, t)dx,$$

the conservation laws require

$$\Gamma_1(t) = \int_{\frac{c}{2}}^{x_{\max}(t)} \gamma_w(x, t)\left(\sqrt{\frac{x+\frac{c}{2}}{x-\frac{c}{2}}} - 1\right)dx \quad (1.10)$$

if one is also to retain the trailing-edge Kutta condition (1938).

Since $\Gamma_a = \Gamma_0 + \Gamma_1$ and $\Gamma_w(t)$ is given by Eq. (1.6), comparison of Eq. (1.9) with Eq. (1.8) yields

$$\Gamma_0(t) - \Gamma(0) = -\int_{+\frac{c}{2}}^{x_{\max}} \gamma_w(x, t)\sqrt{\frac{x+\frac{c}{2}}{x-\frac{c}{2}}}\,dx \quad (1.11)$$

For specified unsteady motion and initial conditions the *lhs* of (1.11) is known (as stated above), and therefore an integral equation determining $\gamma_w(x, t)$ in the wake results. Nowadays this equation is known as the (linearized) "Wagner integral equation" (Wagner, 1925). It has been extended to the nonlinear regime in a recent work by McCune, Lam and Scott, which is partly described in the next section (1990). Also, a similar set of two (2) such integral equations arises in the theory of low aspect ratio wings with leading edge separation (Tavares and McCune, 1993). These recent results, illustrating some more modern applications of the "legacy", are discussed in Section 5.

With these fundamental results in hand the two authors proceeded to determine expressions for the airfoil lift and moment from Eqs. (1.2) and (1.3), recalling integral expressions such as (1.4)–(1.6) and (1.10) and (1.11), in particularly revealing form. They found, in their notation,

$$L(t) = L_0 + L_1 + L_2 \quad (1.12)$$

and

$$M(t) = M_0 + M_1 + M_2, \quad (1.13)$$

where in each case each term has a specific physical meaning, described below.

For example, "L_1" and "M_1" are expressed formally by

$$L_1(t) = +\rho_\infty \frac{d}{dt}\int_{-\frac{c}{2}}^{\frac{c}{2}} x\gamma_0(x, t)dx \quad (1.14)$$

and

$$M_1(t) = +\frac{\rho_\infty}{2}\frac{d}{dt}\int_{-\frac{c}{2}}^{\frac{c}{2}}\left[x^2 - \frac{c^2}{8}\right]\gamma_0(x, t)dx \quad (1.15)$$

and are called the "apparent mass contributions" to the lift and moment, respectively, vanishing for steady flow. As explained by Kármán and Sears, $L_1(t)$, for example, is the contribution to the lift which would occur in unsteady motion even if the airfoil *failed to develop any circulation*. Thus, $L_1(t)$ is understood as the lift due to the inertial reaction of the fluid surrounding the airfoil.

$L_0(t)$ and $M_0(t)$, on the other hand, are the lift and moment that would occur according to the stationary airfoil theory if neither the vortical wake nor the fluid inertia had any effect. These results correspond to *steady* airfoil theory applied as if the actual normal flow boundary conditions of the imposed motion were to be imposed instantaneously and retained as if they might last forever. The authors found

$$L_0(t) = -\rho_\infty U_\infty \Gamma_0(t) \tag{1.16}$$

and

$$M_0(t) = -\rho_0 U_\infty \int_{-\frac{c}{2}}^{\frac{c}{2}} x\gamma_0(x, t)dx. \tag{1.17}$$

Kármán and Sears call these terms the "quasi-steady" lift and moment. In the following sections, however, we prefer to call their nonlinear counterparts the "no-wake" terms since in the high-amplitude case very large unsteady contributions do occur both in L_0 and M_0 (as for example, in severe pitch or plunge), so the expression "quasi-steady" can be misleading.

Finally, $L_2(t)$ and $M_2(t)$ are the so-called "wake-induced" terms. The authors found, in the linear theory,

$$L_2(t) = -\rho_\infty \frac{U_\infty c}{2} \int_{\frac{c}{2}}^{x_{\max}} \frac{\gamma_w(x, t)dx}{\sqrt{x^2 - c^2/4}} \tag{1.18}$$

and

$$M_2(t) = -\left(\frac{c}{4}\right) L_2(t). \tag{1.19}$$

Kármán and Sears call $-L_2$ and $-M_2$ the lift and moment "deficiencies", respectively, in the sense that they represent the extent to which the wake prevents the airfoil from attaining immediately its eventual ("quasi-steady") response to a sudden change in imposed conditions, such as angle-of-attack for example.

The last of these remarkable results, Eq. (1.19), in effect says that following a sudden change the lift deficiency, as caused by wake "induction" effects, always *acts at the quarter-chord* of the airfoil in linear theory. Although this phenomenon was recognized and also shown experimentally by Küssner, its first correct analytic explanation appears to have been given in Kármán and Sears' treatment, published two years later (Küssner, 1936a and 1936b). In the following sections we will find that this particular result holds up remarkably well in the nonlinear case, even for very severe changes.

From these formulations one can note that several basic phenomena in unsteady airfoil response are described directly by "wake integrals" over $\gamma_w(x, t)$. These include the wake induction itself, the lift and moment deficiencies, and various formulations of net circulation, etc. Not least, the Wagner integral equation Eq. (1.11), which *determines* $\gamma_w(x, t)$, emerges as a key to the success of the whole analysis and is itself a wake integral.

In deriving results such as Eqs. (1.12)–(1.19) Kármán and Sears take advantage of the free-vorticity feature noted in Eq. (1.7). It is useful to note the corresponding property of the wake integrals themselves. For example, if we define the delayed time

$$\lambda \equiv t - \frac{x - \frac{c}{2}}{U_\infty} \tag{1.20}$$

for the linear case and note that the circulation element in the wake over the interval dx is $d\Gamma_w = +U_\infty \gamma_w dt$, the wake integrals then have the general property, since $\gamma_w(x, t) = \gamma_w(\lambda)$,

$$\begin{aligned} I_w(t) &= \int_{+\frac{c}{2}}^{x_{\max}(t)} \gamma_w(\lambda) A(x, t)dx \\ &= U_\infty \int_0^t \gamma_w(\lambda) A\left(U_\infty(t-\lambda) + \frac{c}{2}, t\right) d\lambda \\ &= \int_0^t \frac{d\Gamma_w}{d\lambda} A\left(U_\infty(t-\lambda) + \frac{c}{2}, t\right) d\lambda \end{aligned} \tag{1.21}$$

We shall see that this feature of the wake integrals also holds up in the case of large-amplitude motion, provided the characteristic variable, λ, is generalized to allow for the actual nonlinear convection of the wake (McCune et al., 1990; Tavares and McCune, 1993) (see Sections 2 and 3).

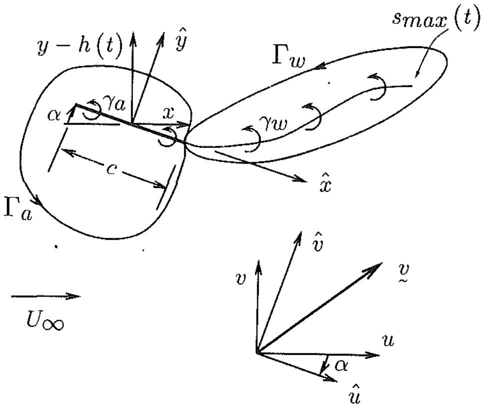

Fig. 2 Airfoil and wake for the nonlinear case

2 Nonlinear Version—Half a Century Later. It turns out that a surprisingly large part of the classical linear analysis can be carried over into the nonlinear regime, even as applied to wings in extreme or severe maneuver (McCune et al., 1990). In the following sections brief accounts are provided of recent work showing lift and moment formulations describing airfoil and slender wing responses to large and rapid imposed motions. In particular, taking our lead from Kármán and Sears, we attempt to illustrate the advantages of expressing key quantities in terms of wake integrals so as to make contact with the Kelvin impulse version of the linear theory such as described in our above review of their work.

An alternative method of calculating loading, lift, and moment proceeds along relatively standard lines by means of the unsteady Bernoulli equation. For example, the corresponding pressure loading across a plate 2-D airfoil is then

$$-\Delta p = \rho_\infty \left[\langle \hat{u}(\beta) \rangle \Delta \hat{u}(\beta) + \Delta \left(\frac{\partial \varphi}{\partial t} \right) \right]. \tag{2.1}$$

One then integrates this loading appropriately over the chord to obtain both lift and moment. (In this paper results are discussed only for a flat plate airfoil in large-amplitude pitch and plunge. Large angles of attack and pitch rate, as well as arbitrary plunging rates are allowed. Effects of thickness and built-in camber can be included readily, and yield very similar results (Lam, 1989).) Here, "β" is a parameter denoting location along the airfoil chord: $c/2 \cos \beta \equiv \hat{x}$ (see Fig. 2). Also, $\langle \hat{u} \rangle$ is the mean tangential velocity at the plate, while $\Delta \hat{u}$ is the corresponding jump.

Reduction of the resulting integrals requires careful attention to the fact that (2.1) is correct only in an inertial frame and that there is a difference between $\Delta(\partial\phi/\partial t)$ and $(\partial/\partial t)\Delta\phi$. One must also take advantage, as in classical treatments, of some convenient integrations by parts. In addition, one uses the fact that the mean tangential velocity at the flat plate airfoil is

$$\langle \hat{u} \rangle = U_\infty \cos \alpha(t) + \hat{u}_w(\beta, t) \tag{2.2}$$

while the airfoil bound vorticity is determined by the corresponding tangential velocity jump:

$$-\Delta \hat{u} \equiv \gamma_a(\beta, t) = \gamma_0(\beta, t) + \gamma_1(\beta, t). \tag{2.3}$$

In the last expression "γ_0" and "γ_1" have *exactly* the same meanings as in Section 1. "$\hat{u}_w(\beta, t)$" is the tangential component of the "wake-induced" velocity at the airfoil surface (see Fig. 2).

In these and subsequent relations the "angle variable" $\beta \equiv \cos^{-1}(2\hat{x}/c)$ has been introduced for convenience. Referring to

Fig. 2, β is in the range 0 to π on the upper surface of the airfoil, where $\sin\beta = +\sqrt{1-\frac{4\hat{x}^2}{c^2}}$, and is in the range π to 2π over the lower airfoil surface. In these terms, one finds

$$\gamma_0(\beta,\, t) = \frac{1-\cos\beta}{\sin\beta} \times \left(2U_\infty \sin\alpha(t) - \frac{2}{\pi} P \int_0^\pi \frac{\hat{v}_{\text{airfoil}}(\kappa,\, t)\,(1+\cos\kappa)}{\cos\kappa - \cos\beta}\, d\kappa\right) \tag{2.4}$$

and

$$\gamma_1(\beta,\, t) = \frac{2(1-\cos\beta)}{\pi\sin\beta} P \int_0^\pi \frac{(-\hat{v}_w(\kappa,\, t)\,(1+\cos\kappa))}{\cos\kappa - \cos\beta}\, d\kappa \tag{2.5}$$

where "κ" is a dummy integration variable along the chord, corresponding to β. In each of these expressions the Kutta condition at the airfoil trailing edge has been applied. The instantaneous boundary condition for the flat plate case leads to

$$\hat{v}_{\text{airfoil}}(\beta,\, t) = \dot{h}(t)\cos\alpha(t) - \hat{x}\dot{\alpha}(t) = \dot{h}\cos\alpha - \left(\frac{c}{2}\cos\beta\right)\dot{\alpha} \tag{2.6}$$

for use in Eq. (2.4). In fact, $\gamma_0(\beta, t)$ is easy to work out explicitly in this case using the Glauert integrals. The result is

$$\gamma_0 = \left(\frac{1-\cos\beta}{\sin\beta}\right)(2U_\infty\sin\alpha - 2\dot{h}\cos\alpha) - c\dot{\alpha}\sin\beta.$$

Moreover, since

$$\Gamma_0 = \int_{-\frac{c}{2}}^{\frac{c}{2}} \gamma_0 d\hat{x},$$

one finds

$$\Gamma_0 = -\pi c(U_\infty\sin\alpha - \dot{h}\cos\alpha) - \left(\frac{\pi c^2}{4}\right)\dot{\alpha}.$$

On the other hand, the quantity $\hat{v}_w(\beta, t)$ to be used in (2.5) is the normal component of the wake-induced velocity at the airfoil. This latter flow must be cancelled at the airfoil surface, giving rise to the additional bound vorticity, γ_1, just as in Section 1 (Kármán and Sears, 1938; Wagner, 1925). We will find that explicit "wake integrals" for $\hat{u}_w$ and $\hat{v}_w$ can be written out below (see Eq. (2.15)).

With these definitions and steps in hand, one is led to the following (intermediate) expressions for lift and moment:

$$L(t) = -\rho_\infty \int_{-\frac{c}{2}}^{\frac{c}{2}} \left(U_\infty + \dot{h}\tan\alpha + \frac{\hat{u}_w}{\cos\alpha}\right)(\gamma_0+\gamma_1)d\hat{x} - \frac{\rho_\infty}{\cos\alpha}\frac{d}{dt}\int_{-\frac{c}{2}}^{\frac{c}{2}}\left(\frac{c}{2}-\hat{x}\right)(\gamma_0+\gamma_1)d\hat{x} \tag{2.7}$$

and

$$M(t) = -\rho_\infty \int_{-\frac{c}{2}}^{\frac{c}{2}} (U_\infty\cos\alpha + \dot{h}\sin\alpha + \hat{u}_w)(\gamma_0+\gamma_1)d\hat{x} - \frac{\rho_\infty}{2}\frac{d}{dt}\int_{-\frac{c}{2}}^{\frac{c}{2}}\left(\frac{c^2}{4}-\hat{x}^2\right)(\gamma_0+\gamma_1)d\hat{x}. \tag{2.8}$$

Note that in Eq. (2.7) the lift has been adjusted to include the leading-edge force in the classical manner.

In this form the expressions for lift and moment look deceptively like their linear-theory counterparts (*before* reduction to their Kelvin impulse forms), almost as if all one had to do is replace U_∞, the free-stream speed, by ($U_\infty\cos\alpha + \dot{h}\sin\alpha + \hat{u}_w$) in order to get the nonlinear contributions. But, in fact, there are some key nonlinear effects "disguised" within γ_1. To make these explicit one needs to express the corresponding wake-related quantities in terms of their appropriate wake-integrals. In so doing one is able to determine the nonlinear equivalents of the impulse formulations described by Kármán and Sears, and once again the results become easier to interpret (McCune et al., 1990).

The real problem with Eqs. (2.7) and (2.8), particularly for practical purposes of numerical evaluation, is that both expressions contain combinations of large first-order terms some of which *almost exactly cancel one another*. Reducing (2.7) and (2.8) by the appropriate use of wake integrals enables one to make these cancellations explicit and exact, leaving only small remainders to be calculated directly. The resulting advantages for numerical calculations are obvious.

To begin this reduction, let us consider the "γ_0" contribution in (2.7) only and note that these can be written

$$\Delta L_0(\text{due to } \gamma_0) = -\rho_\infty\bar{U}\Gamma_0 + \frac{\rho_\infty}{\cos\alpha}\frac{d}{dt}\int_{-\frac{c}{2}}^{\frac{c}{2}}\hat{x}\gamma_0(\hat{x},\, t)d\hat{x} - \frac{\rho_\infty}{\cos\alpha}\left(\frac{c}{2}\frac{d\Gamma_0}{dt}\right) + \tilde{L}_0(t), \tag{2.9}$$

where

$$\tilde{L}_0(t) \equiv \frac{\rho_\infty}{\cos\alpha}\int_{-\frac{c}{2}}^{\frac{c}{2}}\hat{u}_w(\hat{x},\, t)\gamma_0(\hat{x},\, t)d\hat{x} \tag{2.10}$$

and

$$\bar{U} \equiv U_\infty + \dot{h}\tan\alpha \tag{2.11}$$

$\tilde{L}_0(t)$ is an explicitly nonlinear term with no classical counterpart; in practice, however, it turns out not to be difficult to evaluate.

The first two terms in (2.9) correspond immediately to the classical results of Kármán and Sears (1938). The first term is modified from the linear theory "quasi-steady" result only by the additional plunging effect on $\bar{U}$ as written in (2.11). Let us refer to this term here as the "no wake" or as the "Joukowski no wake" term rather than calling it "quasi-steady" since in the nonlinear case the explicitly unsteady contributions are potentially quite large. The second term is precisely the apparent mass as discussed in Section 1. Thus, employing Kármán and Sears' notation:

$$\Delta L_0(\text{due to } \gamma_0) = L_0(t) + L_1(t) - \frac{\rho_\infty}{\cos\alpha}\left(\frac{c}{2}\frac{d\Gamma_0}{dt}\right) + \tilde{L}_0(t) \tag{2.12}$$

where L_0 and L_1 have their original meanings, Kármán and Sears (1938), and $\tilde{L}_0$ is an explicit nonlinear correction. The third term in ΔL_0 will precisely cancel out in the following, so we need not interpret its meaning here.

Following the same procedure for the γ_1-terms yields at the beginning

$$\Delta L_1(\text{due to } \gamma_1) = -\rho\bar{U}\Gamma_1(t) + \frac{\rho_\infty}{\cos\alpha}\frac{d}{dt}\int_{-\frac{c}{2}}^{\frac{c}{2}}\hat{x}\gamma_1(\hat{x},\, t)d\hat{x} - \frac{\rho_\infty}{\cos\alpha}\left(\frac{c}{2}\frac{d\Gamma_1}{dt}\right) + \tilde{L}_1(t), \tag{2.13}$$

where

$$\Gamma_1 \equiv \int_{-\frac{c}{2}}^{\frac{c}{2}} \gamma_1 d\hat{x}$$

and

$$\tilde{L}_1(t) = -\frac{\rho}{\cos\alpha} \int_{-\frac{c}{2}}^{\frac{c}{2}} \hat{u}_w(\hat{x}, t)\gamma_1(\hat{x}, t)d\hat{x} \qquad (2.14)$$

Again, $\tilde{L}_1(t)$ is explicitly nonlinear and has no classical equivalent. As it turns out, it is in (2.13) that most of the cancellations occur or are set up.

To find these, let us note that γ_1 depends on the wake induction at the airfoil, as in Eq. (2.5). In complex-variable notation one can express $\hat{u}_w$ and $\hat{v}_w$ at the airfoil surface in terms of a wake integral:

$$\hat{u}_w(\beta, t) - i\hat{v}_w(\beta, t) = \frac{1}{2\pi i} \int_0^{S_{\max}(t)} \gamma_w(s, t) \frac{1}{\hat{x} - \hat{z}_v} ds$$

$$= \frac{1}{2\pi i} \int_0^t \Gamma_w'(\bar{\lambda}) \frac{1}{\frac{c}{2}\cos\beta - \hat{z}_v(\bar{\lambda}, t)} d\bar{\lambda} \qquad (2.15)$$

In this relation "s" is the cumulative real-variable distance from the trailing edge measured along the distorted wake at any t, and $\hat{z}_v$ is the instantaneous complex location of the vortex element in the wake having real elemental circulation $d\Gamma_w = \gamma_w(s, t)ds$. One obtains "$\hat{z}_v$" from $\hat{z}_v = e^{i\alpha(t)}(x_v + iy_v)$ where x_v and y_v are the vortex element's coordinates in the inertial frame (see Fig. 2.) Let us defer for the moment discussion of the final expression in (2.15) except to say that it is the nonlinear equivalent of equations such as (1.21) and is associated with the actual free-convection properties of the wake (McCune et al., 1990; Tavares and McCune, 1993; McCune, 1987). In particular, $\bar{\lambda}$, is the nonlinear generalization of the "delayed time," λ, identified in Section 1. (See Section 3.)

Using the real part of Eq. (2.15) in Eq. (2.5) and then setting up the necessary integrals for the first two terms in (2.13), one finds in each case that two of the three integrations can be carried out exactly in terms of fundamental integrals, leaving only a wake integral remaining. The results are

$$\Gamma_1(t) = \mathrm{Re}\left(\int_0^t \Gamma_w'(\bar{\lambda})\left(\sqrt{\frac{\hat{z}_v + \frac{c}{2}}{\hat{z}_v - \frac{c}{2}}} - 1\right)dx\right) \qquad (2.16)$$

and

$$\int_{-\frac{c}{2}}^{\frac{c}{2}} \hat{x}\gamma_1(\hat{x}, t)d\hat{x} = \mathrm{Re}\left(\int_0^t \Gamma_w'(\bar{\lambda})\left(\sqrt{\hat{z}_v^2 - \frac{c^2}{4}} - \hat{z}_v\right)d\bar{\lambda}\right) \qquad (2.17)$$

where "Re" denotes "real part."[4] Equation (2.16) is the nonlinear equivalent of Eq. (1.10) and has similar consequences, as discussed below. In both of these expressions $\hat{z}_v \to c/2$ as $\bar{\lambda} \to t$, and $\Gamma'(\bar{\lambda}) = 0$ at $\bar{\lambda} = 0$ (see next Section).

To complete the reduction of (2.13) one takes the time derivative of (2.17) to obtain

$$\frac{\rho_\infty}{\cos\alpha}\frac{d}{dt}\int_{-\frac{c}{2}}^{\frac{c}{2}} \hat{x}\gamma_1 d\hat{x} = \frac{-\rho_\infty}{\cos\alpha}\left(\frac{c}{2}\frac{d\Gamma_w}{dt}\right)$$

$$+\frac{\rho_\infty}{\cos\alpha}\mathrm{Re}\left(\int_0^t \Gamma_w'(\lambda)\frac{\partial\hat{z}_v}{\partial t}\left(\sqrt{\frac{\hat{z}_v + \frac{c}{2}}{\hat{z}_v - \frac{c}{2}}} - 1 - \frac{\frac{c}{2}}{\sqrt{\hat{z}_v^2 - \frac{c^2}{4}}}\right)d\bar{\lambda}\right) \qquad (2.18)$$

where "$\partial\hat{z}_v/\partial t$" is to be taken at fixed $\bar{\lambda}$.

At this point, one sees the cancellations beginning to occur. For example, because of Kelvin's theorem, the leading term in (2.18) exactly cancels the sum of the two time derivatives occurring in (2.12) and (2.13). Also, because $\partial\hat{z}_v/\partial t$ in the wake is comparable with $\bar{U}$ and both reduce to "U_∞" in the linear limit, cancellation will occur in that limit with the $-\rho_\infty\bar{U}\Gamma_1$-term in (2.13) as well, by virtue of Eq. (2.16). Most importantly, one sees the *equivalent wake-induced lift "deficiency" function*, $-L_2(t)$, emerging almost in its classical form, Kármán and Sears (1938).

In fact, in its *equivalent nonlinear version* the lift-deficiency function appears as the last contribution from the bracket in (2.18):

$$L_2^{\text{equivalent}}(t) = \frac{-\rho_\infty}{\cos\alpha}\frac{c}{2}\mathrm{Re}\int_0^t \Gamma_w'(\bar{\lambda})\frac{\frac{\partial\hat{z}_v}{\partial t}}{\sqrt{\hat{z}_v^2 - \frac{c^2}{4}}}d\bar{\lambda} \qquad (2.19)$$

which is to be compared with Eq. (1.18).

Putting this all together, one has at last

$$L(t) = \Delta L_1 + \Delta L_o = L_o + L_1 + L_2 + \tilde{L}(t) \qquad (2.20)$$

where the first three terms have the same physical meaning and (virtually) the same form as their linear equivalents, as in Section 1. $\tilde{L}(t)$ is the *explicit nonlinear term*

$$\tilde{L}(t) = -\frac{\rho_\infty}{\cos\alpha}\int_{-\frac{c}{2}}^{\frac{c}{2}}(\gamma_0 + \gamma_1)\hat{u}_w d\hat{x}$$

$$+\frac{\rho_\infty}{\cos\alpha}\mathrm{Re}\left(\int_0^t \Gamma_W'(\bar{\lambda})\left(\frac{\partial\hat{z}_v}{\partial t} - \bar{U}\cos\alpha\right)\right.$$

$$\left.\times\left(\sqrt{\frac{\hat{z}_v + \frac{c}{2}}{\hat{z}_v - \frac{c}{2}}} - 1\right)d\bar{\lambda}\right), \qquad (2.21)$$

and vanishes by inspection in the linear limit.

Collecting, one has

$$L_0(t) = -\rho_\infty\bar{U}\Gamma_0(t)$$

$$L_1(t) = \frac{\rho_\infty}{\cos\alpha}\frac{d}{dt}\int_{-\frac{c}{2}}^{\frac{c}{2}}\hat{x}\gamma_0(\hat{x}, t)d\hat{x}$$

and

$$L_2(t) = -\frac{\rho_\infty}{\cos\alpha}\frac{c}{2}\mathrm{Re}\int_0^t \Gamma_w'(\bar{\lambda})\frac{\frac{\partial\hat{z}_v}{\partial t}}{\sqrt{\hat{z}_v^2 - \frac{c^2}{4}}}d\bar{\lambda}$$

---

[4] In developing these expressions (McCune et al., 1990; Scott, 1987) one uses the fundamental integral

$$\int_0^\pi \frac{d\theta}{\cos\theta + a} = \frac{\pi}{\sqrt{a^2 - 1}}$$

where in our case "a" is complex and $= -2\hat{z}_v/c$. Thus, for our present purposes the main mathematical complication introduced by the nonlinear distortion of the wake is the need to keep track of the correct branch of the complex square root.

Repeating the above analysis for the moment gives in a similar fashion, we find

$$M(t)=M_0(t)+M_1(t)+M_2(t)+\tilde{M}(t) \tag{2.22}$$

where

$$M_0(t)=-\rho_\infty \overline{U}\cos\alpha \int_{-\frac{c}{2}}^{\frac{c}{2}} \hat{x}\gamma_0(\hat{x},t)d\hat{x}$$

$$M_1(t)=+\frac{\rho_\infty}{2}\frac{d}{dt}\int_{-\frac{c}{2}}^{\frac{c}{2}} \gamma_0(\hat{x},t)\left(\hat{x}^2-\frac{c^2}{8}\right)d\hat{x},$$

and

$$M_2(t)=-\frac{c}{4}L_2(t).$$

The explicit nonlinear moment, $\tilde{M}(t)$, is

$$\tilde{M}(t)=-\rho_\infty \int_{-\frac{c}{2}}^{\frac{c}{2}} \hat{x}(\gamma_0+\gamma_1)\hat{u}_W d\hat{x}$$
$$+\rho_\infty \mathrm{Re}\left(\int_0^t \Gamma'_W(\bar{\lambda})\left(\frac{\partial \hat{z}_\nu}{\partial t}-\overline{U}\cos\alpha\right)\left(\sqrt{\hat{z}_\nu^2-\frac{c^2}{4}}-\hat{z}_\nu\right)d\bar{\lambda}\right) \tag{2.23}$$

It is remarkable that in the nonlinear case M_0 and M_1 are still entirely classical in form and that $M_2(t)$, in its equivalent nonlinear version, *retains the property that L_2 acts precisely through the quarter chord*, McCune et al. (1990).

Returning to Eq. (2.16), one notes that it implies the existence of the nonlinear equivalent of Eq. (1.11). In fact, combined with the Kelvin theorem, Eq. (1.9), it leads to the result

$$\Gamma_0(t)-\Gamma(0)=-\mathrm{Re}\int_0^t \Gamma'_W(\bar{\lambda})\sqrt{\frac{\hat{z}_\nu+\frac{c}{2}}{\hat{z}_\nu-\frac{c}{2}}}\,d\bar{\lambda} \tag{2.24}$$

where, as before, the left-hand side is known for specified imposed airfoil motion. In obtaining (2.24) one uses the fact that

$$\Gamma_W(t)=\int_0^t \Gamma'_W(\bar{\lambda})d\bar{\lambda} \tag{2.25}$$

is the instantaneous total circulation in the wake (see also the next section). In McCune, Lam, and Scott, Eq. (2.24) is referred to as the "*nonlinear Wagner equation*" (1990). In the time-stepping calculations reported in those works it is used to determine the additional vorticity entering the wake at each instant. The remaining wake-integrals contributing to the lift, moment, etc., are then evaluated and catalogued as the run proceeds, thus providing a rapid and convenient calculation of the complete nonlinear airfoil response.

3 Nonlinear Wake Convection. Since the flow is potential on either side of the wake, the wake can be characterized at any point along it by the jump in potential, $\Delta\varphi(s,t)$. Using the Bernoulli equation and requiring that there be no static pressure difference across the free wake leads to the restriction

$$\frac{\partial \Delta\varphi}{\partial t}+\langle \nu\rangle\cdot\nabla\Delta\varphi=0 \tag{3.1}$$

where $\langle \nu\rangle$ is the mean flow velocity vector at the wake, $1/2(\nu^+ + \nu^-)$.

A fundamental, or "characteristic," solution of this equation is the shifted time

$$\bar{\lambda}=t-\bar{\tau}(s,t) \tag{3.2}$$

where $\bar{\tau}$ is the Eulerian drift time for a fluid element within the wake (Lamb, 1945). $\bar{\tau}$ satisfies

$$\frac{\partial\bar{\tau}}{\partial t}+\langle\nu\rangle\cdot\nabla\bar{\tau}=1 \tag{3.3}$$

and represents the time it has taken the fluid element currently at a given location to get there starting from some specified upstream point. For uniform steady motion at U_∞ one has, for example,

$$\bar{\tau}\doteq\frac{x-\text{const.}}{U_\infty},$$

which corresponds to the linearized result in Eq. (1.20). For nonlinear time-stepping calculations on a computer $\bar{\tau}$ is a particularly convenient variable because the drift-time field is generated automatically during the run. $\bar{\lambda}$ in Eq. (3.2) is thus the nonlinear analogue of the quantity in (1.20).

Using this concept one concludes that

$$\Delta\varphi(s,t)=\Delta\varphi(t-\bar{\tau})=\Delta\varphi(\bar{\lambda}) \tag{3.4}$$

is the general solution of Eq. (3.1). But the variation of circulation along the wake at any instant is

$$d\Gamma_w=-d\Delta\varphi$$

so it is also true that

$$d\Gamma_w=d\Gamma_w(\bar{\lambda})\equiv d\bar{\lambda}\Gamma'(\bar{\lambda}). \tag{3.5}$$

In the treatments used in our recent studies, $\bar{\tau}$ is measured from the moment of departing the airfoil trailing edge. In that case one sees that $\bar{\lambda} = t$ (the current time) for a fluid element just entering the wake, while $\bar{\lambda} = 0$ for the element at the furthest reaches of the wake downstream (or rolled-up into its "core"). $\bar{\lambda}$ is a continuous *monotonic* variable along the wake (no matter how deformed or rolled-up the wake may be) and is a conserved quantity during convection. In effect, $\bar{\lambda}$ acts like a "label" for each fluid element in the wake system.

A general wake integral of the form

$$I_W(t)=\int_0^{S_{\max}(t)} \gamma_W(s,t)A(s,t)ds$$

can then be written

$$I_w(t)=\int_0^t \Gamma'(\bar{\lambda})\hat{A}(\bar{\lambda},t)d\bar{\lambda} \tag{3.6}$$

thus providing the nonlinear equivalent of Eq. (1.21). Note in particular that

$$\frac{dI_w}{dt}=\Gamma'(t)\hat{A}(t,t)+\int_0^t \Gamma'(\bar{\lambda})\left.\frac{\partial\hat{A}}{\partial t}\right|_{\text{fixed }\bar{\lambda}} d\bar{\lambda} \tag{3.7}$$

since $\Gamma'(0) = 0$. In fact, one sees that the time derivative at "fixed $\bar{\lambda}$" is the same as a time derivative as *seen by a given fluid element*, i.e., it is identical with the usual convective derivative of fluid mechanics. Further details of this approach to nonlinear wake convection properties are available in the references previously cited, and in Scott (1987).

Figures 3 and 4 show a few samples of "snapshots" of computer-generated wakes. For example, Fig. 3 is a view taken at a fixed time, t, after 20 chord lengths of motion of the wake behind an airfoil oscillating in plunge at moderate amplitude and at a reduced frequency $\omega c/2U_\infty$ = .9. Figure 4 depicts the wake rolling up behind an airfoil following one of the "completed" maneuvers discussed in McCune et al. (1990). The numerical resolution of the roll-up regions in the two examples can be improved by reducing the time step used, down to a limit involving the effective "core size" of the discrete vortices

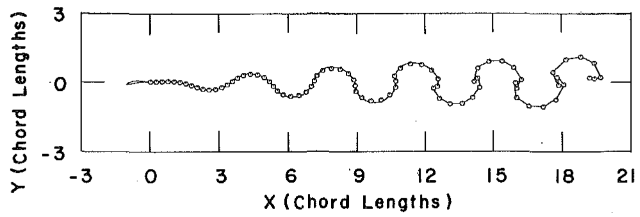

Fig. 3 **Wake behind an airfoil oscillating at moderate amplitude and at $\omega c/2U_\infty$ = .9**

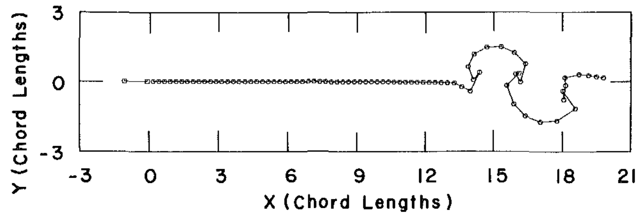

Fig. 4 ***Airfoil wake after a full-sinusoid "completed maneuver." Configuration 20 chord lengths after maneuver inception.***

as used in various numerical wake models available in the literature (Mook et al.; Pullin and Jacobs, 1986; Stremel, 1984; Katz and Weihs, 1978; Levin and Katz, 1981; Hoeijmakers, 1985). In our initial efforts, such as in Scott (1987), we also used such recommended techniques as "vortex splitting", with essentially the same success and the same limitations as described in the literature (Mook et al.; Pullin and Jacobs, 1986; Stremel, 1984; Katz and Weihs, 1978; Levin and Katz, 1981).

4 **Airfoil Response at Large Amplitude—Examples.** In McCune, et al., a number of examples of the application of our nonlinear analysis of the response of an airfoil to rapid and large-amplitude imposed motions were given (1990). For that work the decision was made to improve the effectiveness of the codes relative to Scott (1987), by basing them on the wake-integral formulations described previously. This turned out to be an essential step forward in obtaining more accurately the extensive information we had hoped for on nonlinear airfoil responses. Our first implementation of this approach continued to use the numerical model of the wake based on discrete vortices, together with the core-size and other "adjustments" referred to above. This code was called NLWAKE and was used to obtain all the results reported in McCune et al. (1990). For NLWAKE, once the "wake integral" approach was implemented, we were able to make quite successful comparisons with classical theory and, more importantly, show systematic improvements in those comparisons as numerical resolution was improved.

However, in a parallel work generalizing our study to the response of Joukowski airfoils, Lam developed a code, now called NLWJOU, which corresponds essentially to NLWAKE except for two new features. The first of these, as the name suggests, was the inclusion of thickness and camber for the host (Joukowski) airfoil. The second was the development of an (optional) explicit panel method which could be used in the airfoil wake as a replacement for the discrete vortices previously tried (Lam, 1989). This panel description is somewhat analogous to that used in Hoeijmakers except for the unique feature that we are able to determine the panel vorticity *explicitly* through the use of the nonlinear Wagner Equation (2.24), Lam (1989), rather than the implicit method employed by Hoeijmakers (1985). Lam's NLWJOU results, however, became available too late to be included in McCune et al. (1990); thus, we are reporting them here for the first time. As we show below, the corresponding agreement with classical theory (where such agreement should be expected) is quite satisfying and considerably better than we were able to achieve previously.

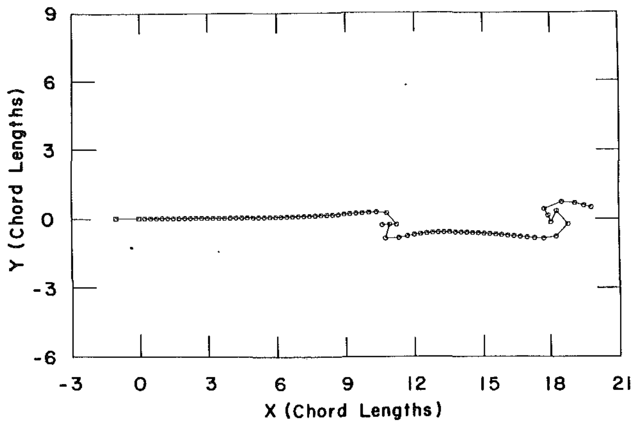

Fig. 5 **Resulting airfoil wake configuration following a "completed step maneuver" of Δα = ±10 deg. The step in angle-of-attack occurs at *t* = 5, the "un-step" at *t* = 37 (i.e., after 8 chord length travel). The wake configuration shown is a "snapshot" after 20 chord length of travel.**

In the following, a few examples of our nonlinear results are given so as to provide comparison with linearized theory.

Step Maneuvers

Figures 5 and 6(*a*, *b*) illustrate nonlinear airfoil behavior during and after a severe "completed maneuver". This maneuver corresponds to a sudden change in angle of attack followed by a return (an "up-step") to the initial incidence condition a short time later. Figure 5 shows the resulting wake as it appears 20 chord lengths after completion of the maneuver. For this example the jump in angle of attack, and the jump back, were ten (10) degrees.

Figures 6(*a*) and 6(*b*) show the airfoil response in terms of the time histories of lift and moment. The initial response is essentially the same as that due to an isolated step. In fact, the development of total lift proceeds initially almost exactly as in the linear theory, Wagner (1925), von Kármán (1938), McCune et al. (1990) with Wagner's "lift deficiency function" dominating the response, by far. In the figure, one can see the explicit nonlinear term $\tilde{L}$ of Eq. (2.21). One can see that it is short-lived both at the beginning of the maneuver and later on when it is re-excited by the "un-step." Thus, despite the severe distortions of the wake, the airfoil response is predominantly classical, except for the short transients shown.

After completion of the maneuver one sees that a substantial residual total lift, due to the remaining *net* upwash from the wake, is present. This decays away only slowly as the wake vorticity is swept downstream. During this decay there are measurable nonlinear effects on the equivalent wake-induced term (or nonlinear lift-deficiency function) which tend to delay somewhat the time after which the transient effect of the maneuver is no longer felt. However, these effects do not appear to be large, and in no case dominant.

The airfoil pitching-moment response, shown in Fig. 6(*b*) illustrates the surprising extent to which the lift-deficiency continues to act almost exactly through the 1/4-chord, even in the nonlinear case. Note that in this example this implies quite substantial residual pitching moment during the decay phase, for some time after the maneuver is completed.

Oscillating Airfoils

From the inception of our studies of nonlinear airfoil theory, beginning with Scott (1987), we have sought to establish conclusive "benchmark" comparisons with classical linear theory.

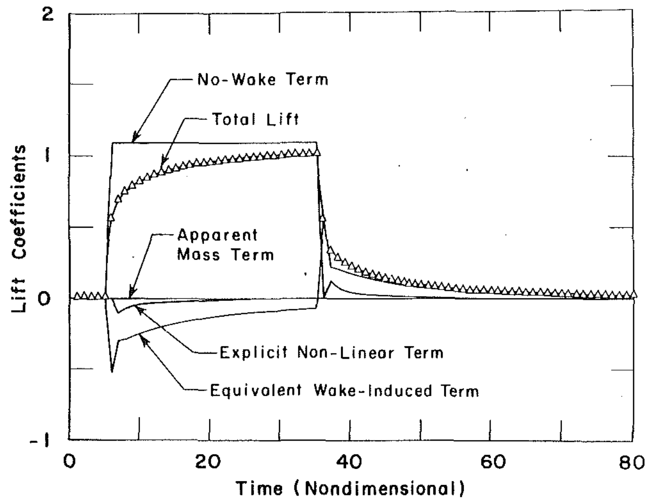

Fig. 6(*a*) Airfoil lift response to the completed step maneuver

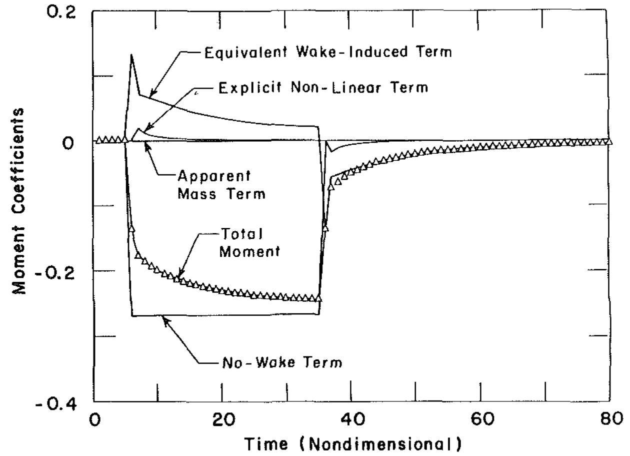

Fig. 6(*b*) Airfoil pitching moment response to the completed step

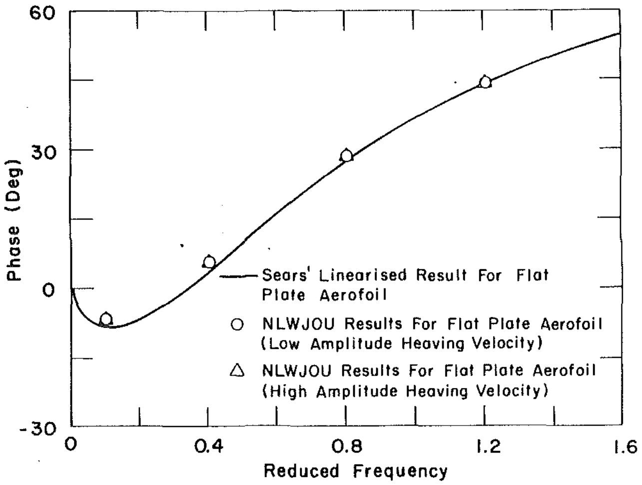

Fig. 7(*a*) Phase shift of airfoil lift versus input plunging motion for an oscillating airfoil. Comparison of nonlinear results with Kármán-Sears as a function of reduced frequency and time-step resolution. These improved nonlinear results were obtained with the code NLWJOU.

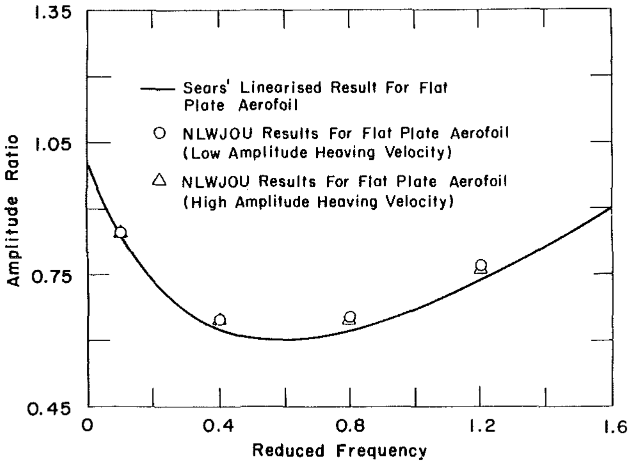

Fig. 7(*b*) Same comparison as in Fig. 7(*a*), but for lift amplitude ratio

The response to a step function, Wagner (1925), was one of these hoped-for benchmarks. We have been gratified by the results, both in our work shown in Figs. 6 and for the "pure" step discussed in McCune et al. (1990).

A more elusive example, however, has been the numerical determination of the phase response of an airfoil to continual repeated oscillation in plunge (heaving) or pitch. It was important here to make contact with Kármán and Sears' linear results (1938), as well as with those of Theodorsen (1935), at least at very low oscillation amplitudes, and to compare our results for phase shift and amplitude ratio with the classical answers of linearized theory.

However, until we reformulated the expressions for lift and moment in the "wake-integral" manner described in Section 2, we were faced with only limited success numerically. We found from the beginning that calculations of phase response are especially sensitive to those numerical errors which arise when one is trying to evaluate small differences between large quantities. Thus, until we decided to reformulate our codes in terms of the wake integrals as discussed above, our main numerical problems were of this nature, and these difficulties showed up primarily during comparisons with Sears and Theodorsen. With the wake-integral reformulation, on the other hand, the success of the comparisons became much improved. As one would hope, the accuracy based on this comparison seemed limited primarily (up to a limit) by the fineness of time resolution one could afford to use in calculating the actual wake evolution. In fact, using our work on NLWJOU, we were able to further improve our numerical wake calculations, leading to the much-improved results shown in Fig. 7 (Lam, 1989).

Figure 7(*a*) shows the calculated phase shifts for an airfoil oscillating in low-amplitude plunge over a substantial range of reduced frequencies, $\omega c/2U_\infty$, as compared with the Kármán-Sears results. Figure 7(*b*) illustrates the corresponding amplitude-ratio comparisons. In addition, Figs. 7(*a*) and 7(*b*) illustrate the effect on the results of increased amplitude. Quite similar results have been found for the pitching moment response, both in phase comparisons and for relative amplitudes. One sees not only that agreement with classical linear theory is excellent, but that the effect of larger amplitudes of oscillation on both the phase shift and amplitude ratio is surprisingly slight, at least for the flat plate comparisons with Sears' classical results. Further new results using Lam's NLWJOU, showing effects of thickness, camber, etc., as well as the use of the explicit panel technique mentioned above, are to be reported in a paper currently under preparation.

5 Results for Slender Wings With Leading Edge Separation. At first glance the treatment of the thin low aspect ratio wing with leading-edge vortex wakes may appear to be quite different from the 2-D unsteady airfoil problem. However, for wings of sufficiently low aspect ratio, one can appeal to the arguments of quasi-two dimensional Munk-Jones slender wing/

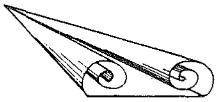

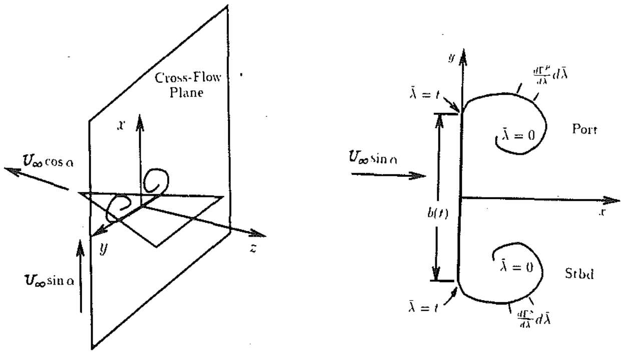

Fig. 8 Cross-flow observation plane and coordinate system for slender wing aerodynamics

body theory (Munk, 1924; Jones, 1946) to attempt an analogous approach. Once cast in the Munk-Jones framework, the basic aerodynamic problem to be solved for the slender wing becomes a close relative of the unsteady airfoil problem, and much useful contact can be made with the techniques pioneered by Kármán and Sears. In fact, effective wake integral formulas can indeed be developed, making use of analogous wake-convection ideas, Kelvin impulse, and classical vortex methods, to produce an efficient aerodynamic theory of slender wings with leading-edge separation, Tavares (1990). In this section, we describe some of these results in the context of the Kármán/Sears legacy.

Figure 8 shows the configuration resulting from the passing of a slender wing through an inertial (x, y, z) coordinate system. The orientation of the cross flow plane is chosen such that it is perpendicular to the surface of the wing. We include a cross flow in the direction of strength $U_\infty \sin\alpha$ from the left such that it "stops" the apparent plunge of the wing trace in the cross flow plane as associated with steady flight of an uncambered wing at angle of attack α. This fixes the wing in the plane $x = 0$, while the wing advances tangent to itself in the $-z$ direction at a rate $U_\infty \cos\alpha$. Viewed in the cross-flow plane, the passing of the wing is then seen as a wing trace of span-wise extent $b(t)$ which lies along the y-axis and which grows in time, while the intersection of the leading-edge vortex sheets and the cross-flow plane form two wake traces. The symbol t is used here in describing the time evolution of events in the cross plane history, and denotes the time since the apex of the wing pierced the cross flow observation plane. The addition of unsteady maneuver of the wing to this description requires accounting for two components of translation of the wing trace and one component of rotation within each cross-flow plane (McCune and Tavares, 1988; Tavares, 1990; Tavares and McCune, 1993).

Within this formulation, the mathematical treatment of the two wake traces is analogous to that of the single airfoil wake treated in previous sections. Once an element of circulation has been shed, it is convected in accordance with the inviscid Helmholtz relation (equivalent to Eq. (3.1)). This allows each element of the port and starboard wake traces to be tagged with the "delayed time" variable $\bar\lambda$, with $\bar\lambda$ varying from 0 at the far reaches of the wakes to t at the edges of the wing trace, as discussed in Section 3. The incremental circulation associated with an element of the port or starboard wake trace, $d\Gamma^P$, and $d\Gamma^S$, respectively, can be written as

$$d\Gamma^P = \frac{d\Gamma^P}{d\bar\lambda}\,d\bar\lambda \text{ and } d\Gamma^S = \frac{d\Gamma^S}{d\bar\lambda}\,d\bar\lambda.$$

Determining the strength of the vorticity on the wing trace is done in the same spirit as for the airfoil. The vorticity distribution on the wing trace is determined in two parts, denoted γ_0 and γ_1. The first part, γ_0, is taken to be the noncirculatory distribution of vorticity which would satisfy the condition of no flow through the wing trace in the absence of a leading-edge wake. For the steady-flight case at fixed α, the distribution γ_0 is given by

$$\gamma_0(y) = -2U_\infty \sin\alpha \frac{y}{\sqrt{\frac{b^2}{4} - y^2}}. \tag{5.1}$$

As in the airfoil problem on the other hand, γ_1 represents the additional vorticity needed to cancel the extra normal component of velocity which arises from wake induction.

If we impose the constraints of smooth flow at each leading edge (i.e., a "Kutta condition" at each edge of the wing trace) and combine these with Kelvin's theorem (which requires that the net circulation about the wing/wake trace system be zero), we obtain a *pair* of constraint equations which must be satisfied at all times in the evolution of the wake traces in order to maintain the required smooth edge flow. For the general cross-flow case, with arbitrary symmetry, this pair of equations plays a role analogous to the classical Wagner integral equation of 2-D airfoil theory as discussed previously (Eqs. (1.11), linearized, and (2.24), nonlinear).

In cases where no roll or sideslip is present, so that the wakes can be taken to be symmetric about the normal axis, Kelvin's theorem, with that symmetry, requires $\Gamma^P(\bar\lambda) = -\Gamma^S(\bar\lambda)$. Such an arrangement of the wake traces then satisfies one of the constraint equations identically, and only one equation remains. For this symmetrical case, and if the wing is also in steady flight, we find that the remaining constraint equation is given by:

$$-2U_\infty \sin\alpha = \frac{1}{\pi}\int_0^t \frac{d\Gamma^P}{d\bar\lambda}\,\mathrm{Re}\left[\frac{i}{\sqrt{(Z_\nu^P)^2 + \frac{b^2}{4}}}\right]d\bar\lambda + \frac{1}{\pi}\int_0^t \frac{d\Gamma^S}{d\bar\lambda}\,\mathrm{Re}\left[\frac{i}{\sqrt{(Z_\nu^S)^2 + \frac{b^2}{4}}}\right]d\bar\lambda \tag{5.2}$$

Here Z_ν^P and Z_ν^S are the complex locations of the vortex elements of the port and the starboard wake traces, respectively. As in the airfoil case they are functions of the shifted time $\bar\lambda$ at time t in the cross-plane history. This equation is analogous with the Wagner equation (2.24). In this case it determines the vorticity distribution in the wake trace(s), since $\Gamma^P = -\Gamma^S$. The general case of arbitrary motion and large amplitude maneuver has been discussed by Tavares (1990) and McCune and Tavares (1988). An example involving asymmetric motion is also included in our discussions, below.

The force and moment exerted on the wing trace can now be determined by calculating the time rate of change of the Kelvin Impulse of the paired vortex system which makes up the wing and wake traces, just as in the work of Kármán and Sears for their case. Thus, for the above example of a planar wing in steady flight at constant angle of attack α, the force on the wing trace at time t is given by:

$$F_{\mathrm{Normal}}(t) = \frac{d}{dt}\left\{p\pi\frac{b^2}{4}U_\infty \sin\alpha\right\}$$

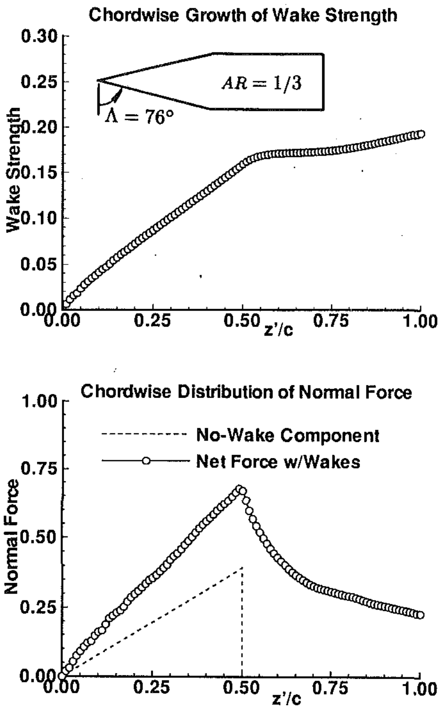

Fig. 9 Aerodynamic performance (loading distribution) of a clipped delta wing at constant angle-of-attack, α = 15 deg, and comparison with no-wake result

$$-\frac{d}{dt}\left\{p\int_0^t \frac{d\Gamma^P}{d\bar{\lambda}}\,\mathrm{Re}\left[i\sqrt{(Z_\nu^P)^2+\frac{b^2}{4}}\right]d\bar{\lambda}\right\}$$

$$-\frac{d}{dt}\left\{p\int_0^t \frac{d\Gamma^S}{d\bar{\lambda}}\,\mathrm{Re}\left[i\sqrt{(Z_\nu^S)^2+\frac{b^2}{4}}\right]d\bar{\lambda}\right\} \tag{5.3}$$

The first term in this equation, which is the force due to the change in the component of impulse associated with the vorticity distribution γ_0, is immediately recognizable as the time rate of change of apparent mass of a flat plate of span "b" (Jones, 1946). This is, of course, exactly the term which appears in Jones' theory for wings with no leading-edge separation. When integrated over the corresponding wing platform this term, by itself, yields the classical slender-wing expression for the lift coefficient, $C_L = (\pi/2)AR\alpha$, in the limit of small angle of attack. On the other hand, the second and third terms in Eq. (5.3) express, in wake integral form, the force component arising from the wakes caused by leading edge separation. Together, they account for all time changes in that part of Kelvin impulse which is associated with the presence of the wakes. These changes naturally include the convection of the vortex elements in the wakes and at the wing edges, and also any changes in the *wake-related* component of vorticity on the wing trace, γ_1.

As an example of a practical calculation carried out using this slender wing approach we consider a clipped delta wing of aspect ratio 1/3 in steady flight at 15 deg angle of attack. This planform is sketched in the upper portion of Fig. 9. In the corresponding unsteady cross-flow problem, the wing trace grows at a constant rate from a point at time $t = 0$, until such time as the wing has penetrated the cross-flow observation plane a distance equal to one-half of its root chord. At this time the "kink" or "clip" in the platform reaches the cross plane, and the span of the trace remains constant thereafter.

The plots in Fig. 9 show the chord-wise growth of wake strength (circulation) and chord-wise distribution of normal force for this case, as obtained from computations in the cross-flow plane. (The variable z'/c on the plots denotes the chordwise distance from the apex, normalized to the root chord.) Consistent with Jones' slender wing theory, that part of the lift associated with the growth of the wing trace itself (without the effect of leading-edge vortices) grows linearly until the kink in the planform is reached, and then drops abruptly to zero. On the other hand, the actual net force on the wing, with the effect of wakes included, does not drop to zero aft of this point. This is a result of the fact that the wakes must continue to evolve, and that they continue to grow in strength over the rear portion of the wing.

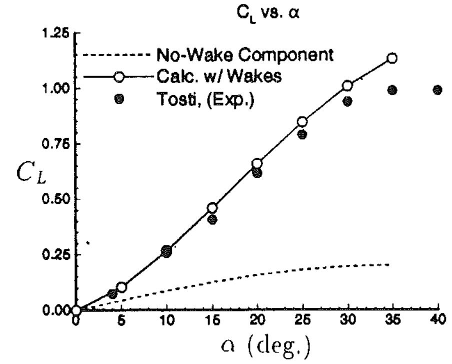

Fig. 10 Comparison for the same "clipped delta" of Fig. 9 of experimental results with predictions of slender wing theory, both without wake (classical) and with wake (present theory), for total lift (C_L) versus α

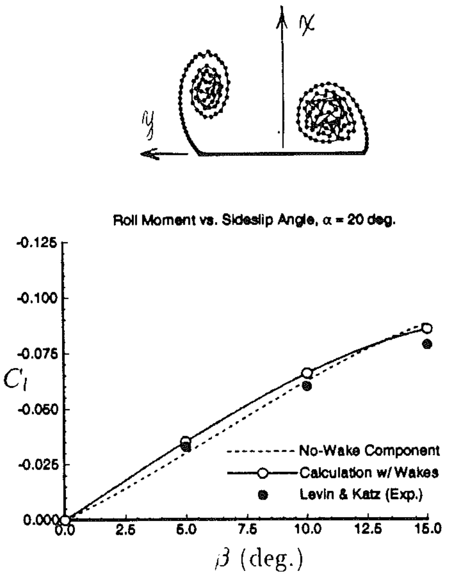

Fig. 11 Aerodynamic response of slender delta wing in side slip at angle of attack. Wake patterns and roll moments (predicted and experimental) are shown.

An example of the relative success of this slender wing method, based on comparison with experiment, is provided by Fig. 10. This plot compares our calculated lift curve for the above clipped delta of aspect ratio 1/3, to the corresponding wind tunnel measurements of Tosti (1947). The dotted line in the figure represents the calculated component of lift which would come about without the leading-edge wakes, Jones (1946). The complete results given in the figure clearly show that, at moderate-to-high angles of attack, the wake-related component of lift dominates for wings of this type. We have found this to be the case for a broad range of slender wing planforms (Tavares, 1990; Tavares and McCune, 1993).

The method also allows treatment of wings in asymmetric maneuver, as illustrated in Fig. 11. (For these calculations Eqs.

(5.2) and (5.3) no longer apply; they are replaced by the appropriate forms which account for non-symmetric wakes (Tavares, 1990; Tavares and McCune, 1993).) The top part of that figure shows the calculated wake patterns of a delta-wing with 80 deg leading-edge sweep, flying at 20 deg angle of attack and with 10 deg of sideslip. The plot in the lower part of the figure compares calculated roll moments for this wing at 20 deg angle of attack with those of the wind tunnel measurements of Levin and Katz over a range of sideslip angles (1984). The dotted line illustrates the component of roll moment which would occur in the absence of leading-edge wakes. (This is the roll moment one would calculate using the slender wing technique of Ribner (1947).) The full figure shows the results when the leading-edge wakes are present. One of the striking results to be noticed in this example is the remarkable adjustment of the wakes during sideslip, leading to the result that although the leading-edge vortices contribute a large fraction of the lift at this angle of attack (56 percent of the total lift at zero sideslip), they contribute only minimally to the rolling moment. As also seen in the figure, the comparison of our computed rolling moment with the experimental results is excellent for the entire range of sideslip angles explored.

The theory described here for the aerodynamics of the slender wing with its wakes also applies to the situation of (severe) dynamic maneuver. For example, the case of a wing undergoing impulsively started plunging motion, starting from a given steady flight condition, can be treated and has been discussed in previous works (see Tavares, 1990; Tavares and McCune, 1993).

For our present purposes, however, we close with a case not previously published which has applications to the phenomenon of "wing rock." This is a matter of particular interest in current studies of the unsteady aerodynamics of low aspect-ratio wings. Wind tunnel experiments, such as those reported by Shanks, for example, have shown that a significant loss of roll damping can occur during imposed rolling motion (1963). Examples of wind tunnel investigations of wing rock using free-to-roll delta wing models have been reported by Levin and Katz (1984), and Jun and Nelson (1988).

The example we consider here is that of a delta-wing, of 80 deg leading-edge sweep and at 30 deg angle of attack, which undergoes an imposed sinusoidal oscillation in roll of 30 deg amplitude. The reduced frequency, $\omega b_0/2U_\infty$, is 0.09 where ω denotes the angular frequency of motion.

Figure 12 shows plots of the calculated centroids of the port and starboard wake traces at the 50 and 100 percent root chord locations at selected roll angles during a cycle of the motion. The centroid locations are plotted in coordinates fixed in the moving wing trace, and are normalized to the local semi-span at the specified chordwise location. The roll angle ϕ is defined positive for the starboard wing down, in keeping with the conventions used in aircraft dynamics. For comparison, the corresponding wake centroid locations which would occur for steady flight at *fixed* roll angles, covering a range of ϕ from -30 deg to $+30$ deg, are shown by the dotted lines. Here, the symbol X indicates the static centroid locations at zero roll angle, for reference.

The static centroid locations reflect the expected conical self-similarity properties of the flow about delta-wings in steady flight when treated in the slender-wing limit. However, when the effects of the dynamic motion are added, this conical similarity property no longer applies. This departure from conicity in the case of dynamic maneuver is clearly seen in the figure. This appears in our calculations in terms of larger relative excursions of the centroids in the direction normal to the wing at the 100 percent root chord location.

It is important to note further that the direction of the "orbits" of the wake centroids about the static location at zero roll angle are the same as those seen for the vortex cores in the experiments of Jun and Nelson, for a similar delta planform undergoing wing rock at the same reduced frequency (1988).

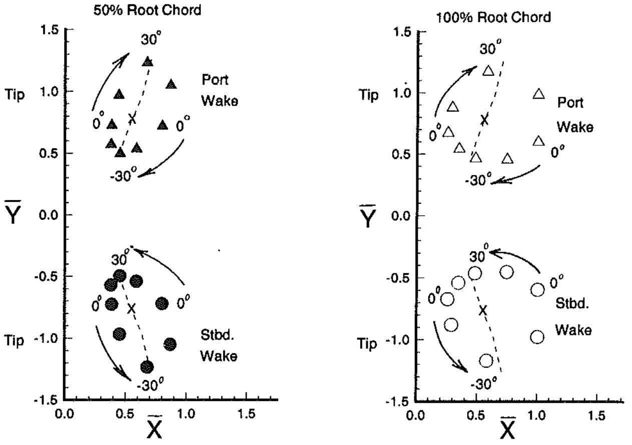

Fig. 12 Example of response of a slender delta undergoing imposed sinusoidal roll at 30 deg angle of attack. Conditions for wing rock are shown to be present at reduced frequency = 0.09. Wake orbits are shown for 50 percent and 100 percent chord.

These results, as shown in Fig. 12, suggest that the present theory, based on the model of a "slender wing plus its wakes," predicts the observed wing rock at least qualitatively; thus, we should be able to expect the results also to exhibit most, if not all, of the aerodynamic features observed. At this writing, we have not yet carried out in our codes the explicit slender wing/wake calculations of the roll moments for such examples. Even so, we believe such a study can provide further useful insight into the wing rock phenomenon, and provide thereby a further illustration of the influence of the Kármán-Sears "legacy." We are encouraged in this expectation by the fact that Arena and Nelson have recently shown that an even simpler model of the wing wakes can lead to an approximate prediction of wing rock as observed for slender wings (1992).

Conclusions

In this paper we have attempted to share a few memories and also some of the lessons learned as part of being a friend, colleague and student of Bill Sears and the tradition he began. It has seemed natural to put these in the context of Bill's relationship with his own teacher, von Kármán. At Cornell some of us had the privilege of meeting Kármán personally during his several visits there; he was always charming and kind to all of us. It's not by accident that everyone loves to tell stories about Kármán.

More than that, the two of them, Kármán and Sears, whether together or apart, always engendered an aura of excellence. The resulting atmosphere has created expectations which (looking back) now seem worthy of Prandtl's school, and those who were to follow. The Kármán and Sears paper that we have featured in this article, and the later works based upon it, are of course only a small part of the rich heritage the two have given us. But the spirit of their paper, in which a fresh look at a difficult problem was taken, and new and definitive insights were gained by applying fundamental and universally recognized principles, symbolizes the Kármán/Sears legacy, and can be an invaluable inspiration to all who aspire themselves to the enrichment of engineering and scientific knowledge.

References

Arena, A. S., and Nelson, R. C., 1992, "A Discrete Vortex Model for Predicting Wing Rock of Slender Wings," AIAA Paper No. AIAA-92-4497-CP, Presented at Conference on Atmospheric Aerodynamics, Hilton Head, S.C., July.

Glauert, H., 1929, "The Force and Moment on an Oscillating Airfoil," British A.R.C., R and M, No. 1242.

Hitzel, S. M., and Schmidt, W., 1984, "Slender Wings with Leading-Edge Separation: A Challenge for Panel Methods and Euler Solvers," *AIAA Journal of Aircraft*, Vol. 21, No. 10, Oct., pp. 751–759.

Hoeijmakers, H. W. M., 1985, "An Approximate Method for Computing Inviscid Vortex Wake Roll-Up," NLR, Amsterdam, The Netherlands, NLR TR85149U.

Hoeijmakers, H. W. M., 1988, "Computational Aerodynamics of Ordered Vortex Flows," NLR Rept. TR 88088 U, National Aerospace Laboratory, Amsterdam, The Netherlands.

Jones, R. T., 1946, "Properties of Low-Aspect-Ratio Pointed Wings Below and Above the Speed of Sound," NACA Report 835.

Jun, Y. W., and Nelson, R. C., 1988, "Leading-Edge Vortex Dynamics on a Slender Oscillating Wing," *AIAA Journal of Aircraft*, Vol. 25, No. 9, Sept., pp. 815–819.

von Kármán, T., and Sears, W. R., 1938, "Airfoil Theory for Non-Uniform Motion," *Journal of Aeronautical Sciences*, Vol. 5, 10, pp. 379–390.

Katz, J., and Weihs, D., 1978, "Behavior of Vortex Wakes from Oscillating Airfoils," *Journal of Aircraft*, Vol. 15, pp. 861–863.

Küssner, H. G., 1936, "Zusammenfassender Bericht über den instationären Auftriebe von Flügeln," *Luftfahrtforschung*, Bd. 13, p. 410.

Küssner, H. G., 1936, "Untersuchung der Bewegung einer Platte beim Eintritt in eine Strahlgrenze," Luftfahforschung, Bd. 13, p. 425.

Lam, C-M. G., 1989, "Nonlinear Wake Evolution of Joukowski Airfoils in Severe Maneuver," M.I.T. M.Sc. thesis, June.

Lamb, Sir Horace, 1945, *Hydrodynamics*, 6th Edition, Dover Publ., N.Y.

Levin, D., and Katz, J., 1981, "Vortex-Lattice Method for the Calculation of the Nonsteady Separated Flow over Delta Wings," *Journal of Aircraft*, Vol. 18, pp. 1032–1037.

Levin, D., and Katz, J., 1989, "Dynamic Load Measurements with Delta Wings Undergoing Self-Induced Roll Oscillations," *AIAA Journal of Aircraft*, Vol. 21, No. 1, Jan., pp. 30–36.

McCorskey, W. J., 1982, "Unsteady Airfoils," *Annual Review of Fluid Mechanics*, Vol. 14, pp. 285–311.

McCune, J. E., "Unsteady Aerodynamics of Wings in Severe Maneuver," Proceedings, AFOSR Workshop II on Unsteady Separated Flow, Colorado Springs, July.

McCune, J. E., and Tavares, T. S., 1988, "Unsteady 3D Aerodynamics of Slender Wings in Severe Maneuver," AIAA Paper No. AIAA 88-3544, *Proceedings*, AIAA 1st National Fluid Dynamics Congress, Cincinnati, Ohio, July.

McCune, J. E., Lam, G., and Scott, M. T., 1990, "Nonlinear Aerodynamics of Two-Dimensional Airfoils in Severe Maneuver," *AIAA Journal*, Vol. 28, pp. 385–393, Mar.

Mook, D. T., et al., 1981, "On the Numerical Simulation of the Unsteady Wake Behind an Airfoil," AIAA-87-0190.

Munk, M., 1924, "The Aerodynamic Forces on Airship Hulls," NACA Report 184.

Pullin, D. I., and Jacobs, P. A., 1986, "Inviscid Evolution of Stretched Vortex Arrays," *Journal of Fluid Mechanics*, Vol. 171, pp. 377–406.

Ribner, H. S., 1947, "The Stability of Low-Aspect-Ratio Triangular Wings at Subsonic and Supersonic Speeds," NACA TN 1423, July.

Sarpkaya, T., 1989, "Computational Methods with Vortices—The 1988 Freeman Scholar Lecture," ASME JOURNAL OF FLUIDS ENGINEERING, Vol. 111, Mar., pp. 5–52.

Scott, M. T., 1987, "Nonlinear Airfoil-Wake Interaction in Large Amplitude Unsteady Flow," M.S. thesis, Dept. of Aeronautics and Astronautics, Massachusetts Institute of Technology, Aug.

Sears, W. R., 1941, "Some Aspects of Non-Stationary Airfoil Theory and its Practical Application," *Journal of Aeronautical Sciences*, Vol. 8, 3, pp. 104–108.

Shanks, R. E., 1963, "Low-Subsonic Measurements of Static and Dynamic Stability Derivatives of Six Flat-Plate Wings Having Leading-Edge Sweep Angle of 70° to 84°," NASA TN D-1822, Apr.

Stremel, P. M., 1984, "A Method for Modeling Finite Core Vortices in Wak Flow Calculations," AIAA-84-0417, Jan.

Tavares, T. S., 1990, "Aerodynamics of Maneuvering Slender Wings with Leading-Edge Separation," Ph.D. thesis, M.I.T. Department of Aeronautics and Astronautics, Sept.

Tavares, T. S., and McCune, J. E., 1993, "Aerodynamics of Maneuvering Slender Wings with Leading-Edge Separation," *AIAA Journal*, Vol. 31, No. 6, June, pp. 977–986.

Theodorsen, T., 1935, "General Theory of Aerodynamic Instability and the Mechanism of Flutter," N.A.C.A. Tech. Rep. No. 490.

Tosti, L. P., 1947, "Low-Speed Static and Damping-in-Roll Characteristics of Some Swept and Unswept Low-Aspect-Ratio Wings," NACA TN 1468.

Wagner, H., 1925, "Über die Entstehung des dynamischen Auftriebes von Tragflügeln," *Zeitschr. f. Angew. Math. u. Mech.*, Bd. 5, p. 17.

Perspective—Aerodynamic Control of Combustion[1]

A. K. Oppenheim
Mechanical Engineering,
University of California,
Berkeley, CA 94720
Honorary Mem. ASME

To do useful work, the exothermic process of combustion should be carried out in an enclosure, as is typically the case with i.c. engines—the subject of this paper's particular concern. To meet the requirements of high efficiency and low pollutant production, this process should be executed at a relatively low temperature—a condition attainable by the use of lean air-fuel mixtures. For this purpose it has to be distributed in space upon multipoint initiation and kept away from the walls to minimize their detrimental effects. In principle, all this can be accomplished by a system referred to as fireball combustion that takes advantage of entrainment and spiral mixing associated with large scale vortex structures of jet plumes. As demonstrated in this paper, the success in such an endeavor depends crucially upon the utilization of the essential elements of classical aerodynamics: the properly distributed sources, expressed in terms of velocity divergences prescribed by the thermodynamic process of combustion and of the vorticity field generated by shear between the jets and the fluid into which they are injected.

Prologue

What aerodynamicist would not be lured by the prospect of employing his craft to control an inferno? Who but who, if it is not Bill Sears himself—a man who contributed so eminently to aerodynamics (vid. e.g., Sears, 1938, 1941, 1948, 1954, 1956)—that should be particularly appreciative of this viewpoint. Presented here is a prescription how this could be accomplished.

Combustion is the oldest technology of mankind. This is perhaps the main reason why it is so much taken for granted; so much so, in fact, that today it finds itself at a much lower level than the significantly younger technology of aeronautics. What is the rationale for this paradoxical state of affairs?

Right from the outset, in the pursuit of aeronautics, Wright brothers and their contemporaries realized that success in the execution and control of an aircraft must be based on a solid background of wind tunnel data and aerodynamics associated primarily with the lift and drag of an airfoil.

In contrast to this, if one examines critically the current state of combustion, one is bound to conclude that, as unbelievably, as it seems, the whole of its industry, occupying today by far the largest economic sector of life on our planet, is based largely on prejudice born out of the belief that, once the fuel is ignited, the rest is in the hands of God (!). Amazingly little attention has been paid so far to proper *execution* of the exothermic process of combustion, let alone its *control*. An aerodynamicist, as we are sure Bill will concur, could not overlook the importance of catering primarily to these two essential functions of the system. It is this topic then that forms the major subject of this paper.

Engines

Let us take a concrete example: the internal combustion engine. Here the consequences of constraints imposed by the walls of the enclosure, its essential ingredients, are immediately recognized as the factors of prime concern. The cylinder-piston enclosure is de facto a site of a manufacturing process where the raw stock is *fuel* and the *product*, fabricated by combustion, is *force* providing the torque for the power train.

Before proceeding any further, there are two questions one should answer: why bother and what can be done about it?

As to why, the reasons are, indeed, most compelling: protection of the environment whose decaying nature is the greatest foe faced by mankind today. In our age of hydrocarbon energy, the goal of advancing the technology of combustion is, indeed, imperative (Oppenheim, 1992a).

The response to the question *how* has been, in fact, implied by the title and in the introduction: disregard the prejudices escalated over the millennia of familiarity with fire, and set out to *foster the technology of controlled combustion.*

It is of interest to observe in this connection that, in contrast to the ancient roots of combustion technology, the concept of control, in a vein similar to controlled flight, is actually brand new—the technology of the future. According to the postulate put forth here, its development should follow in the footsteps of aeronautics.

The equivalent of *wind tunnel* is an *engine combustion simulator*—a device which, in its most elementary form, is a cyl-

---

[1] To Bill Sears—the superb perpetuator of the beauty of aeronautics in the true spirit of its classical founders Clark B. Millikan, his first master, and Theodore von Kármán, his teacher and later, his most famous student—with best wishes for many happy returns.

Contributed by the Fluids Engineering Division for publication in the JOURNAL OF FLUIDS ENGINEERING. Manuscript received by the Fluids Engineering Division April 16, 1993; revised manuscript received September 14, 1993. Associate Technical Editor: D. P. Telionis.

inder of constant volume fitted with transparent plates at both ends for an unobstructed optical insight in the axial direction by the use of Schlieren, interferometer, or laser-induced scattering or fluorescence techniques that are nowadays so readily available. Its raison d'être is based on the recognition that, in order to produce work, the exothermic process of combustion must take place *per force* in an enclosure, where the relatively small change in volume associated with piston motion exerts, in the course of this process, minor influence upon its progress, whereas in the analysis, as shown here, it can be taken into account without any difficulty.

This should be supported by *computational fluid mechanics* which, unlike the conventional approach in this field, should be carried out in a rational sequence of elementary steps, rather than in the form of an all-inclusive, numerical program that can be performed only by the use of a supercomputer, as is in vogue today. Technical aspects of this method of attack are described here.

Fireball

The major goal of engineering is optimization attained by minimizing losses. In an engine cylinder, if proper care is provided for the combustion process to be carried out to completion, the only source of losses is due to contact of the reacting medium with the walls.

A way to reduce these losses significantly is to execute the exothermic process of combustion in form of a fireball created in the midst of the combustion chamber to keep the reacting medium protected from the detrimental effects due to contact with the walls, while maintaining it at as low a temperature as possible—a condition achievable by the use of relatively lean air/fuel mixtures. This can be realized by exploiting the large scale vortex structures of turbulent plumes created by pulsed jets. An engine embodying this principle is the epitome of the so-called *Direct Injection Stratified Charge* (DISC) combustion system.

A forerunner of such engines was developed in the Soviet Union over a period of forty years of research studies directed by Nicholai Nicholaievich Semenov, the Director of the USSR Academy of Sciences Institute of Chemical Physics in Moscow, and the Laureate of the Nobel Prize received for founding the chemical chain reaction theory (Semenov 1944, 1958/59). Its engineering implementation became known as the LAG (Lavinaia Activatsia Gorenia, i.e., Avalanche Activated Combustion—a favorite expression of Semenov to describe the escalating effects of chain branching) engine (Gussak, 1976, 1978, 1983; Gussak, et al., 1976; Gussak and Turkish, 1977; Gussak, et al., 1979; Sokolik and Karpov, 1960), introduced into automobile market as a power plant for Volga cars in 1981. Technologically, it was an awkward system. A four-stroke, three-valve, divided chamber, stratified charge engine, resembling in construction the Honda CVCC, that was capable of operating without knock using an extremely low octane number gasoline, highly diluted with 100 percent excess air (!). Its specific weight in kg/kWhr was consequently prohibitively high.

Conceptually, in a significantly refined version of LAG, fireball combustion is achievable by a PCJ (Pulsed Combustion Jet) system (formerly referred to as PJC; vid. Oppenheim, 1988, 1991, 1992b, 1992c, 1992d; Oppenheim, et al., 1989; Maxson and Oppenheim, 1991; Maxson, et al., 1991; Hensinger, et al., 1992). Upon creating a lean fuel-air mixture within the cloud of a turbulent plume generated by direct injection using pulsed air blast atomizers, for best performance this system should be operated in a two-step mode: injection and combustion. In this case two opposed generators are used, each the size of a 14 mm spark plug, incorporating a 0.5 cm^3 cavity fitted with a conventional ignition gap and fed with rich air-fuel mixture of up to 100 percent excess fuel via a solenoid

Nomenclature

a = stoichiometric coefficient
c = slope of the locus of states on the Le Chatelier diagram; specific heat
C = molar concentration
E = energy
F = full load
h = specific enthalpy
I = total number of reactant species
J = total number of product species
k = c_P/c_R
K = total number of elementary steps
M = mass
p = pressure
P = products; p/p_i; part load
Q = exothermic energy; heat transfer
R = reactants; gas constant
Re = Reynolds number
S = temperature rise due to heat transfer from products
t = time
T = temperature
u = specific internal energy
$\mathbf{u}$ = velocity vector
v = specific volume
V = volume
w = pv
W = w/w_i
Wk = $\int pdV$
α = $(n_c - 1)/n_c$
β = exponent in expression for κ
δ = dilutant gas-fuel mass ratio
Δ = relaxation time
η = V/V_i
θ = crank angle in degrees from TDC
κ = Q_w/E_i
λ = $1/\phi$
μ = M/M_i; viscosity
ξ = vorticity vector
o = stoichiometric air-fuel mass ratio
ϕ = equivalence ratio
χ = v/v_i
ω = Wk/E_i

Subscripts

c = compression
e = expansion
f = final
h = enthalpy
hp = state of equilibrium at initial enthalpy and pressure
i = initial; chemical constituent of reactants
j = chemical constituent of products
k = elementary step
o = overall
p = constant pressure
P = products at equilibrium
r = reaction
R = reactants at frozen composition
t = thermal
u = internal energy
uv = state of equilibrium at initial internal energy and specific volume
v = specific volume
w = walls
ϵ = irrotational
λ = loss
ξ = rotational

Superscripts

I = total number of reactant species
J = total number of product species
K = total number of elementary steps
• = Newtonian symbol of a differential with respect to time

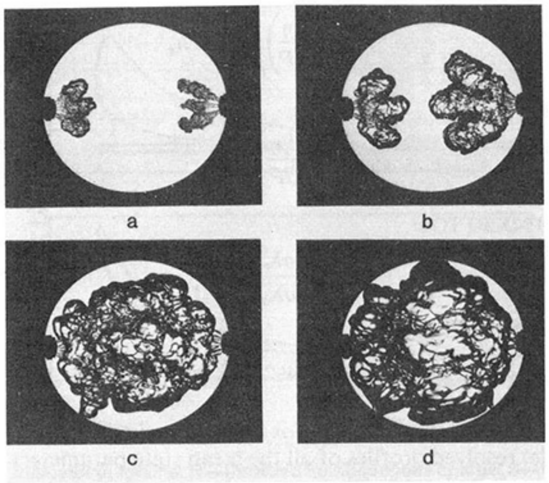

Fig. 1 Schlieren records of jet plumes produced by triple orifice opposed PJC generators. Propane-air mixture at 0.6 equivalence ratio, initially at a pressure of 5 bar and a temperature of 60°C, contained in a cylinder 8.26 cm in diameter and 5 cm wide between transparent end plates; jets generated by the use of 0.5 cm^3 cavities embodies in 14 mm plugs, fed with 1.5 equivalence ratio propane-air mixtures and ignited by conventional spark discharge close to the orifice cup. Orifice diameters: 1.44 mm; Duration of injection: 10 ms (*a*) 2.5 ms; (*b*) 5 ms; (*c*) 10 ms; (*d*) 15 ms after ignition

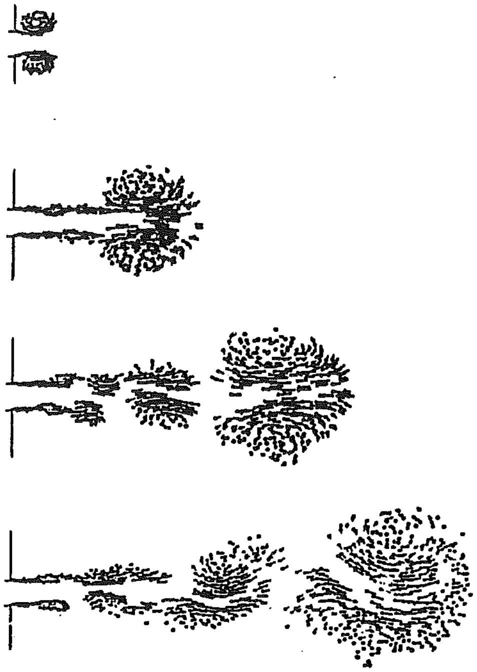

Fig. 2 Formation and structure of a turbulent jet plume. Velocity vector field in consecutive stages of its development determined by numerical solution of the Navier-Stokes equations evaluated by the random vortex method (Ghoniem, et al., 1982). Noted here, especially, should be the large scale vortex structures and the paths of entrainment they induce at their peripheries.

valve. In the two-step process, a turbulent plume of rich mixture is first formed and then, after a short delay to assure satisfactory entrainment, it is ignited by a secondary jet generated by spark-initiated combustion of the mixture residing in the plug's cavity.

The operating characteristics of pulsed jet combustion are illustrated by a sequence of Schlieren photographs in Fig. 1, while the mechanism of a turbulent jet plume is revealed in Fig. 2—a solution of the Navier-Stokes equations obtained by the random vortex method of Chorin (Chorin, 1973, 1978, 1989; Ghoniem, et al., 1982; Oppenheim, 1985; Ghoniem, et al., 1986). Clearly evident here are the paths of entrainment and the spiral mixing taking place in the large scale vortex structures. As it appears there, the jet plume is clearly an aerodynamic body exhibiting the essential features of classical fluid mechanics. In particular, it is of interest to note that when the plume is in the course of combustion, the unburnt hydrocarbons that may have accumulated near the walls ahead of the reacting plume are entrained into it by the sweeping action due to the baroclinic vorticity component (vid. Rotman et al., 1988). The elimination of this pollutant is thus significantly aided by an aerodynamic effect.

Analysis

As conceptually self-evident, in order to treat a combustion process, the aerodynamic considerations must be based upon a profound thermodynamic and thermochemical background. A rational analysis should thus be carried out in three consecutive steps: (A) Thermodynamics, (B) Thermochemistry, and (C) Aerodynamics. The first two are specified in terms of ordinary differential equations, reflecting in essence the fact that the reacting molecules, whose internal energy and chemical transformations are thereby treated, are not aware of the macroscopic properties of the flow field where the reaction takes place. In order to maintain the O.D.E. nature in the formulation of the problem, the effects of diffusion are expressed by fluxes specified in terms of a driving potential, such as the temperature difference, divided by a relaxation time, a constant adopted for this purpose as an adjustable parameter. The computations are, therefore, admittedly only good for an engineering estimate, as most, if not all, modeling analyses are in fact. As usually in such an endeavor, the accuracy of the estimate depends on the skill and experience of the analyst (Oppenheim, 1985; Oppenheim and Maxson, 1993; Gavillet, et al., 1993).

The third step, dealing with fluid mechanics, is expressed, of course, in terms of the partial differential Navier-Stokes equations of motion, and the global continuity equation. The latter provides information about the scalars of velocity divergence. While the dependence on time of these source terms is specified by the thermodynamic solution, their spatial location is prescribed by the inner product of the velocity vector and the density gradient. If the two are coincident at the interface between the burnt and unburnt medium, one has the case of classical deflagration. If they are normal to each other, one gets a non-reacting contact discontinuity with zero contribution to the velocity divergence. Whereas the initial state of combustion products is then specified by the thermodynamic conditions of birth, the initial location in space of velocity divergences that are thereby generated has to be prescribed by the analyst. Its most obvious and interesting place is, of course, in the middle of the large scale vortex structures as brought out in Fig. 2 (Oppenheim, 1986).

The fundamental background of this analytical procedure is as follows.

A. Thermodynamics. The thermodynamic analysis is based on the recognition of the fact that the reactants in an engine cylinder are essentially not at equilibrium, whereas the opposite holds true effectively for the end state of products of the exothermic reaction they undergo. It is incumbent, therefore, on the analyst to specify first this eventual goal. As an example, a locus of states of thermodynamic equilibrium, P, for a propane-air mixture initially at a pressure of 5 bar and a temperature of 65°C, is presented on the plane of internal energy, u, and the product of pressure and specific volume, w, in Fig. 3. Upon the advice of my French peers, such graph is referred to as the *Le Chatelier Diagram*, whereas the multi-

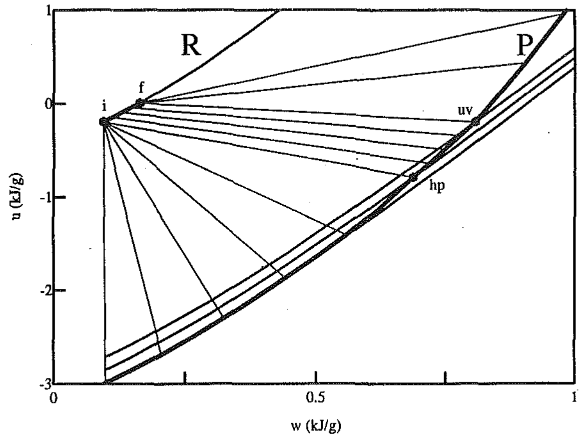

Fig. 3 The Le Chatelier diagram. A particular case of stoichiometric propane-air mixture at initial pressure of 5 bars and temperature of 65°C

dimensional phase space of all the thermochemical parameters as its coordinates should be called a *Le Chatelier space*.

Shown on the diagram also is the locus of states of the reactants, R. At any instant of time the pressure of the products is equal to that of the reactants. From the conservation equations for mass, volume and energy, it follows that constant pressure lines, connecting the corresponding points on R and P, are straight, as delineated by the thin lines on Fig. 3. In an adiabatic enclosure of constant volume, the first bit of reactants is transformed into products at constant enthalpy and pressure, while their last particle is consumed at constant internal energy and volume. The exothermic process is initiated thus at point i on R, leading to hp on P, and is terminated at point f on R, corresponding to uv on P.

The two loci of states, between i and f, as well as between hp and uv, are remarkably straight—a property which occurs at all practical circumstances. In this case, the mass fraction of products at thermodynamic equilibrium (referred to shortly as *mass fraction*) can be evaluated from the three conservation equations to yield:[2]

$$\mu_P = \frac{\omega + \kappa + P^{\alpha} + k(P\eta - P^{\alpha}) - 1}{P + k(P_{uv} - P) - 1} \tag{1}$$

where $\omega \equiv Wk/E_i = 1/c_R \int P d\eta$, while

$$\kappa \equiv Q_w/E_i = \kappa_f[1-(1-\mu_P)^{\beta}] \tag{2}$$

according to the results of heat transfer measurements reported in a companion paper (Maxson et al., 1994).

On this basis, the normalized specific volume of products at equilibrium

$$\chi_P \equiv \nu_P/\nu_i = [\eta - (1-\mu_P)\chi_R]/\mu_P \tag{3}$$

whereas

$$\chi_R \equiv \nu_R/\nu_i = W_R/P = P^{\alpha-1} \tag{4}$$

The initial state is an essential singularity, as at $\mu_P = 0$, $\eta_i = P_i = \chi_R = 1$ so that, according to Eq. (3), $\chi_P = 0/0$. By L'Hospital's rule, however, Eq. (3) yields

$$\chi_{Pi} = 1 + \frac{1/\eta_c + (d\eta/dP)_i}{(d\mu_P/dP)_i} \tag{5}$$

while from Eq. (1)

$$\left(\frac{d\mu_P}{dP}\right)_i = \frac{(k+1/c_R)(d\eta/dP)_i + \alpha(1-k) + k}{k(P_{uv}-1) - \beta\kappa_f/\mu_f} \tag{6}$$

The final state is pinpointed by the conditions of smooth decay, i.e.,

$$\left(\frac{d \ln \eta}{d \ln P}\right)_f = -1/n_e \tag{7}$$

when

$$\left(\frac{d\mu_P}{dP}\right)_f = 0 \tag{8}$$

whereas

$$\mu_f = \frac{\sigma\lambda_r + \delta + 1}{\sigma\lambda_o + \delta + 1} \tag{9}$$

while from Eq. (1)

$$\kappa_f = [P_f^{\alpha} + k(P_{uv} - P_f^{\alpha}) - 1]\mu_f - [P_f^{\alpha} + k(P_f\eta_f - P_f^{\alpha}) - 1] - \omega_f \tag{10}$$

This provides the basis for the evaluation of time (crank angle) resolved profiles of all the mean state parameters of the reactants and products.

B. Thermochemistry. The exothermic reaction proceeds as a consequence of a chemical source and a thermal source. The first is specified in terms of conventional kinetic rate expressions to yield the growth rate of concentration of all the chemical species participating in the exothermic reactions as

$$\dot{C}_i = (a_j - a_i) \sum_{k=1}^{K} \left[a^{1-m_k} \prod_{i=1}^{I} C_i a_{ik} T^{n_k} \exp(-E_k/\Re T) \right] \tag{11}$$

The second expresses the rate of temperature rise as

$$\dot{T} = \dot{Q} + \dot{P} + \dot{S} \tag{12}$$

where $\dot{Q} = -1/\hat{c}_P \left(\sum_{i=1}^{I} \dot{C}_i \hat{h}_i \right)$, while $\hat{c}_P = \sum_{i=1}^{I} C_i \hat{c}_{Pi}(T)$ and $\dot{P} = (v/\hat{c}_P)(dp/dt)$.

In Eq. (12) the last term models the effects of diffusion. In order to maintain its ODE character this is accomplished by introducing a thermal relaxation time, Δ_t, an adjustable constant. Thus

$$\dot{S} = (T_P - T)/\Delta_t \tag{13}$$

C. Aerodynamics. In accordance with the thermodynamic analysis, the flow field is considered to consist of two components: the reactants and the products. The interface zone between them is, in general, unconnected, while the fraction of reacting medium it embodies is negligible. Thus, with matching conditions across the interface, each of the two regimes of the field is governed by the Navier-Stokes equation

$$\frac{\partial \mathbf{u}}{\partial t} = -(\mathbf{u}\cdot\nabla)\mathbf{u} - v\nabla p + \mathrm{Re}^{-1}[\Delta\mathbf{u} + (k\mu^{-1} + 3^{-l})\nabla(\nabla\cdot\mathbf{u})] \tag{14}$$

as well as by the corresponding vortex transport equation

$$\frac{\partial \xi}{\partial t} = -(\mathbf{u}\cdot\nabla)\xi - \nabla v \times \nabla p + \mathrm{Re}^{-1}\nabla\xi \tag{15}$$

The velocity vector, $\mathbf{u}$, according to the Helmholtz decomposition theorem, consists of the rotational component, $\mathbf{u}_{\xi}$, and the irrotational component, $\mathbf{u}_{\epsilon}$

$$\mathbf{u} = \mathbf{u}_{\xi} + \mathbf{u}_{\epsilon} \tag{16}$$

where, by definition, $\nabla \times \mathbf{u}_{\xi} = \xi$, $\nabla \cdot \mathbf{u}_{\xi} = 0$, $\nabla \times \mathbf{u}_{\epsilon} = 0$, while, by virtue of the continuity equation,

$$\nabla \cdot \mathbf{u}_{\epsilon} = \frac{\partial}{\partial t} \ln \chi + (\mathbf{u}\cdot\nabla) \ln \chi \tag{17}$$

In the case of zero Mach number, a condition of the most significant model of turbulent combustion in an engine cyl-

---

[2] In terms of algebraic symbols defined in the Nomenclature.

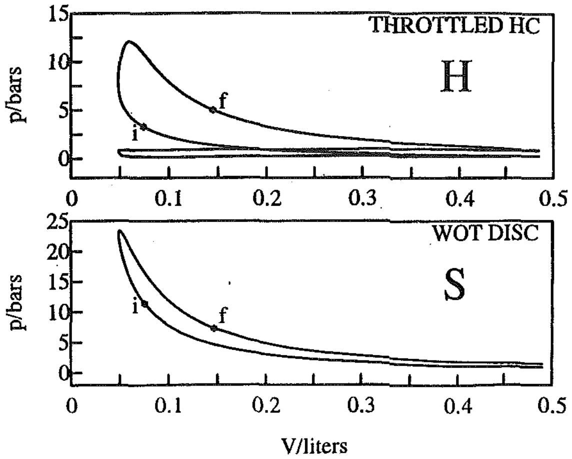

Fig. 4 Indicator diagrams. H—throttled homogeneous charge; S—wide open throttle direct injection stratified charge.

inder, $\nabla \ln \chi = 0$ for both the reactants, R, and products, P, whereas at the interface

$$\nabla \ln \chi \Rightarrow \ln(\chi_P/\chi_R)\delta(\mathbf{x}-\mathbf{x}_i)\mathbf{n} \qquad (18)$$

Here δ is the Dirac delta function, $\mathbf{x}$ is the position vector, subscript i referring to the interface, $\mathbf{n}$ is the unit vector normal to the interface, whereas the values of χ_P/χ_R are prescribed by the thermodynamic analysis per Eqs. (3) and (4).

Initial conditions for the flow field undergoing an exothermic process are specified in terms of the location at a given time of its initial point or points. In the case of a single point, the process spreads out by virtue of Eqs. (17) or (18), in compliance with Eqs. (14) and (15), to form eventually a deflagration front. Multipoint initiation, on the other hand, yields a set of distributed exothermic centers, whereby the combustion process is spread throughout the flow field. In the case of a turbulent jet plume, such as that of Fig. 2, such points can be identified by interrogating the numerical output of inert flow for conditions where $|\mathbf{u}| < \epsilon$, the latter of a sufficiently small value of specify an arbitrarily limited number of points. Obviously they will be then situated at the cores of the large scale vortex structures.

A numerical solution of these equations, subject to initial conditions in a turbulent jet plume presented by Fig. 2 is, as yet, to be completed—a feature rendering this paper the nature of a report on work in progress, rather than a review of past accomplishments.

Illustration

Consider for illustration the case of an engine, such as a four-stroke Renault F7P-700 we used for the development of the modeling analysis described here (Gavillet et al., 1993).

Its indicator diagram at a representative part-load operation, one most often encountered in the European driving test cycle when the engine runs at 2000 rpm, is shown in the upper part of Fig. 4. The engine was operated in the conventional Throttled Homogeneous Combustion (THROTTLED HC) mode. In the fireball mode of combustion attainable by the use of opposed PJC generators, as displayed in Fig. 1, the engine can provide the same net work output expressed in terms of the Indicated Mean Effective Pressure (IMEP) at, as it is known, Wide Open Throttle (WOT), Direct Injection Stratified Charge (DISC) manner of operation. The question is: what advantages can be thereby accrued?

Toward this aim, a parametric analysis was carried out following the method of attack presented here. Shown on the lower part of Fig. 4 is the equivalent indicator diagram we thus determined for a WOT operation of the engine with the same IMEP as that above. For the sake of a parametric study, the initiation and termination of the exothermic process of combustion are assumed to occur in both cases at the same time, while all the other operating parameters remain unchanged. Besides the reference case of throttled homogeneous combustion, marked by H, three cases of wide open throttle DISC, marked by S, were considered: (1) for the same energy loss by heat transfer to the walls, Q_H, as in the reference case; (2) for half as much loss; and (3) for the ultimate case of adiabatic combustion. Operating conditions for all of them are specified in Table 1 with respect to the overall equivalence ratio (the ratio of fuel in the combustible mixture to that of its stoichiometric proportion) in the cylinder, ϕ_o, and that in the reacting zone, ϕ_r. In the case of a homogeneous charge, it should be noted, $\phi_o = \phi_r$, for a stratified charge $\phi_o < \phi_r$.

The performance parameters we evaluated are summarized in Table 2. A bargraph of the Indicated Specific Fuel Consumption (ISFC), NO$_x$ (ISNO$_x$), and CO (ISCO) is presented on Fig. 5. Provided by Figs. 6, 7, 8, 9, and 10 are, respectively,

Table 1 Operating conditions

	Q_W	Φ_0	Φ_r	CASE
H	Q_H	1	1	0
S	Q_H	0.27	0.9	1
	$Q_H/2$	0.19	0.7	2
	0	0.11	0.4	3

Table 2 Performance parameters

Mode of Operation:		Full load		Part Load				
				Throttled HC		WOT DISC		
		EXP	SIM	EXP	SIM	SIM		
Heat loss		Full		Full		Full	Half	Adiabatic
Φ_0 / Φ_r		1.12 / 1.12	1.12 / 1.12	1.00 / 1.00	1.00 / 1.00	0.27 / 0.90	0.19 / 0.70	0.11 / 0.40
Fuel	ISFC (g/kWh)	265	286	324	388	353	275	158
NO$_x$	PPMV	1459	1493	357	368	116	46	2
	mg/g$_f$	31.2	23.9	6.9	6.5	8.8	4.7	0.4
	ISNO$_x$ (g/kWh)	7.0	6.9	2.2	2.5	3.10	1.29	0.06
CO	% V	3.30	3.31	0.66	0.16	0.017	0.007	0.009
	mg/g$_f$	460.3	495.1	87.1	26.5	9.7	5.4	12.0
	ISCO (g/kWh)	103.3	141.5	27.7	5.9	3.4	1.5	1.9

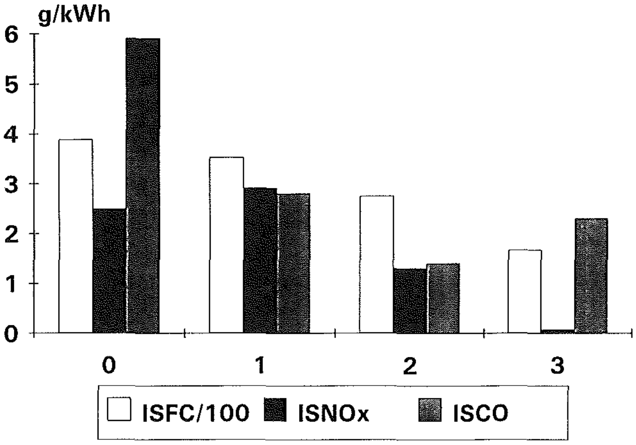

Fig. 5 Indicated specific fuel consumption (ISFC), ISNO$_x$ and ISCO. Four cases specified in Table 1.

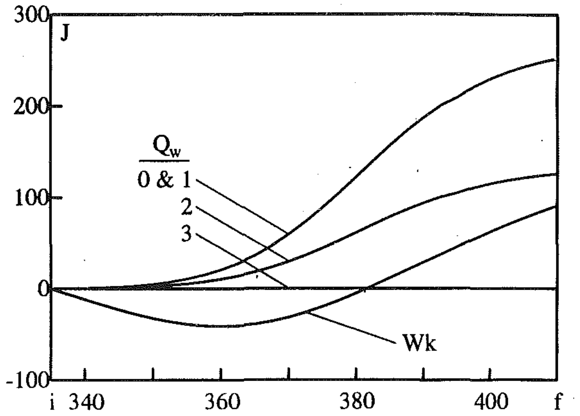

Fig. 6 Profiles of wall heat transfer and piston work. Four cases specified in Table 1.

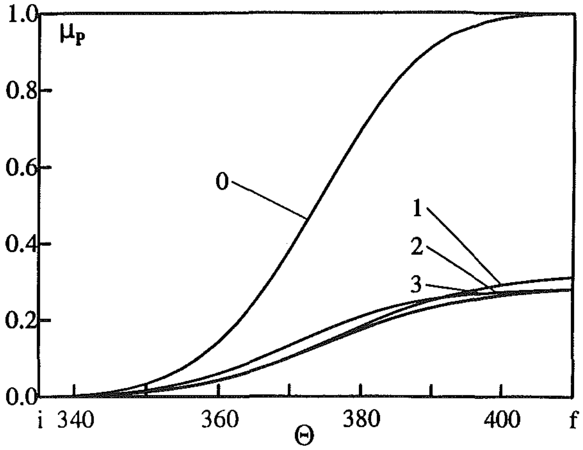

Fig. 7 Profiles of mass fraction of products at equilibrium. Four cases specified in Table 1.

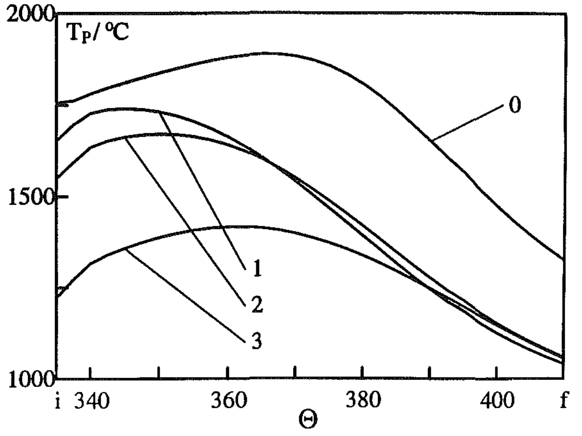

Fig. 8 Temperature profiles of products of equilibrium. Four cases specified in Table 1.

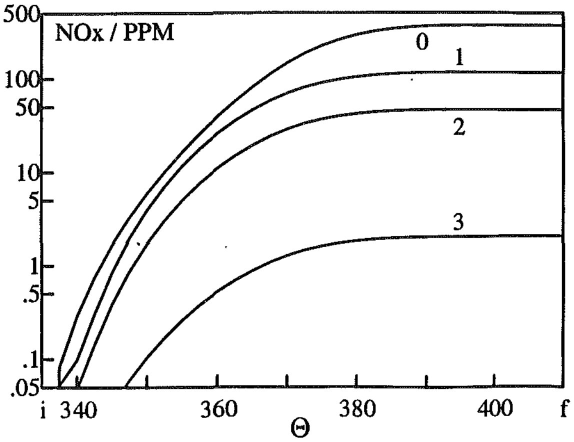

Fig. 9 Profiles of mass fraction of NO_x. Four cases specified in Table 1.

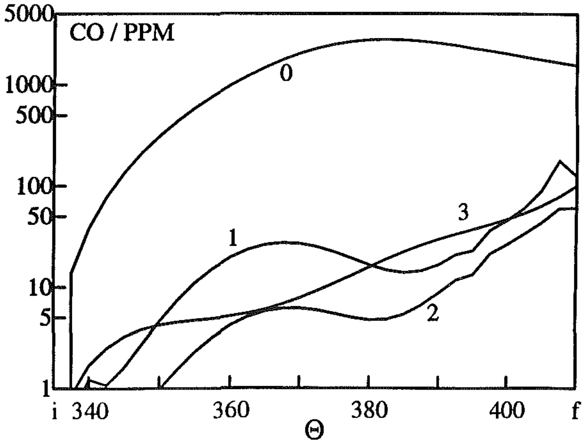

Fig. 10 Profiles of mass fraction of CO. Four cases specified in Table 1.

the wall heat loss profiles in comparison to net piston work delivered in the course of the exothermic process of combustion, the corresponding mass fraction of products at equilibrium that are concomitantly fabricated, their temperature profiles, and the mass fractions of, in turn, nitric oxide and carbon monoxide yields.

A perusal over these results should suffice to appreciate how much, indeed, can be accomplished by developing engines capable of operating efficiently at relatively low temperatures to minimize the production of pollutants—a task that can be attained only by aerodynamic action in, first, creating a turbulent jet plume of a fuel/air mixture within the cylinder-piston enclosure and then initiating the exothermic process of combustion so that it is executed before the reacting medium gets in touch with the walls—the salient feature of the fireball mode of combustion.

Epilogue

The paper is, in effect, an expression of a dream: *to make engines as we make airplanes*, i.e., to establish as close a link between theory and practice in design and construction of internal combustion engines as is traditionally the case in aeronautics, in full recognition of the fluid mechanical nature of the system. The task of tailoring the pressure profile of an indicator diagram on the basis of the aerodynamic properties of turbulent jet plumes is, after all, not unlike that of shaping the lift and drag of an airfoil expressed in terms of a polar diagram, by utilizing the best that fluid mechanics can offer.

Presented here then has been, in effect, a report of as yet unfinished work in progress, rather than a refurbished version of, as yet unpublished old study I set out initially to produce. It is my hope, of course, that the outcome will be thereby more exciting and enjoyable. Moreover, I believe that the theme will be of particular interest to Bill—a man who demonstrated so clearly the essential aspects of *making flying machines* as attested by his classical contribution to the Galcit Aeronautical

Series under the editorial guidance of Theodore von Karman and Clark B. Millikan (Sears, 1942).

In retrospect, albeit the subject of this paper is not entirely along the lines of Bill's professional involvement, there is a peculiar resemblance in the objective of our endeavors: the utilization of aerodynamic principles to combat the detrimental effects of walls—the essential ingredients of any engineering system (vid. Sears et al., 1977; Sears, 1979, 1983; Lee and Sears, 1987; Sears and Erickson, 1988).

Acknowledgment

The author wishes to express his gratitude to Dr. J. A. Maxson, Mr. G. G. Gavillet, and Mrs. S. Frolich for the valuable help they rendered in computations and preparation of the manuscript.

References

Chorin, A. J., 1973, "Numerical Studies of Slightly Viscous Flow," *Journal of Fluid Mechanics*, Vol. 57, pp. 785–796.

Chorin, A. J., 1978, "Vortex Sheet Approximation of Boundary Layers," *J. Comput. Phys.*, Vol. 27, pp. 428–442.

Chorin, A. J., 1989, *Computational Fluid Mechanics*, Academic Press, Boston, San Diego.

Gavillet, G. G., Maxson, J. A., and Oppenheim, A. K., 1993, "Thermodynamic and Thermochemical Aspects of Combustion in Premixed Charge Engines Revisited," SAE Paper 930432, 20.

Ghoniem, A. F., Chorin, A. J., and Oppenheim, A. K., 1982, "Numerical Modelling of Turbulent Flow in a Combustion Tunnel," Philosophic Transactions of the Royal Society London Series, A304, pp. 303–325.

Ghoniem, A. F., Chen, D. Y., and Oppenheim, A. K., 1986, "Formation and Inflammation of Turbulent Jet," *AIAA Journal*, Vol. 24, No. 2, pp. 224–229.

Gussak, L. A., 1976, "High Chemical Activity of Incomplete Combustion Products and a Method of Prechamber Torch Ignition for Avalanche Activation of Combustion in Internal Combustion Engines," *SAE Transactions*, Vol. 84, pp. 2421–2445.

Gussak, L. A., 1978, "LAG-Process, Some Results of Utilization in Transport and Mechanical Engineering," SAE Paper 789651, *Proceedings of the 13th Intersociety Energy Conversion Engineering Conference*, Vol. 3, pp. 2153–2163.

Gussak, L. A., 1983, "The Role of Chemical Activity and Turbulence Intensity in Prechamber-Torch Organization of Combustion in Stationary Flow of a Fuel-Air Mixture," SAE Paper 830592, 14.

Gussak, L. A., Karpov, V. P., Gussak, D. A., 1976, "Torch Ignition in a Stratified Charge Engine," *Archiwum Termodynamiki i Spalania*, Vol. 7, pp. 507–527.

Gussak, L. A., Karpov, V. P., Tikhonov, Yu. V., 1979, "The Application of LAG-Process in Prechamber Engines," SAE Paper 790692, 26.

Gussak, L. A., and Turkish, M. C., 1977, "LAG-Process of Combustion and Its Application in Automobile Gasoline Engines," IMechE Publication C257/76, *Stratified Charge Engines*, The Institution of Mechanical Engineers, London, pp. 137–146.

Hensinger, D. M., Maxson, J. A., Hom, K., and Oppenheim, A. K., 1992, "Jet Plume Injection and Combustion," *SAE Transactions* (Paper 920414), 10.

Lee, D. C. L., and Sears, W. R., 1987, "Experiments with an Adaptable-Wall Wind Tunnel for Large Life," *AIAA Journal of Aircraft*, Vol. 24, No. 6, pp. 371–376.

Maxson, J. A., Ezekoye, O. A., Hensinger, D. M. Greif, R., and Oppenheim, A. K., 1994, "Heat Transfer from Combustion in an Enclosure," (in preparation).

Maxson, J. A., and Oppenheim, A. K., 1991, "Pulsed Jet Combustion—Key to a Refinement of the Stratified Charge Concept," *Twenty-Third Symposium (International) on Combustion*, The Combustion Institute, Pittsburgh, Pa., pp. 1041–1046.

Maxson, J. A., Hensinger, D. M., Hom, K., and Oppenheim, A. K., 1991, "Performance of Multiple Stream Pulsed Jet Combustion Systems," SAE Paper 910565, 9.

Oppenheim, A. K., 1985, "Dynamic Features of Combustion," Philosophic Transactions of the Royal Society London Series, A315, pp. 471–508.

Oppenheim, A. K., 1986, "The Beauty of Combustion Fields and Their Aerothermodynamic Significance," *Dynamics of Reactive Systems Part I: Flames and Configurations, Progress in Astronautics and Aeronautics*, American Institute of Aeronautics and Astronautics, New York, 105, pp. 3–13.

Oppenheim, A. K., 1988, "Quest for Controlled Combustion Engines," *SAE 1988 Transactions, The Journal of Engines*, Vol. 97, No. 6, pp. 1033–6.1039.

Oppenheim, A. K., Beltramo, J., Faris, D. W., Maxson, J. A., Hom, K., and Stewart, H. E., 1989, "Combustion by Pulsed Jet Plumes-Key to Controlled Combustion Engines," *SAE Transactions, The Journal of Engines*, Vol. 98, pp. 175–182.

Oppenheim, A. K., 1991, "Pulsed Jet Combustion—Its Past, Present, and Future," *Archivum Combustionis*, Vol. 11, pp. 1–2, 3–18.

Oppenheim, A. K., 1992a, "Life on Earth at the Point of Inflection," *Proceedings of the Institution of Mechanical Engineers*, C448/076, IMechE 1992-10, pp. 215–220.

Oppenheim, A. K., 1992b, "Is There a Future for the Technology of Combustion in Engines," *Proceedings of International Science Conference on Internal Combustion Engines*, KONES'92, Institute of Aviation, Warsaw, Poland, pp. 336–344.

Oppenheim, A. K., 1992c, "Quo Vadis, Technologia Combustionis?," *Proceedings of 2nd International Conference on Fluidmechanics, Combustion, Emissions and Reliability in Reciprocating Engines*, Istituto Motori, Naples, Italy, pp. 9–14.

Oppenheim, A. K., 1992d, "The Future of Combustion in Engines," *Proceedings of the Institution of Mechanical Engineers*, C448/022, IMech 1992-10, pp. 187–192.

Oppenheim, A. K., and Maxson, J. A., 1993, "Thermodynamics of Combustion in an Enclosure," presented at the 13th International Colloquium on Dynamics of Explosions and Reactive Systems, Nagoya, Japan, *AIAA Progress of Astronautics and Aeronautics* (in press).

Rotman, D. A., Pindera, M. Z., and Oppenheim, A. K., 1988, "Fluid Mechanical Properties of Flames Propagating in Closed Channels," *Dynamics of Reactive Systems Part I: Flames, Progress in Astronautics and Aeronautics*, American Institute of Aeronautics and Astronautics, New York, 113, pp. 251–265.

Sears, W. R., 1938, "Contribution to the Airfoil Theory for Non-Uniform Motion," *Proceedings of the Fifth International Congress of Applied Mechanics*, pp. 483–487.

Sears, W. R., 1941, "Some Aspects of Non-Stationary Airfoil Theory and its Practical Application," *Journal of the Aeronautical Sciences*, Vol. 8, No. 3, pp. 104–108.

Sears, W. R., 1942, *The Airplane and Its Components*, Wiley, New York, viii + 75.

Sears, W. R., 1948, "A New Treatment of the Lifting-Line Wing Theory with Applications to Rigid and Elastic Wings," *Quarterly of Applied Mathematics*, Vol. VI, No. 3, pp. 239–255.

Sears, W. R., 1954, "General Theory of High Speed Aerodynamics" (editor) Vol. VI, *High Speed Aerodynamics and Jet Propulsion*, XIV + 758, Princeton University Press, "Small Perturbation Theory" (author) ibid., 61–121; "Plane Subsonic and Transonic Potential Flow" (authored with Y. H. Kuo) ibid., pp. 490–582.

Sears, W. R., 1956, "Some Recent Developments in Airfoil Theory," *Journal of the Aeronautical Sciences*, Vol. 23, No. 5, pp. 490–499.

Sears, W. R., 1979, "Adaptive Wind Tunnels with Imperfect Control," *AIAA Journal of Aircraft*, Vol. 16, No. 5, pp. 344–348.

Sears, W. R., 1983, "Adaptable Wind Tunnel for Testing V/STOL Configurations at High Lift," *AIAA Journal of Aircraft*, Vol. 20, No. 11, pp. 969–974.

Sears, W. R., and Erickson, Jr., J. C., 1988, "Adaptive Wind Tunnels," *Ann. Rev. Fluid Mech.*, Vol. 20, pp. 17–34.

Sears, W. R., Vidal, R. J., Erickson, Jr., J. C., and Ritter, A., 1977, "Interference-Free Wind-Tunnel Flows by Adaptive-Wall Technology," *AIAA Journal of Aircraft*, Vol. 14, No. 11, pp. 1042–1050.

Semenov, N. N., 1944, "On Types of Kinetic Curves in Chain Reactions," *Comptes Rendus (Doklady) de l'Academie des Sciences de l'URSS* (I) Vol. 43, No. 8, pp. 342–348, (II) Vol. 44, No. 2, pp. 62–66, (III), Vol. 44, No. 6, pp. 241–245.

Semenov, N. N., 1958, *Some Problems in Chemical Kinetics and Reactivity* (Transl. by M. Boudart), Princeton University Press, 1, 239; 2, 1959, 331.

Sokolik, A. S., and Karpov, V. P., 1960, "Torch Ignited Combustion—A Novel Mode of Stratification Combustion and Mixing in Diesels," *USSR Academy of Sciences*, Vol. 9, pp. 125–142.

Tilt Rotor Broadband Hover Aeroacoustics[1]

C. D. Coffen
Assistant Research Engineer.
United Technologies Research Center,
East Hartford, CT 06108

A. R. George
Professor of Mechanical
and Aerospace Engineering,
Cornell University,
Ithaca, NY 14853

To improve the acoustic characteristics of tilt rotor aircraft, the dominant noise mechanisms must be understood. Toward this goal, a method was developed to identify and predict the dominant broadband noise mechanism of a hovering tilt rotor. Predictions are presented for a range of azimuthal observer locations and polar observer angles and are compared to NASA full scale tilt rotor hover noise data. Comparisons between experiment and prediction indicate that the polar and azimuthal directionality trends are captured. The predicted sound spectrum levels are generally within 5 dB of the experiment. The results of this study indicate that the highly turbulent recirculating fountain flow is the dominant broadband noise mechanism for a tilt rotor aircraft in hover.

1 Introduction

This paper will report on some important progress in understanding and predicting the dominant source of broadband noise generated by a hovering tilt rotor aircraft. This mechanism has been identified as unsteady lift on the rotor blades generated by the reingestion of the highly turbulent recirculating fountain flow.[2] Experiments were conducted on a twelfth scale model tilt rotor in hover mode in order to characterize the unsteadiness, turbulence intensity, integral scale, and spatial extent of the fountain flow. The results of our experimental study (Coffen et al., 1991) are used as input to a modified version of Amiet's noise prediction code (Amiet, 1989). Several analytical techniques are available for predicting the broadband noise due to rotor interaction with a turbulent inflow field: Homicz and George (1974), George and Kim (1977), and Amiet (1976). Amiet's method is used as a starting point because it is the only analysis which can be modified to account for azimuthally varying inflow turbulence. This analysis also accounts for blade-to-blade correlations, includes rapid distortion theory (not used in the current study), and has been shown to accurately predict turbulence ingestion noise in previous studies (Amiet, 1976; Simonich et al., 1989). Of special interest to the celebration of Professor W. R. Sears' 80th birthday is Amiet's use of the classical Sears function (Sears, 1939) as the airfoil response function to turbulent inflow.

The fundamental geometry of the tilt rotor aircraft, shown in Fig. 1, consists of prop-rotors mounted on tiltable nacelles which are located at or near the tips of a fixed (non-tilting) wing. The prop-rotor is sufficiently large so that the benefits of low disk loading are gained for efficient hover flight. The prop-rotor is designed to provide the desired performance balance between the axial-flow hover requirement and the axial-flow airplane mode requirement (Rosenstein and Clark, 1983; McVeigh et al., 1983; Paisley, 1987). Tilt rotor aircraft are being seriously considered as future commercial transports. Their unique design allows them to take-off and land vertically (or with very short ground rolls) then convert into conventional airplane mode for cruise. The need for only small verti-ports in strategic locations, such as near city centers, make the tilt rotor's use very attractive. The limiting factors for tilt rotor aircraft commercialization include cost, safety, the existence of verti-ports, and noise. Clearly, with the possibility of operating close to densely populated areas, it is imperative that the tilt rotor's noise radiation be acceptable to the public.

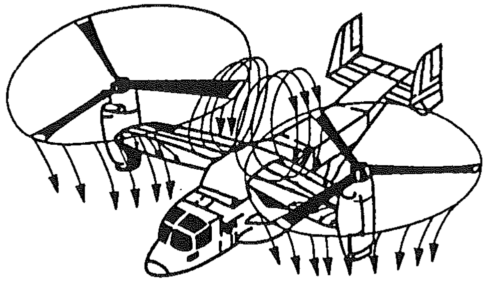

Fig. 1 Schematic of the hover mode wake/flow patterns (McVeigh et al., 1988)

The importance of tilt rotor acoustics makes it vital to better understand the noise mechanisms. In addition to exhibiting most of the noise mechanisms of a conventional helicopter, the tilt rotor is also affected by other noise mechanisms. The tilt rotor introduces a number of unique prop-rotor/airframe aerodynamic interactions that result in important noise and performance problems. Fortunately, tilt rotors can be operated with more degrees of freedom than helicopters and thus may have more potential for operational noise reductions (George et al., 1989). Minimizing the acoustic signal can be accomplished in two ways: by reduction in the strength of the basic mechanisms, and by understanding and then controlling the strong directionality of the observed radiation. Improved un-

---

[1] This paper is dedicated to Professor W. R. Sears on the occasion of his 80th birthday and in celebration of his teaching, research, and friendship.

[2] Discrete noise prediction techniques, hover flow characterization and visualization, and blade vortex interaction noise are discussed in Coffen and George (1990), Coffen et al. (1991), Rutledge et al. (1991), Coffen (1992), and George et al. (1992).

Contributed by the Fluids Engineering Division for publication in the JOURNAL OF FLUIDS ENGINEERING. Manuscript received by the Fluids Engineering Division, January 15, 1993; revised manuscript received July 12, 1993. Associate Technical Editor: D. P. Telcoms.

derstanding of tilt rotor noise will aid in minimizing noise radiation for the existing tilt rotor and help determine the proper design changes for future generations of tilt rotor aircraft.

2 Tilt Rotor Fountain Effect

The operational configuration of a hovering tilt rotor aircraft is such that the presence of the wing and fuselage beneath the rotor strongly affects the aerodynamics by introducing complex unsteady recirculating flows. Figure 1 shows a simplified schematic of this fountain flow while Fig. 2 is an actual photo from a flow visualization study conducted on a one-twelfth scale model tilt rotor (Coffen et al., 1991). The wing and fuselage provide a partial ground plane in the near wake which causes the development of an inboard-bound spanwise flow over the wing and fuselage surface. At the aircraft's longitudinal plane of symmetry, the opposing flows collide, producing an unsteady "fountain flow" with upward velocity components. This fountain flow, characterized by higher than ambient turbulence intensity levels and smaller integral scale, is then reingested by the rotors, resulting in azimuthally varying inflow turbulence levels. The interaction of the rotors with this highly turbulent spatially non-uniform flow causes significant broadband noise which is radiated preferentially to the rear of the aircraft (the direction of motion as the blade passes through the fountain).

3 Summary of Amiet's Method

Amiet's method for predicting noise generated by turbulent flow into a rotor has been documented previously in the literature (Amiet, 1975; Amiet, 1976; Amiet, 1989). The following is a summary of the theory involved in the method and includes a brief description of the implementation of the classical Sears function. Initially, Amiet's analysis was applied to the case of an airfoil convecting rectilinearly through a turbulent flow field (Amiet, 1975). Amiet later extended this analysis to include the effects of the rotary motion of an airfoil (propeller or rotor blade) (Amiet, 1976). In this study, Amiet's method was further modified in order to account for azimuthally varying inflow turbulence.

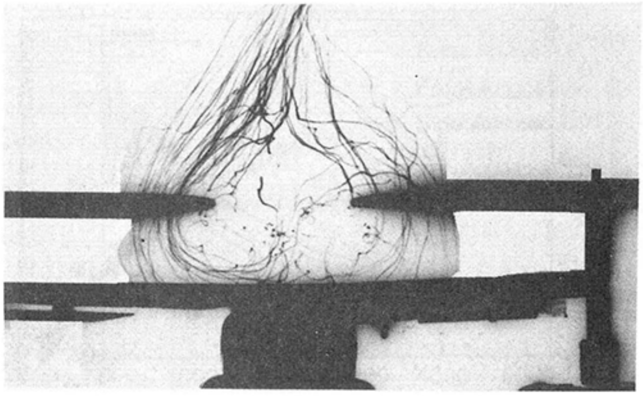

Fig. 2 Computer enhanced digitized photo of the fountain flow. Viewer is in front of the model looking down the fuselage. Helium filled soap bubbles are injected over the center of the wing on the rotor/rotor axis. This illustrates the spanwise flow, fountain height and recirculation. 1/2 second exposure time.

3.1 Airfoil in Rectilinear Motion. An airfoil passing through a turbulent flow field experiences an unsteady loading due to the fluctuating airfoil angle of attack. This unsteady loading translates into unsteady surface pressures which propagate to the far field as noise. Amiet's analysis assumes that a vertical gust convects perpendicular to the leading edge of a flat plate airfoil. Linearized theory is assumed throughout the analysis. When the gust impinges on the airfoil, a surface dipole distribution is induced to oppose the gust flow and satisfy the condition of no flow through the airfoil surface. This surface dipole distribution creates a pressure jump across the upper and lower surfaces which acts as an effective distributed force on the airfoil. The far-field noise can be calculated by noting that a force imposed by the fluid produces a dipole pressure field response (acoustic sources). These acoustic dipole sources are equal in strength to the force induced on the airfoil by the convecting turbulent gusts. Amiet's analysis provides an expression for the far-field acoustic power spectral density in terms of the turbulence velocity spectrum and the airfoil response function. The product of these two functions can be described as the transfer function between the turbulent inflow velocity fluctuations and the far-field acoustics:

$$S_{pp}(\mathbf{x}, \omega) = \left(\frac{\omega z \rho_0 b}{c_0 \sigma^2}\right)^2 \pi U d \left| \mathcal{L}\left(x, k_x, \frac{\omega y}{c_0 \sigma}\right)\right|^2 \Phi_{ww}\left(k_x, \frac{\omega y}{c_0 \sigma}, \mathbf{M}\right) \quad (1)$$

3.2 Airfoil Response Functions: The Sears Function. The rotor blades' unsteady lift response to an incident gust is the fundamental source of the turbulence ingestion noise mechanism. At low Mach number and reduced frequency, the Sears function can be used with good accuracy (an alternate response function is used for larger values of Mach number and reduced

Nomenclature

b = semi-chord
d = semi-span
c_0 = sound speed
ρ_0 = ambient fluid density
U = free stream velocity
W = mean convection velocity through the rotor
u', v', w' = Cartesian components of rms velocity
J_0, J_1 = Bessel functions of the first kind
k = magnitude of wave number vector
k_x, k_y, k_z = Cartesian wave numbers of turbulence
$\mathcal{L}$ = effective lift
M = free stream Mach number
$\mathbf{M}_t$ = Mach number of the source relative to the observer
$\mathbf{M}_r$ = Mach number of the source relative to the ambient fluid
S_{pp} = PSD of far field sound
S = Sears function
$\mathbf{x}$ = observer location with respect to the rotor hub
x, y, z = chordwise, spanwise, and normal Cartesian coordinates
$\beta = \sqrt{1-M^2}$
$\sigma = \sqrt{x^2+\beta^2(y^2+z^2)}$
ω = circular frequency
ω_0 = Doppler shifted frequency
γ = azimuthal angle
Φ_{ww} = velocity spectrum of turbulence
E = Von Kármán energy spectrum of turbulence
F_{11} = longitudinal velocity spectrum of turbulence
$f(M) = \dfrac{(1-\beta)\ln M+\beta}{\ln(1+\beta)-\ln 2}$
OS = unit vector from the observer to the retarded source

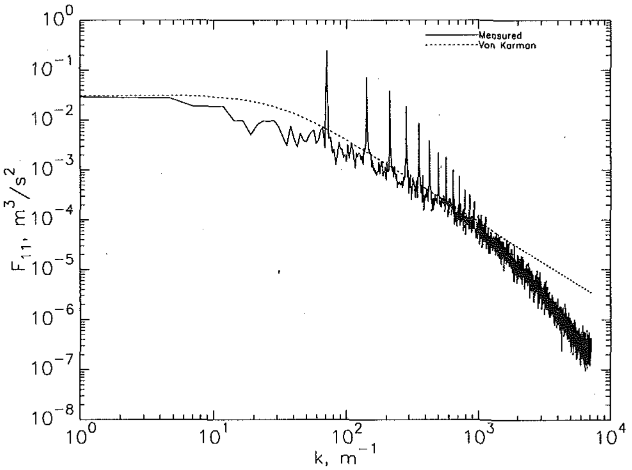

Fig. 4 Comparison of Measured and Von Kármán longitudinal velocity spectrum of fountain flow turbulence for the 1/12 scale model tilt rotor

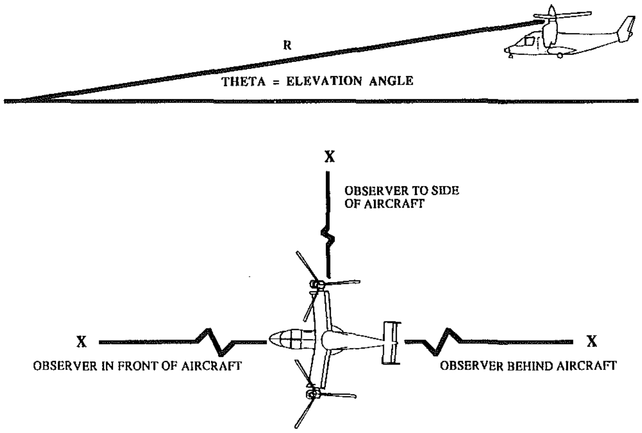

Fig. 5 Schematic of observer locations for the predictions and experiment

frequency). Amiet shows that the effective lift, $\mathfrak{L}$, can be expressed as:

$$\mathfrak{L}\left(x,\, k_x,\, \frac{\omega y}{c_0\sigma}\right)=\frac{1}{\beta}\, S\left(\frac{k_x}{\beta^2 b}\right)\, e^{i\frac{k_x}{\beta^2 b}f(M)}\, \left(J_0\left(\frac{\mathbf{M}k_x x}{b\beta^2\sigma}\right) - iJ_1\left(\frac{\mathbf{M}k_x x}{b\beta^2\sigma}\right)\right) \quad (2)$$

In this expression, S is the classical Sears function described in the following: Sears and Keuthe (1939), Von Kármán and Sears (1938), and Sears (1940). This application demonstrates the practical importance of Sears' work on unsteady flow problems. A numerical calculation of this analysis would not be possible without the groundwork provide by Sears and others in understanding the fundamentals of airfoil response to unsteady flows. One should also note that while there are several different techniques for calculating turbulence ingestion noise, the methods of Homicz and George (1974), and George and Kim (1977) also make use of the Sears function in their respective analyses.

3.3 Airfoil in Rotary Motion. A fundamental difference between Amiet's method and the other noted methods is that the rotary motion of the blade element is approximated as a series of rectilinear motions. Two effects cause the observer fixed instantaneous sound spectrum of a rotating source to vary periodically in time. First, the orientation of the source radiation directivity relative to a fixed observer changes as the blade rotates. This causes the spectrum amplitude to modulate at the rotor rotational frequency. Second, the retarded time effects, due to the source alternately moving away and towards the observer, cause an alternate compression and dilation of the time scale of the signal. Finding the exact spectrum of a broadband noise signal modified in these two ways would be difficult. An approximation can be made by assuming that the frequencies of interest are much greater than the rotor rotational frequencies. The rotor rotation period, T, is divided into short time segments, ΔT. A spectrum is calculated for each time segment during which it is assumed that the rotor blade is moving rectilinearly. These "instantaneous" spectra are averaged resulting in a spectrum which is the equivalent of the output of a constant bandwidth spectrum analyzer that has insufficient resolution to display the rotation harmonics. The technique for calculating the azimuthally averaged spectrum of a rotating source modeled by rectilinear motion is described in Amiet (1976) and Schlinker and Amiet (1981) with the result expressed as:

$$S_{pp}(\mathbf{x},\, \omega_0)=\frac{1}{2\pi}\int_{\gamma=0}^{2\pi}\left(\frac{\omega}{\omega_0}\right)^2 S_{pp}(\mathbf{x},\, \omega,\, \gamma)d\gamma \quad (3)$$

Equation (3) is used with Eq. (1) to predict the far-field acoustics of turbulence ingestion noise.

4 Calculation Procedure (Modified Amiet's Method)

Amiet's method can be used to calculate the noise due to azimuthally varying turbulence because the analysis makes the rectilinear motion approximation. In the numerical implementation, the blade span is discretized into segments and the blade rotation is reduced to a series of rectilinear motions which approximate the rotary trajectory of the blade. Spatial variations were implemented by associating appropriate turbulence characteristics with each blade segment and azimuthal location. The implementation requires keeping track of where the observer is located with respect to the motion of the blade and the blade's azimuthal location, because the Doppler amplification factor changes as the blade rotates towards and away from the observer. This relationship determines the azimuthal directionality of the broadband noise as the observer's location relative to the blade as it passes through the high levels of turbulence in the fountain flow determines the relative amplitude of the broadband noise.

The azimuthally varying turbulence was defined in such a way as to approximate the measured spatial variations in turbulence properties measured in the one-twelfth scale model experiments. Figure 3 indicates the spatial variations in turbulence level in the inflow field. The contour levels are the measured quantity $\sqrt{(u'^2+v'^2+w'^2)/3}$ and are only useful to identify the spatial extent of the highly turbulent recirculating flow. The vertical gust component of the turbulence, w', which causes the unsteady blade loading, was not directly deduced from this data as the measurements also include the fluctuating velocity due to the potential flow generated by the blade passing underneath the hot wire probe. However, the yellow and green shading clearly indicates a region of highly turbulent inflow which the rotor blade encounters as it rotates toward the rear of the aircraft.

4.1 Turbulence Spectra. Amiet's method assumes that the turbulence velocity spectrum, $\Phi_{ww}(k_x, k_y, k_z)$, is related to $E(k)$, the Von Kármán energy spectrum as function of the magnitude of the wave vector, k, by

$$\Phi_{ww}(k_x,\, k_y,\, k_z)=\frac{E(k)}{4\pi k^2}\left(1-\frac{k_z^2}{k^2}\right) \quad (4)$$

The accuracy of the Von Kármán energy spectrum vis-a-vis the actual inflow turbulence is an important assumption in predicting the acoustic spectra. This assumption was examined by comparing an experimentally obtained fountain turbulence

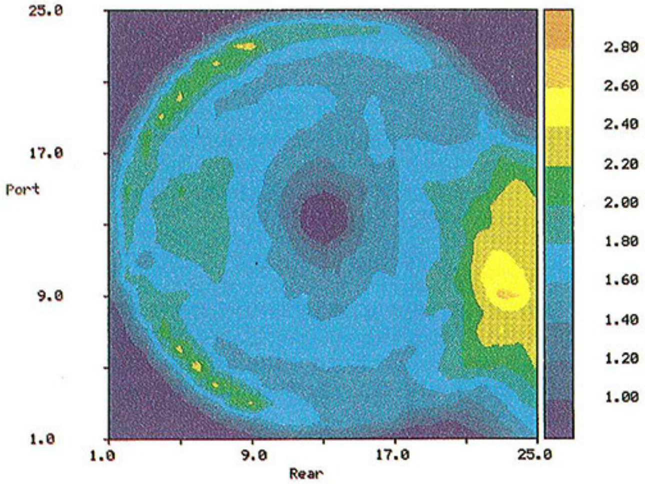

Fig. 3 Contour plot of rms inflow velocity: $(u'^2 + v'^2 + w'^2/3)^{0.5}$ (m/s). Port rotor, rotates clockwise, 24 inch diameter blade. Yellow and green shading corresponds to high levels of turbulence in the reingestion zone over the wing (the fuselage is to the right of the plot with the tail toward the bottom of the page).

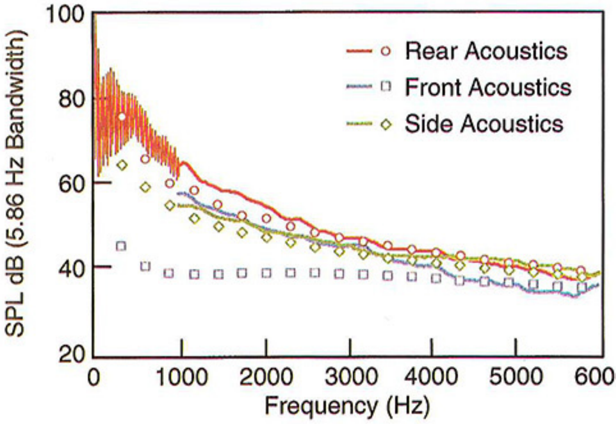

Fig. 6 Comparison of experimental and predicted broadband noise spectra. Rear, side, and front aircraft acoustics, θ = 7.2 deg (50′ hover height). Lines are experiment, symbols are prediction. The broadband part of the experimental spectra are faired, and front and side spectra are truncated below 1000 Hz.

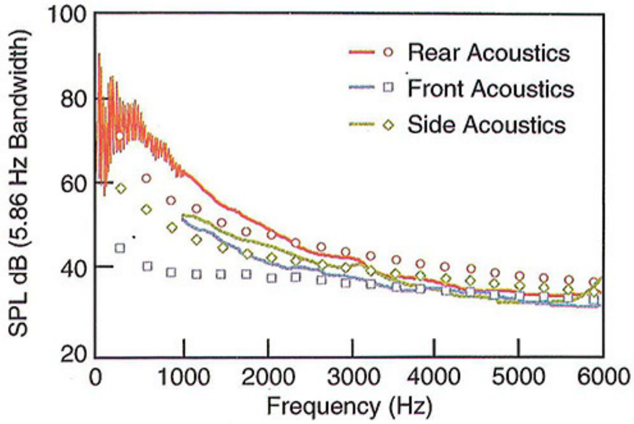

Fig. 7 Comparison of experimental and predicted broadband noise spectra. Rear, side, and front aircraft acoustics, θ = 12.7 deg (100′ hover height). Lines are experiment, symbols are prediction. The broadband part of the experimental spectra are faired, and front and side spectra are truncated below 1000 Hz.

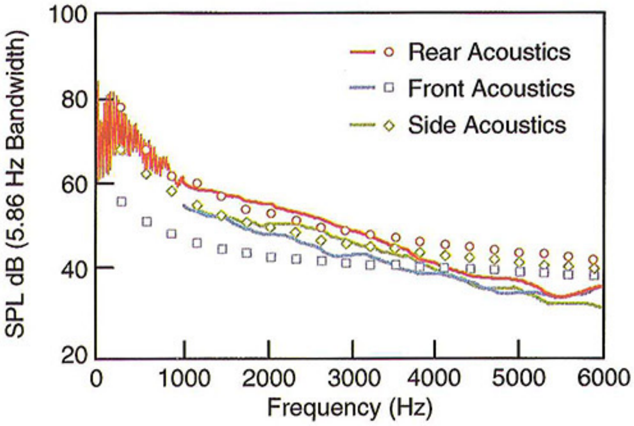

Fig. 8 Comparison of experimental and predicted broadband noise spectra. Rear, side, and front aircraft acoustics, θ = 23.0 deg (200′ hover height). Lines are experiment, symbols are prediction. The broadband part of the experimental spectra are faired, and front and side spectra are truncated below 1000 Hz.

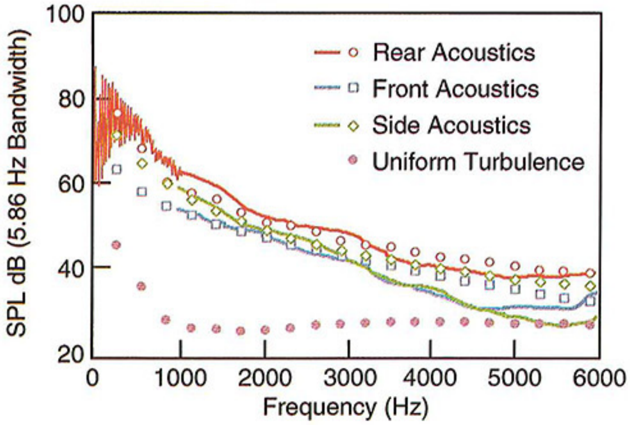

Fig. 9 Comparison of experimental and predicted broadband noise spectra. Rear, side, and front aircraft acoustics, θ = 45.7 deg (500′ hover height). Lines are experiment, symbols are prediction. The broadband part of the experimental spectra are faired, and front and side spectra are truncated below 1000 Hz.

spectrum to the Von Kármán spectrum as follows: The longitudinal spectrum of the turbulence, $F_{11}(k)$, for the one-twelfth scale model was obtained from the power spectral density of the inflow which was measured with a hot wire placed in the highly turbulent region over the wing. Assuming isotropic turbulence, the energy spectrum is related to the longitudinal spectrum by:

$$E(k) = k^3 \frac{d}{dk}\left(\frac{1}{k}\frac{d}{dk}F_{11}(k)\right) \tag{5}$$

Integrating twice with respect to k and setting the constants of integration to zero gives an analytical expression for the longitudinal spectrum based on the Von Kármán energy spectrum. Figure 4 is a comparison between the experimental data and the Von Kármán spectrum and exhibits good agreement for wave numbers less than 10^3 m^{-1}. One should note that the discrete peaks in the experimental spectra are related to the blade passing frequencies and are caused by the potential field of the rotating blade. In calculating $F_{11}(k)$ for the Von Kármán spectrum, the rms turbulence velocity is obtained by integrating the area under the experimentally obtained $F_{11}(k)$ of inflow velocity and the turbulent length scale is assumed to be equal to the chord of the rotor blade. For the purposes of the XV-15 acoustic predictions presented below, w' in the reingestion area of the rotor disk is assumed to scale from the one-twelfth scale experiment with the rotor disk area averaged convection velocity, W. This velocity is calculated from the known thrust of the XV-15 in hover, and is calculated from inflow measurements in the experiment. The turbulence length scale is assumed to scale with blade chord length. For regions of the rotor disk not in the reingestion zone, representative atmospheric turbulence is assumed: the integral scale is taken to be 90 percent of the hover height and the rms turbulence velocity is given the typical value of 1 m/s.

5 Predicted Spectra

Predicted and measured noise spectra are presented in Figs. 6-9 for four polar observer angles. Each of these figures has curves for experiment[3] and prediction for three azimuthal observer locations: front, side, and rear aircraft acoustics (see Fig. 5 for directionality definitions). These predictions are in good agreement with the experimental data as both the polar and azimuthal directionality trends are captured. The predicted spectrum levels are generally within 5 dB of experiment with the following exceptions: The **front** acoustic predictions are 5-15 dB low over a portion of the spectrum for the 7.2, 12.7, and 23 deg polar angle observer locations. The part of the spectrum where the predictions do not agree increases for lower aircraft hover heights (smaller polar angles). At these lower hover heights, there may be some recirculation due to the ground plane which would increase the ambient turbulence intensities above the 1 m/s assumed for the predictions, and result in higher than predicted noise levels. One should note that the low frequency discrete noise is due to the mean flow of the fountain and is not treated in this paper. Analysis and predictions of discrete noise due to the fountain mean flow are presented in Coffen and George (1990), Rutledge et al. (1991), and Coffen (1992).

The good agreement between the predictions and experimental data indicate that the highly turbulent recirculating fountain flow has been correctly identified as the dominant broadband noise mechanism for a hovering tilt rotor. The predictions capture the azimuthal directionality trends; the levels are higher for an observer behind the aircraft with the levels decreasing as the observer location is moved around the aircraft to the front. The effect of azimuthally varying turbulence characteristics on the noise directionality is further illustrated in Fig. 9 which has a prediction based on uniform atmospheric turbulence (labeled **Uniform Turbulence**). This prediction underpredicts the noise levels by 10-25 dB depending on frequency and is independent of azimuthal observer location. The azimuthal variations in noise levels can be explained by aeroacoustic theory which shows that the noise is amplified in the direction that the source is moving (Lowson, 1965). Because the blade is moving toward the rear of the aircraft as it passes through this highly turbulent region, noise is radiated preferentially to the rear with levels decreasing to a minimum at the front of the aircraft where the blades are moving away from the observer as they pass through the reingestion zone.

6 Conclusion

Modifications to Amiet's method of predicting turbulence ingestion noise have resulted in a means of predicting broadband rotor noise generated by azimuthally varying inflow turbulence. For the results presented here, the azimuthal variations are based on one-twelfth scale model tilt rotor hover experiments. Noise predictions based on this method compare well, both levels and trends, with full scale hover acoustics tests conducted by NASA on the XV-15. The good correlation between these broadband predictions and experiment indicates that the highly turbulent, reingested inflow is the dominant broadband noise mechanism for a hovering tilt rotor. As alluded to previously, these strong directional dependences can be taken advantage of to minimize the aircraft's operational noise annoyance. The pilot should operate the aircraft such that the rear of the aircraft faces away from areas that would be most adversely affected by the noise.

Acknowledgments

This research was supported by NASA Ames grant NAG-2-554 and partly by the NASA-Cornell University Space Grant Program. We also acknowledge many helpful conversations with Roy K. Amiet and the crucial contributions of Charles K. Rutledge (NASA Langley).

References

Amiet, R. K., 1975, "Acoustic Radiation from a Airfoil in a Turbulent Stream," *Journal of Sound and Vibration*, Vol. 41, pp. 407-420.

Amiet, R. K., 1976, "Noise Produced by Turbulent Flow into a Propeller or Helicopter Rotor," AIAA Paper 76-560.

Amiet, R. K., 1989, "Noise Produced by Turbulent Flow into a Rotor: Theory Manual for Noise Calculation," NASA CR 181788.

Coffen, C. D., and George, A. R., 1990, "Analysis and Prediction of Tilt Rotor Hover Noise," *Proceedings of the 46th Annual Forum & Technology Display for the American Helicopter Society*, Washington, DC.

Coffen, C. D., George, A. R., Hardinge, H., and Stevenson, R., 1991, "Flow Visualization and Flow Field Measurements of a 1/12 Scale Tilt Rotor Aircraft in Hover," *Proceedings of the American Helicopter Society Technical Specialist' Meeting*, Philadelphia, PA.

Coffen, C. D., 1992, "Tilt Rotor Hover Aeroacoustics," Masters thesis, Department of Mechanical and Aerospace Engineering, Cornell University, Ithaca, NY; also NASA CR 177598.

Homicz, G. F., and George, A. R., 1974, "Broadband and Discrete Frequency Radiation from Subsonic Rotors," *Journal of Sound and Vibration*, Vol. 36, pp. 151-177.

George, A. R., Kim, Y. N., 1977, "High Frequency Broadband Rotor Noise," *AIAA Journal 15*, No. 11, pp. 538-545. Also AIAA Paper No. 76-561 (1976).

George, A. R., 1984, "Comparisons of Broadband Noise Mechanisms, Analyses, and Experiments on Rotors," *Journal of Aircraft*, Vol. 21, No. 8, pp. 583-592.

George, A. R., Smith, C., Maisel, M., and Brieger, J., 1989, "Tilt Rotor Aircraft Aeroacoustics," *Proceedings of the 45th Annual Forum & Technology Display of the American Helicopter Society*, Boston, MA.

George, A. R., Coffen, C. D., and Ringler, T. D., 1992, "Advances in Tilt Rotor Noise Prediction," DGLR/AIAA Paper 92-02-087. *Proceedings of the DGLR/AIAA 14th Aeroacoustics Meeting*, Achen, Germany.

Lowson, M. V., 1965, "The Sound Field of Singularities in Motion," *Proceedings of the Royal Society of London*, Series A, Vol. 286, pp. 559-572.

McVeigh, M. A., Rosenstein, H., and McHugh, F. J., 1983, "Aerodynamic Design of the XV-15 Advanced Composite Tilt Rotor Blade," *Proceedings of the 39th Annual Forum of the American Helicopter Society.*

McVeigh, M. A., Grauer, W. K., and Paisley, D. J., 1988, "Rotor/Aircraft Interactions on Tiltrotor Aircraft," *Proceedings of the 44th Annual Forum of the American Helicopter Society.*

Paisley, D. J., 1987, "Rotor Aerodynamics Optimization for High Speed Tilt Rotors," *Proceedings of the 43rd Annual Forum of the American Helicopter Society.*

Rosenstein, H., and Clark, R., 1983, "Aerodynamic Development of the V-22 Tilt Rotor," AIAA Paper No. AIAA-86-2678.

Rutledge, C. K., Coffen, C. D., and George, A. R., 1991, "A Comparative Analysis of XV-15 Tilt Rotor Hover Test Data and WOPWOP Predictions Incorporating the Fountain Effect," *Proceedings of the American Helicopter Society Technical Specialist' Meeting*, Philadelphia, PA.

Schlinker, R. H., and Amiet, R. K., 1981, "Helicopter Rotor Trailing Edge Noise," NASA CR 3470.

Sears, W. R., and Keuthe, A. M., 1939, "The Growth of the Circulation of an Airfoil Flying Through a Gust," *Journal of Aeronautical Sciences*, Vol. 6, pp. 376-378.

Sears, W. R., 1940, "Some Aspects of Non-Stationary Airfoil Theory and its Practical Application," *Journal of Aeronautical Sciences*, Vol. 8, pp. 104-108.

Simonich, J. C., Schlinker, R. H., and Amiet, R. K., 1989, "Experimental Assessment of Helicopter Rotor Turbulence Ingestion Noise in Hover," NASA CR 181792.

Von Kármán, T., and Sears, W. R., 1938, "Airfoil Theory for Non Uniform Motion," *Journal of Aeronautical Sciences*, Vol. 5, pp. 379-390.

---

[3] Rutledge et al. (1991) contains a complete description of the experimental method used to obtain the full scale acoustic measurements.

H. M. Atassi

J. Fang

S. Patrick

Aerospace and Mechanical Engineering,
University of Notre Dame,
Notre Dame, IN 46556

Direct Calculation of Sound Radiated From Bodies in Nonuniform Flows

Sound radiated from a single airfoil and a cascade of airfoils in three-dimensional gusts is directly calculated. Euler's equations are linearized about the mean flow of the airfoil or cascade. The velocity field is split into a vortical part and a potential part. The latter is governed by a single nonconstant-coefficient convective wave equation. For a single airfoil, the radiated sound is calculated using Kirchhoff's method from the mid field of the unsteady pressure obtained through the unsteady aerodynamic solver. The results indicate the importance of the contribution of the quadrupole effects to the sound field. For a cascade of airfoils, the acoustic pressure is directly obtained by solving the partial differential equation. The results show that, as the maximum Mach number on the blade surface nears unity, there is a significant rise in the local unsteady pressure, and also a significant increase in the upstream acoustic pressure.

1 Introduction

The motion of a body in a nonuniform or unsteady flow produces fluctuating forces along the body surface and radiates sound in the far field. This is, for example, what happens in the case of an aircraft wind moving into a gust (Sears, 1941), or that of a turbomachine blade row rotating in the wake of a row of guide vanes (Kemp and Sears, 1955). In the frame of reference of the body, the upstream nonuniformities are seen as convected vortical disturbances. This noise generation mechanism, known as *interaction noise*, is thus a consequence of the interaction of the body with incoming upstream nonuniformities. Interaction noise is therefore closely related to the unsteady aerodynamics of nonuniform flows since the radiated sound is, in fact, the far-field manifestation of such flows.

Until recently, interaction noise was calculated using Lighthill's acoustic analogy (Lighthill, 1952) and the Ffowcs Williams-Hawkings equation (Ffowcs Williams and Hawkings, 1969). In this approach, the unsteady pressure along the body surface is equivalent to a dipole distribution. All other effects including sound refraction by the mean flow, and sound produced by the unsteady flow surrounding the body were treated as quadrupole effects. The dipole distribution along the body surface can be obtained from measurements or from analytical or numerical solutions. The calculation of the sound resulting from the quadrupole effects requires the evaluation of volume integrals of the unsteady flow quantities. This approach has been used extensively to calculate the sound radiated from airfoils in turbulent flows (Amiet, 1976) and propeller and turbomachinery noise (Lowson, 1970; Wright, 1971; Hanson, 1980; Farassat, 1981). In these treatments, the unsteady loading on the blades is calculated from linear aerodynamic theories which assume uniform mean flow and do not, generally, account for the distortion of the incoming nonuniformities by the mean flow of the blades. This distortion was found to have a significant effect on the unsteady aerodynamic response of loaded airfoils and blades (Goldstein and Atassi, 1976; Atassi, 1984). Moreover, the radiation part of these analyses also assumes that the sound propagates in a uniform medium and thus these analyses do not fully account for the quadrupole generated sound. Atassi et al. (1993) have shown that, for an airfoil in a gust at moderate and high subsonic Mach numbers and high frequencies, the intensity of the quadrupole generated sound is significant and comparable in magnitude to that of the dipole generated sound. For loaded airfoils, Goldstein et al. (1974) and more recently Patrick et al. (1993) have shown that the quadrupole contribution to the sound field is important and strongly depends on the airfoil mean loading, the upstream mean-flow Mach number, and the gust parameters.

In order to accurately calculate the sound radiated from real lifting bodies at subsonic and transonic speeds, it is necessary to fully account for both the dipole and quadrupole contributions to the sound field. This implies that all unsteady flow quantities must be determined throughout the volume surrounding the body. However, if the unsteady flow surrounding the body is accurately known, the radiated sound can then be *directly* calculated as the far field of the unsteady flow. This would then obviate the need to use the acoustic analogy to calculate the radiated sound.

---

[1] This paper is dedicated to Professor W. R. Sears on the occasion of his 80th birthday. Professor Sears' enthusiasm for research, his profound physical insight, and his personable demeanor continue to influence the thinking and touch the lives of generations of investigators.

Contributed by the Fluids Engineering Division for publication in the JOURNAL OF FLUIDS ENGINEERING. Manuscript received by the Fluids Engineering Division April 3, 1993; revised manuscript received September 16, 1993. Associate Technical Editor: D. P. Telonis.

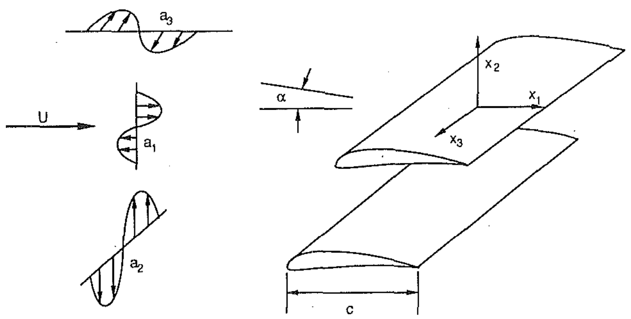

Fig. 1 Cascade of airfoils in three-dimensional gusts

In the present paper, sound is *directly* calculated for a single airfoil and for a cascade of airfoils subject to upstream three-dimensional vortical disturbances in subsonic flows. The results examine the effects of the mean-flow Mach number and incidence, the upstream gust parameters and the airfoil and cascade geometry on the sound pressure level and its directivity. For a cascade, the effect of the local Mach number as it approaches unity is also investigated. The numerical results are validated by comparison with analytical and semi-analytical solutions for a broad range of reduced frequencies and Mach numbers.

2 Mathematical Formulation

Consider an airfoil or a cascade of airfoils placed at an angle of attack α to a flow with a uniform mean upstream velocity U_∞ in the x_1 direction (Fig. 1). We further assume that an unsteady, nonuniform disturbance, $\mathbf{u}_\infty(\mathbf{x}, t)$ is imposed on the upstream flow so that the total incoming upstream velocity can be written as

$$\mathbf{V}(\mathbf{x}, t) = U_\infty \mathbf{i}_1 + \mathbf{u}_\infty(\mathbf{x}, t) \quad \text{as} \quad x_1 \to -\infty \tag{1}$$

where $\mathbf{x} = \{x_1, x_2, x_3\}$ with x_3 in the span direction.

Observation and comparison between linear and nonlinear computations (Atassi, 1994) suggest that the unsteady pressure field in attached unsteady flows is accurately described by Euler equations linearized about the mean flow of the body. We therefore assume the fluid to be inviscid and nonheat conducting with constant specific heats. Moreover, in the present paper, we consider only subsonic mean flows. The flow velocity $\mathbf{V}(\mathbf{x}, t)$, pressure $p(\mathbf{x}, t)$, density $\rho(\mathbf{x}, t)$, and entropy $s(\mathbf{x}, t)$ are then linearized about their mean values

$$\mathbf{V}(\mathbf{x}, t) = \mathbf{U}(\mathbf{x}) + \mathbf{u}(\mathbf{x}, t) \tag{2}$$

$$p(\mathbf{x}, t) = p_0(\mathbf{x}) + p'(\mathbf{x}, t) \tag{3}$$

$$\rho(\mathbf{x}, t) = \rho_0(\mathbf{x}) + \rho'(\mathbf{x}, t) \tag{4}$$

$$s(\mathbf{x}, t) = s'(\mathbf{x}, t) \tag{5}$$

The mean flow velocity $\mathbf{U}(\mathbf{x})$, pressure, $p_0(\mathbf{x})$, and density, $\rho_0(\mathbf{x})$ are calculated from steady solvers and are assumed to be known quantities. Then following Goldstein (1978) and Atassi and Grzedzinski (1989), we split the unsteady velocity into two parts

$$\mathbf{u}(\mathbf{x}, t) = \mathbf{u}^{(R)} + \nabla\phi \tag{7}$$

where the rotational velocity $\mathbf{u}^{(R)}$ satisfies the equation

$$\frac{D_0}{Dt}\mathbf{u}^{(R)} + \mathbf{u}^{(R)} \cdot \nabla \mathbf{U} = 0 \tag{8}$$

and the boundary conditions

$$\mathbf{u}^{(R)} \cdot \tau = 0 \tag{9}$$

$$\mathbf{u}^{(R)} \cdot \mathbf{n} = 0 \tag{10}$$

along the body surface Σ and its wake $\mathcal{W}$. $(D_0/Dt) \equiv \partial/\partial t + \mathbf{U} \cdot \nabla$ is the material derivative based on the mean flow, and τ and $\mathbf{n}$ represent the unit vectors tangential and normal to the body surface and its wake. The potential function ϕ satisfies the equation

$$\frac{D_0}{Dt}\left(\frac{1}{c_0^2}\frac{D_0\phi}{Dt}\right) - \frac{1}{\rho_0}\nabla\cdot(\rho_0\nabla\phi) = \frac{1}{\rho_0}\nabla\cdot(\rho_0\mathbf{u}^{(R)}) \tag{11}$$

and the boundary conditions

$$\nabla\phi \cdot \mathbf{n} = 0 \tag{12}$$

$$\Delta[\nabla\phi \cdot \mathbf{n}] = 0 \tag{13}$$

$$\nabla\phi + \mathbf{u}^{(R)} \to \mathbf{u}_\infty + \mathbf{u}_{ac} \quad \text{as} \quad x_1 \to -\infty \tag{14}$$

where $\mathbf{u}_{ac}$ is the far-field acoustic velocity which vanishes for a single airfoil but may be nonzero for a cascade. c_0 is the mean speed for sound of the fluid, and Δ denotes the jump across the wake. The analytical expression of the unsteady vortical velocity $\mathbf{u}^{(R)}$ was given by Atassi and Grzedzinski (1989) in terms of the upstream gust conditions and the Lagrangian coordinates of the mean flow. The unsteady pressure depends solely on the potential function ϕ and is given by

$$p' = -\rho_0 \frac{D_0\phi}{Dt} \tag{15}$$

We also assume that the upstream disturbance $\mathbf{u}_\infty(\mathbf{x}, t)$ can be written in terms of a Fourier integral, and we consider, without loss of generality, only one Fourier component

$$\mathbf{u}_\infty(\mathbf{x}, t) = \mathbf{a}\exp\{i[\omega t - \mathbf{k}\cdot\mathbf{x}]\} \tag{16}$$

where $\mathbf{a} = \{a_1, a_2, a_3\}$ is the magnitude of the disturbance, $\mathbf{k} = \{k_1, k_2, k_3\}$ is the wave number vector, and ω is the frequency. We nondimensionalize all lengths with respect to half of the airfoil chord length c, and all velocities with respect to the mean flow upstream velocity U_∞. The reduced frequency is then defined as $k_1 = (\omega c)/(2U_\infty)$.

In order to obtain numerical solutions for the boundary-value problem defined by Eqs. (11)–(14), the boundary condition at infinity must be replaced by a radiation condition at the outer boundary of the computational domain. Scott and Atassi (1990) and Fang and Atassi (1993a) have developed suitable outflow boundary conditions for a single airfoil and for a cascade of airfoils, respectively. They use the approximation that the outer computational boundaries are located far enough from the body so that the mean flow quantities are constant along and outside the computational domain. The governing Eq. (11) then reduces to a constant-coefficient, convective wave equation. However, because of the discontinuity of the potential function ϕ along the wake lines, these conditions are formulated in terms of the unsteady pressure p' which satisfies the equation

$$\frac{1}{c_0^2}\frac{D_0^2 p'}{Dt^2} - \nabla^2 p' = 0 \tag{17}$$

outside the computational domain. For a single airfoil, Eq. (17) is further simplified using the Sommerfeld radiation condition. For a cascade of airfoils, p' is expanded in terms of plane waves

$$p' = \sum_{n=-\infty}^{\infty} c_{n+}p'_{n+} + \sum_{n=-\infty}^{\infty} c_{n-}p'_{n-}, \tag{18}$$

where $c_{n_\pm}$ are complex constants and $p'_{n_\pm}$ have the general form

$$p'_{n_\pm} = e^{i[\omega t - \mathbf{k}_{n_\pm}\cdot\mathbf{x}]}, \tag{19}$$

where $\mathbf{k}_{n_\pm}$ are complex acoustic wave numbers. This outflow condition accounts for all propagating and decaying modes. Substituting this expansion into Eq. (17) and introducing the cascade quasi-periodicity conditions show that $\mathbf{k}_{n_\pm}$ represent an unsteady pressure field with the following far field characteristics: (i) an exponentially decaying field, (ii) an exponential amplifying field, (iii) constant amplitude waves propagating away from the row of the blades, or (iv) constant amplitude waves propagating toward the cascade. Those nonwave type terms whose amplitudes amplify exponentially in the far field are physically not acceptable. For a gust problem without far-field acoustic sources, those terms which represent inward propagating waves are also to be eliminated. Consequently, p' on the boundary can be constructed as a sum of all decaying terms (i) and propagating waves (iii).

It should be pointed out that the decaying terms (i) must be considered for accurate sound prediction especially when the sound level is low. Moreover, since multi-mode acoustic radiations may occur in the far field, it is necessary to consider all possible acoustic modes.

3 Numerical Scheme

The boundary-value problem for ϕ defined by Eqs. (11)–(14) and (16) is solved for two-dimensional body geometries. In this case, it is possible to factor out the dependence on t and x_3, and introduce the new function

$$\psi(x_1, x_2) = \phi e^{-i(\omega t - k_3 x_3)} \tag{20}$$

Substituting Eq. (20) into (11), we obtain a second order partial differential equation for $\psi(x_1, x_2)$. This equation is solved numerically using a second order finite difference scheme as outlined in Scott and Atassi (1990) and Fang and Atassi (1993).

The far-field calculations are, however, different for the single airfoil and the cascade.

3.1 Single Airfoil. A numerical code, Gust3D, was developed by Scott and Atassi (1990) for calculating the unsteady flow quantities in the field surrounding an airfoil in a subsonic flow with imposed upstream vortical disturbance. The code calculates the solution to the nonconstant-coefficient, inhomogeneous, convective wave Eq. (11) in the frequency domain. Because of the loss of accuracy in the far field of the computational domain, the unsteady quantities in this region cannot be used when calculating the unsteady acoustic pressure. Instead, Kirchhoff's method is used to obtain the far-field pressure. This takes advantage of the accuracy of the solution in the near and mid-field regions, by using the unsteady quantities on a Kirchhoff surface, located in these regions. Outside the Kirchhoff surface the unsteady pressure is governed by Eq. (17). Factoring out the dependence on time and the third spatial component, transforming to the Prandtl-Glauert coordinates, and following a transformation introduced by Reissner (1951):

$$\tilde{P} = p' e^{-i(k_1 t - k_3 x_3 + M K_1 x_1)} \tag{21}$$

where

$$K_1 = \frac{k_1 M_\infty}{\beta_\infty^2} \tag{22}$$

the governing equation reduces to the two-dimensional Helmholtz equation in the Prandtl-Glauert plane for $\tilde{P}$

$$(\tilde{\nabla}^2 + K^2)\tilde{P}(\tilde{x}_1, \tilde{x}_2) = 0 \tag{23}$$

where the tilde denotes Prandtl-Glauert coordinates and

$$K^2 = \frac{k_1^2 M_\infty^2}{\beta_\infty^4} - \frac{k_3^2}{\beta_\infty^2} \tag{24}$$

Green's theorem gives the value of $\tilde{P}$ in the far field based on the value of $\tilde{P}$ on the Kirchhoff surface.

$$\tilde{P}(\tilde{\mathbf{x}}) = \frac{1}{2\pi}\int_\Sigma \left[\tilde{P}(\tilde{\mathbf{y}}) \frac{\partial G_f}{\partial n}(\tilde{\mathbf{y}} \mid \tilde{\mathbf{x}}) - G_f(\tilde{\mathbf{y}} \mid \tilde{\mathbf{x}}) \frac{\partial \tilde{P}}{\partial n}(\tilde{\mathbf{y}}) \right] d\Sigma \tag{25}$$

where $\tilde{\mathbf{y}}$ is the source point, $\tilde{\mathbf{x}}$ is the observation point, s is the Kirchhoff surface, $\mathbf{n}$ is the outward normal to the surface and

$$G_f(\tilde{\mathbf{y}} \mid \tilde{\mathbf{x}}) = -\frac{i\pi}{2} H_0^{(2)}(KR), \quad R = |\tilde{\mathbf{y}} - \tilde{\mathbf{x}}| \tag{26}$$

Two numerical derivatives must be performed to calculate $\partial\tilde{P}/\partial n$. This results in large inaccuracies in the calculation of $\tilde{P}$. To avoid this difficulty, a modified Green's function is determined which is identically zero along the Kirchhoff surface. The new Green's function is

$$G(\tilde{\mathbf{y}} \mid \tilde{\mathbf{x}}) = G_f(\tilde{\mathbf{y}} \mid \tilde{\mathbf{x}}) + \sum_{m=0}^{N} H_m^{(2)}(K r_k) a_m \cos[m(\theta_y - \theta_x)] \tag{27}$$

where

$$a_0 = -\frac{1}{2\pi H_0^{(2)}(K r_k)} \int_0^{2\pi} G_f(\tilde{\mathbf{y}} \mid \tilde{\mathbf{x}}) d(\theta_y - \theta_x), \tag{28}$$

$$a_m = -\frac{1}{\pi H_m^{(2)}(K r_k)} \times \int_0^{2\pi} G_f(\tilde{\mathbf{y}} \mid \tilde{\mathbf{x}}) \cos[m(\theta_y - \theta_x)] d(\theta_y - \theta_x) \tag{29}$$

and $r_k = |\tilde{\mathbf{y}}|$, or the radius of the Kirchhoff surface. So the far-field values of $\tilde{P}$ are given simply by

$$\tilde{P}(\tilde{\mathbf{x}}) = \frac{1}{2\pi}\int_\Sigma \left[\tilde{P}(\tilde{\mathbf{y}}) \frac{\partial G}{\partial n}(\tilde{\mathbf{y}} \mid \tilde{\mathbf{x}}) \right] d\Sigma \tag{30}$$

Details are given in Patrick (1993).

3.2 Cascade of Airfoils. For a cascade of airfoils, a computer code, CASGUST, was developed to calculate the entire unsteady pressure field and the sound simultaneously. Special efforts are made to ensure the far-field accuracy. As a result, the sound is obtained directly from the far field of the unsteady pressure without the use of Kirchhoff's method.

The calculation is based on a nonorthogonal, body-fitted, H-mesh for a single extended cascade passage. The grid system consists of mean flow streamlines and a family of straight lines parallel to the cascade stagger. The number of grid points used in the present work is 80 × 169.

It is known that the dispersive and dissipative effects due to numerical discretizations can severely distort the pressure field in acoustic calculations as the pressure waves propagate through the grid of numerical computation. Since the out-flow condition being used is an *exact* condition that requires an accurate match between the near field and the far field, the distortion of the pressure in the entire field is minimized.

Since the error is cumulative in the grid system, it is more advantageous to employ a relatively small computational domain from upstream to downstream. On the other hand, in order to use the plane wave expansion in the out-flow boundary, the domain must be large enough so that the out-flow boundary mean flow is approximately uniform. For typical cascade configurations, our numerical experience shows that a computational domain extending one half chord from the blade to the out-flow boundary is adequate.

In order to resolve the acoustic waves numerically, a certain number of grid points per wave length is needed. This is particularly important for sound calculations with high reduced frequencies. Our experience shows that in general 15 grid points per wave length is the minimum required. If the coefficients and the source term of the governing equation are calculated using the same grid system, which is not necessary but convenient, this grid system must be able to resolve not only the acoustic waves but also the incoming gust vortical wave which, in general, has a different wave length from the acoustic waves. Moreover, the acoustic waves may include a number of modes

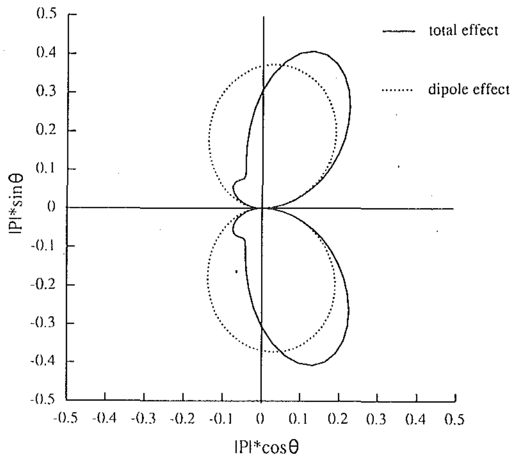

Fig. 2 Pressure directivity for a symmetric airfoil with a thickness ratio 6 percent, $M_\infty = 0.6$, $k_1 = 2.0$

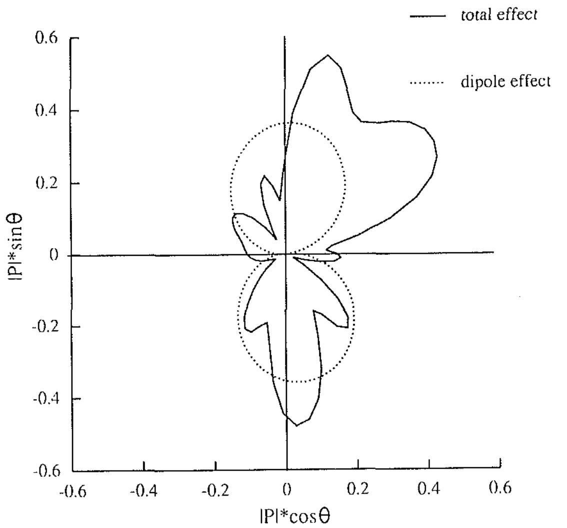

Fig. 3 Pressure directivity for a 4 percent cambered airfoil with a thickness ratio 6 percent, $M_\infty = 0.6$, $k_1 = 2.0$

with different wave numbers. In general, the upstream propagating modes have smaller wave lengths than downstream propagating modes. Note that as the local Mach number approaches unity, the wave lengths of the upstream propagating modes become very small while that of downstream propagating modes become larger. For high harmonic modes, the wave number in the stagger line direction is proportional to the harmonic number.

4 Results and Discussion

In what follows, the unsteady pressure and the unsteady lift coefficients are defined by

$$P = \frac{p'}{\rho_\infty U_\infty a_2 e^{i\omega t} e^{-ik_3x_3}} \tag{31}$$

$$C_L = \frac{L}{\pi \rho_\infty c U_\infty a_2 e^{i\omega t} e^{-ik_3x_3}} \tag{32}$$

where p' is the aerodynamic pressure and L is the aerodynamic lift.

4.1 Single Airfoil. The results of the investigation into the sound radiated from a single airfoil in a nonuniform subsonic flow all reinforce the importance of including the quadrupole terms as the Mach number, reduced frequency, or mean-flow loading increases.

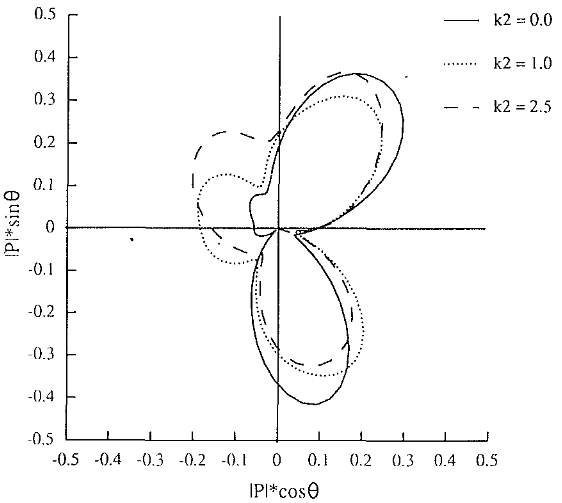

Fig. 4 Total pressure directivity for a 2 percent cambered airfoil with a thickness ratio 12 percent, $M_\infty = 0.5$, $k_1 = 2.5$ and varying k_2

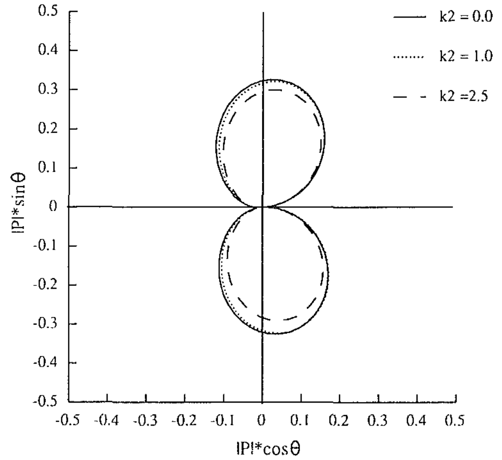

Fig. 5 Dipole pressure directivity for a 2 percent cambered airfoil with a thickness ratio 12 percent, $M_\infty = 0.5$, $k_1 = 2.5$ and varying k_2

Figure 2 compares the total sound directivity pattern and the dipole sound directivity pattern for a simple symmetric, 6 percent thick airfoil at zero angle of attack in a flow with upstream Mach number 0.6 and a transverse gust with reduced frequency 2.0. The quadrupole contribution to the radiated sound is seen as the difference between the two plots. This indicates that the development of lobes in the directivity pattern as quadrupole effects rather than noncompact source effects.

Figure 3 shows the quadrupole effects for the sound radiated from an airfoil with mean loading. The same flow conditions as for Fig. 2 are used, but here the airfoil has 4 percent camber and 6 percent thickness ratio. The dipole pattern is smooth. However, a non-symmetric, multi-lobe pattern appears in the total directivity and is entirely due to quadrupole effects.

The effect of a two-dimensional gust with transverse and longitudinal components is shown in Figs. 4 and 5. The figures show the total directivity and dipole directivity, respectively, for a 2 percent cambered, 12 percent thick airfoil, with a free-stream Mach number of 0.5. The gust reduced frequency is 2.5 and the longitudinal wave number of the gust, k_2, is varied from 0 to 2.5. As k_2 increases, the sound level in the upstream direction increases. The increase is not seen in the dipole radiation and is a result of including the quadrupole effects.

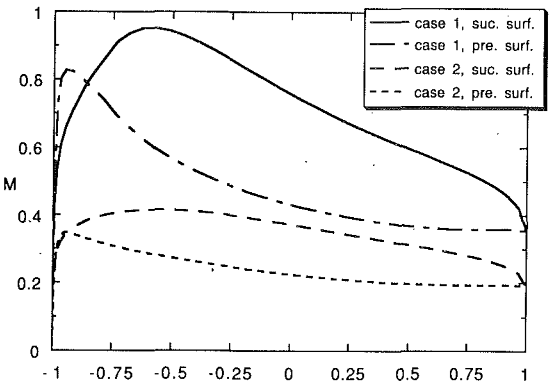

Fig. 6 Distribution of Mach number on the blade surface

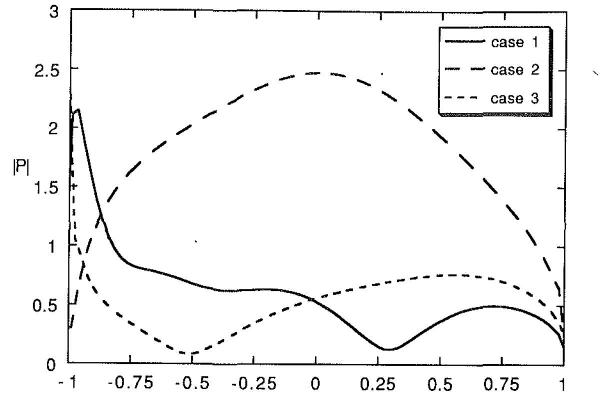

Fig. 8 Magnitude of the unsteady pressure on the blade pressure surface

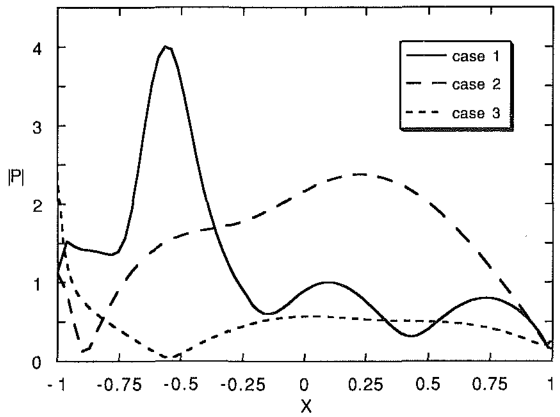

Fig. 7 Magnitude of the unsteady pressure on the blade suction surface

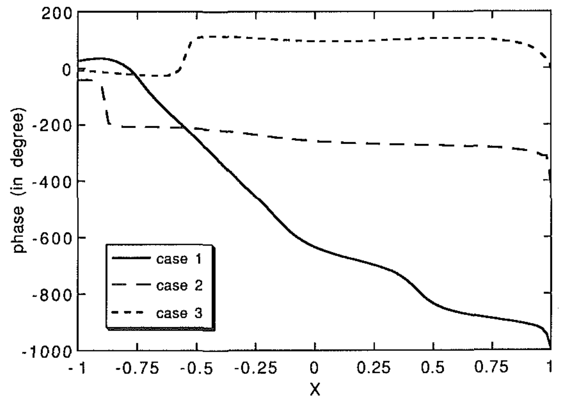

Fig. 9 Phase of the unsteady pressure on the blade suction surface

These results reinforce the importance of the quadrupole effects on the radiated sound.

4.3 Cascade of Airfoils. CASGUST was validated in an earlier work by Fang and Atassi (1993b) by comparison with semi-analytical solutions (Ventres, 1980) for flat plate cascades. For a large range of reduced frequencies, 0 to 30, the agreement between the two codes is excellent.

In the present work, we have examined the effects of the mean-flow Mach number and the upstream gust parameters on both the unsteady pressure on the blades surface and the far-field radiated sound for a loaded cascade. To this end, we have considered an exit guide vane (EGV) cascade operating at high-subsonic (case 1) and low-subsonic (case 2) conditions. The results are compared with that of an unloaded flat-plate cascade (case 3) with the same upstream mean-flow condition as case 1. The blade of EGV has a thickness distribution of a NACA0012 airfoil on a circular arc camber line with height at midchord of 13 percent of the chord. The cascade spacing is $s/c=0.6$ and stagger $\chi=15$ deg. The inlet flow angle is 40 deg. For case 1, the upstream mean flow Mach number $M_\infty=0.6$, the maximum Mach number $M_{\max}=0.952$ occurs at $x=-0.57$ on the blade suction surface. For case 2, $M_\infty=0.3$ and $M_{\max}=0.415$ occurs at $x=-0.57$ on the suction surface. The distribution of the mean-flow Mach number on the blade surface is plotted in Fig. 6. For case 3, the cascade spacing is the same as for case 1 and the stagger is $\chi=40$ deg. The upstream vortical disturbances for all cases are transverse gusts with the reduced frequency k_1 varying from 0 to 10.

For $k_1=4$, the entire unsteady pressure field is calculated for cases 1, 2 and 3. The magnitudes of the unsteady pressure on both the blade suction and pressure surfaces are plotted in Figs. 7 and 8, respectively. For case 1 the magnitude possesses a sharp peak where the total mean-flow Mach number approaches its maximum value, close to unity. The peak value is 6 times larger than that for a flat plate cascade at the same upstream Mach number. Similarly, on the pressure-surface for case 1, the magnitude of the unsteady pressure increases rapidly where the local Mach number becomes large near the leading edge. The peak value on the pressure surface, however, is smaller than that on the suction-surface because of the smaller $M_{\max}$. We conjecture that this sharp rise in the magnitude of the unsteady pressure is due to the near-sonic local flow condition. The near-sonic velocity acts as a barrier preventing the acoustic waves from propagating upstream. For cases 2 and 3, the local Mach numbers are well below unity and there is no rapid change in the magnitude of the unsteady pressure except at the leading edge.

The phases of the unsteady pressure on the blade surface for cases 1, 2 and 3 are shown in Figs. 9 and 10 for the suction surface and the pressure surface, respectively. The phase for case 1 on the suction surface possesses a much larger total variation than that of cases 2 and 3.

The magnitudes of the unsteady lift coefficients C_L are shown in Fig. 11 for cases 1 and 3. For low reduced frequency, the magnitude of the unsteady lift for case 1 is smaller than that of an unloaded flat plate cascade. It is also shown that the unsteady lift is sensitive to the acoustic cut-on/off phenomena which occur at $k_1=2.9$, 5.8, and 8.6 upstream, and 4.4 and 8.8 downstream for case 1.

Figures 12, 13, and 14 show the magnitude of the first, second and third acoustic modes upstream for cases 1 and 3, respectively. On the upstream, the first mode cuts on at $k_1=2.9$,

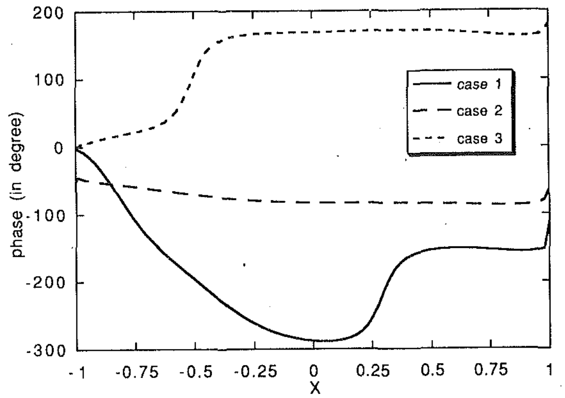

Fig. 10 Phase of the unsteady pressure on the blade pressure surface

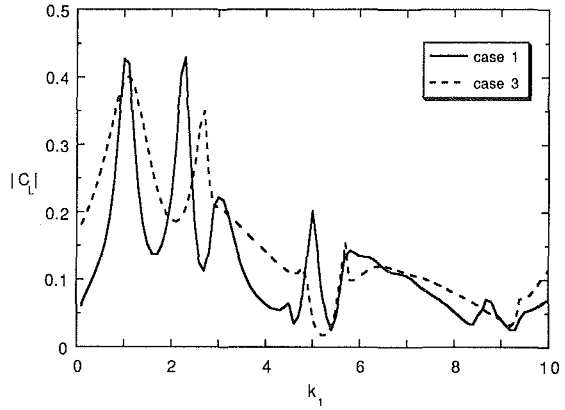

Fig. 11 Magnitude of the unsteady lift coefficient

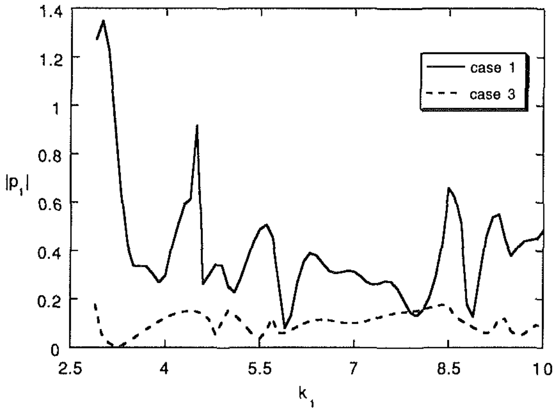

Fig. 12 Magnitude of the first acoustic mode upstream for case 1, compared with that of case 3

the second mode at $k_1 = 5.8$, and the third mode at $k_1 = 8.6$. These cut-on frequencies are the same for both cases 1 and 3 because they have identical upstream flow conditions.

The magnitude of these modes for case 1 is significantly larger than that of case 3. It can be shown by unsteady pressure field animation that the large-magnitude pressure waves, that are generated in the region near to the suction surface where the mean flow is close to sonic condition, propagate toward the upstream rather than the downstream. Since the magnitude of the unsteady pressure is significantly larger as the mean flow on the blade suction surface nears sonic condition, the magnitudes of the upstream acoustic modes can be significantly larger than that of a corresponding unloaded flat plate cascade at the same upstream mean flow Mach number.

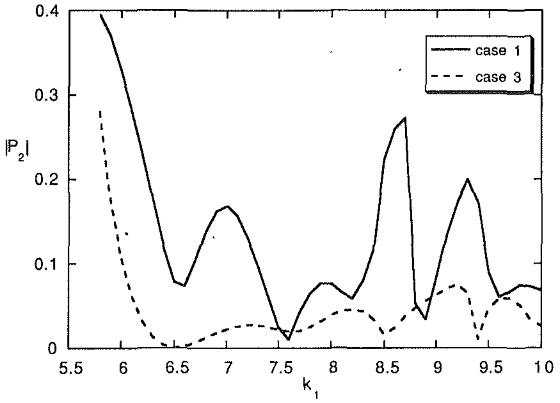

Fig. 13 Magnitude of the second acoustic mode upstream for case 1, compared with that of case 3

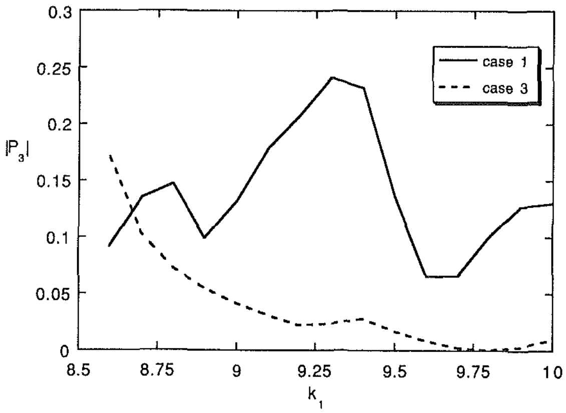

Fig. 14 Magnitude of the third acoustic mode upstream for case 1, compared with that of case 3

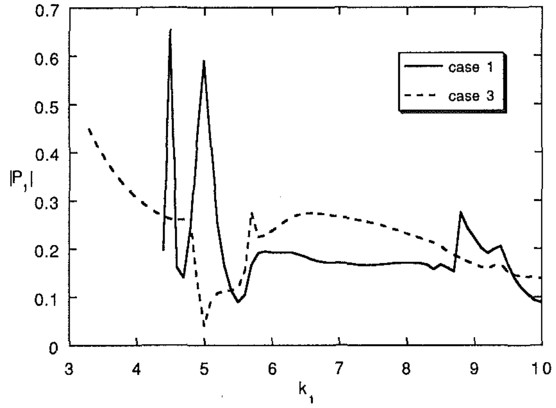

Fig. 15 Magnitude of the first acoustic mode downstream for case 1, compared with that of case 3

Figures 15 and 16 show the magnitudes of the first and the second acoustic modes downstream for cases 1 and 3. For case 1, the cut-on frequencies are $k_1 = 4.4$ for the first mode and $k_1 = 8.8$ for the second mode. The third mode does not cut on in this range of the reduced frequency. These cut-on frequencies are higher than that for case 3, where the first mode cuts on at $k_1 = 3.3$, the second mode at $k_1 = 6.5$ and the third mode at $k_1 = 9.7$. This difference is due to the modification of the downstream mean flow by the mean blade loading, namely, the lower Mach number and the different mean flow direction in the downstream.

Although the cut-on frequencies are modified for case 1

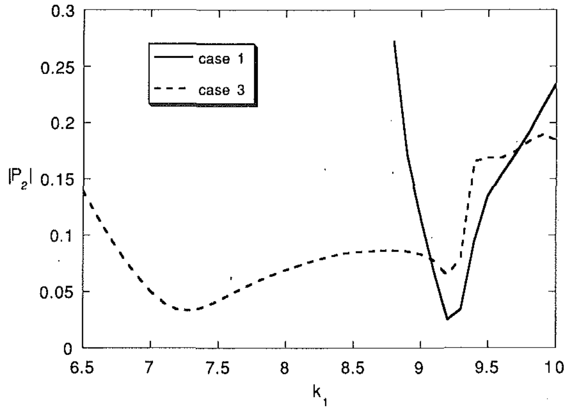

Fig. 16 Magnitude of the second acoustic mode downstream for case 1, compared with that of case 3

downstream, the difference in the magnitude of the acoustic modes between cases 1 and 3 are, in general, less significant on the downstream than that on the upstream. However, for a small range of reduced frequencies close to the cut-on frequencies, the difference in the magnitude of the acoustic modes becomes relatively large.

5 Conclusions

Direct methods for the calculation of sound radiated from a single airfoil and a cascade of airfoils subject to three-dimensional vortical disturbances are developed. For a single airfoil, the radiated sound is calculated from the unsteady pressure mid-field using the Kirchhoff's method. For a cascade of airfoils, the radiated sound and the entire unsteady pressure field are calculated simultaneously.

The study of the radiated sound field from a single airfoil in a gust indicates that the dipole contribution alone does not completely describe the sound field. Refraction by the mean flow and the sound radiated by the unsteady flow surrounding the airfoil must be included for high Mach numbers, high reduced frequencies and loaded airfoils.

The unsteady pressure field and radiated sound are studied for cascades of loaded airfoils operating in high- and low-subsonic mean flows. This study shows that as local mean-flow Mach number approaches unity, the magnitude of local unsteady pressure rises significantly. This generates unsteady pressure waves propagating upstream with large magnitude and small wave length. As a result, the radiated sound level upstream of the cascade rises significantly.

Acknowledgments

This work is supported by NASA Lewis Research Center under grant NAG 3-732. The authors would like to thank Dennis Huff of NASA Lewis Research Center for his support and assistance.

References

Amiet, R. K., 1976, "High Frequency Thin-Airfoil Theory for Subsonic Flow," *AIAA Journal*, Vol. 14, No. 8, pp. 1076–1082.

Atassi, H. M., 1984, "The Sears Problem for Lifting Airfoil Revisited-New Results," *Journal of Fluid Mechanics*, Vol. 141, pp. 109–122.

Atassi, H. M., 1994, *Aerodynamics and Aeroacoustics*, K. Y. Fung, ed., World Scientific, pp. 119–169.

Atassi, H. M., and Grzedzinski, J., 1989, "Unsteady Disturbances of Streaming Motions Around Bodies," *Journal of Fluid Mechanics*, Vol. 209, pp. 385–403.

Atassi, H. M., Dusey, M., and Davis, C. M., 1993, "Acoustic Radiation from a Thin Airfoil in Nonuniform Subsonic Flows," *AIAA Journal*, Vol. 31, No. 1, pp. 12–19.

Fang, J., and Atassi, H. M., 1993a, "Compressible Flows with Vortical Disturbances Around a Cascade of Loaded Airfoils," *Unsteady Aerodynamics, Aeroacoustics and Aeroelasticity of Turbomachines and Propellers*, H. M. Atassi, ed., Springer-Verlaga, pp. 149–176.

Fang, J., and Atassi, H. M., 1993b, "Direct Calculation of Sound Radiated from a Loaded Cascade in a Gust," *Computational Aero- and Hydro-Acoustics*, ASME FED-Vol. 147, pp. 111–116.

Farassat, F., 1981, "Linear Acoustic Formulas for Calculation of Rotating Blade Noise," *AIAA Journal*, Vol. 19, No. 9, pp. 1122–1130.

Ffowcs William, J. E., and Hawkings, D. L., 1969, "Sound Generated by Turbulence and Surfaces in Arbitrary Motion," *Philosophical Transactions of the Royal Society*, Vol. 264A, pp. 321–342.

Goldstein, M. E., 1978, "Unsteady Vortical and Entropic Distortions of Potential Flows Round Arbitrary Obstacles," *Journal of Fluid Mechanics*, Vol. 89, Part 3, pp. 433–468.

Goldstein, M. E., and Atassi, H. M., 1976, "A Complete Second-Order Theory for the Unsteady Flow about an Airfoil Due to a Periodic Gust," *Journal of Fluid Mechanics*, Vol. 74, pp. 741–765.

Goldstein, M. E., Dittmar, J. H., and Gelder, T. F., 1974, "Combined Quadrupole-Dipole Model for Inlet Flow Distortion Noise," NASA TN D-7676.

Hanson, D. B., 1980, "Helicoidal Surface Theory for Harmonic Noise of Propellers in the Far Field," *AIAA Journal*, Vol. 18, No. 10, pp. 1213–1220.

Kemp, N., and Sears, W. R., 1955, "The Unsteady Forces Due to Viscous Wakes in Turbomachines," *Journal of Aeronautical Sciences*, Vol. 22, No. 7, pp. 478–483.

Lighthill, J. M., 1952, "On Sound Generated Aerodynamically. I. General Theory," *Proceedings of the Royal Society of London*, Series A, Vol. 211A, pp. 564–487.

Lowson, M. V., 1970, "Theoretical Studies of Compressor Noise," *Journal of the Acoustical Soceity of America*, Vol. 47, pp. 371–185.

Patrick, S. M., Davis, C. M., and Atassi, H. M., 1993, "Acoustic Radiation from a Lifting Airfoil in Nonuniform Subsonic Flow," *ASME Computational Aero- and Hydro-Acoustics*, Vol. 147, pp. 41–46.

Reissner, E., 1951, "On the Application of Mathieu Functions in the Theory of Subsonic Compressible Flow Past Oscillating Airfoils," NACA-TN-2363.

Scott, J. R., 1991, "Compressible Flow with Periodic Vortical Disturbances Around Lifting Airfoils," NASA Technical Memorandum, 103742.

Scott, J. R., and Atassi, H. M., 1990, "A Finite-Difference, Frequency-Domain Numerical Scheme for the Solution of the Linearized Unsteady Euler Equations," *Computational Fluid Dynamics Symposium on Aeropropulsion*, NASA Conference Publication 3078, pp. 55–104.

Sears, W. R., 1941, "Some Aspects of Non-Stationary Airfoil Theory and Its Practical Application," *Journal of the Aeronautical Sciences*, Vol. 8, No. 3, pp. 104–108.

Ventres, C. S., 1980, "Nonsteady Compressible Aerodynamics Code for Linear Cascades," NASA Lewis Technic Memorandum.

Wright, S. E., 1971, "Discrete Radiation from Rotating Periodic Sources," *Journal of Sound and Vibration*, Vol. 17, No. 4, pp. 437–498.

Response of a Thin Airfoil Encountering a Strong Density Discontinuity[1]

F. E. Marble
California Institute of Technology,
Karman Laboratory of Fluid Mechanics
and Jet Propulsion,
Pasadena, CA 91125

Airfoil theory for unsteady motion has been developed extensively assuming the undisturbed medium to be of uniform density, a restriction accurate for motion in the atmosphere, Glauert (1929), Burgers (1935), Theodorsen (1935), Kussner (1936), Karman and Sears (1938), Kinney and Sears (1975). In some instances, notably for airfoils comprising fan, compressor and turbine blade rows, the undisturbed medium may carry density variations or "spots," resulting from non-uniformaties in temperature or composition, of a size comparable to the blade chord. This condition exists for turbine blades, Marble (1975), Giles and Krouthen (1988), immediately downstream of the main burner of a gas turbine engine where the density fluctuations of the order of 50 percent may occur. Disturbances of a somewhat smaller magnitude arise from the ingestion of hot boundary layers into fans, Wortman (1975), and exhaust into hovercraft. Because these regions of non-uniform density convect with the moving medium, the airfoil experiences a time varying load and moment which we propose to calculate.

1 Introduction

If the fluid is treated as incompressible and the velocity disturbances, caused by the shape and attitude of the airfoil, are small in comparison with the uniform free stream velocity U, then the density field, assumed known at some time, is given as $\rho(\xi - Ut, \eta)$. The complicating feature of the problem arises from the vorticity $\bar{\omega}$ generated by the interaction of the convected density field with the pressure field generated by the airfoil. For a continuous distribution of density, this vorticity satisfies the linearized relation.

$$\left(\frac{\partial}{\partial t}+U\frac{\partial}{\partial \xi}\right)\bar{\omega}=\frac{1}{\rho^2}\,\text{grad}\,p\times\text{grad}\,\rho \tag{1}$$

Therefore, if grad ρ is large (of zeroth order), the vorticity $\bar{\omega}$ is of the same mathematical order as the pressure field of the airfoil and hence of size comparable to that distributed on the airfoil camber line. Clearly, then, solution of the thin airfoil problem involves determination of the unknown field vorticity as well as the unknown vorticity shed from the trailing edge as a result of the unsteady motion. Note that in this problem, in contrast with the conventional problem of kinematically unsteady airfoils, the time dependence arises solely from the convection of the non-uniform density fluid past the airfoil. We may note also that when the density field is of perturbation order but the pressure field is of zeroth order, a related problem arises which has been examined by Marble and Candel (1977) in a particular context, and by Goldstein (1978) under more general circumstances.

The case that will be examined in this paper is the response of a plane lifting airfoil to the passage of a strong density discontinuity normal to the direction of uniform motion of the main stream. In this circumstance a vortex sheet is formed on the density discontinuity where it is generated at a rate proportional to the pressure gradient, produced by the airfoil, along the density discontinuity. The problem will be formulated through representing the lifting plane airfoil as a sheet of vortex elements whose distribution is determined to satisfy the boundary conditions on the airfoil in the presence of (*i*) the vortex sheet shed form the trailing edge of the airfoil and (*ii*) the vorticity generated in free stream by nonuniform density. Thus it will use techniques familiar from conventional formulation of thin airfoil theory but, because of the non-uniform density field, will require the introduction of some novel features.

One of these concerns the linearized field generated by a single vortex element in the presence of a strong plane density discontinuity convected by a uniform free stream of velocity U parallel to the horizontal axis. A very convenient representation of this field, believed to be new, is presented which greatly simplifies determination of the vorticity distribution on the airfoil.

The determination of the distribution of wake vorticity introduces a second novel issue because, as the density jump passes over the airfoil, Kelvin's theorem may not be applied in the usual fashion. However through considering the local impulsive generation of airfoil loading, Burgers (1935), Karman and Sears (1938), it is shown that the relationship between

---

[1] Dedicated to Professor W. R Sears on the occasion of his 80th birthday.

Contributed by the Fluids Engineering Division for publication in the JOURNAL OF FLUIDS ENGINEERING. Manuscript received by the Fluids Engineering Division June 29, 193; revised manuscript received September 23, 1993. Associate Technical Editor: D. P. Telionis.

airfoil circulation and shed vorticity may be indeed be represented in a form identical with that for an airfoil in a uniform density field.

2 Vortex Element Near a Moving Density Jump

When the fluid is uniform, an element of vorticity $\gamma(\xi_1)\, d\xi_1$, where $\gamma(\xi_1)$ is the vorticity distribution on the airfoil, has a complex potential

$$w_0(\zeta, t) = \frac{i\gamma(\xi_1, t)d\xi_1}{2\pi} \ln(\zeta - \xi_1) \tag{2}$$

where $\zeta = \xi + i\eta$ is the complex variable in the airfoil plane and ξ_1 is the coordinate of the vorticity element. When, however, the flow has a density jump from ρ_1 on the right to ρ_2 on the left, Fig. 1, the potential of the field has a discontinuity at $\xi = \lambda(t)$ but is regular on either side of this discontinuity. Therefore the actual field of the vorticity element requires the addition of a potential $w_1(\zeta, t)$ for $\xi > \lambda$ and a potential $w_2(\zeta, t)$ for $\xi < \lambda$. These potentials must vanish in the far field, produce equal values of $u(\lambda, \eta)$, the ξ-velocity component at $\xi = \lambda$, and equal values of the perturbation pressure on either side of the discontinuity, $p_1(\lambda, \eta) = p_2(\lambda, \eta)$. These pressure perturbations are related to the potentials through the Bernoulli integral,

$$\frac{\partial \varphi_i}{\partial t} + U\left(\frac{\partial \varphi_o}{\partial \xi} + \frac{\partial \varphi_i}{\partial \xi}\right) = \frac{p_i}{\rho_i}$$

and the condition to be satisfied at $\xi = \lambda(t)$ is

$$\rho_1\left(\frac{\partial \varphi_1}{\partial t} + U\frac{\partial \varphi_1}{\partial \xi}\right) - \rho_2\left(\frac{\partial \varphi_2}{\partial t} + U\frac{\partial \varphi_2}{\partial \xi}\right) = -(\rho_1 - \rho_2)\left(\frac{\partial \varphi_0}{\partial t} + U\frac{\partial \varphi_0}{\partial \xi}\right) \tag{3}$$

In satisfying this condition it must be kept in mind (*i*) that the potentials depend upon $\lambda(t)$ and that $d\lambda/dt = U$, and (*ii*) that the strength of the vorticity elements representing the airfoil will depend upon time because of the unsteady flow field.

The supplementary potentials w_1 and w_2 are analytic in the entire ζ-plane although in each case only a portion of the field is used to describe the physical solution. These potentials, see Appendix, have the nature of partial images of the actual vortex element and are, in fact

$$w_1(\zeta, t) = \frac{i\gamma(\xi_1, t)d\xi_1}{2\pi}\left(\frac{\rho_1 - \rho_2}{\rho_1 + \rho_2}\right) \ln((\zeta - \lambda) + (\xi_1 - \lambda)) \tag{4}$$

$$w_2(\zeta, t) = \frac{i\gamma(\xi_1, t)d\xi_1}{2\pi}\left(\frac{\rho_1 - \rho_2}{\rho_1 + \rho_2}\right) \ln((\zeta - \lambda) - (\xi_1 - \lambda)) \tag{5}$$

which hold for $\xi > \lambda$, the situation shown in Fig. 1. Specifically for $\xi < \lambda$, the complex potential $w_0 + w_1$ consists of the actual vortex element plus a vortex at the image point with strength $(\rho_1 - \rho_2)/(\rho_1 + \rho_2)$ times that of the original. On the other hand, when $\xi_1 < \lambda$ the complex potential $w_0 + w_2$ consists of the original vortex plus a coincident vortex of strength $(\rho_1 - \rho_2)/(\rho_1 + \rho_2)$ times that of the original.

When the density jump has moved downstream of the vortex element, $\lambda > \xi_1$, the corresponding supplementary potentials are

$$w_1(\zeta, t) = \frac{i\gamma(\xi_1, t)d\xi_1}{2\pi}\left(\frac{\rho_1 - \rho_2}{\rho_1 + \rho_2}\right) \ln((\zeta - \lambda) - (\xi_1 - \lambda)) \tag{6}$$

$$w_2(\zeta, t) = \frac{i\gamma(\xi_1, t)d\xi_1}{2\pi}\left(\frac{\rho_1 - \rho_2}{\rho_1 + \rho_2}\right) \ln((\zeta - \lambda) + (\xi_1 - \lambda)) \tag{7}$$

The complementary potentials, Eqs. (4), (5), allow calculation of the vorticity distribution on the discontinuity.

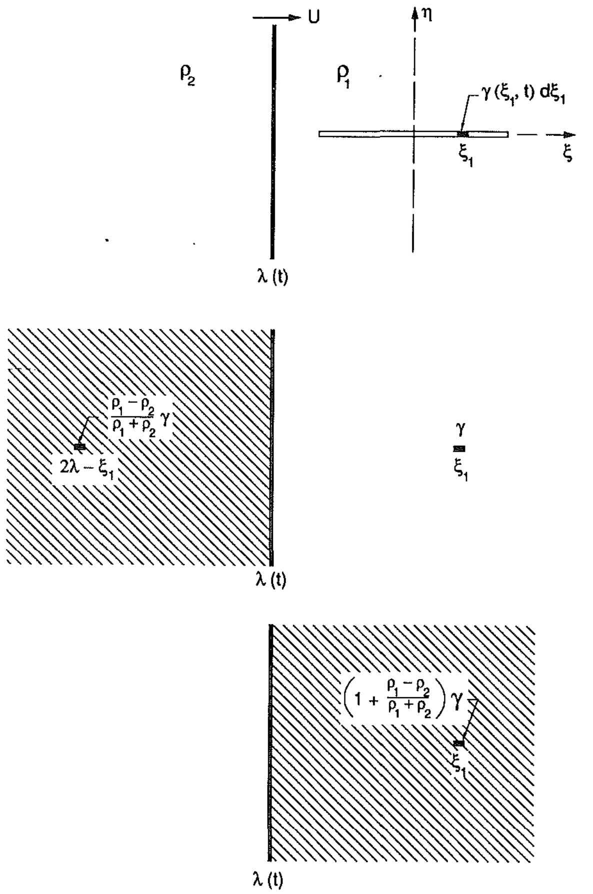

Fig. 1 Construction of flow field induced by a vortex near a convecting density jump

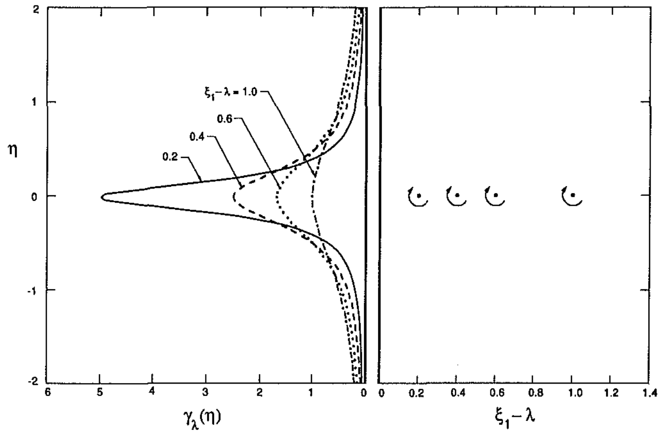

Fig. 2 Vorticity induced on density discontinuity by airfoil vortex element at various positions

$$\gamma_\lambda(\eta) = -v(\lambda_+, \eta) + v(\lambda_-, \eta) = \Im \frac{d}{d\zeta}(w_1 - w_2)_{\xi = \lambda} \tag{8}$$

When the density jump is upstream of the vorticity element, $\lambda < \xi_1$, we find

$$\lambda_\lambda(\eta) = \frac{\gamma(\xi_1, t)d\xi_1}{\pi}\left(\frac{\rho_1 - \rho_2}{\rho_1 + \rho_2}\right)\frac{\xi_1 - \lambda}{(\xi_1 - \lambda)^2 + \eta^2} \tag{9}$$

and this vorticity distribution is shown in Fig. 2 for several relative locations of the density jump and the vorticity element. As the density jump convects towards the vorticity element $\gamma(\xi_1, r)$, the vorticity distribution $\lambda_\lambda(\eta)$ concentrates nearer the

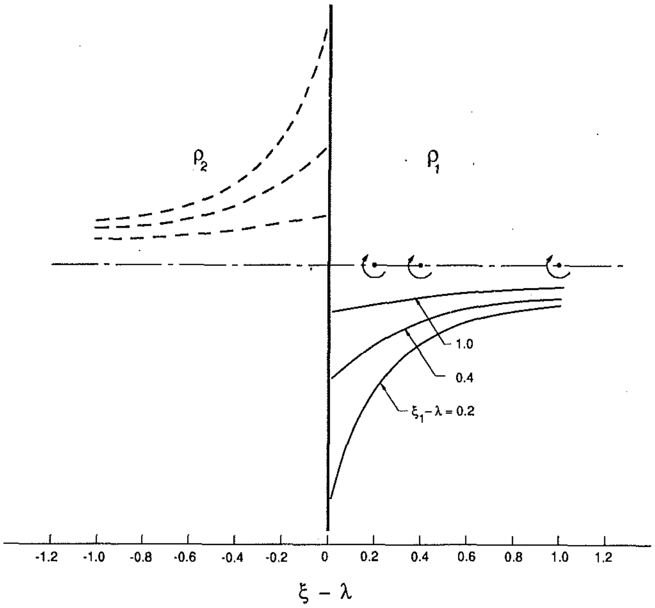

Fig. 3 Downwash induced by the vortex sheet formed on the density discontinuity

airfoil axis and has a higher maximum value. It is also easily shown, either by application of Kelvin's theorem or by direct integration of Eq. (9), that the total vorticity on the density jump is

$$\int_{-\infty}^{\infty} \gamma_\lambda(\eta)d\eta) = \frac{\gamma(\xi_1, t)d\xi_1}{2\pi} \left(\frac{\rho_1 - \rho_2}{\rho_1 + \rho_2}\right) \tag{10}$$

the strength of the "image vortex" we employed to construct the solution. After the density jump has passed downstream of the airfoil vorticity element, the vorticity distributions repeat themselves but with opposite sign, as might be inferred from the appropriate image vortex given by Eqs. (6), (7).

From the viewpoint of airfoil theory, the important consequence of this calculation is the downwash velocity, v (ξ, 0), which is induced at the plane of the airfoil, that is $-1 \le \xi_1 \le 1$. When the density jump is upstream of the airfoil vortex element, $\xi_1 > \lambda$, the vertical velocity induced by the density jump is

$$v(\xi, 0) = -\left(\frac{\rho_1 - \rho_2}{\rho_1 + \rho_2}\right) \frac{\gamma(\xi_1, t)\, d\xi_1}{2\pi} \frac{1}{(\xi - \lambda) + (\xi_1 - \lambda)}; \ \xi > \lambda \tag{11}$$

$$v(\xi, 0) = -\left(\frac{\rho_1 - \rho_2}{\rho_1 + \rho_2}\right) \frac{\gamma(\xi_1, t)\, d\xi_1}{2\pi} \frac{1}{(\xi - \lambda) - (\xi_1 - \lambda)}; \ \xi < \lambda \tag{12}$$

and after the density jump has passed the vorticity element, $\xi_1 < \lambda$, the corresponding downwash velocity is

$$v(\xi, 0) = \left(\frac{\rho_1 - \rho_2}{\rho_1 + \rho_2}\right) \frac{\gamma(\xi_1, t)\, d\xi_1}{2\pi} \frac{1}{(\xi - \lambda) + (\xi_1 - \lambda)}; \ \xi < \lambda \tag{13}$$

$$v(\xi, 0) = \left(\frac{\rho_1 - \rho_2}{\rho_1 + \rho_2}\right) \frac{\gamma(\xi_1, t)\, d\xi_1}{2\pi} \frac{1}{(\xi - \lambda) - (\xi_1 - \lambda)}; \ \xi > \lambda \tag{14}$$

The downwash velocity induced by the vortex sheet on the density jump is shown in Fig. 3 for several positions of the density jump with respect to the vortex element. As is evident for the potentials w_1 and w_2, the downwash is anti-symmetric about the density jump and has maximum absolute value at the density jump of magnitude proportional to $1/|\xi_1 - \lambda|$.

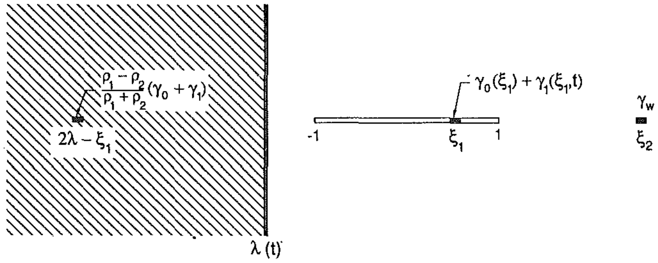

Fig. 4 Sources of downwash induction

It is important to note that the foregoing discussion pertains only to vortices that are in relative motion with respect to the density jump or whose strength varies with time. In contrast, when we consider the vortex elements that comprise the wake, the situation, as demonstrated in the Appendix, is quite different. If we follow a particular vortex element that has been shed into the wake (*i*) it is stationary with respect to the density discontinuity, and (*ii*) it is of constant strength. It therefore induces a steady flow of perturbation order at the density jump and hence generates a pressure field of second order. As a consequence the vorticity on the discontinuity is influenced to only the second order and, to the present order of calculation, the potential associated with a vortex element moving in the wake has a potential continuous across the density jump.

3 Vorticity Distribution on a Thin Airfoil

The problem of thin airfoil theory is to determine the vorticity distribution along the camber line that provides flow tangential to the given airfoil shape $\eta_1(\xi)$ and regularity at the trailing edge. For steady flow of uniform density about this airfoil shape, the vorticity distribution $\gamma_0(\xi_1)$ is assumed known. For our problem, however, additional components of downwash are induced at the foil by (*i*) vorticity on the density discontinuity and (*ii*) the wake vorticity resulting from the unsteady character resulting from the convective motion of the density field. This additional downwash then necessitates a supplementary vorticity distribution $\gamma_1(\xi_1)$ on the airfoil to satisfy the boundary conditions. It is this vorticity distribution that must be found to allow pressure, force and moment on the airfoil to be calculated.

The sources of downwash are sketched in Fig. 4. At each point ξ on the airfoil, the induced vertical velocity $v(\xi, 0)$ must cause the fluid to move tangentially to the airfoil surface, that is

$$v(\xi, 0) = U \frac{d\eta_1}{d\xi} \tag{15}$$

But the known vorticity distribution $\gamma_0(\xi_1)$ induces a flow that satisfies the condition given by Eq. (15)

$$\frac{1}{2\pi} \int_{-1}^{1} \frac{\gamma_0(\xi_1)}{\xi - \xi_1} d\xi_1 = U \frac{d\eta_1}{d\xi} \tag{16}$$

and consequently the remaining induction must give zero vertical velocity on the line segment $-1 < \xi \le 1$.

The remaining induction falls into three categories:

1. The direct induction of the supplementary vorticity distribution $\gamma_1(\xi_1)$ on the airfoil itself

$$\frac{1}{2\pi} \int_{-1}^{1} \frac{\gamma_1(\xi_1, t)}{\xi - \xi_1} d\xi_1 \tag{17}$$

2. The induction of the vorticity distribution on the density jump resulting from the airfoil vorticity $\gamma_0(\xi_1) + \gamma_1(\xi_1, t)$. Using the technique introduced in Section 2, this is

$$\frac{1}{2\pi}\left(\frac{\rho_1-\rho_2}{\rho_1+\rho_2}\right)\int_{-1}^{\lambda}\frac{\gamma_0+\gamma_1}{\xi-2\lambda+\xi_1}\,d\xi_1 -\frac{1}{2\pi}\left(\frac{\rho_1-\rho_2}{\rho_1+\rho_2}\right)\int_{\lambda}^{1}\frac{\gamma_0+\gamma_1}{\xi-\xi_1}\,d\xi_1 \qquad (18)$$

for values of $\xi<\lambda$, and

$$\frac{1}{2\pi}\left(\frac{\rho_1-\rho_2}{\rho_1+\rho_2}\right)\int_{-1}^{\lambda}\frac{\gamma_0+\gamma_1}{\xi-\xi_1}\,d\xi_1 -\frac{1}{2\pi}\left(\frac{\rho_1-\rho_2}{\rho_1+\rho_2}\right)\int_{\lambda}^{1}\frac{\gamma_0+\gamma_1}{\xi-2\lambda+\xi_1}\,d\xi_1 \qquad (19)$$

for values of $\lambda>\xi$.

3. The induction of the wake vorticity

$$\frac{1}{2\pi}\int_{1}^{\infty}\frac{\gamma_w}{\xi-\xi_2}\,d\xi_2 \qquad (20)$$

recalling, from the comment at the end of Section 2, that a wake vortex element does not require an "image" in the density discontinuity.

The expressions in Eqs. (18), (19) are written explicitly for the position $\lambda(t)$ of the density jump lying between the leading and trailing edges of the airfoil. When the density jump is upstream of the leading edge of the airfoil, only the second term in each expression survives; similarly, when the density jump is downstream of the trailing edge, only the first term remains in each expression.

For points ξ on the airfoil where $\lambda<\xi\leq 1$, the sum of these parts vanishes at each point ξ of the range.

$$\int_{-1}^{1}\frac{\gamma_1}{\xi-\xi_1}\,d\xi_1+\left(\frac{\rho_1-\rho_2}{\rho_1+\rho_2}\right)\left(\int_{-1}^{\lambda}\frac{\gamma_1+\gamma_0}{\xi-\xi_1}\,d\xi_1 -\int_{\lambda}^{1}\frac{\gamma_1+\gamma_0}{\xi-2\lambda+\xi_1}\,d\xi_1\right)+\int_{1}^{\infty}\frac{\gamma_w}{\xi-\xi_2}\,d\xi_2=0 \qquad (21)$$

A corresponding integral equation, utilizing Eq. (18) rather than Eq. 19, holds at each value of ξ in the range $-1<\xi<\lambda$. When the wake vorticity γ_w is functionally related to the supplementary vorticity $\gamma_1(\xi_1, t)$, these relations constitute an integral equation determining γ_1 as a function of position on the airfoil and time.

4 Vorticity Distribution in the Wake

The strength and distribution of the wake vorticity is determined by the vorticity $\gamma_w'(\tau)$ shed at any time, τ, and by the fact that, in the linearized approximation, this vorticity element is transported with free-stream velocity U along the horizontal axis. Then the vorticity in the wake is just

$$\gamma_w\left(t-\frac{\xi_2-1}{U}\right)=\gamma'_w(\tau) \qquad (22)$$

that is, the wake vorticity at a position $\xi_2>1$ at time t is equal to that shed from the trailing edge at the earlier time

$$\tau=t-\frac{\xi_2-1}{U} \qquad (23)$$

The usual argument to demonstrate that the shed vorticity element $\gamma_w'(t)U\,dt$ is given by the negative of the change of total circulation about the airfoil in the same time period

$$\gamma_w'(t)\;U\,dt=-\frac{d\Gamma}{dt}\,dt \qquad (24)$$

involves the application of Kelvin's theorem to a contour encompassing the entire airfoil. And although this familiar argument may be carried out when the density jump is either upstream or downstream of the airfoil, the presence of the discontinuous potential raises complications as the density jump passes over the airfoil. Instead, we shall employ the concept of the impulsive generation of lift described by Burgers (1935) which was used by Karman & Sears (1938) as the basis of their unsteady airfoil theory.

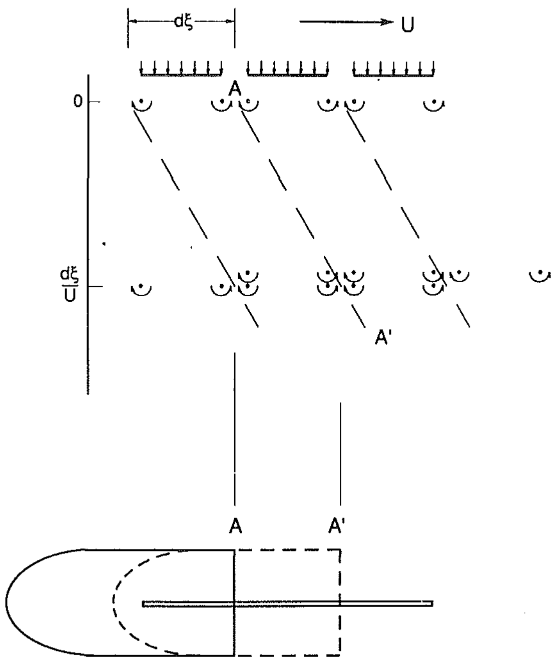

Fig. 5 Generation of lift by successive impulses-conservation of vortex pairs

An impulsive load δI applied along an element $\delta\xi$ of the horizontal axis creates a vortex pair, each vortex having a circulation Γ, according to the relation $\delta I=\rho\Gamma\,\delta\xi$ where ρ is density of the fluid in which impulse is applied. This vortex pair then drifts downstream with the free stream velocity U. A succession of impulses applied to the same element $\delta\xi$ produces a corresponding succession of vortex pairs drifting downstream along the ξ axis. Now let us chose the time intervals between these impulses to be $\delta t=\delta\xi/U$ and the impulses to be of the same magnitude

$$\delta I=\int_0^{\delta t}f\,dt$$

f being the equivalent steady load on the element. Then each impulse generates a vortex at the downstream edge of the element equal and opposite to the vortex transported from the leading edge and which was generated by the previous impulse. As a consequence there remains only the vortex of circulation Γ at the upstream edge of the element and a vortex of strength $-\Gamma$, the one generated at the downstream edge of the element by the initial impulse, drifting far downstream. The former constitutes the "bound vortex" representing the lift on the element (more appropriately designated the "regenerate" vortex) while the latter constitutes the "starting vortex," This configuration constitute the basis for the Karman-Sears (1938) formulation of the theory of airfoils in nonuniform motion.

The complete airfoil consists of a distribution of such elements, each with its peculiar load which may vary with time, and each producing its succession of vortex pairs. Figure 5 illustrates this representation by an airfoil of three elements. At the start of the motion, $t=0$, each element produces a vortex pair according to its load and each of these vortex pairs moves downstream with the undisturbed velocity U. A second set of impulses is applied at a time $\delta\xi/U$ later, the resulting set of vortex pairs moves correspondingly and each successive set of impulses contributes its own set of vortex pairs. The residual

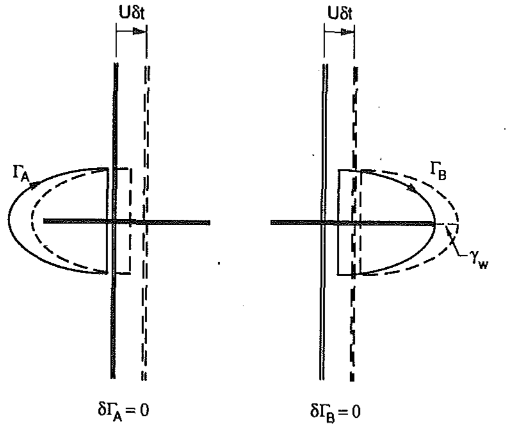

Fig. 6 Relation of shed vorticity to airfoil circulation

vortices moving away from the trailing edge constitute the vortex wake.

Now if we choose a point A between two elements of the airfoil, the field to the left of this point consists of a collection of vortex pairs. Furthermore, if we move with the undisturbed fluid, this region continues to consist of vortex pairs, more being generated at each successive impulse. As a consequence, the circulation in the region does not change with time in spite of the fact that the loading of the airfoil may be changing.

This situation may be interpreted as shown also in Fig. 5. As the contour moves with the fluid the time derivative of the circulation Γ about this contour vanishes. Furthermore, any contour that moves with the fluid across the airfoil has a circulation that does not change, simply because any loading changes that occur create vortex pairs which remain within the contour in question.

These observations are particularly useful in determining the shed vorticity as the density discontinuity is passing over the airfoil. Referring to Fig. 6, consider the contour including the portion of the airfoil to the left of the discontinuity, lying entirely within the fluid of density ρ_2. Our argument regarding the elementary impulses holds and, as a consequence, the circulation Γ_A does not change with time. On the other hand, consider the contour which contains the remaining portion of the airfoil and lying entirely within the fluid of density ρ_1. Again, as we move with the fluid, the circulation Γ_B about this contour does not change. Hence as it moves downstream, the contour covers an element $U\delta t$ of the ξ-axis comprising a vorticity element $\gamma'_w(t)\,U\delta t$ of the wake vorticity. Now in the time δt

$$\delta\Gamma_A + \delta\Gamma_B = \delta\int_{-1}^{1} \gamma_1(\xi_1, t)\,d\xi_1 + \gamma'_w(t)\,U\delta t = 0$$

so that the shed wake vorticity is

$$\gamma'_w(t) = -\frac{1}{U}\frac{d}{dt}\int_{-1}^{1} \gamma_1(\xi, t)\,d\xi_1 \tag{25}$$

This result is remarkable as well as very useful! For as a consequence, we have the unanticipated advantage that the usual relationship between airfoil circulation and shed vorticity holds even as the density jump passes over the airfoil.

Equation (25), together with the relation given in Eq. (23), allows the wake vorticity distribution $\gamma_w(\xi_1, t)$ to be expressed in terms of $\gamma_1(\xi_1, t)$ so that Eq. (22) becomes an integral equation for $\gamma_1(\xi_1, t)$.

5 Pressure Distribution, Lift and Moment

If we denote by u_+, p_+ and u_-, p_- the velocity and pressure perturbations on the upper and lower surfaces of the airfoil, the the linearization momentum equation gives

$$\frac{\partial u}{\partial t} + U\frac{\partial u}{\partial \xi} = -\frac{1}{\rho}\frac{\partial p}{\partial \xi} \tag{26}$$

where the density may be ρ_1 or ρ_2 depending upon the region in which Eq. (26) is applied. Now the vorticity representing the airfoil, $\gamma(\xi, t)$, is equal to $u_+ - u_-$ and $p_+ p_- = \Delta p$ is the airfoil load per unit area in the downward direction. By writing Eq. (26) for the upper and lower surfaces and subtracting the results we obtain the following relation between the vorticity and the airfoil loading.

$$\frac{\partial \gamma}{\partial t} + U\frac{\partial \gamma}{\partial \xi} = -\frac{1}{\rho}\frac{\partial \Delta p}{\partial \xi} \tag{27}$$

When the fluid density is uniform this may be integrated from the trailing edge, $\xi = 1$, at which point $\gamma = 0$ and $\Delta p = 0$. Then

$$\rho\int_{\xi}^{1} \frac{\partial \gamma}{\partial t}\,d\xi - \rho U\gamma(\xi, t) = \Delta p(\xi, t) \tag{28}$$

and when the density jump is upstream of the leading edge of the airfoil, this hold for $-1 < \xi \leq 1$ and $\rho = \rho_1$. The lift on the airfoil is just

$$L = \int_{-1}^{1} (-\Delta p)\,d\xi = \rho_1 U\int_{-1}^{1} \gamma(\xi)\,d\xi$$
$$-\rho_1\frac{d}{dt}\int_{-1}^{1} d\xi\int_{\xi}^{1} \gamma(\xi_1)\,d\xi_1 = \rho_1 U\Gamma - \rho_1\frac{d}{dt}\int_{-1}^{1} (1+\xi)\gamma(\xi)\,d\xi \tag{29}$$

Likewise, after the density jump has passed downstream of the trailing edge of the airfoil, the lift is given by an expression identical with Eq. (29) with the the exception that ρ_1 is replaced by ρ_2. In each case $\gamma(\xi, t) = \gamma_0(\xi) + \gamma_1(\xi, t)$ and consequently

$$\Gamma(t) = \int_{-1}^{1} \gamma_0(\xi)\,d\xi + \int_{-1}^{1} \gamma_1(\xi, t)\,d\xi = \Gamma_0 + \Gamma_1(t) \tag{30}$$

When the density jump lies between the leading and trailing edges of the airfoil, Eq. (28) holds with $\rho = \rho_1$ so long as $\xi > \lambda$. For the range $\lambda > \xi > -1$, Eq. 27 must be integrated from $\xi = \lambda$ to the left, which gives

$$\rho_2\int_{\xi}^{\lambda} \frac{\partial \gamma}{\partial t}\,d\xi + \rho_2\,U(\gamma(\lambda) - \gamma(\xi)) = -(\Delta p(\lambda) - \Delta p(\xi)) \tag{31}$$

Now the conditions at the density jump require that the pressure and the horizontal velocity components are continuous. As a consequence $\Delta p(\xi)$ and $\gamma(\xi)$ are continuous at $\xi = \lambda$ so that when we write the loading integral, Eq. (28), for the range $\lambda < \xi \leq 1$,

$$\rho_1\int_{\lambda}^{1} \frac{\partial \gamma}{\partial t}\,d\xi - \rho_1 U(\lambda) = \Delta p(\lambda) \tag{32}$$

where the values of $\gamma(\lambda)$ and $\Delta p(\lambda)$ are identical with those occurring in Eq. (32).

Note further that because $d\lambda/dt = U$, Eq. (32) may be written

$$\rho_1\int_{\lambda}^{1} \frac{\partial \gamma}{\partial t}\,d\xi - \rho_1 U\gamma(\lambda) = \rho_1\frac{d}{dt}\int_{\lambda(t)}^{1} \gamma(\xi, t)\,d\xi = \Delta p(\lambda) \tag{33}$$

and similarly for Eq. (31)

$$\rho_2\frac{d}{dt}\int_{\xi}^{\lambda} \gamma(\xi, t)\,d\xi - \rho_2 U\gamma = -\Delta p(\lambda) + \Delta p(\xi) \tag{34}$$

The value of the pressure loading $\Delta p(\lambda)$ at the discontinuity may be eliminated between Eq. (33) and Eq. (34) to give the loading $\Delta p(\xi)$ in the range $-1 < \xi < \lambda$

$$\Delta p(\xi) = \rho_2 U\gamma(\xi) + \rho_1 \frac{d}{dt}\int_\lambda^1 \gamma(\xi)d\xi + \rho_2 \frac{d}{dt}\int_\xi^\lambda \gamma(\xi)d\xi \quad (35)$$

Together with the relation valid for the range $\lambda < \xi < 1$

$$\Delta p(\xi) = -\rho_1 U\gamma(\xi) + \rho_1 \frac{d}{dt}\int_\xi^1 \gamma(\xi)d\xi \quad (36)$$

the loading is then determined for all points of the airfoil.

The lift may now be computed, using Eqs. (35) and (36), during passage of the discontinuity over the airfoil

$$L = \int_{-1}^1 (-\Delta p)d\xi = \rho_2 U\int_{-1}^\lambda \gamma(\xi)d\xi + \rho_1 U\int_\lambda^1 \gamma(\xi)d\xi$$

$$-\int_{-1}^\lambda d\xi\left\{\rho_1 \frac{d}{dt}\int_\lambda^1 \gamma(\xi_1)d\xi_1 + \rho_2 \frac{d}{dt}\int_\xi^\lambda \gamma(\xi_1)d\xi_1\right\}$$

$$-\int_\lambda^1 d\xi\left\{\rho_1 \frac{d}{dt}\int_\xi^1 \gamma(\xi_1)d\xi_1\right\}$$

which, after partial integration, gives

$$L = \rho_2 U\int_{-1}^\lambda \gamma(\xi)d\xi + \rho_1 U\int_\lambda^1 \gamma(\xi)d\xi$$

$$-\rho_2 \frac{d}{dt}\int_{-1}^\lambda (1+\xi)\gamma(\xi)d\xi - \rho_1 \frac{d}{dt}\int_\lambda^1 (1+\xi)\gamma(\xi)d\xi \quad (37)$$

Likewise, the counter-clockwise moment about the mid-chord point is

$$M = \rho_2 U\int_{-1}^\lambda \gamma(\xi)\xi d\xi + \rho_1 U\int_\lambda^1 \gamma(\xi)\xi d\xi$$

$$-\rho_2 \frac{d}{dt}\int_{-1}^\lambda \frac{1}{2}(\xi^2-1)\gamma(\xi)d\xi - \rho_1 \frac{d}{dt}\int_\lambda^1 \frac{1}{2}(\xi^2-1)\gamma(\xi)d\xi \quad (38)$$

6 Application to the Flat Plate Airfoil

A flat plate airfoil of chord 2 at a small angle of attack α has a vorticity distribution

$$\gamma_0(\xi) = 2U\alpha\sqrt{\frac{1-\xi}{1+\xi}} \quad (39)$$

for steady motion in a uniform medium. As a consequence the integral equation for $\gamma_1(\xi, t)$, Eq. (21), becomes, for $\lambda < -1$ ahead if the leading edge of the airfoil,

$$\int_{-1}^1 \frac{\gamma_1(\xi_1, t)}{\xi - \xi_1} d\xi_1 - \frac{\rho_1 - \rho_2}{\rho_1 + \rho_2}\int_{-1}^1 \frac{\gamma_1(\xi_1, t)}{\xi - 2\lambda + \xi_1} d\xi_1$$

$$+\int_1^\infty \frac{\gamma_w(t - (\xi_2 - 1)/U))}{\xi - \xi_2} d\xi_2 = \alpha\left(\frac{\rho_1 - \rho_2}{\rho_1 + \rho_2}\right)$$

$$\times\left(1 - \sqrt{\frac{\xi - 2\lambda + 1}{\xi - 2\lambda - 1}}\right) \quad (40)$$

where

$$\gamma_w(\tau) = -\frac{1}{U}\frac{d}{dt}\int_{-1}^1 \gamma_1(\xi_1, \tau)d\xi_1 \quad (41)$$

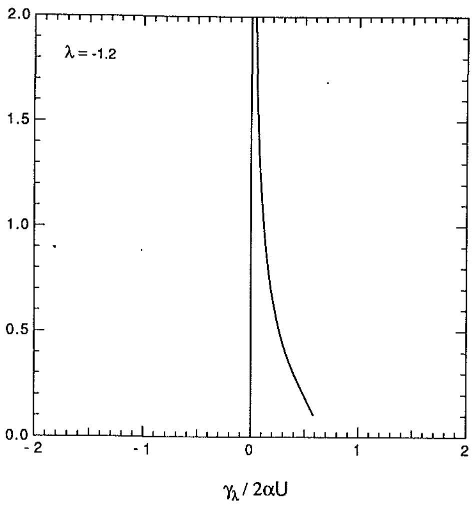

Fig. 7 (*a*) Vorticity on density jump

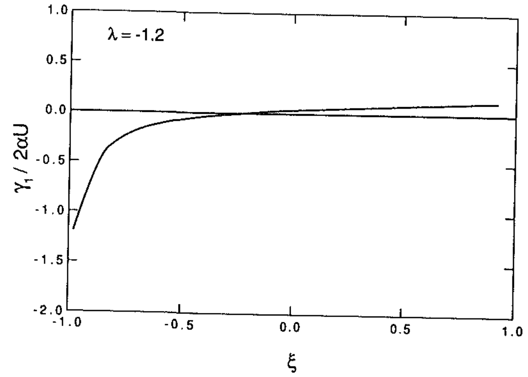

Fig. 7 (*b*) Vorticity on airfoil

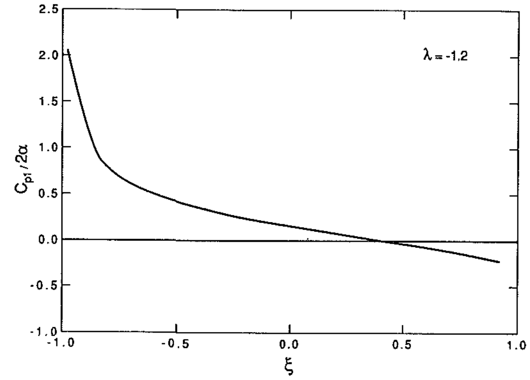

Fig. 7 (*c*) Pressure on airfoil

Fig. 7 Flow induced on plane airfoil by the density discontinuity, $\rho_2/\rho_1 = 0.5$, $\lambda = -1.2$

Corresponding expressions are easily obtained for the density jump over the airfoil, $-1 < \lambda \leq 1$, and for the density jump downstream of the airfoil, $1 < \lambda$. Although we may proceed analytically when either $\lambda < -1$ or $\lambda > 1$, the situation is more complex when the discontinuity is passing over the airfoil and consequently $\gamma_1(\xi_1, t)$ was calculated numerically. The airfoil chord line was divided into elements, a point vortex was located at the quarter point of each element and downwash was computed at the three-quarter point of each element. The resulting matrix was inverted to find values of $\gamma_1(\xi_1, t)$ at the discrete points of the airfoil. For most of the calculations 20 elements were used. Spot calculations using 40 points showed no substantial changes.

Examples of the vorticity distribution on the airfoil, vorticity distribution on the density jump, and pressure distribution on the airfoil are shown in Figs. 7 and 8 for values of $\lambda = -1.2$ and $\lambda = -0.8$, respectively. As the density jump approaches the leading edge of the airfoil, Fig. 7(*a*) shows that a distri-

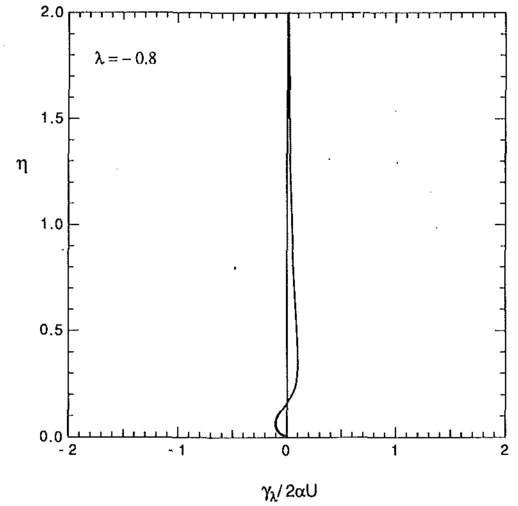

Fig. 8 (*a*) Vorticity on density jump

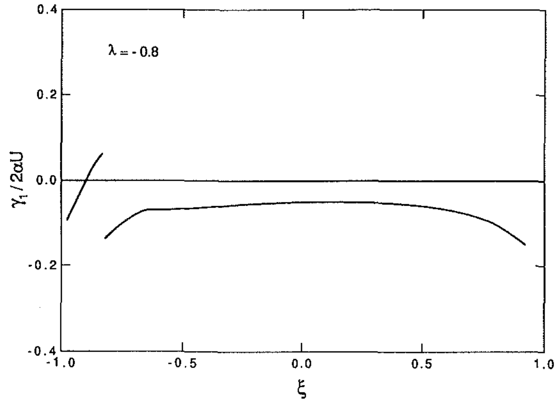

Fig. 8 (*b*) Vorticity on airfoil

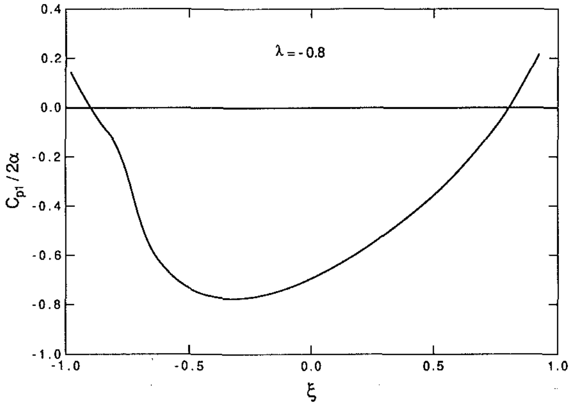

Fig. 8 (*c*) Pressure on airfoil

Fig. 8 Flow induced on plane airfoil by the density discontinuity, $\rho_2/\rho_1 = 0.5$, $\lambda = -0.8$

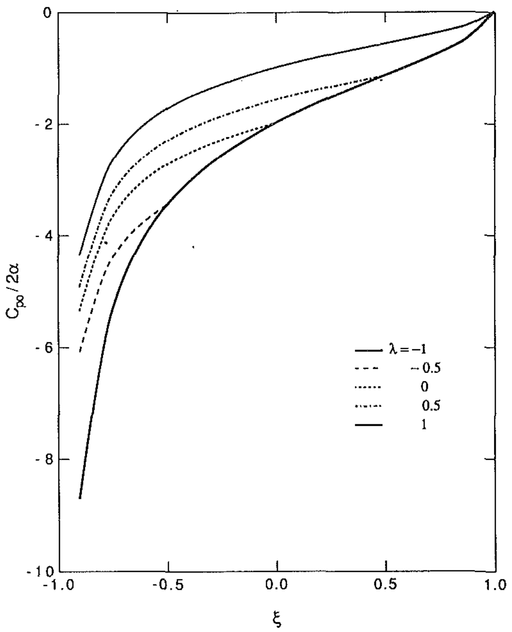

Fig. 9 Pressure distribution due to passage of density jump, initial vorticity $\gamma_0(\xi)$, $\rho_2/\rho_1 = 0.5$

bution of positive vorticity is induced on the density jump when $\lambda = -1.2$. The sign of the distribution follows directly from Eq. (9) because the vorticity distribution $\gamma_1(\xi_1, t)$ is dominated by the initial loading $\gamma_0(\xi_1)$, Eq. (36). As a consequence the density jump induces a downwash at the leading edge producing the negative vorticity γ_1 show in Fig. 7(*b*). The resulting pressure coefficient perturbation (the negative of the loading), Fig. 7(*c*), shows a strong unloading of the leading edge corresponding to the action of a downward gust. It is important to notice here that, in contrast to the effect of the sharp edge gust, Karman and Sears (1938), the density discontinuity has a downwash field that precedes its arrival.

The situation changes when the density jump lies within the airfoil chord, shown in Fig. 8. The vorticity distribution on the discontinuity, Fig. 8(*a*), shows the effect of strong leading edge vorticity γ_0 which now lies to the left of the density jump, largely negating the effect of the vorticity of the same sign lying to the right. Figure 8(*b*) shows a comparably small induced vorticity on the airfoil. The significant pressure coefficients in Fig. 8(*c*) arise largely from the local temporal variation of vorticity, the time-differentiated term of Eq. (35) and Eq. (36). The pressure distribution of Fig. 8(*c*) implies a significant adverse pressure gradient induced on the lower surface.

Now because the position of the airfoil and the velocity of the undisturbed flow are constant during the encounter with the density jump, the potential and the vorticity distribution $\gamma_0(\xi)$ given in Eq. (39) are independent of time. However, the pressure coefficient induced by this vorticity is time dependent because, specifically, the variable position $\lambda(t)$ of the discontinuity appears in the limits of the integrals of Eq. (35). When the discontinuity is ahead of the airfoil, that is $\lambda < -1$,

$$C_{p0} \equiv \frac{\Delta p}{1/2\rho_1 U^2} = -4\alpha\sqrt{\frac{1-\xi}{1+\xi}} \tag{42}$$

and after it has passed downstream, $\lambda > 1$,

$$C_{p0} = -4\alpha\frac{\rho_2}{\rho_1}\sqrt{\frac{1-\xi}{1+\xi}} \tag{43}$$

During the process of passage, however, the pressure ahead of the discontinuity, $-1 < \xi < \lambda$,

$$C_{p0} = -4\alpha\frac{\rho_2}{\rho_2}\sqrt{\frac{1-\xi}{1+\xi}} - 4\alpha\left(1-\frac{\rho_2}{\rho_2}\right)\sqrt{\frac{1-\lambda}{1+\lambda}} \tag{44}$$

and downstream of the discontinuity, $\lambda < \xi \leq 1$,

$$C_{p0} = -4\alpha\sqrt{\frac{1-\xi}{1+\xi}} \tag{45}$$

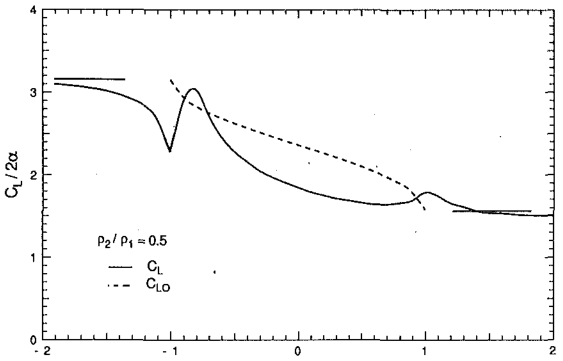

Fig. 10 **Lift coefficient during passage of density discontinuity over the airfoil, $\rho_2/\rho_1 = 0.5$**

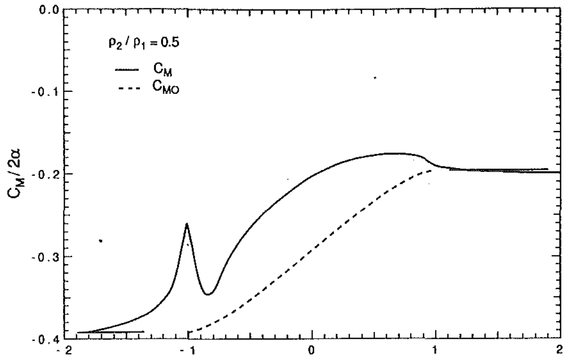

Fig. 11 **Moment coefficient during passage of density discontinuity over the airfoil, $\rho_2/\rho_1 = 0.5$**

which we note is unchanged from its value when the discontinuity was far upstream of the airfoil. Figure 9 shows C_{p0} (ξ) for several values of λ during the period the discontinuity is passing over the airfoil. The C_{p0} distribution for $\lambda = -1$ holds for all $\lambda < -1$ and the C_{p0} distribution for $\lambda = 1$, equal to ρ_2/ρ_1 times the C_{p0} distribution for $\lambda = -1$, holds for all $\lambda > 1$ after the discontinuity has left the trailing edge. The changes in the C_{p0} distribution take place from the leading edge and progress following the density jump; this feature rests upon (*i*) the fact that C_{p0} (1) = 0 and (*ii*) pressure continuity across the density jump. These values of C_{p0} are, generally, larger than the values of C_{p1} and we may anticipate that the forces on the airfoil will to a considerable extent be dominated by C_{p0} and thus confined to the period when the density jump is actually passing over the airfoil.

The lift coefficient C_{L0} resulting from the pressure coefficient C_{p0} is easily calculated, remembering that the airfoil chord is equal to 2,

$$C_{L0} = -\frac{1}{2}\int_{-1}^{1} C_{p0}\,d\xi$$

$$= 2\alpha\left\{\frac{\rho_2}{\rho_1}\int_{-1}^{\lambda}\sqrt{\frac{1-\xi}{1+\xi}}\,d\xi + \left(1+\frac{\rho_2}{\rho_1}\sqrt{\frac{1-\lambda}{1+\lambda}}\int_{-1}^{\lambda} d\xi\right.\right.$$

$$\left.+\int_{\lambda}^{1}\sqrt{\frac{1-\xi}{1+\xi}}\,d\xi\right\} = 2\pi\alpha\left\{1-\left(1-\frac{\rho_2}{\rho_1}\right)\left(1-\frac{1}{\pi}\cos^{-1}\lambda\right)\right. \quad (46)$$

This is shown as the broken line in Fig. 10.

The clockwise moment about the airfoil midpoint is also easily calculated, again recalling that the airfoil chord is 2,

$$C_{M0} = \frac{1}{4}\int_{-1}^{1} C_{p0}\xi\,d\xi = \frac{1}{4}(2\alpha)\left\{\frac{\rho_2}{\rho_1}\int_{-1}^{\lambda}\sqrt{\frac{1-\xi}{1+\xi}}\,\xi\,d\xi\right.$$

$$\left.+\left(1-\frac{\rho_2}{\rho_1}\right)\sqrt{\frac{1-\lambda}{1+\lambda}}\int_{-1}^{\lambda}\xi\,d\xi + \int_{\lambda}^{1}\sqrt{\frac{1-\xi}{1+\xi}}\,\xi\,d\xi\right\}$$

which may be evaluated as

$$C_{Mo} = \frac{\pi}{4}\alpha\left\{1-\left(1-\frac{\rho_2}{\rho_1}\right)\left(1-\frac{1}{\pi}\cos^{-1}\lambda + \frac{\lambda}{\pi}\sqrt{1-\lambda^2}\right)\right\} \quad (47)$$

This result appears as the broken line in Fig. 11.

The complete solutions for the lift and moment coefficients shown in Figs. 10 and 11 were obtained by numerically solving Eqs. (40) and (41) for the $\gamma_1(\xi, t)$, the additional vorticity distribution induced by the density jump. Integration was begun with the density jump 2 chord lengths upstream, $\lambda = -4$, and continued until the density jump had passed 2 chord lengths downstream, $\lambda = 4$. At $\lambda = -4$ the values of γ_1 were negligible and the vorticity shed from the trailing edge correspondingly small. As the discontinuity moved downstream, the successive distributions $\gamma_1(\xi, t)$ allowed determination of the γ_m values to be used at each succeeding value of λ.

The unique features of the problem are most readily described with reference to the lift coefficients shown in Fig. 10. As the density jump approaches within about one half chord of the leading edge, the downwash, induced as illustrated in Figs. 2 and 3, generates a reduction of the airfoil vorticity distribution, Fig. 7(*b*), and the consequent lift reduction, Fig. 9, for $\lambda < -1$. As the discontinuity passes the leading edge, the flow following the density jump constitutes a strong upwash, creating a situation resembling the sharp-edge gust. In fact, the cusp appearing at $\lambda = -1$ is related to the lift growth for a sharp-edged gust shown in Fig. 8 of Karman and Sears (1938). The subsequent rise in C_L overshoots the value of C_{L0} to a degree that evidently exceeds that shown simply because the number of intervals used to describe the airfoil surface was not sufficient to resolve the peak.[2] The moment coefficient, Fig. 11, reflects these events in local loading. The response as the density jump passes off the trailing edge is relatively mild, largely because the values of $\gamma_0(\xi)$ are small in this region and consequently the near-field reflected vorticity is small.

Initially it seems surprising that the variations in lift and moment are confined so closely to the period when the density discontinuity is passing directly over the airfoil, particularly so in view of our experience with other examples of unsteady airfoil behavior. Significant response to a sharp-edge gust, for example, continues until the gust has passed 5 to 10 chord lengths downstream. The difference lies in the fact that in the present case the flow field is kinematically identical when the discontinuity is far upstream and when it has passed far downstream and, in particular, the circulation about the airfoil is the same in both cases. Consequently, the shed vortex sheet contains zero net vorticity and behaves much like a vortex pair with a spacing of the order of the airfoil chord whose induced field dies out as $1/\lambda^2$ rather than as $1/\lambda$.

References

Burgers, J. M., 1935, "Problems of Non-Uniform Motion," *Aerodynamic Theory*, Springer, W. F. Durand, ed., pp. 280-310.

Giles, M. B., Krouthen, B., 1988, "Numerical Investigation of Hot Streaks in Turbines," Paper AIAA-88-3015, 24th Joints Propulsion Conference, Boston.

---

[2] One reviewer has pointed out that Basu and Hancock, J.F.M., Vol. 87, Pt. 1, pp. 159-178, 1978, observed a numerical anomaly resembling the behavior of the lift coefficient as the discontinuity passes the trailing edge. Although calculations of C_{L0} do not show this, the author cannot completely rule out the possibility.

Glauert, H., 1929, "The Force and Moment on an Oscillating Aerofoil," British A.R.C., R.&M. No. 1242, 1929.

Goldstein, M. E., 1978, "Unsteady Vortical and Entropic Distortions of Potential Flows Round Arbitrary Obstacles," *Journal of Fluid Mechanics*, Vol. 89, Part 2, pp. 433–468.

Karman, Th. v., Sears, W. R., 1938, "Airfoil Theory for Non-Uniform Motion," *Jour. Aero Sci*, Vol. 5, pp. 379–390.

Kinney, R. B., and Sears, W. R., 1975, "Unsteady Aerodynamics," *Symposium Proceedings*, Vol. I and Vol. II, University of Arizona, Tucson, R. B. Kinney, ed.

Kussner, H. G., 1936 "Zusammenfassender Bericht uber den instationaren Auftrieb von Flugeln," *Luftfahrtforschung*, Bd 13, pp. 410–424.

Marble, F. E. and Candel, S. M., 1977, "Acoustic Distribution from Gas Nonuniformities Convected Through a Nozzle," *Journal of Sound and Vibration*, Vol. 55, No. 2, pp. 225–243.

Marble, F. E., 1975, "Response of a Nozzle to an Entropy Disturbance-Example of Thermodynamically Unsteady Aerodynamics," *Unsteady Aerodynamics*, Vol. II, Symposium Proceedings, University of Arizona, Tucson, R. B. Kinney, ed.

Theodorsen, Th., 1935, "General Theory of Aerodynamic Instability and the Mechanism of Flutter," N.A.C.A. Technical Report No. 496, Washington, D.C.

Wortman, A., 1975, "Unsteady Flow Phenomena Causing Weapons Fire-Aircraft Engine Inlet Interference Problems, Theory and Experiments," *Unsteady Aerodynamics*, V. I., Symposium Proceedings, University of Arizona, Tucson, R. B. Kinney, ed.

APPENDIX

Field of A Source-Vortex Near a Moving Density Discontinuity

Consider source element $\sigma(0, t)\, d\xi_1$ and a vortex element $\gamma(0, t)\, d\xi_1$ located, without loss of generality, at the origin of the $\zeta = \xi + i\eta$ plane. The complex potential is

$$w_0 = \frac{(\sigma + i\eta)\, d\xi_1}{2\pi} \ln(\zeta)$$

$$\equiv (f(t) + ig(t)) \ln(\zeta) \qquad \text{(A-1)}$$

The density discontinuity is located at $\xi = \lambda(t)$, ref Fig. 1, and moves with the undisturbed stream velocity so that $d\lambda/dt = U$. We propose to write the supplementary potentials in the form

$$w_1 = (A_1 f + iB_1 g) \ln(\zeta - 2\lambda) \qquad \text{(A-2)}$$

and

$$w_2 = (A_2 f + iB_2\, g) \ln(\zeta) \qquad \text{(A-3)}$$

The potential w_1 has its singularity at the reflection point of the actual singularity and is regular to the right of the discontinuity. The potential w_2 is coincident with the actual singularity and is regular to the left of the discontinuity. The complete solutions $w_0 + w_1$ and $w_0 + w_2$ must satisfy the condition that the ξ-component of velocity be continuous at the density jump, $\xi = \lambda$, so that

$$\Re\left\{\frac{dw_1}{d\zeta}\ (\xi + i\lambda, t)\right\} = \Re\left\{\frac{dw_2}{d\zeta}\ (\xi + i\lambda, t)\right\} \qquad \text{(A-4)}$$

because w_0 is continuous at $\zeta = \lambda + i\eta$. The condition of Eq. A-4 is satisfied if

$$A_2 = -A_1 \equiv A;\ B_2 = B_1 \equiv B \qquad \text{(A-5)}$$

The other condition to be satisfied is that the pressure be continuous across the density jump. The perturbation pressures are given by

$$p_1/\rho_1 = \Re\left\{\left(\frac{\partial}{\partial t} + U\frac{d}{d\zeta}\right)\ (w_0 + w_1)\right\}$$

$$p_2/\rho_2 = \Re\left\{\left(\frac{\partial}{\partial t} + U\frac{d}{d\zeta}\right)\ (w_0 + w_2)\right\} \qquad \text{(A-6)}$$

so that pressure continuity yields the relation

$$\rho_1\, \Re\left\{\frac{\partial w_1}{\partial t} + U\frac{d\, w_1}{d\zeta}\right\} - \rho_2\, \Re\left\{\frac{\partial w_2}{\partial t} + U\frac{dw_2}{d\zeta}\right\}$$

$$= -(\rho_1 - \rho_2)\Re\left\{\frac{\partial w_0}{\partial t} + U\frac{dw_0}{d\zeta}\right\} \qquad \text{(A-7)}$$

at $\zeta = \lambda + i\eta$. If we use the values of the potentials, Eqs. (A-1), (A-2), (A-3) and the Eq. (A-5), ensuring continuity of the streamwise velocity, Eq. (A-7) may be put in the form

$$[(\rho_1 + \rho_2)A + (\rho_1 - \rho_2)]f' \ln\sqrt{\lambda^2 + \eta^2}$$

$$+ [(\rho_1 + \rho_2)B - (\rho_1 - \rho_2]g' \tan^{-1}\left(\frac{\eta}{\lambda}\right)$$

$$+ [(\rho_1 + \rho_2)A + (\rho_1 - \rho_2)]Uf\frac{\lambda}{\lambda^2 + \eta^2}$$

$$+ [-(\rho_1 + \rho_2)B + (\rho_1 - \rho_2)]Ug\frac{\eta}{\lambda^2 + \eta^2} = 0 \qquad \text{(A-8)}$$

For our suggested form of the solution to be valid, Eq. (A-8) must be satisfied for all values of η and t. Because each function multiplying a square bracket is distinct, *each* of the square brackets must vanish. But these four relations consists of two identical pairs and consequently

$$A = -\frac{\rho_1 - \rho_2}{\rho_1 + \rho_2} = A_2 = -A_1;\quad B = \frac{\rho_1 - \rho_2}{\rho_1 + \rho_2} = B_1 = B_2 \qquad \text{(A-9)}$$

This completes verification of the solution for the auxiliary potentials given in Eqs. (A-2) and (A-3).

We should note the special case that occurs when (i) the source and vortex strengths are independent of time, and (ii) the discontinuity is stationary with respect to the source-vortex point. This is equivalent to setting the $\partial/\partial t$ and U to zero in the pressure relations, Eq. (A-6), so that the pressure disturbance vanish, to the order of our calculation, and it follows that the supplementary potentials vanish.

This circumstance arises specifically for vortices moving with the flow, such as elements of the vortex sheet shed from the trailing edge of the airfoil. These satisfy the conditions (i) and (ii) above and hence their potential is continuous through the density jump.

It is simple to generalize this result to a source element and a vortex element at an arbitrary position ξ_1 along the real axis. When the density jump is upstream of the source-vortex element, $\xi_1 > \lambda$, the solution may be written down from the result just obtained,

$$w_0(\zeta, t) + w_1(\zeta, t) = \frac{\sigma(\xi_1, t)d\xi_1}{2\pi}\left\{\ln(\zeta - \xi_1)\right.$$

$$\left. + \frac{\rho_1 - \rho_2}{\rho_1 + \rho_2}\ln(\zeta - \lambda) + (\xi_1 - \lambda))\right\}$$

$$+ \frac{i\gamma(\xi_1, t)d\xi_1}{2\pi}\left\{\ln(\zeta - \xi_1) + \frac{\rho_1 - \rho_2}{\rho_1 + \rho_2}\ln\ ((\zeta - \lambda) + (\xi_1 - \lambda)\right\}$$

$$\text{(A-10)}$$

$$w_0(\zeta, t) + w_2(\zeta, t) = \frac{\sigma(\xi_1, d\xi_1}{2\pi}\left\{\ln(\zeta - \xi_1) - \frac{\rho_1 - \rho_2}{\rho_1 + \rho_2}\ln(\zeta - \xi_1)\right\}$$

$$+ \frac{i\gamma(\xi_1, t)d\xi_1}{2\pi}\left\{\ln(\zeta - \xi_1) + \frac{\rho_1 - \rho_2}{\rho_1 + \rho_2}\ln\ (\zeta - \xi_1)\right\} \qquad \text{(A-11)}$$

On the other hand, when the density discontinuity has passed downstream of the source-vortex point, this singularity now lies in the region of density ρ_2. The analytic formulation of the solution is not altered, the only modification is the interchange of indices 1 and 2 when they refer to the fluid densities and the regions of validity of the solutions. Therefore for $\xi_1 < \lambda$ the solutions may be written down directly

$$w_0(\zeta, t) + w_1(\zeta, t) = \frac{\sigma(\xi_1, t)d\xi_1}{2\pi}\left\{\ln(\zeta-\xi_1) + \frac{\rho_1-\rho_2}{\rho_1+\rho_2}\ln(\zeta-\xi_1)\right\} + \frac{i\gamma(\xi_1, t)d\xi_1}{2\pi}\left\{\ln(\zeta-\xi_1) - \frac{\rho_1-\rho_2}{\rho_1+\rho_2}\ln(\zeta-\xi_1)\right\} \quad \text{(A-12)}$$

$$w_0(\zeta, t) + w_2(\zeta, t) = \frac{\sigma(\xi_1, t)d\xi_1}{2\pi}\left\{\ln(\zeta-\xi_1) - \frac{\rho_1-\rho_2}{\rho_1+\rho_2}\ln((\zeta-\lambda)+(\xi_1-\lambda)\right\} + \frac{i\gamma(\xi_1, t)d\xi_1}{2\pi}\left\{\ln(\zeta-\xi_1) - \frac{\rho_1-\rho_2}{\rho_1+\rho_2}\ln(\zeta-\lambda)+(\xi_1-\lambda)\right\} \quad \text{(A-13)}$$

J. Swirydczuk[2]

M. C. Wilder[3]

D. P. Telionis

Department of Engineering Science
and, Mechanics,
Virginia Polytechnic Institute
and State University,
Blacksburg, VA 24061-0219

The Interaction of Coherent Vortices With Short Flat Plates[1]

(Data Bank Contribution*)

The interaction between a vortex and a small plate, are studied experimentally in a water tunnel using a computer-controlled laser-Doppler velocimeter. The interaction is proved to be a strong source of secondary and tertiary vorticity, the formation of which can be controlled by a selection of the plate dimensions, and cross-sectional shape. It is demonstrated that shorter plates with sharp edges are more efficient in breaking up oncoming vortical structures, while they create lower levels of secondary and tertiary vorticity. Such devices could be employed to control the amplitude of pressure fluctuations and the generation of noise in many practical applications.

1 Introduction

In the past decade, fluid mechanics research has seen a renewed emphasis in a new and exciting area, the control and management of fluid mechanics phenomena. This was pursued via passive and active devices. A typical example is the control of vortical structures in a turbulent boundary layer. One idea pursued by many investigators in the early 80's was to insert a thin flat plate in the boundary layer in order to break up the large vortices. It was proven that such plates and other similar devices influence greatly the subsequent development of the turbulent boundary layer, for distances as large as fifty boundary-layer thicknesses downstream. Such devices are known today with the acronym LEBU for "Large Eddy Break Up" devices. The reader can trace the early contributions in Bushnell (1984).

LEBU's should not be considered only as means of reducing drag in turbulent boundary layers. The success of such devices in breaking up vortical structures could be exploited in a variety of engineering applications. For example, vortex manipulators could improve the operation of hydraulic machinery at off-design operation, or alter the sound generation characteristics of helicoper rotors, or ship propellers.

In most of the early experimental contributions on the topic, measurements were made downstream of the LEBU to assess the effect on skin friction. It was found that considerable reductions in skin friction can be achieved but the overall net effect on drag is questionable, because such devices introduce form drag. A recent review of contributions on the topic is found in Anders (1990). In all the experimental studies referenced there, no information is supplied on the flow properties in the immediate vicinity of the device. In the present contribution, we try to fill this void by presenting velocity and vorticity data upstream, over, and immediately downstream of short flat plates. The spirit of this effort is in line with the work of Sears (Sears and Kuethe, 1939; Sears, 1940) who first investigated the interaction of flow disturbances with solid bodies and to whom this paper is dedicated.

All earlier experimental investigations of LEBU effects were conducted so far with fully developed turbulent boundary layers. It was therefore impossible to identify and track individual vortices and observe their breakup by a LEBU. In the present contribution, we create a row of coherent vortices and allow them to interact with a flat plate. Moreover, the vortical structures upstream and downstream of the plate are scaled up in comparison to turbulent-boundary-layer-flow structures, thus allowing us to perform detailed, local measurements. A similar study of coherent isolated vortices and their interaction with small cylinders and flat plates has been reported by Homa et al. (1988). In this study, the authors employ flow visualization techniques which help them identify the phenomenon of secondary vortex formation. In the present study, we provide ensemble-averaged LDV measurements for such fields. Rockwell and his coworkers (Rockwell, 1983) laid the foundation for the interaction of coherent vortical structures with sharp edges. However, in Homa et al. (1988) the vortices are self-propelled. There is no mean flow. As a result, the interaction of one of the two vortices with a plate induces a reversal in the direction of the motion of the primary and secondary vortices. This is unlikely to occur if vortices are drifting with a stream.

Analytical and numerical efforts have actually been reported on the flow structure around a LEBU (Dowling, 1985; Balakumar and Widnall, 1986; Kinney et al., 1988). In such studies the effect of devices on fluctuating quantities are reported, but usually these are constrained by simplifying assumptions. Kin-

---

[1] This paper is dedicated to Professor W. R. Sears on occasion of his 80th birthday. Professor Sears' cheerful spirit in the search of the unknown and his love of fluid mechanics is being transmitted to many lines of investigators. The present authors have been fortunate to become members of one of these lines.

[2] Present Address: Institute of Fluid-Flow Machinery, Polish Academy of Sciences, Gdańsk, Fiszera 14, Poland.

[3] Present Address: NASA Ames Research Center, Moffet Field, CA 94035.

*Data have been deposited to the JFE Data Bank. To access the file for this paper, see instructions on p. 794 of this issue.

Contributed by the Fluids Engineering Division for publication in the Journal of Fluids Engineering. Manuscript received by the Fluids Engineering Division July 22, 1992; revised manuscript received September 17, 1993. Associate Technical Editor: F M. White.

ney and his co-workers provide some information on the development of vortical structures but these are very limited.

There is a body of literature on problems related to the present but with geometries which involve very long walls. For example, Doligalski and Walker (1984) explored the interaction of a discrete vortex with an infinite flat plate and studied the generation of secondary vorticity. The interaction of vortical structures with the sharp edge of a wedge is the topic of investigations by Ziada and Rockwell (1982) and Kaykayoglu and Rockwell (1985). A comprehensive review of earlier contributions on this topic is given by Rockwell (1983).

A review of the literature already cited indicates some unexplored issues. Homa et al. (1988), with their flow visualization method, have captured the vorticity shed from the leading edge but did not report on the vorticity shed in the form of a shear layer from the trailing edge of the LEBU. On the other hand, Dowling (1985) modeled analytically the vorticity shed at the trailing edge but ignored the leading edge effect and the stall vortex. Here we provide quantitative information on the vorticity shed from both the leading and trailing edge and investigate their interaction with the disturbing vortical structure. We present laser-Doppler velocimetry data for a variety of plates interacting with a street of coherent vortices. These data were conditionally averaged and subsequently extrapolated via a modified Taylor's hypothesis to provide quasi-instantaneous frames of phenomena developing in time.

2 Experimental Setup and Facilities

The experiments were carried out in the VPI water tunnel (see Koromilas and Telionis, 1980 for the details of the tunnel construction), with a free-stream speed U, equal to 12.5 cm/s. Vortices were generated by a NACA 0012 airfoil of chord length, C, equal to 101.6 mm, pitching about its quarter chord. The sinusoidal pitching motion had an amplitude of ± 10 deg about the airfoil position corresponding to a zero degree angle of attack. The airfoil was driven by a DC motor, through a four-bar-linkage system. The initial point of each cycle of the pitching motion was detected by an optical sensor mounted on a rotational part of the pitching mechanism.

A number of thin plates, having different dimensions *and/or* shapes, were mounted in the tunnel as target elements undergoing vortex-body interaction. Each plate was located at a distance, $\Delta l = 2.375$ C downstream of the neutral position of the trailing edge of the pitching airfoil (see Fig. 1). The offset of the plate position, Δh, with respect to the axis of the pitching airfoil could be adjusted for each experiment. The angle of attack of the plate was always equal to zero degrees.

Measurements were carried out using a two-component, three-beam, He-Ne laser-Doppler velocimeter (LDV), arranged in a back-scatter mode, interfaced with two counter-type signal processors. Bragg cells made it possible to detect reversed flow. The velocity signals were stored on mini-disks for further calculations. The velocity measurements were carried out within the rectangular domain $-0.20 < x/C < 0.90$, $-0.45 < y/C < 0.30$. The origin of this coordinate system was located at the leading edge of the target plate (Fig. 1). The displacement of the LDV measuring volume along rows and columns was executed by two computer-controlled stepping motors. Linear transducers were employed to provide a direct feedback of position. In this way, the measuring volume was positioned with an accuracy of 10^{-2} mm.

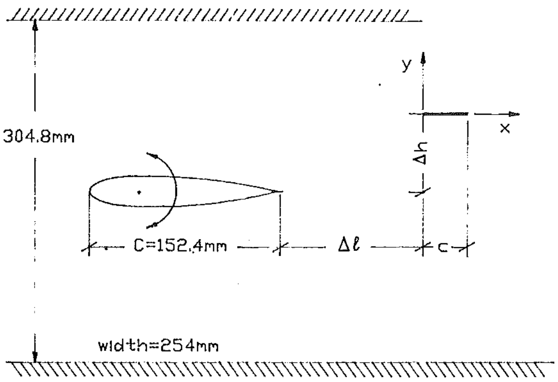

Fig. 1 Schematic of the test section showing the pitching airfoil and the target plate

Each velocity data set along a station consisted of data recorded at points separated by $\Delta y/C = 0.0187$, and along two vertical columns at a distance from each other Δx equal to Δy. At each point, 200 instantaneous values of the velocity components were obtained to describe the time history of the velocity during one pitching period. In order to eliminate random fluctuations, the time histories were conditionally averaged over 20 periods. The averaging process was triggered at a fixed phase of the pitching motion. For each measuring point, the data set was supplemented by the free-stream velocity value U, measured by a separated LDV unit, at a point located upstream of the pitching airfoil. Instantaneous values of the velocity components were thus reduced on line by the free-stream velocity. This experimental hardware and software was developed earlier by Wilder et al. (1990).

Phase-averaged velocity data obtained along a station, consisting of a pair of columns, were smoothed and employed to calculate vorticity, according to the standard formula, $\Omega = \partial v/\partial x - \partial u/\partial y$. The random error in velocity measurements was less than 3 percent but such errors could significantly reduce the uniformity in calculated vorticity components.

Data obtained along each station were extrapolated for short distances both upstream and downstream of the station. The extrapolation was achieved by invoking the Taylor hypothesis locally, i.e., in accordance with the equation $D\Omega/Dt = 0$. Vorticity was assumed to convect for short distances with the velocity measured locally. In other words, vorticity at short distances upstream and downstream of a station, x_o was calculated by assuming that the vorticity at a point (x_o, y) is displaced unchanged by the local velocity $u(x_o, y)$, $v(x_o, y)$ and that these velocity components do not change for a few steps Δx, upstream or downstream. It is important to note that

Nomenclature

C = chord length of pitching airfoil, mm
c = plate chord length, mm
N = primary negative vortex
P = primary positive vortex
SN = secondary negative vortex
SP = secondary positive vortex
NV = secondary negative vorticity
t = time, s
T = time period of pitching airfoil, s
U = free-stream velocity, cm/s
u, v = local and/or instantaneous flow velocity components, cm/s
x/C, y/C = position of the measuring column with respect to the plate leading edge (see Fig. 1)
Δh = plate offset with respect to airfoil rotation axis, mm
Δl = distance between trailing edge of the pitching airfoil and leading edge of the plate, mm
Γ = circulation, measure of fluid transported vorticity, cm^2/s
Ω = vorticity, 1/s

according to the traditional Taylor's hypothesis, vortical patterns would displace frozen in space. Here this is assumed to hold only locally, and the circulation about small material contours is preserved, in accordance to the Kelvin-Helmholtz theorem.

This technique allows us to expand information along a station, i.e., a double column of data to eight columns. The process can be visualized as opening a "window" onto the field (Wilder et al., 1990). Thus, five to seven stations in the field can be opened to overlapping windows which thus can cover the entire flow field. The effect of viscosity is neglected in this process but it is assumed that this is negligible for short streamwise distances.

The experimental uncertainty of the method has been carefully studied. The bias errors introduced by beam alignments, beam angles, processing of the Doppler signal etc. have been individually estimated (Wilder, 1991). The overall bias error was found to be less than 0.5 percent of the average measured quantities. Random errors were also very small. However, the actual field contained free-stream turbulence, which on some occasions exceeded the level of 1 percent. Calculating vorticity from the measured velocity components introduces more uncertainties because of the fact that differences of measured quantities are required. To minimize these effects, the experimental data were smoothed by the ISML DSURF routine. (ISML User's Manual 1987) which is based on the Akima (1978) method. It was estimated that errors in the levels of vorticity calculated by such methods may be as large as 10 percent of the corresponding maximum value.

It has been known that the vortex wake shed from a pitching airfoil forms a double row of vortices with sense of rotation opposite to that of the Kármán vortex street. The present authors have earlier presented extensive data on the wake of a pitching airfoil and the character of the vortical structures that organize a short distance downstream of its trailing edge (Mathioulakis et al., 1985; Poling and Telionis, 1987). The data obtained for a free development of the wake indicate that the vortices have a circular, or sometimes slightly ellipsoidal shape, with a visible core of finite vorticity. The highest Ω values in the vortex core vary within the limits of $\pm(12-18)\mathrm{s}^{-1}$, depending on the vortex sign. The diameter of the circular area occupied by the vortex core is approximately equal to 0.3 C to 0.4 C. The main vortices are accompanied sometimes by smaller vortical structures. The number and location of these vortices with respect to the main vortex varied, perhaps due to some small, long, periodic or even irregular fluctuations in the airfoil pitching motion. This demonstrates the sensitivity of the process of vortex shedding to disturbances in the airfoil motion (Swirydczuk, 1990).

The time history of the vorticity crossing the measuring column

$$\Delta\Gamma_c = \Delta x \int \Omega dy \tag{1}$$

is shown in Fig. 2. In this plot, two peaks are distinguishable, which refer to the passage of the positive, P, and negative, N, vortex. The areas defined by the two curves represent the positive and negative amounts of vorticity crossing the measuring column in one pitching period. Although for each individual diagram these values are slightly different, their balance within an error of about 10 percent is a measure of both the symmetry of the phenomenon, and the accuracy of the measurement.

3 The Vortex-Plate Interaction

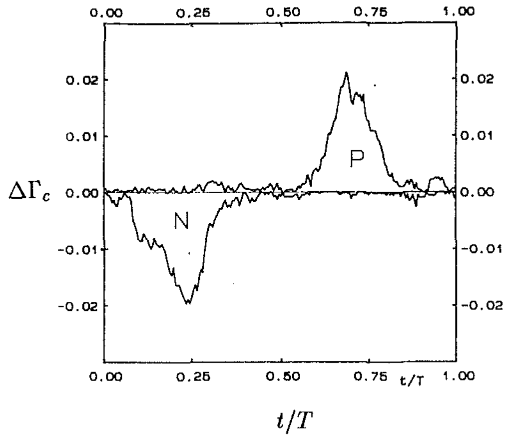

Fig. 2 Time history of vorticity passing the measuring column at $x/C = -0.3000$. Uncertainty estimate in vorticity calculation ± 0.001.

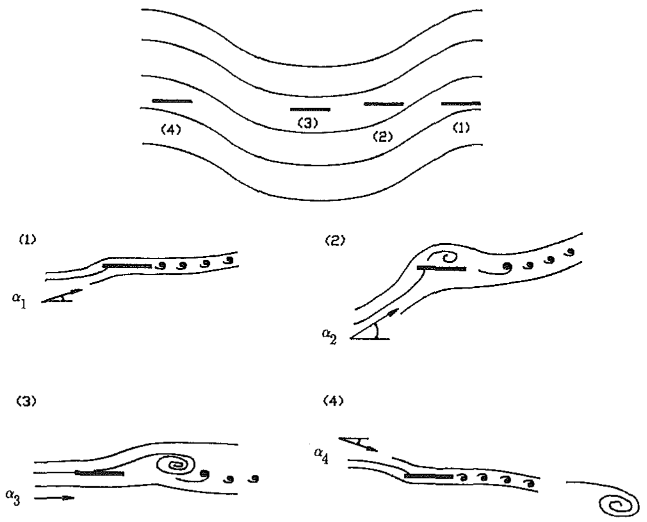

Fig. 3 Schematic sketch of four instances as a counterclockwise rotating vortex passes over the flat plate

In the frame of reference attached to the flat plate, the flow streamlines downstream of the pitching airfoil present the familiar wave pattern shown schematically in Fig. 3 (Mathioulakis et al., 1985). The following events should then be anticipated for the flow over the plate. As a positive (counterclockwise) vortex approaches, the plate experiences an increase in the angle of attack (position 1). In response, it builds up negative circulation, while simultaneously it sheds a shear layer of positive (counterclockwise) vorticity. Soon, the flow separates from the leading edge and a stall vortex develops (position 2). This vortex is called secondary vortex by Homa et al. (1988). When the disturbing vortex reaches the plate, the angle of attack reduces again (position 3). The stall vortex is swept away and convects downstream with the disturbing vortex and its remnants. Before these vortical structures leave the vicinity of the plate, the angle of attack changes sign and the trailing edge starts shedding negative vorticity (position 4). The negative disturbing vortex is approaching and the events are repeated, except that the signs of all quantities are reversed.

The target plate was mounted in the tunnel so as to meet the upper row of vortices shed by the pitching airfoil. The plate used in the first part of the experiment had a length c, equal to 25.4 mm, and a thickness, b, equal to 1.0 mm. The plate location offset, Δh (Fig. 1), was varied within the limits of 5 mm to 25 mm. This made it possible to record the interaction for various relative paths of the center of the vortex core with respect to the plate.

A sequence of instantaneous frames of vorticity contours is presented in Fig. 4. In this figure, the approaching counterclockwise rotating vortex induces same-sign trailing-edge vorticity and eventually a strong, negative leading-edge separation vortex. In the terminology of airfoil theory this is the stall

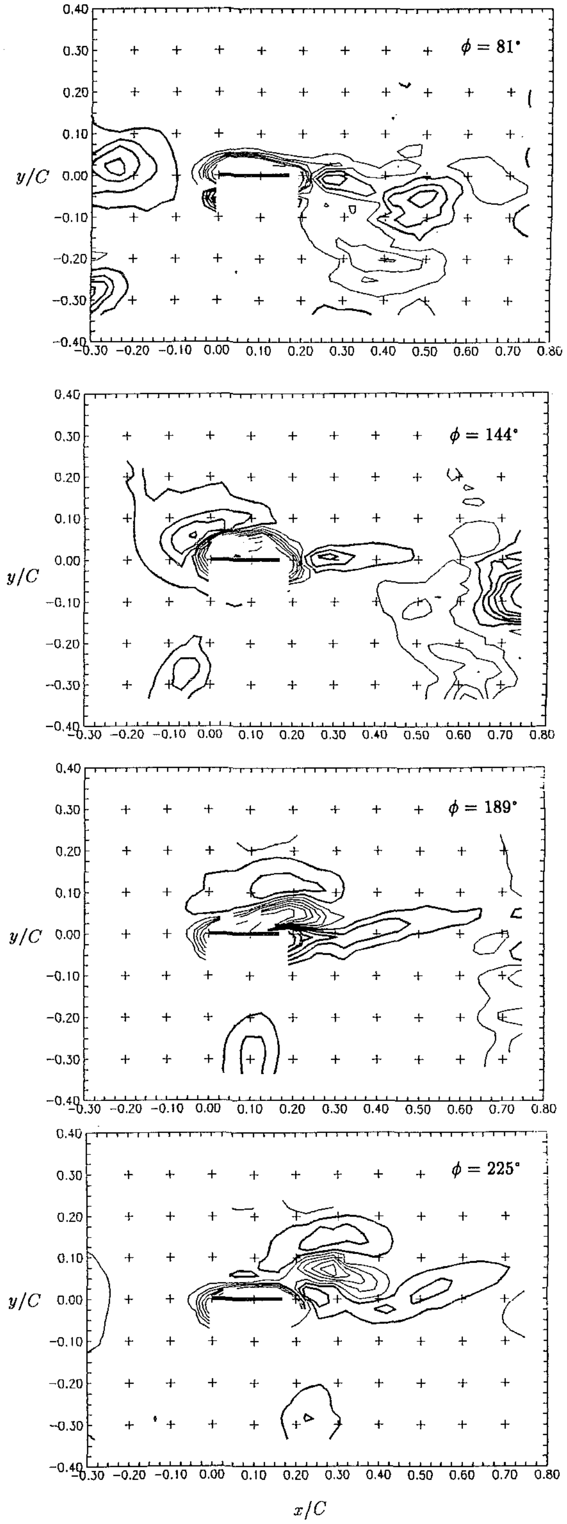

Fig. 4 Vorticity contours for the 25.4 mm plate, Δh = 10 mm. Thick and thin lines represent positive (counterclockwise) and negative vorticity, respectively. The levels in positive and negative contour lines correspond to dimensionless values of 2,6,10,15,20,30, and 50, starting from the open domain. Spatial uncertainty estimate of contours: ±0.01 C in both directions.

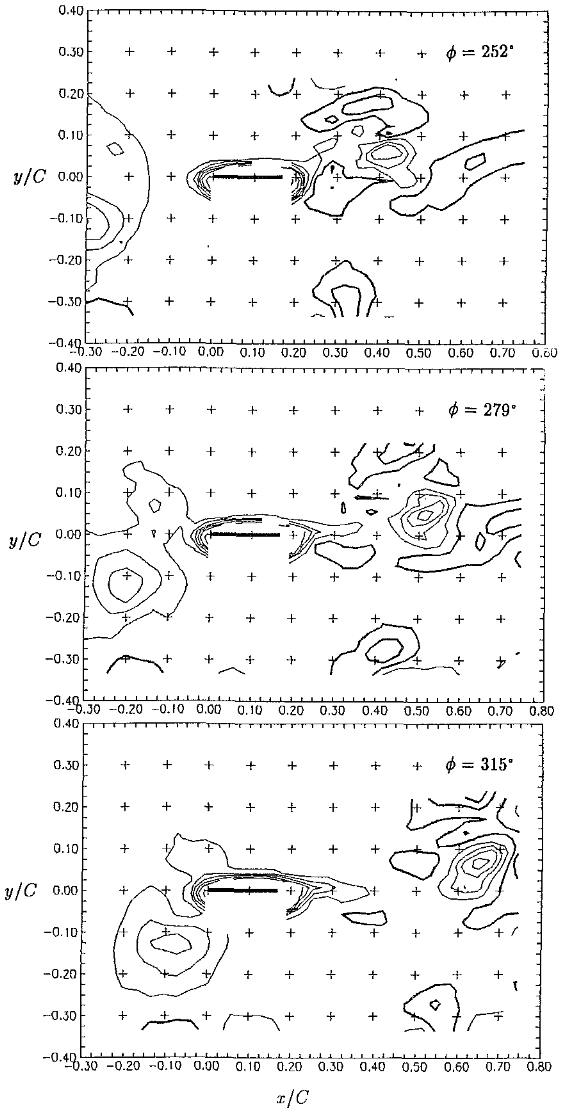

Fig. 4 (Cont.)

vortex, but here we will refer to it as the secondary vortex. This vortex remains attached to the plate and continues growing until the incident vortex reaches the middle of the plate. The incident vortex is cut into two pieces, which appear emerging on the downstream edge, separated by the negative stall vortex. The trailing edge vorticity, which we will call here the tertiary vortex, is stretched out as shown in the frame ϕ = 144 deg and eventually merges with the lower half of the oncoming vortex. All three vortical structures are convected downstream along an inclined trajectory.

A very basic issue deserves now some discussion: whether vortices of opposite sense could annihilate each other if allowed to interact. It is well known that a pair of vortices of opposite sense are perfectly compatible and propagate as a pair, with no mixing and negligible viscous interaction. A good example can be found in Homa et al. (1988). In the present case, we have a triplet of vortices, the outer two rotating in the counterclockwise direction and the middle one in the clockwise direction. These senses of rotations are again compatible and yet, the vortices appear to experience considerable reduction in strength. We attribute this to a level of turbulent mixing, the only mechanism of mutual cancellation of positive and negative vorticity. It is also interesting to notice that the three vortices emerge from their interaction with the plate very elongated in form. But a little downstream, they appear to reform axisymmetric patterns, a phenomenon that Melander et al. (1982) have identified and termed "axisymmetrization."

If this device is employed to control a turbulent boundary layer, then the mechanism of its operation is probably the following. It cuts large vortical structures to smaller pieces while simultaneously it generates a vortex of the opposite sense, which through turbulent mixing will reduce further the vorticity of the turbulent boundary layer.

Table 1 Strength of secondary vortex, Γ/uC, downstream of 25.4 mm plate

$\Delta h^{\backslash x/C}$	0.3375	0.5250	0.7125	0.9000
25 mm	−0.2106	−0.1850	−0.1546	−0.1949
15 mm	−0.2183	−0.2217	−0.1139	- -
12 mm	−0.2635	−0.2301	−0.2102	−0.1902
10 mm	−0.2236	−0.2064	−0.1651	−0.1802
5 mm	−0.3679	−0.2479	−0.1680	−0.1802

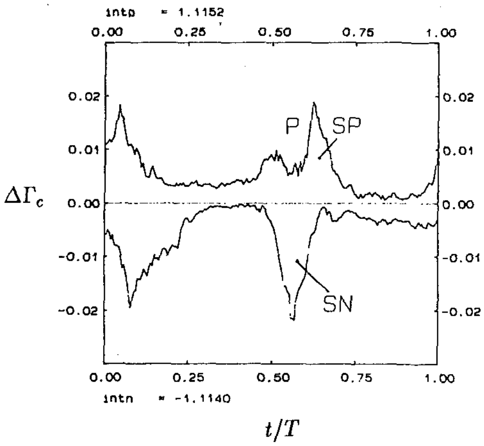

Fig. 5 Time history of vorticity passing the measuring column; Δh = 10 mm, x/C = 0.5250

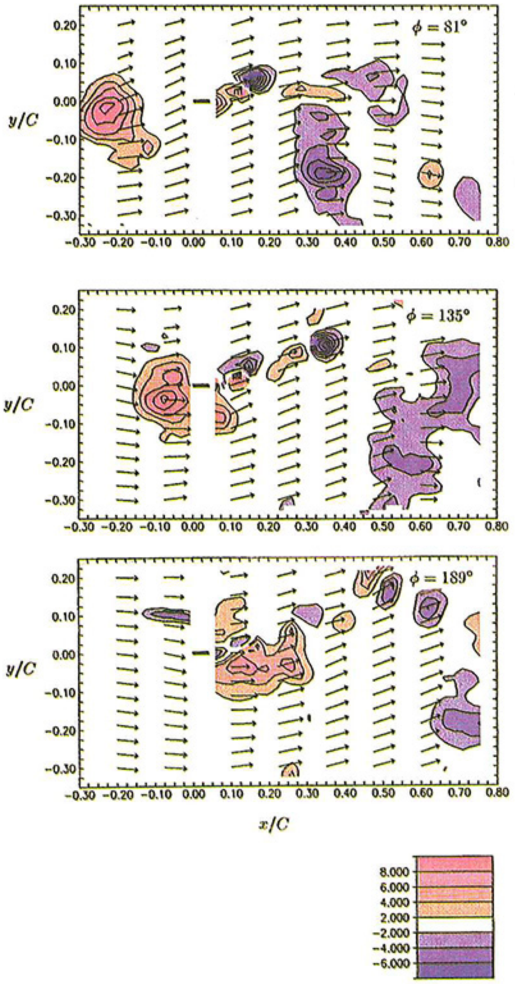

Fig. 6 Vorticity contours for the 6.35 mm rectangular plate, Δh = 10 mm

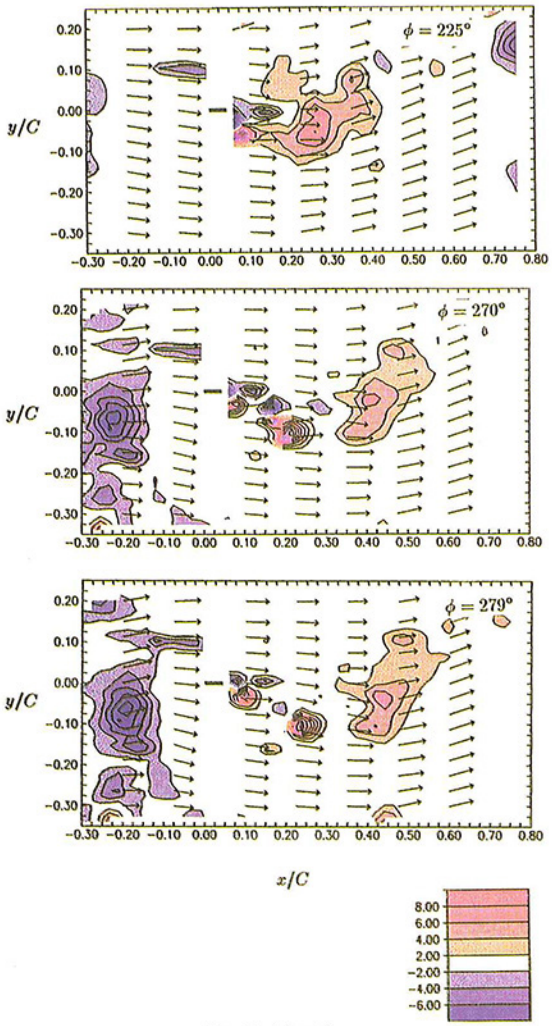

Fig. 6 (Cont.)

Data were also obtained for other Δh displacements and have been deposited in the JFE Data Bank. Here we only present some integral quantities obtained from these data. The dimensionless strength, $\Gamma/(UC)$, of the negative secondary vortex, obtained by integration, is presented in Table 1. It is apparent that the strongest negative vortices were created when the primary vortex passes above the plate (Δh = 5 mm), in qualitative agreement with the results presented by other authors (Meier et al., 1986).

The time history of the vorticity, as calculated by Eq. (1), crossing a station downstream of the plate is presented in Fig. 5. Positive, strong positive, and negative spikes are present, in contrast to a uniform structure of the undisturbed case of Fig. 2.

4 The Effects of Plate Length and Shape. Three target plates, having chord lengths 25.4, 12.7, and 6.35 mm, were examined. For all the cases, the plate offset, Δh, was set equal to 10 mm. A sequence of frames showing the vortical pattern development over the 6.35 mm plate is shown in Fig. 6. In this figure we also display instantaneous velocity vectors. Velocity is measured along a tight grid in the y direction, but here we present data only along a few points to preserve the clarity of the figure. It is now clear that large angles of attack are induced on the irrotational flow about the plate, while the oncoming disturbing vortex is still at some distance upstream. The oncoming vortex is split again and its two pieces are separated by vorticity of the opposite sense. However, the magnitude of the positive vorticity is reduced, compared to the 25.4 mm plate wake. This is also true for the negative vorticity, i.e., the

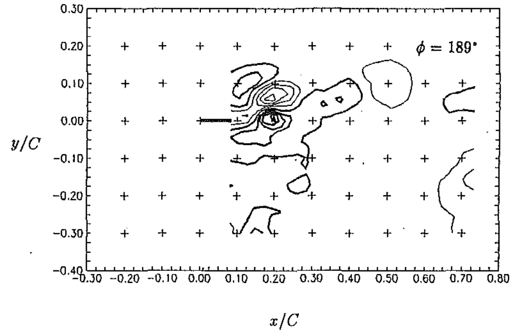

Fig. 7 Vorticity contours for the 12.7 mm rectangular plate, Δh = 10 mm. Contour definitions as in Fig. 4.

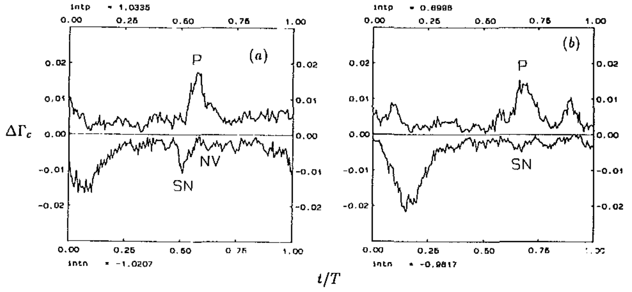

Fig. 8 Time history of vorticity for c = 12.7 mm, Δh = 10 mm passing the measuring column at (*a*) x/C = 0.3375; (*b*) x/C = 0.5250. Uncertainty estimate in vorticity calculations: ±0.03.

secondary vortex induced on the plate because of its interaction with the oncoming vortex is also smaller compared to the longer plates.

A sequence of little vortices is observed drifting along the direction of the local velocity, namely inclined upward when a counterclockwise vortex is interacting with the plate and downward when a clockwise vortex is interacting with the plate. These vortices are vaguely reminiscent of Kelvin-Helmholz vortices. However, unlike $K-H$ vortices, the present sequence has an alternating sense of direction. Moreover, their wavelength is about two orders of magnitude smaller than the $K-H$ wavelength. A rough estimate of the latter could be given by $L = 2\pi/\alpha$ where the wave number α is equal to 0.446 ($\delta\omega/2$) and the vorticity thickness, $\delta\omega$, can be assumed equal to the thickness of the vorticity layer shown in Fig. 6. Here we estimated from the second frame, ϕ = 135 deg, that the thickness of the layer of the series of vortices is comparable to the chord of the plate.

Due to lack of space, we present in Fig. 7 only one frame of the wake of the 12.7 mm plate. The pattern is similar to the ones discussed earlier. The intensity of the vortices downstream of the plate is a little larger than for the case of the shorter plate. In Fig. 8 are shown the circulation history diagrams obtained at x/C = 0.525 for the 12.7 mm plate. The peak corresponding to the secondary vortex is less regular in Fig. 8(*a*) than in Fig. 6. The secondary vortex in this case disintegrated sooner than the one created behind the 25.4 mm plate. For various values of x/C, its strength, is given in Table 2.

For the shortest plate (c = 6.35 mm), the vorticity contour image was even less regular. The amount of negative vorticity, produced during the vortex-plate interaction, was too small to create a regular negative vortex. The result was that the core of the primary vortex was cut apart by a sequence of small irregular areas of negative vorticity.

Apart from the rectangular cross-section, two other shapes of the target plate were examined. One of them was a 12.7 mm plate with rounded edges. A frame of vorticity contours over such a plate is presented in Fig. 9. A schematic of the plate shape is included in the frame of the figure. These patterns should be compared with those of Fig. 7, which were obtained with a plate of identical chord length but with rectangular corners. Apparently the plate with rounded edges reduces the peaks of both positive and negative vorticity. The strength of the negative vorticity calculated by integration at downstream stations is presented in Table 3.

Table 2 Range of strength of secondary vortex downstream of the 12.7 mm plate

x/C	0.2250	0.3375	0.5250	0.7125	0.9000
$\dfrac{\Gamma}{UC}$	0.17—0.21	0.11—0.13	0.03—0.07	0.02—0.06	0.03—0.04

Table 3 Strength Γ/UC of secondary vortex downstream of 12.7 mm plate

x/C	0.2250	0.3375	0.5250	0.7125
rectangular	−0.2106	−0.1304	−0.0703	−0.0350
rounded	−0.1458	−0.0923	−0.0419	−0.0424

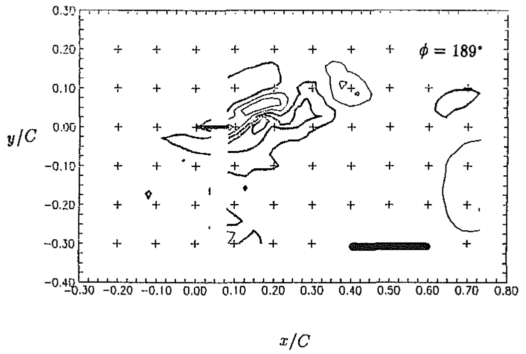

Fig. 9 Vorticity contours for a 12.7 mm plate with rounded edged, Δh = 10mm. Contour definitions as in Fig. 4.

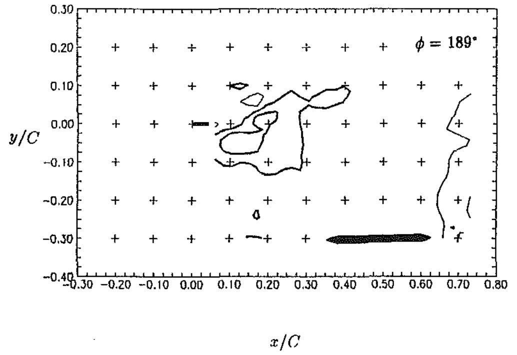

Fig. 10 Vorticity contours for the 6.35 mm plate with sharp edges, Δh = 10 mm. Contour definitions as in Fig. 4.

The most interesting results in this investigation we obtained with a 6.35 mm plate which was tapered carefully on both sides to form sharp edges. The top and bottom surfaces were given a curvature, allowing the shape to merge smoothly into wedge-shaped edges. A schematic sketch of the plate is inserted in Fig. 10, which presents the frame at ϕ = 189 deg over this plate. This can be compared directly to the corresponding frame of Fig. 7. Although the patterns are very similar, a significant decrease in strength of both positive and negative vorticity can be observed.

5 JFE Data Bank Contributions

The raw data obtained by the authors have been deposited in the JFE Data Bank. The readers will find in the files velocity components measured along eight x/C columns for different values of the phase angle. Unfortunately, due to lack of computer space, it was not possible to save all realizations of velocity records. The data were ensemble averaged on the line, while the experiment was in progress. The readers can use these data to explore in their own way the physics of the problem, plot results in whatever form they see fit, calculate vorticity and reconstruct vorticity contours.

The data files contain all the data employed in the construction of the figures of this paper, as well as many more data which could not be represented by figures due to lack of space. Complete data sets are included for the three plate chords, for rectangular, rounded and sharp-edged plates. The files also include instructions on the data format. To access the file of this paper, see instructions on p. 794 of this issue.

6 Conclusions

Velocity measurements were obtained over short plates during their interaction with oncoming coherent vortices. It was proved that the phenomena developing in time, are repeatable within the accuracy of the measuring devices employed. This allowed us to reconstruct the entire field by measuring at each point in space during different realizations of the motion. We were therefore able to construct "quasi-instantaneous" vorticity fields.

Our results describe the detailed structure of the interaction of a vortex with short flat plates. The vorticity shed at the trailing edge of the plate in response to its changing circulation and the vorticity building up into the stall vortex are captured. All these vortical structures are shed and interact with the remnants of the oncoming vortex.

It was demonstrated that shorter plates are more efficient in reducing the strength of the oncoming vortices. Moreover, they produce secondary vorticity with smaller magnitudes than do longer plates. Finally, a short tapered plate with sharp edges proved to be the most efficient attenuator of the oncoming vortical structure.

Acknowledgment

One of the authors (J. S.) was sponsored by the Kościuszko Foundation, an American Center for Polish Culture, under the Exchange Visitor Program No. P 3/3000. The work of the second author (M. C. W.) was supported by NASA grant no. NGT-50123.

References

Akima, H., 1978, "A Method of Bivariate Interpolation and Smooth Surface Fitting for Irregularly Distributed Data Points," *ACM Transactions on Mathematical Software 4*, Vol. 2.

Anders, J. B., 1990, "Outer-Layer Manipulators for Turbulent Drag Reduction," *Progress in Astronautics and Aeronautics: Viscous Drag Reduction in Boundary Layers*, Vol. 123, D. M. Bushnell and J. N. Hefner, eds., AIAA, Washington, DC, pp. 263-284.

Balakumar, P., and Widnall, S. E., 1986, "Application of Unsteady Aerodynamics to Large-Eddy Breakup Devices in a Turbulent Flow," *Physics of Fluids*, Vol. 29, No. 6, pp. 1779-1787.

Bushnell, D. M., 1984, "Body Turbulent Interaction," AIAA Paper No. 84-1527.

Doligalski, T. L., and Walker, J. D. A., 1984, "The Boundary Layer Due to a Convected Two-Dimensional Vortex," *Journal of Fluid Mechanics*, Vol. 139, pp. 1-28, 1984.

Dowling, A. P., 1985, "The Effect of Large-Eddy Breakup Devices on Oncoming Vorticity,"*Journal of Fluid Mechanics*, Vol. 160, pp. 447-463.

Homa, J., Lucas, M., and Rockwell, D., 1988, "Interaction of Impulsively Generated Vortex Pairs with Bodies," *Journal of Fluid Mechanics*, Vol. 197, pp. 571-594.

Kaykayoglu, R., and Rockwell, D., 1985, "Vortices Incident Upon a Leading Edge: Instantaneous Pressure Fields," *Journal of Fluid Mechanics*, Vol. 156, pp. 439-446.

Kinney, R. B., Taslim, M. E., and Hung, S. C., 1988, "A Hybrid Computational Approach to Multiple-Body Viscous-Flow Problems: Application to Large-Eddy Breakup in a Boundary Layer," *Journal of Computational Physics*, Vol. 78, pp. 378-404.

Koromilas, C. A., and Telionis, D. P., 1980, "Unsteady Laminar Separation: An Experimental Study," *Journal of Fluid Mechanics*, Vol. 97, pp. 378-384.

Mathioulakis, D. S., Kim, J., Telionis, D. P., and Mook, D. T., 1985, "The Near Wake of a Pitching Airfoil," 18th AIAA Fluid Mechanics, Plasma Dynamics and Laser Conference, AIAA Paper #85-162.

Meier, G. E. A., and Timm, R., 1986, "Unsteady Vortex Airfoil Interaction," *Proc. AGARD Conf. No. 386 Neuilly sur Seine*, France, Paper No. 16.

Melander, M. V., McWilliams, J. C., and Zabusky, N. J., 1987, "Axisymmetrization and Vorticity-Gradient Intensification of an Isolated Two-Dimensional Vortex Through Filamentation," *Journal of Fluid Mechanics*, Vol. 178, pp. 137-159.

Poling, D. R., and Telionis, D. P., 1987, "The Trailing Edge of a Pitching Airfoil at High Reduced Frequencies," ASME JOURNAL OF FLUIDS ENGINEERING, Vol. 109, pp. 410-414.

Rockwell, D., 1983, "Invited Lecture: Oscillation of Impinging Shear Layers," *AIAA Journal*, Vol. 21, No. 5, May, pp. 645-664.

Sears, W. R., and Kuethe, A. M., 1939, "The Growth of the Circulation of an Airfoil Flying through a Gust," *Journal of Aeronautical Sciences*, Vol. 6, No. 9, 1939, pp. 376-378.

Sears, W. R., 1940, "Operational Methods in the Theory of Airfoils in Non-Uniform Motion," *Journal of the Franklin Institute*, Vol. 230, No. 1, 1940, pp. 95-111.

Swirydczuk, J., 1990, "A Visual Study of the Interaction of a Free Vortex with the Wake Behind an Airfoil," *Experiments in Fluids*, Vol. 9, pp. 181-190.

Wilder, M. C., Pesce, M. M., Telionis, D. P., Poling, D. R., and Dadone, L., 1990, "Blade-Vortex Interaction Experiments—Velocity and Vorticity Fields," AIAA Paper No. 90-0030.

Ziada, S., and Rockwell, D., 1982, "Vortex-Leading Edge Interaction," *Journal of Fluid Mechanics*, Vol. 118, May, pp. 79-107.

Eigen-Functions of Linearized Unsteady Boundary Layer Equations[1]

S. H. Lam
Department of Mechanical and
Aerospace Engineering,
Princeton University,
Princeton, NJ 08544

N. Rott
Department of Aeronautics and Astronautics,
Stanford University,
Stanford, CA 94305

The Lam and Rott theory of linearized unsteady boundary layers is revisited, and some new results are obtained. The exact outer eigen-solution for a flat plate found in the original paper is shown to be a special case of the Prandtl-Glauert transposition theorem. The streamwise coordinate-dependent factor of the inner eigen-solutions, first found by M. E. Goldstein for the flat plate, is generalized for arbitrary pressure gradients.

1 Introduction

In 1960, we did research on unsteady laminar boundary layers under the general supervision of Professor William R. Sears in support of his comprehensive research program on steady and unsteady aerodynamics (Sears, 1956), and issued a Cornell University Graduate School of Aeronautical Engineering Report (Lam and Rott, 1960) entitled "Theory of Linearized Time-dependent Boundary Layers." This report derived, for the first time, *eigen-solutions* to the linearized unsteady laminar boundary layer equations. In addition, it showed that the "low-frequency" series solution obtained has an infinite radius of convergence, and computed 15 terms of this series. Even though it was never published in the open literature, this work has been noted, used and extended by several authors. Ackerberg and Phillips (1972) noted that Lam and Rott "anticipated the use of matched (asymptotic) expansions," and presented an alternative analysis supplemented by direct numerical solutions of the governing partial differential equations using a finite difference method. Later, Goldstein (1983) pointed out that the Lam and Rott eigen-solutions accounted for nonparallel flow effects—and thus provided the mechanism to progressively shorten the long wavelength components of upstream disturbances to match the shorter wavelengths of the Tollmien-Schlichting waves downstream. He showed that the "lowest order asymptotic eigen-solution of the unsteady boundary-layer equations turns into a spatially growing Tollmien-Schlichting wave." In addition, he pointed out that, for the flat plate case, both previous works missed a power law factor in the eigen-solutions, and showed that this missing factor is important in the calculation of higher order terms. These eigen-solutions were found to be useful (Goldstein, Sockol and Sanz, 1983, Kerschen, 1990) in the study of the *receptivity* of boundary layers (Reshotko, 1976).

In other developments, Brown and Stewartson (1974) studied the leading order linear partial differential equation which governed the Lam and Rott eigen-solutions, and constructed an "exact solution" for a model problem in terms of a contour integral using Laplace Transform. They showed that the "most significant exponentially decaying term" of the asymptotic representation of this exact analytical solution far downstream was in agreement with the Lam and Rott results. Van Dyke (1974) cited the 15 terms Lam and Rott low-frequency series solution as a rare example in analytical mechanics of a series solution with infinite radius of convergence.

It is now a third of a century since the original Cornell University report appeared. We are rewriting this work to honor Professor William R. Sears on his 80th birthday, and to acknowledge to him our debts for his inspirations, friendship and support throughout the years. Originally, we had planned to simply edit the original manuscript and to publish it without changing the technical content. However, it seemed appropriate to refer to developments since 1960, and in the process of editing and rewriting, some new results were obtained. In particular, our original "exact" outer eigen-solution for the flat plate case is found to be valid for arbitrary pressure gradients. In addition, the streamwise coordinate-dependent factor of the inner eigen-solutions, missed by all investigators prior to 1983, is rederived here without requiring that pressure gradient of the basic steady flow be zero.

2 Statement of the Problem

The laminar, constant property, two-dimensional time-dependent boundary layer equations are:

$$\frac{\partial u}{\partial x}+\frac{\partial v}{\partial y}=0 \tag{1a}$$

and

$$\frac{\partial u}{\partial t}+u\frac{\partial u}{\partial x}+v\frac{\partial u}{\partial y}=-\frac{1}{\rho}\frac{dp}{dx}+\nu\frac{\partial^2 u}{\partial y^2} \tag{1b}$$

where

$$-\frac{1}{\rho}\frac{dp}{dx}=\frac{\partial U_\infty}{\partial t}+U_\infty\frac{\partial U_\infty}{\partial x} \tag{1c}$$

and U_∞, the freestream velocity, is given by

---

[1] Dedicated to Professor W. R. Sears on occasion of his 80th birthday.

Contributed by the Fluids Engineering Division for production in the JOURNAL OF FLUIDS ENGINEERING. Manuscript received by the Fluids Engineering Division June 24, 1993; revised manuscript received September 23, 1993. Associate Technical Editor: D. P. Telionis.

$$U_\infty(x,t)=U_o(x)+\epsilon U_1(x)\exp(-i\omega t) \qquad (2)$$

where $U_o(x)$ and $U_1(x)$ are given functions of x and ϵ is a small dimensionless parameter. For the sake of simplicity, the frequency ω is considered real and positive.

Since ϵ is small, we express u and v as follows:

$$u=U(x,y)+\epsilon u'(x,y,t)+O(\epsilon^2), \qquad (3a)$$

$$v=V(x,y)+\epsilon v'(x,y,t)+O(\epsilon^2), \qquad (3b)$$

where (U, V) is an exact steady-state solution and (u', v') represents the time-dependent perturbation. The equations governing (u', v') are linearized:

$$\frac{\partial u'}{\partial x}+\frac{\partial v'}{\partial y}=0 \qquad (4a)$$

and

$$\frac{\partial u'}{\partial t}+U\frac{\partial u'}{\partial x}+V\frac{\partial u'}{\partial y}+u'\frac{\partial U}{\partial x}+v'\frac{\partial U}{\partial y}=-\frac{1}{\rho}\frac{dp'}{dx}+\nu\frac{\partial^2 u'}{\partial y^2} \qquad (4b)$$

where

$$-\frac{1}{\rho}\frac{dp'}{dx}=\exp(-i\omega t)\,(-i\omega U_1+(U_oU_1)_x) \qquad (4c)$$

For later convenience, we differentiate (4*b*) with respect to y to obtain:

$$\frac{\partial u_y'}{\partial t}+U\frac{\partial u_y'}{\partial x}+V\frac{\partial u_y'}{\partial y}+u'\frac{\partial U_y}{\partial x}+v'\frac{\partial U_y}{\partial y}=\nu\frac{\partial^2 u_y'}{\partial y^2} \qquad (5)$$

It is important to note that the boundary layer approximations are assumed to be valid for the perturbation velocities. In particular, $u_y' \gg v_x'$ is assumed. Under this approximation, u_y' can be interpreted to be the perturbation vorticity, and (5) can be interpreted to be the linearized vorticity equation. The initial and boundary conditions for this parabolic partial differential equation are the standard ones.

2.1 The Choice of Independent Variables. We write the total streamfunction ψ for the flow as follows:

$$\psi=\sqrt{2\nu xU_o(x)}F(x,\eta)+\epsilon\psi'(x,y,t) \qquad (6)$$

where the basic steady flow solution $F(x, \eta)$ is assumed to be known, η is the usual nondimensional normal coordinate of the basic steady boundary layer, $\eta \equiv y\sqrt{U_o(x)/2\nu x}$, and ψ' is the streamfunction of the time-dependent perturbation.

For problems with sinusoidal time dependence, ψ' can be expressed in terms of only two independent variables, ξ and η, where ξ, the *reduced frequency* parameter, is given by $\xi \equiv i\omega x/U_o(x)$. For any given basic flow (we shall exclude from our consideration the "pure" stagnation point case, i.e., $U_o(x) \propto x$ for all x, which is an exception), ξ will be a function of x. Hence, for fixed ω, the whole range of $|\xi|$ from zero to infinity is of interest.

The solution $\psi'(\xi, \eta)$ when expressed as a power series in ξ is called the *low-frequency* series solution.

For large values of ξ, an alternative choice of coordinates is more appropriate: $\alpha \equiv \xi^{-1/2} = \sqrt{U_o(x)/i\omega x}$, $\beta \equiv y\sqrt{i\omega/\nu}$. The solution $\psi'(\alpha, \beta)$ when expressed as a power series in α is called the *high-frequency* series solution.

2.2 The Literature in 1960. Special cases of this class of problems had already been reported in the literature prior to 1960. For example, Lighthill (1954) and Illingworth (1958) studied the flat plate case. Rott (1956) and Glauert (1956) studied the pure stagnation point case. The flat plate case presents certain interesting mathematical pecularities, and it provided the primary motivation for Lam and Rott (1960).

The low-frequency solution, a series in powers of ξ, can be straightforwardly calculated. Lighthill and Illingworth computed the first two terms, and Lam and Rott computed the first 15 terms. In addition, Lam and Rott showed that the low-frequency series solution has an infinite radius of convergence, and proved an uniqueness theorem.

The high-frequency solution is a series in powers of α. Lighthill carried only one term in his calculation, while Illingworth carried the expansion to order α^3, and included the effects of compressibility. His higher-order velocity profiles behave like polynomials in β for β large, and Illingworth was satisfied that they only blow up algebraically and not exponentially. Rott and Rosenzweig (1969) suggested that the high-frequency solution might have an "inner and outer" structure. The Lam and Rott analysis, which was done before the method of matched asymptotic expansion became widely accepted, showed that the solution had indeed an inner and outer structure for large ξ, and constructed an uniformly valid composite high-frequency solution which satisfied all boundary conditions.

The high frequency series solution for the flat plate is mathematically an asymptotic solution valid far downstream. The question posed by Lam and Rott was: what would be the response of a laminar boundary layer far downstream to some arbitrary time-dependent perturbation imposed at some upstream station? The Lighthill and Illingworth high-frequency series solution could not answer this question, for their theory did not provide the needed degrees of freedom. Noting that solutions to initial-value problems for linear parabolic partial differential equations is usually expressed in terms of their eigen-solutions, Lam and Rott proceeded to look for them and succeeded in finding them for the linearized unsteady boundary layer equations. In principle, the desired solution far downstream would then be given as a superposition of these eigen-solutions on top of the Lighthill-Illingworth high-frequency series solution.

3 The Eigen-Solutions

Equations (4*a*) and (4*b*), with the latter's "forcing term" dp'/dx deleted (i.e., setting $U_1 = 0$), constitute a system of linear *homogeneous* partial differential equation. Solutions to this PDE system satisfying *null* freestream and wall boundary conditions are called *eigen-solutions*. We are interested in the construction of eigen-solutions when ξ is large.

It is now well established that the large ξ eigen-solution has an inner and outer structure. In the following sections, separate outer and inner eigen-solutions will be found and matched with each other.

3.1 A Special Exact Outer Eigen-Solution. Consider the following transformation of dependent and independent variables:

$$x_*\equiv x, \quad y_*\equiv y-\epsilon B(x,t), \quad t_*\equiv t, \qquad (7a)$$

and

$$u(x,y,t)=u_*(x_*,y_*,t_*), \qquad (7b)$$

$$v(x,y,t)=v_*(x_*,y_*,t_*)+\epsilon u_*(x_*,y_*,t_*)B_x(x,t)+\epsilon B_t(x,t) \qquad (7c)$$

where $B(x, t)$ is any arbitrary differentiable function of x and t, and ϵ is a dimensionless parameter which need *not* be small—for the moment. It can readily be verified that $u_*(x_*, y_*, t_*)$ and $u_*(x_*, y_*, t_*)$ satisfy the unsteady boundary layer equations in the transformed variables (for the same externally imposed pressure gradient). In other words, *the unsteady boundary layer equations are invariant under this transformation.* Hence, a special exact solution is:

$$u_*=U(x_*,y_*), \quad v_*=V(x_*,y_*). \qquad (8)$$

Physically, this result says that the effects of a flexible wall with time-dependent motion located at $y_{\text{wall}} = \epsilon B(x, t)$ can be removed by a coordinate transformation—provided that the movements of the wall do not disturb the externally imposed pressure gradient. This special property of the boundary-layer equations was first noted by Prandtl (1938) for $B = B(x)$, and was later generalized by Glauert (1957) for $B = B(x, z, t)$ for three-dimensional unsteady compressible flows. It is commonly referred to as the Prandtl-Glauert transposition theorem.

If we now assume that ϵ is small, then (8) can be expanded to yield:

$$u_* = U(x,y) - \epsilon B(x,t)\, U_y(x,y) + O(\epsilon^2), \tag{9a}$$

$$v_* = V(x,y) - \epsilon B(x,t)\, V_y(x,y) + O(\epsilon^2). \tag{9b}$$

Using (9*a*), (9*b*) in (7*b*) and (7*c*) and comparing the results to (3*a*) and (3*b*), we obtain:

$$u'(x,y,t) = -B(x,t)\, U_y(x,y) + O(\epsilon^2), \tag{10a}$$

$$v'(x,y,t) = [B(x,t)\, U(x,y)]_x + B_t(x,t) + O(\epsilon^2). \tag{10b}$$

Equations (10*a*) and (10*b*) satisfy (4*a*) and the homogeneous version of (4*b*) exactly—for any differentiable but otherwise arbitrary $B(x, t)$—as can be verified readily by direct substitution. Note that u' is null as required at the edge of the boundary-layer ($y \rightarrow \infty$), but the no-slip condition is *not* satisfied at the wall ($y = 0$).

This special exact solution for the flat plate case ((10*a*) and (10*b*)) was first found by Lam and Rott, and was used as part of the outer solution in their flat plate high-frequency analysis. The fact that it is a valid outer eigen-solution for the general case (without requiring the basic pressure gradient to be zero, or the frequency to be high), and that it was in fact the linearized version of the Prandtl-Glauert transposition theorem, was discovered only during the rewriting of this paper. Note that it possesses *no* degree of freedom to accommodate for arbitrary upstream initial conditions, hence it cannot be used to represent their effects downstream. Nevertheless, we shall call it the *outer eigen-solution* because it will be used as the outer solution to match with the inner eigen-solutions.

3.2 The High-Frequency Inner Eigen-Solutions. Let the perturbation eigen streamfunction ψ' be expressed as follows:

$$\psi'(x,y,t) \equiv \left[\exp(-i\omega t)\exp\left(\int^x \frac{K dx'}{\sigma(x')}\right)\right] P(x,y) \tag{11}$$

where K is a dimensional (complex) constant to be determined and $\sigma(x)$ is the slope of the basic steady streamwise velocity profile at the wall:

$$\sigma(x) \equiv (U_y)_{y=0}. \tag{12}$$

We have:

$$u' = \frac{\partial \psi'}{\partial y} = \left[\exp(-i\omega t)\exp\left(\int^x \frac{K dx'}{\sigma(x')}\right)\right] P_y, \tag{13a}$$

$$v' = -\frac{\partial \psi'}{\partial x} = - \left[\exp(-i\omega t)\exp\left(\int^x \frac{K dx'}{\sigma(x')}\right)\right] \left(\frac{K}{\delta} P + P_x\right). \tag{13b}$$

When ω is sufficiently large, a thin inner layer of thickness $\beta = O(1)$ is expected adjacent to the wall to accommodate for the no-slip boundary condition. It is clear that in this thin layer, the unsteady term, the viscous term, and the convection term of the boundary-layer momentum equation must all play a role.

Using (13*a*) and (13*b*) in (5), we obtain:

$$-i\omega P_{yy} + \frac{K}{\sigma} U P_{yy} - \nu P_{yyyy} = Q \tag{14}$$

where the unsteady, viscous and one of the K-dependent convective terms have been placed on the left hand side, while all the remaining (convective) terms are placed on the right hand side and are collectively denoted by Q:

$$Q \equiv U_{yy}\left(P_x + \frac{K}{\sigma} P\right) - U P_{yyx} - V P_{yyy} - U_{xy} P_y. \tag{15}$$

In the vicinity of the wall, the basic steady velocity profiles can be expressed as follows:[2]

$$U = \sigma y - \frac{1}{4\nu}\frac{dU_o^2}{dx} y^2 + \frac{1}{48\nu}\frac{d\sigma^2}{dx} y^4 + \ldots, \tag{16a}$$

$$V = -\frac{1}{2}\frac{d\sigma}{dx} y^2 + \frac{1}{12\nu}\frac{d^2 U_o^2}{dx^2} y^3 - \frac{1}{240\nu}\frac{d^2\sigma^2}{dx^3} y^5 + \ldots. \tag{16b}$$

Using (16*a*), (16*b*) in (14), we obtain:

$$(-i\omega + Ky) P_{yy} - \nu P_{yyyy} = \tilde{Q} \tag{17}$$

where

$$\tilde{Q} \equiv Q - \frac{K}{\sigma}(U - \sigma y) P_{yy}. \tag{18}$$

We now introduce a new set of dimensionless independent variable $\tilde{x}$ and ζ to replace x and y:

$$\tilde{x} \equiv \frac{x}{L}, \quad \zeta \equiv \zeta_k + \frac{y}{\Delta_k} \tag{19}$$

where L is the characteristic length of the basic steady flow problem, and ζ_k and Δ_k are constants to be determined. We obtain:

$$G_{\zeta\zeta} - \left(-\frac{i\omega\Delta_k^2}{\nu} + \frac{K\Delta_k^3}{\nu}(\zeta - \zeta_k)\right) G = -\frac{\Delta_k^4}{\nu}\tilde{Q} \tag{20}$$

where

$$G \equiv P_{\zeta\zeta} \tag{21}$$

and is proportional to the vorticity of the perturbation.

To simplify (20), we choose:

$$\frac{K\Delta_k^3}{\nu} = 1, \quad \text{or } K = \frac{\nu}{\Delta_k^3}, \tag{22a}$$

$$-\frac{i\omega\Delta_k^2}{\nu} = \zeta_k, \quad \text{or } \Delta_k = \left(\frac{\nu^{1/2}(-\zeta_k)^{1/2}}{\omega^{1/2}}\right) e^{-i\pi/4} \tag{22b}$$

so that (20) becomes, for small y (near the wall):

$$\begin{aligned} \mathfrak{L}^{(\zeta)}(G) &= -\frac{\Delta_k^4}{\nu}\tilde{Q} \\ &= \epsilon_{k1}\tilde{Q}_1 + \epsilon_{k2}\tilde{Q}_2 + O(\epsilon_{k1}\epsilon_{k2}) \end{aligned} \tag{23}$$

where $\mathfrak{L}^{(\zeta)}(*)$ is the self-adjoint *Airy* operator

$$\mathfrak{L}^{(\zeta)}(*) \equiv \frac{d^2}{d\zeta^2}(*) - \zeta(*), \tag{24}$$

and $\tilde{Q}_1$ and $\tilde{Q}_2$ are given by:

$$\tilde{Q}_1 \equiv (\zeta - \zeta_k) P_{\zeta\zeta\tilde{x}} + \frac{1}{\sigma}\frac{d\sigma}{d\tilde{x}}\left[P_\zeta - \frac{1}{2}(\zeta - \zeta_k)^2\left(P_{\zeta\zeta\zeta} - \frac{(\zeta - \zeta_k)^2}{12} P_{\zeta\zeta} + P\right)\right], \tag{25a}$$

$$\tilde{Q}_2 \equiv \frac{1}{U_o}\frac{dU_o}{d\tilde{x}}\left(P - \frac{1}{2}(\zeta - \zeta_k)^2 P_{\zeta\zeta}\right). \tag{25b}$$

The dimensionless parameters ϵ_{k1} and ϵ_{k2} are given by:

---

[2] It is essential that the term proportional to y^4 in U be kept in this analysis. The omission of this term was responsible for the failure of the earlier analyses (Lam and Rott, 1960; Ackerberg and Phillips, 1972; and Brown and Stewartson, 1974) to obtain the correct x-dependent factor for the leading order eigen-solution.

$$\epsilon_{k1}(\tilde{x}) \equiv \left(\frac{\sigma\nu^{1/2}}{\omega^{3/2}L}\right)(-\zeta_k)^{3/2}e^{-i3\pi/4}, \tag{25c}$$

$$\epsilon_{k2}(\tilde{x}) \equiv \left(\frac{U_o^2}{\sigma(\nu\omega)^{1/2}L}\right)(-\zeta_k)^{1/2}e^{-i\pi/4}. \tag{25d}$$

In general, the magnitude of the ratio $\epsilon_{k2}/\epsilon_{k1}$ is a large number:

$$\frac{\epsilon_{k2}}{\epsilon_{k1}} = \frac{i\Pi_k}{(-\zeta_k)}, \quad \Pi_k(\tilde{x}) \equiv \frac{\omega U_o^2}{\nu\sigma^2}. \tag{26}$$

In the limit of asymptotically large ω, both parameters ϵ_{k1} and ϵ_{k2} are small—provided that ζ_k is $O(1)$. Expanding G,

$$G = G^{(o)} + \epsilon_{k1}G^{(1)} + \epsilon_{k2}G^{(2)} + \ldots \tag{27}$$

we obtain the governing ODE for the leading order term:

$$\mathcal{L}^{(\zeta)}(G^{(o)}) = 0. \tag{28}$$

It is straightforward to show that the boundary conditions for $G^{(o)}(\tilde{x}, \zeta)$ are (under the boundary-layer approximations):

$$\lim_{y\to\infty} G^{(o)}(\tilde{x},\zeta) \to 0, \quad \text{(edge condition)}, \tag{29a}$$

$$G_\zeta^{(o)}(\tilde{x},\zeta\to\zeta_k) = 0, \quad \text{(wall condition)}. \tag{29b}$$

Integrating (28) with respect to ζ once, recognizing that $G^{(o)} = P_{\zeta\zeta}^{(o)}$, and imposing (29$b$) and the no-slip condition at the wall, we obtain:

$$P_{\zeta\zeta\zeta}^{(o)} - \zeta P_\zeta^{(o)} + P^{(o)} = 0 \tag{30}$$

which shall be found useful later.

The solution of (28) can in general be expressed as linear combinations of *Airy Functions* $A_i(\zeta)$ and $B_i(\zeta)$ (Jeffery and Jeffery, 1972). Only $A_i(\zeta)$, which decays exponentially for $|\arg(\zeta)| \leq \pi/3$ and oscillates and decays algebraically for $\arg(\zeta) = \pi$, is consistent with the above boundary conditions. Discarding[3] $B_i(\zeta)$, we have:

$$G^{(o)} = a(\tilde{x})A_i(\zeta) \tag{31}$$

where the amplitude factor $a(\tilde{x})$ may indeed depend on $\tilde{x}$ was first pointed out by Goldstein (1983). The only requirement at this point on $a(\tilde{x})$ is that it be smooth and differentiable when $\tilde{x} = O(1)$.

The edge condition (29a) requires $\arg(\zeta) \leq \pi/3$ as $y \to \infty$. The phase of the right-hand side of (22b) had been chosen to satisfy this requirement—with the understanding that square roots of positive real numbers are positive and real. The ζ_k are the eigen-values for this problem, and they are determined by (29b) to be the zeros of $dA_i/d\zeta$—which all lie on the negative real axis. Ordering them in ascending magnitudes, we have:

$$\zeta_0 = -1.019, \quad \zeta_1 = -3.248, \quad \zeta_2 = -4.820, \quad \zeta_3 = -6.163, \quad \zeta_4 = -7.372, \ldots$$

Note that $|\zeta_k|$ is proportional to $k^{2/3}$ for large k. In principle, G should be represented by a linear combination of G_k's, each of which is associated with its own ζ_k. In what follows, the G's we deal with are G_k's but their k-subscripts are omitted to minimize clutter.

We can compute $P_y^{(o)}$ and $P^{(o)}$ from $G^{(o)}$ by direct integration:

$$P_y^{(o)} = \frac{P_\zeta^{(o)}}{\Delta_k} = \frac{a(\tilde{x})}{\Delta_k}\int_{\zeta_k}^{\zeta} A_i(\zeta')d\zeta', \tag{32}$$

$$P^{(o)} = a(\tilde{x})\int_{\zeta_k}^{\zeta}(\zeta - \zeta')A_i(\zeta')d\zeta'. \tag{33}$$

Note that $P_y^{(o)}$ is finite as $\zeta \to \infty$. In other words, the value of u' at the outer edge of this inner layer is nonzero, and an outer layer is required to satisfy the requirement that u' should be zero at the outer edge of the basic steady boundary layer.

All $G^{(n)}$'s for $n > 0$ are required to satisfy the same homogeneous wall conditions as $G^{(o)}$, but are allowed algebraic behaviors for their edge conditions in accordance with standard matched asymptotic expansion procedures (Van Dyke, 1964; Cole, 1968). The leading order matching will be done in Section 3.4.

3.3 The Determination of *a(x̃)*. To obtain an equation for $a(\tilde{x})$, we multiply (23) by $A_i(\zeta)$ and integrate with respect to ζ from ζ_k to infinity. Since $\mathcal{L}^{(\zeta)}(*)$ is a self-adjoint operator and $\mathcal{L}^{(\zeta)}(A_i) = 0$, the left-hand side can be shown to vanish identically by the use of (29a) and (29b):

$$\int_{\zeta_k}^{\infty} A_i(\zeta')\mathcal{L}^{(\zeta')}(G(\zeta'))d\zeta' = [A_iG_\zeta - (A_i)_\zeta G]_{\zeta k}^{\infty} + \int_{\zeta_k}^{\infty} G(\zeta')\mathcal{L}^{(\zeta')}(A_i(\zeta'))d\zeta' = 0. \tag{34}$$

We have:

$$\int_{\zeta_k}^{\infty}(\epsilon_{k1}\tilde{Q}_1(\tilde{x},\zeta') + \epsilon_{k2}\tilde{Q}_2(\tilde{x},\zeta'))A_i(\zeta')d\zeta' \approx 0 \tag{35}$$

which must be satisfied for all $\tilde{x}$.

Using (30), (31), (32) and (33) in (35), we obtain, after considerable algebra:

$$\frac{1}{a_k}\frac{da_k}{d\tilde{x}} - \Gamma_{k1}\frac{1}{\sigma}\frac{d\sigma}{d\tilde{x}} + i\Pi_k\Gamma_{k2}\frac{1}{U_o}\frac{dU_o}{d\tilde{x}} \approx 0 \tag{36}$$

where Γ_{k1} and Γ_{k2} are k-dependent universal real constants

$$\Gamma_{k1} \equiv \frac{3}{2} - \frac{I_{k1}}{24}, \quad \Gamma_{k2} \equiv \frac{1}{(-\zeta_k)}\left(I_{k3} - \frac{I_{k2}}{2}\right), \tag{37a}$$

and

$$I_{ko} \equiv \int_{\zeta_k}^{\infty}(\zeta' - \zeta_k)A_i^2(\zeta')d\zeta', \tag{37b}$$

$$I_{k1} \equiv \frac{1}{I_{ko}}\int_{\zeta_k}^{\infty}(\zeta' - \zeta_k)^4A_i^2(\zeta')d\zeta', \tag{37c}$$

$$I_{k2} \equiv \frac{1}{I_{ko}}\int_{\zeta_k}^{\infty}(\zeta' - \zeta_k)^2A_i^2(\zeta')d\zeta', \tag{37d}$$

$$I_{k3} \equiv \frac{1}{I_{ko}}\int_{\zeta_k}^{\infty}A_i(\zeta'')\int_{\zeta_k}^{\zeta''}(\zeta'' - \zeta')A_i(\zeta')d\zeta'd\zeta''. \tag{37e}$$

Integrating (36), we obtain:

$$a_k \propto \sigma^{\Gamma_{k1}}\exp\left(-i\Gamma_{k2}\int^{\tilde{x}}\Pi_k\frac{d\ln U_o}{d\tilde{x}}d\tilde{x}\right). \tag{38}$$

When U_o = constant, (38) reduces to the flat plate results obtained by Goldstein (1983) and Goldstein, Sockol and Sanz (1983).

3.4 Matching the Outer and Inner Eigen-Solutions. At the edge of this inner layer ($y \to \infty$), we have from (32):

$$P_{y,\infty}^{(o)}(\tilde{x}) \equiv \lim_{y\to\infty} P_y^{(o)} = \frac{a(\tilde{x})}{\Delta_k}C_k, \tag{39a}$$

where C_k, which depends only on k, is:

$$C_k \equiv \int_{\zeta k}^{\infty} A_i(\zeta')d\zeta'. \tag{39b}$$

Matching the values of u' given by (10a) and (13a) at the

---

[3] In the original report, Lam and Rott had noted that if $B_i(\zeta)$ were kept, a continuous spectrum of eigen-values would exist. The corresponding eigen-functions, however, decay only algebraically at the edge of the inner layer. This option is discarded because the corresponding matching outer solution is not available.

junction of the outer and inner layers, we obtain, after using (22*a*), (22*b*) and (26) to eliminate K and Π_k in favor of physical parameters:

$$B(\tilde{x},t)\propto \frac{C_k\sigma^{\Gamma_{k1}-1}}{\Delta_k}\exp\left[-i\left(\omega t+\frac{\omega}{\nu}\int^{\tilde{x}}\frac{\Gamma_{k2}}{2\sigma^2}\frac{dU_o^s}{d\tilde{x}}d\tilde{x}\right)\right]$$
$$\times\exp\left[(-1+i)\left(\frac{\omega^{3/2}L}{(2\nu)^{1/2}(-\zeta_k)^{3/2}}\int^{\tilde{x}}\frac{d\tilde{x}'}{\sigma(\tilde{x}')}\right)+\ldots\right] \qquad (40)$$

It is seen that the leading effect of nonzero pressure gradients is to introduce a purely oscillatory factor (with a comparatively much longer wavelength) into the boundary-layer eigen-solutions.

4 The Low-Frequency Series Solution

We shall also present the Lam and Rott analysis of the low-frequency series solution here because the mathematics used is interesting and is similar to that used in the previous sections.

Let the perturbation streamfunction ψ' be expressed as follows:

$$\psi'=\exp(i\omega t)\sqrt{2\nu x U_o U_1}\sum_{n=0}^{\infty}(2\xi)^n g^{(n)}(\eta). \qquad (41)$$

Restricting our attention to the class of problems defined by:

$$U_o(x)\propto x^m, \qquad (42a)$$

$$U_1(x)\propto x^{m_1}\exp\left(i\omega m_2\int^x\frac{dx}{U_o(x)}\right) \qquad (42b)$$

we can obtain a system of ODE's for all the $g^{(n)}$'s. The ODE for $g^{(n)}$'s for $n \geq 2$ is:

$$g_{\eta\eta\eta}^{(n)}+(1+m)Fg_{\eta\eta}^{(n)}-2(n(1-m)+(m+m_1))F_\eta g_\eta^{(n)}$$
$$+((2n+1)(1-m)+2m_1)F_{\eta\eta}g^{(n)}$$
$$=g_\eta^{(n-1)}+m_2(F_\eta g_\eta^{(n-1)}-F_{\eta\eta}g^{(n-1)}),\quad n\geq 2 \qquad (43)$$

where $F(\eta; m)$ represents the basic steady similar solution. The boundary conditions are:

$$g^{(n)}(0)=g_\eta^{(n)}(0)=0,\quad g_\eta^{(n)}(\infty)=0,\quad n\geq 1. \qquad (44)$$

Lam and Rott numerically computed 15 terms of this series for the special case of a flat plate with $m = m_1 = m_2 = 0$. In addition, the leading approximation to $g^{(n)}$ for asymptotically large n was obtained as outlined below.

For large n, a new independent variable τ is introduced to replace η:

$$\tau=(2(1-m)nA)^{1/3}\eta,\quad A\equiv F_{\eta\eta}(0). \qquad (45)$$

The basic solution $F(\eta)$ can be expressed in terms of τ as follows:

$$F(\eta)=\frac{A\eta^2}{2}+\ldots=\frac{A^{1/3}\tau^2}{2(2(1-m)n)^{2/3}}+\ldots \qquad (46)$$

We now express $g^{(n)}$ formally in terms of a set of basis functions Z_k's:

$$g^{(n)}=\sum_{k=1}^{\infty}b_k D_k^{(n)}Z^{(k)}(\tau) \qquad (47)$$

where the b_k's are constants independent of n, and $D_k^{(n)}$ is a function of k and n to be determined. Substituting into (43), we obtain for $n >> 1$:

$$Z_{\tau\tau\tau}^{(k)}-\tau Z_\tau^{(k)}+Z^{(k)}=-z_k Z_\tau^{(k)}+O(n^{-1/3}) \qquad (48)$$

where z_k is given by

$$z_k\equiv\frac{D_k^{(n-1)}}{(2(1-m)nA)^{2/3}D_k^{(n)}} \qquad (49)$$

and is required to be independent of n. Note that m_1 and m_2 do not appear in either (48) or (49), indicating the results obtained below are valid for arbitrary U_1.

Solving (49) for $D_k^{(n)}$, we obtain:

$$D_k^{(n)}\propto\frac{1}{[z_k]^n[n!]^{2/3}[2(1-m)A]^{2n/3}}. \qquad (50)$$

The presence of the $[n!]^{2/3}$ factor in the denominator indicates that the low-frequency series is an integral function of 2/3 order (Copson, 1955) and has an infinite radius of convergence. Differentiating (48) with respect to τ, and introducing a new independent variable z by

$$z\equiv z_k+\tau \qquad (51)$$

we obtain:

$$\mathfrak{L}^{(z)}(Z_{zz}^{(k)})=0. \qquad (52)$$

The boundary conditions can be shown to be:

$$\lim_{\eta\to\infty} Z_{zz}^{(k)}(z)\to 0,\quad \text{(edge condition)}, \qquad (53a)$$

$$Z_{zzz}^{(k)}(z=z_k)=0,\quad \text{(wall condition)}. \qquad (53b)$$

Again, the solution $Z_{zz}^{(k)}$ is the Airy Function $A_i(z)$, and the z_k's are the zeros of dA_i/dz; in other words, the z_k's are negative and real, and are identical to the ζ_k's which appeared earlier.

Since z_k appears in the denominator of $D_k^{(n)}$, the basis function Z^1 associated with the smallest magnitude of z_k is the most important. Lam and Rott took only the $k = 1$ term from (47) and used the *Stirling approximation* for the factorial to show that theoretically $g_{\eta\eta}^{(n)}(0)$ should have the following n-dependence for large n:

$$\ln|g_{\eta\eta}^{(n)}(0)|=c_1+c_2n-\frac{2n}{3}\ln n \qquad (54)$$

where c_1 and c_2 are constants. The values of $g_{\eta\eta}^{(n)}(0)$ numerically computed by Lam and Rott were found to be reasonably accurately represented by this formula for $15 \geq n \geq 6$ with $c_1 = 0.62$ and $c_2 = -2.6$.

The above result represents only the "inner" solution valid near the wall. It can readily be matched to the special exact outer eigen-solution obtained earlier to provide an uniformly valid eigen-solution.

5 Summary and Discussions

In the present paper, we revisit and present the two major results of the 1960 unpublished Lam and Rott Cornell Report: the uniformly valid eigen-solutions of the linearized unsteady boundary-layer equations in the high-frequency asymptotic limit, and the leading approximation to terms in the low-frequency series solution in the large index limit. In the latter case, the presentation here is essentially identical to the original presentation; only minor changes were made for the purpose of streamlining the presentation. In the former case, however, some new results were obtained in the course of the rewriting, and they are incorporated into the presentation.

Firstly, we show here that the special Lam and Rott exact "outer solution" for a flat plate is merely the linear version of the Prandtl-Glauert transposition theorem which is valid for *any* basic steady flow—with or without pressure gradients. Second, their original eigen-solutions did not satisfy the required null boundary condition for u' at the freestream edge. In the present work, the special exact outer solution is used to match on to their inner eigen-solutions to yield uniformly valid eigen-solutions. Third, Lam and Rott did not recognize that their (inner) eigen-solutions should have a streamwise coordinate-dependent factor—as was pointed out by Goldstein 23 years later. In the present work, Goldstein (1983) derivation, which was limited to a basic steady flow with zero pressure gradient, is extended to deal with the general case.

Under the boundary-layer approximations, the velocity perturbations in the boundary layer generate no pressure response. Physically, however, the vertical velocity perturbation at the outer edge of the boundary layer will interact with the free-stream irrotational flow, generating a pressure response. The main mathematical consequence of this effect is that the right-hand side of (29*b*) will no longer be zero, and the eigen-values ζ_k determined by a modified (29*b*) will become complex. This pressure-coupling has been treated by Smith (1979) for the case of the flat plate, and is responsible for the "connection" between the boundary-layer eigen-solutions and the Orr-Sommerfeld eigen-solutions.

The analytical result obtained for $a(\tilde{x})$ for arbitrary pressure gradients is expected to be a useful resource for future studies on boundary layer receptivities (Goldstein and Hultgren, 1989; Hammerton and Kerschen, 1991; Kerschen, 1993).

Acknowledgment

The authors are grateful to Dr. M. E. Goldstein, Prof. E. J. Kerschen, and Prof. M. D. Van Dyke for their encouragements and assistance in the preparation of this manuscript.

The research was funded in 1959–1960 by the Office of Scientific Research of the Air Research and Development Command, United States Air Force, Contract AF49(638)-544. The authors acknowledge the help of Ms. Ann Walbran of the Cornell Computing Center who performed the original calculations.

References

Ackerberg, R. C., and Phillips, J. H., 1972, "The Unsteady Laminar Boundary Layer on a Semi-Infinite Flat Plate Due to Small Fluctuations in the Magnitude of the Free-Stream Velocity," *Journal of Fluid Mechanics*, Vol. 51, pp. 137–157.

Brown, S. N., and Stewartson, K., 1974, "On the Propagation of Disturbances in a Laminar Boundary Layer. II," *Proceedings of the Cambridge Philosophical Society*, Vol. 73, pp. 505–514.

Cole, J. D., 1968, *Perturbation Methods in Applied Mathematics*, Blaisdell Pub. Co., Waltham, Mass.

Copson, E. T., 1955, *An Introduction to the Theory of Functions of a Complex Variable*, University Press, Oxford, England.

Glauert, M. B., 1956, "The Laminar Boundary Layer on Oscillating Plates and Cylinders," *Journal of Fluid Mechanics*, Vol. 1, Part, 1, pp. 97–110.

Glauert, M. B., 1957, "A Boundary Layer Theorem, with Applications to Rotating Cylinders," *Journal of Fluid Mechanics*, Vol. 2, pp. 89–99.

Goldstein, M. E., 1983, "The Evolution of Tollmien-Schlichting Waves Near a Leading Edge," *Journal of Fluid Mechanics*, Vol. 127, pp. 59–81.

Goldstein, M. E., 1991, "Boundary Layer Receptivity to Long Wave Free-stream Disturbances," *Annual Review of Fluid Mechanics*, Vol. 21, pp. 137–166.

Goldstein, M. E., Sockol, P. M., and Sanz, J., 1983, "The Evolution of Tollmien-Schlichting Waves Near a Leading Edge. Part 2. Numerical Determination of Amplitudes," *Journal of Fluid Mechanics*, Vol. 129, pp. 443–453.

Hammerton, P. J., and Kerschen, E. J., 1991, "Effect of Nose Bluntness on Leading-Edge Receptivity," *Instability, Transition and Turbulence*, Proceedings of the Workshop on Instability, Transition and Turbulence during July 8 to August 2, 1991, M. Y. Hussaini, A. J. Kumar, C. L. Streett, eds., ICASE/NASA LaRC Series, Springer-Verlag, pp. 441–451.

Illingworth, C. R., 1958, "The Effects of a Sound Wave on the Compressible Boundary Layer on a Flat Plate," *Journal of Fluid Mechanics*, Vol. 3, pp. 471–493.

Jeffery, H., and Jeffery, B., 1972, *Methods of Mathematical Physics*, 3rd Edition, Cambridge University Press, pp. 508–511.

Kerschen, E. J., 1990, "Boundary Layer Receptivity Theory," *Applied Mechanics Review*, Vol. 43, pp. S152–S157.

Kerschen, E. J., 1993, private communications.

Lam, S. H., and Rott, N., 1960, "Theory of Linearized Time-Dependent Boundary Layers," Graduate School of Aeronautical Engineering Report AFOSR TN-60-1100, Cornell University, Ithaca, N.Y.

Lighthill, M. J., 1954, "The Response of Laminar Skin Friction and Heat Transfer to Fluctuations in the Stream Velocity," *Proceedings of the Royal Society*, Series A, Vol. 224, pp. 1–23.

Prandtl, L., 1938, "Zur Berechnung der Grezschichten," *Zeitschrift fuer Angewwandte Mathematik und Mechanik*, Vol. 18, pp. 77–82.

Reshotko, E., 1976, *Annual Review of Fluid Mechanics*, Vol. 8, pp. 311–349.

Rott, N., 1956, "Unsteady Viscous Flow in the Vicinity of a Stagnation Point," *Quarterly of Applied Mathematics*, Vol. XIII, No. 4, pp. 444–451.

Rott, N., and Rosenzweig, M. L., 1960, "On the Response of the Laminar Boundary Layer to Small Fluctuations of the Free-Stream Velocity," *Journal of the Aerospace Sciences*, Vol. 27, No. 10, pp. 741–748.

Sears, William, R., 1956, "Some Recent Developments in Airfoil Theory," *Journal of the Aeronautical Sciences*, Vol. 23, No. 2, pp. 490–499.

Smith, F. T., 1979, "On the Non-Parallel Flow Stability of the Blasius Boundary Layer," *Proceedings of the Royal Society, London*, Series A, Vol. 366, pp. 91–109.

Van Dyke, M. D., 1964, *Perturbation Methods in Fluid Mechanics*, Academic Press.

Van Dyke, M. D., 1974, "Analysis and Improvement of Perturbation Series," *Quart. J. Mech. Appl. Math.*, Vol. XXVII, Part 4, pp. 425–435.

The Rayleigh Problem for the Interior of a Torus[1]

W. J. Rae
Professor.
Mem. ASME

C. J. Ollila
Graduate Student.

Department of Mechanical and
Aerospace Engineering,
State University of New York at Buffalo,
Buffalo, NY 14260

This paper contains a description of the low Reynolds number flow inside a torus which has been set impulsively in motion about its central axis. The moving wall drags with it a primary flow confined to a sheath that grows steadily toward the center of the torus cross section. The primary flow in turn produces centrifugal and Coriolis accelerations which lead to secondary flows in the cross-sectional plane. At very long time the secondary flows subside, and the primary flow approaches a condition of solid-body rotation. The present analysis treats this problem in the thin-torus limit, where the cross-sectional radius is small compared to the toroidal radius, and is restricted to wall velocities small enough to support a low Reynolds-number assumption. At this level of approximation, the flow is characterized by a single dimensionless parameter, analogous to the Dean number.

Introduction

Flow inside a toroidal enclosure is found in a number of problems of engineering interest. The literature describing such flows begins with the celebrated work of W. R. Dean (1927, 1928), who examined the flow driven by a pressure gradient inside a loosely wound helical coil; his results illustrated the secondary flow that develops, and quantified the additional pressure drop required to pump a given mass flow. His analysis forms the starting point for the extensive literature of flows in toroidal channels, for both steady and unsteady flows. Treatments of the steady-flow case include a variety of numerical results (for example, McConalogue and Srivistava, 1968; Austin and Seader, 1973; Greenspan, 1973; Collins and Dennis, 1975; Dennis, 1980; Dennis and Ng, 1982), as well as analytical/numerical discussions of multiple solutions in certain ranges of the Dean number (VanDyke, 1978; Yang and Keller, 1986). The problems addressed in the unsteady-flow case include such flows as those in the human aorta (Lin and Tarbell, 1980; Yearwood and Chandran, 1984) and the semicircular canals of the human ear (Van Buskirk et al. 1976). These flows have been studied in a number of papers (for example Lyne, 1970; Zalosh and Nelson, 1973; Smith, 1975; Munson, 1976).

More recently (Schuring, et al., 1982), Dean's work has been useful in interpreting the flow inside a rolling pneumatic tire. The tire-flow studies were motivated by the need to quantify the heat-transfer path in which energy generated in the flexing tread region is convected by the contained air from the tread region toward the rim.

A central feature of the tire-flow studies was a series of airflow measurements made with a three element hot-wire anemometer (Rae and Skinner, 1984) inserted through the rim into the interior of a tire that was rolling under a preset load on a large-diameter drive wheel in the Calspan Corporation's Tire Test Facility. During the initial phases of that test program, the response of a single-element hot wire was examined with the wheel held up off the driving surface; the wheel was set in motion impulsively by an air motor connected to the axle. The result of this experiment is shown in Fig. 1, taken from Schuring et al. (1982). The rise time of the wheel's angular velocity is about five seconds; during this period, a hot wire near the center of the cross section recorded the same speed as that of the wheel, indicating that the air it was passing through was still at rest. Later, as the air came into solid-body rotation, the anemometer signal diminished to zero. This response could be used for calibration purposes, and to help in identifying the signals corresponding to forward and reverse flow over the three-element assembly used in the later tests.

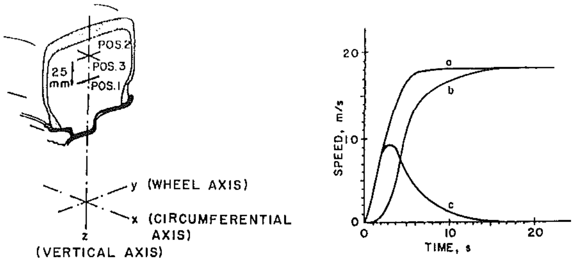

Hot wire positions and orientations. Center position: 1 wheel axis (y-) direction. Advanced position: 2 wheel axis (y-direction), 3 circumferential (x-) direction

Cavity air speed during tire spin-up. Tire unloaded. Hot wire position 1. a - absolute hot-wire speed, b - absolute cavity air speed, c - relative cavity air speed

Fig. 1 Hot-wire anemometer measurements (from Schuring, Skinner, and Rae 1982)

In order to interpret the data of Fig. 1, a search was made for the solution of the Rayleigh problem corresponding to the impulsive start of the flow in a toroidal enclosure. We were not able to find such a solution; all of the papers cited above deal with a stationary wall, except for the work of Munson (1976), which treats the case of a torus oscillating sinusoidally about its central axis. The work presented here is a first step toward the construction of a solution for the case where the

---

[1] This paper is dedicated to Bill Sears, in celebration of his 80th birthday and in gratitude for his teaching, his research, his wisdom, his humor, and his friendship.

Contributed by the Fluids Engineering Division for publication in the JOURNAL OF FLUIDS ENGINEERING. Manuscript received by the Fluids Engineering Division, April 3, 1993; revised manuscript received September 13, 1993. Associate Technical Editor, D. P. Telionis.

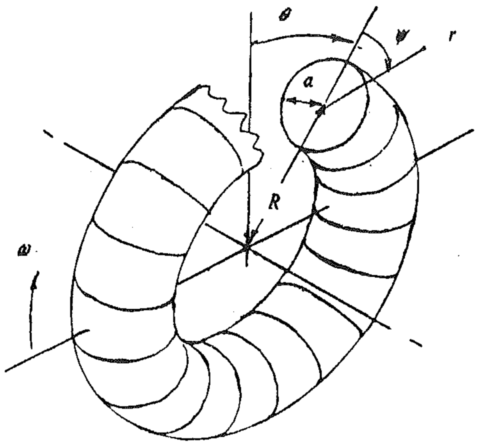

Fig. 2 Torus geometry and coordinates

torus is impulsively set in motion about its central axis. The solution presented contains the first several terms in an expansion in powers of the parameter analogous to the Dean number of the steady, pressure-driven case. Further (numerical) studies appropriate for higher values of this parameter are under way, and will be reported later.

The basic equations and the approximations made are presented in Section 1. This is followed by details of the expansion procedure. The leading term of the primary flow in the thin-torus limit is the same as the classical solution for the temperature distribution in a cylindrical bar subjected to a step-function surface temperature change (Carslaw and Jaeger, 1947). The higher-order terms are found by a Crank-Nicholson procedure and by a set of quadratures similar to those that apply for the pressure-driven case. For that case the leading term of the primary flow is the parabolic Poiseuille profile, and the quadratures can be expressed in simple form. In the present case, the leading term is a Fourier-Bessel series, and the resulting quadratures are done numerically. Section 3 contains numerical results showing the time development of the velocity patterns, and the final section is addressed to extensions of this work that are needed to more closely approximate the real tire flow, which involves much higher Reynolds numbers, more complex cross-sectional geometry, and a larger value of the ratio of the cross-sectional radius to the wheel radius.

In preparing this work, the first author has again had many occasions to recall the wonderful years spent learning fluid mechanics from Bill Sears, and to reflect on his many contributions to the fields of viscous and boundary-layer flows (Sears, 1948, 1954) and of small-perturbation expansions (Sears, 1950, 1954), as well as his deft use, in the classroom, of the Rayleigh analogy to explain the physics of boundary-layer development. The present work is offered with great thanks as evidence that the directions he suggested then are still being applied by his students today.

1 Basic Equations

Figure 2 shows the coordinate system introduced by Dean (1927); θ is the circumferential angle in the direction of wheel rotation, while ψ and r are polar coordinates in the cross-sectional plane. The radius of the centerline of the torus is denoted by R, while a is the radius of the cross section. Note that these coordinates are fixed in space; the torus is set in motion relative to this system.

In the thin-torus limit $a << R$, the equations are the same as those of Dean (1927), with the addition of time derivatives in the momentum equations (u, v, and w are velocity components in the r, ψ, and θ directions, respectively):

$$\frac{\partial u}{\partial r}+\frac{u}{r}+\frac{1}{r}\frac{\partial v}{\partial \psi}=0$$

$$\frac{\partial u}{\partial t}+u\frac{\partial u}{\partial r}+\frac{v}{r}\frac{\partial u}{\partial \psi}-\frac{v^2}{r}-\frac{w^2\cos\psi}{R}$$
$$=\frac{-1}{\rho}\frac{\partial p}{\partial r}-\frac{\nu}{r}\frac{\partial}{\partial \psi}\left(\frac{\partial v}{\partial r}+\frac{\nu}{r}-\frac{1}{r}\frac{\partial u}{\partial \psi}\right)$$

$$\frac{\partial v}{\partial t}+u\frac{\partial v}{\partial r}+\frac{v}{r}\frac{\partial v}{\partial \psi}+\frac{uv}{r}+\frac{w^2\sin\psi}{R}$$
$$=\frac{-1}{\rho r}\frac{\partial p}{\partial \psi}+\nu\frac{\partial}{\partial r}\left(\frac{\partial v}{\partial r}+\frac{v}{r}-\frac{1}{r}\frac{\partial u}{\partial \psi}\right)$$

$$\frac{\partial w}{\partial t}+u\frac{\partial w}{\partial r}+\frac{v}{r}\frac{\partial w}{\partial \psi}=+\nu\left(\frac{\partial^2 w}{\partial r^2}+\frac{-1}{r}\frac{\partial w}{\partial r}+\frac{1}{r}\frac{\partial}{\partial \psi}\left[\frac{1}{r}\frac{\partial w}{\partial \psi}\right]\right)$$

Here p, ρ, and ν are the pressure, density, and kinematic viscosity; w will be referred to as the primary flow, u and v as the secondary flow. A stream function can be defined for the secondary flow:

$$u=\frac{-1}{Rr}\frac{\partial f}{\partial \psi},\ v=\frac{1}{R}\frac{\partial f}{\partial r}$$

The equation satisfied by this stream function is found by eliminating the pressure between the two secondary-flow momentum equations. In terms of the dimensionless variables

$$\phi=f/\nu,\ \eta=r/a,\ W=w/\omega R,\ \tau=\frac{\nu t}{a^2}$$

the basic equations become:

$$\eta\frac{\partial}{\partial \tau}\tilde{\nabla}^2\phi+\left(\frac{\partial \phi}{\partial \psi}\frac{\partial}{\partial \eta}-\frac{\partial \phi}{\partial \eta}\frac{\partial}{\partial \psi}\right)\tilde{\nabla}^2\phi-\eta\,\tilde{\nabla}^4\phi$$
$$=AW\left(\cos\psi\frac{\partial W}{\partial \psi}+\eta\sin\psi\frac{\partial W}{\partial \eta}\right)$$

$$\frac{\partial W}{\partial \tau}+\frac{1}{\eta}\frac{\partial \phi}{\partial \psi}\frac{\partial W}{\partial \eta}-\frac{1}{\eta}\frac{\partial \phi}{\partial \eta}\frac{\partial W}{\partial \psi}=\tilde{\nabla}^2 W;\ \tilde{\nabla}^2\equiv\frac{\partial^2}{\partial \eta^2}+\frac{1}{\eta}\frac{\partial}{\partial \eta}+\frac{1}{\eta^2}\frac{\partial^2}{\partial \psi^2}$$

where

$$A\equiv 2\left(\frac{\omega R\bullet a}{\nu}\right)^2\bullet\frac{a}{R}$$

is a dimensionless parameter that plays a role analogous to the Dean number in the pressure-driven case.

2 Series Solution for Small A

The solution can be expanded for small A in a series analogous to that of the Dean problem:

$$W=W_0+AW_1+A^2W_2+\ldots$$
$$\phi=A\phi_1+A^2\phi_2+\ldots$$

The leading term W_0 satisifies the boundary conditions:[2]

$$W_0(\tau,\eta=1,\psi)=1;\ \frac{\partial W_0}{\partial \eta}(\tau,0,\psi)=0$$

The solution is the same as that for the temperature in a cylindrical bar subjected to a step-function change in surface temperature (Carslaw and Jaeger, 1947)

$$W_0(\tau,\eta)=1-2\sum_{n=1}^{\infty}e^{-\beta_n^2\tau}\frac{J_0(\beta_n\eta)}{\beta_n J_1(\beta_n)}$$

---

[2] Details of the expansion procedure are available from the first author.

where the β_n are the roots of

$$J_0(\beta)=0$$

Note that W_0 is independent of ψ; this leads to simplifications in the partial differential equations at the next two orders. When this is done in the equation for ϕ_1, it is clear that the solution must be of the form:

$$\phi_1(\tau,\eta,\psi)=\phi_{is}(\tau,\eta)\sin\psi$$

The boundary condition $u=v=0$ on $\eta=1$ requires that

$$\phi_{is}=\frac{\partial\phi_{is}}{\partial\eta}=0 \text{ on } \eta=1$$

Upon calculating the quantities $\tilde\nabla^2\phi_1$, $\tilde\nabla^4\phi_1$, one finds

$$\tilde\nabla^2\phi_1=g_1(\tau,\eta)\sin\psi;\; g_1\equiv\left(\frac{\partial^2}{\partial\eta^2}+\frac{1}{\eta}\frac{\partial}{\partial\eta}-\frac{1}{\eta^2}\right)\phi_{is}(\tau,\eta)$$

and

$$\tilde\nabla^4\phi_1=\sin\psi\left(\frac{\partial^2}{\partial\eta^2}+\frac{1}{\eta}\frac{\partial}{\partial\eta}-\frac{1}{\eta^2}\right)g_1$$

Thus the equation to be solved becomes

$$\frac{\partial}{\partial\tau}g_1(\tau,\eta)-\left(\frac{\partial^2}{\partial\eta^2}+\frac{1}{\eta}\frac{\partial}{\partial\eta}-\frac{1}{\eta^2}\right)g_1(\tau,\eta)=W_0\frac{\partial W_0}{\partial\eta}$$

Having found g_1 (numerically, by a Crank-Nicholson method) one can reconstruct the function ϕ_{is} by integrating

$$\frac{d^2\phi_{is}}{d\eta^2}+\frac{1}{\eta}\frac{d\phi_{is}}{d\eta}-\frac{\phi_{is}}{\eta^2}=g_1(\eta;\tau)$$

in which τ appears only as a parameter. This equation can be solved by quadratures; let

$$\phi_{is}=\eta p(\eta) \text{ and } q=\eta^3p'$$

It is found that

$$\phi_{is}=\eta\,(I_2(\eta)-I_2(1))$$

where

$$I_2(\eta)=\int_0^\eta\frac{I_1(s)ds}{s^3},\; I_1(\eta)=\int_0^\eta\eta^2g_1(\eta,\tau)d\eta$$

The solution for W_1 must satisfy

$$\frac{\partial W_1}{\partial\tau}-\tilde\nabla^2W_1=-\frac{1}{\eta}\frac{\partial\phi_1}{\partial\psi}\frac{\partial W_0}{\partial\eta}$$

It is clear by inspection that the angular dependence of W_1 must be of the form:

$$W_1(\tau,\eta,\psi)=W_{ic}(\tau,\eta)\cos\psi$$

(These angular dependences are the same as those which apply for the steady case; their general form is given, for example, by McConalogue and Srivastava (1968) and by VanDyke (1978)). The equation to be solved is

$$\frac{\partial W_{ic}}{\partial\tau}-\frac{\partial^2W_{ic}}{\partial\eta^2}-\frac{1}{\eta}\frac{\partial W_{ic}}{\partial\eta}+\frac{W_{ic}}{\eta^2}=-\frac{\phi_{is}}{\eta}\frac{\partial W_p}{\partial\eta}$$

with boundary conditions

$$W_{ic}(\eta=0)=W_{ic}(\eta=1)=0$$

A Crank-Nicholson technique was also used to calculate this quantity.

Inspection of the governing equation for ϕ_2 shows that it must have the following angular dependence:

$$\phi_2(\tau,\eta,\psi)=\phi_{2s}(\tau,\eta)\sin 2\psi$$

It is then found that

$$\tilde\nabla^2\phi_2=\sin 2\psi\left(\frac{\partial^2\phi_{2s}}{\partial\eta^2}+\frac{1}{\eta}\frac{\partial\phi_{2s}}{\partial\eta}-\frac{4\phi_{2s}}{\eta^2}\right)$$

and that

$$\tilde\nabla^4\phi_2=\sin 2\psi\left\{\frac{\partial^2}{\partial\eta^2}+\frac{1}{\eta}\frac{\partial}{\partial\eta}\right\}\left[\frac{\partial^2\phi_{2s}}{\partial\eta^2}+\frac{1}{\eta}\frac{\partial\phi_{2s}}{\partial\eta}\frac{4\phi_{2s}}{\eta^2}\right]-\frac{4}{\eta^2}\left[\frac{\partial^2\phi_{2s}}{\partial\eta^2}+\frac{1}{\eta}\frac{\partial\phi_{2s}}{\partial\eta}-\frac{4\phi_{2s}}{\eta^2}\right]$$

This suggests the definition

$$g_2(\tau,\eta)=\frac{\partial^2\phi_{2s}}{\partial\eta^2}+\frac{1}{\eta}\frac{\partial\phi_{2s}}{\partial\eta}-\frac{4\phi_{2s}}{\eta^2}$$

Then

$$\tilde\nabla^2\phi_2=g_2\sin 2\psi$$

and

$$\tilde\nabla^4\phi_2=\sin 2\psi\left\{\frac{\partial^2}{\partial\eta^2}+\frac{1}{\eta}\frac{\partial}{\partial\eta}-\frac{4}{\eta^2}\right\}g_2$$

So the equation for ϕ_2 becomes an equation for $g_2(\tau,\eta)$:

$$\eta\frac{\partial}{\partial\tau}g_2-\eta\left(\frac{\partial^2}{\partial\eta^2}+\frac{1}{\eta}\frac{\partial}{\partial\eta}-\frac{4}{\eta^2}\right)g_2=$$

$$=\frac{1}{2}\left(\eta W_{ic}\frac{\partial W_0}{\partial\eta}-W_0W_{ic}+\eta W_0\frac{\partial W_{ic}}{\partial\eta}\right)$$

After g_2 is found, the quantity ϕ_{2s} is found by integrating

$$\frac{d^2\phi_{2s}}{d\eta^2}+\frac{1}{\eta}\frac{d\phi_{2s}}{d\eta}-\frac{4}{\eta^2}\phi_{2s}=g_2$$

This integration can be expressed in quadratures; use of the functions

$$\phi_{2s}=\eta^2p_2,\; q_2=\eta^5p_2'$$

leads to

$$\phi_{2s}=\eta^2\,[I_4(\eta)-I_4(1)]$$

where

$$I_4(\eta)=\int_0^\eta\frac{I_3(\eta)}{\eta^5}d\eta$$

and

$$I_3(\eta)=\int_0^\eta\eta^3g_2\,d\eta$$

3 Results

Figures 3–6 show the flow field as given by the leading terms in the primary and secondary flows. The primary flow, shown in Fig. 3, is identical to the temperature fields given in Carslaw and Jaeger. Note that a value of the dimensionless time τ on the order of 1.0 is required to bring the flow into solid-body rotation. All of the Crank-Nicholson calculations reported here were done with $\Delta\eta=0.005$, $\Delta\tau=0.001$. Several calculations

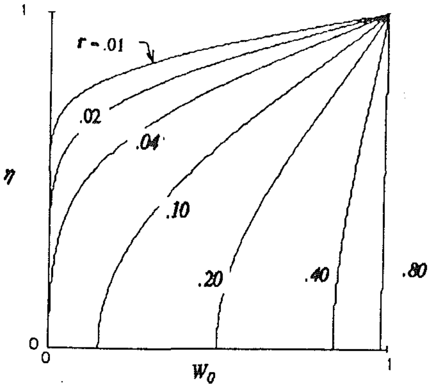

Fig. 3 W_0 profiles

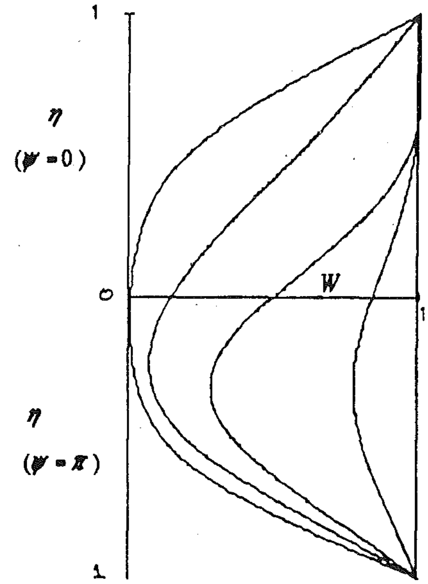

Fig. 4 Profiles of $W_0 + AW_1$; $A = 3000$

were done with step sizes twice these; no differences were found.

Figure 4 shows the effect of including the second term in the series for W. These curves, for a value of A equal to 3000,[3] pertain to the symmetry plane of the torus, and show that the effect of the second term is to retard the velocity on the inner half of the plane and to increase it on the outer half.

The magnitude of the second term W_{ic} varies as a function of time. Thus for a given value of A, the ratio of the magnitude of the second term to that of the first will also vary, and it is not always possible to choose a value that displays the effect of the higher-order term while still keeping the value of the second term small compared to that of the first.

Streamlines corresponding to the leading term in the secondary flow, ϕ_1, are shown in Fig. 5: initially, the flow in the growing boundary layer near the wall is driven toward the outer part of the torus by the centrifugal forces, and returns in a region near the symmetry plane. Nine streamlines are shown in each of these figures, for stream-function values ranging from ten percent to ninety percent of the range between the maximum and minimum values in the field at that instant. The steamlines show only the pattern, but not the magnitude, of the flow velocities.

The term ϕ_{is} has a maximum on the line $\psi = 90$ degrees and near the wall. This maximum moves inward as time increases; its magnitude grows until a dimensionless time around 0.2, after which the motion begins to subside as the primary flow approaches solid-body rotation.

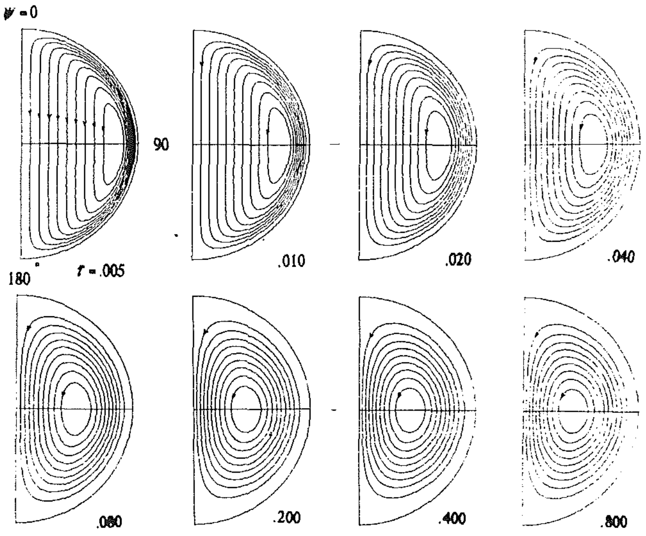

Fig. 5 ϕ_1 contours

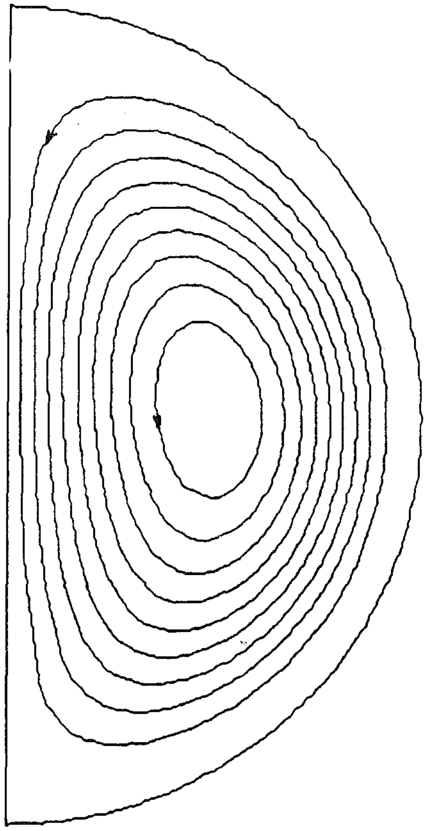

Fig. 6 Contours of $\phi_1 + A\phi_2$; $A = 10^4$

The effects of the next-order term ϕ_2 are shown in Fig. 6, for the value $A = 10{,}000$. This value was chosen so as to make the second terms roughly ten percent of the leading terms, at a time level around 0.2. The selection of an appropriate value for A encounters the same problem in the secondary-flow case as was discussed above in connection with the primary flow, namely that the relative magnitudes of the two terms vary with time. The value $A = 10{,}000$ was chosen to illustrate that the center of the circulating region migrates toward the outer portion of the torus when the second-order term is included.

4 Discussion

The solution presented above suggests that the length of time required for the contained flow to come into solid-body rotation is about one characteristic viscous-diffusion time, and that the higher-order terms in both the primary and secondary flows reach their peak amplitude at around one fifth of this time, after which they begin to decay. The secondary flow has the behavior that would be expected: at early time, a thin layer

---

[3] The values of A used in these examples appear at first glance to be too large for a "small-A" expansion. The fact is that the functions which are multiplied by A are themselves very small; the values of A have been chosen so as to yield values of the product AW_1 on the order of one tenth of the leading term (and a similar choice has been made for successive terms in the other series expansions). Evidently the inhomogeneous terms in the differential equations for the functions of order higher than W_0 are proportional to a small numerical factor, which in principle could be absorbed into the parameter A. A comparable factor appears in the classical Dean problem, and can be identified exactly because of the analytical nature of the solution (see Van Dyke 1978, where results are expressed in terms of the classical Dean number divided by 576). In the present problem, there is no analytic basis for identifying this factor.

is dragged along by the wall, and is centrifuged toward the outer rim of the torus. As this layer grows toward the centerline of the cross section, the magnitude of the circulation subsides.

This solution can serve as the starting point for numerical studies in which the thin-torus approximation and the restriction to small values of the parameter A are avoided. It will be interesting to see whether these calculations encounter multiple solutions or perhaps regions where more than one vortex appears. The problem may also be suitable for further study by the method of formula manipulation (see Van Dyke, 1978), although the need for numerical integration of the $W-$ and $g-$ fields may be an obstacle to this.

Such extensions may suggest new approaches to the more complex problem of flow in a rolling, deformed torus. That problem, discussed by Rae (1983) and by Wey (1985), differs by being steady in a coordinate system which translates with the axle, but is made geometrically more complicated by the variations in the tire cross section, which make the problem fully three-dimensional: all quantities vary in the θ-direction, including pressure gradients. It retains the moving-wall boundary conditions, and so the primary flow is nearly one of solid-body rotation, diminished slightly by the flow impedance at the footprint. The distributions of all quantities are periodic in the θ-direction. The pressure distribution is dictated by the requirements that it be periodic and that it have a gradient in the footprint region sufficient to force the flow through the constriction there.

One new approach that is suggested by the present work is to calculate the deformed rolling-torus problem by a time-marching scheme applied to the incremental flow that represents the difference from solid-body rotation. In the calculations done by Wey, the entire flow was used in order to avoid numerical stability problems caused by reverse-flow regions. A time-marching technique would not suffer from this problem, and use of the incremental flow would enable the calculation to be more accurate.

Finally, the present work may also provide the starting point for improved analysis of the time-dependent flow in a partial torus having closed ends, as in the case of the human-ear semicircular canals.

References

Austin L. R., and Seader, J. D., 1973, "Fully Developed Viscous Flow in Coiled Circular Pipes," *AIChE Journal*, Vol. 19, pp. 85-94.

Carslaw, H. S., and Jaeger, J. C., 1974 *Conduction of Heat in Solids*, Oxford, Clarendon Press, pp. 174-176.

Collins, W. M. and Dennis, S. C. R., 1975, "The Steady Motion of a Viscous Fluid in a Curved Tube," *Quarterly Journal of Mechanics and Applied Mathematics*, Vol. 28, pp. 133-156.

Dean, W. R., 1927, "Note on the Motion of Fluid in a Curved Pipe" *Philosophical Magazine* (7), Vol. 4, pp. 208-233.

Dean, W. R., 1928, "The Streamline Motion of Fluid in a Curved Pipe," *Philosophical Magazine* (7), Vol. 5, pp. 673-695.

Dennis, S. C. R., 1980, "Calculation of the Steady Flow through a Curved Tube Using a New Finite-Difference Method," *Journal of Fluid Mechanics*, Vol. 99, pp. 449-467.

Dennis, S. C. R., and Ng, M., 1982, "Dual Solutions for Steady Laminar Flow through a Curved Tube," *Quarterly Journal of Mechanics and Applied Mathematics*, Vol. 35, pp. 305—324.

Greenspan, D., "Secondary Flow in a Curved Tube," *Journal of Fluid Mechanics*, Vol. 57, pp. 167-176.

Lin, J. Y., and Tarbell, J. M., 1980, "An Experimental and Numerical Study of Periodic Flow in a Curved Tube," Journal of Fluid Mechanics, Vol. 100, pp. 623-638.

Lyne, W. H., 1970, "Unsteady Viscous Flow in a Curved Pipe," *Journal of Fluid Mechanics*, Vol. 45, pp. 13-31.

McConalogue, D. J., and Srivastava, R. S., 1968, "Motion of a Fluid in a Curved Tube," *Proceedings of the Royal Society*, Vol. A307, pp. 37-53.

Munson, B. R., 1976, "Secondary Flows in a Slowly Oscillating Torus," *The Physics of Fluids*, Vol. 19, pp. 1823-1825.

Rae, W. J., 1983, "Flow Inside a Pneumatic Tire: A Peristaltic-Pumping Analysis for the Thin-Tire Limit at Very Low Forward Speed," *Journal of Applied Mechanics*, Vol. 105, pp. 255-258,

Rae, W. J., and Skinner, G. T., 1984, "Measurements of Air Flow Velocity Distributions Inside a Rolling Pneumatic Tire," SAE Paper No. 840066, Feb.

Schuring, D. J., Skinner, G. T., and Rae, W. J., 1982, "Contained Air Flow in a Radial Tire," SAE Transactions, Vol. 90, pp. 705-712.

Sears, W. R., 1948, "The Boundary Layer of Yawed Cylinders," *Journal of the Aeronautical Sciences*, Vol. 15, pp. 49-52.

Sears, W. R., 1954, "Boundary Layers in Three-Dimensional Flow," *Applied Mechanics Reviews*, Vol. 7, pp. 281-285.

Sears, W. R., 1950, "The Linear Perturbation Theory for Rotational Flow," *Journal of Mathematics and Physics*, Vol. 28, pp. 268-271.

Sears, W. R., 1954, "Small Perturbation Theory," Section C of *General Theory of High Speed Aerodynamics*, Volume 2 of *High Speed Aerodynamics and Jet Propulsion* Princeton University Press.

Smith, F. T., 1975, "Pulsatile Flow in Curved Tubes," *Journal of Fluid Mechanics*, Vol. 71, pp. 15-42.

VanBuskirk, W. C., et al., 1976, "The Fluid Mechanics of the Semicircular Canals," *Journal of Fluid Mechanics*, Vol. 78, pp. 87-98.

VanDyke, M. D., 1978, "Extended Stokes Series: Laminar Flow through a Loosely Coiled Pipe," *Journal of Fluid Mechanics*, Vol. 86, pp. 129-145.

Wey, M. J., 1985, "Numerical Simulation of a Flow Inside a Loaded Rotating Tire," PhD Thesis State University of New York at Buffalo.

Yang, Z-H., and Keller, H. B., 1986, "Multiple Laminar Flow through Curved Pipes," *Advances in Numerical and Applied Mathematics*, Institute for Computer Applications in Numerical and Applied Mechanics Report No. 86-18, J. C. South, Jr., and M. Y. Hussaini, eds.

Yearwood, T. L., and Chandran, K. B., 1984, "Physiological Pulsatile Flow Experiments in a Model of the Human Aortic Arch," *Journal of Biomechanics*, Vol. 15, pp. 683-704.

Zalosh, R. G., and Nelson, W. G., 1973, "Pulsating Flow in a Curved Tube," *Journal of Fluid Mechanics*, Vol. 59, pp. 693-705.

Segmented Domain Decomposition Multigrid Solutions for Two and Three-Dimensional Viscous Flows[1]

Kumar Srinivasan

Stanley G. Rubin

Department of Aerospace Engineering
and Engineering Mechanics,
University of Cincinnati,
Cincinnati, OH 45221

Several viscous incompressible two and three-dimensional flows with strong inviscid interaction and/or axial flow reversal are considered with a segmented domain decomposition multigrid (SDDMG) procedure. Specific examples include the laminar flow recirculation in a trough geometry and in a three-dimensional step channel. For the latter case, there are multiple and three-dimensional recirculation zones. A pressure-based form of flux-vector splitting is applied to the Navier-Stokes equations, which are represented by an implicit, lowest-order reduced Navier-Stokes (RNS) system and a purely diffusive, higher-order, deferred-corrector. A trapezoidal or box-like form of discretization insures that all mass conservation properties are satisfied at interfacial and outflow boundaries, even for this primitive-variable non-staggered grid formulation. The segmented domain strategy is adapted herein for three-dimensional flows and is extended to allow for disjoint subdomains that do not share a common boundary.

Introduction

Strong viscous-inviscid interactions, associated with high Reynolds number (Re) laminar flows, are quite frequently characterized by the appearance of large flow gradients that are most significant in small or "thin" domains of finite extent, and in one or more directions, e.g., boundary or shear layers/regions, triple deck structures, and vortical zones. In three dimensions, secondary flows and geometry, e.g., corners, can significantly influence the extent of "viscous regions." This was recognized in the late 1940's and early 1950's in the work of a number of researchers, including W. R. Sears (1954). Outside of these regions, the flow is generally more highly diffused or inviscid and the flow gradients are less severe. However, the flow character in these "smoother" regions, which generally encompass the major portion of the flow domain, can be significantly influenced by the interaction associated with the thin high gradient viscous layers. In order to efficiently and accurately assess this class of viscous interacting flows with discrete computational methods, (1) significant local grid refinement is required in the high shear layers, (2) coarser meshes are to be specified in the inviscid regions in order to reduce computational cost and improve overall accuracy, and (3) simple, but efficient, domain decomposition techniques, that effectively communicate information between the disparate flow domains, and at the same time maintain all conservation properties, are desired.

In the present investigation, a segmented domain decomposition multigrid (SDDMG) strategy is combined with a pressure-based form of flux-vector discretization in order to achieve these goals. The governing Navier-Stokes equations are evaluated with an implicit, lowest-order in Re, reduced Navier-Stokes (RNS) subsystem (Rubin and Tannehill, 1992) that is combined, when necessary, with an explicit purely diffusive deferred-corrector (DC) in the thin viscous layers. Local directional refinement that is driven by specified flow parameters and accuracy limits is achieved by sequentially dividing the overall flow domain into a variety of subdomains. Each level of the multigrid hierarchy consists of a system of segmented, possibly disjoint, subdomains which are of equal or lesser extent than on all of the coarser grid predecessors. The boundaries of these multidimensional subdomains are defined by specified directional and global resolution requirements. A related approach has been presented earlier (Fuchs, 1986; Thompson and Ferziger, 1989), although no attempt was made to meet the differing needs for refinement in two or more coordinate directions. In the present investigation this is achieved through a domain decomposition procedure that allows for segmentally varying grid resolution in two or more directions throughout the flow field. The SDDMG procedure provides the requisite grid refinement, and, through the multigrid component, information is very effectively transferred between high and low gradient domains that have distinctly different grid structures. In addition, the equation solver can be adjusted from subdomain to subdomain, e.g., a sparse matrix direct solver, preconditioned LU procedure or other factorization or line/plane relaxation, etc., can be used in high

---

[1] This paper is dedicated to Professor W. R. Sears on occasion of his 80th birthday. His significant contributions to fluid mechanics research, development and education are greatly appreciated.

Contributed by the Fluids Engineering Division for publication in the JOURNAL OF FLUIDS ENGINEERING. Manuscript received by the Fluids Engineering Division February 10, 1993; revised manuscript received April 21, 1993. Associate Technical Editor: D. P. Telionis.

frequency, strong interaction, domains. Line/plane relaxation is found to be more computationally efficient in moderate interaction domains.

The use of pressure-based flux vector splitting and a trapezoidal or box-like discretization for the implicit RNS subsystem leads to a precise prescription of the surface normal boundary conditions on all global and local subdomain boundaries. This ensures that interfacial and global mass conservation requirements are automatically satisfied. This is generally not the case with characteristic-based Navier-Stokes schemes, and overlapping domain decomposition procedures, where special conditions are required in order to satisfy interfacial and/or global conservation conditions. The primitive variable formulation to be considered herein is also directly applicable on nonstaggered grids. *This differs from many other incompressible, primitive variable, Navier-Stokes formulations, that apply pressure Poisson or artificial compressibility concepts and either require staggered grids, and/or satisfy the discrete form of the continuity equation (Eq. (1a)) only approximately.*

Governing Equations and Discretization

The governing Navier-Stokes equations are shown here in Cartesian coordinates. They are written for incompressible three-dimensional flow in nonconservation form, as an RNS system added to a diffusive deferred-corrector.

$$\frac{\partial u}{\partial x}+\frac{\partial v}{\partial y}+\frac{\partial w}{\partial z}=0 \tag{1a}$$

$$u\,\frac{\partial u}{\partial x}+v\,\frac{\partial u}{\partial y}+w\,\frac{\partial u}{\partial z}+\frac{\partial p}{\partial x}=\frac{1}{\mathrm{Re}}\left(\frac{\partial^2 u}{\partial y^2}+\frac{\partial^2 u}{\partial z^2}\right)+\mathrm{DC}_x \tag{1b}$$

$$u\,\frac{\partial v}{\partial x}+v\,\frac{\partial v}{\partial y}+w\,\frac{\partial v}{\partial z}+\frac{\partial p}{\partial y}=\frac{1}{\mathrm{Re}}\left(\frac{\partial^2 v}{\partial z^2}\right)+\mathrm{DC}_y \tag{1c}$$

$$u\,\frac{\partial w}{\partial x}+v\,\frac{\partial w}{\partial y}+w\,\frac{\partial w}{\partial z}+\frac{\partial p}{\partial z}=\frac{1}{\mathrm{Re}}\left(\frac{\partial^2 w}{\partial y^2}\right)+\mathrm{DC}_z \tag{1d}$$

where $\mathrm{DC}_x=1/\mathrm{Re}(\partial^2 u/\partial x^2)$, $\mathrm{DC}_y=1/\mathrm{Re}(\partial^2 v/\partial x^2)$, and $\mathrm{DC}_z=1/\mathrm{Re}(\partial^2 w/\partial x^2)$ (u, v, w) are the Cartesian velocities in the (x, y, z) directions, respectively. These equations when transformed to generalized curvilinear body fitted coordinates (ξ, η, ζ) are given for two-dimensional compressible applications in Pordal et al. (1992b), and for three-dimensions in Pordal et al. (1992a). Here x (or ξ) is a body fitted coordinate direction and is approximately streamline oriented; y (or η) is approximately normal to the surface and, for the three-dimensional step channel, z (or ζ) is normal to the side walls. The RNS approximation is given by the lowest-order (in Re) system obtained by omitting the purely diffusive deferred-corrector (DC) terms. The RNS system is in effect a composite of the inviscid Euler and second-order boundary-layer equations (Rubin and Tannehill, 1992). The DC terms are retained selectively, either explicitly or implicitly in some subdomains, or globally throughout the flowfield, when they are important.

A pressure based form of flux vector splitting (Rubin, 1988) is applied to discretize the governing equations. Trapezoidal or "box" two point differencing is used for all normal and azimuthal derivatives; three point central (i, j, k) differencing (in y and z) is applied for the axial momentum equation (Eq. (1b)) and for z gradients in Eq. (1c), y gradients in Eq. (1d). Further details on the pressure and convective discretization can be found in Srinivasan and Rubin (1992b).

Grid Structure, Refinement Strategy, and Multigrid Implementation

The first two grid levels in the multigrid hierarchy cover the entire computational domain. The mesh size is initially coarse in all directions. In fact, the first mesh point from wall boundaries generally lies outside of the thin viscous or boundary layer. Subsequent multigrid levels are decomposed into a discrete number of abutting or disjoint subdomains, for which refinement is required in one or more directions. This pattern is defined by the directional refinement criteria. Each successive multigrid level derives part of its topology from the subdomaining pattern of the coarser predecessor. Within each subdomain, of a given multigrid level, the refinement is specified independently. Thus, each subdomain of a multigrid level can act as a parent for a subdomain or subdomains at the next finer multigrid level. If in a given multigrid level, a particular subdomain is refined in only one direction, e.g., y, then on subsequent multigrid levels, further refinement within this subdomain is performed only in the y-direction. A similar strategy is adopted for the x-direction. In the present analysis, segmenting has not been implemented in the z-direction. For the backstep geometry considered herein, the flow patterns are only mildly three-dimensional and therefore do not require very fine grids or segmentation in the z-direction. For the present study a full nonsegmented multigrid strategy is applied in the z-direction. A future paper will discuss the full three-dimensional SDDMG method and solutions.

Only subdomains that result from refinement, of a parent subdomain, in more than one direction require further decomposition according to the direction selective refinement specification. If two neighboring subdomains have the same grid spacing in all directions then the refinement strategy combines them into a single subdomain. For the three-dimensional results presented here, the segmentation is more sophisticated and allows for regions of similar refinement to be defined as disjoint subdomains if necessary. A tolerance defining the maximum number of stations, e.g., n_s, in the x direction, that are permitted between points requiring similar refinement is specified. Thus if two blocks needing x refinement are separated by more than n_s stations, then they are defined as separate blocks. For the present three-dimensional calculations n_s is chosen to be two.

In most adaptive gridding methods on any grid level, an estimate of the truncation error of the discretized system of equations is used to identify those regions that require finer grid resolution (Thompson and Ferziger, 1989). The overall truncation error estimates, however, do not provide information on the specific direction(s) that require refinement. Therefore, for regions requiring higher resolution, the grid is refined in both directions, even though only one coordinate gradient may be significant. In order to achieve directional refinement adaptivity it is necessary to monitor the truncation error of selected gradients or derivatives. For the problems considered herein, the truncation error for the pressure and vorticity gradients, e.g., p_x and u_{yy}, are monitored in order to define the regions that require refinement in, x and y, respectively.

The truncation error estimate is obtained from the solution on two successive grids of the multigrid hierarchy. In order to determine the truncation error in x (and/or y) derivative, the finer of the two grids must have regions that are refined in the x (and/or y) direction(s). Although the p_x and u_{yy} terms are the key derivatives for the present analysis, the truncation error of these terms alone will not suffice to ensure that uniform accuracy is achieved throughout the flow domain. The global truncation error for the full discrete system of equations is monitored for this purpose. It is important to emphasize that grid stretching is never applied, expect as the grids change discretely from subdomain to subdomain. Solutions are first obtained on two coarse grids, with full multigrid implementation. From these two full grid solutions, the truncation error of the key derivatives and also of the global discrete system is estimated using a Richardson extrapolation procedure (Srinivasan and Rubin, 1992a, 1992b). Note that although different meshes are used in the different subdomains, within each subdomain, uniform meshes are specified. This subdomaining process is applied to the third and higher levels of the multigrid hierarchy.

For the RNS system of equations (Eqs. (1*a*–1*d*)), i.e., NS without the DC, a relaxation or global space marching procedure (in x) is applied for the trough and channel geometries. The convergence rate of this relaxation procedure is significantly improved if the extent of the domain in the two directions is reduced. *The current segmented domain decomposition multigrid procedure, in effect, reduces the extent of subdomains with finer grids and achieves convergence rates comparable to coarse grids even on fine grids.*

In the present application, the multigrid method is implemented in a Full Approximation Storage (FAS) mode. For two-dimensional calculations, three different modes of multigrid are implemented; namely, xy refinement, x refinement, and y refinement, and appropriate modes are used in each subdomain. For three-dimensional SDDMG calculations seven different modes would be necessary, i.e., x, y, z, xy, yz, xz, and xyz refinement. When segmentation is prescribed, then the fine grid is comprised of more than one subdomain, each with its own refinement requirements. The details of implementation of the multigrid components namely relaxation, restriction and prolongation, and for the addition of the DC terms can be found in (Srinivasan and Rubin, 1992a).

Interdomain Transfer Boundary Conditions and Conservation at Grid Interfaces

For a given subdomain, the following boundary conditions are to be prescribed from the known boundary conditions of the global domain or from the multigrid restriction or prolongation:

u, v, w at the inflow; (p is not required but is obtained from the solver)

u, v, w at all solid boundaries;

u, w, p at all free (y) boundaries;

u, v, p at all free (z) boundaries;

At the outflow, $(x=x_{\max})$, $p_x=0$ for external flows; $p=$constant for internal flows; at an interface outflow, $x=x_o<x_{\max}$, p is prescribed, either from the current grid level computation or from multigrid transfers, u, v, w are not required at any outflow boundary when $u>0$; when $u<0$ (this can occur if the subdomain boundary is located within a separation zone) u, v, w are prescribed either from current grid calculation or from multigrid transfers, or a FLARE type approximation (Srinivasan and Rubin, 1991, 1992a) removes the need for any outflow velocity condition. It is significant that p at solid boundaries, v at free (y) boundaries, w at free (z) boundaries are calculated as part of the solution in a given grid level. For external flows, if a subdomain has its outflow at some $(x<x_{\max})$, then the boundary condition on pressure changes from Neumann to Dirichlet type. For internal flow, the outflow boundary condition for the pressure is always of Dirichlet type. Also, if the lower boundary of a subdomain is at some $y>0$, only u, p and either v or w are prescribed depending on whether it is a free z or free y boundary, respectively.

In time-dependent, characteristic-based, Navier-Stokes computations that use locally embedded grids, boundary conditions are required for all variables, i.e., u, v, w, and p on all boundaries. In addition, special care has to be taken to ensure that mass conservation is not violated locally or globally. With pressure-based flux-vector splitting and the trapezoidal or "box" formulation, this difficulty does not occur as the normal velocity v in y, w in z or u in x, is not prescribed at the (y) upper or (z) crossflow, or (x) outflow boundaries. Only the tangential component u is prescribed at the upper interface or interdomain boundary. The pressure-based box-type differencing allows for the exact calculation of the normal velocity component from the continuity equation at the outer free boundaries, and for the pressure from the normal momentum equation at the body surfaces. Therefore mass and momentum conservation is automatically satisfied on all levels, for all subdomains.

Table 1 Comparison of computer resource requirements for trough

Aspect	Geometry	Two-D adaptive	One-D adaptive	Full MG with stretched grid
CPU	Trough ($D=0.03$)	18.03%	—	100.0%
	Trough ($D=0.015$)	7.10%	16.80%	100.0%
Memory	Trough ($D=0.03$)	16.32%	—	100.0%
	Trough ($D=0.015$)	5.10%	63.4%	100.0%

Results

All of the calculations, including the three-dimensional studies presented herein, are initiated on the coarsest grid, with uniform flow velocity and pressure. On the finer grids, the interpolated coarse grid solution fields are sequentially applied as initial approximations. Convergence to the final solution is improved with better initial approximations (Rubin and Himansu, 1989). The SDDMG framework introduces this element in a natural and convenient fashion. It is significant that for the examples presented herein, Reynolds number continuation is not required in order to obtain a solution for any of the prescribed values of Re. Even for highly interactive, large Re flows the solution is obtained directly with uniform initial values.

Example 1. Flow Over a Trough. The first problem to be considered is the large Re, laminar flow over a trough configuration. Both unseparated and reverse flows are computed with the SDDMG refinement strategy. The trough surface is specified by $y_b=-D\,\mathrm{sech}[4(x-x_0)]$, where D represents the maximum depth. This occurs at the location x_0. The values $x_0=2.5$ and Re $=80{,}000$ are used for the present calculation. The grid obtained from the two-dimensional adaptive procedure, for $D=0.03$ ($\mathrm{Re}_D=2400$) and with a region of flow reversal, is shown in Fig. 1. Note that refinement in the ξ direction is quite extensive for this recirculating geometry. This is due to the fact that the maximum vorticity occurs near the outer edge of the separation bubble. As a result refinement in the η direction extends to a significantly large distance from the body. For an attached flow the subdomains are much smaller in extent. Also note the sudden increase in the extent of the region where η refinement is performed. This signifies the increase in boundary layer thickness as a result of flow separation. This is followed by a reduction in the extent of η refinement toward the outflow. This represents the region beyond reattachment where the boundary layer thickness is reduced. Figure 2 provides comparisons of the skin friction for the separated ($D=0.03$) case.

The full refinement calculation is performed with a stretched η grid. Multigrid acceleration is also applied to enhance the convergence of the full refinement calculation. Thus the gain in computational efficiency is to be fully attributed to the adaptive strategy. In addition it is important that only the finest grid is converged to a residual norm of 10^{-4} in the case of the full refinement calculation since it is not efficient to obtain fully converged solutions on coarser grids. On the other hand, in the adaptive calculations, each multigrid level is fully converged before progressing to the next level for two reasons; (*a*) a fully converged solution is required in the truncation error estimation process, (*b*) the extent of the fine grid is local and hence, in portions of the flow field, the solution is obtained only on the coarser grids. Good agreement is obtained and significant gains in computer resource requirements are achieved (Table 1). The locations of the separation and reattachment points computed by the two-dimensional adaptive calculation are at $\xi = 2.31$ and $\xi = 2.54$, respectively; the values predicted by nonadaptive full multigrid refinement are at $\xi = 2.31$ and $\xi = 2.53$.

Example 2. Flow in a Two/Three-Dimensional Backstep Channel. For this flow, which is dominated by rather large recirculation regions, it is possible to complete the calculation for all Re considered herein by prescribing uniform initial flow conditions. This is true even for the relatively difficult, although somewhat artificial, two-dimensional calculation with Re = 800 (based on channel height). For this Re value, separation bubbles, are evident on each wall. Reynolds number continuation, as applied in many other reported NS solvers (Gartling, 1990), is not required for the present calculations.

Two-Dimensional Laminar Flow. The laminar flow in a backstep channel has been studied extensively both through numerical computations and experiments. This flow is characterized by large recirculation zones, both on the upper and lower walls for large enough values of Re. Typically, the theoretical results agree with the experimental results for Re < 400.

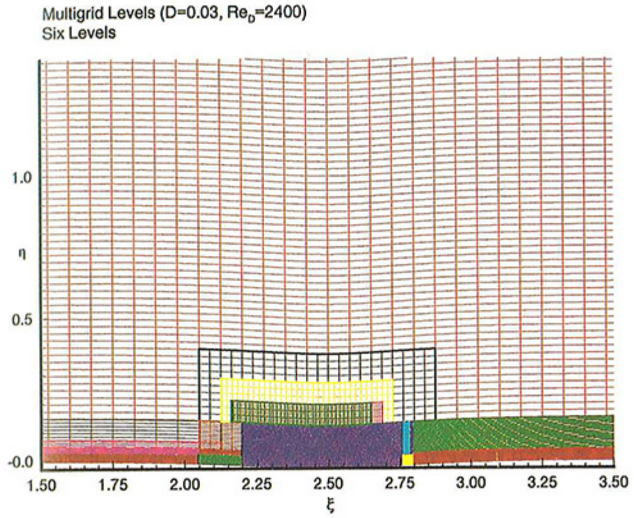

Fig. 1 Segmented grid for the (D = 0.03) trough geometry; Re = 80,000; comprises six multigrid levels

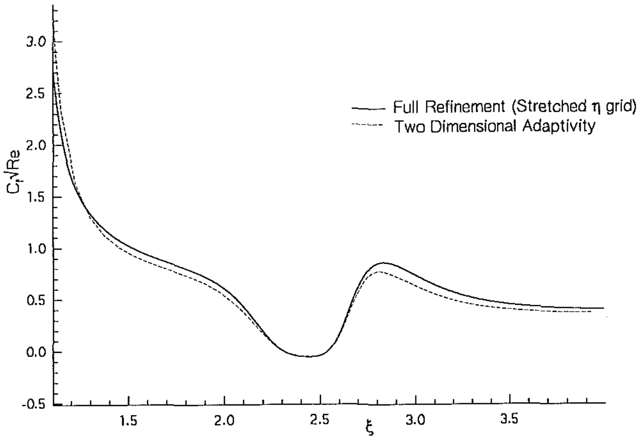

Fig. 2 Comparison of skin friction parameter; D = 0.03 trough; Re = 80,000

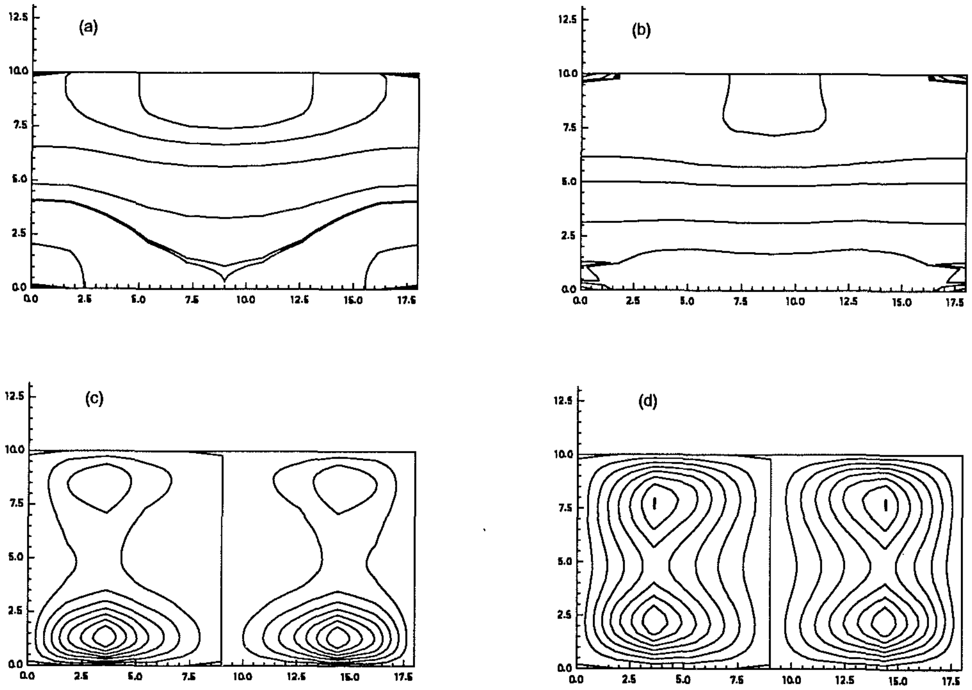

Fig. 3 (*a*), (*b*) Pressure contours in the *yz* plane at x = 7.125 and x = 10.5, respectively. (*c*), (*d*) *w* (velocity component) in *yz* plane at x = 7.125 and x = 10.5, respectively; Re = 800; three-dimensional flow in a backward facing step channel.

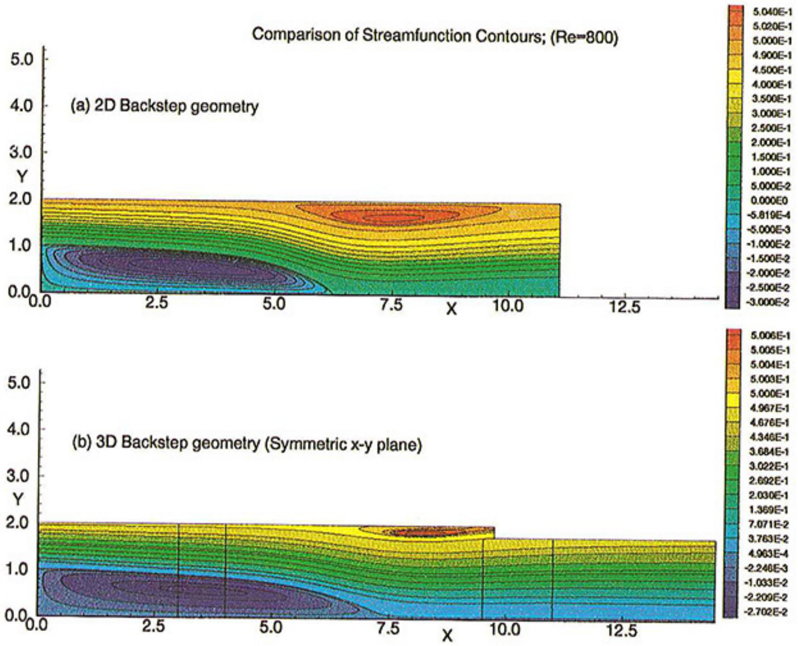

Fig. 4 Comparison of streamfunction contours (2*D* versus 3*D*); Re = 800

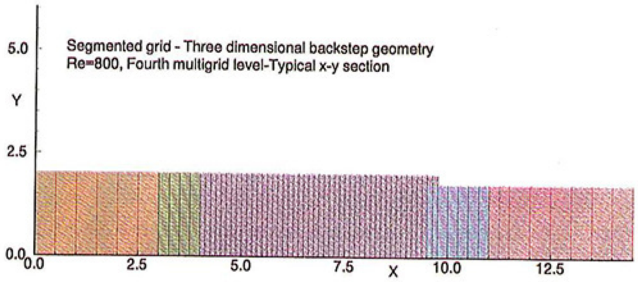

Fig. 5 Segmented multigrid levels (typical *x-y* section); three-dimensional backward facing step; (Re = 800); four multigrid levels are shown: five subdomains in finest level; *Y* scaled by a factor of 5

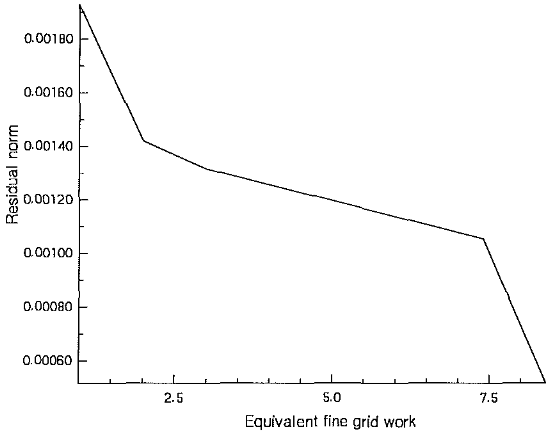

Fig. 6 Convergence history of fourth segmented multigrid level

For Re > 400, the numerical results underpredict the primary separation bubble length. It is significant that for this Re range there is a second recirculation zone on the upper wall of the channel. Although this leads to only mild three-dimensionality in the flow field, a considerable relief effect on the axial flow occurs, and hence the extent of the recirculation is altered appreciably. The Re = 800 flow is an excellent test case for the three-dimensional computations. Detailed two-dimensional SDDMG results for Re ≤ 800 which include the nonreflectivity of the outflow boundary conditions and effect of the DC terms can be found in Srinivasan and Rubin (1992a). For Re = 800 the reattachment length was found to be 6.18, whereas the experimental value in Armaly et al. (1983), is 7.25. The benchmark solution gives a value of 6.10.

Three-Dimensional Laminar Flow. In order to confirm the three dimensionality of the backstep geometry flowfield for Re = 800, a full three-dimensional calculation is performed applying the SDDMG technique. The three-dimensional flow has been simulated experimentally by Armaly et al. (1983). They used a model with aspect ratio 1:18 to conduct the experiments. This is considered here for the three-dimensional calculation. Figure 3 represents the pressure and azimuthal velocity contours at two different axial locations. The first location ($x = 7.125$), is very close to the reattachment and, hence, the flow is more three-dimensional at this location than the second location ($x = 10.5$), which is downstream of both separation bubbles. This is evident in the pressure contours which remain almost horizontal for the second location. Note that the w-velocity component is perfectly symmetrical about the mid plane. The values of w are much larger at location 2 compared to location 1. Figure 4 displays the stream function contours for this geometry. The lower reattachment length is obtained as 7.25 which is in excellent agreement with the experimental value.

Figure 5 displays the segmented grid for the three-dimensional calculation. Note that the finest grid resolution in the streamwise direction is required around the separation zone. There are four different subdomains in the finest multigrid level. The equivalent, nonadapted fine grid contains about 150,000 grid points. The adaptive strategy reduces the number of grid points by nearly 40 percent. Figure 6 shows the convergence history of the residual norm in the finest grid level. The coarse grid calculations are taken into account by multiplying them by a factor proportional to the number of grid points.

Summary

A segmented domain decomposition multigrid method has been used to efficiently compute incompressible laminar flows with regions of recirculation. A low order RNS system of equations, a fully consistent primitive variable nonstaggered grid solver, accurate mass conservation at subdomain interfaces and global boundaries, nonreflective outflow boundary conditions and a pressure-based flux-split discretization are the key features of the procedure. The SDDMG procedure allows for efficient grid definition consistent with asymptotic theory and for effective transfer of information to and from fine grid high gradient regions to coarse grid "inviscid" regions.

Significant gains in computer resources have been achieved when compared to standard full refinement methods. Good agreement is obtained between the present solutions, full refinement computations, and other published results. The computational cost is several times smaller than that required by most other NS methods (Gartling, 1990). All the two-dimensional computations (backstep and trough geometries) were completed in less than 10 min on an IBM 320 Risc/6000 workstation. The CPU required for the three-dimensional calculation ($Re = 800$) is about 3 hours. All solutions are initiated with uniform flow approximations and Reynolds number continuation is not required, even for the relatively complex $Re = 800$ case. Grid convergence has been established efficiently through the SDDMG procedure. The flux-split discretization allows for direct computation of the normal velocity and therefore mass conservation at grid interfaces and subdomain boundaries is achieved in a simple fashion. Extension of this procedure for compressible and turbulent flow applications is currently in progress.

Acknowledgment

This research was supported by the NASA Lewis Research Center (J. Adamczyk, Technical Monitor), grant no. NAG-397. The Cray Y-MP at the Ohio Super computer was used for these computations.

References

Armaly, B. F., Durst, F., Pereira, J. C. F., and Schonung, B., 1983, "Experimental and Theoretical Investigation of Backward Facing Step Flow," *Journal of Fluid Mechanics*, Vol. 127, pp. 473-496.

Fuchs, L., 1986, "A Local Mid-Refinement Technique for Incompressible Flows," *Computers and Fluids*, Vol. 14, pp. 69-81.

Gartling, D. K., 1990, "A Test Problem for Outflow Boundary Condition—Flow Over Backward Facing Step," *International Journal of Numerical Methods in Fluids*, Vol. 11, pp. 953-967.

Pordal, H. S., Rubin, S. G., and Khosla, P. K., 1992, "A Three-Dimensional Pressure Flux-Split RNS Formulation: Application to Subsonic/Supersonic Flow in Inlets and Ducts," presented at the 13th International Conference Numerical Methods and Fluid Dynamics, Rome, July 6-10.

Pordal, H. S., Khosla, P. K., and Rubin, S. G., 1992, "Transient Behavior of Supersonic Flow Through Inlets," *AIAA Journal*, Vol. 30, No. 3, pp. 711-719.

Rubin, S. G., and Srinivasan, K., "Adaptive Multigrid Domain Decomposition Solutions for Viscous Interacting Flows," *Proceedings of the 5th Symposium on Numerical and Physical Aspects of Aerodynamic Flows*, January 13-15, California State University, Long Beach, CA.

Rubin, S. G., and Himansu, A., 1989, "Convergence Properties of High Reynolds Number Separated Flow Calculations," *International Journal of Numerical Methods in Fluids*, Vol. 9, pp. 1395-1411.

Rubin, S. G., 1988, "RNS/Euler Pressure Relaxation and Flux Vector Splitting," *Computers and Fluids*, Vol. 16, pp. 485-490.

Rubin, S. G., and Tannehill, J. C., 1992, "Parabolized/Reduced Navier Stokes Computational Techniques," *Annual Review of Fluid Mechanics*, Vol. 24, pp. 117-144.

Sears, W. R., 1954, "Boundary Layers in Three Dimensional Flow," *Appl. Mech. Rev.*, Vol. 7, pp. 281-285.

Srinivasan, K., and Rubin, S. G., 1992, "Adaptive Multigrid Domain Decomposition Solutions for Incompressible Viscous Flows," *International Journal of Numerical Methods in Fluids*, Vol. 15, pp. 1333-1355.

Srinivasan, K., and Rubin, S. G., 1991, "Flow Over a Backward Facing Step Using the Reduced Navier-Stokes Equations," *Proceedings of the Mini Symposium on Outflow Boundary Conditions*, Stanford University, California, July.

Srinivasan, K., and Rubin, S. G., 1992, "Segmented Domain Decomposition Multigrid Solutions for Two and Three Dimensional Viscous Flows," *Proceedings of the Symposium on Adaptive Multilevel Hierarchical Computational Strategies*, Noor, A. K., ed., AMD-Vol. 157, ASME Winter Annual Meeting, Anaheim, California, Nov. 8-13, pp. 249-274.

Thompson, M. C., and Ferziger, J. H., 1989, "An Adaptive Multigrid Technique for the Incompressible Navier-Stokes Equations," *Journal of Computational Physics*, Vol. 82, pp. 94-121.

An Integral Method for Turbulent Boundary Layers on Rotating Disks

S. Abrahamson

S. Lonnes

Aerospace Engineering and Mechanics,
University of Minnesota,
Minneapolis, MN 55455

An integral method for computing turbulent boundary layers on rotating disks has been developed using a power law profile for the tangential velocity and a new model for the radial profile. A similarity solution results from the formulation. Radial transport, boundary layer growth, and drag on the disk were computed for the case of a forced vortex freestream flow. The results were compared to previous similarity solutions. The method was extended to a Rankine vortex freestream flow. Differential equations for boundary layer parameters were developed and solved for different Reynolds numbers to look at the net entrainment, boundary layer growth, and drag on the disk.

Introduction

The boundary layers on rotating disks have significant impact on the performance of rotating machinery. In many rotating machines such as centrifugal compressors, the boundary layers unavoidably contribute viscous heating to the device, but they may also be used significantly for cooling by capitalizing on the forced convection they provide. In computer disk drives, viscous heating is significant but there are other more concentrated sources of heat, such as the heat from the motors which spin the disks and move the actuators. In this application, the boundary layers on the rotating disks drive secondary circulation and thus provide convective heat transfer, which tends to homogenize the temperature field. Thus they help to maintain the dimensional tolerances in the drive by reducing nonuniform thermal expansion. Additionally, the boundary layers on the rotating disks in disk drives are important to the transport of particulate contaminants out of the rotating assembly towards a filter.

The high Reynolds numbers and the geometric complexity of many rotating machines make their associated flow fields difficult to calculate using computational fluid dynamics, especially when trying to resolve the boundary layers on the disks, which may be laminar near the center of rotation and turbulent at larger radii. Integral methods offer a convenient means for determining the effects of turbulent boundary layers. Since the freestream flow is dominated by rotation, the flow outside the boundary layers is often much less difficult to determine once one can account for boundary layer effects.

The first integral approach to computing the turbulent boundary layer on a rotating disk was performed by von Kármán (1921). The geometry he considered was a single disk of infinite radius rotating at speed Ω, while the fluid far away from the disk did not rotate. Within the boundary layer, the profile of the tangential velocity was assumed to have a power law form which, when viewed in the reference frame rotating with the disk, was similar to two-dimensional flat-plate turbulent boundary layers. The profile for the radial or crossflow velocity was assumed to have the same power law dependence; however, the power law was modulated by a function (the actual form is presented below) which assured zero radial velocity in the freestream. When substituted into the momentum integral equations, these assumptions lead to evolution equations for the boundary layer thickness and a scale factor for the crossflow (radial velocity) profile. Von Kármán obtained an exact, similarity type solution to these equations by assuming that the crossflow scale factor was constant and that the boundary layer thickness had a power law dependence on the radial coordinate.

Newman (1983) determined that the same set of assumptions leads to a class of solutions for the cases where the freestream flow rotates in solid body motion at some fraction K of the disk rotation rate, i.e., when the flow at infinity is a force vortex.

Cham and Head (1969) used an integral method cast in the rotating reference frame to compute turbulent boundary layer effects. A tangential velocity profile which depended upon the shape factor and momentum thickness Reynolds number was assumed, while the crossflow profile was dependent upon the tangential profile and the surface flow angle. An additional model for the entrainment into the boundary layer was required in order to obtain a solution. Their results showed good agreement to their own experimental data and the data of Case (1966).

In this paper we refine the crossflow model used by Newman (1983) and von Kármán (1921) and look at the effects of the new model on Newman's class of solutions. In addition, we consider the case where the freestream flow is a Rankine vortex, with a forced vortex core of radius r_h, and a potential vortex

---

Contributed by the Fluids Engineering Division for publication in the JOURNAL OF FLUIDS ENGINEERING. Manuscript received by the Fluids Engineering Division July 23, 1992; revised manuscript received January 7, 1993. Associate Technical Editor: J. A. C. Humphrey.

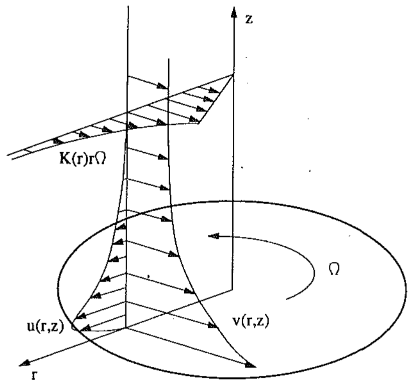

Fig. 1 Sketch of flow geometry and velocity profiles

at radii greater than r_h. In this case, the parameter K becomes a function of the radial coordinate r. This emulates the geometry of a device with a rotating hub. Weak radial injection from the hub provides a flow whose tangential velocity is governed by conservation of angular momentum, like the potential vortex. The introduction of a length scale r_h precludes the possibility of a similarity type solution, but the analysis does lead to a simple set of ODEs which are easy to integrate numerically. At large radial distances from the origin, K tends to zero and the solution tends towards the von Kármán solution but the radial massflow remains elevated.

Problem Formulation

Consider the flow in the vicinity of an infinite radius disk rotating with angular velocity Ω. The boundary layer is assumed turbulent and the fluid outside of the boundary layer has tangential velocity $K(r)r\Omega$, as shown in Fig. 1. In the papers by von Kármán (1921) and Newman (1983) the function K was constant. In this paper we will allow for the possibility of a weak radial flow emerging from a rotating hub. The freestream value of the radial velocity is considered to be negligible, but a consequence of the radial flow is that the freestream tangential velocity is governed by conservation of angular momentum. The functional form of K will be discussed later.

A cylindrical coordinate system (r, θ, z) is used with corresponding velocity (u, v, w). The flow is assumed axisymmetric, and w is assumed negligible. The boundary conditions on the disk ($z = 0$) are $u = v = 0$, and in the freestream ($z \geq \delta(r)$) are $u = 0$ and $v = K(r)r\Omega$, where $\delta(r)$ is the local boundary layer thickness.

A form for the boundary layer profiles must be assumed in order to use an integral method. Both Newman and von Kármán assumed power law forms for the profiles.

$$v = r\Omega[1-(1-K)\xi^n]$$

$$u = \alpha r\Omega\xi^n(1-\xi)$$

where ξ is a scaled boundary layer coordinate $\xi = z/\delta(r)$ and α is an entrainment scale factor. Note that in the reference frame rotating with the disk, the scaled tangential velocity has the standard power law form:

$$\frac{-v}{(1-K)r\Omega} = \xi^n$$

In this paper we follow their development except we use the general form cast in the rotating reference frame and then transform it to the inertial frame.

$$v_{\text{rot}}(r, z) = -G(\xi)$$

$$u(r, z) = g(\xi)G(\xi)$$

(u is unaffected by the reference frame). $G(\xi)$ is given by

$$G(\xi) = (1-K)r\Omega\xi^n$$

so the tangential profile in the laboratory (inertial) reference frame is the same as used by von Kármán and Newman

$$v_{\text{lab}}(r, z) = r\Omega[1-(1-K)\xi^n] \tag{1}$$

The crossflow profiles assumed by the previous investigators, while convenient for evaluation of the integrals which arise, do not represent the data very well. Measurements of the velocity profiles in the vicinity of a rotating disk, using both hot wire anemometry and pressure probes, have been made by Cham and Head (1969) and by Littell and Eaton (1991) and are reproduced in Figs. 2, which are, respectively, plots of the radial and tangential velocity profiles. The velocities were recorded in the laboratory reference frame, translated to rotating coordinates and scaled by the local disk speed, V. The normal distances from the disk were scaled using the momentum thickness of the tangential profile, θ_{11}. The local disk Reynolds numbers range from 3.4×10^5 to 2.0×10^6 in these profiles and although there is scatter between different profiles, there is no discernable Reynolds number trend to the scatter, indicating the possibility of a self-similar or equilibrium boundary layer. Additionally, as shown in the figure there is considerably less fullness in the measured profiles than the one assumed by von Kármán and Newman. Using the sinusoidal form of the crossflow profile given by the linear Ekman layer solution as

Nomenclature

A_j = integration constant (there are 6)
b = crossflow profile parameter
c = crossflow profile parameter
G = tangential velocity profile function
g = modulation function to G for crossflow profile
K = freestream relative velocity function = $v(\delta, r)/r\Omega$
m = exponent used in boundary layer thickness function
n = velocity profile power law exponent
P = shear stress function
Q = volumetric radial transport
Re = Reynolds number = $r^2\Omega/\nu$
r = radial coordinate
r_h = hub radius
r_* = dimensionless radial coordinate = r/r_h
s = near-wall velocity magnitude (rotating reference frame)
S = characteristic velocity
u = radial velocity component
v = tangential velocity component
w = axial velocity component
z = axial coordinate
Z = integration limit, $Z \geq \delta(r)$
α = crossflow profile entrainment factor
α_* = $\alpha(1-K)$
β = boundary layer thickness parameter
δ = boundary layer thickness
δ_* = dimensionless boundary layer thickness = δ/r_h
ν = kinematic viscosity
Ω = disk rotation rate
θ = tangential coordinate
ρ = density
τ = shear stress
ξ = scaled boundary layer coordinate = z/δ

Subscripts

h = evaluated at the hub
lab = laboratory or inertial reference frame
rot = rotating reference frame
r = radial component
θ = tangential component
w = evaluated at the wall (disk surface)

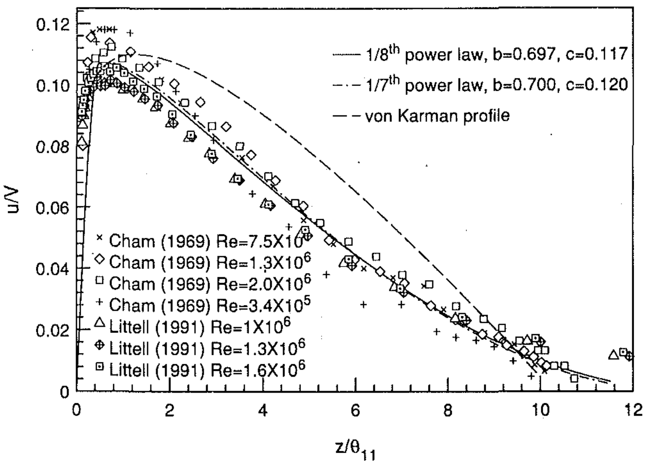

Fig. 2(a) Crossflow velocity profile data and models

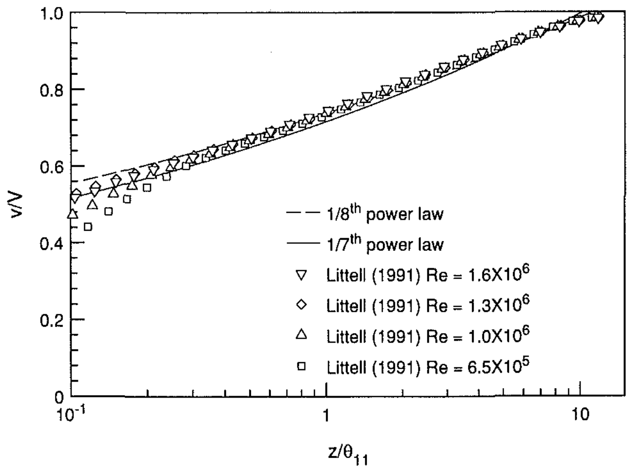

Fig. 2(b) Tangential velocity profile data and models

a guide, a form for $g(\xi)$ was assumed in order to give better agreement to the measurements

$$g(\xi)=\alpha(1-\sin^b(c\xi))$$

or

$$u(r,\, z)=\alpha(1-K)r\Omega\xi^n[1-\sin^b(c\xi)] \tag{2}$$

where α is a scale factor whose magnitude is dependent upon the entrainment rate. In equilibrium situations such as the cases described by Newman, α is constant. When the freestream flow is not in solid body rotation, α may be dependent upon r. The parameters b and c were obtained from a least-squares fit to the data of Littell and Eaton (1991) and Cham and Head (1969) after assuming a value for n (either 1/7 or 1/8). Figure 2(a) shows a comparison between the assumed radial velocity profile and the data. A comparison between the assumed tangential profile and the data of Littell and Eaton (1991) is shown in Fig. 2(b). In this figure, Re is in the range from 6.5×10^5 to 1.6×10^6. For this range of Reynolds numbers, the 1/8th profile appears to be a slightly better fit.

The momentum integral equations require the shear stress evaluated on the disk. Newman points out that although the derivatives of the assumed profiles become undefined on the surface, the ratio of the stresses is obtained from the limiting behavior of the profiles

$$\frac{\tau_r}{\tau_\theta}=\lim_{\xi\to 0}\left|\frac{u}{v_{\text{rot}}}\right|=\alpha$$

In the near-wall region, ($\xi \ll 1$)

$$\xi^n=\frac{-v_{\text{rot}}}{(1-K)r\Omega}=\frac{u}{\alpha(1-K)r\Omega}$$

and the velocity magnitude is

$$s=(1-K)r\Omega\xi^n[1+\alpha^2]^{1/2}$$

Defining

$$S=(1-K)r\Omega[1+\alpha^2]^{1/2}$$

we can write

$$\frac{s}{S}=\xi^n$$

Following Newman and von Kármán we require s to fit the law of the wall so

$$\frac{s}{(\tau_w/\rho)^{1/2}}=C_n\left[\frac{z(\tau_w/\rho)^{1/2}}{\nu}\right]^n$$

Schlichting (1968) provides the constant C_n from standard turbulent boundary layer correlations, depending upon the choice of n. Using $\tau_w = [\tau_\theta^2 + \tau_r^2]^{1/2}$ we use the relationships between the velocity components and s to determine the shear stresses.

$$\frac{\tau_r}{\rho}=C_n^{-\frac{2}{n+1}}\alpha(1-K)r\Omega S^{\frac{1-n}{1+n}}\left(\frac{\nu}{\delta}\right)^{\frac{2n}{n+1}} \tag{3}$$

$$\frac{\tau_\theta}{\rho}=C_n^{-\frac{2}{n+1}}(1-K)r\Omega S^{\frac{1-n}{1+n}}\left(\frac{\nu}{\delta}\right)^{\frac{2n}{n+1}} \tag{4}$$

In the inertial reference frame the momentum integral equations for the boundary layer on the rotating surface are

$$\frac{d}{dr}\left\{r^2\int_0^Z uvdz\right\}-Kr^2\Omega\,\frac{d}{dr}\left\{r\int_0^Z udz\right\}=r^2\,\frac{\tau_\theta}{\rho}$$

and

$$\frac{d}{dr}\left\{r\int_0^Z u^2dz\right\}-\int_0^Z[v^2-(Kr\Omega)^2]dz=-r\,\frac{\tau_r}{\rho}$$

for the tangential and radial directions, respectively, and where Z is some arbitrary point outside the boundary layer (in practice, $Z = \delta$). When the assumed profiles are substituted into the integral equations, four integrals need to be evaluated.

$$\int_0^Z udz=A_1\alpha_*r\Omega\delta$$

$$\int_0^Z u^2dz=A_2\alpha_*^2(r\Omega)^2\delta$$

$$\int_0^Z uvdz=[A_1-A_3(1-K)]\alpha_*(r\Omega)^2\delta$$

$$\int_0^Z[v^2-(Kr\Omega)^2]dz=[A_4+A_5K+(A_6-1)K^2](r\Omega)^2\delta$$

where $\alpha_* = \alpha(1 - K)$. The constants in the first three integrals, A_1 to A_3 arise from numerical integration of the profiles and the other constants are simple functions of n. Defining a general shear stress function

$$P=C_n^{-\frac{2}{n+1}}[(1-K)^2+\alpha_*^2]^{\frac{1-n}{2(1+n)}}\left(\frac{\nu}{\delta\Omega}\right)^{\frac{2n}{n+1}}r^{\frac{2}{n+1}}$$

and substituting the above integrals and P into the integral equations to yield expressions for the evolution of α_* and δ.

$$\frac{d\alpha_*}{dr}=\frac{R_2-\alpha_*R_1}{\alpha_*\delta} \tag{5}$$

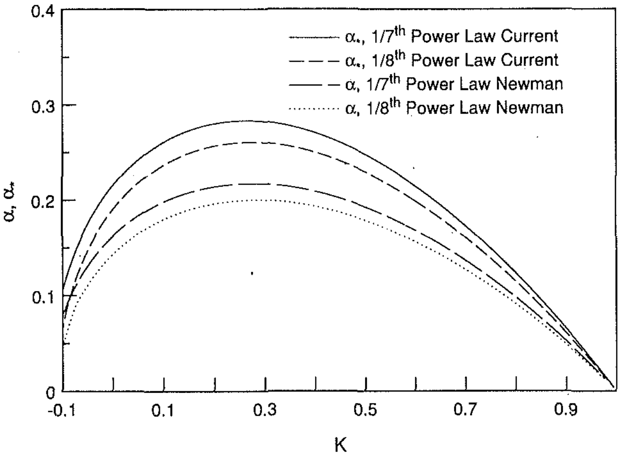

Fig. 3 Radial flow entrainment parameter

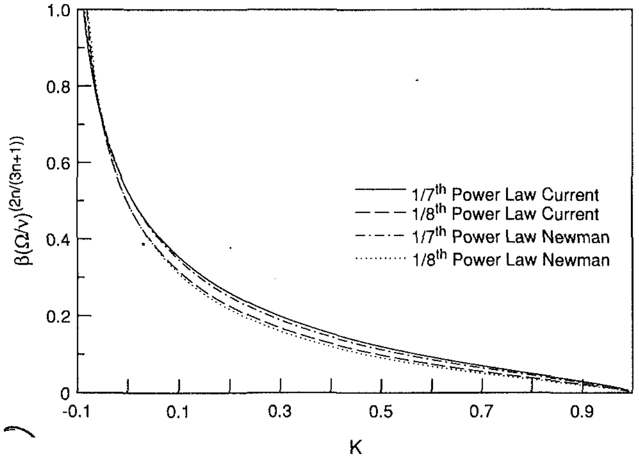

Fig. 4 Boundary layer thickness parameter

$$\frac{d\delta}{dr}=\frac{2\alpha_* R_1-R_2}{\alpha_*^2} \tag{6}$$

where

$$R_1=\left(\frac{1}{A_1-A_3}\right)\frac{P}{r^3}-\alpha_*\delta\left\{\frac{A_3}{A_1-A_3}\,\frac{1}{1-K}\,\frac{dK}{dr}+\left[\frac{4}{1-K}-\left(\frac{2K}{1-K}\right)\left(\frac{A_1-2A_3}{A_1-A_3}\right)\right]\frac{1}{r}\right\} \tag{7}$$

and

$$R_2=-3\,\frac{\alpha_*^2\delta}{r}+\frac{1}{A_2}\,[A_4+A_5K+(A_6-1)K^2]\,\frac{\delta}{r}-\frac{\alpha_*}{A_2}\,\frac{P}{r^2} \tag{8}$$

Solutions

So far we have left $K(r)$ as a completely general function. We now consider two classes of solutions. First we consider the forced vortex case where K is constant and see the impact of the new cross flow model on previous results. Second we consider K to be a function of r, so the freestream is a Rankine vortex.

Forced Vortex Freestream. If K is constant, we recover the von Kármán and Newman problems. Assume α_* is constant and a power law form for the boundary layer thickness: $\delta=\beta r^n$. As in the previous solutions, we find a relationship between m and n.

$$m=\frac{1-n}{3n+1}$$

The corresponding values for α_* and β are

$$\alpha_*^2=\frac{A_4+A_5K+(A_6-1)K^2}{A_1\left[m+\dfrac{2(2-K)}{(1-K)}\right]+A_2(m+3)-A_3(m+4)} \tag{9}$$

$$\beta\left(\frac{\Omega}{\nu}\right)^{\frac{2n}{3n+1}}=\left\{\frac{\alpha_* C_n^{-\frac{2}{n+1}}[(1-K)^2+\alpha_*^2]^{\frac{1-n}{2(1+n)}}}{A_4+A_5K+(A_6-1)K^2-A_2\alpha_*^2(m+3)}\right\}^{\frac{n+1}{3n+1}} \tag{10}$$

Figures 3, 4, and 5 are comparisons between the current results expressed by Eqs. (9) and (10) and the results of Newman. Figure 3 is a plot of the radial flow entrainment parameter α, computed for the range of K from -0.1 to 1.0 using both the current method and that of Newman, for both 1/7th and 1/8th power laws. In the figure, it is clear that the current calculations show a larger value for α_* at all values of K. However, since the assumed profile in Eq. (2) is much less full than that assumed by either Newman or von Kármán it is not surprising to see compensation in the form of a larger maximum. In Fig. 4 we see that the boundary layer thickness parameter $\beta(\Omega/\nu)^{2n/3n+1}$ is approximately the same in both the current and Newman's calculations, indicating that the boundary layer growth is similar. Figure 5 is a plot of the net radial outflow in the boundary layer, computed using the current method and Newman's method for K in the range from -0.1 to 1.0. From the figure it is clear that the entrainment is overpredicted by the previous work, despite the increased values of α_* in the current work. The net entrainment correlation, $Q=k_m r^3\Omega \mathrm{Re}_r^{2n/3n+1}$ for the case where $K=0$ is given by

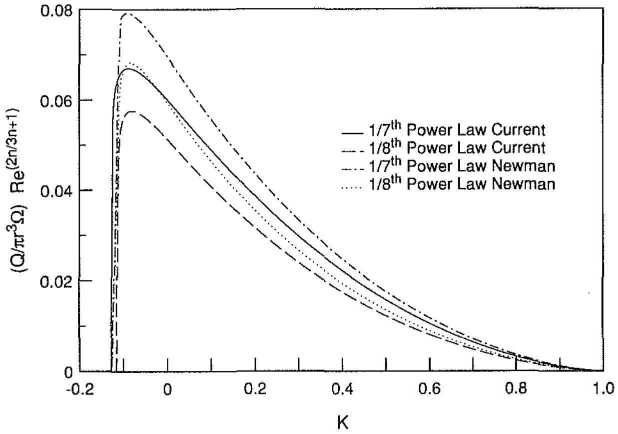

Fig. 5 Radial transport in the boundary layer

$$Q=0.200r^3\Omega\mathrm{Re}_r^{-1/5}$$

for the 1/7th power law profile and

$$Q=0.165r^3\Omega\mathrm{Re}_r^{-2/11}$$

for the 1/8th power law profile, which are 8.5 and 11.5 percent lower than the values obtained by von Kármán (1921). Figure 6 also compares the dimensionless entrainment as calculated using the current method, as calculated by von Kármán (1921) and measurements made by Cham and Head (1969) and Case (1966). Correlations are shown for both the 1/7th and 1/8th power law profiles. From the figure it is clear that the current calculations predict less entrainment than von Kármán's results. The two best fits appear to be the 1/7th power law as computed by von Kármán and the 1/8th power law from the current calculations, with the current results giving a slightly better fit to the Cham and Head data. Recall from Fig. 2(*b*) that the tangential velocity data are best fit by the 1/8th power law for the range of Re available, so it makes sense for it to

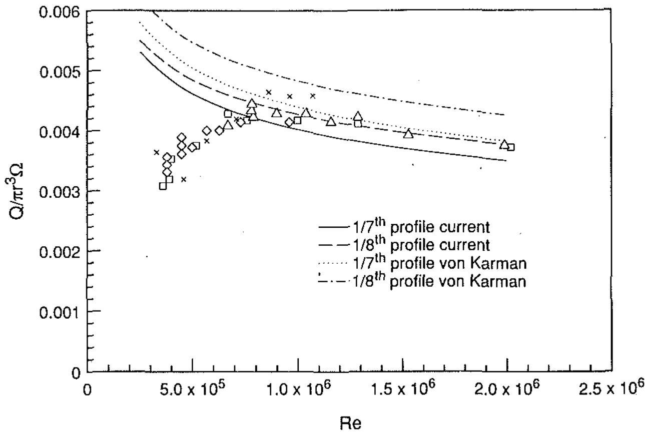

Fig. 6 Comparison to experimental entrainment data

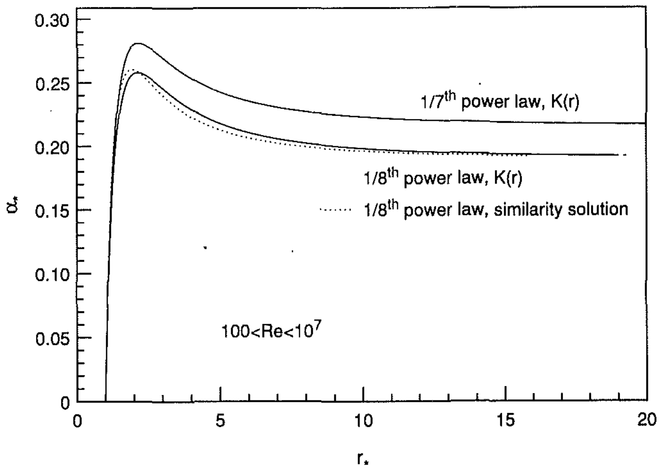

Fig. 7 Crossflow entrainment parameter comparison ($K = K(r)$)

give a better estimate of the flow. Neither method yields good results for Reynolds numbers less than approximately 8.5×10^5 because they fail to account for laminar and transitional boundary layer effects. At larger Re, these effects are small in comparison to the turbulent boundary layer effects.

Rankine Vortex Freestream. Consider the case where K is a function of r. In particular, if a weak radial flow is introduced at some radial location r_h, like the cooling flow emitted from a rotating hub such as that in a gas turbine engine or a computer disk drive, the tangential velocity of the freestream flow is governed by conservation of angular momentum, so for $r > r_h$

$$K(r)r^2\Omega = r_h^2\Omega$$

or

$$K(r) = \left(\frac{r_h}{r}\right)^2$$

It is assumed that the presence of the hub is equivalent to $K(r) = 1$ for $r \leq r_h$.

The introduction of the length scale r_h into the problem precludes the possibility of a similarity solution, and requires numerical integration to obtain the functions $\alpha_*(r)$ and $\delta(r)$. Additionally, when cast in dimensionless form, Eqs. (5) through (8) look unchanged except for the substitution of $\delta_* = \delta/r_h$ and $r_* = r/r_h$ for δ and r, respectively

$$\frac{d\alpha_*}{\mathrm{d}r_*} = \frac{R_{2*} - \alpha_* R_{1*}}{\alpha_*\delta_*} \tag{11}$$

$$\frac{d\delta_*}{dr_*} = \frac{2\alpha_* R_{1*} - R_{2*}}{\alpha_*^2} \tag{12}$$

where

$$R_{1*} = \left(\frac{1}{A_1 - A_3}\right)\frac{P_*}{r_*^2} - \alpha_*\delta_*\left\{\frac{A_3}{A_1 - A_3}\,\frac{1}{1-K}\,\frac{dK}{dr_*} + \left[\frac{4}{1-K} - \left(\frac{2K}{1-K}\right)\left(\frac{A_1 - 2A_3}{A_1 - A_3}\right)\right]\frac{1}{r_*}\right\} \tag{13}$$

and

$$R_{2*} = -3\,\frac{\alpha_*^2\delta_*}{\mathrm{r}_*} + \frac{1}{A_2}\,[A_4 + A_5 K + (A_6 - 1)K^2]\,\frac{\delta_*}{r_*} - \frac{\alpha_*}{A_2}\,\frac{P_*}{r_*^2} \tag{14}$$

and where the boundary layer function P_* exhibits an explicit Reynolds number dependence through the definition of

$$P_* = \frac{P}{r_h^2} = C_n^{-\frac{2}{n+1}}[(1-K)^2 + \alpha_*^2]^{\frac{1-n}{2(1+n)}}[\delta_*\mathrm{Re}_h]^{-\frac{2n}{n+1}} r_*^{\frac{2}{n+1}} \tag{15}$$

where $\mathrm{Re}_h = r_h^2\Omega/\nu$.

The revised forms (11) and (12), were integrated using a fourth order Runge-Kutta scheme along with initial conditions at $r_* = 1$ determined from the similarity solutions above. Due to the fact that $\alpha_* = \delta_* = 0$ at $r_* = 1$ the initial conditions were actually specified at $r_* = 1.005$. There was little sensitivity to the initial conditions. If the initial values of α_* or δ_* were within an order of magnitude of the similarity solution values, the computed results were virtually identical.

Figure 7 shows $\alpha_*(r_*)$ for both power law profiles as well as a comparison to α_* obtained from the similarity solution using the 1/8th power law. For the $\alpha_*(r_*)$ results, five different Reynolds numbers are plotted together, ranging from 10^2 to 10^7. Although the lower values are rather ridiculous for a turbulent boundary layer, they are plotted to show the universality of the function $\alpha_*(r_*)$ since all five curves coincide. For the 1/8th profile, α_* rises quickly from its 0 value at $r_* = 1$ to a maximum of approximately 0.258 around $r_* = 2.13$, and then gradually decays. At $r_* = 20$, $K(r_*) = 0.0025$ and the value of α_* is still 16 percent higher than the similarity solution value of von Kármán. A similar behavior is observed for the 1/7th power law profiles. As an approximation to the numerically integrated solution, one might be tempted to use the values of α_* obtained from the similarity solution at the same values of $K(r_*)$. A comparison between the two cases for the 1/8th power law profile is also shown in Fig. 7. Although the two curves have similar shape, Fig. 7 shows that the use of the similarity solution would over-predict α_* by as much as 13 percent when r_* is in the range from 1.1 to 1.6, and underpredict α_* for r_* greater than 1.6. At large r_* the $K(r_*)$ solution asymptotically approaches the $K = 0$ similarity solution.

The next three figures are comparisons between the numerical integration where $K = K(r)$ (Note that as $r \to \infty$, $K(r) \to 0$) and the similarity solution with $K = 0$. Figure 8 compares the dimensionless entrainment. Both calculations were made using $\mathrm{Re}_h = 10^6$ and used the 1/8th power law profiles. Near the hub ($r_h = 1$) the similarity solution greatly overpredicts the entrainment because of the large difference in the rotation rates of the disk and fluid or alternatively, because the similarity solution has no ability for α_* to accommodate the true boundary condition at the hub. At larger distances from the hub both calculations achieve the same growth rate, with the similarity solution exceeding the Rankine vortex result.

Figure 9 shows the boundary layer thickness as a function of radial distance at $\mathrm{Re}_h = 10^6$. The numerical results ($K = K(r)$) from both the 1/7th and 1/8th power law results are shown and compared to the similarity solution with $K = 0$. The $K = K(r)$ results show that the boundary layer corresponding to the 1/8th power law profile grows faster than the 1/7th power law. Additionally, the $K(r)$ calculations with the

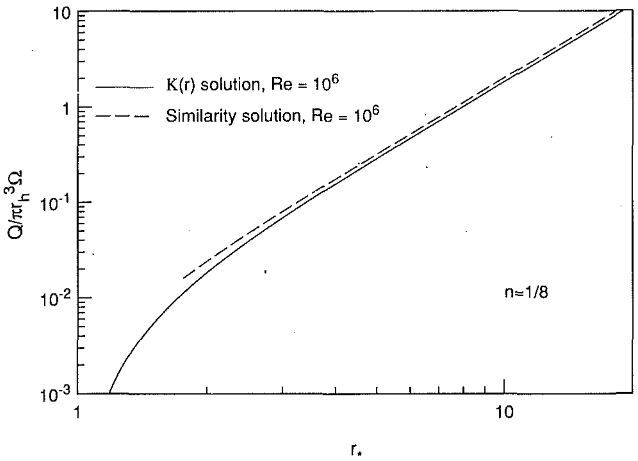

Fig. 8 Net entrainment comparison

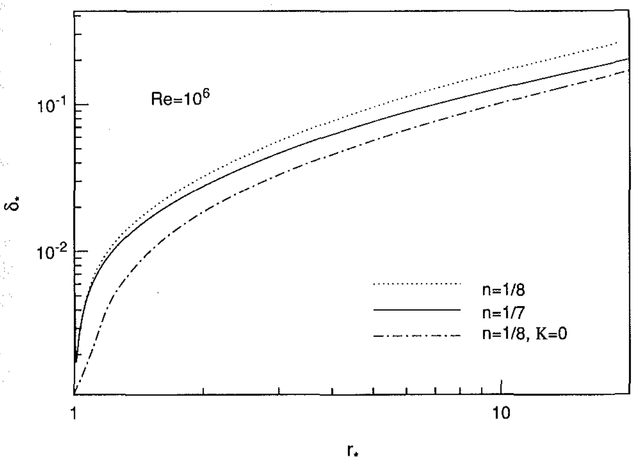

Fig. 9 Boundary layer thickness comparison

1/8th power law profile initially grow much faster than the similarity ($K = 0$) results. At large values of r, $K \to 0$ and the growth rate of the two become comparable, although the $K(r)$ results are larger than the $K = 0$ results. At a fixed distance from the hub, δ_* is a decreasing function of Re due to the increased strain in the layer. Without artificial means of tipping the boundary layer, the boundary layer is likely to be laminar for Re $< 2.9 \times 10^5$ (Gregory et al., 1955). However, turbulence in the freestream will precipitate early transition in the boundary layer, so any practical means of introducing radial freestream flow in an application may provide the trip mechanism and result in a turbulent boundary layer at lower Re.

Another parameter to consider is the torque on the disk due to the wall shear stress. As with the entrainment calculations in Fig. 8, at large distances from the hub the Rankine vortex cases achieve the same dependence on r_* as the similarity solution. Figure 10 shows the comparison between the disk torque due to the boundary layer for both the similarity ($K = 0$) cases and the $K = K(r)$ solution. For $r_* > 4$ the two solutions are virtually indistinguishable. For $r_* < 4$ the similarity solution predicts greater torque on the disk than the Rankine vortex case, as would be expected from the difference in K.

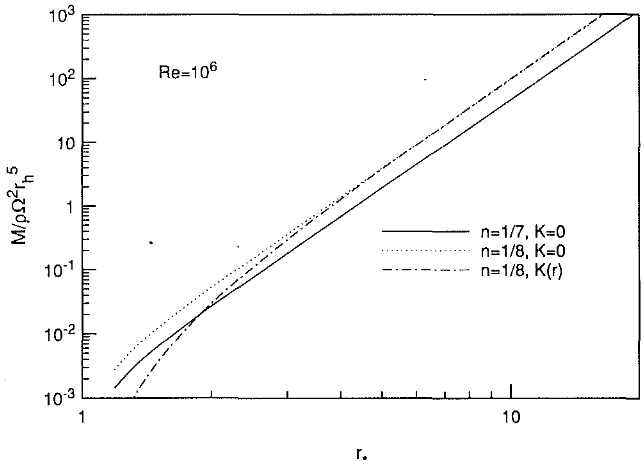

Fig. 10 Disk torque comparison

Conclusions

A simple integral method for computing the effects of turbulent boundary layers on rotating disks has been developed using the concept of self-similar velocity profiles in the radial and tangential directions. Under the assumption that the flow in the freestream is a forced vortex rotating at some fraction of the disk rotation, a self-similar solution has been determined which agrees well with the data and represents a refinement of previous solutions. Additionally, the approach has been extended to the case where the freestream flow is a Rankine vortex. Differential equations for the boundary layer growth and a crossflow profile scale factor were developed and solved. The crossflow profile scale factor has a Reynolds number invariant form and the boundary layer was shown to grow faster than boundary layer in the forced vortex case. The entrainment into the boundary layer was slower in the Rankine vortex calculations than in the forced vortex flow. At large radial distances from the vortex core, the boundary layer thickness, net entrainment and torque due to shear stress tended to the same dependences on the local Reynolds numbers as in the force vortex case. The primary effects from the Rankine vortex freestream seemed confined to the first several core radii; however, in many applications, the size of the device is confined to the same region, so use of the similarity results would overpredict the pumping effects of the disk boundary layers and the torque required to spin the disk.

References

Case, P., 1966, "Measurements of Entrainment by a Free Rotating Disk," *Journal of the Royal Aeronautical Society*, Vol. 71, pp. 124-126.

Cham, T.-S., and Head, M. R., 1969, "Turbulent Boundary Layer on a Rotating Disk," *Journal of Fluid Mechanics*, Vol. 37, No. 1, pp. 129-147.

Gregory, N., Stuart, J. T., and Walker, W. S., 1955, "On the Stability of Three-Dimensional Boundary Layers with Application to the Flow Due to a Rotating Disk," *Philosophical Transactions A*, Vol. 248, pp. 155-199.

Littell, H., and Eaton, J., 1991, "Experimental Investigation of the Three-Dimensional Boundary Layer on a Rotating Disk," *Proceedings of the 8th Symposium on Turbulent Shear Flows*, Munich, Aug. 91, pp. 30-4:1-5.

Newman, B. G., 1983, "Flow and Heat Transfer on a Disk Rotating Beneath a Forced Vortex," *AIAA Journal*, Vol. 21, No. 8, pp. 1066-1070.

Schlichting, H., *Boundary Layer Theory*, McGraw-Hill, New York, NY, 1979, pp. 596-602.

von Kármán, T., 1921, "Über Laminare und Turbulente Reibung," *Zeitschrift für Angewandte Mathematic und Mechanik*, Vol. 1, pp. 233.

Unsteady Flow in the Obstructed Space Between Disks Corotating in a Cylindrical Enclosure

W. R. Usry

J. A. C. Humphrey

R. Greif

Department of Mechanical Engineering,
University of California at Berkeley,
Berkeley, CA 94720

Time-resolved measurements of the circumferential velocity component were obtained with a laser-Doppler velocimeter in the space between the center pair of four disks corotating in air in an axisymmetric cylindrical enclosure. The separate influences on the flow of two obstructions of similar shapes but having different lengths were investigated. The results show that both obstructions significantly alter the mean and rms distributions of velocity in quantitatively different but qualitatively similar ways. Both obstructions also alter the characteristic frequencies of flow oscillations associated with large scale motions present in the flow, apparently of the type that arise in unobstructed configurations. The measurements suggest that an obstruction can induce bimodal states of motion over frequency ranges that depend on the obstruction's length. The presence of an obstruction increases the strength of the cross-stream secondary motion in the inter-disk space by redirecting fluid moving in the circumferential direction towards the radial direction. While this reduced the magnitude of the velocity deficit in the obstruction wake, for the cases investigated the flow did not recover within one revolution from the effects of either obstruction.

Introduction

The flow of air in the space between a pair of corotating disks is of considerable importance to information storage systems in the computer industry. This is because flow oscillations resulting from obstructions, the transport of particulates and the convection of heat resulting from temperature differences among system components, contribute to alignment inaccuracies and, hence, to the degraded performance of the read-write magnetic heads that are supported at submicron distances from the rotating disk surfaces.

Although the rotating disk storage devices used in the computer industry are very complex, laboratory models have allowed an investigation of the essential characteristics of this class of flows. Schuler et al. (1990) review the quantitative experimental studies performed in unobstructed corotating disk flow configurations. The review by Humphrey et al. (1991) covers the small amount of work related to obstructed configurations, where the obstruction is in the shape of a rigid parallelepiped of rectangular cross-section that passes through the enclosure side wall into the space between the disks and is radially aligned along the symmetry plane between them. The work reviewed includes: (*a*) the first quantitative time-averaged measurements of velocity clearly showing the marked effects of an obstruction upon the flow, obtained by Tzeng and Humphrey (1991) using a laser-Doppler velocimeter (LDV); (*b*) the benefits of streamlining obstructions in order to minimize drag and eddy shedding, demonstrated by Yamaguchi et al. (1990) with a hot-wire anemometer (HWA); and, (*c*) the study on the increase in viscous dissipation resulting from rectangular obstructions between corotating disks, by Hudson and Eibeck (1991), subsequently analyzed in considerable detail by Humphrey et al. (1992).

Using the two-equation turbulence model developed by Chang et al. (1990), three-dimensional numerical simulations of obstructed corotating disk flows have been performed by Chang and Li (1990) for the configuration and flow conditions corresponding to the experiment of Tzeng and Humphrey (1991). Although limited, the comparisons between measurements and computations of mean velocity show qualitative agreement. However, corresponding predictions of the rms velocity reveal discrepancies with respect to the measurements which point to the need to improve the numerical calculation and turbulence modelling methodologies. For this, more extensive and accurate measurements of the mean and rms velocities, as well as the characteristic flow oscillation frequencies, are needed to guide and test developments.

This paper presents the main LDV and HWA results of an experimental investigation aimed at quantifying the influence of a thin rectangular obstruction on the isothermal flow of air in the space between coaxial disks corotating in a fixed cylindrical enclosure. In this regard, it is of special interest to determine the effect of an obstruction on the characteristic frequencies of flow oscillations associated with large-scale motions present in the flow, of the type which arise in unobstructed configurations (Abrahamson et al., 1988).

Contributed by the Fluids Engineering Division for publication in the JOURNAL OF FLUIDS ENGINEERING. Manuscript received by the Fluids Engineering Division April 29, 1992; revised manuscript received November 30, 1992. Associate Technical Editor: Ho Chih-Ming.

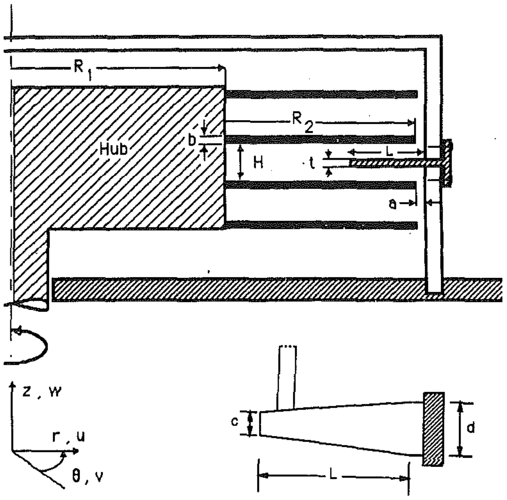

Fig. 1 Side view of the test section and top view of the obstruction (insert) with relevant length scales, coordinate system and velocity components defined. In the figure: R_1 = 56.4 mm, R_2 = 105.3 mm, H = 9.5 mm, a = 2.7 mm, and b = 1.9 mm. For the long obstruction: c = 6.9 mm, d = 10.2 mm, L = 31.8 mm, and t = 2.0 mm. For the short obstruction: c = 8.5 mm, d = 10.2 mm, L = 15.9 mm and t = 2.0 mm.

Experimental Apparatus and Instrumentation

The experimental apparatus and the LDV methodology used in this study have been described in detail in Schuler et al. (1990). Briefly, the apparatus consists of a motorized test section with the base of the test section fixed to a large inertial granite slab supported on a steel stand. The test section, together with definitions of relevant variables and dimensions, is shown schematically in Fig. 1. It consists of four, coaxial, equidistant aluminum disks mounted on a common hub in a fixed cylindrical enclosure. The enclosure was modified to allow the insertion of an obstruction in the space between the center pair of the four corotating disks.

Two obstructions of varying rectangular cross-section, one short (L = 15.9 mm) and one long (L = 31.8 mm), were machined out of Plexiglas (see Fig. 1). Either obstruction could be inserted radially through a slot in the enclosure wall so that it laid in the inter-disk midplane with its largest pair of flat surfaces oriented parallel to the midplane. The penetration depth of the obstruction is defined by the radial location of its tip, r_{tip}, relative to the rotating system axis of symmetry. Thus, on a dimensionless basis, $r_{\text{tip}}/R_2 = 1 + (a - L)/R_2$ (Fig. 1) and $r_{\text{tip}}/R_2 = 0.88$ for the short obstruction while $r_{\text{tip}}/R_2 = 0.73$ for the long.

The disks are rotated by a spindle that is connected to the hub clamping them and to a DC servo motor located underneath the test section. The motor is equipped with a DC tachometer, a linear servo-amplifier, a digital stroboscope tachometer and a frequency counter. The hub clamping the disks is composed of a stack of three black-anodized aluminum rings. The rings were painted with orange fluorescent enamel to reduce backscattered light, thus enhancing the signal-to-noise ratio.

The side and top walls of the cylindrical enclosure are made of 1/4 inch Plexiglas to allow optical access for the LDV measurements. A 3/8 in. diameter hole drilled through the enclosure wall allows the periodic introduction of 0.5–2 micron mineral oil droplets for the LDV measurements. Tape was used to cover 75 percent of this hole to minimize possible perturbations to the flow. Data rates as high as 5000 Hz could be obtained after seeding the flow and allowing it to equilibrate prior to taking the measurements.

The LDV system consists of a DANTEC 55X modular optics system aligned 25 deg off-axis in a backscatter mode. A description of the system and a list of its relevant parameters are provided in Schuler et al. (1990). A 5/8 Doppler burst validation criterion, set to 1.5 percent, was used with the counter set to "combined" measurement mode.

The LDV system is mounted on the surface of a traversing table connected to three stepping motors controlled by an IBM PC/AT. Table movements allow the relative displacement of the optical probe volume to within ±100 microns over a range of 18 cm. For this study the optical probe volume was moved in the radial and axial directions only. Geometrical symmetries inherent in the test section facilitated the alignment of the optical probe volume relative to the enclosure side wall inner surface and the facing surfaces of the center pair of disks. It was possible to locate the probe volume to within ±50 microns from a disk surface and ±500 microns from the enclosure side wall inner surface.

Limited optical access near the obstructions, and the higher quality spectra obtainable from continuous velocity signals, motivated us to obtain additional data with a HWA. In this regard we note that it was the frequency content of the HWA signal which was important to measure. The HWA probe was mounted on a pair of 0.5 mm diameter brass wires shown schematically in the insert to Fig. 1. The sensor was a tungsten wire 5 micrometers in diameter and 1 mm in effective length that was soldered to the support wires. The sensor was aligned in the radial direction and was sensitive to both the circumferential and axial components of velocity. Velocity time records were obtained immediately downstream of the obstruction, and immediately upstream of the same obstruction by flipping it 180 deg to make the hotwire face the approaching flow. The HWA sensor was controlled by a constant temperature type hotwire controller (TSI Model 1010). The output signal of the anemometer was amplified 33 times and the DC component

Nomenclature

a = clearance between disk tip and enclosure wall
b = disk thickness
c = obstruction width at the tip
d = obstruction width at the base
f = frequency of mean flow oscillation
H = disk spacing
L = obstruction length
N = nondimensional mean flow frequency ($=2\pi f/\Omega$)
r = radial coordinate
r_{tip} = radial location of obstruction tip ($=R_2 + a - L$)
R_1 = hub radius
R_2 = disk radius
R = nondimensional radius ($=r/R_2$)
Re = Reynolds number ($= \Omega R_2^2/\nu$)
t = obstruction thickness
v = mean circumferential velocity component
V = nondimensional mean circumferential velocity component ($=v/\Omega R_2$)
$\tilde{v}$ = rms of the circumferential velocity component
$\tilde{V}$ = nondimensional rms of the circumferential velocity component ($=\tilde{v}/\Omega R_2$)
z = axial coordinate
Z = nondimensional axial coordinate ($=z/H$)
θ = circumferential coordinate (measured with respect to the obstruction)
Ω = angular speed of rotation in radians/second unless otherwise noted

was suppressed by an operational amplifier with a gain that was flat from DC up to 10 kHz. The signal was sampled periodically and stored in an IBM PC-AT through a 12 bit analog-to-digital converter. The maximum sampling frequency was 3030 Hz.

Measurement Procedure and Uncertainty Considerations

Measurements of the circumferential velocity component were made using the green-light channel of the LDV system. All the measurements were taken in the space between the center pair of disks in the test section. Radial profiles of velocity were taken along the midplane between the center pair of disks ($Z = z/H = 0$) for four different circumferential locations (20, 90, 180, and 270 deg) downstream of the short or long obstruction. In addition, axial profiles were obtained at four radial locations ($R = r/R_2 = 0.71$, 0.78, 0.92, and 1.00) for different circumferential locations relative to the obstruction present in the flow.

Software was written to perform both the data collection and its initial reduction. At each measurement location, 2500 validated Doppler bursts and their time increments were accumulated in the buffer interface and then stored in the PC/AT memory. Mean and rms values were obtained by ensemble averaging the instantaneous quantities. (Corresponding mean and rms time averages were in excellent agreement with the ensemble averages.) These calculations included a check-and-correct procedure to eliminate measurements falling beyond 5 standard deviations. Typically, not more than 5 measurements in 2500 were discarded this way. The data rate was controlled to be low enough to insure that an accurate long-term mean velocity could be obtained, but high enough to resolve non-turbulent oscillations known to arise in the flow.

The velocity time series were subsequently transferred to a DEC-Station 3100 to calculate their autocorrelation functions and spectra. Allowance was made for the random variation in arrival times in the velocity data by using the slotted autocorrelation technique discussed by Bell (1986). This technique clusters data from a time series into an autocorrelation function with equally spaced time-bins. The Fourier transform of the autocorrelation then yields the energy spectrum. A trial-and-correct procedure allows the optimum bin time-size to be obtained for calculating the autocorrelation functions from which a spectrum is subsequently determined.

For data collection with the HWA, software was written to take 8192 samples from the hotwire signal at equally spaced time intervals. The time records of velocity were then transferred to the DEC-Station 3100 where their spectra were calculated using a commercial package for evenly spaced data.

The main sources of uncertainty affecting the mean and rms LDV measurements were: the beam angle and optical probe volume location, due to refraction of the beams by the curved Plexiglas wall; additional (random) refraction effects; velocity bias; filter bias; velocity gradient broadening; inhomogeneous particle seeding; and, finite data-sample size. Each of these uncertainties has been discussed and quantified by Schuler et al. (1990) where it is argued that they are all small everywhere except for the regions very close to the disks and the enclosure side wall where the effects of positioning error and velocity gradient broadening are important. In this work it is estimated that, except very near these surfaces, systematic uncertainties in the mean and rms velocities were typically 0.2 and 5.0 percent, respectively. Maximum uncertainties were 5 and 50 percent, respectively. Corresponding values of random uncertainties in both the mean and rms velocities are estimated to be about 0.8 percent, typically. Maximum values were 1.3 percent for the mean and 3 percent for the rms velocity. Calibration of the HWA anemometer was unncessary since the time information from the velocity record was sufficient to compute the energy spectra.

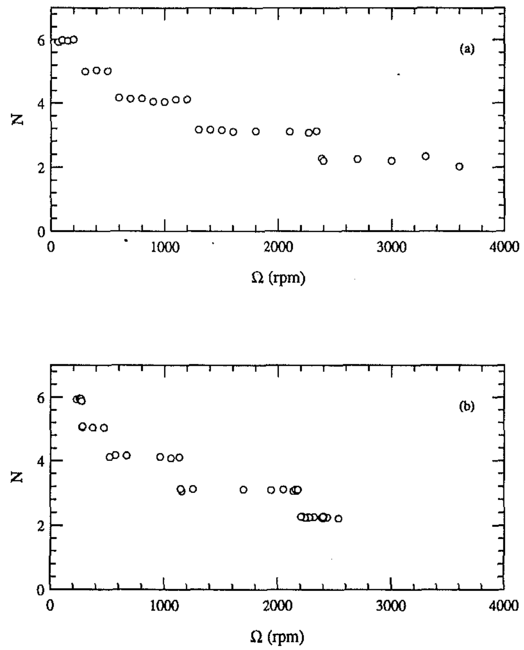

Fig. 2 Dominant dimensionless unobstructed flow frequency versus rpm for (*a*) rpm increasing and (*b*) rpm decreasing

Results and Discussion

A. Unobstructed Flow Measurements (Flow Oscillations). Time-resolved measurements of the circumferential velocity component in the present flow configuration without an obstruction have been presented by Schuler et al. (1990) and Usry et al. (1990). The latter reported a transition from steady axisymmetric flow to unsteady circumferentially-periodic flow between 60 and 64 rpm ($\mathrm{Re} = 4.88 \times 10^3$, approximately). The transition was found to coincide with the appearance of six circumferentially distributed axially aligned vortical structures of the type visualized by Abrahamson et al. (1988).

New time-resolved measurements of the circumferential velocity component are provided here at the radial location $r = 93$ mm ($R = r/R_2 = 0.89$) on the midplane between the two center disks, for values of Ω ranging from 60 rpm to 4200 rpm ($4.59 \times 10^3 < \mathrm{Re} < 2.91 \times 10^5$). For each rpm, the system was brought to the target rotational speed from a lower rotational speed, and the flow was allowed to equilibrate for a minimum of 100 revolutions prior to measuring a velocity time-record. Each time-record obtained displayed a distinct sinusoidal-like oscillation whose frequency, f, was determined from the corresponding energy spectrum. Figure 2(*a*) shows the variation of $N = 2\pi f/\Omega$ with respect to rpm. The data appear as a staircase pattern over the range of rotational speeds examined and show that the dominant frequencies of the large-scale flow oscillations are close to integer multiples of the disk angular velocity. This finding strongly supports the notion that it is the periodic passage past the measurement probe-volume of large scale flow structures that induces the oscillations observed. The relatively sharp transitions between the near-integer values shown in the figure were reproducible.

Figure 2(*b*) shows the corresponding distribution of N for the system brought to its target rotational speeds from higher (rather than lower) values. A comparison between the two sets of results reveals a rotationally-dependent hysteresis in the values of the rotational speeds marking the transitions in N.

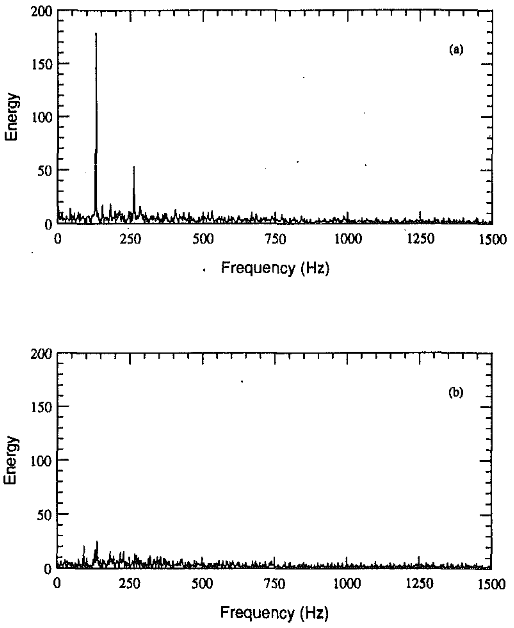

Fig. 3 Energy spectra obtained with a hotwire anemometer immediately downstream of an obstruction in a flow at Re = 2.64×10^5 (3600 rpm) (*a*) short obstruction and (*b*) long obstruction

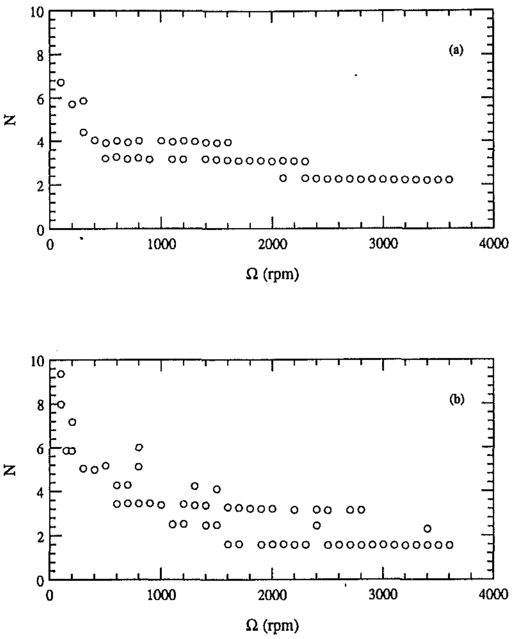

Fig. 5 Dominant dimensionless obstructed flow frequency versus rpm immediately upstream of the (*a*) short obstruction (*b*) long obstruction

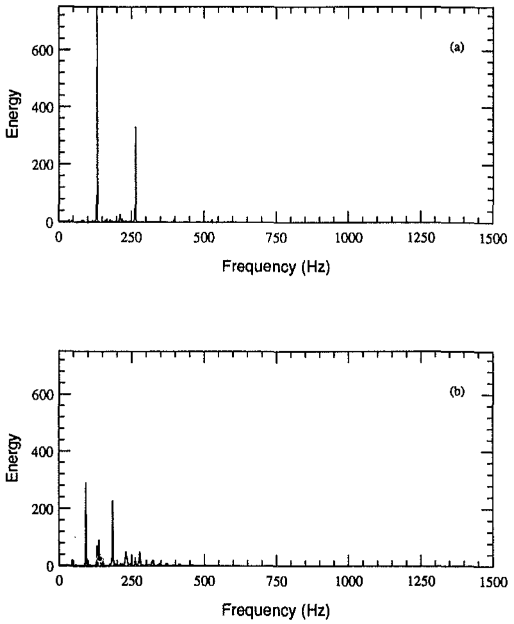

Fig. 4 Energy spectra obtained with a hotwire anemometer immediately upstream of an obstruction in a flow at Re = 2.64×10^5 (3600 rpm) (*a*) short obstruction and (*b*) long obstruction

B. Obstructed Flow Measurements (Flow Oscillations). Energy spectra obtained from the hotwire measurements of velocity at 3600 rpm (Re = 2.64×10^5) are shown in Fig. 3 for the measurement position immediately downstream of the two obstructions, and in Fig. 4 for the measurement position immediately upstream of the two obstructions. Downstream of the short obstruction Fig. 3(*a*) shows a dominant frequency at 132 Hz corresponding to $N = 2.2$. Downstream of the long obstruction Fig. 3(*b*) shows three relatively weak peaks at 93, 137, and 183 Hz, respectively, with that at 137 Hz corresponding to $N = 2.3$. For the unobstructed flow, shown in Fig. 2, a value of N close to 2 is expected.

The spectra measured upstream of the long and short obstructions (Fig. 4) show the same dominant frequencies as those measured downstream of these obstructions but with much larger energy content. This suggests that the motions responsible for the oscillations attempt to reestablish themselves within one revolution of the disks. In this regard, the short obstruction spectra reveal frequencies with much larger energy content than observed for the long obstruction at both the upstream and downstream locations. It will be shown below that both obstructions significantly alter the mean and rms velocities in the inter-disk space. However, the above results imply that the shorter obstruction has a weaker influence on the time dependent properties of the flow. Clearly, as the penetration depth of an obstruction is decreased, the inter-disk fluid motion should gradually acquire the unobstructed flow characteristics.

Energy spectra obtained at rotational speeds less than 1400 rpm (not provided here) showed evidence of eddy shedding for the long obstruction only. For example, at 900 rpm an eddy shedding frequency of 800 Hz, corresponding to St = $ft/\Omega R_2 = 0.16$, was measured for this obstruction. The energy at high frequency started appearing at 100 rpm, approximately, and persisted up to the highest frequency the instrumentation could resolve (1500 Hz at 1400 rpm). It is expected that eddy shedding from the long obstruction would continue at rotational speeds greater than 1400 rpm. Figure 5 shows the variation of the dimensionless frequency, N, with respect to disk speed of rotation for the obstructed flows. These data differ in a significant way from the unobstructed flow results shown in Fig. 2. For both the long and short obstructions there are ranges of the rotational speed for which at least two values of N are possible. Therefore, there are no clear-cut values of disk rotational speed marking possible transitions between the different values of N. For example, for the short obstruction we find $N = 3.2$ or 3.8 for $500 < \Omega < 1600$ rpm, and for the long obstruction $N = 2.2$ or 3.2 for $2100 < \Omega < 2300$ rpm, approximately.

In the unobstructed flow case we know that the quantity N, when rounded to the nearest integer value, coincides with the number of large-scale vortical structures periodically distributed in the circumferential direction. The present duality of frequencies observed for the obstructed flows suggests that the effect of an obstruction is to induce bimodal states of motion in the inter-disk space. While the data are insufficient to un-

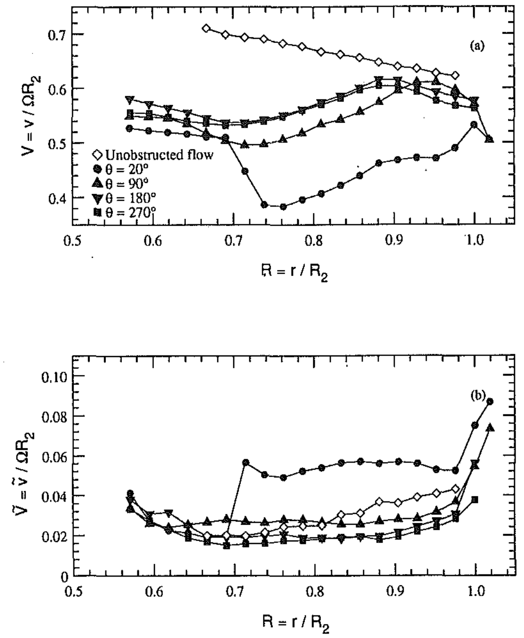

Fig. 6 Radial profiles of the dimensionless circumferential mean velocity (*a*) and its root mean square (*b*) downstream of the long obstruction between the center pair of four disks corotating at Re = 2.64 × 10^5 (3600 rpm) in the cylindrical enclosure

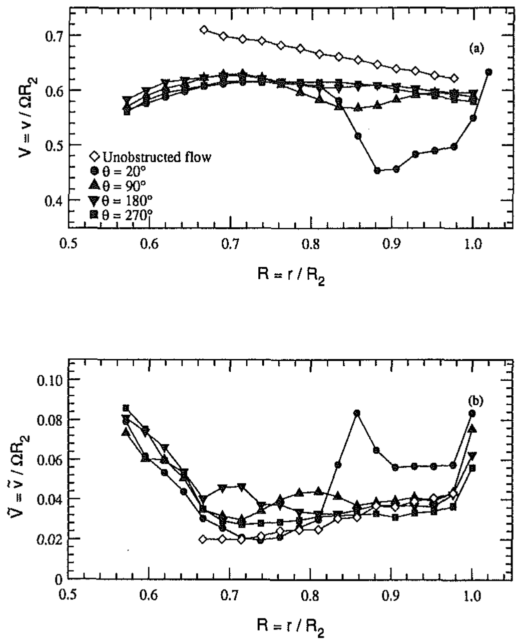

Fig. 7 Same as Fig. 6 for the case of the short obstruction

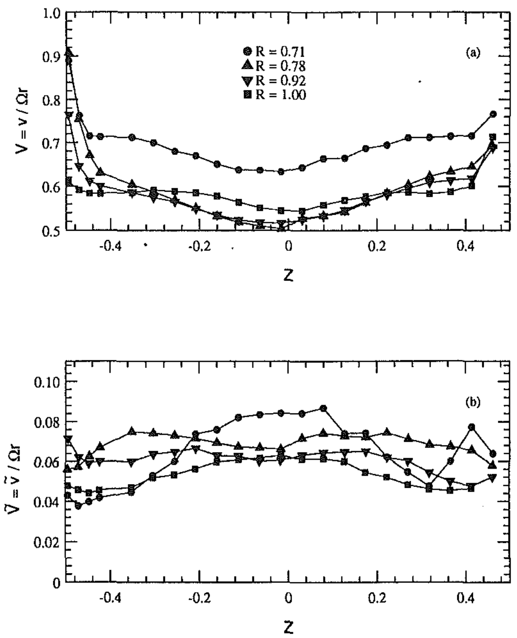

Fig. 8 Axial profiles of the dimensionless circumferential mean velocity (*a*) and its root mean square (*b*) between the center pair of four disks corotating at Re = 2.64 × 10^5 (3600 rpm) 20 deg downstream of the long obstruction in the cylindrical enclosure

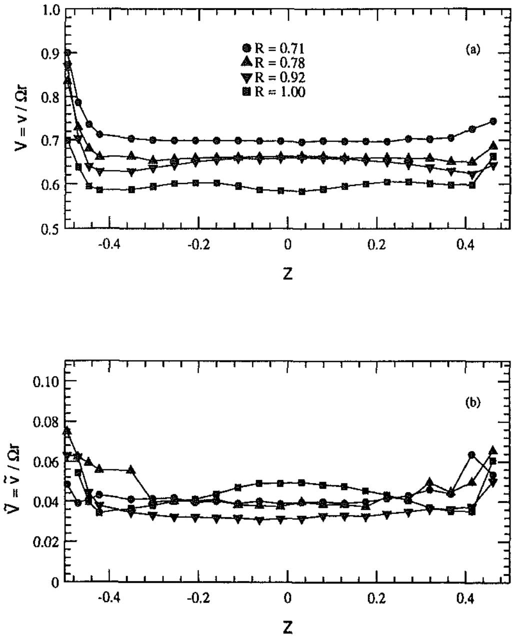

Fig. 9 Same as Fig. 8 for the case 90 deg downstream of the long obstruction

ambiguously attribute the bimodal states of motion to alternations between the number of vortical axially-aligned unobstructed-type flow structures, from the spectra it is clear that the energy content of these motions is considerably larger in the case of the short obstruction than the long, in keeping with the notion that the short obstruction flow is closer to the unobstructed flow in its time-dependent characteristics.

C. Obstructed Flow Measurements (Mean and RMS Velocities). Radial and axial profiles of the mean and rms velocities for the obstructed flow cases at 3600 rpm are provided in Figs. 6 to 11. The radial traverses taken along the midplane between the disks ($Z = 0$) are plotted in Figs. 6 and 7. For comparison, corresponding profiles for the unobstructed flow are included. Figures 8 and 9 show axial traverses for various radial locations at circumferential locations, 20 and 90 degrees downstream of the long obstruction, respectively. Figures 10 and 11 provide the corresponding plots for the short obstruction.

The motion of air in the unobstructed space between corotating disks would be described everywhere by solid body rotation if the gap dimension were $a = 0$ and the enclosure wall were rotating at the same angular velocity as the disks. However, the enclosure is stationary and this results in a lower air velocity in the core of the flow relative to the disk velocity. Near the disks the centrifugal force acting on the air in the

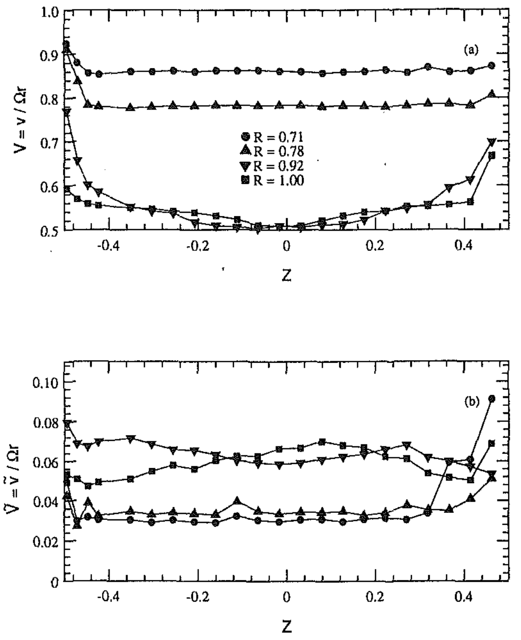

Fig. 10 Same as Fig. 8 for the case 20 deg downstream of the short obstruction

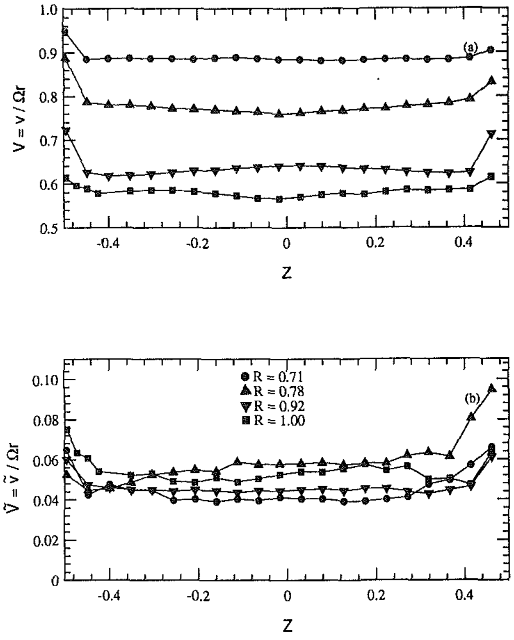

Fig. 11 Same as Fig. 8 for the case 90 deg downstream of the short obstruction

disk Ekman layers overcomes the inwardly-directed radial pressure gradient force while the opposite is true in the core of the flow. This results in a cross-stream secondary motion that displaces the air radially outward along the disk surfaces towards the enclosure side-wall, and radially inward toward the hub in the core of the flow. The secondary motion transfers a deficit of circumferential momentum from the enclosure sidewall into the core of the flow and this results in a larger fraction of the flow that deviates from solid body rotation than can be attributed to radial diffusion effects alone. A second source of circumferential momentum deficit is due to the obstruction. This is shown by the marked reductions in the mean circumferential velocity, relative to the unobstructed flow case, plotted in Fig. 6(*a*). Past the obstruction the flow attempts to recover its undisturbed state but is unable to do so in the course of one revolution.

The first rms profile immediately downstream of the long obstruction, shown in Fig. 6(*b*) displays considerably larger values of this quantity than the corresponding profile for the unobstructed flow case. However, the rms profiles further downstream show relatively constant uniform values which are actually lower than the rms values for the unobstructed flow. The reduction in the rms is attributed to a disruption of the periodic passage of the large-scale axially-aligned vortical structures present in the unobstructed flow.

The mean velocity profiles for the short obstruction, shown in Fig. 7(*a*), are similar to those for the long obstruction with two noteworthy differences. First, the radial extent of the reduced velocity immediately downstream of the obstruction is considerably smaller. Second, recovery of the flow is faster. The rms values in Fig. 7(*b*) are very high 20 deg downstream of the tip of the obstruction. The gradual displacement of the maxima in the rms profiles (from $R = 0.86$ at 20 deg, to $R = 0.8$ at 90 deg, to $R = 0.7$ at 180 deg) suggests that this high rms fluid is convected towards smaller radii by the cross-stream secondary motion. We believe that this explains the higher values of the rms velocity at all circumferential locations with radii less than $R = 0.66$ in the figure. An estimate of the mean radial velocity (v_r) along the inter-disk midplane can be obtained from the sequential locations of these elevated rms levels. This yields $v_r = -1.4$ m/s which, nondimensionally, is $v_r/\Omega R_2 = -0.035$. In contrast, for a disk rotating freely in the laminar flow regime Batchelor (1951) has shown that v_r is approximately equal to $\Delta\Omega^* r$. Taking $\Delta\Omega$ as the rotational speed of a disk minus the rotational speed of the bulk of the air between a pair of disks, the dimensionless velocity computed from this expression at $R = 0.7$ is $v_r/\Omega R_2 = +0.056$.

The axial variations of the mean and rms velocity profiles for the long obstruction, shown in Figs. 8 and 9, reveal in further detail how the flow evolves past the obstruction. Between 20 and 90 deg, the mean velocity profiles already show a significant recovery from the strong influence of the obstruction. The midplane velocities at 90 deg for $R = 0.78$ and $R = 0.92$ increase as a result of the cross-stream secondary flow which is augmented by the higher value of $\Delta\Omega$ caused by the obstruction. Air near the disks moves at essentially the disk speed of rotation while further away its circumferential velocity is substantially reduced by the obstruction relative to the value that would exist in the absence of an obstruction.

The rms profiles in Fig. 8(*b*) show that the turbulence intensity in the wake of the long obstruction is highest near the tip which is at $r_{\text{tip}}/R_2 = 0.73$. The profiles for $R = 0.78$ and for $R = 0.92$ display maxima on either side of the obstruction where the flow shears past it. A comparison among these four profiles shows the extent to which the wake has spread in the axial direction by the time the 20 deg location is reached. A similar comparison among the profiles at 90 deg (Fig. 9(*b*)) shows much more uniform distributions, again supporting the notion of a strong mixing action due to the combined effects of the cross-stream secondary flow and enhanced turbulent diffusion. The rms values at $R = 1.0$ are larger than the background turbulence on the midplane ($Z = 0$) as a result of the collision of the Ekman layers in the vicinity of $Z = 0$ on the enclosure side wall.

The axial profiles of mean velocity 20 deg downstream of the short obstruction (Fig. 10(*a*)) show almost no variation at the two radial locations ($R = 0.71$ and 0.78) that are less than the radial location of the obstruction tip ($r_{\text{tip}} = R_2 = 0.88$). The other two profiles reveal the presence of a large wake similar to the long obstruction case. The corresponding rms values at 20 deg (Fig. 10(*b*)) are low at the two inner radii and high at the two outer radii. The mean profiles 90 deg downstream of this obstruction (Fig. 11(*a*)) again show that a recovery is under way. By the 90 deg location, the two higher levels of the rms at large radii have been reduced while the two lower levels at small radii have been increased. These observations support the picture of a flow that is strongly mixed by the combined effects of turbulent diffusion and advective transport by the secondary motion.

Conclusions

Laser-Doppler measurements of the circumferential component of velocity obtained in the region between a pair of disks corotating in a fixed cylindrical enclosure reveal that the presence of a thin rectangular obstruction significantly affects the average and time dependent features of the flow to an extent dictated by the penetration depth of the obstruction in the inter-disk space. Hotwire spectra reveal bimodal states of motion for both long and short obstructions, and eddy shedding for the long obstruction only. The blockage due to an obstruction increases the strength of the cross-stream secondary motion, helping to reestablish the character of an unobstructed flow within one revolution. However, for the conditions investigated here recovery is not achieved within one revolution. Larger obstruction blockage ratios, typical of current and forthcoming disk storage designs, are the subject of continuing research.

Acknowledgments

This investigation was supported by the Computer Mechanics Laboratory of the University of California at Berkeley and by the IBM Almaden Research Center in San Jose, CA. We are sincerely grateful for this support and for the interest shown in the work by our colleagues at IBM. Special thanks go to Dr. T. Kawamura of Gifu National College of Technology (Japan) for his assistance in setting up the hotwire anemometer used in the study.

References

Abrahamson, S. D., Koga, D., and Eaton, J. E., 1988, "An Experimental Investigation of the Flow Between Shrouded Corotating Disks," Report No. MD-50, Thermoscience Division, Department of Mechanical Engineering, Stanford University.

Bell, W. A., 1986, "Spectral Analysis Of Laser Velocimeter Data With the Slotted Correlation Method," *Proceedings of the AIAA/ASME Fourth Fluid Mechanics, Plasma Dynamics and Lasers Conference.*

Batchelor, G. K., 1951, "Note on a Class of Solutions of the Navier-Stokes Equations Representing Steady Rotationally-Symmetric Flow," *Quarterly Journal of Mechanics and Applied Mathematics*, Vol. 4, No. 1, pp. 29-41.

Chang, C. J., Humphrey, J. A. C., and Greif, R. 1990, "Calculation of Turbulent Convection Between Corotating Disks in Axisymmetric Enclosures," *International Journal of Heat and Mass Transfer*, Vol. 33, pp. 2701-2720.

Chang, C. J., and Li, H., 1990, "Three-Dimensional Numerical Simulation of Flows For Corotating Disks," *Proceedings of the 1990 ASME International Computers in Engineering Conference and Exhibition*, Boston, MA, Vol. 2, pp. 387-392.

Hudson, A. J., and Eibeck, P. A., 1991, "Torque Measurements of Corotating Disks in an Axisymmetric Enclosure," ASME JOURNAL OF FLUIDS ENGINEERING, Vol. 113, pp. 648-653.

Humphrey, J. A. C., Chang, C. J., Li, H., and Schuler, C. A., 1991, "Unobstructed and Obstructed Rotating Disk Flows: A Summary Review Relevant to Information Storage Systems," *Advances in Information Storage Systems*, Vol. 1, pp. 79-110.

Humphrey, J. A. C., Schuler, C. A., and Iglesias, I., 1992, "Analysis of Viscous Dissipation in Disk Storage Systems and Similar Flow Configurations," *Physics of Fluids A*, Vol. 4, pp. 1415-1427.

Schuler, C. A., Usry, W., Weber, B., Humphrey, J. A. C., and Greif, R., 1990, "On the Flow in the Unobstructed Space Between Shrouded Corotating Disks," *Physics of Fluids A*, Vol. 2, pp. 1760-1770.

Tzeng, H,. and Humphrey, J. A. C., 1991, "Corotating Disk flow in an Axisymmetric Enclosure With and Without a Bluff Body," *International Journal of Heat and Fluid Flow*, Vol. 12, No. 3, pp. 184-201.

Usry, W. R., Schuler, C. A., Humphrey, J. A. C., and Greif, R., 1990, "Unsteady Flow Between Corotating Disks in an Enclosure With an Obstruction," *Proceedings Fifth International Symposium on Applications of Laser Techniques to Fluid Mechanics*, July 9-12, Lisbon, Portugal.

Yamaguchi, Y., Talukder, A. A., Shibuja, T., and Tokuyama, M., 1990, "Air Flow Around Magnetic-Head-Slider Suspension and Its Effect on Slider Flying-Height Fluctuation," *Proceedings of INTERMAG 1990 CONFERENCE, Trans. on Magnetics.*

C. R. Truman
Associate Professor.
Mem. ASME

S. A. Shirazi[1]
Research Assistant.

Department of Mechanical Engineering,
University of New Mexico,
Albuquerque, NM 87131

F. G. Blottner
Distinguished Member of Technical Staff,
Computational Aerodynamics Division 1556,
Sandia National Laboratories,
Albuquerque, NM 87185

Noniterative Solution for Pressure in Parabolic Flows

Parabolic flows in which the pressure variation in the streamwise (or marching) direction is unknown a priori include internal thin shear layers, shock-boundary layer interactions, and inverse boundary layers with specified displacement thickness or shear stress. The pressure is typically obtained through an additional iteration beyond that required to determine the velocity components (and other dependent variables). A generalized block-tridiagonal procedure is discussed in which pressure is determined within the iteration for velocity components to substantially reduce computation time. The increase in algebraic complexity in the solution procedure is small; no increase in the size of the block matrices is required. The method applies to any marching solution in which a scalar dependent variable is constant across the flow, but varies in the streamwise or marching direction.

Introduction

Finite-difference techniques for two-dimensional thin shear layers take advantage of the block-tridiagonal structure of the linearized difference equations in an efficient factorization solution procedure (see, for example, Blottner, 1975). Three-dimensional flows with small crossflow (Cebeci, 1974) or rotational symmetry (e.g., Truman and Jankowski, 1985) also result in block-tridiagonal systems. However, for parabolic flows in which pressure is constant across the shear layer (e.g., the y-direction) but varies in the streamwise or marching direction (e.g., the x-direction), the pressure $p(x)$ is unknown a priori and must be determined simultaneously with the velocity components. In the present method, this additional unknown and corresponding constraint are treated as additional elements in the standard block-tridiagonal form of the linearized difference equations. Examples of flows in which the pressure must be computed simultaneously with the velocity components are: (i) internal flows, including ducts and diffusers; (ii) inverse boundary layers, with specified displacement thickness or wall shear stress; and (iii) shock-boundary layer interactions. The scalar constraint may take the form of integral conservation of mass, a specified displacement thickness or wall shear stress, or conditions at the edge of the boundary layer.

Previous methods of solution for such flows include an integral form of conservation of mass used by Bodoia and Osterle (1961) to compute flow development in a plane Poiseuille channel. Since a Gaussian elimination procedure was used, this quadrature was simply solved simultaneously with the difference equations for mass and momentum. The efficiency afforded by tridiagonal solvers, however, required that the constraint used to determine the pressure be uncoupled from the remaining difference equations. Most implicit methods employ an iteration procedure for the pressure (Anderson et al., 1984); the nonlinear eigenvalue method (Cebeci and Chang, 1978) is an example. In this method, the pressure is treated as an eigenvalue in the system of linearized difference equations. Additional iterations, beyond those required to solve the nonlinear difference equations, are required to determine the eigenvalue. Although this iteration for the eigenvalue (pressure) typically converges in three iterations, the solution of an internal or inverse boundary layer is three times more expensive than the standard boundary-layer solution.

In the mechul function method (Cebeci and Bradshaw, 1977), the pressure is treated as an additional unknown at each grid point, and the basic block-tridiagonal structure is retained. The idea of computing the pressure $p(x, y)$ even when its variation across the boundary layer was negligible was used by Cebeci and Chang (1978) to compute duct flows. For thin shear layers, the transverse momentum equation reduces to $\partial p/\partial y = 0$. In the mechul function approach, however, this equation is retained and pressure $p(x, y)$ is included as an unknown along with the velocity components $u(x, y)$ and $v(x, y)$. A recent inverse boundary layer application by Kaufman and Hoffman (1985) for specified wall shear found that using $\partial p/\partial y = 0$ led to an instability. They instead used $\partial^2 p/\partial y^2 = 0$ across the boundary layer, with $\partial p/\partial y = 0$ enforced at the wall. The present work shows that such manipulations are unnecessary, since the pressure can be determined simultaneously with the velocity components without iteration. The present approach also provides a more efficient solution procedure.

Description of Generalized Method

Although the unknown pressure and scalar constraint must be added to the block-tridiagonal structure of the linearized difference equations, the solution can proceed in almost the usual manner. It is a misconception that additional iterations are required or that the block size must be increased by in-

---

[1] Presently Assistant Professor, Department of Mechanical Engineering, University of Tulsa, Tulsa, OK 74104.

Contributed by the Fluids Engineering Division for publication in the JOURNAL OF FLUIDS ENGINEERING. Manuscript received by the Fluids Engineering Division January 25, 1993; revised manuscript received January 25, 1993. Associate Technical Editor: P. D. Telionis.

cluding a transverse variation of the pressure which is then set to zero. The present method is a generalization of those used to determine pressure in shock-boundary layer interactions (Reyhner and Flügge-Lotz, 1968) as well as in duct flows and inverse boundary layers (Kwon et al., 1984). The linearized difference equations are partitioned between a block-tridiagonal system for the velocity components and a scalar constraint for the pressure. An upper/lower triangular matrix factorization is performed in the usual manner. The coefficients of the scalar equation are eliminated during the forward sweep to determine the pressure directly; no initial guess for pressure is required. During the backward sweep, the pressure is used to determine the velocity components (and other dependent variables). Indeed, the procedure applies for any marching solution in which a scalar dependent variable varies only in the marching direction, and is determined from an equation involving the other dependent variables and (possibly) the scalar variable itself.

To illustrate the new method for the solution for pressure, consider the system of linearized difference equations for a parabolic two-dimensional incompressible flow (see, e.g., Blottner, 1975). The pressure p, which varies only in the streamwise direction, is included as an unknown in this system. The other unknowns are represented by the n-length vector $\overline{W}_j$ of the remaining dependent variables, which includes the two velocity components and, in the case of the Box method (Keller and Cebeci, 1972), the shear stress. The n boundary conditions at one boundary ($j=1$) are

$$\mathbf{B}_1\overline{W}_1+\mathbf{C}_1\overline{W}_2+\overline{G}_1 p=\overline{D}_1. \tag{1}$$

These boundary conditions would include, for example, no-slip and no-penetration conditions. The n transport equations at internal grid locations are expressed as

$$\mathbf{A}_j\overline{W}_{j-1}+\mathbf{B}_j\overline{W}_j+\mathbf{C}_j\overline{W}_{j+1}+\overline{G}_j p=\overline{D}_j, \tag{2}$$

for $j=2, \ldots, J-1$. These would include conservation of mass and streamwise momentum. The n boundary conditions at the other boundary ($j=J$) are

$$\mathbf{A}_J\overline{W}_{J-1}+\mathbf{B}_J\overline{W}_J+\overline{G}_J p=\overline{D}_J. \tag{3}$$

The scalar constraint used to determine the pressure can be written as

$$\overline{a}_1^T\overline{W}_1+\overline{a}_2^T\overline{W}_2+\cdots+\overline{a}_J^T\overline{W}_J+gp=d, \tag{4}$$

where the superscript T denotes the transpose. This is the most general form of the scalar constraint; some specific examples are discussed below. The coefficients are given by $n\times n$ block matrices $\mathbf{A}_j$, $\mathbf{B}_j$, and $\mathbf{C}_j$, $n\times 1$ vectors $\overline{D}_j$, $\overline{G}_j$, and $\overline{a}_j$, and scalars d and g.

Writing this system of equations in matrix form shows the resulting "nearly" block-tridiagonal form is $\mathbf{A}\,\mathbf{W}=\mathbf{D}$, or

$$\left[\begin{array}{ccccc|c} \mathbf{B}_1 & \mathbf{C}_1 & & & & \overline{G}_1 \\ \mathbf{A}_2 & \mathbf{B}_2 & \mathbf{C}_2 & & & \overline{G}_2 \\ & & \ddots & & & \vdots \\ & & \mathbf{A}_{J-1} & \mathbf{B}_{J-1} & \mathbf{C}_{J-1} & \overline{G}_{J-1} \\ & & & \mathbf{A}_J & \mathbf{B}_J & \overline{G}_J \\ \hline \overline{a}_1^T & \overline{a}_2^T & \cdots & \overline{a}_{J-1}^T & \overline{a}_J^T & g \end{array}\right] \left[\begin{array}{c} \overline{W}_1 \\ \overline{W}_2 \\ \vdots \\ \overline{W}_{J-1} \\ \overline{W}_J \\ \hline p \end{array}\right] = \left[\begin{array}{c} \overline{D}_1 \\ \overline{D}_2 \\ \vdots \\ \overline{D}_{J-1} \\ \overline{D}_J \\ \hline d \end{array}\right] \tag{5}$$

The efficient solution methods for pressure developed by Reyhner and Flügge-Lotz (1968) and Kwon et al. (1984) have been generalized in the present method by noting that the usual solution procedure of factorizing the coefficient matrix $\mathbf{A}$ into lower- and upper-triangular matrices $\mathbf{L}$ and $\mathbf{U}$ can be carried out to yield $\mathbf{L}\,\mathbf{U}\,\mathbf{W}=\mathbf{D}$, where

$$\mathbf{L}=\left[\begin{array}{ccccc|c} \mathbf{I} & & & & & \\ \hat{\mathbf{A}}_2 & \mathbf{I} & & & & \\ & & \ddots & & & \\ & & \hat{\mathbf{A}}_{J-1} & \mathbf{I} & & \\ & & & \hat{\mathbf{A}}_J & \mathbf{I} & \\ \hline \hat{a}_1^T & \hat{a}_2^T & \cdots & \hat{a}_{J-1}^T & \hat{a}_J^T & 1 \end{array}\right] \tag{6a}$$

and

$$\mathbf{U}=\left[\begin{array}{ccccc|c} \hat{\mathbf{B}}_1 & \mathbf{C}_1 & & & & \hat{G}_1 \\ & \hat{\mathbf{B}}_2 & \mathbf{C}_2 & & & \hat{G}_2 \\ & & \ddots & & & \vdots \\ & & & \hat{\mathbf{B}}_{J-1} & \mathbf{C}_{J-1} & \hat{G}_{J-1} \\ & & & & \hat{\mathbf{B}}_J & \hat{G}_J \\ \hline & & & & & \hat{g} \end{array}\right] \tag{6b}$$

The caret indicates matrices, vectors and scalars formed from the elements in the original matrix $\mathbf{A}$ in Eq. (5) through the recursion relations defined in Truman et al. (1988). Then following the usual factorization procedure $\mathbf{U}\,\mathbf{W}=\mathbf{L}^{-1}\,\mathbf{D}=\hat{\mathbf{D}}$, where $\hat{\mathbf{D}}=[\hat{D}_1, \hat{D}_2, \ldots, \hat{D}_J, \hat{d}]^T$ is determined from $\mathbf{L}\,\hat{\mathbf{D}}=\mathbf{D}$. Then the unknowns $\mathbf{W}=[\overline{W}_1, \overline{W}_2, \ldots, \overline{W}_J, p]^T$ are determined quite easily from $\mathbf{U}\,\mathbf{W}=\hat{\mathbf{D}}$. The pressure is determined first from $\hat{g}p=\hat{d}$, or $p=\hat{d}/\hat{g}$. Then the n-length vectors $\overline{W}_J$, $\overline{W}_{J-1}$, $\ldots$, $\overline{W}_1$ are obtained through backward substitution to arrive at the solution for the linearized system. Further details of this method including recursion relations are given by Truman et al. (1988). The nonlinearity inherent in the momentum equations requires iteration and new coefficient matrices are computed. Thus the pressure is obtained simultaneously with the velocity components (and other dependent variables) in each iteration to solve the nonlinear difference equations.

The formation of the coefficient vectors $\hat{a}_j$ and $\hat{G}_j$ requires additional floating-point operations relative to those required to compute $\hat{\mathbf{A}}_j$ and $\hat{\mathbf{B}}_j$. An operations count for the present method is compared with those for the nonlinear eigenvalue and mechul function methods in Truman et al. (1988). Comparisons for several examples are carried out in the Results section.

The general form of the scalar constraint (4) can represent a variety of conditions. Only a few nonzero elements actually appear in the vector coefficients $\overline{a}_j$ and $\overline{G}_j$ in most cases. Note that g and d may be zero but that $\hat{g}$ and $\hat{d}$ will be nonzero after the factorization. Some of the more common examples of the scalar constraint are: (i) integral conservation of mass using quadrature formulas; (ii) integral conservation of mass using a stream-function formulation (Cebeci and Chang, 1978); (iii) the streamwise momentum equation written at the centerline of a duct or channel (Anderson et al., 1984; Cebeci and Chang, 1978); (iv) specified wall shear stress (Keller and Cebeci, 1972); (v) specified displacement thickness (Anderson et al., 1984); (vi) pressure-velocity relation in a shock-boundary layer interaction (Reyhner and Flügge-Lotz, 1968). For some forms of the scalar constraint, including (ii) and (iv) above, the pressure may be determined with a reduced set of recursion relations, as shown in Truman et al. (1988).

The present method for the solution for pressure in parabolic flows simply takes advantage of the "nearly" block-tridiagonal structure of the linearized difference equations in an efficient factorization scheme. A similar approach was used to develop recursion relations for the solution of cyclic block-tridiagonal systems (Napolitano, 1985) which arise in problems with periodic boundary conditions. Towne and Hoffman (1984) developed a form similar to Eq. (5) for the solution of the streamwise pressure in a three-dimensional parabolic procedure. Towne and Hoffman also showed that even in a com-

Table 1 Comparison of efficiency of solution methods for turbulent internal thin shear layers

Test case	Block size *n*	Computation Time (CPU s, IBM 3032/4341) Nonlinear eigenvalue	 Generalized block-tridiagonal	Savings
Parallel-plate channel entrance region (Cebeci and Chang, 1978)	2	3.6	1.9	47%
Source flow between stationary disks (Truman and Jankowski, 1985)	3	28	10	64%
Source flow between rotating disks (Truman and Jankowski, 1985)	5	87	30	66%

pressible form, integral conservation of mass can be written in the form of Eq. (4) when the density is expressed in terms of pressure through the ideal gas relation. In a novel method used by Van Dalsem and Steger (1987) for separated three-dimensional boundary layers, the pressure terms in the momentum equations were replaced by applying the momentum equations evaluated at the wall and at the wake centerline. The resulting augmented scalar tridiagonal system of equations is solved by LU decomposition, in a manner very similar to the present method. Jang et al. (1989) employed a factorization technique similar to the present work to efficiently solve a bordered block-tridiagonal system which occurs when turbulent viscosity terms are fully linearized in a boundary-layer method.

Results

Several test cases are used to demonstrate the efficiency of the present technique as compared to the nonlinear eigenvalue method (Cebeci and Chang, 1978). Each test case is an internal incompressible flow in which the Box method was employed with an algebraic turbulence model. These results are summarized in Table 1.

The theoretical savings in computational time can be estimated by assuming that the nonlinear eigenvalue solution required three iterations at each marching step compared to each solution of the nonlinear difference equations in the new method for a savings of about two-thirds. These savings are somewhat diminished by the additional recursion relations in the matrix factorization in the new method. It is clear, as the number of variables n increases, the additional work required by the new method is negligible compared to the savings achieved by eliminating the iterations in the nonlinear eigenvalue method. The mechul function approach for the three examples in Table 1 would require computation times which were greater than the present method by 85, 57 and 33 percent, respectively. Moreover, storage requirements for the mechul function method would be larger by the factor $[(n+1)/n]^2$. Figure 1 shows the theoretical operation count per transverse grid point, which is proportional to computation time, for the standard and generalized block-tridiagonal methods as well as that for the mechul function where block size is increased to $n+1$. As n increases, the advantage of the present generalized method over the mechul function method decreases, but the savings in time and storage for typical values of n is significant. The savings achieved by using the generalized block-tridiagonal method over the nonlinear eigenvalue method are dramatic, since the latter typically requires three iterations with the standard block-tridiagonal method.

Conclusion

A generalization of an efficient solution method of parabolic flows in which the pressure is unknown a priori was presented.

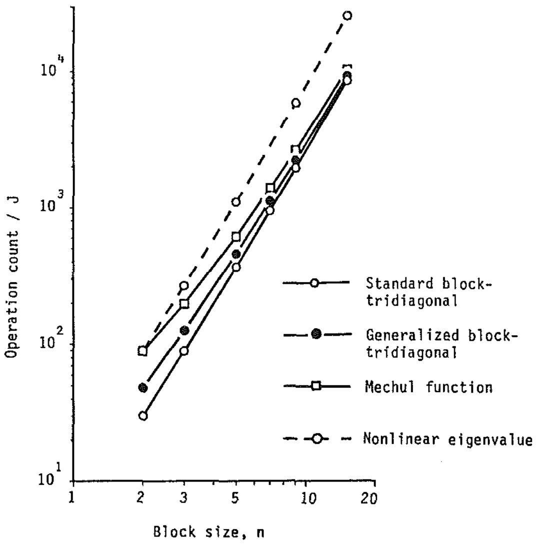

Fig. 1 Block-tridiagonal operation count (per transverse grid point) versus block size

The present method shows that solution methods such as the nonlinear eigenvalue and mechul function approaches are not necessary since an efficient solution can be achieved in nearly the usual manner as used for standard block-tridiagonal systems. The generalized block-tridiagonal procedure can be employed for parabolic flows in which a scalar variable does not vary across the shear layer but varies in the marching direction. Besides pressure, as described herein, other such dependent variables arise. For example, the variation of the shock layer thickness in the streamwise direction is unknown in marching solutions for supersonic flows past blunt bodies. Barnett et al. (1982) and Davis and Blottner (1987) describe specific applications of the general procedure discussed herein for parabolized Navier-Stokes and (hyperbolic) Euler equations, respectively.

The efficiency of the present method becomes increasingly important with the inclusion of additional transport equations for energy or turbulence quantities. For example, the present method has been used to predict turbulent source flow between rotating disks (Shirazi and Truman, 1988) at approximately one-third cost of the nonlinear eigenvalue method. A two-equation turbulence model was employed, and the coefficient matrices were composed of 9×9 block matrices.

Acknowledgment

This work was supported by the Computational Aerodynamics Division, Sandia National Laboratories, Albuquerque (SNLA), and the Department of Mechanical Engineering, University of New Mexico.

References

Anderson, D. A., Tannehill, J. C., and Pletcher, R. H., 1984, *Computational Fluid Mechanics and Heat Transfer*, Hemisphere, WA, pp. 363-391, 417-468.

Barnett, M., Davis, R. T., and Rakich, J. V., 1982, "Implicit Boundary Conditions for the Solution of the Parabolized Navier-Stokes Equations for Supersonic Flows," *Journal of Computational Physics*, Vol. 48, pp. 168-181.

Blottner, F. G., 1975, "Investigation of Some Finite-Difference Techniques for Solving the Boundary Layer Equations," *Computer Methods in Applied Mechanics and Engineering*, Vol. 6, pp. 1-30.

Bodoia, J. R., and Osterle, J. F., 1961, "Finite Difference Analysis of Plane Poiseuille and Couette Flow Developments," *Applied Scientific Research*, Vol. 10, pp. 265-276.

Cebeci, T., 1974, "Calculation of Three-Dimensional Boundary Layers. I. Swept Infinite Cylinders and Small Cross-Flow," *AIAA Journal*, Vol. 12, pp. 779-786.

Cebeci, T., and Bradshaw, P., 1977, *Momentum Transfer in Boundary Layers*, Hemisphere-McGraw Hill, New York, pp. 367-371.

Cebeci, T., and Chang, K. C., 1978, "A General Method for Calculating Momentum and Heat Transfer in Laminar and Turbulent Duct Flows," *Numerical Heat Transfer*, Vol. 1, pp. 39-68.

Davis, R. T., and Blottner, F. G., 1987, "A Spatial Marching Technique for the Inviscid Blunt Body Problem," *Aerodynamics of Hypersonic Lifting Vehicles*, AGARD Conference Proceedings 428-21.

Jang, H.-M., Cebeci, T., and Keller, H. B., 1989, "A Preferred Approach to the Linearization of Turbulent Boundary-Layer Equations," *Computers & Fluids*, Vol. 17, pp. 571-578.

Kaufman, K. C., and Hoffman, G. H., 1985, "Inverse Laminar Boundary Layer Problems with Assigned Shear. The Mechul Function Revisited," *International Journal for Numerical Methods in Fluids*, Vol. 5, pp. 1035-1045.

Keller, H. B., and Cebeci, T., 1972, "An Inverse Problem in Boundary-Layer Flows: Numerical Determination of Pressure Gradient for a Given Wall Shear," *Journal of Computational Physics*, Vol. 10, pp. 151-161.

Kwon, O. K., Pletcher, R. H., and Lewis, J. P., 1984, "Prediction of Sudden Expansion Flows Using the Boundary-Layer Equations," ASME JOURNAL OF FLUIDS ENGINEERING, Vol. 106, pp. 285-291.

Napolitano, M., 1985, "A Fortran Subroutine for the Solution of Periodic Block-Tridiagonal Systems," *Communications in Applied Numerical Methods*, Vol. 1, pp. 11-15.

Reyhner, T. A., and Flügge-Lotz, I., 1968, "The Interaction of a Shock Wave with a Laminar Boundary Layer," *International Journal of Non-Linear Mechanics*, Vol. 3, pp. 173-199.

Shirazi, S. A., and Truman, C. R., 1988, "Prediction of Turbulent Source Flow Between Corotating Disks with an Anisotropic Two-Equation Turbulence Model," ASME *Journal of Turbomachinery*, Vol. 110, pp. 187-194.

Towne, C. E., and Hoffman, J. D., 1984, "Computation of Viscous Flow in Planar and Axisymmetric Ducts by an Implicit Marching Procedure," AIAA Paper 84-0256 (also NASA TM-83567).

Truman, C. R., and Jankowski, D. F., 1985, "Prediction of Turbulent Source Flow Between Stationary and Rotating Discs," *International Journal of Heat and Fluid Flow*, Vol. 6, pp. 69-78.

Truman, C. R., Shirazi, S. A., and Blottner, F. G., 1988, "Noniterative Solution for Pressure in Parabolic Flows," *Advances and Applications in Computational Fluid Dynamics*, O. Baysal, ed., FED-Vol. 66, ASME, New York, pp. 121-127.

Van Dalsem, W. R., and Steger, J. L., 1987, "Efficient Simulation of Separated Three-Dimensional Viscous Flows Using the Boundary-Layer Equations," *AIAA Journal*, Vol. 25, pp. 395-400.

Shiki Okamoto
Department of Mechanical Engineering,
Shibaura Institute of Technology,
Tokyo, Japan

Shozo Seo
Toshiba Monofrax Co., Ltd.
Chiba, Japan

Kouichirou Nakaso

Itsurou Kawai

Department of Mechanical Engineering,
Shibaura Institute of Technology,
Tokyo, Japan

Turbulent Shear Flow and Heat Transfer Over the Repeated Two-Dimensional Square Ribs on Ground Plane

This paper describes the flow structure over the repeated two-dimensional square ribs of side length D, *placed at a pitch S on a ground plane. The value of S/D which most augments the turbulence of the free stream and, hence the heat transfer is calculated. The region of interest in this investigation is far downstream where the velocity and temperature distributions follow similarity rules. The time-mean velocity, static pressure, and the velocity vectors were measured by Pitot-and static pressure tubes and a three hole cylindrical yawmeter. The turbulence intensities and integral scale were obtained using a hot wire anemometer. The mean temperature distribution was measured by thermocouples and the local heat transfer coefficient was then calculated. It is found that at $S/D=9$ the turbulence intensity is maximized. As a result of this effect and the fact that for $S/D=9$ the flow reattaches within a groove, the heat transfer is also maximized. The measurements show how the location of reattachment depends on S/D and that high local heat transfer coefficient coincides with the reattachment point. The average heat transfer coefficient and the pressure drop correlation is quantified.*

1 Introduction

The flow over rough walls has been hitherto investigated in relation to the drag of a rough wall as well as early establishment of a turbulent boundary layer which augments the heat transfer. Nikuradse (1933) studied first the turbulent flow in pipes roughened by sand and Schlichting (1936) investigated the resistance of a wall with repeated roughness elements. Perry et al. (1969) studied the turbulent boundary layer developing over a rough wall and proposed to divide them into two types: "*d*-type," independent of the size of roughness element for value of $S/D \leqq 4$, (where S is the pitch between adjoining roughness elements and D is the height of roughness element) and "*k*-type" which is dependent on the roughness size for $S/D > 4$. Antonia and Luxton (1971) studied the "*k*-type" and Osaka et al. (1984) investigated the "*d*-type" boundary layer.

In connection with the problem of augmenting the heat transfer, Nunner (1956) measured the heat transfer and the pressure loss in the pipe where the inner wall was roughened by wires of various sizes. Webb et al. (1971) studied the relation between the heat transfer and the resistance of tubes roughened by the repeated ribs for the cases of $10<S/D<40$, and Berger and Hau (1979) measured the mass- and heat transfer in pipe roughened with the repeated square ribs for cases of $3 < S/D < 10$. Rao and Picot (1970), and Edwards and Sheriff (1961) studied the heat transfer on the inner tube of annulus and the ground plane in the test section of wind tunnel using wires as promoters for various values of S/D. Optimum values of S/D to augment the heat transfer were given at $S/D=7$ by Rao and Picot (1970), and at $S/D=10$ by Edwards and Sheriff (1961), and Han et al. (1978).

In the references mentioned so far, no information is presented on the detailed flow structure. This was undertaken by Hijikata et al. (1984) and Mori et al. (1985) who studied the flow between adjoining ribs among repeated two-dimensional ribs on the ground plane for the single case of $S/D=15$. Ichimiya et al. (1983) measured the flow over repeated ribs on the lower insulated wall of duct whose upper wall was heated for cases of $S/D=5$, 7, and 15. However, these studies were performed for limited case of S/D and did not, as a consequence, describe the variation of flow properties with the pitch ratio S/D nor, in particular, include information on maximum heat transfer.

The present paper describes the detailed study of the flow structure over repeated two-dimensional square ribs on the ground plane for various values of S/D and indicates the value of S/D which is optimal in augmenting turbulence.

2 Experimental Apparatus and Measurement Procedures

The experiment was carried out in a blow down wind tunnel having a 500 mm × 500 mm working section of 2000 mm length. The ground plate, an aluminum plate of 4 mm thickness, was set with a spacing of 25 mm from the lower wall of

---

Contributed by the Fluids Engineering Division for publication in the JOURNAL OF FLUIDS ENGINEERING. Manuscript received by the Fluids Engineering Division March 24, 1992; revised manuscript received May 24, 1993. Associate Technical Editor: J. Humphrey.

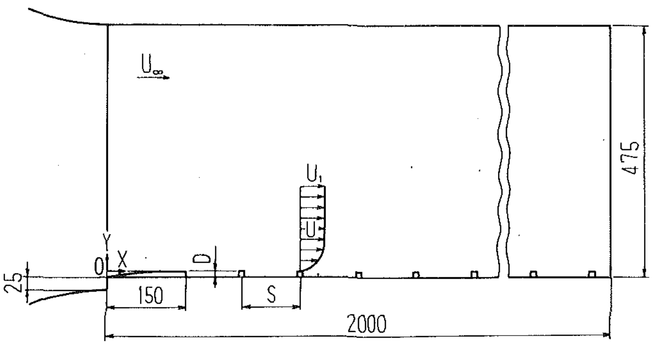

(*a*) **Test section**

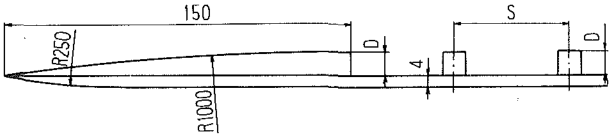

(*b*) **Details of ribs and inlet of duct**

Fig. 1 Apparatus and nomenclature

tunnel exit in order to avoid the boundary layer developed on the tunnel wall, as shown in Fig. 1. A half-ogival forebody of 150 mm length was placed on the leading-edge portion of the ground plate. Two-dimensional square ribs with side length $D=10$mm were aligned at regular pitch, S, on the lower wall of the test section and were varied to provide $S/D=2$, 3, 4, 5, 7, 9, 13, and 17. The trough thus created between two square ribs will be referred as a groove. The time-mean velocity, static pressure, and the velocity vectors were measured by Pitot- and static pressure tubes, and a three hole cylindrical yawmeter of 6 mm diameter. The turbulence intensities, and integral length scale were obtained using an F.F.T. Analyzer connected to a hot wire anemometer. Use of the anemometer in the recirculation zone was avoided by restricting measurements to a position of Y greater than zero, where Y is measured from the top of the ribs. This slightly unusual choice of origin, as opposed to the ground plane, was made to emphasize this aspect. Only the three-hole probe was used for negative Y, in other words, within the recirculation zone, and the probe was aligned to the direction of the mean flow by nulling the pressure difference between the outer holes. For the purpose of qualitative depiction of the flow pattern and measurement of the recirculation length, this technique was adequate. Measurements were made at 14 axial locations corresponding to the centers of the square ribs and the grooves for a free stream velocity of $U_\infty=16.0$ m/s corresponding to $\mathrm{Re}=U_\infty D/\nu=1.0\times10^4$.

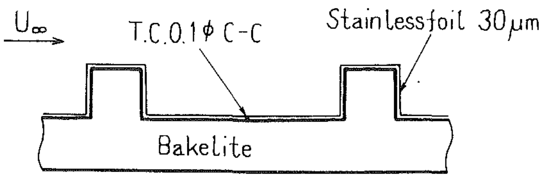

Fig. 2 Heater arrangement in heat transfer experiment

The heat transfer experiment was done in a blow down wind tunnel having a 100 mm × 100 mm working section of 1500 mm length. The heated surface of the ground plate consisted of a stainless steel foil (thickness = 0.03 mm) which was supplied by a constant heat flux of an alternating current of 100V. The foil was attached on to insulating bakelite plate to prevent heat loss as shown in Fig. 2. The temperature of the heated surface T_w was measured by copper-constantan thermocouples of 0.1 mm diameter which were set on the stainless steel foil. Measurements were made at five downstream groove centers and five locations between the two-adjoining square ribs by using the probes as shown in Fig. 3, for a free-stream velocity of $U_\infty=12.0$m/s, corresponding to $\mathrm{Re}=U_\infty D/\nu=7500$.

3 Experimental Results and Discusssions

3.1 Velocity Profiles in Shear Layer Over Repeated Square Ribs. Flow visualizations are presented first in order to provide a qualitative picture of the flow field. Flow visualization was performed in a water channel with flow corresponding to $\mathrm{Re}\fallingdotseq 500$. Figure 4 shows photographs of the flow and vortices generated behind a rib for the cases of $S/D=2$, 5, and 9. The combined effect of flow reattachment and the intensified turbulence behind the ribs are the key to heat transfer enhancement. A small stable vortex exists in the groove for $S/D=2$ and, for $S/D=5$, a larger stable vortex occupies the entire groove, without reattachment of the separation streamline on the floor of the groove. For $S/D=9$, in contrast, this streamline reattaches to the floor of the groove at about 4D. This result was confirmed in the wind tunnel, at the Reynolds number used later, by the three hole probe.

The turbulent shear layer and the velocity profiles not shown here, tend to similarity with increasing distance. Therefore the

Nomenclature

C_p = pressure coefficient $=(P-P_\infty)/(\rho U_\infty^2/2)$
D = side length of square section of two-dimensional ribs
L_x = integral scale in X-direction
P = static pressure
P_∞ = static pressure in free stream
q = heat flux
Re = Reynolds number $=U_\infty D/\nu$
S = pitch between the centers of two adjoining square ribs
T, T_w, T_∞ = mean temperature, wall temperature and mean temperature in free stream
U = time-mean velocity
U_1 = velocity at outer edge of shear layer
U_∞ = velocity in free stream
u' = X component of fluctuation velocity
X, Y, Z = coordinates with origin above 10 mm at the center of the leading edge of the ground plane (see Fig. 1). X is chosen along the ground plane, Y and Z for the vertical and horizontal directions, respectively
$\overline{X}$ = distance in X-direction from the center of the rib
$\overline{Y}$ = distance in Y-direction from the base in the groove
$\overline{X}_r$ = distance from the center of square rib to the reattachment point
α = local heat transfer coefficient $=q/(T_w-T_\infty)$
α_0 = local heat transfer coefficient on the smooth surface without ribs
$\overline{\alpha}$ = average heat transfer coefficient
δ = thickness of turbulent shear layer
ν = kinematic viscosity of air
ρ = density of air

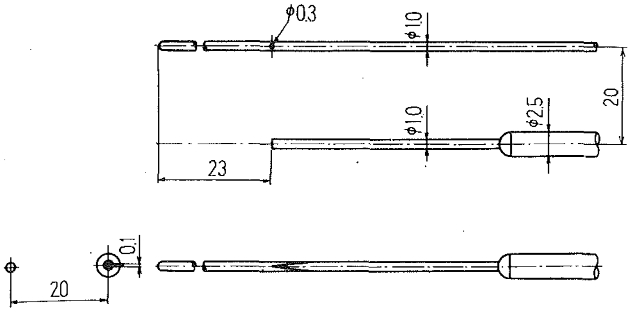

(*a*) **Pitot and static pressure tubes**

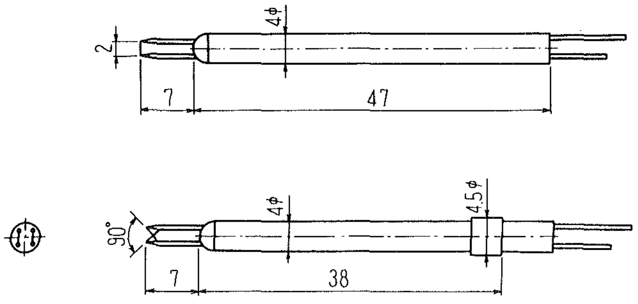

(*b*) **Hot wire probe**

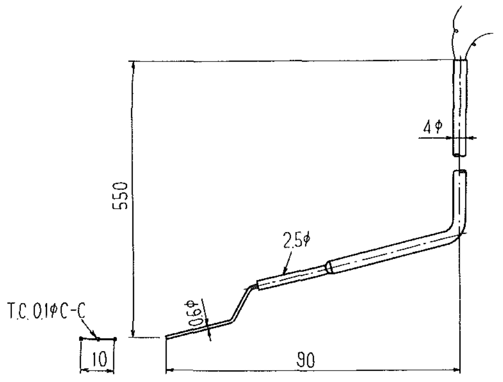

(*c*) **Thermocouple probe**

Fig. 3 Sketches of probes

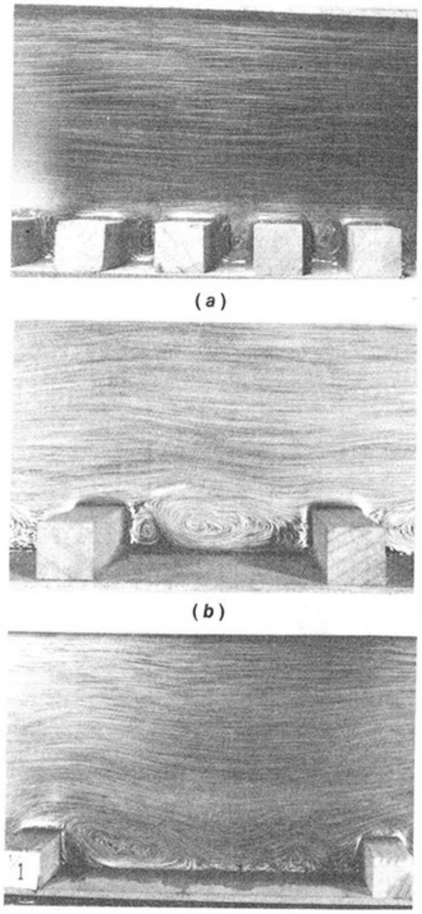

Fig. 4 Photographs of vortices in water channel. Reynolds number is approximately 500. (*a*) *S/D* = 2; (*b*) *S/D* = 5; (*c*) *S/D* = 9

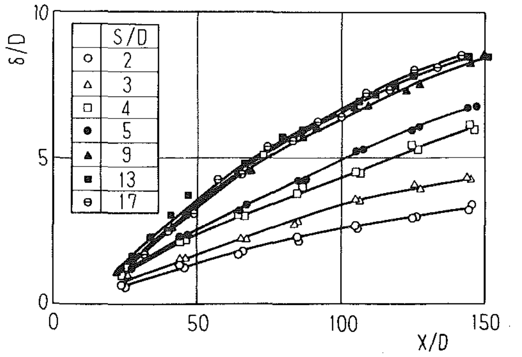

Fig. 5 Thickness of shear layer (uncertainty in δ/D = 0.05 and in *X/D* = 0.10)

ribs can be seen as the roughness element on the flat plate. The thickness of the turbulent shear layer was defined by the value of Y where U is equal to $0.99U_1$. Figure 5 shows the variation of the thickness of the turbulent shear layer with the pitch ratio S/D. This and the figure that follow, serve to define the region of interest in this investigation, namely the region of large X/D where the velocity and temperature distribution follow similarity rules closely. In the range of $2 \leqq S/D \leqq 9$, thickness increases with increase in the downstream distance, as for a conventional turbulent boundary layer on a flat plate, but it is almost unchanged in the range of $S/D \geqq 9$. Apparently, the interaction between the ribs reaches a maximum at $S/D \fallingdotseq 9$ and beyond this spacing no additional disturbance is introduced.

In order to examine the development of the similarity in the shear layers, Fig. 6 shows the velocity profiles in the sections at the centers of ribs and grooves between two ribs in the case of $S/D = 9$ and at a distance of about 70 and 46, respectively. Although the velocity profiles above the rib centers are somewhat different from the 1/3 power law profile, the profiles at $Y/\delta > 0.1$ above the groove centers are close to the 1/3 power law profile, except for $X/D = 28.0$.

Figure 7(*a*) shows the variation of the velocity profile in a section at the similar profile region, near $X/D = 142$, with the pitch ratio S/D. The difference between the velocity profiles above the rib for the various values of S/D is concentrated in the region of $Y/\delta < 0.5$. The velocity profiles at $Y/\delta > 0.1$ for $S/D = 3$, 4, and 5 are close to the 1/3 power law profile. Figure 7(*b*) shows that the velocity profiles above the last groove center, near $X/D = 147$, concentrate in a narrow range which is different from the case of the rib. The 1/3 power law in the velocity profile means that the displacement thickness increases in the downstream distance and large pressure losses occur. This is different from the case of a conventional turbulent boundary layer.

3.2 Turbulence Intensities in Shear Layer over Repeated Ribs.

The augmentation in heat transfer with changes in S/D is

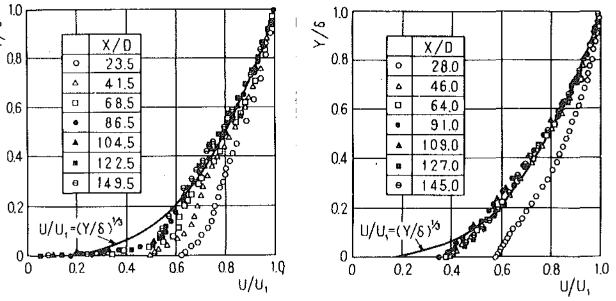

(a) (b)

Fig. 6 Velocity profile in shear layer for $S/D=9$ ((a) rib; (b) groove (Uncertainty in $Y/\delta=0.02$ and and in $U/U_1=0.04$))

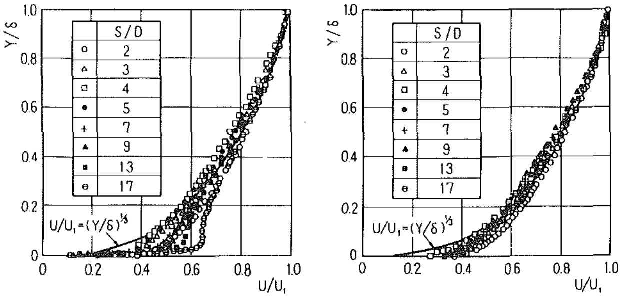

(a) (b)

Fig. 7 Velocity profile in shear layer in similar profile region ((a) rib; (b) groove (Uncertainty in $Y/\delta=0.02$ and in $U/U_1=0.04$))

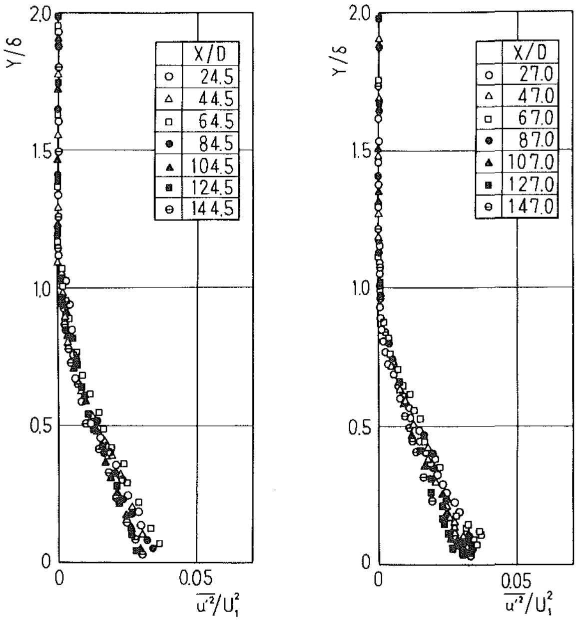

(a) (b)

Fig. 8 X-component of turbulence intensity for $S/D=5$ ((a) rib; (b) groove (Uncertainty in $Y/\delta=0.02$ and in $\overline{u'^2}/U_1^2=0.0015$))

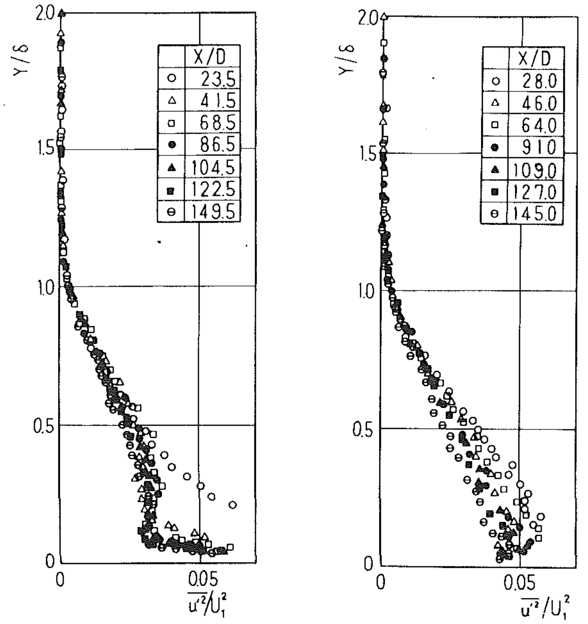

(a) (b)

Fig. 9 X-component of turbulence intensity for $S/D=9$ ((a) rib; (b) groove (Uncertainty in $Y/\delta=0.02$ and in $\overline{u'^2}/U_1^2=0.0015$))

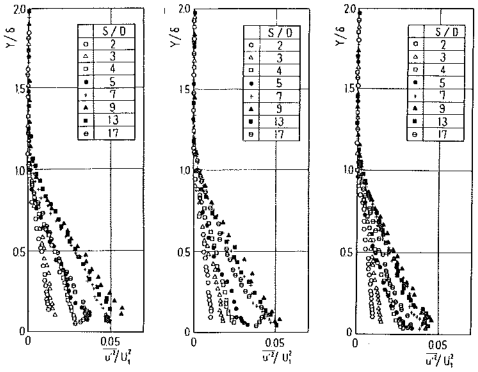

(a) (b) (c)

Fig. 10 X-component of turbulence intensity at groove center ((a) $X/D=69$; (b) $X/D=108$; (c) $X/D=147$ (Uncertainty in $Y/\delta=0.02$ and in $\overline{u'^2}/U_1^2=0.0015$))

due to the change in the turbulence intensity. Figures 8 and 9 show the X-component of turbulence intensity in the shear layer at the rib and groove centers for the cases of $S/D=5$ and 9. The profiles of turbulent intensity become self-preserving at locations farther downstream in contrast to the mean velocity for the case of $S/D=5$ shown in Fig. 8. The profiles of turbulence intensity in the shear layer at the rib center become self-preserving by $X/D=40$ for the case of $S/D=9$ as shown in Fig. 9(a). But Fig. 9(b) shows that the turbulence intensity in the shear layer at the groove decays with an increase in the downstream distance, and in particular it does not achieve a self-preserving profile with $X/D=145$ in contrast to the velocity profiles at the same position. In order to examine the variation in turbulence intensity with the pitch ratio S/D, profiles of turbulence intensity were measured at three typical positions, $X/D=69$, 108, 147, for the groove centers. Figure 10 shows the variation of turbulence intensity in the shear layer with the pitch ratio S/D at three positions. It is found that the turbulence intensity increases with S/D for $S/D \leqq 9$ and decreases for $S/D > 9$. Figure 11 summarizes the important parts of Fig. 10 and shows the variation of turbulence intensity at the positions of $Y/\delta=0.1$ to 0.5 in the groove with the pitch ratio S/D, in order to indicate the optimum pitch ratio to augment the turbulence intensity as a turbulence promoter. This figure shows that the turbulence intensity attains maximum at $S/D=9$. When the two-dimensional square ribs are aligned on the wall as a turbulence promoter, the pitch ratio $S/D=9$ is optimum to augment the turbulence intensity. Moreover, the effects of the Reynolds number on the optimum S/D seem to be few, since Rao and Picot (1970) reported that the optimum pitch ratio was almost same in the range of $Re=6\times10^4 \sim 1.2\times10^5$. It therefore appears that the effect of Reynolds number may be insignificant.

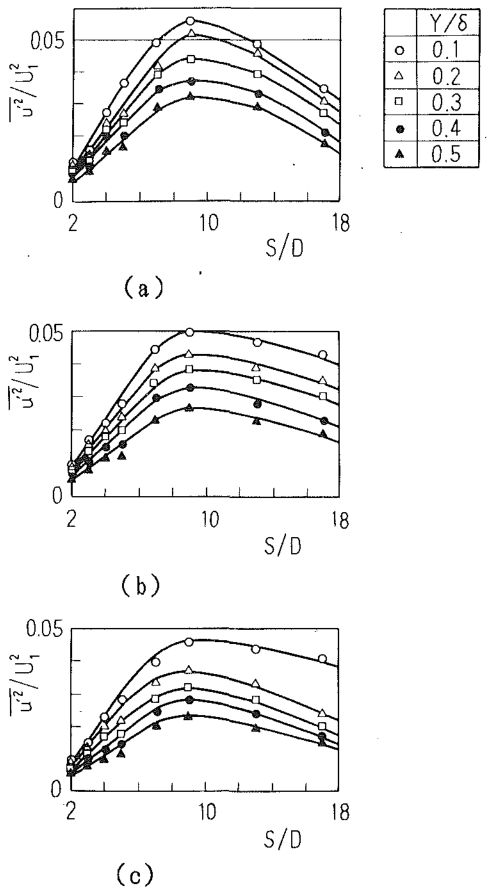

Fig. 11 Variation of *X*-component of turbulence intensity at groove center with *S/D* (*a*) *X/D* = 69, (*b*) *X/D* = 108; (*c*) *X/D* = 147 (Uncertainty in *S/D* = 0.10 and in $u'^2/U_1^2 = 0.0015$)

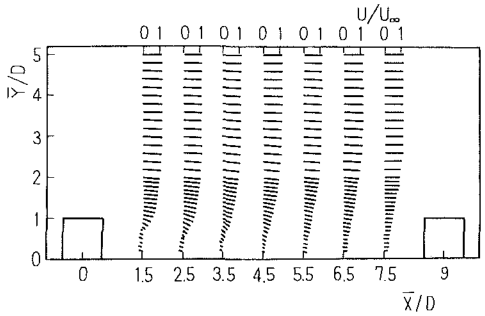

Fig. 12 Velocity vectors in flow above the groove for *S/D* = 9 (Uncertainty in $U/U_\infty = 0.06$ and $\overline{Y}/D = 0.10$ and in $\overline{X}/D = 0.10$)

3.3 Flow Pattern and Turbulent Eddies in the Groove. Figure 12 shows the air velocity vectors in the flow in the groove for the case of $S/D = 9$, where the velocity vectors were measured by using the three hole probe. It was found from this figure that there is back-flow in the region of $\overline{X}/D \leqq 4$ behind the upstream square ribs and favorable flow in the region of $4 \leqq \overline{X}/D \leqq 7.5$. Hence the free streamline leaving the edge of the upstream square rib encloses the recirculation region and reattaches to the ground plate at $\overline{X}/D \fallingdotseq 4$ as shown in Fig. 12.

The length of recirculation region, namely the distance from the rib center to the reattachment point, as a function of pitch ratio S/D is shown in Fig. 13. The reverse ratio is used as an abscissa in order to include the special case of a single rib. Other experimental results are also plotted for the sake of comparison. Mantle (1966) reported that the free streamline leaving the leading edge of a square rib does not reattach in the groove for the case of $S/D < 6.6$, and reattaches at $\overline{Xr}/D = 4$ for the case of $6.6 \leqq S/D \leqq 12$ and at $\overline{Xr}/D = 8.5$ for the case of infinite pitch ratio, namely, the case of single rib. Mori et al. (1985) showed $\overline{Xr}/D = 4.5$ for the case of $S/D = 15$. The results in Fig. 13 can be used as a correlation for finding the recirculation length in other figures. The present result ($\overline{X}/D = 4$) is consistent with the results by Mantle (1966) and Mori et al. (1985). Okamoto (1979) reported that the turbulence intensity is largest immediately behind the reattachment point in the shear flow behind a flat plate normal to a plane boundary and pointed out, that the same can be assumed to occur in the groove.

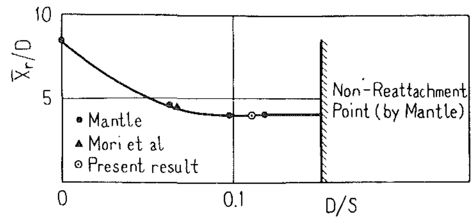

Fig. 13 Reattachment point (Uncertainty in $\overline{X}r/D = 0.10$ and in *D/S* = 0.04)

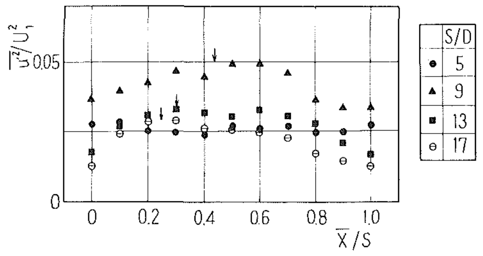

Fig. 14 *X*-component of turbulence intensity at *Y/δ* = 0.1 above groove Vertical arrow denotes the reattachment point, deduced from Fig. 13. (Uncertainty in $\overline{U'^2}U_1^2 = 0.0075$ and in *X/S* = 0.015)

As mentioned in Section 3.2, the turbulence intensity in the groove decays gradually with an increase in the downstream distance for the case of $S/D = 9$. Figure 14 shows that the variation of turbulence intensity at $Y/\delta = 0.1$, in the groove in the range $X/D = 116.5 \sim 133.5$, is a function of the pitch ratio S/D. The mark "↓" in this figure denotes the position of the reattachment point for the cases of $S/D = 17$, 13, and 9 taken from Fig. 13. The turbulence intensity has almost constant value in the groove for the case of $S/D = 5$. However, for the cases of $S/D = 9$, 13, and 17 the turbulence intensity attains a maximum near the reattachment point. For the case of $S/D = 5$, the recirculation region occupies the whole groove between the square ribs without reattachment. Hence the turbulence intensity becomes low as compared with those of $S/D = 9$, 13, and 17. On the other hand, for the case of $S/D > 5$, the flow over the ribs reattaches to the groove surface. The reattachment point corresponds to the position of the maximum turbulent intensity near the ground plane and is near the midpoint in the groove for the case of $S/D = 9$. Furthermore, for the cases of $S/D = 13$ and 17, the turbulence intensities decrease as compared with that for $S/D = 9$. The distance from the reattachment point to the next downstream square rib is longer for the cases of $S/D = 13$ and 17 than for $S/D = 9$. Hence the turbulence intensity is high over the whole groove zone $S/D = 9$, and larger for $S/D = 13$ than for $S/D = 17$.

The integral scale, which identifies the average scale of the large eddy, was obtained by integrating the auto-correlation function

$$L_x = U\int_0^\infty R_u(\tau)d\tau$$

where the convection velocity was estimated by the local time-

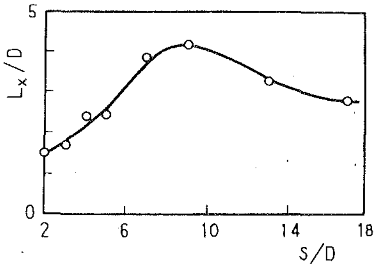

Fig. 15 Integral scale at $Y/D = 0.5$ above groove center (Uncertainty in $Lx/D = 0.23$ and in $S/D = 0.10$)

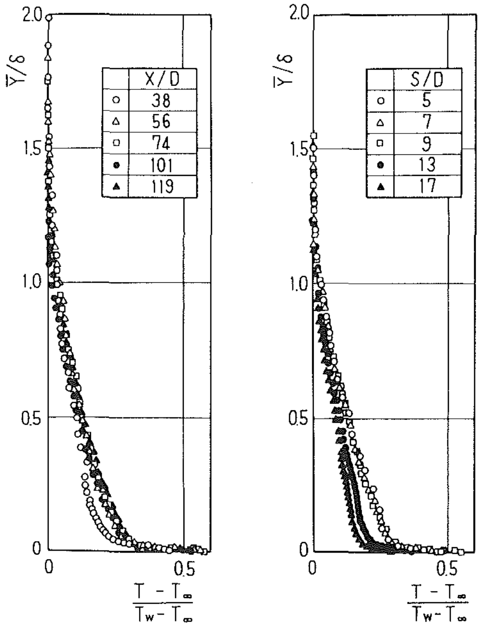

(a) (b)

Fig. 16 Temperature profiles at groove center (a) $S/D = 9$; (b) $X/D = 115$ (Uncertainty in $\overline{Y}/D = 0.12$ and in $(T - T_\infty)/(T_w - T_\infty) = 0.0102$)

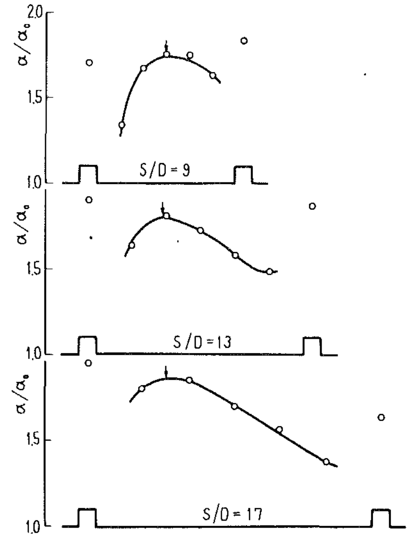

Fig. 17 Local heat transfer coefficient in groove for $S/D = 9$, 13, and 17 (↓: reattachment point, deduced from Fig. 13) (Uncertainty in $\alpha/\alpha_0 = 0.059$)

Table 1 Ratio of heat transfer coefficient

	S/D	$\alpha/\overline{\alpha}$
Present result	9	1.04
	13	1.03
	17	1.01
Hishida	5	1.00
	20	1.01
Berger and Hau	3	1.00
	5	1.05
	7	1.07
	10	1.08

mean velocity according to Taylor's hypothesis. Figure 15 shows the integral scale in the shear layer at $Y/D = 0.5$ above the midpoint in the groove. The integral scale becomes largest at $S/D = 9$, which means that the average scale of the large eddy is maximum, implying effective dispersion of hot air from the groove to the free stream. The integral scale becomes small for the case of $S/D < 5$ as predicted by Perry et al. (1969) who pointed out that the eddies shed from the roughness element into the flow will be negligible for a *d*-type rough wall.

3.4 Mean Temperature Profiles in Shear Layer Over Repeated Square Ribs and Heat Transfer Coefficient. Figure 16(*a*) shows the development of the temperature profiles with downstream distance. The distribution eventually becomes independent of X/D except in the region of small X/D behind the half-ogival forebody. Figure 16(*b*) shows the comparison of temperature profile near $X/D = 115$ for different values of S/D. The difference between temperature profiles for the various values of S/D occurs near the ground plane. This is due to the heated rib effects on the temperature profile at the groove center for the small value of S/D.

Figure 17 shows the distribution of local heat transfer coefficient in the groove between the two adjoining ribs for the cases of $S/D = 9$, 13, and 17. For all three cases, the distribution attains a maximum which is nearly coincident with the reattachment point of the separated streamline from the upstream rib. This indicates that high local heat transfer rate occurs around the reattachment point. The average heat transfer coefficient $\overline{\alpha}$ between the two ribs was compared with the local heat transfer coefficient at the groove center between the two adjoining ribs. Table 1 shows the ratio of the local heat transfer coefficient α at the groove center to the average heat transfer coefficient $\overline{\alpha}$ in the groove. The present result and the results of Hishida (1989) and Berger and Hau (1979) are shown in Table 1. It appears that the local heat transfer coefficient α at the groove center is close to the average heat transfer coefficient in the groove. This confirms the fact that it was reasonable to use the local heat transfer coefficient at the groove center in place of the average heat transfer coefficient in the groove in the comparison of the heat transfer coefficient for the value of S/D. Figure 18 shows the ratio of local heat transfer coefficient α at the groove center to the heat transfer coefficient α_0 at the smooth surface without ribs, which will be used to investigate the streamwise variation of the local heat transfer coefficient. The local heat transfer coefficient increases with downstream distance for all cases of S/D. When the repeated square ribs are used as a heat transfer promoter, it is important to find the optimum value of S/D between the two adjoining ribs. In order to find the optimum value, Figure 19 shows the variation of ratio α/α_0 with S/D near $X/D = 115$ and 135. It is found again that the value of α/α_0 attains a maximum near $S/D = 9$, which is hence the optimum value which augments the heat transfer coefficient.

3.5 Pressure Distribution in Shear Layer Over Repeated Square Ribs. When the repeated square ribs on the ground plane are utilized as the technique of augmenting heat transfer, the increased pressure loss due to the square ribs is an undesirable cost to be paid. The variation of pressure distribution in the shear layer with the pitch ratio S/D was investigated. Figure 20 shows the pressure distribution at $Y/D = 1.5$ above the groove center. The pressure is reduced with an increase in the downstream distance independently of S/D. It is found

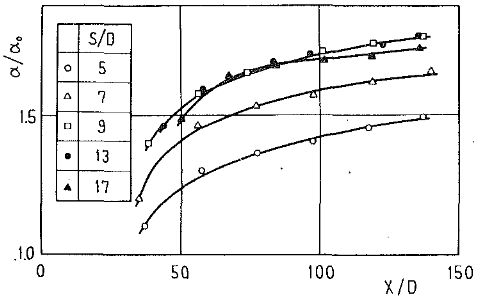

Fig. 18 **Local heat transfer coefficient at groove center (Uncertainty in $\alpha/\alpha_0 = 0.059$)**

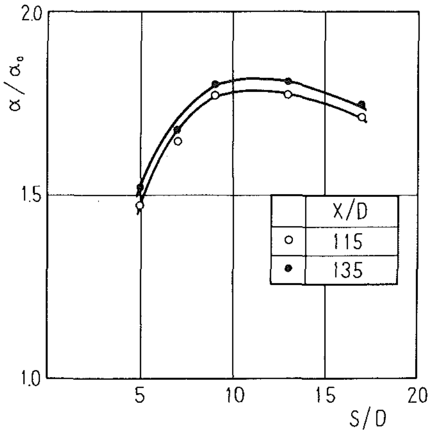

Fig. 19 **Local heat transfer coefficient near $X/D = 115$ and 135 (Uncertainty in $\alpha/\alpha_0 = 0.059$)**

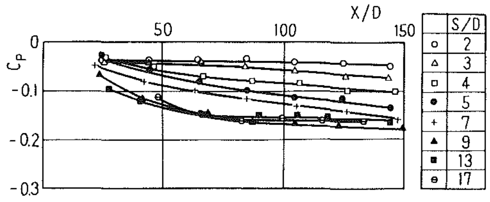

Fig. 20 **Pressure distribution at $Y/D = 1.5$ above groove center (Uncertainty in Cp = 0.0848)**

that the pressure decreases in the range of $S/D \leqq 9$ as the value of S/D increases, and the loss is larger at $S/D = 9$. Furthermore the pressure loss for $S/D = 13$ and 17 become slightly smaller than that for $S/D = 9$. Hence, when the optimum pitch ratio, $S/D = 9$ of the repeated square ribs is used as a promoter, the pressure loss is a maximum.

4 Conclusions

This paper presented the flow structure over the repeated two-dimensional square ribs, of side length D, placed at a pitch S on a ground plane to find the value of S/D which most augments the turbulence of the free stream and, hence the heat transfer. The results of the present study are summarized as follows:

(1) The thickness of the turbulent shear layer at a given value of X/D increases with S/D in the range of $2 \leqq S/D \leqq 9$, but is almost unchanged beyond $S/D = 9$. The velocity profiles, in the similar profile region above the last rib center and groove center, are concentrated as a whole in a narrow region close to the 1/3 power law profile.

(2) The profiles of turbulent intensity in the shear layer become self-preserving above both the ribs and grooves for the case of $S/D \leqq 5$. But for the case of $S/D = 9$, the turbulence intensity in the shear layer above the grooves falls with increasing downstream distance and does not achieve a self-preserving profile. In contrast, the profile becomes self-preserving in the shear layer above the ribs unlike the velocity profile at the same position.

(3) The pitch ratio $S/D = 9$ is optimum to augment the turbulence intensity and the heat transfer. A repeated two-dimensional square rib configuration with $S/D = 9$ is therefore recommended as a promoter.

(4) The free streamline leaving a rib corner reattaches to the ground plate at $\overline{X}/D \fallingdotseq 4$ for $S/D = 9$. The turbulence intensity is largest immediately downstream the reattachment point and decreases gradually to the next rib. Hence for the case of $S/D \leqq 5$, the turbulence intensity becomes relatively low due to non-reattachment. Moreover, the distance from the reattachement point to the next square rib is longer for $S/D = 13$ and 17 than for $S/D = 9$ so that the turbulence intensity decays in the flow downstream of the recirculation region.

(5) The average scale of the large eddy, deduced from the integral scale, is largest at $S/D = 9$. The integral scale becomes small for $S/D < 5$.

(6) When the optimum pitch ratio $S/D = 9$ of the repeated square ribs is used as the promoter, the pressure loss attains its maximum.

References

Antonia, R. A., and Luxton, R. E., 1971, "The Response of a Turbulent Boundary Layer to an Upstanding Step Change in Surface Roughness," ASME Vol. 93, pp. 22–34.

Berger, F. P., and Hau, K.-F., F.-L., 1979, "Local Mass/Heat Transfer Distribution on Surfaces Roughened With Small Square Ribs," International Journal of Heat Mass Transfer, Vol. 22, pp. 1645–1656.

Edwards, F. J., and Sheriff, N., 1961, "The Heat Transfer and Friction Characteristic for Forced Convection Air Flow over a Particular Type of Rough Surface," International Development in Heat Transfer, Part II, pp. 415–425.

Han, J. C., Glicksman, L. R., and Rohsenow, W. M., 1978, "An Investigation of Heat Transfer and Friction for Rib-Roughened Surfaces," *International Journal of Heat Mass Transfer*, Vol. 21, pp. 1143–1156.

Hijikata, K., Mori, Y., and Ishiguro, H., 1984, Turbulence Structure and Heat Transfer of Pipe Flow with Cascade Smooth Turbulence Surface Promoters," *Transactions of the JSME*, Vol. 50-458B, pp. 2555–2562.

Hishida, M., 1989, "Heat Transfer of Ribbed Surface," *Transactions of the JSME*, Vol. 55-518B, pp. 3166–3171.

Ichimiya, K., Yokoyama, M., and Shimomura, R., 1983, "Effects of Several Roughness Elements for the Heat Transfer from a Smooth Heated Wall," *Proceedings of ASME/JSME Thermal Engineering Joint Conference*, Vol. 1, pp. 359–364.

Mantle, P. L., 1966, "A New Type of Roughened Heat Transfer Surface Selected by Flow Visualization Techniques," *Proceedings of 3rd International Heat Transfer Conference*, Vol. 1, pp. 45–55.

Mori, Y., Hijikata, K., and Ishiguro, H., 1985, "Fundamental Study of Heat Transfer Augmentation by Smooth Turbulence Surface Promoters," *Transactions of the JSME*, Vol. 51-461B, pp. 160–168.

Nikuradse, J., 1933, "Stromüngsgesetze in Rauhen Rohren," VDI-Forschungsheft 361.

Nunner, W., 1956, "Wärmeübergang und Druckabfall in Rauhen Rohren," VDI-Forschungsheft 455, pp. 1–38.

Okamoto, S., 1979, "Shear Layer Behind Two-Dimensional Flat Plate Normal to Plane Boundary," *Theoretical and Applied Mechanics*, Vol. 27, pp. 563–570.

Osaka, H., Nakamura, I., and Kageyama, Y., 1984, "Time Averaged Quantities of a Turbulent Boundary Layer over a d-Type Rough Surface," *Transactions of the JSME*, Vol. 50-458B, pp. 2299–2306.

Perry, A. E., Schofield, W. H., and Joubert, P. N., 1969, "Rough Wall Turbulent Boundary Layers," *Journal of Fluid Mechanics*, Vol. 37-2, pp. 383–413.

Rao, C. K., and Picot, J. J. C., 1970, "The Effect of Turbulence Promoters on Heat and Momentum Transfer for Air Flow in an Annulus," *Proceedings of 4th International Heat Transfer Conference*, F.C.4.8., pp. 1–12.

Schlichting, H., 1936, "Experimentalle Untersuchung zum Rauhigkeitsproblem," *Ingenieur-Archiv*, Vol. 7, pp. 1–34.

Webb, R. L., Eckert, E. R. G., and Goldstein, R. J., 1971, "Heat Transfer and Friction in Tubes with Repeated-Rib Roughness," *International Journal of Heat Mass Transfer*, Vol. 14, pp. 601–617.

Turbulent Flow in Two-Inlet Channels

Hsiao C. Kao
NASA-Lewis Research Center,
Cleveland, OH 44135

The problem of turbulent flows in two-inlet channels has been studied numerically by solving the Reynolds-averaged Navier-Stokes equations with the $k-\epsilon$ *model in a mapped domain. Both the high Reynolds number and the low Reynolds number form were used for this purpose. In general, the former predicts a weaker and smaller recirculation zone than the latter. Comparisons with experimental data, when applicable, were also made. The bulk of the present computations used, however, the high Reynolds number form to correlate different geometries and inflow conditions with the flow properties after turning.*

Introduction

There is a fairly wide range of engineering applications involving branches and junctions, such as side inlets, slot injection, ejectors, etc., from which two streams merge. Merging of two streams is usually not a simple process and will incur losses in total pressure. The common mode of investigation is to conduct experiments to find the effect of geometry and flow conditions on the pressure losses. Consequently, measured pressure data are generally available, but "corresponding information on the underlying flow processes is extremely scarce," Ward-Smith (1980). In view of this situation, we propose to secure some of the information through numerical calculations. The geometry chosen is a two-dimensional, two inlet channel and the flow in it is assumed to be incompressible and turbulent.

A two-inlet channel flow often possesses the characteristics of both free and wall turbulent shear flow. The former takes place in the region where two streams meet and the latter near the surface. In the wall dominated region the flow is prone to separation. Thus, the objectives here are twofold: (1) to examine the geometry and the flow conditions that affect flow separation and (2) to see whether they can be changed to suppress it.

Transformation and Computational Domain

Geometry in Physical Plane. The geometry of a schematic two-inlet channel is shown in Fig. 1(*a*). It illustrates the following features. The width of the main channel before and after the branch channel need not be the same. If the width of the main channel upstream of the junction (referred to as the fore channel hereafter) plus the width of the branch channel is greater than the width of the main channel downstream of the junction (the aft channel), the flow undergoes a contraction and will usually accelerate after merging. This is somewhat equivalent to the flow in a convergent channel and is less prone to flow separation. The converse of this situation is approximately equivalent to the flow in a divergent channel and is very prone to flow separation. For this reason, these cases are not treated here.

The intermediate case, where the width of the fore channel plus the width of the branch channel equals the aft channel width, is of interest and will be considered. Attention will also be given to a special class of geometry in which the cross sections of the fore and aft channels are the same. This is of interest from the practical point of view since side inlets and injection slots resemble this geometry.

Other geometric characteristics are: The intersection angle

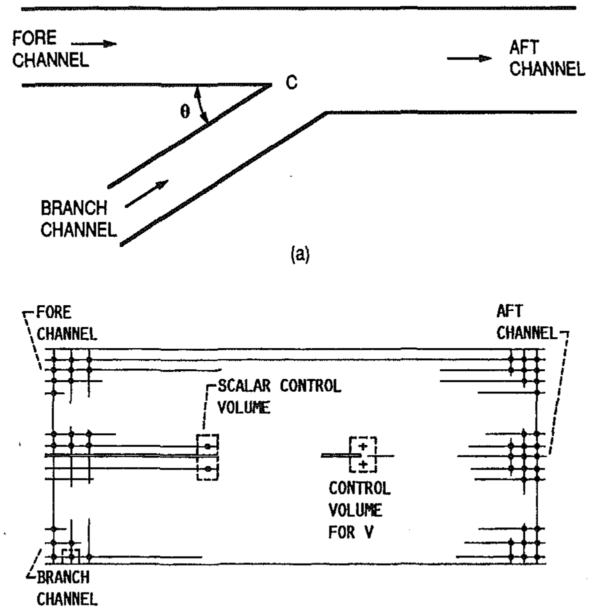

(a)

(b)

Fig. 1 Schematic depiction of computational domain, branch cut, and control volumes.

Contributed by the Fluid Engineering Division for publication in the JOURNAL OF FLUIDS ENGINEERING. Manuscript received by the Fluids Engineering Division May 20, 1992; revised manuscript received February 18, 1993. Associate Technical Editor: D. P. Telionis.

of the main and branch channel is acute, the lower surface of the branch channel usually merges with the lower surface of the main channel smoothly, but the junction is always sharp (point C in Fig. 1(*a*)).

Transformation and Computational Network. The computational grids comprise the streamlines and potential lines obtained by conformal mapping, which are boundary-conforming, orthogonal, and any number of grid points can be packed near the boundary and in the flow field. The computational domain is rectangular. A cut extending from the entrance to the junction divides the domain into an upper part, which maps into the fore channel, and a lower part into the branch channel. This is illustrated in Fig. 1 (*b*). The mapping used here is based on the Schwarz-Christoffel transformation. The basic procedure and equations can be found, for example, in Milne-Thomson (1968). Closed-form solutions can be obtained for special cases with θ equal to even fractions of π, but numerical procedures have to be used for arbitrary angles.

It is convenient to have an orthogonal grid next to the surface, since application of a wall function requires distances normal to the boundary. However, the main advantage of using stream and potential lines to form computational grids comes from the fact that the transformed velocity vectors even in a viscous flow are approximately aligned with the potential flow streamlines. This enables us to use staggered grids even when there is a large turning in the channel. If this is not done and velocity components are expressed in the physical space, a severe skewness in relation to the cell boundaries will result.

Governing Equations, Turbulence Modeling and Boundary Conditions

Governing Equations. The Reynolds-averaged conservation equations for mass and momenta in an incompressible two-dimensional turbulence flow are

$$\frac{\partial}{\partial\phi}(hU)+\frac{\partial}{\partial\psi}(hV)=0 \tag{1}$$

$$\begin{aligned}\frac{\partial}{\partial\phi}(\rho hU^2)+\frac{\partial}{\partial\psi}(\rho hUV)+\rho UV\frac{\partial h}{\partial\psi}-\rho V^2\frac{\partial h}{\partial\phi}&=-h\frac{\partial P}{\partial\phi}\\ +2\frac{\partial}{\partial\phi}\left[\mu\left(\frac{\partial U}{\partial\phi}+\frac{V}{h}\frac{\partial h}{\partial\psi}\right)\right]&+\frac{\partial}{\partial\psi}\left\{\mu h\left[\frac{\partial}{\partial\phi}\left(\frac{V}{h}\right)+\frac{\partial}{\partial\psi}\left(\frac{U}{h}\right)\right]\right\}\\ +\mu\left[\frac{\partial}{\partial\phi}\left(\frac{V}{h}\right)+\frac{\partial}{\partial\psi}\left(\frac{U}{h}\right)\right]\frac{\partial h}{\partial\psi}&-2\frac{\mu}{h}\times\left(\frac{\partial V}{\partial\psi}+\frac{U}{h}\frac{\partial h}{\partial\phi}\right)\frac{\partial h}{\partial\phi}\\ -\frac{\partial}{\partial\phi}\left(\rho h\overline{u^2}\right)-\frac{\partial}{\partial\psi}(\rho h\overline{uv})&-\rho\overline{uv}\frac{\partial h}{\partial\psi}+\rho\overline{v^2}\frac{\partial h}{\partial\phi}\end{aligned} \tag{2}$$

$$\begin{aligned}\frac{\partial}{\partial\phi}(\rho hUV)+\frac{\partial}{\partial\psi}(\rho hV^2)+\rho UV\frac{\partial h}{\partial\phi}-\rho U^2\frac{\partial h}{\partial\psi}&\\ =-h\frac{\partial P}{\partial\psi}+\frac{\partial}{\partial\phi}\left\{\mu h\left[\frac{\partial}{\partial\phi}\left(\frac{V}{h}\right)+\frac{\partial}{\partial\psi}\left(\frac{U}{h}\right)\right]\right\}&\\ +2\frac{\partial}{\partial\psi}\left[\mu\left(\frac{\partial V}{\partial\psi}+\frac{U}{h}\frac{\partial h}{\partial\phi}\right)\right]+\mu\left[\frac{\partial}{\partial\phi}\left(\frac{V}{h}\right)+\frac{\partial}{\partial\psi}\left(\frac{U}{h}\right)\right]\frac{\partial h}{\partial\phi}&\\ -2\frac{\mu}{h}\left(\frac{\partial U}{\partial\phi}+\frac{V}{h}\frac{\partial h}{\partial\psi}\right)\frac{\partial h}{\partial\psi}-\frac{\partial}{\partial\phi}(\rho h\overline{uv})-\frac{\partial}{\partial\psi}\left(\rho h\,\overline{v^2}\right)&\\ -\rho\overline{uv}\frac{\partial h}{\partial\phi}+\rho\overline{u^2}\frac{\partial h}{\partial\psi}&\end{aligned} \tag{3}$$

where ϕ and ψ are the dimensionless potential and stream functions, and h is the metric coefficient. The symbol μ is the coefficient of molecular viscosity and is assumed to be a constant. The symbols U, V, and P are the time-averaged velocity components in the potential and stream line directions and pressure. The quantities with overscores are the turbulence stresses.

Turbulence Modeling. The momentum equations contain turbulence stress terms, which have to be modeled. On the basis of Boussinesq's assumption, we have

$$\begin{aligned}-\rho h\overline{u_iu_j}=-\left[\frac{2}{3}\rho hk-\frac{\mu_t}{h}\left(U_i\frac{\partial h}{\partial\xi_i}+U_j\frac{\partial h}{\partial\xi_j}\right]\right)\delta_{ij}&\\ +\mu_t h\left[\frac{\partial}{\partial\xi_j}\left(\frac{U_i}{h}\right)+\frac{\partial}{\partial\xi_i}\left(\frac{U_j}{h}\right)\right]&\end{aligned} \tag{4}$$

where U_i, u_i and U_j, u_j are the average and fluctuating velocity components in the directions of ξ_i and ξ_j, and δ_{ij} is the Kronecker delta. They are related to the symbols in Eqs. (1) to (3) as follows

$$U_1=U,\ U_2=V,\ u_1=u,\ u_2=v,\ \xi_1=\phi,\ \xi_2=\psi$$

To close the system we choose the $k-\epsilon$ model and define

$$\mu_t=c_\mu f_\mu\rho\frac{k^2}{\epsilon} \tag{5}$$

where ϵ is the dissipation rate of the turbulence, c_μ an empirical constant, and f_μ equals unity in the high Reynolds number form and is a function of turbulence Reynolds numbers in the low Reynolds number form. The quantities k and ϵ are to be calculated according to the following two simplified equations

Nomenclature

C_f = skin friction coefficient, $\frac{\tau_w}{1/2\rho\overline{V}_e^2}$
H = channel width, $H_a=0.18$ m nominally
k = turbulence kinetic energy, $\left(\frac{\overline{u^2}+\overline{u^2}+\overline{w^2}}{2}\right)$
k^+ = $\frac{k}{V_\tau^2}$
T = turbulence intensity, $\frac{k}{\overline{V}^2}$
U,V = mean velocity components in ϕ and ψ directions
$\overline{V}$ = cross-sectionally averaged value of V
$\overline{V}_e$ = $\overline{V}$ at exit
V_τ = friction velocity, $\left(\frac{\tau_w}{\rho}\right)^{1/2}$
u,v = velocity fluctuations in ϕ and ψ directions
y_w = distance normal to wall
y^+ = wall coordinate, $\frac{\rho V_\tau y_w}{\mu}$
ϵ^+ = $\frac{\mu\epsilon}{\rho V_\tau^4}$
μ = dynamic viscosity, 1.824×10^{-5} kg/m
μ_t = eddy viscosity
ρ = density, 1.177 kg/m^3
τ_w = wall shear stress

Subscripts

a, b, f = aft, branch and fore channels

$$\frac{1}{h^2}\frac{\partial}{\partial\phi}(\rho Uhk)+\frac{1}{h^2}\frac{\partial}{\partial\psi}(\rho Vhk)=\rho G-\rho\epsilon$$
$$+\frac{1}{h^2}\frac{\partial}{\partial\phi}\left[\left(\mu+\frac{\mu_t}{\sigma_k}\right)\frac{\partial k}{\partial\phi}\right]+\frac{1}{h^2}\frac{\partial}{\partial\psi}\left[\left(\mu+\frac{\mu_t}{\sigma_k}\right)\frac{\partial k}{\partial\psi}\right] \quad (6)$$

$$\frac{1}{h^2}\frac{\partial}{\partial\phi}(\rho Uh\epsilon)+\frac{1}{h^2}\frac{\partial}{\partial\psi}(\rho Vh\epsilon)=f_1c_{1\epsilon}\rho\frac{\epsilon}{k}G$$
$$-f_2c_{2\epsilon}\rho\frac{\epsilon^2}{k}+\frac{1}{h^2}\frac{\partial}{\partial\phi}\left[\left(\mu+\frac{\mu_t}{\sigma_\epsilon}\right)\frac{\partial\epsilon}{\partial\phi}\right]$$
$$+\frac{1}{h^2}\frac{\partial}{\partial\psi}\left[\left(\mu+\frac{\mu_t}{\sigma_\epsilon}\right)\frac{\partial\epsilon}{\partial\psi}\right] \quad (7)$$

in which G is the production rate of the turbulence kinetic energy and is given by

$$\rho G=-\rho\sum_{i,j}^{2}\overline{u_iu_j}T_{ij}=2\frac{\mu_t}{h^2}\left(\frac{\partial U}{\partial\phi}+\frac{V}{h}\frac{\partial h}{\partial\psi}\right)^2$$
$$+\mu_t\left[\frac{\partial}{\partial\psi}\left(\frac{U}{h}\right)+\frac{\partial}{\partial\phi}\left(\frac{V}{h}\right)\right]^2+2\frac{\mu_t}{h^2}\left(\frac{\partial V}{\partial\psi}+\frac{U}{h}\frac{\partial h}{\partial\phi}\right)^2 \quad (8)$$

There are a number of empirical constants in these equations, which are given as $c_\mu=0.09$, $c_{1\epsilon}=1.44$, $c_{2\epsilon}=1.92$, $\delta_k=1.0$, and $\delta_\epsilon=1.217$. In addition, f_1 and f_2 are equal to unity for the HRN (high Reynolds number) form, and become two functions of turbulence Reynolds numbers for the LRN (low Reynolds number) form. This two-equation model with standard constants has been used widely for practical problems, and is known to give better results for internal flows with confined walls than for external flows (Rodi, 1981 and Simpson, 1987).

Most calculations in this report were carried out by applying the HRN model along with Chieng and Launder's (1980) wall function. A selected number of reference cases was, however, computed by both the HRN form and the LRN form of the $k-\epsilon$ model. For the latter Lam and Bremhorst's (1981) formulation is used. A brief description of these two forms are given below.

Wall Function and Its Extension. The HRL form of the $k-\epsilon$ model is invalid near the surface; a wall function is needed to join the wall region to the turbulent flow outside. The type of the wall function used here is the Chieng and Launder formulation together with Johnson and Launder's (1982) modification. Since details are available in these references, they will not be repeated here.

In applying the wall function to calculations of shock-wave boundary-layer interactions with flow separation, Viegas, Rubesin, and Horstman (1985) observed that one could actually get a better agreement with experimental data by using an extended Chieng-Launder wall function than the LRN form of the Jones-Launder k-ϵ model. For this reason, an attempt is made here to incorporate this extension in the present computation.

Low Reynolds's Number $k-\epsilon$ Model. As mentioned earlier, the LRN form used here is the Lam-Bremhorst type. Hence, the functions f_μ, f_1, and f_2 in Eqs. (5) and (7) are essentially Lam-Bremhorst's expressions modified slightly for the transformed coordinates. The function f_1 becomes, however, singular at the surface. Thus some measure has to be taken to avoid this difficulty.

Schmidt and Patankar (1988) suggest to add a small constant, say 10^{-10}, to the quantities in the formula, so that they will not become too large or too small near the surface. This method was tried in the present calculation, but it appears that the calculated results may differ, depending on the size of this small constant. An alternative method is, therefore, proposed to put some restrictions on μ_t to prevent it from becoming extremely small near the surface by specifying

$$\mu_t=\mu_t+\frac{\delta}{5}, \text{ if } \mu_t<\delta$$

where δ is a small quantity in the range of 10^{-7} to 10^{-15}. The criterion of choosing δ is through a trail-and-error procedure, so that μ_t increases almost smoothly from the surface to the outer layer. In this manner, the original formulas given by Lam and Bremhorst can be used directly. The shortcoming is, of course, that δ is not a fixed number and has to be determined for every case.

Inflow and Outflow Conditions. The procedure of acquiring boundary conditions at entrances is first to make a calculation in a straight channel of constant width by solving Eqs. (1) to (8), and then to employ the exit quantities from this calculation as inflow conditions for the present problem. In this manner, the upstream length in a computational domain can be reduced. To solve this simplified problem of a straight channel, both inflow and outflow conditions are still needed. The inflow conditions are based on the digitized value of Smyth's measurements (1979) upstream of the expansion. The missing quantity ϵ is obtained by the empirical formula.

$$\epsilon=\frac{c_\mu^{3/4}k^{3/2}}{\ell_m}$$

with the mixing length ℓ_m given by Nikuradse's formula.

The outflow conditions are the usual assumption of zero streamwise gradients at exit. Although the channel length is normally chosen sufficiently long to establish a nearly fully developed state for mean quantities, turbulence structure in the core region may still undergo changes, especially when Smyth's measurements for k are scaled down to a reduced level.

We now return to the problem of two-inlet channel. Although the approaching velocity can be of any magnitude at the entrance, we generally assume that velocities in the branch channel are higher than that in the main channel to simulate approximately the various engineering applications. In addition, it may resemble the outflow of a half-jet.

Inflow conditions once prescribed will remain unchanged throughout iteration cycles. A question may then be raised about the upstream influence of the junction. This may not be serious for the following two reasons: (*a*) from Smyth's measurements it is seen that no step influence is detectable even at a station one-fifth of the duct height upstream of the step; (*b*) Bramley and Dennis's (1982) eigenvalue analysis shows that a perturbation from the Poiseuille flow in a straight channel decays much faster in the upstream direction than in the downstream direction.

Finally, outflow conditions for the aft channel are prescribed in the same manner as for a straight channel. The streamwise velocity components are, however, adjusted after every iteration to ensure that the total flux is conserved.

Discretization and Numerical Computation

Discretization of Governing Equations. As seen, the solution domain in Fig. 1(*b*) contains a branch cut. This is the boundary between the fore and branch channel and represents a solid surface on each side of the cut. Thus we have to place the control volumes accordingly, especially since a staggered grid for velocity components is used. At the extremity of this line, which represents the intersecting point of the fore and branch channel walls, a problem arises concerning the relative position of the control volumes. The layout which we adapted is depicted in an insert in Fig. 1(*b*). In this arrangement the last scalar control volume on either side of this cut has a solid

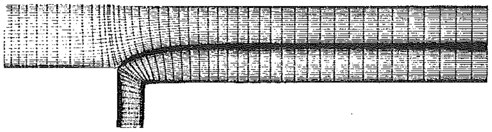

Fig. 2 Grid layouts. Case 3b, Table 1

boundary, but the last V control volume has a cell surface comprised of both solid and open boundaries. The error caused by these partially open cells will probably be limited to a local region, owing to small grid spacing there.

With the control volume and the staggered grid defined, the governing differential equations can now be discretized. We use the quadratic upwind scheme of Leonard (1979) (QUICK) for the two momentum equations, and the hybrid scheme of Spalding for the k and ϵ equations. This choice stems mainly from the fact that the primary concern here is with the mean quantities and not with the turbulence structure.

Grid Distribution. A representative case of the grid distribution for a routine computation using the high Reynolds number form is shown in Fig. 2. There are 50×60 grid points in the channel with its aft channel length equal to approximately six times the width (for the purpose of illustration the length has been truncated). For the computation using the low Reynolds number form, the grid distribution has to be modified, so that a sufficient number of points will be in the viscous sublayer $y^+ \leq 10$. However, since the application of the LRN form in the present study is confined to the lower surface where flow separation occurs and the validity of a wall function becomes questionable, only a moderate increase of grid points is called for.

Solution Procedure, Boundary Conditions, and Accuracy. There are five equations for five dependent variables (the continuity equation is converted into a pressure-correction equation through the SIMPLE method of Patankar and Spalding), which are to be solved iteratively in a sequential manner, proceeding from V to U, P, k, and ϵ. The cycle is repeated as necessary until the convergence criteria are met. The residuals of the continuity and two momentum equations in their finite difference forms summed over the entire solution domain divided by the inflow flux and momentum are the gauges for convergence. Iterations usually terminate if all three values are less than 0.005. (For reference cases this number is generally reduced by a factor of 5.) In each iteration cycle, we always use underrelaxation to stabilize the computation. The underrelaxation factors are, however, different for different variables.

Since the quadratic upwind discretization is used for the U and V components, each control volume requires two grid points outside each cell face. Thus, if the solution domain covers the entire space, it will be necessary to supplement these components by extrapolation. To avoid this difficulty, we restrict the quadratic interpolation in a region excluding all grid points nearest to a solid wall, and then apply the hybrid method at these rows and columns. The solutions to the discretized momentum equations are obtained by the line-sweeping pentadiagonal matrix algorithm alternative in both directions, whereas the solution to the other three equations are obtained by a tridiagonal algorithm, line-sweeping from the upstream to downstream and in one direction only.

In the HRN form, the boundary conditions for V, k and ϵ are imposed through the wall function. In the LRN form, integration is carried out directly to the surface, boundary conditions for U, V, and k are the no-slip condition and $k=0$ at the wall. The boundary condition for ϵ is zero gradient at the wall in the normal direction $\partial\epsilon/\partial n = 0$.

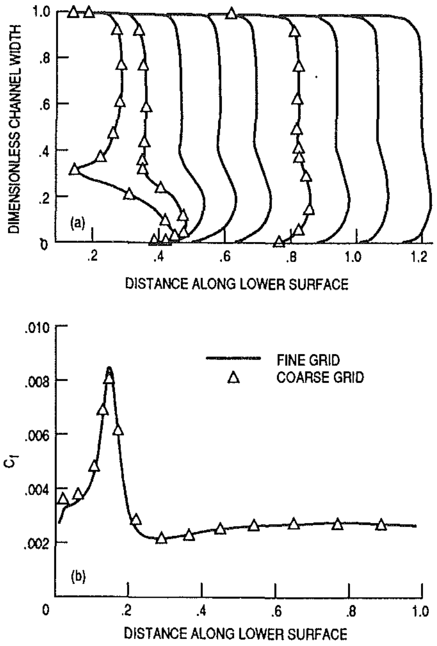

Fig. 3 Grid refinement study. (*a*) Dimensionless mean velocities, (*b*) skin friction coefficient. (See the text for the explanation of velocity profiles in (*a*)).

We next discuss the problem of numerical accuracy related to grid spacing by comparing the results from a coarse grid against those from a fine grid. The coarse grid has 45×52 points, which is somewhat coarser than that for a routine calculation, whereas the finer grid comprises 64×96 points with a nearly uniform increase in the transverse direction from 52 points to 96 and a local increase in the streamwise direction in the junction area.

These results based on the HRN form are shown in Fig. 3. However, in order to read Fig. 3(*a*) a few remarks are in the order. The distance along the channel lower surface is the actual length measured in meters, the channel width is dimensionless and greatly magnified, and the staggered profiles are V components made dimensionless by referring to $4\bar{V}e$ and displaced according to the position of a station. The first profile is taken at a station immediately downstream of point C (Fig. 1(*a*)) and is approximately 0.14 m from the branch entrance. It has a "cusp," which is the low velocity region caused by merging of two boundary layers, whose magnitude equals approximately 5 percent of the peak velocity. Below the cusp is a high velocity region near the wall formed by the high speed stream from the branch channel. This cusp diminishes quickly and becomes a small depression in the profile throughout, which suggests that the flow never reaches a truly fully developed stage in a length equal to approximately six times the channel width.

In order to put these results to a further test, we select a more sensitive quantity than the mean velocity in Fig. 3(*b*) to show the difference. Again the difference is seen to be fairly small. These comparisons seem to assure us that the grid used in a routine computation, which is always somewhat finer than 45×52, is adequate and the solutions obtained are reasonably grid-independent. Finally we observe that the flow is attached everywhere. This is the result of an area contraction and small difference in incoming velocities.

Results and Discussion

It is possible to enumerate a number of parameters that exert some influence on the flow development in a two-inlet channel. Some of these parameters are

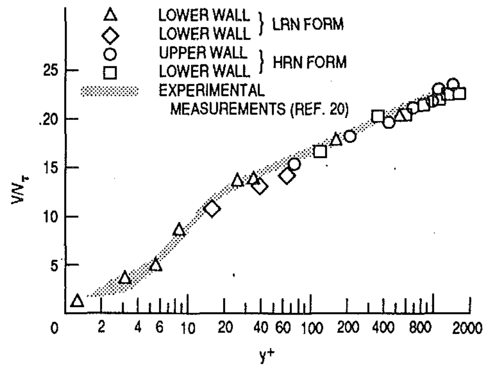

Fig. 4 Comparisons of experimental and computational data for mean streamwise velocities (case 1a, Table 1; see the text for the explanation of diamond symbols)

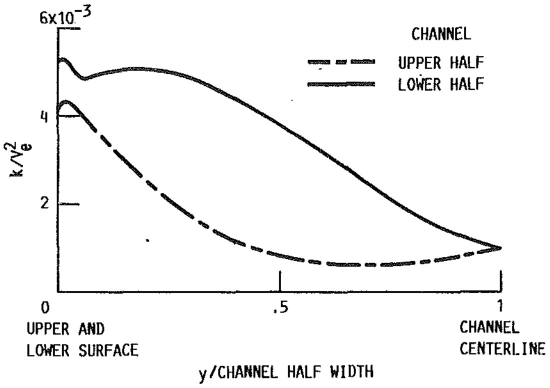

Fig. 5 Turbulence intensity profile in a cross section near exit (case 1a, Table 1)

$$R_a=\frac{H_f+H_b}{H_a},\ R_u=\frac{\overline{V}_b}{\overline{V}_f},\ T_b=\frac{k_b}{\overline{V}_b^2},\ T_f=\frac{k_f}{\overline{V}_f^2},$$

$$Re_b=\frac{\rho\overline{V}_bH_b}{\mu},\ \mathrm{Re}_f=\frac{\rho\overline{V}_fH_f}{\mu},\ \theta,\ S_c=\frac{H_a}{r_c},\qquad(9)$$

where H, $\overline{V}$, μ, and r_c denote, respectively, the height of the channel, cross-sectionally avergered mean streamwise velocity, dynamic viscosity and the smallest radius of curvature at the turning point of the lower surface. The symbol k refers to the minimum value of the turbulent kinetic energy in the core region at the entrance. The subscripts b and f refer to the branch and fore channel at entrance, and a to the aft channel at exit.

The parameter R_a signifies the area variation of a channel. For instance, if $R_a=1.0$, the total area is constant, and if $R_a > 1.0$, it is a convergent-like channel. The parameter R_u is the velocity ratio of two incoming streams and is a dominant factor for the flow development. The symbols T_b and T_f denote the turbulence intensities at the entrance of the branch and fore channel, respectively. They also affect the flow development but play a less important role than others. Re_b and Re_f are the corresponding Reynolds numbers. The notation θ refers to the angle subtended at the junction by the centerlines of the fore and branch channel, and S_c is the sharpness ratio at the turning point of the lower surface. Both of these are dominant parameters.

In addition to the above quantities, there is one more parameter, which has a controlling effect on flow separation. This is the area ratio of the branch channel to the fore channel. A large ratio is found to facilitate flow separation. This parameter is, however, not included in the present study.

Following the numerical procedure indicated above, we carried out various computations with different combinations of these parameters. Some of these obtained results will be presented and discussed later. For the time being we focus mainly on comparisons of computation with experiment to give some credibility to the present method. A direct comparison is not feasible at present for lack of experimental data. There exists, however, a fairly large volume of test data for fully developed turbulent channel flows, which can be used for comparison with calculated results near the channel exit.

Comparison With Measurements Based on the observation that velocity profiles near the exit remain virtually unchanged, it is assumed that the flow is nominally fully developed and can be compared with experimental data (Hussian and Reynolds, 1975, e.g.). To do this we have to supplement the HRN computation by the LRN computation, so that there are enough computational data points in the viscous sublayer. A standard example is selected for this purpose, and comparisons are illustrated in Figs. 4 and 6. We first discuss Fig. 4. There are two groups of data points in this figure. One is from the HRN form, the other from the LRN form, and an overlap region where there are points from both groups. In addition, these data points are taken randomly from different streamwise stations near the exit.

In order to see how fast the flow can regain the nominally fully developed state after turning, we choose a station approximately three channel widths downstream from the junction and plot its mean velocities. These are the three diamond symbols in Fig. 4 located slightly below the experimental curve. The discrepancy at $y^+ \simeq 80$ is quite noticeable, but decreases gradually, and become unrecognizable below $y^+=10$ (not shown). This trend of merging computations to experiment in the wall region suggest that even though the flow in the core region may still be changing, that in the wall region is near the state of full development.

Thus far only mean quantities have been compared. We now bring in two figures to describe turbulence quantities. In Fig. 5, where turbulence kinetic energies are plotted, we see a large difference in intensity between the upper and lower portion of the channel, which is an indication that the flow is still in a state of transition. This finding seems to correlate well with experimental results, since it is known Kobata et al. (1983); Ward-Smith (1980) that it requires much longer distance for turbulence structure to attain a fully developed state than for mean quantities. In the present case, the large disturbance in turbulence structure takes place mainly in the shear layer where two streams merge, resulting in a high rate of production. An aggregate of this fluid is then convected downstream to form a hump in the profile in the lower portion in contrast to the upper one, which is in a more or less fully developed state.

In Fig. 6 the dimensionless k^+ and ϵ^+ are plotted and compared to the composite test data in Patel et al., 1985. These data points are mostly the counterparts of Fig. 4. The fact that they all fall into the shaded area of test data seems to suggest that the turbulence structure wherever in wall regions is nearly fully developed.

Comparisons of Different Forms of $k-\epsilon$ Model. As stated previously, computations for some reference cases have been carried out by employing both the HRN and LRN forms. For the former we experimented with two slightly different types of wall function: the Chieng-Launder wall function and its extended form proposed by Viegas et al. To solve the problem, we still employ the basic formulation of the HRN form along with the Chieng-Launder wall function everywhere, except along the lower surface where these variations are applied. Thus, for the purpose of comparison the relevant quantities are the calculated results along the lower surface.

Plotted in Fig. 7(*a*) are the mean velocity profiles obtained by these different representations, which shows practically no difference between two types of wall function and some differences between the HRN form and LRN form. In order to read this figure, the remarks made previously for Fig. 3(*a*) are still valid, except that the station where the first velocity profile is taken is now quite far from the junction and there is a fairly large recirculation zone over the lower surface, whose magnitude equals approximately 25 percent of the peak velocity found in the area where two streams merge. This recirculation zone terminates in an area between the second and third profile. Notice that all profiles become, however, fairly symmetric near the exit. In fact, they are more symmetric than the attached flow in Fig. 3(*a*). This seemingly incongruity seen here and elsewhere may be explained by arguing that the presence of a flow separation promotes mixing and, therefore, facilitates the transformation to a fully developed state.

Next we consider the variation of skin friction along the lower surface in Fig. 7(*b*). A quick look at this figure shows a considerable disparity between these two forms, especially in the flow separation region and shortly after reattachment. Such differences are perhaps not unexpected, since it is often said that the wall function treatment is invalid in this region. Furthermore, it does not appear that the extended form proposed by Viegas et al. showed any appreciable improvement, in contrast to their finding with the shock boundary layer interaction problem. Finally our experience with this problem seems to show that if the turbulence near the surface is not in a local equilibrium, calculated skin friction based on the HRN and LRN forms will differe, even if the flow is attached everywhere (Fig. 11).

Effects of Parameters on Flow Properties. In the above, only a few selected examples were solved but more stringent convergence criteria were used with the hope that more meaningful comparisons with experiments and each other may be had. In the following, our attention is shifted to conducting calculations by using the HRN form alone and with less stringent criteria but for a large number of cases with diverse parameters and their combinations, so that a cross-examination can be made to uncover their influence on flow properties after turning. Some of the outcomes are summarized in Table 1.

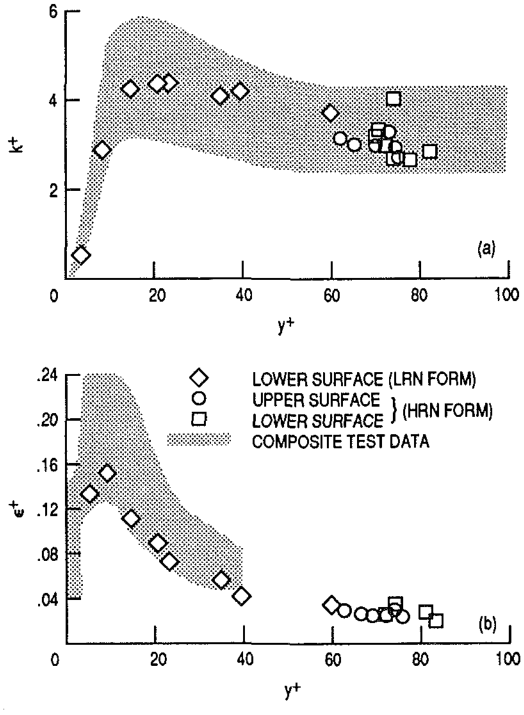

Fig. 6 Comparison of experimental and computational data (case 1a, Table 1). (*a*) Turbulence kinetic energy, (*b*) dissipation rate.

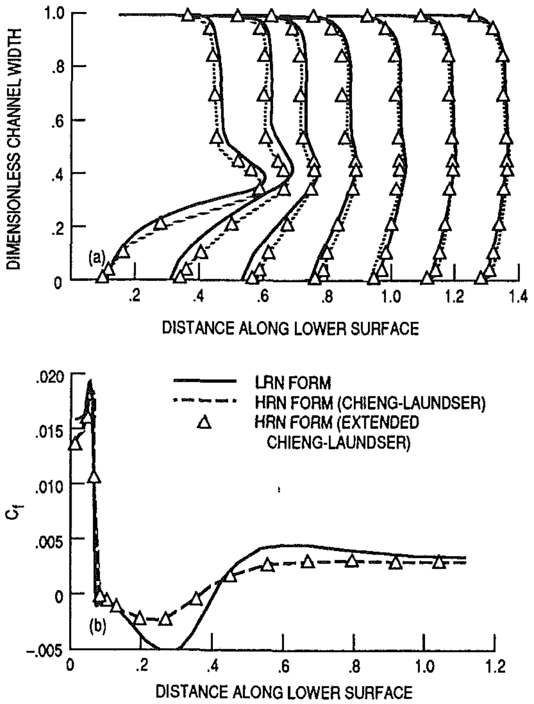

Fig. 7 Comparisons among different representations (case 1b, Table 1). (*a*) Dimensionless mean velocity $(\overline{V}/\overline{V}_e)$ (*b*) skin friction coefficient.

Table 1

Case	Parameter to be changed	Effect on flow	Attached flow (*a*)	Separated flow (*b*)	Graphical representation
1	R_u	Large	$R_u=2.0$	$R_u=3.0$	Fig. 9
2	T_b, T_f	Small	$T_b=2.22\times10^{-3}$ $T_f=2.18\times10^{-3}$	$T_b=1.30\times10^{-3}\sim0.36\times10^{-3}$ $T_f=2.18\times10^{-3}\sim0.36\times10^{-3}$	None
3	S_c	Large	$S_c=15.15$	$S_c=41.15$	Figs. 2, 10
4	R_a	Large	$R_a=1.0$	$R_a=1.33$	Fig. 9
5	θ	Large	$\theta=75$ deg	$\theta=90$ deg	Fig. 11

Notes:
1 $R_a=1.0$, $T_b=2.22\times10^{-3}$, $T_f=2.18\times10^{-3}$, $\mathrm{Re}_b=2.32\times10^5$, $\mathrm{Re}_f=6.28\times10^5$, $S_c=8.77$; (*a*) $R_u=2.0$ ($\overline{V}_b=128.6$m/s, $\overline{V}_f=64.3$ m/s), (*b*) $R_u=3.0$ ($\overline{V}_b=128.6$ m/s, $\overline{V}=42.8$ m/s).
2 $R_u=2.0$, $R_a=1.0$, $S_c=8.77$;
3 $R_u=2.0$, (*a*) $R_a=1.21$, (*b*)$=1.18$;
4 $R_u=3.0$, (*a*) $S_c=8.77$, (*b*) $S_c=4.05$;
5 $R_u=3.0$, $R_a\simeq1.0$.

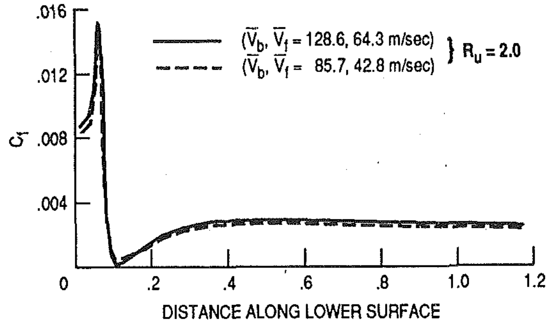

Fig. 8 Flow with same R_u ratio

Fig. 9 Mean velocity profiles for $R_u = 3.0$ (case 1b, Table 1)

There are five cases listed in this table. Each case except number 2 describes the effect of changing one single parameter with the remaining ones nominally fixed. In addition, each case is accompanied by a note, whose purpose is to furnish information on some pertinent parameters. Note 1 is an exception, which lists every parameter involved. In every case, except 5, $\theta = 90$ deg.

Since some of these parameters, which are the ratios of two physical quantities, do not appear explicitly in the governing equations or boundary conditions, it is perhaps appropriate to demonstrate, at least for one case, that the relevant factor is the ratio not the individual quantities. The example chosen here is Case 1 in Table 1. However, instead of increasing R_u to 3.0, we repeat the calculation by fixing R_u and reducing each velocity by half with other parameters unchanged. The results of these two calculations are compared in Fig. 8. Note that mean velocities are not plotted, since the difference is too small to be discerned.

The purpose of Case 1 is to show the effect of the velocity ratio on the flow properties. When the velocity ratio is equal to 2.0, no flow separation is observed. If this ratio is increased to 3.0, a large zone of back flows appears. The recovery from the flow separation in this case is, however, relatively quick at least as far as mean quantities are concerned. This can be seen from the plot (Fig. 9), where the mean velocity profile nearly regains a fully developed mode in a relatively short distance. This property of a quick recovery appears to be a characteristic of a constant-area channel ($R_a = 1.0$). If $R_a > 1.0$, this is no longer true and will be discussed later.

The object of Case 2 is to see whether a variation of turbulence level in the branch channel makes a difference in flow properties in the aft channel. The findings indicate that a low turbulence level T_b in the core region facilitates flow separation after turning. For instance, the flow is attached for the combination given in (*a*) and show a very small separation in (*b*). However, this is not a dominant factor; other factors are far more important.

All parameters in Case 3 are nearly identical, except the sharpness ratio S_c (see Fig. 2 for the geometry of Fig. 10(*b*). To appreciate visually the difference in two conditions, we plot the mean velocities in Fig. 10, to show what a sharp corner can do to the flow after turning. Note that the velocity profiles in both cases at exit are rather skewed. This is apparently a common characteristic for convergent-like channels with $R_a > 1.0$. In fact, even for two streams with two equal inflow velocities, considerable skewness still exists at the exit.

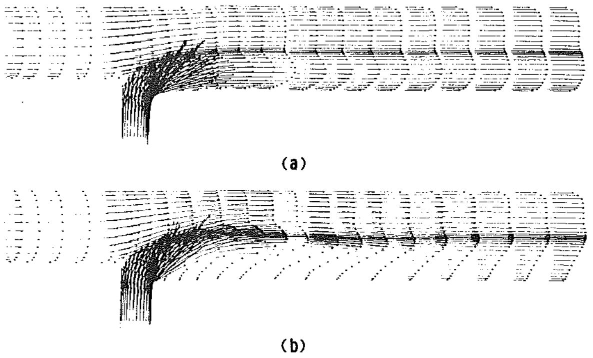

Fig. 10 Mean velocity profiles. (*a*) Case 3a, Table 1, (*b*) Case 3b, Table 1 (channel length used in computation was longer than that in Fig. 2).

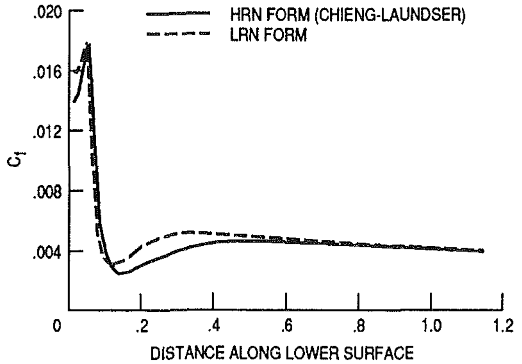

Fig. 11 Two-inlet channel flow with $\theta = 75$ deg, $R_u = 3.0$

Two computer runs in Case 4 were made with essentially identical inflow conditions but different channel area ratios. (Through S_c in two cases are not exactly the same, it is not critical, since a further flattening of a smooth corner does not usually have much of an impact.) A velocity ratio of 3.0 with $R_a = 1.0$ causes a massive flow separation (Fig. 9), whereas the same velocity ratio with a convergent-like channel of $R_a = 1.33$ engenders an attached flow throughout. Thus, this is an important factor.

In Case 5 we again use the separated flow of Case 1(*b*) ($R_u = 3.0$) to study the effect of changing θ and to demonstrate the fact that disparity may still occur between two forms of the $k - \epsilon$ model for attached flows, if the turbulence in the wall region is locally out of equilibrium. To see this, we reduce θ from 90 to 75 deg and perform two calculations, one by the HRN form and the other by the LRN form. Again the more sensitive quantity of the skin friction coefficient is plotted in Fig. 11 to show the effectiveness of changing θ, the occurrence of disparity after turning, and its disappearance later.

In the above although we made a preliminary investigation of flow separation at the junction influenced individually by different ratios, the collective effect and their interactions have not been examined. For the practical purpose this collective effect may be more important than individual parameters.

Concluding Remarks

The problem of turbulent flows in two-inlet channels has been investigated numerically by solving the Reynolds-averaged Navier-Stokes equations together with the high Reynolds number and low Reynolds number forms of the $k - \epsilon$ modeling. In addition to comparisons with experimental data, cross-references are made among computed results to find dominant parameters for the flow properties downstream of the junction.

References

Bramley, J. S., and Dennis, S. C. R., 1982, "The Calculation of Eigenvalues for the Stationary Perturbation of Posieuille Flow," *Journal of Computational Physics*, Vol. 47, pp. 179–198.

Chieng, C. C., and Launder, B. E., 1980, "On the Calculation of Turbulent Heat Transport Downstream from an Abrupt Pipe Expansion," *Numerical Heat Transfer*, Vol. 3, pp. 189–207.

Hussain, A. K. M. F., and Reynolds, W. C., 1975, "Measurements in Fully Developed Turbulent Channel Flow," ASME JOURNAL OF FLUIDS ENGINEERING, Vol. 97, No. 4, pp. 568–580.

Johnson, R. W., and Launder, B. E., 1982, "Discussion of 'On the Calculation of Turbulent Heat Transport Downstream from an Abrupt Pipe Expansion,'" *Numerical Heat Transfer*, Vol. 5, pp. 493–496.

Kobata, T., Yoshino, Y., Masuda, S., and Ariga, I., 1983, "Turbulent Flows in Entrance Region of Two-Dimensional Straight Channel with Inlet Disturbance," *JSME Bulletin*, Vol. 26, No. 220, pp. 1711–1718.

Lam, C. K. G., and Bremhorst, K., 1981, "A Modified Form of the $k-\epsilon$ Model for Predicting Wall Turbulence," ASME JOURNAL OF FLUIDS ENGINEERING, Vol. 103, pp. 456–460.

Leonard, B. P., 1979, "A Stable and Accurate Convective Modelling Procedure Based on Quadratic Upstream Interpolation," *Computer Methods in Applied Mechanics and Engineering*, Vol. 19, pp. 59–98.

Milne-Thomson, L. M., 1968, *Theoretical Hydrodynamics*, 5th ed., MacMillan Co., New York, NY.

Patel, V. C., Rode, W., and Scheuerer, G., 1985, "Turbulence Models for Near-Wall and Low Reynolds Number Flows: A Review," *AIAA Journal*, Vol. 23, No. 9, pp. 1308–1319.

Rodi, W., 1981, "Progress in Turbulence Modelling for Incompressible Flows," AIAA Paper 81-0045.

Schmidt, R. C., and Patankar, S. V., 1988, "Two-Equation Low-Reynolds-Number Turbulence Modeling of Transitional Boundary Layer Flows Characteristic of Gas Turbine Blades," NASA CR-4145.

Simpson, R. L., 1987, "Two-Dimensional Turbulent Separated Flow," *AIAA Journal*, Vol. 25, pp. 775–776.

Smyth, R., 1979, "Turbulent Flow Over a Plane Symmetric Sudden Expansion," ASME JOURNAL OF FLUIDS ENGINEERING, Vol. 101, pp. 348–353.

Viegas, J. R., Rubesin, M., W., and Horstman, C. C., 1985, "On the Use of Wall Function as Boundary Conditions for Two-Dimensional Separated Compressible Flows," AIAA Paper 85-0180.

Ward-Smith, A. J., 1980, *Internal Fluid Flow: The Fluid Dynamics of Flow in Pipes and Ducts*, Clarendon Press, Oxford, pp. 138 and 435.

Prediction of Turbulent Flows in Rotating Rectangular Ducts

B. A. Younis
Department of Civil Engineering,
City University,
London, U.K.

This paper reports on progress made in the development of a numerical predictive procedure for turbulent flows in rotating rectangular ducts. The unknown turbulent stresses were approximated with the $k-\epsilon$ model of turbulence while Speziale's (1987) nonlinear stress-strain relationship was utilized to capture the turbulence-driven secondary motions. Data from stationary rectangular ducts of aspect ratios in the range 1:1 to 10:1 were used to check the model. It was found that the occurrence and consequences of these motions were well reproduced. Application of the model to rotating rectangular ducts yielded results which suggest that the interactions between the pressure and turbulence-driven motions are far more important than hitherto suspected.

1 Introduction

Turbulent flows in which Prandtl's first and second kind of secondary motion are simultaneously present are often encountered in the fields of propulsion and power generation. Examples include flows through the curved, noncircular intakes and transition ducts of jet engines and in the rotating cooling passages of gas turbine blades. The difficulty in the prediction of such flows stems from the presence of a large number of complicating influences. Johnston et al. (1972), in a study of rotating channels (see Fig. 1 for geometry and coordinates), found that the body forces associated with rotation severely modified the mean-flow and turbulence fields in different ways. On the stable, suction, side of the channel, turbulence activity was diminished and eventually, for high rotation rates, completely suppressed such that the flow relaminarized at relatively high Reynolds number. In contrast, on the unstable, pressure, side turbulent activity was significantly enhanced and the turbulent eddies aggregated into large-scale Gortler-type vortices (see also Johnston, 1974). Moreover, and irrespective of whether the flow is laminar or turbulent, the same centrifugal forces set up pressure gradients which in turn drive Prandtl's first kind of secondary motions; those modify the flow field even further by causing, for example, an-outward shift of the contours of streamwise velocity. For rotating ducts of noncircular cross section, an additional complication is present in the form of Prandtl's second kind of secondary motions that exist in planes perpendicular to the streamwise direction of flow (Gessner, 1973). These motions, which are driven primarily by the anisotropy of the turbulent normal stresses and hence have no counterpart in laminar flow, are also known to significantly modify the gross features of the mean flow: in rectangular ducts for example, they cause the contours of main velocity to bulge toward the corners and shift the position of maximum wall shear stress away from the center planes.

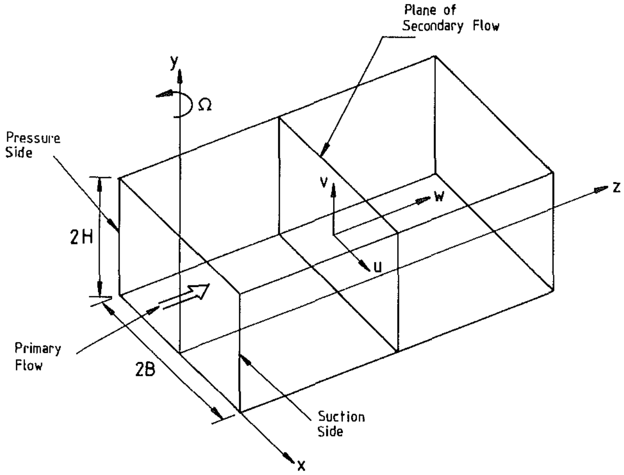

Fig. 1 Flow geometry and coordinates system

Almost all two-equation models of turbulence now in use in practical calculation methods utilize Boussinesq's linear stress-strain relationship in conjunction with the isotropic eddy-viscosity hypothesis, viz.

$$-\overline{u_iu_j} = \nu_t\left(\frac{\partial U_i}{\partial x_j}+\frac{\partial U_j}{\partial x_i}\right)-\frac{2}{3}\,\delta_{ij}k \qquad (1)$$

$$\nu_t = C_\mu\,\frac{k^2}{\epsilon} \qquad (2)$$

where k and ϵ are the turbulent kinetic energy and its dissipation rate, respectively.

It is well known that those models, in their standard form, fail badly to predict the observed effects of rotation unless specifically modified in some respect. Several alternative modifications, mainly to the length-scale equation, have been proposed and used with varying degrees of success. But while the deficiency in such models for rotation has received much attention, another, and equally important one, has been virtually

---

Contributed by the Fluids Engineering Division for publication in the JOURNAL OF FLUIDS ENGINEERING. Manuscript received by the Fluids Engineering Division September 23, 1991; revised manuscript received January 9, 1993. Associate Technical Editor: R. L. Panton.

ignored: in fully developed flows, these models obtain the normal stresses as being identically equal and since the turbulence-driven secondary motions are generated mainly by the turbulence anisotropy, no such motions are predicted. Past workers in the fields of rotating or curved noncircular ducts were quite content with this defect in two-equation models arguing that the turbulence driven motions are an order of magnitude smaller than the pressure-driven flow and can therefore be neglected without major loss in accuracy. The results reported in this paper do not support such an approach but rather they indicate that the interactions between the two kinds of secondary motions exert unexpectedly large influence on the flow behavior, particularly in the near-wall regions.

2 Prediction Method

The rotating duct geometry and coordinate system are defined in Fig. 1. The flow is assumed to be steady, incompressible, and of constant properties.

Equations of Motion. The equations to be solved are

Continuity:

$$\frac{\partial U}{\partial x}+\frac{\partial V}{\partial y}+\frac{\partial W}{\partial z}=0 \tag{3}$$

Momentum:

$$\frac{DU}{Dt}=\frac{\partial}{\partial x}\,(-\overline{u^2})+\frac{\partial}{\partial y}\,(-\overline{uv})-\frac{1}{\rho}\frac{\partial p}{\partial x}-2\Omega W \tag{4}$$

$$\frac{DV}{Dt}=\frac{\partial}{\partial x}\,(-\overline{uv})+\frac{\partial}{\partial y}\,(-\overline{v^2})-\frac{1}{\rho}\frac{\partial p}{\partial y} \tag{5}$$

$$\frac{DW}{Dt}=\frac{\partial}{\partial x}\,(-\overline{uw})+\frac{\partial}{\partial y}\,(-\overline{vw})-\frac{1}{\rho}\frac{\overline{\partial p}}{\partial z}-2\Omega U \tag{6}$$

where

$$\frac{D\phi}{Dt}\equiv\frac{\partial U\phi}{\partial x}+\frac{\partial V\phi}{\partial y}+\frac{\partial W\phi}{\partial z} \tag{7}$$

The flow is assumed to be fully turbulent and hence the absence of molecular diffusion. Further, and consistent with the usual boundary-layer approximations, terms representing diffusion in the streamwise direction have been dropped. For reasons given below, the pressure gradient term in Eq. (6) is a cross-sectional averaged one which is uncoupled from the pressure field $p(x,y)$ associated with the secondary velocities (Eqs. (4) and (5)).

Turbulence Model. Since the linear stress-strain relationship is inadequate for the present application, it seems logical to consider the next higher level of approximation i.e., one which is *quadratic* in the mean rate of strain.

There have been several proposals in the published literature. Lumley (1970) identified the scaling parameters that enter into a generalized constitutive relation and expressed it as a finite tensor polynomial. Pope (1978) pointed out that Lumley's results were invalid because he had made "illicit use" of the alternating tensor density and then proceeded to propose an alternative stress-strain relationship. That, however, turned out to be of limited use for three-dimensional flows being, according to the originator, "so intractable as to be of no value." Speziale (1978) followed a different approach by postulating a particular form for the stress tensor and then specified it by applying several well-known constraints such as coordinate invariance, realizability and, material frame indifference in the limit of two-dimensional turbulence. The proposed relation is of the form:

$$\begin{aligned}-\overline{u_iu_j}=\nu_t\left(\frac{\partial U_i}{\partial x_j}+\frac{\partial U_j}{\partial x_i}\right)-\frac{2}{3}\,\delta_{ij}k\\+C_Dl^2\left(D_{im}D_{jm}-\frac{1}{3}\,D_{mn}D_{mn}\delta_{ij}\right)\\+C_Dl^2\left(\overset{\circ}{\overline{D}}_{ij}-\frac{1}{3}\,\overset{\circ}{\overline{D}}_{mm}\,\delta_{ij}\right)\end{aligned} \tag{8}$$

where

$$D_{ij}=\frac{1}{2}\left(\frac{\partial U_i}{\partial x_j}+\frac{\partial U_j}{\partial x_i}\right) \tag{9a}$$

$$\overset{\circ}{\overline{D}}_{ij}=\frac{\partial \overline{D}_{ij}}{\partial t}+U_m\,\frac{\partial}{\partial x_m}\,\overline{D}_{ij}-\frac{\partial U_i}{\partial x_m}\,\overline{D}_{mj}-\frac{\partial U_j}{\partial x_m}\,\overline{D}_{mi} \tag{9b}$$

$$l=2C_\mu k^{3/2}/\epsilon \tag{10}$$

By expanding Eq. (8), the difference between the two normal stresses acting in the cross-stream planes (i.e., the primary source of streamwise vorticity) is obtained as

$$\begin{aligned}(\overline{v^2}-\overline{u^2})=2\nu_t\left(\frac{\partial U}{\partial x}-\frac{\partial V}{\partial y}\right)+\frac{1}{3}\,l^2\,C_D\left[\left(\frac{\partial V}{\partial y}\right)^2-\left(\frac{\partial U}{\partial x}\right)^2\right]\\-\frac{17}{24}\,l^2C_D\left[\left(\frac{\partial U}{\partial y}\right)^2-\left(\frac{\partial V}{\partial x}\right)^2\right]\\+2C_Dl^2\left(U\,\frac{\partial^2 U}{\partial x^2}-V\,\frac{\partial^2 V}{\partial y^2}\right)\end{aligned} \tag{11}$$

Clearly, the difference is nonzero, even in fully developed flow conditions, and the new quadratic relation is thus capable of producing the turbulence-driven secondary motions. Equation (11) suggests a similarity between the present nonlinear model and the Algebraic Stress Model (ASM) approach used by Demuren and Rodi (1984) for flows in stationary noncircular ducts and by Bo et al. (1991) for heat transfer in rotating square ducts in that both models give the Reynolds stresses as an explicit function of various mean-flow and turbulence parameters. But all similarities end here: the nonlinear model contains combinations of the mean rate of strain gradients that

Nomenclature

B, H = duct dimensions (Fig. 1)
$C_1, C_2, C\mu, C_D$ = coefficients in turbulence model
D_{ij} = mean rate of strain tensor
G = turbulence kinetic energy generation rate
k = turbulence kinetic energy
p = static pressure
Re = Reynolds number
Ro = Rossby number ($=2\Omega B/W_{\text{Bulk}}$)
U, V, W = time-averaged velocities in the spanwise, normal and axial directions, respectively
$\overline{u_iu_j}$ = Reynolds-stress tensor
x, y, z = spanwise, normal, and axial coordinates, respectively
δ_{ij} = Kronecker delta
ϵ = turbulence energy dissipation rate
ϕ = generalized variable
ν_t = kinematic eddy viscosity
ρ = density
$\sigma_k, \sigma_\epsilon$ = Prandtl numbers for k and ϵ
Ω = angular velocity

are absent from ASM, it does not involve a "wall-reflection" term with a wall-damping function, which is quite badly behaved in the corner regions, and finally, unlike ASM, the nonlinear model formulation is always coordinate invariant.

The turbulence kinetic energy and its dissipation rate are obtained from the solution of their standard differential equations:

$$\frac{Dk}{Dt}=\frac{\partial}{\partial x}\left(\frac{\nu t}{\sigma_k}\frac{\partial k}{\partial x}\right)+\frac{\partial}{\partial y}\left(\frac{\nu_t}{\sigma_k}\frac{\partial k}{\partial y}\right)+G-\epsilon \tag{12}$$

$$\frac{D\epsilon}{Dt}=\frac{\partial}{\partial x}\left(\frac{\nu_t}{\sigma_\epsilon}\frac{\partial \epsilon}{\partial x}\right)+\frac{\partial}{\partial y}\left(\frac{\nu_t}{\sigma_\epsilon}\frac{\partial \epsilon}{\partial y}\right)+C_1\frac{\epsilon}{k}G-C_2\frac{\epsilon^2}{k} \tag{13}$$

where

$$G=-\overline{u_iu_j}\left(\frac{\partial U_i}{\partial x_j}+\frac{\partial U_j}{\partial x_i}\right) \tag{14}$$

The values assigned to the model coefficients are the most frequently used ones, viz.

C_μ	σ_k	σ_ϵ	C_1	C_2	C_D
0.09	1.0	1.3	1.44	1.92	1.68

The single new coefficient C_D introduced by the new model was assigned the value of 1.68 obtained by the model originator by reference to pipe flow data.

It should be mentioned that Hur et al. (1990) have applied the same nonlinear model (Eq. (8)) to the companion problem of curved duct flow but with the turbulence kinetic energy and length scale specified empirically rather than determined from the solution of differential transport equations as is done here.

Model Enhancement for Rotation. That two-equation models of turbulence do not account adequately for the effects of rotation is mainly due to the complete absence from the models' equations of rotation-dependent terms: a term 4 $\overline{uw}$ Ω appears as a source (or sink) in the equation for streamwise fluctuating velocity while a term which is equal but of opposite sign appears in the equation for the fluctuating velocity component normal to the axis of rotation and the two terms cancel out when the equations are summed to obtain the equation for k. Proposals for sensitizing the equations for rotation have thus to rely on making one of the source terms of the ϵ-equation a function of a suitably-defined rotation parameter. Howard et al. (1980) evaluated three alternative proposals; the one adopted here was probably the best to emerge from their study and entails re-defining the coefficient C_2 in Eq. (13) thus:

$$C_2=1.92\left(1+0.2\left(\frac{k}{\epsilon}\right)^2 2\Omega\frac{\partial W}{\partial x}\right) \tag{15}$$

Solution Procedure. The mean-flow and turbulence model equations were solved using a three-dimensional finite-volume method. The method is parabolic in the streamwise direction, since the solution at a particular section of a duct is not affected by events downstream of it, but elliptical in the cross-stream planes where pressure and diffusive influences exhibit no predetermined direction. The algorithm is that of Patankar and Spalding (1972) which requires the axial pressure gradient to be uncoupled from the pressure field associated with the secondary velocities. Starting from guessed initial distributions for all dependent variables, the secondary velocities U and V were solved for and then corrected to satisfy continuity using the SIMPLE algorithm. The primary velocity W was then solved and again corrected, this time by reference to global continuity and linearized momentum equations, to satisfy overall mass-balance constraints. Finally, k and ϵ were solved for and used to update the eddy viscosity. For developing flows, a new longitudinal station would be chosen next and the above sequence repeated. For fully developed flows, no forward steps were executed but rather the solution sequence was repeated at the same section until a fully converged solution was attained (with all normalized residuals falling below 10^{-5}).

In all the transport equations solved, the diffusion and the convection terms were discretized using Patankar's (1980) Power-Law Differencing Scheme. Most calculations were also repeated using Peric's (1985) second-order accurate Linear-Upwind Differencing Scheme in order to check the sensitivity of the computed solutions to numerical diffusion. The usual grid-independence tests were also performed. The implementation of the nonlinear model does not differ in detail from that for the usual linear model expect that a large number of additional terms that are non-linear in the velocity gradients emerge and those were simply incorporated as source terms. Evaluation of the second derivatives was rather cumbersome particularly for the grid nodes closest to the walls. The practice finally adopted here was to obtain those terms, when appropriate, by formal differentiation of the standard logarithmic law of the wall. The latter also provided the basis for the wall boundary conditions employed here: its extension for three-dimensional rotating flows is described in detail in Gibson and Younis (1986).

3 Results and Discussion

Predictions were obtained for three different flow geometries, each chosen to test a particular feature of the turbulence model. The first was stationary rectangular ducts with aspect ratios in the range 1:1 - 10:1 chosen to assess the performance of the non-linear relationship for turbulence-driven secondary motions. The second flow geometry was that of a channel of infinite aspect ratio rotated about an axis normal to the direction of the mean flow. The objective here was to test the validity of the modifications made to the dissipation-rate equation to account for rotational effects. The third, and most difficult geometry considered, was that of a rotating duct of small aspect ratio where all complicating influences are present at once.

For all cases, grid dependency checks were performed by doubling the number of grid nodes used and comparing the results. Symmetry was utilized whenever appropriate to reduce the size of the solution domain. For the stationary ducts, results of the two grids 20×20 and 40×40 (covering only a quarter of the duct) were virtually indistinguishable. The large-aspect-ratio rotating duct required 50 nodes to span the distances between opposite walls while the small-aspect-ratio rotating duct required a 40×40 gird. All grids used were nonuniformly distributed with the greater concentration occurring near the walls.

Stationary Rectangular Ducts. Figure 2 compares the predicted and measured mean velocity fields in a square duct. It is immediately clear from the plot of secondary-velocity vectors that the present nonlinear stress-strain relationship has produced the turbulence anisotropy required to drive this motion. The plot indicates the presence of eight vortices, symmetrical about the wall and corner bisectors. The largest secondary velocities occur along the corner bisectors and amount to approximately 3 percent of the streamwise velocity. The strength and position of the secondary-flow cells are generally well predicted as can be seen from Fig. 2(*b*) where the streamlines are compared with the measurements of Gessner and Jones (1965). The contours of the main flow (presented at 80 and 90 percent of maximum value) shown in Fig. 2(*c*) demonstrate the importance of the secondary motion: the bulge in the contours toward the corners is caused by the secondary velocities transporting slow moving fluid from the near-wall region into the duct's center and carrying fast moving fluid from there towards the corners. The present predictions are compared

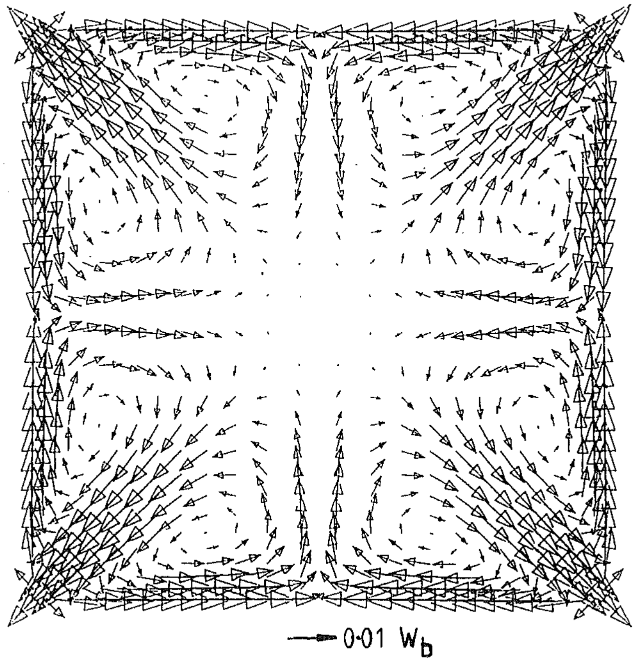

Fig. 2(*a*)

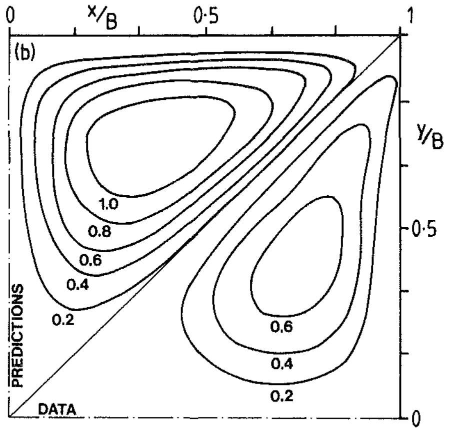

Fig. 2(*b*)

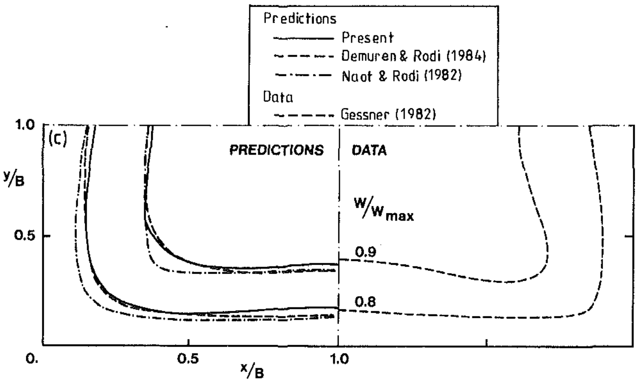

Fig. 2(*c*)

Fig. 2 Square duct results: (*a*) predicted flow vectors, (*b*) secondary flow streamlines, data of Gessner and Jones (1965), (*c*) contours of primary velocity

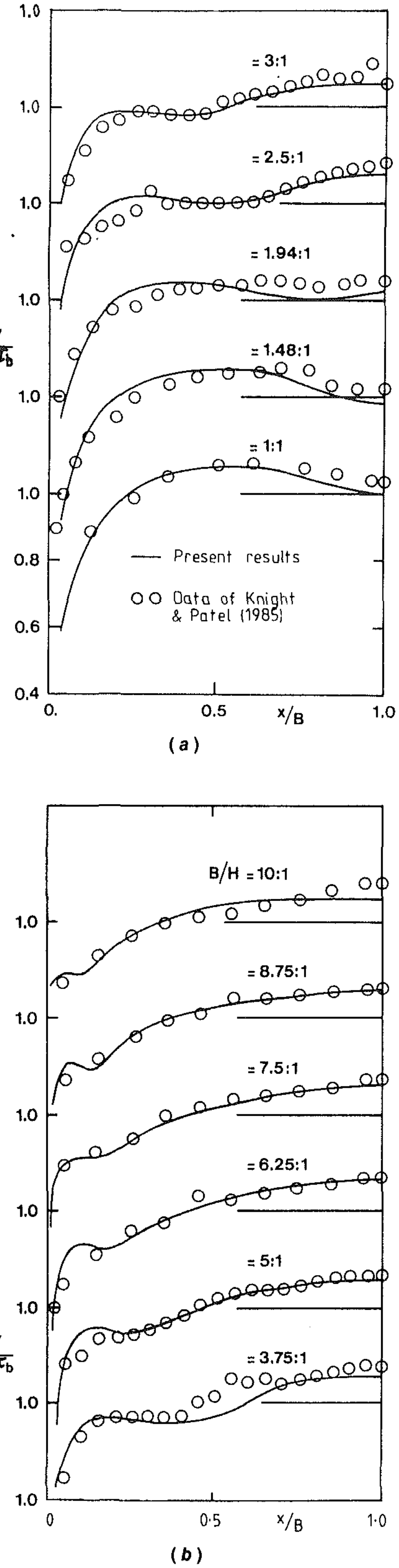

Fig. 3 Predicted and measured wall shear stress for rectangular stationary ducts

with the data of Gessner (1982) and also with Algebraic Stress Model results of Naot and Rodi (1982) and Demuren and Rodi (1984). It is clear that the present two-equation model yields results that are at least comparable to those obtained with the more difficult models.

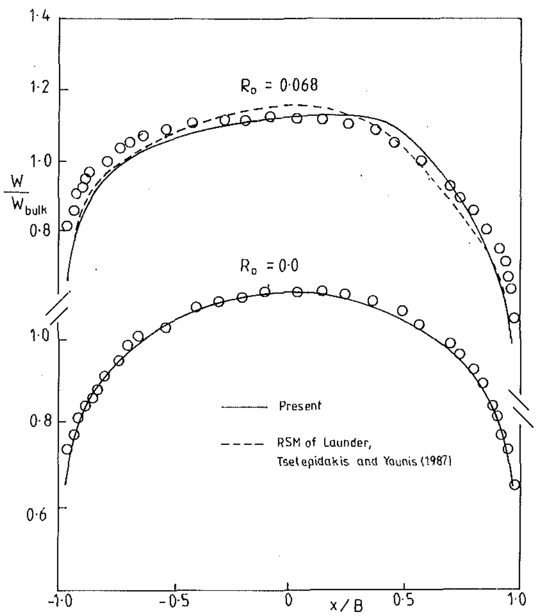

Fig. 4 **Mean velocity profiles in high-aspect-ratio duct. O data of Johnston et al. (1972) at Re = 35,000**

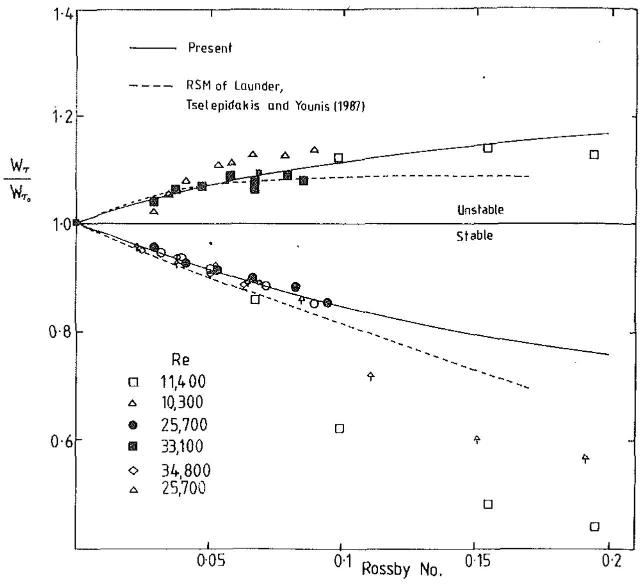

Fig. 5 **Effects of rotation on wall friction for high-aspect-ratio duct. Data of Johnston et al. (1972)**

Knight and Patel (1985) obtained detailed measurements of wall shear stress in ducts of various aspect ratios and these are compared with the present predictions in Fig. 3. The distortion to the axial velocity wrought by the secondary motion has led to the displacement of the point of maximum wall shear stress away from the center plane and towards the corner. A region of 'stress deficit' is thus created in the middle of the duct, migrating towards the corners with increasing aspect ratio. This behavior is consistent with approach to two-dimensional flow conditions. Both the extent of this deficit region, as well as the rate at which it moves toward the corners, are very well predicted except for aspect ratio of 3.75:1 where the unexpected rise in wall shear stress half way between the corner and the center plane is not reproduced in the predictions. Another difference appears at aspect ratio of 10:1 where the data indicate attainment of two-dimensional conditions while the model shows residual effects near the corners arising from finite secondary velocities there.

Rotating High-Aspect-Ratio Ducts. The measurements of Moore (1967) suggest that for rotating ducts of aspect ratios greater than about 7:1, the flow resembles that between infinite rotating parallel planes: the Coriolis force in the direction normal to the planes is everywhere balanced by the pressure gradient and the secondary velocities are too weak to influence the mainstream flow. Rotation is thus the only complicating effect present and such flows have been used to test the performance of various turbulence models (e.g., Howard et al., 1987 and Launder et al., 1987).

In Fig. 4, the predicted mean velocity distributions are compared with the data of Johnson et al. (1972) taken at Re = 35,000. Both calculations and data correspond to fully-developed flow conditions. Two values of Rossby number ($2\Omega B/W_{\mathrm{bulk}}$) are compared viz. 0. and 0.068. The predictions of Launder et al. (1987) with a differential Reynolds-stress model are also plotted. The effect of rotation is to cause a shift in the location of maximum axial velocity and this is correctly reproduced by both models. It should be noted that the standard $k-\epsilon$ model, when not modified for rotation, is completely insensitive to rotation and would thus have produced symmetric velocity distribution. The modification introduced to the ϵ-equation (Eq. (15)) has increased the eddy viscosity near the unstable side (where the velocity gradient is positive) leading to a thinner boundary layer there but lowering it on the stable side where the boundary layer is seen to be thicker than in the stationary flow.

The effects of rotation on wall shear stress are demonstrated in Fig. 5 where the friction velocity on each wall, normalized by the same quantity at zero rotation and same Reynolds number, is shown as a function of Rossby number. The present results are again compared with the Reynolds-stress model predictions of Launder et al. (1987). On the unstable side, rotation enhances turbulent activity leading to increased wall shear stress levels. At Ro = 0.1, for example, friction velocity is some 10 percent higher than for the non-rotating channel. The reverse occurs on the stabilized suction side where wall stress is diminished. The sudden drop in measured wall friction at Ro = 0.1 is due to flow relaminarization which cannot be reproduced by high Reynolds-number turbulence models such as the present.

Rotating Low-Aspect-Ratio Ducts. Wagner and Velkoff (1972) obtained measurements in a developing flow in a rectangular duct of aspect ratio of 2.7:1 rotated about an axis normal to the flow direction (Fig. 1). Rotation here produces a Coriolis acceleration in the position x-direction which results in higher pressures in the negative x-direction. The pressure gradients setup act to accelerate the slow moving fluid adjacent to the walls from the high-pressure region into the low pressure one with faster moving fluid returning in the opposite direction for continuity to be satisfied. In order to investigate the effects of rotation without the added complexity of the turbulence-driven motions, the coefficient C_D in Eq. (8) was set to zero to recover the usual linear stress-strain relationship and render the present model identical to that of Howard et al. (1980). The present model predictions of the mean flow distorted therefore only by rotation are shown in Fig. 6(*b*) where it can be seen that the expected patterns of pressure-driven motions are reproduced and where it is evident that the returning flow has displaced the location of maximum mainstream velocity toward the pressure side. The results for $C_D = 1.68$ are shown in Fig. 6(*c*): the striking feature to emerge there is the presence of two vortices adjacent to the suction side that are remnants of the larger ones that existed in the stationary duct (see Fig. 6(*a*)).

Wagner and Velkoff reported measurements of mean axial velocity taken along the ducts central plane at several rotation speeds; these are compared with the present predictions in Fig.

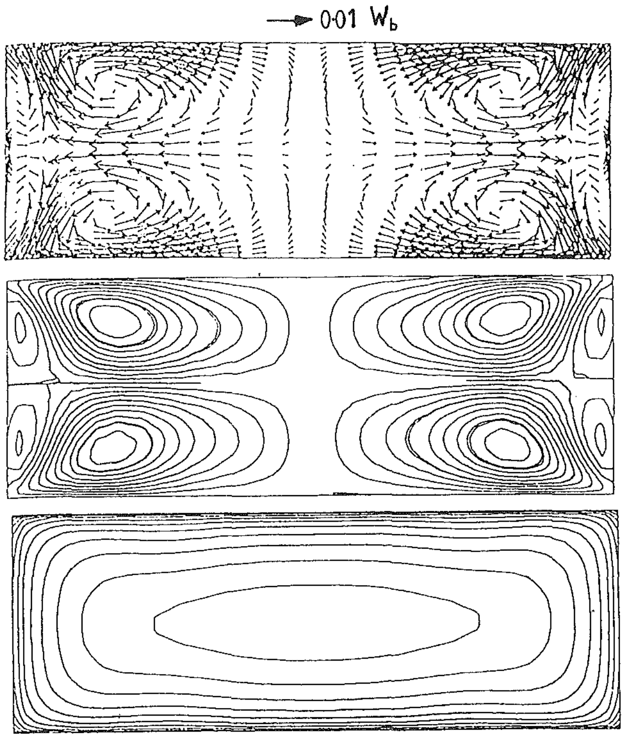

(a)

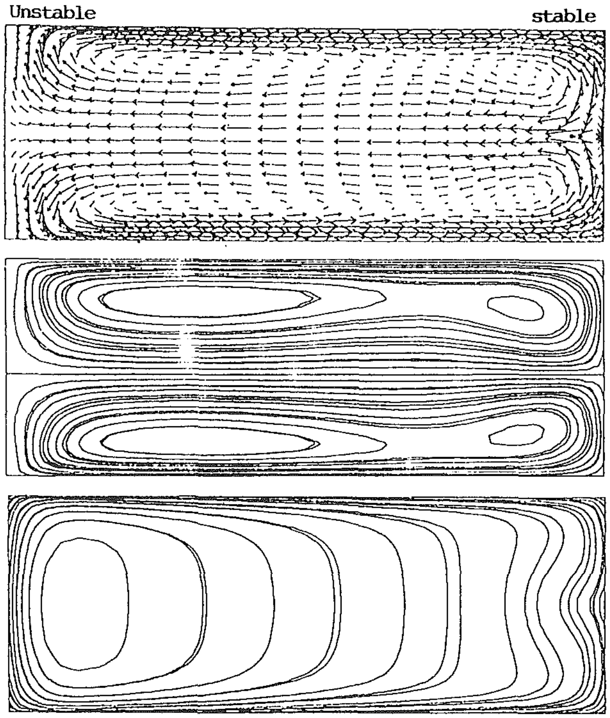

(c)

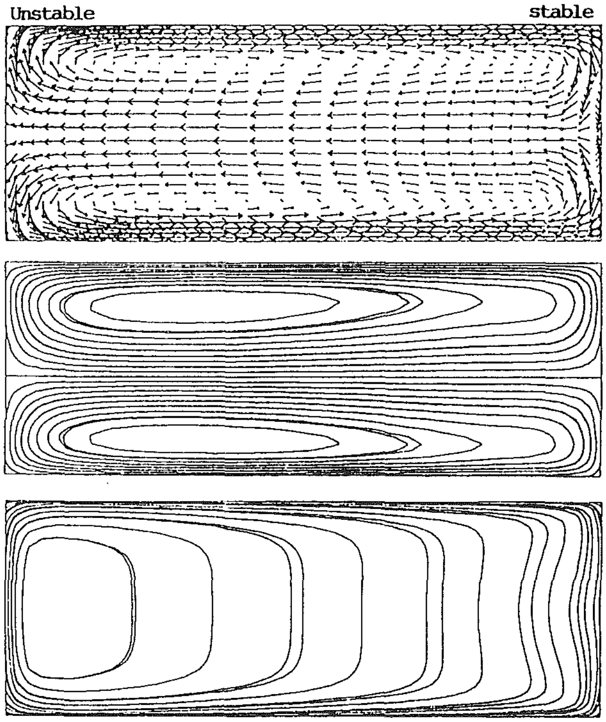

(b)

Fig. 6 Predicted secondary velocity vectors and streamlines and mainstream velocity contours in a 2.71: 1 duct. (*a*) stationary duct, (*b*) and (*c*) rotating duct without and with turbulence-driven motions

7. The calculations correctly reproduce the measured reduction in boundary layer thickness on the pressure side and increase on the suction side, but fail to capture the flat central portion apparent in the data. It should be noted that the measurements were obtained at a location where the flow was still developing while in the calculations fully developed conditions had to be assumed in the absence of suitable inlet conditions. For the zero rotation case, the differences between the linear and nonlinear stress-strain relationships are attributable solely to their sensitivity to turbulence-driven motion. At the lowest rotation rate, the differences are quite pronounced, particularly in the near-wall regions where the turbulence and the pressure-driven motions are approximately of the same order. At higher rotation rates, the pressure-driven motion is dominant and the two models produce almost indistinguishable profiles.

The effects of the interaction between the two kinds of secondary motion on the wall friction coefficient are shown in Fig. 8: the friction velocity obtained with the linear model is about 10 percent higher on the pressure side and 8 percent lower on the suction side compared with the nonlinear model results. The reason for this behavior may be inferred from Fig. 6 and, in particular, from the plots of secondary velocity vectors presented there. Near the pressure side, the turbulence-driven motion opposes the pressure-driven one: some cancellation occurs leading to a reduction in the extent to which the location of maximum streamwise velocity is shifted towards the pressure side. The velocity gradients there are now smaller than before leading to lower shear stress. The reverse applies very near the suction side where the pressure- and turbulence-driven motions are in the same direction.

4 Concluding Remarks

The occurrence of turbulence-driven secondary motions in noncircular ducts is well predicted with a standard $k-\epsilon$ model used in conjuction with a nonlinear stress-strain relationship. In particular, the distortion to mainstream velocity contours and displacement of point of maximum wall shear stress away from duct's center plane are well reproduced. For fully developed flows in rotation, the model produced the correct response of the turbulence on the pressure side where wall shear stress increased above non-rotating levels and on the suction side where the reverse occurred. For a low aspect ratio rotating duct, the model revealed a complex pattern of interacting pressure and turbulence-driven secondary motions par-

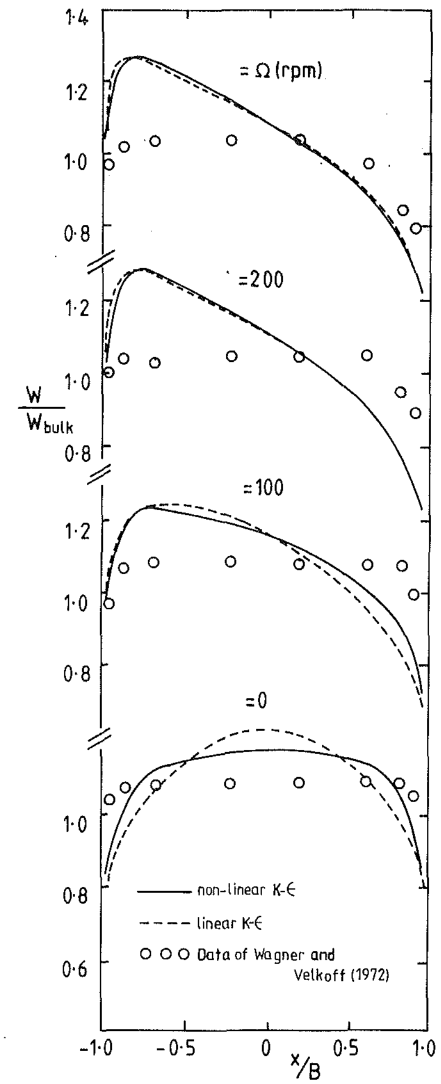

Fig. 7 Primary velocity profiles in low-aspect-ratio duct. Data of Wagner and Velkoff (1972).

ticularly in the shear-wall regions. The consequences of this interaction on wall shear stresses were unexpectedly large and tend to confirm the need to account properly for all the complicating effects present.

References

Bo, T., Iacovides, H., and Launder, B. E., 1991, "The Prediction of Convective Heat Transfer in Rotating Square Ducts," *Proceedings 8th Symposium on Turbulent Shear Flows*, Munich-Germany, pp. 24.4.1-24.4.6.

Demuren, A. O., and Rodi, W., 1984, "Calculation of Turbulence-Driven Secondary Motion in Non-Circular Ducts," *Journal of Fluid Mechanics*, Vol. 140, pp. 189-222.

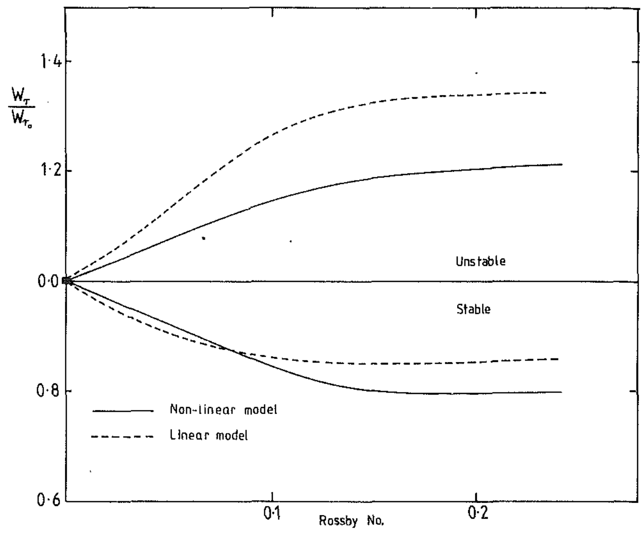

Fig. 8 Effects of rotation on wall shear stress in low-aspect-ratio duct

Gessner, F. B., 1973, "The Origin of Secondary Flow in Turbulent Flow Along a Corner," *Journal of Fluid Mechanics*, Vol. 58, pp. 1-25.

Gessner, F. B., 1982, "Corner Flow (Secondary Flow of the Second Kind," *Proceedings of 1980-81 AFOSR-HTTM Stanford Conference*, (ed. Kline, S et al, ed., pp. 182-212.

Gessner, F. B., and Jones, J. B., 1965, "On Some Aspects of Fully Developed Turbulent Flow in Rectangular Channels," *Journal of Fluid Mechanics*, Vol. 23, pp. 689-713.

Gibson, M. M., and Younis, B. A., 1986, "Calculation of Boundary Layers With Sudden Transverse Strain," ASME JOURNAL OF FLUIDS ENGINEERING, Vol. 108, pp. 470-475.

Howard, J. H. G., Patankar, S. V., and Bordynuik, R. M., "Flow Prediction in Rotating Ducts Using Coriolis-Modified Turbulence Models," ASME JOURNAL OF FLUIDS ENGINEERING, Vol. 102, pp. 456-461.

Hur, N., Thangam, S., and Speziale, C. G., 1990, "Numerical Study of Turbulent Secondary Flows in Curved Ducts," ASME JOURNAL OF FLUIDS ENGINEERING, Vol. 112, pp. 205-211.

Johnston, J. P., 1974, "The Effects of Rotation on Boundary Layers in Turbomachine Rotors," NASA SP-304, pp. 207-249.

Johnston, J. P., Halleen, R. M., and Lezius, D. K., 1972, "Effects of Streamwise Rotation on the Structure of Two-Dimensional Fully Developed Turbulent Channel Flow," *Journal of Fluid Mechanics*, Vol. 56, pp. 533-557.

Knight, D. W., and Patel, M., 1985, "Boundary Shear Stress in Smooth Rectangular Ducts," *ASCE Journal of Hydraulic Engineering*, Vol. 111, pp. 29-47.

Launder, B. E., Tselepidakis, D. P., and Younis, B. A., 1987, "A Second-Moment Closure Study of Rotating Channel Flow," *Journal of Fluid Mechanics*, Vol. 183, pp. 63-75.

Lumley, J. L., 1970, "Toward a Turbulent Constitutive Relation," *Journal of Fluid Mechanics*, Vol. 41, pp. 413-434.

Moore, J., 1967, "Effects of Coriolis on Turbulent Flow in Rotating Channels," MIT Gas Turbine Lab. Report 89.

Naot, D., and Rodi, W., 1982, "Calculation of Secondary Currents in Channel Flow," *ASCE Journal of Hydraulic Division*, Vol. 108, (HY8), pp. 948-968.

Patankar, S. V., and Spalding, D. B., 1972, " A Calculation Procedure for Heat, Mass and Momentum Transfer in Three-Dimensional Parabolic Flows," *International Journal of Heat and Mass Transfer*, Vol. 15, pp. 1787-1806.

Peric, M., 1985, Ph.D thesis, Mechanical Engineering Department, Imperial College, London.

Pope, S. B., 1975, "A More General Effective-Viscosity Hypothesis," *Journal of Fluid Mechanics*, Vol. 72, pp. 331-340.

Speziale, C. G., 1987, "On Nonlinear $k-l$ and $k-\epsilon$ Models of Turbulence," *Journal of Fluid Mechanics*, Vol. 178, pp. 459-475.

Wagner, R. E., and Velkoff, H. R., 1972, "Measurements of Secondary Flows in a Rotating Duct," ASME *Journal of Engineering for Power*, Vol. 94, pp. 261-270.

Large Amplitude Wall Pressure Events Beneath a Turbulent Boundary Layer

C. C. Karangelen
Lecturer,
Department of Mechanical Engineering,
The Catholic University of America,
Washington, DC 20064
Assoc. Mem. ASME

V. Wilczynski
Associate Professor,
The U.S. Coast Guard Academy,
New London, CT 06320-4192

M. J. Casarella
Professor,
Department of Mechanical Engineering,
The Catholic University of America,
Washington, DC 20064

Experimental data on the temporal records of the wall pressure fluctuations beneath a turbulent boundary layer have been acquired in a low-noise flow facility. The pressure data were first analyzed using long-time averaging techniques to determine the statistical properties and the results were compared to the baseline data of Schewe (1983). Next, the pressure records were conditionally sampled at various k threshold levels ($p'_w \geq k \cdot p_{rms}$) to detect large amplitude, positive and negative events which were then averaged and analyzed to determine their shape, duration, and frequency of occurrence. The intermittent large amplitude events are very short in duration, occur rather infrequently in time, but are a major contributor to the high frequency content of the wall pressure fluctuations. As an example, events where $p'_w \geq |3 \cdot p_{rms}|$ have an average duration of 14 viscous time units, occur 5 percent of the time and contribute 49 percent to the RMS value. The time between events appears to have a lognormal statistical distribution. The frequency of occurrence of the large amplitude events are consistent with the burst rate for flow structures and thus support the conjecture that the large amplitude events are associated with the near-wall bursting process.

Background

The wall pressure fluctuations beneath a turbulent boundary layer have received numerous experimental investigations and these have been reviewed by Willmarth (1975), Blake (1986), and Eckelmann (1990). Many of the earlier studies were concerned with obtaining quality data over a wide spectral range. Measurement errors due to transducer size and contamination by facility-related noise were major concerns in the high and low frequency regions, respectively. The recent investigation by Farabee and Casarella (1991) had overcome some of these problems. Data were obtained in a low-noise facility over a broad region of the spectrum and appropriate scaling laws for the low, mid, and high frequency ranges were established. It was concluded that flow structures in the inner and outer layers of the boundary layer contribute to the high and low frequency ranges of the spectrum, respectively. Because these data were obtained by unconditional averaging techniques, the contributions from intermittent organized events in the inner layer, sometimes referred to as the bursting process, were not distinctly observed in the spectrum of the wall pressure.

Several investigations have recently been made using conditional averaging techniques to examine the relationship between intermittent high amplitude wall-pressure peaks and flow structures in the near wall region. The most recent work is that of Haritonidis et al. (1990). Their results conclude that the wall pressure and flow structures in the buffer region are most prominently coupled through the normal component of velocity. No direct relationship between the wall pressure and isolated "*uv*" peak events was observed. Furthermore, by examining the weighted probability density $P(u, v)$ of u and v with the wall pressure, as well as the conditional averages of near-wall flow events and pressure peak events, they concluded that:

"Positive (peak) pressures are primarily associated with the fourth quadrant or sweep type events while negative (peak) pressures are associated with both the second and third quadrant or ejections and interactions inward, respectively."

"Quadrant," in the above quotation, refers to the u-v quadrant method developed by Lu and Willmarth (1973) for the statistical analysis of u-v stress events. It was also used in the Haritonidis study to detect isolated shear stress events. The quadrants are obtained by plotting the statistical data on a two axis graph, with u on the horizontal axis, v on the vertical axis. The result is a scatter plot which may be interpreted as a joint probability distribution, $p(u, v)$.

In Haritonidis et al. (1990), it was also stated that a one-to-one correspondence between pressure events and flow events does not exist. These findings contradict some earlier results of Johansson et al. (1987). It is apparent from these and other studies that the various coupling mechanisms between flow structures, in both the inner and outer layers of the boundary layer, and wall pressure fluctuations are quite complex.

The present research is an extension of the work of Farabee and Casarella (1991) by focusing on the use of conditional sampling techniques to analyze the data and investigate the

---

Contributed by the Fluids Engineering Division for publication in the JOURNAL OF FLUIDS ENGINEERING. Manuscript received by the Fluids Engineering Division May 22, 1992. Associate Technical Editor: D. M. Bushnell.

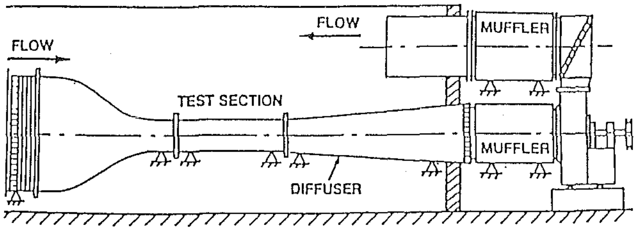

Fig. 1 The CUA wind tunnel facility

causality between flow structures and wall pressure events. As the first phase of this investigation, the authors obtained extensive data exclusively on the large amplitude positive and negative pressure events. The shapes, duration and frequency of occurrence of these events were computed (Karangelen, 1991) and these findings are detailed in this paper. Research now in progress (Wilczynski, 1991) consists of simultaneously measuring the (hot-wire) velocity at various locations across the boundary layer and the (pinhole microphone) wall pressure fluctuations.

Experimental Facility

A complete discussion of the facility, measurement techniques, and background noise can be found in Farabee and Casarella (1991) while a review of the data acquisition system and developed software is contained in Karangelen (1991). The following is a brief overview of the experimental facility.

Flow Facility and Measurement Techniques. The measurements were made in the wind tunnel at The Catholic University of America. The tunnel, illustrated in Fig. 1, has a 0.61 m square cross section with a 2.44 m long test section. Air is drawn through the tunnel by a low-speed centrifugal blower that is located downstream of the test section in an adjacent room. Acoustic mufflers are located upstream and downstream of the blower to minimize blower generated background noise. Exhaust air from the blower is circulated back into the room containing the tunnel allowing the air to be continuously recirculated. The inlet air first passes through a turbulence management section that consists of a honeycomb section and a series of screens of different mesh sizes. The contraction section was carefully designed to have a gradual static pressure distribution with no local separation on the wall. Boundary-layer trip wires are located on the test wall of the contraction section, upstream of the start of the test section, to ensure a fully developed turbulent boundary layer at the measurement locations. The wall pressure measurements were obtained at a location of approximately 1500 trip heights downstream of the trip wire. Tunnel free-stream velocity can be continuously varied from 6 to 30 m/s. Typical boundary-layer properties for the data to be presented are listed in Table 1.

Table 1 Summary of TBL characteristics

U_0 (m/s)	δ (cm)	δ^* (cm)	θ (cm)
15.5 (±0.1)	2.78 (±0.01)	0.45 (±0.01)	0.33 (±0.01)
28.3 (±0.1)	2.78 (±0.01)	0.43 (±0.01)	0.32 (±0.01)
u_τ/U_0	R_θ	d^+	δ^+
0.0403	3332	32.0	1169
0.0379	5929	56.6	2010

Wall pressure measurements were made on the smooth wall in the test section. To minimize spatial averaging effects, wall pressure fluctuations were measured with flush mounted 0.79 mm diameter pinhole microphones. The pinhole transducer consisted of a Bruel and Kjaer 0.3175 cm (1/8 in.) condenser microphone on which a blank cap, containing a 0.79 mm diameter hole ($33 \leq d \cdot u_\tau/\nu \leq 66$) was attached. The volume enclosed by the cap was kept small to ensure the Helmholtz resonance frequency of the cap system was above the frequency range of interest in the wall pressure measurements. A comparison calibration showed that the Helmholtz frequency occurs at approximately 25 Khz.

Special efforts were made during the measurements of the wall pressure to minimize the effects of both background noise and spurious free-stream turbulence levels. The spectral features of the free stream turbulence and the cross-spectra between free-stream velocities and wall pressure fluctuations were massed in order to assess the sources of noise contamination on the measurements (Helal et al., 1989). The data were found to be noise-free for frequencies above 70 Hz.

Data Acquisition Techniques. The data acquisition system (MASSCOMP 5450 Unix-based workstation) allowed pressure data to be simultaneously sampled, digitized, stored, and analyzed. In the experimental approach used to collect and analyze the wall pressure data, the power spectrum of the wall pressure signal are first examined using the dual channel FFT analyzer (HP 3562A) to determine the spectral features and the quality of the data. The temporal records of this pressure signal are then filtered to avoid aliasing, digitized, and stored on the hard disk. The data are also high pass filtered (f_{c0} = 70 Hz) to eliminate facility noise, and stored as a new record on the workstation's hard disk for post-processing.

The sampling rate was selected such that the time between sequential samples does not exceed one viscous time unit using the criteria:

$$f_{\text{sample}} > \frac{1}{t_\nu} = \frac{u_\tau^2}{\nu}.$$

At a free-stream velocity of 15.5 m/s, the data were sampled for 10 seconds at a 30 Khz sampling rate. This resulted in a time between samples of 0.8 viscous units. Data records were obtained over a range of flow speeds from 12 to 27 m/s.

Nomenclature

d = microphone diameter
d^+ = microphone diameter scaled on inner variables
f_{c0} = analog filter cutoff frequency
f_{sample} = digital sampling frequency
k = threshold value
$p(u, v)$ = joint probability distribution of u, v
p_{rms} = RMS pressure
p_w' = pressure fluctuation measured at the wall
q = dynamic head
RMS = root mean square
R_θ = Reynolds number based on momentum thickness
t = time
t^+ = time scaled on inner variables
$\langle t \rangle$ = average time, in units of t^+, between large amplitude events
Δt = average duration, in units of t^+, of large amplitude events
u = streamwise velocity component
u_τ = frictional velocity
U_0 = free-stream velocity
v = velocity component perpendicular to the wall
δ = boundary-layer thickness
δ^+ = boundary-layer thickness scaled on inner variables
δ^* = displacement thickness
θ = momentum thickness

Experimental Results

The wall pressure data were first examined using long-time averaging techniques to determine the statistical properties for comparison to the published data. Some of these results will be briefly reported in this paper. The data records were then conditionally sampled to detect large amplitude, positive and negative events. These events were averaged and analyzed to determine the characteristic shapes and the frequency of occurrence. These results will be presented in some detail.

Statistical Properties of Wall Pressure Fluctuations. The data to be presented will show that the probability distribution of amplitudes has features which are clearly different from a Gaussian signal. Specifically, in comparison to the Gaussian signal, the wall pressure fluctuations have more large negative and positive amplitudes. A comparison of the higher moments of the probability distribution between the present data and the Gaussian random signal illustrates the distinctions. The data exhibited a slight negative coefficient of skewness (-0.18, with a variance of .0025) with 0.0 for Gaussian data, and a larger coefficient of kurtosis (4.94, with a variance of .044) rather than 3.0 for the Gaussian signal. The negative skewness in the data indicates an asymmetry in the probability density distribution, with a slightly greater occurrence of negative amplitudes. The deviation in the kurtosis (flatness) value indicates that more large amplitude events are present. Also, it is expected that a signal with a high level of intermittency should have a high flatness value. In summary, the difference between Gaussian statistics and that seen by the measured data appears to be attributed to intermittent large amplitude pressure fluctuations, with a slight bias towards more negative events.

Schewe (1983) measured the probability distribution and its moments using transducers of various sizes. He demonstrated that the skewness and kurtosis values for increasingly large transducers approach that expected for a random Gaussian signal and concluded that measurements with large transducers lack the ability to discriminate the inherent features of the data. As more and more pressure producing events occur on the active face of a transducer, each can be considered an individual random process with its own probability density function. As the transducer size is increased, more pressure events are detectable simultaneously by the transducer. By virtue of the Central Limit Theorem, the statistics of the transducer output will approach Gaussian values with increasing transducer size.

The statistics of the present data were compared with the Schewe (1983) data to validate the quality of the data. Figure 2 compares the RMS value, skewness coefficient and kurtosis coefficient of the present data with Schewe's results for various dimensionless transducer sizes ($d^+ = d \cdot u_\tau / \nu$).

It is somewhat misleading to compare the statistical data from investigations at different Reynolds numbers in the form shown in Fig. 2 since it is difficult to separately account for both the effects of transducer size, which limits the high frequency resolution, and the variations of the wall pressure fluctuations with Reynolds number. This issue, as well as the scaling laws for the RMS values, are discussed in Farabee and Casarella (1991).

Skewness and kurtosis values from a direct numerical simulation of the pressure fluctuations in a turbulent channel flow were reported by Kim (1989). The d^+ for his simulation can be estimated from the streamwise grid spacing where $d^+ = \Delta x^+ = 17$. At the wall, the numerical simulation results obtained a skewness value of $-.10$ and a kurtosis value of 5.0. These values are consistent with those of Schewe and the present data.

Some warnings are in order regarding the interpretations of the statistical data. It should be noted that if the temporal record of the wall pressure contains both deterministic and random structures, a pronounced effect on the long-time statistics is expected (Alfredsson and Johansson, 1990). Furthermore, Sreenivasan (1991) states that intermittent (flow) structures cannot be described efficiently by the statistics of the distribution. He further states that for Gaussian data, the mean and variance describe the process completely; however, for highly intermittent structures, the first few moments give little clue as to their nature.

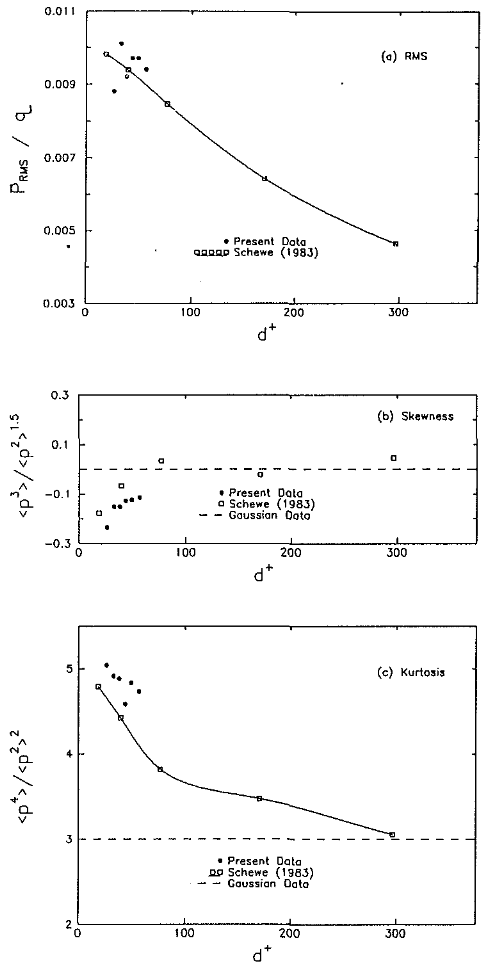

Fig. 2 Comparison of present data with the results of Schewe (1983). Experimental data have an error of approximately +/− 10 percent of magnitude.

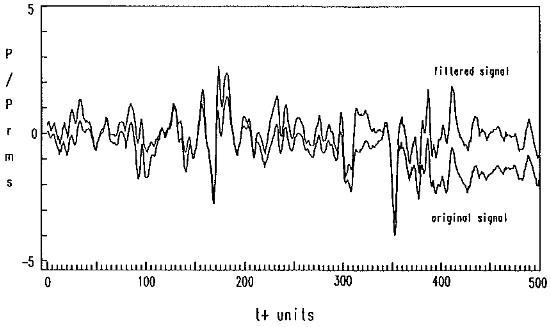

Fig. 3 Excerpt of a digital temporal record of the wall pressure signal at U_0 = 15.5 m/s. (Filtered signal has been bandpass filtered between 70 and 15,000 Hz)

Conditional Sampling of Large Amplitude Events. Visual inspection of the time records of the wall pressure revealed large amplitude events as seen in Fig. 3. A conditional sampling

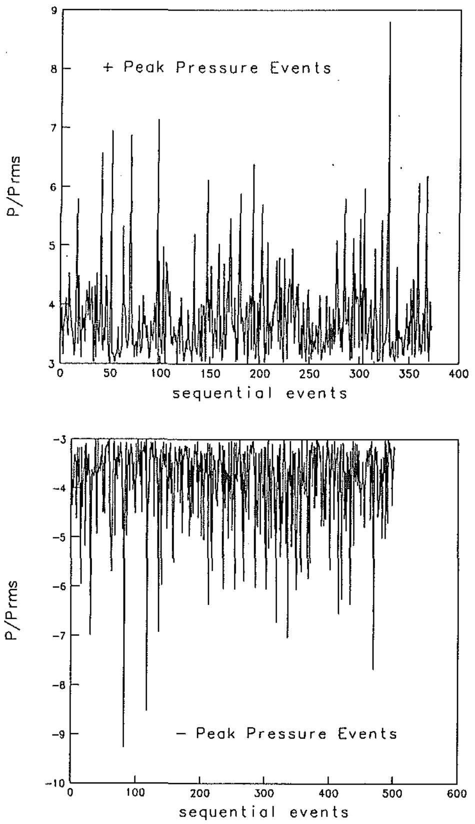

Fig. 4 Sequential large amplitude wall pressure events in excess of 3 RMS values for U_0 = 15.5 m/s: (*a*) positive events; (*b*) negative events

approach to investigate the statistics of these pressure events was used. Peak pressure events were extracted from the contiguous time record if a measurement exceeded the threshold k, established by $p_w' \geq k{\bullet}p_{\text{rms}}$ for all positive peaks, and $p_w' \leq -k{\bullet}p_{\text{rms}}$ for all negative peaks. When the amplitude exceeded the threshold, an event was declared present. The time of occurrence of the event was colocated with the peak's maximum amplitude for positive events, and minimum amplitude for negative events. The duration of the event, Δt, was defined by the event's pre and post threshold zero crossings. It should be noted that many thresholds were investigated. The results to be presented are for a threshold $k = 3$ and these results show features that are typical of events using thresholds from 1 to 5.

Figures 4(*a*) and (*b*) are plots of peak positive and negative amplitudes, respectively, of events exceeding a threshold of $k = 3$ and displayed in sequential order of occurrence. The maximum positive pressure measured was 8.7 p_{rms} while the maximum negative pressure was $-9.2\ p_{\text{rms}}$. Figures 5(*a*) and (*c*) display the shape of events obtained by averaging the full ensemble of positive (or negative) events while Figs. 5(*b*) and (*d*) show an overlay of a subset of the individual events. Figures 6(*a*) through (*d*) are from the dame data records used in Fig. 5; however, these results were obtained by first normalizing each of the event's data points by their peak amplitude, then averaging the full ensemble of normalized events. From these results, it appears that the shape and duration of the events are independent of the event's amplitude since normalization had no noticeable effect on the averaged shape. In both cases, the positive and negative large amplitude events have clearly defined asymmetric wavelet shapes. These features are qualitatively similar to those obtained by Schewe (1983), Johansson et al. (1987), and Haritonidis et al. (1990).

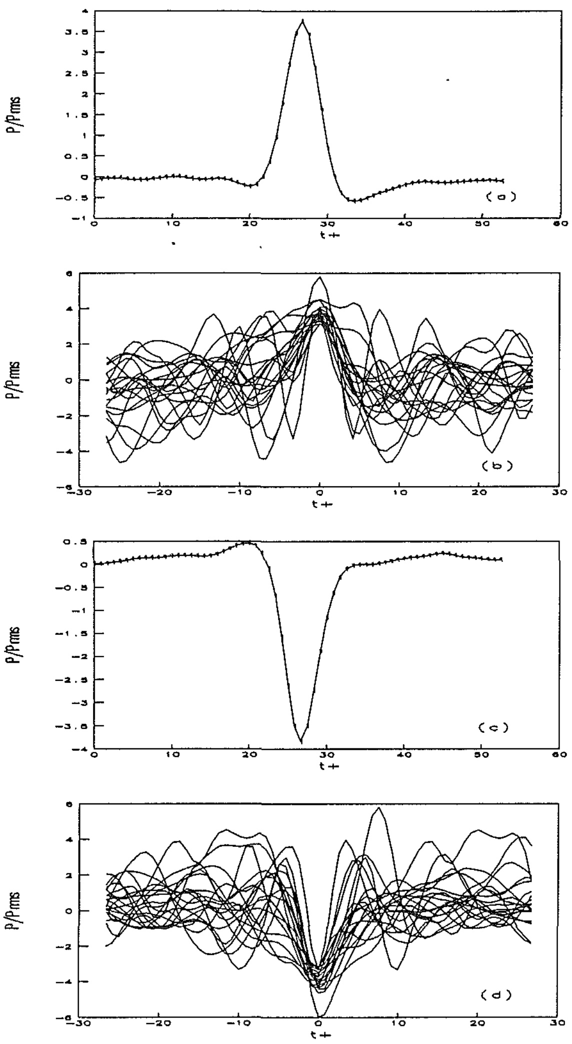

Fig. 5 Average and overlay of positive and negative large amplitude wall pressure events (k = 3.0; U_0 = 15.5 m/s)

The statistical properties of the events for various threshold values are presented in Table 2. The table lists the percentage of the total time and total RMS value that both positive and negative events contribute to the wall pressure fluctuations. The contributions were determined by computing the RMS values from all events that exceeded the current threshold. Consider, for example, the threshold $k = 3$. The data show that large amplitude events in excess of this threshold ($p_w' \geq 3{\bullet}p_{\text{rms}}$) occur approximately 5 percent of the time and contribute to approximately 49 percent of the RMS value. These values (5 percent, 49 percent) are larger than that reported by Schewe (1 percent, 40 percent) and Johansson (6 percent, 18 percent). These differences are partially attributed to the methods used to estimate the contributions. Schewe's values were determined directly from higher moments of the probability density function. A comparison of the present results for $k = 3$ using this procedure show only 38 percent contribution to the RMS value compared to 49 percent contribution determined by considering the full event. Clearly, the probability distribution approach only takes into account that portion of the individual event that exceeds the threshold. The RMS calculations which incorporate the full event based on the axes crossings appear to be more realistic.

Frequency of Occurrence of Large Amplitude Events. An investigation of the time-dependent behavior of the wall pressure events was also pursued. This was done by determining

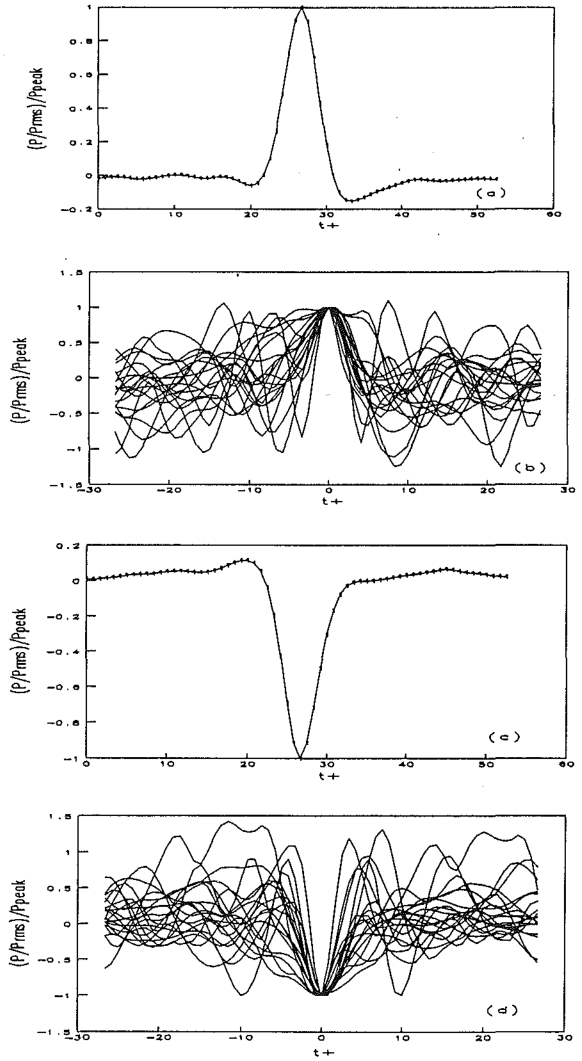

Fig. 6 Average and overlay of positive and negative large amplitude wall pressure events with normalized amplitudes (k = 3.0; U_0 = 15.5 m/s)

Table 2 Statistical properties of combined positive and negative large amplitude events. Mean values reported with standard deviations from the mean shown in parenthesis

k	%RMS	(err)	%Time	(err)
0.0	100.0	(----)	100.0	(----)
1.0	96.7	(0.13)	65.9	(0.63)
2.0	75.8	(0.37)	22.2	(0.36)
3.0	49.4	(0.80)	5.3	(0.16)
4.0	30.9	(1.41)	1.3	(0.12)
5.0	19.6	(1.78)	0.4	(0.06)
6.0	14.5	(0.92)	0.1	(0.03)

Table 3 Statistical properties of large amplitude events. Mean values reported with standard deviations from the mean show in parenthesis

(*a*) Positive large amplitude events

k	%Time	(err)	$\langle t \rangle$	(err)	Δt	(err)
0.0	50.87	(0.17)	20.66	(0.45)	10.10	(0.25)
1.0	33.57	(0.24)	48.02	(1.33)	15.56	(0.41)
2.0	10.47	(0.16)	164.9	(6.11)	16.54	(0.72)
3.0	2.15	(0.06)	724.5	(51.0)	14.58	(0.67)
4.0	0.47	(0.03)	2897.4	(280.7)	13.04	(0.92)
5.0	0.12	(0.02)	11454.	(3019.)	12.26	(0.79)

(*b*) Negative large amplitude events

k	%Time	(err)	$\langle t \rangle$	(err)	Δt	(err)
0.0	49.12	(0.17)	20.64	(0.44)	9.72	(0.22)
1.0	32.66	(0.24)	47.82	(1.77)	15.06	(0.48)
2.0	11.52	(0.24)	144.9	(6.53)	15.96	(0.79)
3.0	3.17	(0.16)	496.1	(31.6)	14.98	(1.33)
4.0	0.88	(0.07)	1640.0	(246.7)	13.64	(1.13)
5.0	0.26	(0.05)	4939.0	(938.9)	12.18	(1.45)

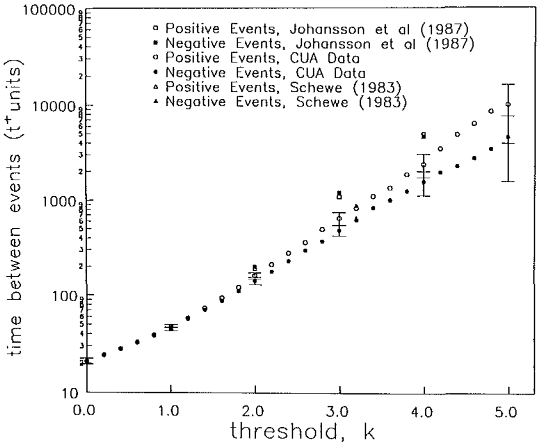

Fig. 7 The average time between large amplitude wall pressure events versus threshold for U_0 = 15.5 m/s. Error bars represent three standard deviations from the mean.

the statistical features of the duration of the events, and the time between events. The frequency of occurrence is defined as the reciprocal of the average time between events. For the purpose of this discussion, the 'time between events' is the time elapsed from the trigger point of one peak event to the next trigger point. The trigger point is defined as the time at which the signal exceeds the threshold condition. The time measurements are scaled on inner wall variables using the relationship

$$t^+ = \frac{tu_\tau^2}{\nu}.$$

The average duration of the events and the average "time between events" are tabulated in Table 3. This table contains separate information on both the positive and negative events. The average durations vary with threshold, but are approximately 10 to 16 viscous time units. There is negligible difference between the duration of the positive and negative events for calculations based on a large number of events. Schewe (1983) reported an average duration of 12 viscous time units. The present data are also consistent with the values obtained by Johansson et al. (1987).

As expected, the tabulated data show that the average value of the time between events increases with increasing values of the threshold for detecting events. For thresholds $k > 2$, the behavior appears to follow an exponential relationship as shown by the (approximate) linear fit using semi-logarithmic scaling in Fig. 7. The values obtained by Johansson et al. (1987) for thresholds of 1, 2, 3, and 4 as well as Schewe (1983) for a threshold of 3.2 are also included in the Fig. 7. The limited data points of Schewe are in agreement with the present data while the Johansson data show some variations. As the threshold increases beyond k = 2, the average time between negative events is consistently less than the time between positive events. A corollary to this observation is that there are significantly more negative peaks than positive peaks over the same time record for peaks whose amplitudes exceeded k = 2.

The time between events for sequentially detected positive and negative events having a threshold of k = 3 are shown in Figs. 8(*a*) and (*b*). For this figure, events exceeding a threshold of k = 3 are sorted by sign into positive and negative

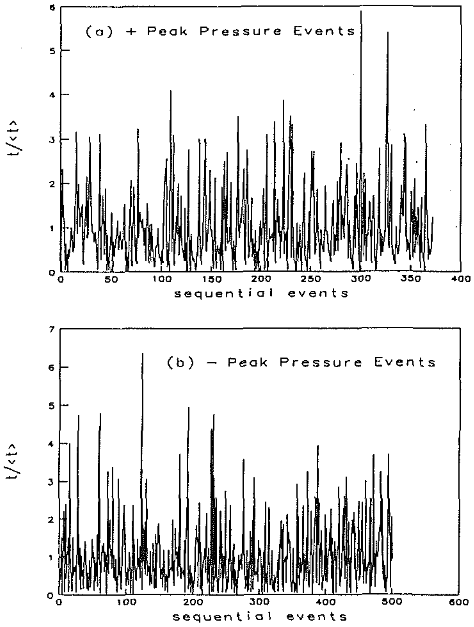

Fig. 8 Time between sequential events that exceed the 3 RMS value at U_0 = 15.5 m/s for: (*a*) positive events; (*b*) negative events

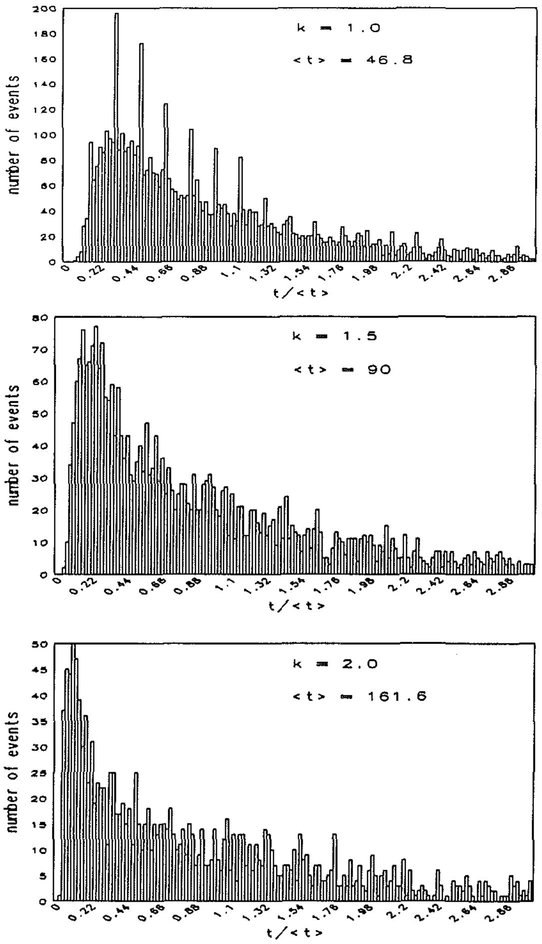

Fig. 9 Histogram of the distribution of time between positive large amplitude events at threshold values of 1.0, 1.5, and 2.0 for U_0 = 15.5 m/s

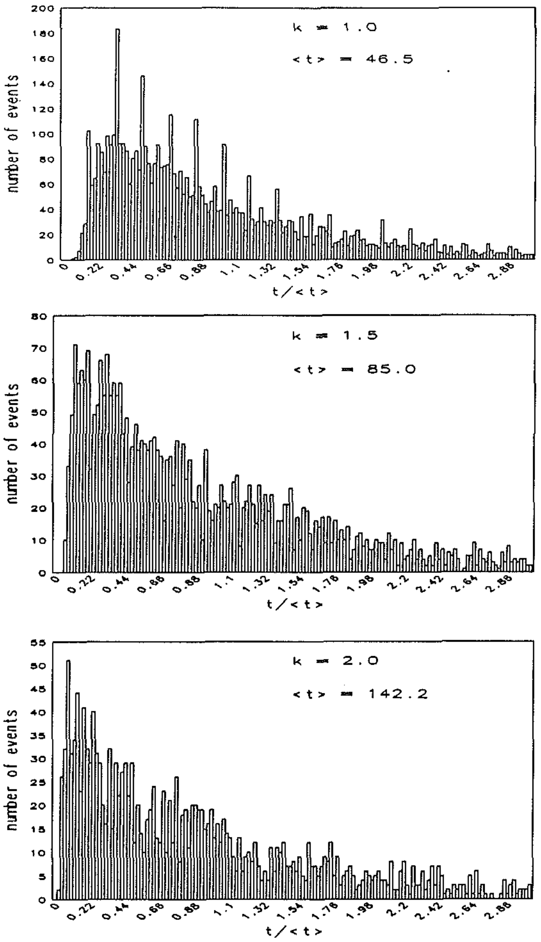

Fig. 10 Histogram of the distribution of time between negative large amplitude events at threshold values of 1.0, 1.5, and 2.0 at U_0 = 15.5 m/s

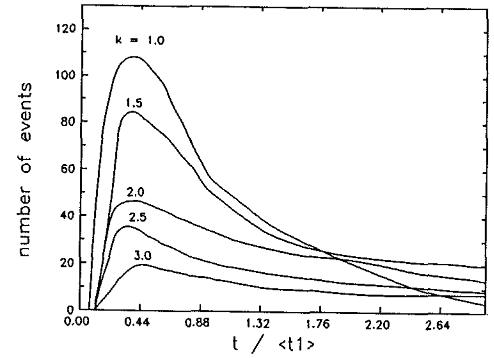

Fig. 11 Distribution of normalized time (re. ⟨*t*⟩ for the threshold *k* = 1) between negative peak pressure events for U_0 = 15.5 m/s

events and shown in their respective order of occurrence. As seen in the figures, there is no apparent order to the sequence of events. However, it does appear that several events below the average time occur prior to the occurrence of a long time delay between events. A preliminary examination of the relationship between positive and negative events revealed a pattern of 4 or 5 sequential negative events followed by a sequence of 3 or 4 positive events along the time record.

Histograms of the time between events for *k* = 1.0, 1.5, and 2.0 are shown in Figs. 9 and 10 for the positive and negative peaks, respectively. In each of the plots, the time between events has been normalized by the average value of time for that particular threshold. The results for higher values of *k* appear to follow the overall trend but were limited by the small sample size for the total number of events. Figure 11 is a composite histogram of the time between events for the negative peaks over a range of threshold. In this figure, the time for each data set was normalized by the average time for the $k = 1$ threshold. To a first approximation, the distributions of time between events appear to follow a family of lognormal distributions (Karangelen, 1991).

A (Gaussian) white noise temporal record, which was band-pass filtered over the same frequency range as the real data, was analyzed and compared to the actual data shown in Fig. 9. As expected, the Gaussian results produced an equal number of positive and negative events with a classical lognormal distribution for the time between events for both positive and negative data sets. For the threshold of $k = 2$, the relative peak location and histogram shape appeared similar to the real data. The details can be found in Karangelen (1991).

Some Concluding Remarks

The goal of this investigation was to obtain noise-free wall pressure data in a quiet flow facility and to extend the database on the statistical features of wall pressure fluctuations. In the course of analyzing the extensive data, several significant observations have been made.

- Digital samples of wall pressure fluctuations demonstrate non-gaussian statistics.
- Large amplitude wall pressure events are major contributors to the RMS; 49 percent of the RMS value comes from events whose normalized peak pressures exceed a threshold of three times the RMS value and occur only 5 percent of the time.
- Negative wall pressure events are seen to occur more frequently than positive events for all thresholds exceeding $k = 2$.
- The probability distribution of time between events demonstrates quasi-lognormal behavior.

In this study, the focus of attention was to examine the large amplitude wall events in order to gain some new insight on the coupling between intermittent near wall flow structures and the wall pressure events. It had been proposed by Haritonidis et al. (1990) that the *negative pressure events* are associated with *outward ejections and inward interactions* of low speed fluid, while *positive pressure events* are associated with the *sweeps* of high-speed fluid toward the wall.

As previously discussed, there is some controversy regarding a one-to-one correspondence between "bursting events" and the large amplitude wall pressure events (Eckelmann, 1990; Haritonidis et al., 1990). This correspondence implies that for every ejection and/or sweep event that occurs locally in the near wall flow, there is a corresponding and exclusive large amplitude event seen in the pressure signatures at the wall. It futher implies that one can use the pressure signal received at the wall to trigger the detection of the burst events within the flow. This question was further addressed by Wilczynski (1992) and it is not possible to explicitly answer it with the present results. However, the secondary question, of whether the frequency of occurrence of wall pressure events (or average time between events) correlates with the occurrence of organized flow events, may shed some light on this issue.

For channel flows, Tiederman (1990) detected burst events using velocity measurements in the flow. He reported an average time between burst events of 90, scaled on inner variables, and this value was seen to be independent of Reynolds number. For boundary layer flows, the time between events is reported to be closer to 300 (Blackwelder and Haritonidis, 1983 and Willmarth and Sharma, 1984). By using these values as upper and lower bounds, the average time between events corresponds to a range between $2 \leq k \leq 3$ on Fig. 7 and thus is consistent with the occurrence of large amplitude wall pressure events.

Though the present results cannot resolve the basic issues regarding a one-to-one correspondence between bursting events and large amplitude wall pressure fluctuations, the analyses of the database on wall pressure events support the conjecture that there is a distinct relationship between intermittent events in the flow and large amplitude wall pressure events. This work has also provided a framework to pursue concurrent measurements of the velocity and wall pressure fluctuations in an effort to better understand the relationship between turbulent structures and wall pressure fluctuations. The recent data acquired by Wilczynski (1992) are now under extensive analyses to resolve these issues. Some of these findings were reported at the ASME winter meeting (NCA-Vol. 13, pgs. 165–80) and will be submitted for publication.

Acknowledgments

This research was sponsored by the Office of Naval Research under Contract No. N00014-88-K-0141 and grant No. N00014-91-J-1925.

References

Alfredsson, P. H., and Johansson, A. V., 1984, "Time Scales in Turbulent Channel Flow," *Physics of Fluids*, Vol. 27, pp. 1974–1981.

Blackwelder, R. F., and Haritonidis, J. H., 1983, "Scaling of the Bursting Frequency in Turbulent Boundary Layers," *Journal of Fluid Mechanics*, Vol. 132, p. 87–103.

Blake, W. K., 1986, *Mechanics of Flow-Induced Sound and Vibration*, Vol. II, Academic Press, New York, NY.

Bogard, D. G., and Tiederman, W. G., 1986, "Burst Detection with Single Point Velocity Measurements," *Journal of Fluid Mechanics*, Vol. 162, pp. 389–413.

Eckelmann, H., 1990, "A Review of Knowledge on Pressure Fluctuations," *Near Wall Turbulence*, S. J. Kline and N. H. Afgan, eds., Hemisphere Publishing Corporation, New York, NY, pp. 328–347.

Farabee, T. M., and Casarella, M. J., 1991, "Spectral Features of Wall Pressure Fluctuations Beneath Turbulent Boundary Layers," *Physics of Fluids A*, Vol. 3, No. 10, pp. 2410–2420.

Haritonidis, J. H., Gresko, L. S., and Breuer, K. S., 1990, "Wall Pressure Peaks and Waves," *Near Wall Turbulence*, S. J. Kline and N. H. Afgan, eds., Hemisphere Publishing Corporation, New York, NY, pp. 397–417.

Helal, H. M. S., Casarella, M. J., and Farabee, T. M., 1989, "An Application of Noise Cancellation Techniques to the Measurement of Wall Pressure Fluctuations in a Wind Tunnel," ASME Winter Annual Meeting, Report No. H00563 NCA 5, p. 49.

Johansson, A. V., Her, J., and Haritonidis, J. H., 1987, "On the Generation of High-Amplitude Wall Pressure Peaks in Turbulent Boundary Layers and Spots," *Journal of Fluid Mechanics*, Vol. 175, pp. 119–142.

Karangelen, C. C., 1991, "Temporal and Spectral Features of Wall Pressure Fluctuations Beneath a Turbulent Boundary Layer," Ph.D. dissertation, The Catholic University of America.

Kim, J., 1989, "On the Structure of Pressure Fluctuations in Simulated Turbulent Channel Flow," *Journal of Fluid Mechanics*, Vol. 205, pp. 421–451.

Lu, S. S., and Willmarth, W. W., 1973, "Measurements of the Structure of the Reynolds Stress in a Turbulent Boundary Layer," *Journal of Fluid Mechanics*, Vol. 60, p. 481.

Schewe, G., 1983, "On the Structure and Resolution of Wall-Pressure Fluctuations Associated with Turbulent Boundary-Layer Flow," *Journal of Fluid Mechanics*, Vol. 134, pp. 311–390.

Sreenivasan, K. R., 1991, "Fractals and Multifractals in Fluid Turbulence," *Annual Review of Fluid Mechanics*, Vol. 23, pp. 539–600.

Tiederman, W. G., 1990, "Eulerian Detection of Turbulent Bursts," *Near Wall Turbulence*, S. J. Kline and N. H. Afgan, eds., Hemisphere Publishing Corporation, New York, NY, pp. 874–887.

Wilczynski, V., 1991, "Correlation Between Organized Flow Structures and Large Amplitude Events Beneath a Turbulent Boundary Layer," presented at the 44th Annual Meeting of the American Physical Society.

Wilczynski, V., 1992, "Organized Turbulent Structures and Their Induced Wall Pressure Fluctuations," Ph.D. dissertation, The Catholic University of America.

Willmarth, W. W., 1975, "Pressure Fluctuations Beneath Turbulent Boundary Layers," *Annual Review of Fluid Mechanics*, Vol. 7, pp. 13–38.

Willmarth, W. W., and Sharma, L. K., 1984, "Study of Turbulent Structure with Hot Wires Smaller than the Viscous Length," *Journal of Fluid Mechanics*, Vol. 142, pp. 121–149.

W. B. Brower, Jr.
Rensselaer Polytechnic Institute,
Troy, NY 12180

E. Eisler
Orbital Sciences Corporation,
Tempe, AZ 85283

E. J. Filkorn
United States Air Force,
Griffiss AFB, NY 13441

J. Gonenc
University of Connecticut,
Storrs, CT

C. Plati
Ossining, NY 10562

J. Stagnitti
General Electric Co.,
Schenectady, NY 12306

On the Compressible Flow Through an Orifice

A new theory for the compressible flow through an orifice is presented which provides a significant advance over the approach currently employed. As the flow approaches the critical regime (local sonic condition), measurements diverge from the theoretical result due to the non-one-dimensionality of the flow. Nevertheless, a straightforward correlation is available, and the measurements for different pipe/orifice geometries all appear to lie in the vicinity of a single, universal curve. As the flow approaches the incompressible condition the correlation factor (the discharge coefficient) becomes unity.

Introduction

The measurement of an incompressible mass-flow-rate by means of an orifice installed in a pipe was first developed by the Verein deutscher Ingenieure in 1912. It eventually was taken over to become the German 1952 Standard Orifice; see NACA TM 952 for the details. Referring to Fig. 1, if the properties of the fluid are known, and if the orifice is machined to the specifications therein, calculation of the flow rate depends only on the measurement of the static-pressure drop $\Delta p \equiv p_2 - p_3$ across the orifice plate, and a discharge coefficient C, which is obtained from a universal plot provided in the same reference. The discharge coefficient is plotted as a function of the upstream Reynolds number and the orifice/pipe area-ratio $A_2/A_1 \equiv A_{21}$.

As indicated in the figure, the flow separates from the orifice contour and becomes a free jet where the static pressure on the jet boundary is equal to that of the bounding fluid in the surrounding plenum. A short distance downstream (typically a few pipe diameters) of the orifice the jet area becomes a minimum, and the local flow becomes (nearly) uniform. The expression for the mass rate-of-flow is

$$\dot{m} = C\rho A_2 \sqrt{2\Delta p/\rho}.$$

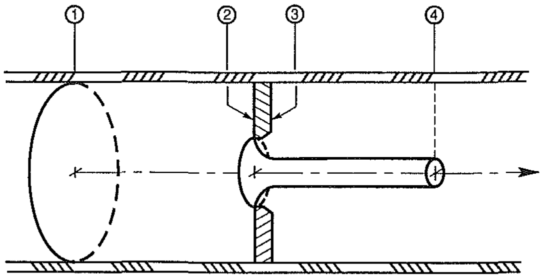

Fig. 1 Schematic of gas flow through an orifice

The introduction of the discharge coefficient bypasses the fact that there is no theory linking the plenum pressure $p_3 = p_4$[1] bounding the jet, with the jet minimum-area A_4, and the orifice area $A_2 = A_3$. The plot is made with C as ordinate, and with the upstream Reynolds-number as abscissa. It incorporates a series of curves with the area ratio A_{21} as parameter. As a practical matter the value of the discharge coefficient for any fixed value of A_{21} is constant if the Reynolds number is sufficiently high, and gradually increases as the Reynolds number decreases.

In the case of the flow of a perfect gas the problem is more

Contributed by the Fluids Engineering Division for publication in the JOURNAL OF ENGINEERING FOR FLUIDS. Manuscript received by the Fluids Engineering Division March 16, 1992; revised manuscript received June 7, 1993. Associate Technical Editor: R. L. Panton.

---

[1] One reviewer of this paper questioned our claim that the pressure on the back face of the orifice, measured by an annular array of pressure taps, was in fact equal to the plenum pressure. We made hundreds of measurements of the difference of these two pressures, for a variety of orifice geometries, and never found any significant deviations from zero.

complex. The method chosen to deal with this was to modify the preceding incompressible-flow formula by the introduction of a second multiplier, called the expansion factor, which depends on the area ratio A_{21}, the static-pressure ratio $p_3/p_2 \equiv p_{32}$, the ratio of specific heats, and an empirical contraction factor which relates to the sharpness of the orifice machined-edge. The density to be used for a gas is the static density at station 1. For a given pipe/orifice geometry the latter value tends to decrease as the flow rate increases; it is thus a variable. Consequently, some means must be provided for calculating it. The most straightforward way is to measure the local static-pressure and static-temperature, both of which are variables. The desired density is then calculated from the equation of state. Furthermore, one must still calculate the upstream Reynolds number to be able to compute the discharge coefficient. Since this is not known in advance an iterative calculation must be performed. The theory is limited to subcritical flow.

Objectives of the Current Study

If station 1 is not too far upstream of the orifice, we can expect viscous flow-losses between stations 1 and 4—unlike the case of a venturi where the rapidly moving portion of the flow is bounded by a solid wall—to be small. This is not to say, as the jet downstream of station 4 expands to fill the pipe, that significant viscous losses will not eventually result. Thus, in the current work we seek a new theory which is based (principally) on inviscid one-dimensional flow relations. It is also our objective to obtain a simple expression which can be used in the supercritical regime.

To achieve this, it is our contention that it is greatly preferable to employ, rather than the static-pressure drop across the orifice $\Delta p \equiv p_2 - p_3$, the relationship between the total-pressure $p_1^0 \equiv p^0$, just upstream of the orifice, and the downstream static-pressure p_4, which will appear in terms of the ratio p_4/p^0. This choice, it will be seen, leads to a substantial simplification over earlier approaches.

A Note on Previous Work

Various authors, starting early in this century, have undertaken the analysis of this flow with varying amounts of success. One of the more successful is due to Cunningham (1951)[2] in which he utilizes a one-dimensional theory which incorporates the momentum equation. In spite of the fact that it depends on one unverified assumption[3] and, additionally, on the assumption that the pressure at the minimum area in supercritical flow can be taken as uniform over a section and equal to the plenum pressure, his data points lie close to his theoretical expression in the two cases presented. Cunningham chooses the static-pressure ratio (in the current notation p_4/p_1), as the independent variable, which makes for more awkward algebra than with the ratio p_4/p^0 used herein. In his principal finding he compares the theoretical contraction-ratio $A_4/A_2 \equiv A_{42}$ (current notation) with experiment, and finds good agreement, although there is no explanation of how the experimental jet-area A_4, at the station where the flow is thought to be sonic, was determined. Unfortunately the failure to report his results in the form of a discharge coefficient has limited the utility of the work.

Proposed Theory

A principal novelty of the current work is the introduction of a theoretical model of the flow from the orifice, station 2, where the flow is clearly not one-dimensional, to station 4, where the flow is presumed to become (almost) uniform, a condition which is realized, in fact, only in sub-critical flow.

The Relations of Compressible Flow. At station 1, which is presumed to be at most a few diameters upstream of the orifice, the flow is also treated as uniform. The restrictions of steady, isoenergetic, inviscid (and thus isentropic), perfect-gas flow are imposed. Under these restrictions the flow total-conditions T^0, p^0, ρ^0, as well as $\dot m$, are constant throughout.

For the mass rate-of-flow we have

$$\dot m = \rho_4 u_4 A_4 = \frac{\rho_4}{\rho^0}\frac{u_4}{a_4}\frac{a_4}{a^0}\rho^0 a^0 A_4. \tag{1}$$

The isentropic condition yields

$$\rho_4/\rho^0 = (p_4/p^0)^{1/\gamma} = (a_4/a^0)^{2/(\gamma-1)}. \tag{2}$$

Therefore,

$$a_4/a^0 = (p_4/p^0)^{(\gamma-1)/2\gamma}, \tag{3}$$

$$\rho_4 a_4/\rho^0 a^0 = (p_4/p^0)^{(\gamma+1)/2\gamma}. \tag{4}$$

From the compressible-flow energy equation:

$$a^{02} = a_4^2 + \frac{\gamma-1}{2}u_4^2. \tag{5}$$

Combining (5) with (2), with p_4/p^0 as the independent variable,

$$\frac{u_4}{a_4} = \left(\frac{2}{\gamma-1}\left(\left(\frac{p^0}{p_4}\right)^{(\gamma-1)/\gamma} - 1\right)\right)^{1/2}. \tag{6}$$

Substitution of (4) and (6) into (1) produces an expression for the theoretical mass-flow-rate:

$$\dot m_t = \left(\frac{2}{\gamma-1}\left(\frac{p_4}{p^0}\right)^{2/\gamma}\left(1-\left(\frac{p_4}{p^0}\right)^{(\gamma-1)/\gamma}\right)\right)^{1/2}\rho^0 a^0 A_4. \tag{7}$$

Note in (7), if we introduce the equation of state for a perfect gas $p = \rho R T$ and the expression for the total speed-of-sound $a^0 = (\gamma R T^0)^{1/2}$, we have the combination

$$\rho^0 a^0 = p^0(\gamma/RT^0)^{1/2}, \tag{8}$$

a form which is more readily computed from direct measurement.

---

[2] Cunningham gives several of the early references.

[3] *He assumes, following Buckingham (1931), that the unknown force on the orifice plate can be calculated by comparing it to a fictitious, incompressible flow of the same mass-flow-rate.*

Nomenclature

A = cross-sectional area of a duct
a = speed of sound
C = discharge coefficient
D = duct diameter
M = Mach number
$\dot m$ = mass rate-of-flow
p = pressure
$\dot Q$ = volume rate-of-flow
R = gas constant
u = flow speed
γ = ratio of specific heats
ρ = density

Superscripts

o = denotes total (stagnation) conditions
* = denotes sonic condition

Subscripts

a = denotes actual
t = denotes theoretical
1, 2, 3, 4 = denote flow stations in duct

Busemann's Relation for the Contraction Coefficient of a Free Jet. There is no closed-form theoretical expression available for the contraction coefficient of a jet in axi-symmetric, compressible flow. However, for the corresponding two-dimensional, planar case by use of conformal mapping in the hodograph plane, Busemann (1937)[4] obtained the following exact result:

$$\frac{A_4}{A_2}=\frac{\pi}{\pi+2\rho_4/\rho^0}. \tag{9}$$

The one-dimensionality of the flow at station 4 is, of course, attained theoretically only infinitely far downstream. In fact, at the station several duct-opening widths downstream, the jet thickness differs little from its asymptotic value. We caution that (9) is strictly valid only in the limit of an infinite upstream plenum, i.e., for the case when $A_{21}\to 0$. It is further restricted to flow speeds in the jet not greater than sonic.

To apply a planar-flow relation to axisymmetric flow needs some justification, not to mention verification. We first note from (9), that in the case of incompressible flow, where $\rho_4/\rho^0\to 1$,

$$\lim_{\rho_4/\rho^0\to 1}\frac{A_4}{A_2}=\frac{\pi}{\pi+2}=0.6110. \tag{10}$$

Thus Busemann's expression reduces to the classical result of Kirchhoff (1869) for an infinite plenum, also obtained by the method of conformal mapping.

For the axisymmetric case, the earliest result is due to Garabedian (1956) using some fierce mathematics. He obtained

$$\frac{A_4}{A_2}=0.5793. \tag{11}$$

His student Bloch (1967), using the method of steepest descent in a computerized numerical solution, found that

$$\frac{A_4}{A_2}=0.59135\pm 0.00004. \tag{12}$$

The exact axisymmetric value for A_{42} in incompressible flow is thus only three percent less than the exact two-dimensional value.

It therefore seems plausible that we can apply Busemann's expression to the axisymmetric, compressible flow with a reasonable prospect that resulting errors should be minor. We must, however, in an actual flow, be prepared for the possibility that the discharge coefficient (defined below) may be dependent on the orifice/pipe area-ratio A_{21}.

Thus, combining (7), (9), and (2), our final expression for the theoretical mass-flow-rate is

$$\dot{m}_t=\left(\frac{2}{\gamma-1}\left(\frac{p_4}{p^0}\right)^{2/\gamma}\left(1-\left(\frac{p_4}{p^0}\right)^{\frac{\gamma-1}{\gamma}}\right)\right)^{1/2}\times\left(1+\frac{2}{\pi}\left(\frac{p_4}{p^0}\right)^{\frac{1}{\gamma}}\right)^{-1}\rho^0 a^0 A_2. \tag{13}$$

There is a hidden pitfall. Equation (13) has a certain similarity to the corresponding relation for the flow through a deLaval nozzle. However, unlike a fixed nozzle, where a maximum flow-rate is established as soon as the critical pressure is established in the throat, a free jet will respond to pressures lower than critical. Experiments on orifice flow by Perry (1944)[5] have shown that as the downstream-pressure decreases, the flow rate (and, effectively, the area A_4) gradually increases.

A comprehensive theoretical study by Alder (1979) of the flow through an orifice from an infinite upstream plenum clearly delineates the reasons why the flow rate continues to increase. Downstream of the minimum area the jet becomes supersonic. Furthermore, the jet boundaries expand everywhere to adjust to the lower pressure, thus producing a higher flow-rate. We would not expect the related problem of finite upstream and downstream plenum boundaries to affect these qualitative conclusions. It is worth noting that the condition used by Alder to locate the jet boundary is precisely the condition used in this work that $p_3=p_4$. It turns out, when the pressure downstream is lower than critical, that the location of the jet minimum-area moves closer to the orifice station as the plenum pressure continues to decrease. Furthermore, the flow at this station is not uniform. The flow is extremely complex, and there appears to be no rational way of representing it by one-dimensional theory.

The critical pressure p^* is given by

$$\left(\frac{p^*}{p^0}\right)=\lim_{M_4\to 1}\left(\frac{p_4}{p^0}\right)=\left(\frac{2}{\gamma+1}\right)^{\frac{\gamma}{\gamma-1}}, \tag{14}$$

where $p^*/p^0 = 0.528$ for $\gamma = 7/5$ (i.e., for air).

A Computational Rule. To illustrate the absurdity of attempting to compute the flow rate by substituting a supercritical pressure in (13), we note in the limit as $p_4/p^0\to 0$, that $\dot{m}\to 0$. We therefore propose the following rule for the application of (13): for $1>p_4/p^0\geq p^*/p^0$, Eq. (13) shall be used as written, for computing the flow rate. For $0 \leq p_4/p^0 < p^*/p^0$, we replace the unknown value of $\dot{m}_t$ by a reference value, $\lim_{p_4\to p^*}[\dot{m}_t]\equiv\dot{m}_{t\max}$, which is the maximum value of the theoretical mass rate-of-flow in the sub-critical regime. Thus

$$\dot{m}_{t\max}=\left(\frac{2}{\gamma+1}\right)^{\frac{\gamma+1}{2(\gamma-1)}}\left(1+\frac{2}{\pi}\left(\frac{\gamma}{\gamma+1}\right)^{\frac{1}{\gamma-1}}\right)^{-1}\rho^0 a^0 A_2, \tag{15a}$$

$$=0.4123\rho^0 a^0 A_2,\ \text{for } \gamma=7/5. \tag{15b}$$

There is no suggestion, for downstream pressures less than the critical value, that the flow rate has become constant. On the contrary, it continually increases as the pressure decreases. However, as Alder has conclusively shown, supercritical flow downstream of the orifice cannot be represented by any one-dimensional model. Therefore we choose simply to replace $\dot{m}_t$ over the entire supercritical regime by its initial value when $p_4=p^*$. The error incurred thereby is overcome by correlating the discharge coefficient with experiment, a common-enough technique.

Definition of the Discharge Coefficient. We define the discharge coefficient as the ratio of the actual, to the theoretical mass-flow-rate, i.e.,

$$C=\dot{m}_a/\dot{m}_t. \tag{16}$$

In calculating C, $\dot{m}_t$ is replaced by $\dot{m}_{t\max}$ in the supercritical regime. We recognize the possibility that C may be dependent on the orifice/pipe area ratio A_{21}.

The Experimental Setup

Our measurements were made in the RPI gas-dynamics inflow-facility using a specially fabricated test-section sketched in Fig. 2. The two test-sections employed were fabricated from either copper or plastic pipe-segments which join together through flanges. Two sizes of pipe were employed, nominally 2 in. (copper), and 4 in. (plastic) in diameter, respectively. The actual dimensions are $D_2=2.033$ in (5.164 cm), and 3.790 in. (9.627 cm), respectively. The inlets were turned from wooden blocks, custom fitted to provide a smooth transition to each

---

[4] Cunningham (1951, p. 634) refers to a group of earlier efforts, including two by Busemann, to compute the contraction coefficient of a compressible jetflow.

[5] Actually a number of earlier researchers had established this flow behavior years earlier. See Cunningham (1951) for some of the references.

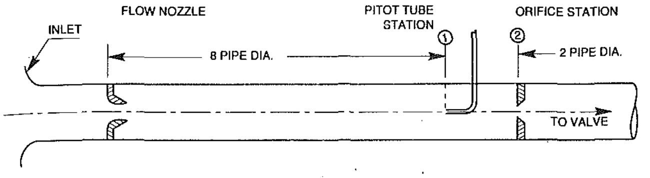

Fig. 2 Schematic of test facility

pipe inside-diameter. About 10 diameters downstream from the inlet a specially machined flange allows for the installation of interchangeable, custom-made VDI flow-nozzles of different outlet diameters which were employed to measure the actual flow rates. In general the flow-nozzle used had an exit diameter sufficiently large that compressibility effects in the flow nozzle were avoided in calculating the actual flow rate. The calibration curves were verified by pitot-tube field surveys downstream of the nozzles.

About eight diameters further downstream a mount is provided for a commercial pitot-static tube which is the station for the measurement of the local total-pressure p^0 upstream of the orifice. Our measurements showed that the local value was only slightly smaller than the atmospheric value at the inlet. The decrease reflects flow losses due to the inlet, the flow nozzle, and the pipe.

The orifice station is located ten diameters downstream from that of the flow-nozzle. The flanges are fitted with pressure taps, arrayed in an annulus, so that the values are effectively averaged to produce the pressures p_2 and p_3, as required. The flanges also accommodate interchangeable orifice plates which are fabricated to ISO (formerly VDI) standards. A ball valve is located about ten diameters beyond the orifice station to regulate the flow. Several diameters ahead of the ball valve a second pitot-static tube is located to provide the downstream static-pressure p_4. It also provides a capability for measuring the total-pressure drop through the orifice, if desired. All pressure measurements were made with manometers, using either water or mercury as fluid. For at least one run the flow rate was sufficiently high that it was necessary to use a second ball-valve further downstream, which is a part of the permanent piping-system leading to the vacuum pumps, in order to obtain the necessary sensitivity to increment the flow rate.

The flow is maintained with a bank of five vacuum pumps, each rated at 100 cfm, which empty a vacuum reservoir of about 2300 ft^3 (65 m^3) downstream of the test rig. Consequently, the inlet total-pressure and temperature are always essentially the local atmospheric values. Due to the inability to adjust the inlet total-conditions, systematic studies on the effects of varying the upstream Reynolds number for a specific orifice/pipe geometry are not possible. Consequently, for a given orifice/pipe geometry, where the flow rate varies from the no-flow condition to the maximum attainable with the set up, the Reynolds number changes with every data point, increasing with the flow rate.

Note on Experimental Difficulties. The original (and over-optimistic) plans were to test a substantial number (6 or 7) of orifices for each pipe size. As it turned out the number of useful data runs is rather smaller than planned. For the case where the flow-nozzle diameter was only slightly larger than the orifice, compressibility effects in the flow nozzle were experienced, and mass-flow-rate measurements became inaccurate. If the flow-nozzle diameter was (relatively) too large then the sensitivity became so small that useful measurments of the flow rates could not be obtained over the whole range of the run.

If the orifice diameter was too small, in the absolute sense, the actual flow-rate was so low that the Reynolds number upstream of the flow nozzle fell below the minimum value 10^4 at which the VDI flow-nozzle is calibrated. On the other hand, if the orifice diameter was too large (particularly in the 4-inch pipe), then the pumps could not handle the larger flow-rates capable of being passed by the orifice, and the low pressures in the downstream plenum necessary to obtain the higher flow-rates could not be maintained.

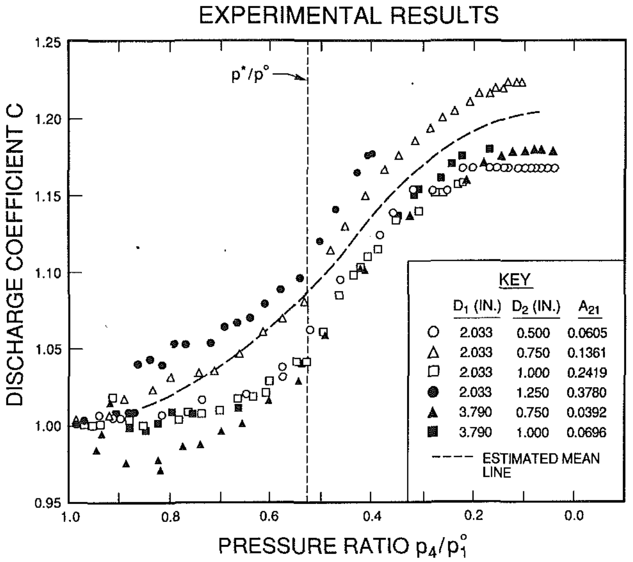

Fig. 3 Plot of discharge-coefficient C versus p_4/p^0 for various values of A_{21}

The consequence of these limitations is that we are restricted to presenting results for only four orifices in the two-inch pipe (D_2 = 0.500, 0.750, 1.000, and 1.250 inches), and two in the four-in. pipe (D_2 = 0.750 and 1.000 in.)

Experimental Results

All reported results are contained in Fig. 3. As previously indicated, we believe that the appropriate variable on which to correlate the data is the pressure ratio p_4/p^0. The upstream Reynolds number is different for every data point for a given run. For completeness, however, we note that the range of Reynolds numbers in the two-inch pipe was from 5.3×10^3 to 1.9×10^5. In the four-inch pipe the range was from 3.05×10^3 to 6.8×10^4.

It is apparent that each set of points for a fixed value of A_{21} defines a unique curve. A mean line has been drawn in arbitrarily such that the great majority of data points lies within the band of $\Delta C = \pm 0.04$ from the mean line. Several reviewers have correctly noted that the plot of the various curves is not monotonic with variations in the orifice/pipe area-ratio A_{21}. The principal offender is the curve for $A_{21} = 0.2419$ which should lie between the pair of curves above the faired line to maintain monotonicity. A review of the data has not revealed any explanation for this fact. More encouraging is the fact that the curve for $A_{21} = 0.0605$ in the two-inch test-section and the curve for $A_{21} = 0.0696$ in the four-inch test-section fall almost on top of each other.

Our finding that the flow rate increases continuously as the pressure ratio p_4/p^0 decreases confirms the work of earlier investigators. Furthermore, the discharge coefficient C increases similarly, and the initiation of the rise is evident well before the critical pressure-ratio p^*/p^0 is reached. We attribute the probable reason for this rise to interaction of the flow just upstream of the orifice station with the jet immediately downstream of the orifice, as it experiences the onset of supersonic flow. This is another indication that the one-dimensional flow equations have been put to a substantial test in this application. It is not likely that other one-dimensional modifications applied to the current theory will result in substantial improvements.

The data points at the left end of the plot exhibit the greatest scatter. This is the region of the lowest flow rates, where a small deviation in the absolute value of a measured pressure-difference shows up as a relatively large change in the calculated value of the corresponding flow rate. In the limit as $p_4/p^0 \rightarrow 1$, $C \rightarrow 1$. The limiting case corresponds to incompressible flow, and the preceding equations reduce to a very simple expression for the incompressible-flow analog of (13). This expression is omitted since we have not conducted any measurements in a liquid flow.

On the right side of the plot, anomalies appear where several of the curves become horizontal. It is our belief this indicates that the flow has become choked somewhere in the system which consequently will not accept higher flow rates.

We have previously noted it is possible that the correlation of the discharge coefficient C may involve dependency on the parameter A_{21}. If there is such dependency it appears to be small. The acquisition of the data presented required us to push the capabilities of our test-facility to its limits, and we must leave further refinement to experimenters who have facilities with greater capabilities.

Thus there remains a need for comprehensive independent verification over a wide range of the parameter A_{21}. Furthermore, to increase the range of the test Reynolds number one must have a pressurized facility, or use a different gas. It is our contention that, to the first approximation, and for Reynolds numbers within our test range, viscous effects may be neglected.

Conclusions

1. For the first time known to the authors, a formula (Busemann's formula, Eq. (9)]) has been provided which provides a simple expression for the contraction coefficient for an axi-symmetric subcritical jet emitted from an orifice. Although the formula was derived for planar jet-flow from a slit, our measurements provide (indirect) evidence that it can be applied to axi-symmetric flow with only modest error, at worst.
2. Within the range of Reynolds number of our measurements, it is clear that viscous effects play but a small, probably negligible role in orifice flow.
3. It is shown that the appropriate parameter to employ as independent variable in correlating the mass-flow-rate is the ratio of the downstream plenum static-pressure to the total pressure just upstream of the orifice. Use of this variable reduces, and perhaps eliminates, the need to introduce the ratio of the orifice-area to the pipe-area as a parameter.
4. Use of the theory allows a correlation of our experimental values for mass-flow-rate in terms of a discharge coefficient, where almost all of the experimental points lie within $\Delta C = \pm 0.04$ of a universal curve (an estimated mean line). This correlation includes the entire range of downstream pressures, including both subcritical and supercritical flows.
5. We recommend independent verification of our measurements to eliminate possible uncertainties, and to extend the range of Reynolds number for which our results apply.
6. The authors believe that the new theory represents the ultimate use of one-dimensional theory to analyze gas flow through an orifice. Due to the essential non-one-dimensionality of the jet in orifice flow, as shown by Alder (1979), more sophisticated techniques must be employed if further improvements are sought.

Acknowledgment

The writers wish to thank Professor Joseph H. Smith, former Assistant Dean of Engineering at Rensselaer Polytechnic Institute, for providing financial support in acquiring and constructing the equipment and models used in this study.

References

Alder, G. M., 1979, "The Numerical Solution of Choked and Supercritical Ideal Gas Flow Through Orifices and Convergent Conical Nozzles," *Jour. Mech. Eng. Sci.*, Vol. 21, No. 3, pp. 197–203.

Bloch, E., 1967, "Numerical Solution of Free Boundary Problems by the Method of Steepest Descent," *Physics of Fluids*, Supplement II, Vol. 12, pp. 129–132.

Buckingham, E., 1931, "Note on Contract Coefficients for Jets of Gas," US Bureau of Standards Journal of Research, Vol. 6, p. 765.

Busemann, A., 1937, "Hodographenmethode der Gasdynamik, "*Zeitschrift f̈ r̈ angewandte Math. und Mech.*," Vol. 17, No. 2.

Cunningham, R. A., 1951, "Orifice Meters With Supercritical Compressible Flow," Trans. ASME, Vol. 73, p. 625.

Garabedian, P., 1956, "Calculation of Axi-symmetric Cavities and Jets," *Pacific Journal of Mathematics*, Vol. 6, pp. 611–684.

Kirchhoff, G., 1869, "Zur Theorie freier Flussigkeitstrahlen," *J. Reine Angewandte Math.*, Vol. 70, p. 289.

NACA TM 952, 1940, "Standards for Discharge Measurement with Standardized Nozzles and Orifices," German Industrial Standard 1952, translated from the Geman Fourth edition, VDI-Verlag, GmbH, Berlin 1937.

Perry, J. A., 1949, "Critical Flow Through Sharp-Edged Orifices," *Trans.* ASME, Vol. 73, p. 625.

Acoustic Properties of Solid-Liquid Mixtures and the Limits of Ultrasound Diagnostics—I: Experiments

(Data Bank Contribution*)

C. M. Atkinson

H. K. Kytömaa

Department of Mechanical Engineering,
Massachusetts Institute of Technology,
Cambridge, MA 02139

Ultrasound as a technique for interrogating two-phase mixtures has the advantages of being nonintrusive, it has a very high frequency response, and is able to penetrate typically opaque highly concentrated mixtures. There exists, however, an inherent compromise in the choice of the frequency of the ultrasound between maximizing spatial resolution and ensuring adequate beam penetration. To this end, the propagation of ultrasound in solid-liquid mixtures has been investigated experimentally for a range of frequencies and concentrations of the dispersed phase. The measured attenuation has been shown to depend roughly linearly on frequency for $0.1 < kr < 0.75$ *(where the wavenumber* $k = 2\pi/\lambda$*, and* λ *and* r *are the wavelength and particle radius, respectively), and quadratically for* $kr > 0.75$*. As a function of solids concentration, the attenuation displays a maximum at a solids fraction of about 30 percent for the present system of silica beads in water. This robust and reproducible result contradicts models of attenuation that rely on linear superposition of single particle effects. The intensity field produced by a circular disk transducer in a two phase medium at* $kr \sim 1$ *shows excellent agreement with the Rayleigh integral with a modified wavenumber and attenuation parameter, and it allows for the prediction of the transducer beam geometry in two phase mixtures for a wide range of frequencies and solids fractions. The limitations of ultrasonic wave propagation as a nonintrusive diagnostic technique, in terms of spatial resolution, have been discussed. Acknowledging these limitations, an ultrasonic instrument for determining the velocity of moving particles at or near maximum packing was built. Preliminary results from this prototypical ultrasonic Doppler velocimeter show good agreement with observations of the settling velocity of silica beads at high concentrations.*

1 Introduction

Highly concentrated solid-liquid mixtures are encountered in a number of chemical and transport processes, such as the transport of slurries, drilling muds, pastes, concrete, and polymer melts. Flows of such mixtures are often susceptible to blockages and bridging, and are typically difficult to monitor and control. These problems have motivated the development of nonintrusive diagnostics to describe the internal mechanics of these flows. In this paper the use of ultrasound in flowing or static multiphase mixtures is addressed as a means of monitoring internal flow properties. Ultrasound (typically in the range of tens of kilohertz to several megahertz) has several distinct advantages over other methods of measurement in the investigation of highly concentrated mixtures. It is truly nonintrusive (unlike resistive or capacitive point probes such as those described by Shook et al., 1982, or Hsu et al., 1989), it has an inherently high frequency response, and can thus be used for the measurement of dynamic or transient phenomena; it can penetrate highly concentrated and optically opaque mixtures (unlike laser Doppler anenometry or other optical techniques which require index of refraction matching, as described by Yianneskis and Whitelaw (1984)) and it has the capability of providing good spatial resolution. Acoustic wave propagation has been used for some time in the measurement of single phase flowrates (for in vivo blood flow measurements (McLeod, 1967)) and in low concentration two phase mixtures (Hilgert and Hofmann, 1986). Several proprietary devices are available that measure fluid velocities in predominantly single phase systems, such as water pipelines (cf. Controlotron Cor-

---

*Data have been deposited to the JFE Data Bank. To access the file for this paper, see instructions on p. 794 of this issue.

Contributed by the Fluids Engineering Division of THE AMERICAN SOCIETY OF MECHANICAL ENGINEERS and presented at the ASME-JSME 4th International Symposium on Liquid Solid Flow, Portland, OR, June 24-26, 1991. Manuscript received by the Fluids Engineering Division February 20, 1991; revised manuscript received September 18, 1992. Associate Technical Editor: E. E. Michaelides.

poration, Nusonics and Texas Nuclear); these devices are also considered suitable for measurements in suspensions with low solids loading. These devices infer fluid velocity by measuring the Doppler shift scattered from particles moving along with the fluid.

Acoustic wave propagation as a nonintrusive technique has certainly not been used to its full potential in highly concentrated mixtures, due mainly to the difficulties posed by signal attenuation. There exists an inherent compromise in the selection of operating frequency for an acoustic device between the need to minimize the wavelength for better spatial resolution, and maximizing the wavelength for better penetration of such mixtures. To this end, experiments were carried out to determine the acoustic characteristics of solid-liquid mixtures as a function of solids fraction and frequency. Based on these findings, we delineate the distinct advantages of acoustics as a method of interrogating these mixtures, and the limitations of the technique. The mechanics of sound production by a circular disc transducer and its propagation in a single phase medium are reviewed, and based on the experimental findings, the theory is extended to attenuating monodisperse solid-liquid mixtures. We show that the judicious choice of the frequency and other operating parameters allow the use of acoustic wave propagation for the measurement of particle concentration and velocity in systems of particles up to the maximum packing concentration. Based on these findings a prototype Doppler velocimeter was constructed. Preliminary measurements of particle velocity in a sedimenting system, using this device, are presented for very high solids concentration.

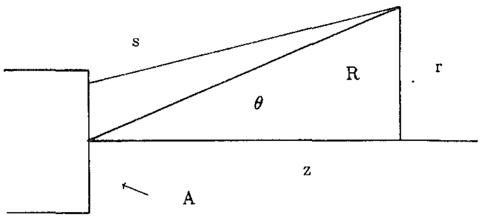

Fig. 1 The geometry of the intensity field due to a plane piston transducer

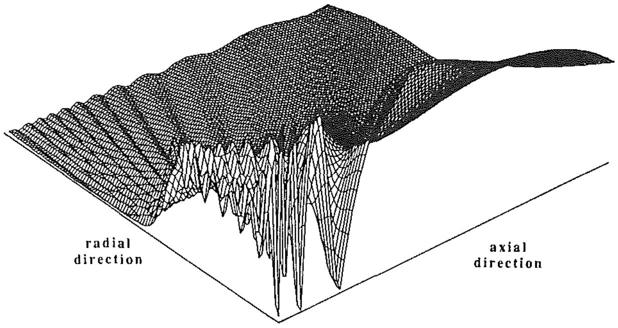

Fig. 2 One half of the radially symmetrical intensity profile for a plane piston transducer, calculated using the Rayleigh integral (Eq. (1)), with $ka = 40$. In this isometric view, the axial direction, which has a total length of 10x the transducer radius, is angled to the right. The radial direction is to the left in this square domain. The intensity goes through several maxima in the near field, and then decreases as $1/x^2$ in the far field, as well as falling off sharply in the radial direction.

2 The Theory of Linear Acoustics—A Review

The experimental study utilizes a flat, unfocussed ultrasonic transducer; it is therefore appropriate to first outline the characteristics of the acoustic field eminating from such a transducer in a pure fluid. A more complete review of the classical theory may be found elsewhere (see, for example, Morse and Ingard, 1978). If a circular planar piston transducer is induced to vibrate, it will cause sound to be radiated into the medium in which it is immersed. All points on the face of the piston act as monopoles oscillating in phase with one another. Away from the piston face, the monopole fields interfere both constructively and destructively. By linear superposition, the velocity potential $\phi(\mathbf{x},t)$ at any point in the fluid is given by the Rayleigh integral (Morse and Ingard, 1978):

$$\phi(\mathbf{x},t) = \int_A u \frac{e^{-iks}}{2\pi s}\, dA, \tag{1}$$

where $\mathbf{x}$ is the position vector of the target point, u is the velocity distribution across the face of the transducer, s is the distance from each point on the face of the transducer to the target, k is the wavenumber, and A is the area of the emitting surface, as indicated in Fig. 1. The velocity, $\mathbf{u}$, of the fluid at any point is given by $\mathbf{u} = \nabla\phi$, where ϕ is the velocity potential. The acoustical pressure deviation from the undisturbed datum, p_0, is given by $p' = i\rho_0\omega\phi$, where ρ_0 is the datum fluid density (Temkin, 1981). The Rayleigh integral has been simplified and evaluated in approximate analytical forms by numerous investigators (cf. Adach and Chivers, 1990; Goodsitt et al., 1982; Harris, 1981). Here it is integrated numerically and the radially symmetric intensity profile, normalized with respect to the maximum value, is shown in Fig. 2 for the case $ka = 40$, where a is the transducer radius (the profile shown is actually one-half of the radially symmetric profile). The acoustic field has the following characteristics. The amplitude goes through a number of local maxima and minima in the near-field or Fresnel region while far from the piston face, the amplitude decays monotonically (as $1/x^2$). In the intermediate region between the near and far fields, the intensity of the sound wave goes through a final maximum at the point of natural focus of the transducer. The distance from the transducer face to this point is referred to as the natural focal length, in reference to the (analytically) similar case in geometrical optics. In the far-

Nomenclature

a = transducer radius
A = transducer area
c = sound speed
f = frequency
$H(\omega)$ = frequency response transfer function
i = $\sqrt{-1}$
k = wavenumber (complex)
L = penetration depth or distance
p = acoustic pressure
r = particle radius
R = distance from center of transducer
s = distance from transducer face
t = time
T = period
$\mathbf{u}$ = fluid velocity
V = signal amplitude
$\mathbf{x}$ = position vector
α = attentuation parameter
κ = bulk modulus
λ = wavelength
μ = viscosity
∇ = gradient
ω = frequency
ϕ = velocity potential
ρ = density

Subscripts

eff = effective
f = liquid
p = particle
Re = real part
s = solid
trans = transmitted
0 = ambient

Superscripts

$\underline{\ }'$ = perturbation
$\bar{\ }$ = bulk medium property

field, the transducer beam intensity is a maximum along its axis and falls off with increasing radial distance from the center axis. The Rayleigh integral is sufficiently general to describe the acoustic field due to a transducer of any geometry oscillating with an arbitrary velocity distribution, as was demonstrated for a focussed transducer by O'Neil (1949).

3 Acoustic Wave Propagation in an Attenuating Medium

In an attenuating medium, the wavenumber of a propagating acoustic wave, k, is generally complex and involves the angular frequency of oscillation, ω, the sound speed, c, and the frequency dependent attenuation parameter, $\alpha(\omega)$, which is unique to the medium concerned,

$$k=\frac{\omega}{c}-i\alpha(\omega)=k_{\mathrm{Re}}-i\alpha(\omega). \tag{2}$$

Several theories exist that relate $\alpha(\omega)$ to fluid and particle properties, the particle concentration and the frequency of excitation, and a comprehensive review of these theories for the attenuation of sound in suspensions has been given by Harker and Temple (1988). The acoustic field for a linearly attenuating medium can be readily computed with the Rayleigh integral, with the substitution of a modified wavenumber to take into account differences in sound speed and attenuation. For all points sufficiently far from the emitting surface such that $R \gg a$, where R is the distance from the center of the transducer face, it follows that $s \simeq R$. For these conditions, the purely geometrical effect of the integration over the transducer face may be uncoupled from the attenuation term to give the resultant velocity potential as

$$\phi(\mathbf{x}) \simeq e^{-\alpha R}\int_A u\,\frac{e^{-k_{\mathrm{Re}}s}}{2\pi s}\,dA \tag{3}$$

The condition $R \gg a$ is not particularly restrictive when it is considered that the transition to the far-field of an unfocussed transducer typically occurs at a distance of several times the transducer radius, and that intensity measurements are typically performed in the far-field. Thus by measuring the velocity potential distribution in an attenauting medium, the attenuating parameter for that fluid can be calculated.

Considering a non-homogeneous multiphase system consisting of discrete solid particles suspended in a fluid, for the case in which the wavelength of the sound is much larger than the particle radius, or $\lambda \gg r$, the behavior of the medium is known to become attenuative and to assume the above representation with a modified wave speed (Allegra and Hawley, 1972 and Waterman and Truell, 1961). The validity of this representation and the functional dependence of the attenuation parameter α with respect to λ for the case $\lambda \leq r$ is further investigated in this study.

4 Ultrasonic Wave Propagation—Experimental Procedure

4.1 Experimental Apparatus. Experiments were performed to measure the intensity field of an unfocussed circular disc transducer in single phase and multiphase systems. In particular, acoustic velocity, attenuation and beam geometry were measured. These experiments were conducted in a water bath of 30 cm width, 60 cm length, and 25 cm height. The transmitting transducer was attached to a housing with three degrees of linear motion provided by an $x-y$ stage which itself was placed on a movable rail. The transducer could thus be moved axially and radially with respect to the receiver in a controlled and measureable fashion (Fig. 3). The receiving transducer was mounted on a 3 mm aluminum plate in a rigid mounting in the water bath. The transmitter which was typically operated in a tone-burst mode, was driven by a frequency generator (Wavetek Model 166) via a 100 W RF amplifier (Amplifier Research AR15). The frequency generator was triggered internally to emit bursts of 10–20 sinewaves in the frequency range 100 kHz to 1.0 MHz. The receiver was connected to an ultrasonic amplifier (Panametrics 5052PR) with variable gain in the range 0 db to 60 db, and the amplified signal was then filtered (Krohn-Hite 3320) at a cut-off frequency of twice the emitted frequency in each experiment. The transmitted and received signals were displayed simultaneously on a digital oscilloscope from which the requisite information could be measured. The magnitudes of the transmitted and received signals were compared to evaluate the attenuation and beam geometry features, and the delay time between the transmitted and the received signals was measured to give the sound speed.

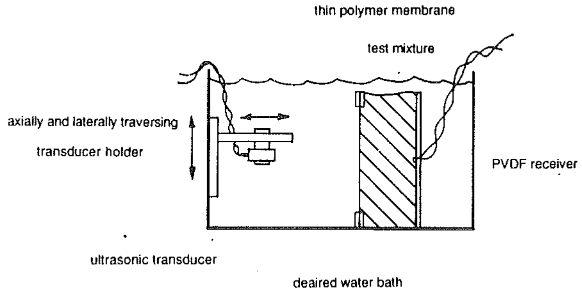

Fig. 3 Experimental apparatus for the measurement of sound speed and attenuation in single phase and packed bed mixtures. The test medium is separated from the rest of the water bath by a 10 μm polythene film.

4.2 Transducers. The transmitting transducer was a flat unfocussed and highly damped, broadband immersion transducer of radius a = 9.5 mm, and nominal natural frequency 1.0 MHz (Panametrics, V302). The intensity fields generated by the unfocussed transmitter was measured by a 1.0 mm diameter bilaminar polyvinylidene fluoromer (PVDF) hydrophone (Pennwalt Corp.). The piezoelectric polymer PVDF has several distinct advantages in its use for acoustic receivers, including the fact that transducers may be tailor-made to virtually any dimension, and such hydrophones have a very flat frequency response from DC to several MHz. The receiver used in these experiments was chosen for its small size and hence the local nature of its reception characteristics. The frequency response of the transmitter-receiver system was measured under controlled conditions in pure water for each separate experiment to allow effects associated with the medium, such as attenuation and beam geometry to be separated from the system characteristics.

4.3 Transducer Alignment. The acoustic intensity field produced by a transducer varies greatly with position, and consequently accurate positioning of the transmitting and receiving transducers is critical. Initial coaxial alignment is achieved in an iterative fashion. The receiver is positioned at roughly the distance known to correspond to the focal length of the transmitter at the particular frequency of operation, and is then traversed axially and laterally in small increments until the maximum is detected. The transmitter is then moved back and forth along the axis and at each axial position, it is translated radially to ensure that the two are indeed aligned coaxially. This procedure is conducted prior to all measurements.

4.4 Transducer Operation. Often ultrasonic instruments are operated in a pulsed mode, in which the transducer is excited by a pulse of relatively high amplitude and short duration. The transducer then rings down for some period of time (the length of which depends on the degree of mechanical and electrical damping inherent in the unit) at its natural or

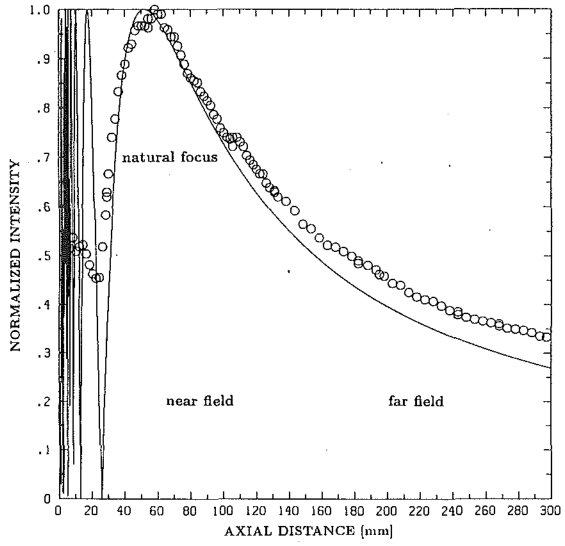

Fig. 4 Axial intensity profile for a 9.5 mm radius, 1 MHz transducer in water, normalized with respect to the maximum value at the point of natural focus. The theoretical curve is calculated using the Rayleigh integral (Eq. (1)).

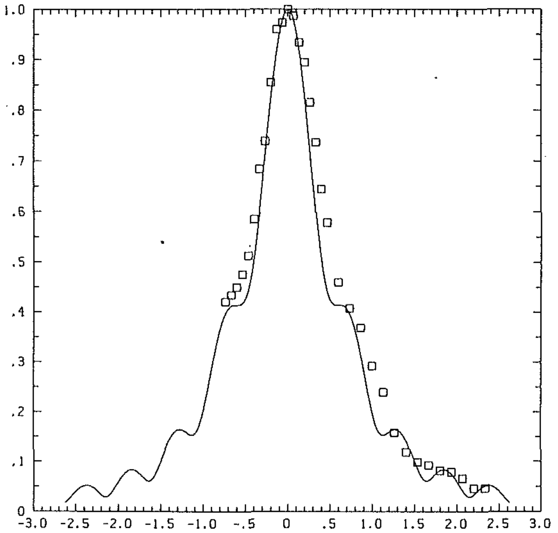

Fig. 5 Radial intensity profiles for a 9.5 mm transducer, operating at 0.95 MHz in water, at (*a*) 58.4 mm, (*b*) 89.4 mm, and (*c*) 151.4 mm. The radial distance is nondimensionalized with respect to the transducer radius.

preferred frequency of operation. In contrast, in the present experiments the transducer was excited by a tone burst or wave packet of adjustable frequency and amplitude. The length of the tone burst is limited to less than the time of arrival of the first echo reflected by boundaries in the system and the repetition rate or the time between successive bursts is adjusted to be longer than the time required for all extraneous reverberations to die away. A burst duration of 10–20 full waves at a repetition rate of about 1 kHz was found to be satisfactory. To avoid nonlinear effects, the amplitude of the emitted signals were kept low. In these experiments, the maximum pressure excursion measured was of the order of 0.15 kPa (Atkinson, 1991), and the typical value was somewhat less than this. At these pressure amplitudes, cavitation, which could corrupt the measurements, does not occur.

5 Experimental Results

5.1 Acoustic Field in Degassed Water. It has previously been shown that commercial flat transducers create acoustic fields that are very close to those predicted theoretically (Adach and Chivers, 1990). Prior to making measurements for the purpose of characterizing the ultrasonic properties of concentrated solid–liquid mixtures, the acoustic field in degassed water was measured as a verification of satisfactory operation of the ultrasonic transducer. This was done in terms of an axial and three radial traverses. The location of the natural focus of a transducer is a near linear function of the reduced transducer radius. The axial distribution for the 9.5 mm radius, 1 MHz transducer has a measured natural focus at 58.4 mm as shown in Fig. 4 while the corresponding calculated value is 52 mm. This discrepancy is probably the consequence of the uncertainty in the effective radius of the active piezo-electric ceramic element, which can also be the source of the minor and typical error in the axial intensity decay. The radial profiles in intensity were measured at 58.4, 89.4, and 151.4 mm. These are shown in normalized form in Fig. 5, and they agree relatively well with the result of the Rayleigh integral particularly at the greater axial distance. The measurements show qualitative agreement with the off-peak oscillations in predicted intensity. Based on the measurements shown and many others it is found that the measured fields consistently show good predictability in the far field and a lesser agreement in the Fresnel region.

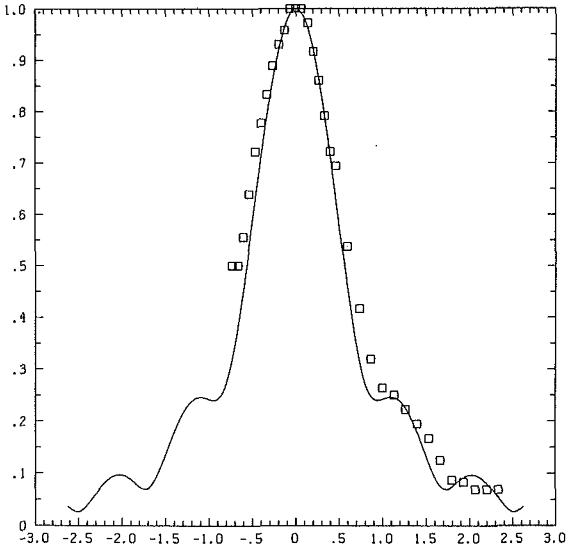

Fig. 5(*b*)

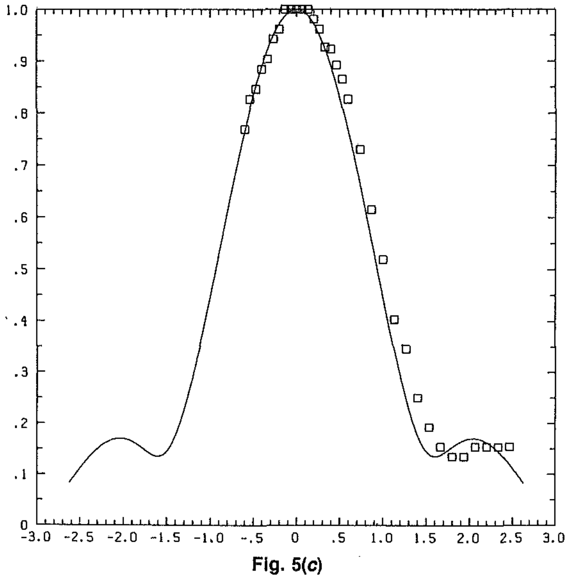

Fig. 5(*c*)

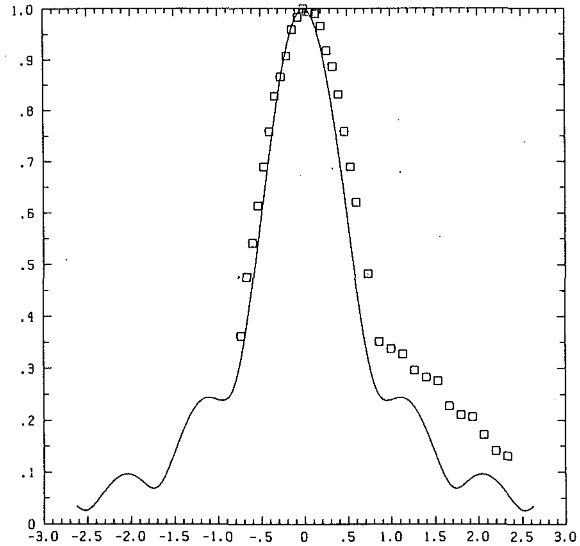

Fig. 6 **Radial intensity profiles for a 9.5 mm transducer, operating at 0.30 MHz in a packed bed of 1.0 mm glass beads in water ($kr \approx 0.55$), at (*a*) 50 mm, (*b*) 75 mm, and (*c*) 100 mm. The radial distance is nondimensionalized with respect to the transducer radius.**

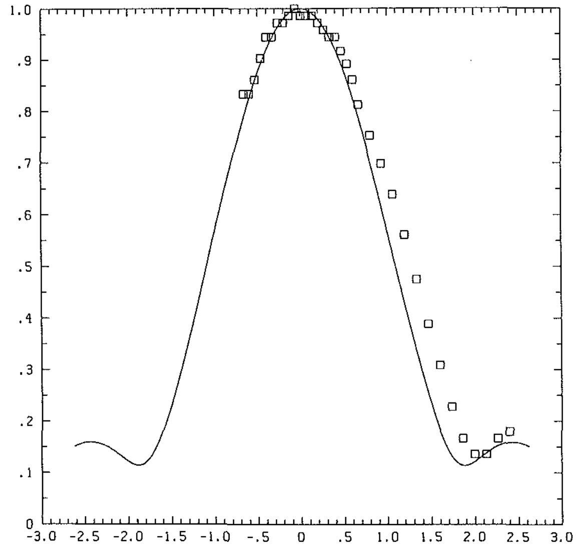

Fig. 6(*b*)

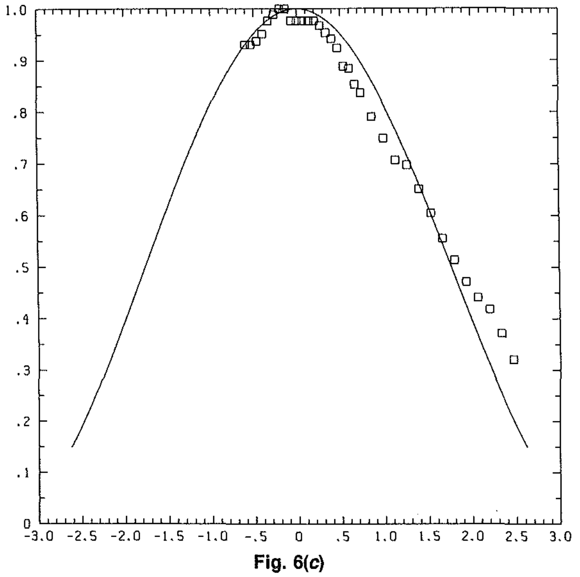

Fig. 6(*c*)

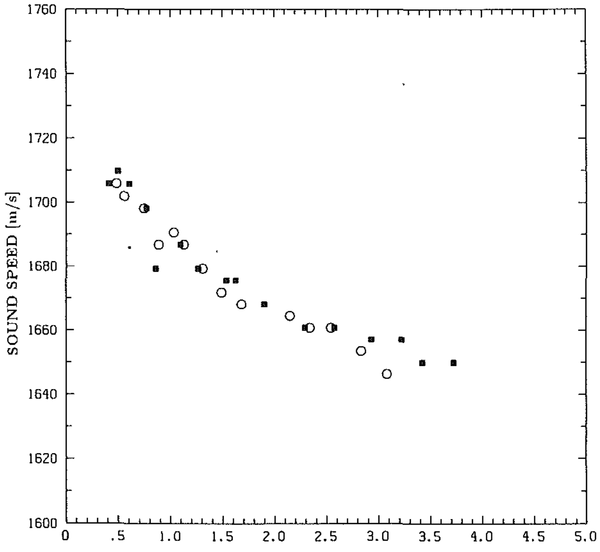

Fig. 7 **Phase speed of sound in a packed bed of 1.0 mm glass beads in water as a function of *kr*, showing a minor monotonic decrease at higher frequencies**

5.2 Acoustic Field in Packed Beds. The properties of packed beds were characterized by means of similar acoustic field measurements for various fixed dimensions of the test cell. The active transducer was positioned directly against the acoustically transparent window of the container that held the packed mixture of 1.0 mm nominal diameter glass beads in water (the actual average diameter of the beads was 1.034 mm, with a standard deviation of 0.100 mm). Radial beam traverses were made for each axial separation between the transmitter and receiver (50, 75, and 100 mm), and are shown in Fig. 6 for a frequency of 0.30 MHz. To calculate the amplitude of the corresponding non-attenuating acoustic fields (i.e., the acoustic field due solely to geometric effects) for the purpose of comparison, the medium sonic velocity is required. To this end, the acoustic phase velocity was measured for the packed bed as a function of frequency.

5.3 Phase Velocity in Packed Beds of Glass Beads and Water. The phase velocity was derived from time of flight measurements between the two stations. The method was first used with water alone to verify the accuracy of the technique. The pure water data showed good agreement with accepted data in the literature (Del Grosso and Mader, 1972). In the packed bed of glass spheres and water, the phase speed shown in Fig. 7 displays a gentle, monotonic decrease as a function of frequency, with no evidence of scale effects when *kr* becomes of order one or greater. The sound speed undergoes a total change of four percent over the frequency range studied, which is not considered significant as it is of the order of the error in the measurement. The monotonic nature of this change does not support the truncated theoretical representation of the "multiple scattering" model (Anson and Chivers, 1989) which shows great fluctuations of sonic velocity with *kr*. Further, it is interesting to note that only one wave speed was detected in these settled bed experiments. Plona (1982) has shown that porous media of finite solids stiffness may display three types of wave, a slow compressional, a shear and a fast compressional wave in order of ascending speed. The present results show a complete absence of the fast compressional wave which could either be the result of the method of emission favoring only one wave mode, or that the stiffness of the solids matrix is minimal in these experiments. As is shown below in the fluidized bed experiments, the absence in detectable difference between the sound speed in the settled and incipiently fluidized

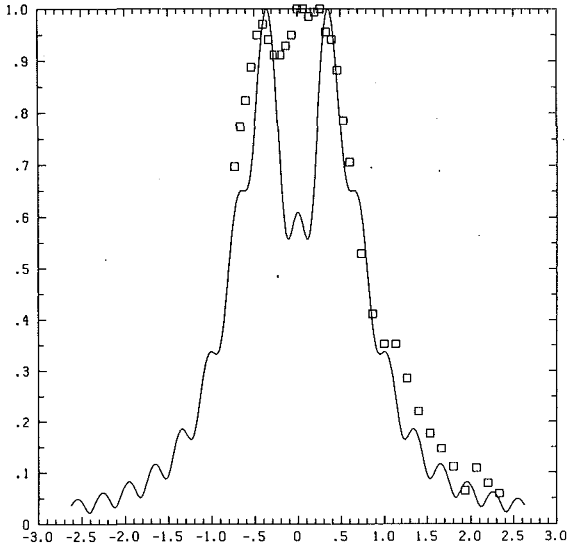

Fig. 8 Radial intensity profiles for a 9.5 mm transducer, operating at 0.80 MHz in a packed bed of 1.0 mm glass beads in water *(kr* ≈ 1.5), at (*a*) 25 mm, (*b*) 50 mm, and (*c*) 75 mm. The agreement of the experimental data with the Rayleigh theory persists for higher values of *kr*.

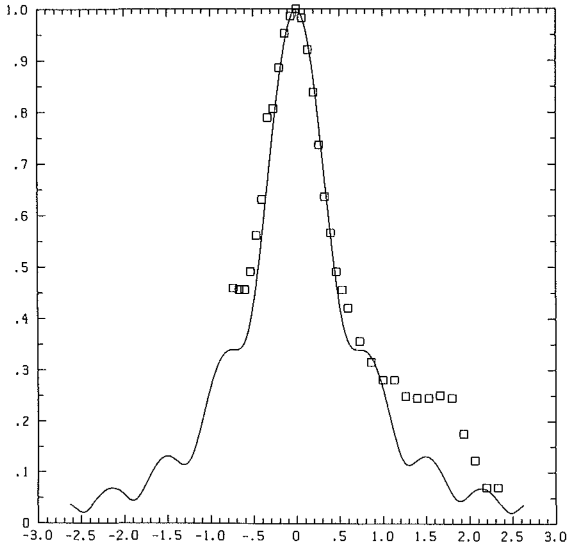

Fig. 8(*b*)

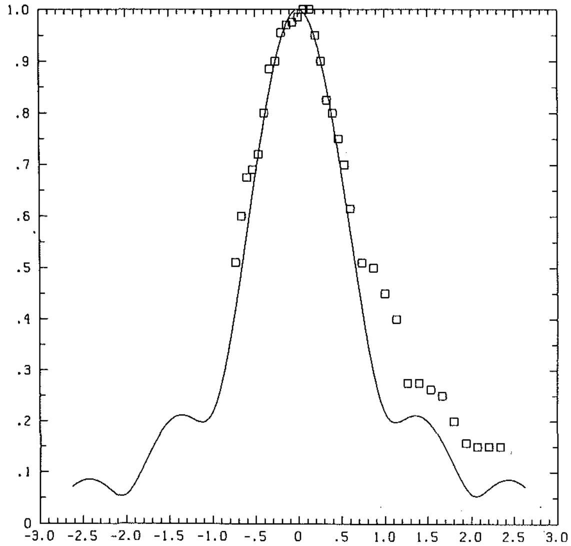

Fig. 8(*c*)

states leads the authors to believe that the settled beds are effectively cohesionless.

5.4 Comparison With Rayleigh Theory. The acoustic field in a nonattenuating medium can be fully represented by the wave speed and the transducer geometry alone. The radial beam profiles corresponding to the above packed bed conditions were computed and are shown together with the data in Fig. 6. In this figure, both the calculated and measured curves are normalized with their respective peak values. Although the dimensional magnitudes of these maxima differ, the geometrical similarity between the theoretical curves and the data is striking, particularly near the axis, and the Rayleigh theory is well able to represent beam width. It is hypothesized that the decay of beam amplitude, which the unattenuated theory fails to capture, may be described by the attenuated version of the Rayleigh integral (Eq. (1)). Using this representation, numerical values of the attenuation parameter, α, could then be derived from measurements. It should be noted that the far field intensity decays due to both geometrical spreading and due to the presence of solids. Typically the inverse square geometrical attenuation effect has not been taken into account in previous investigations (Machado et al., 1983) which leads to an overestimation of the attenuation due to scattering. The purpose of the present measurements is to extend the investigation of the effect of wavelength down to $kr \approx 1$, and to include the effect of solids concentration (discussed in Section 6.2) on the attenuation in mixtures. To address the former, further traverses for $f = 0.8$ MHz ($kr = 1.5$) were obtained. These are shown in Fig. 8, with the corresponding unattenuated Rayleigh results based on the measured mixture phase speed. The agreement persists even for high values of kr. It appears, therefore, that for this specific application, an equivalent single phase characterization of the two component mixture is appropriate. Such a representation is adopted here and is utilized to represent all measured mixture attenuation values in this study.

5.5 Attenuation in Packed Beds. Since the attenuation in pure water is found to be negligible compared to the attenuation in the the packed mixture, it is convenient to present the attenuation, α, relative to degassed water measurements. In quantifying attenuation, the following factors were recognized to affect the amplitude of the received signal:

(*a*) the frequency response $H(\omega)$ of the transmitter-receiver combination,

(*b*) the position of the measuring location relative to the natural focus, and

(*c*) the signal loss due to the presence of solids.

The received axial signal amplitude (V_{water}) through degassed water at a fixed separation, L, between transmitter and receiver can therefore be presented as

$$V_{\text{water}} = V_{\text{trans}} H(\omega) \mathcal{R} \left\{ \int_A u \frac{e^{-i(\omega/c_{\text{water}})L}}{2\pi L} dA \right\}, \tag{4}$$

while the corresponding amplitude received through the mixture is

$$V_{\text{mixt}} \simeq V_{\text{trans}} H(\omega) e^{-\alpha L} \mathcal{R} \left\{ \int_A u \frac{e^{-i(\omega/c_{\text{mixt}})L}}{2\pi L} dA \right\}. \tag{5}$$

This relation is subject to the same condition $L >> a$ seen with Eq. (3). Dividing (5) by (4), an expression emerges for the attenuation parameter:

$$\alpha \simeq \frac{1}{L} [\ln V_{\text{water}} - \ln V_{\text{mixt}}] + \ln \left[\frac{\cos(\omega/c_{\text{mixt}})L}{\cos(\omega/c_{\text{water}})L} \right]. \tag{6}$$

This form was used to evaluate α from experiments performed in the constant dimension test section for L = 50, 75, and 100 mm. The trigonometric correction factor in Eq. (6) accounts for the relative axial position of the receiver with respect to

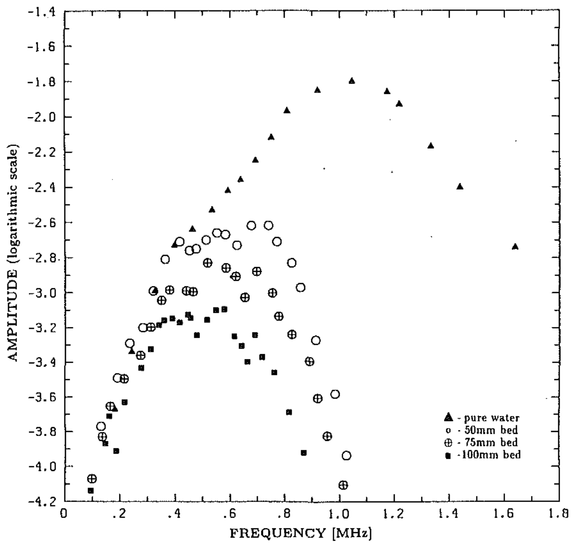

Fig. 9 Typical unreduced data showing the attenuation as a function of frequency for pure water and packed beds of 1 mm glass beads

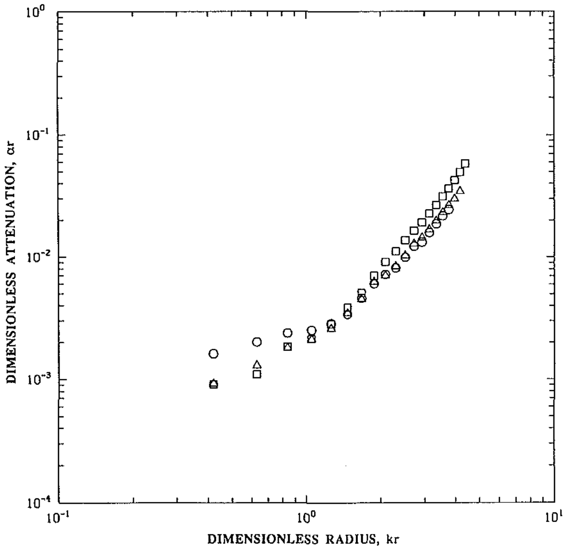

Fig. 10 Dimensionless representation of the attenuation data of Fig. 9, showing (αr) as a function of the reduced frequency (kr). At low frequencies, the attenuation appears to depend linearly on frequency, while the change in slope indicates a quadratic dependence on frequency for $kr > 0.75$.

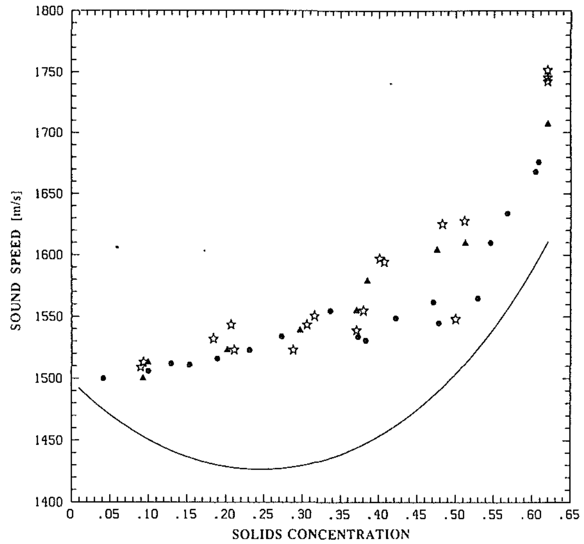

Fig. 11 Sound speed in a fluidized bed of 1.0 mm glass beads in water as a function of solids fraction. The theoretical curve is the prediction using the phenomenological model of Urick (1947), outlined in the Appendix. The experimental sound speed (for $kr \sim 1$), in contrast, shows no minimum at intermediate concentrations. Symbols represent different runs for the same experimental conditions.

the natural focus, and it is named the geometrical factor. At the axial distances considered, namely $L = 50$, 75 and 100 mm, the magnitude of this factor is small with a maximum deviation of the order of 20 percent. However, all measurements were adjusted to take this correction into account. The experiments consist of measuring the received signal for a full range of excitation frequencies. Typical unreduced data for these tests are shown in Fig. 9 for both water and settled beds. The degassed water curve contains the combined transmitter-receiver frequency characteristics with a maximum at 0.9 MHz, which is consistent with the nominal transmitter natural frequency of 1 MHz, and the high receiver natural frequency. The mixture signal amplitudes show little deviation from the water values at low frequencies, but they typically begin to deviate from the water curve at a frequency of approximately 0.4 MHz ($kr = 0.75$). These resulting attenuation parameter values are presented in Fig. 10 in dimensionless form (αr) as a function of the reduced frequency kr. The log-log presentation of the data exhibits two distinct regions. At low frequencies, the attenuation parameter appears to depend approximately linearly on frequency, while the change in slope indicates an apparently quadratic dependence on frequency for $kr > 0.75$. Further tests were carried out to verify these findings and to characterize the effect of solids fraction using a similar apparatus with the additional ability of fluidizing the mixture.

6 Fluidized Bed Acoustic Experiments

In order to obtain attenuation and wave speed behavior of acoustic propagation in systems of varying concentration, experiments were conducted in a fluidized bed. Here the concentration of the solid-liquid mixture could be varied by adjusting the upwards velocity of liquid through a bed of particles initially suspended on a porous plate. An ultrasonic transducer transmitter-receiver pair was mounted horizontally on the vertically aligned 100 mm tube. Liquid-solid fluidized beds are kinematically quite stable with small local fluctuations of solids fraction, due to the discrete nature of solid-liquid systems (Foscolo and Gibilaro, 1985). Although such fluctuations are present, the period of oscillation of the acoustic wave propagation used ($T = 1/\omega = 1/2\pi f$) is very much smaller than the characteristic time scale of acceleration of the individual particles ($T_p = r^2\rho_p/18\mu_f$, so that the particles may be considered to be frozen in space, particularly for tone bursts of short duration. In these experiments 1.0 mm glass beads were fluidized in water, and the typical frequencies of the sound used were in the range 100 kHz to 1.0 MHz ($kr = 0.2 \sim 2$).

6.1 Sound Speed Variation With Concentration. The variation of the speed of sound with solids fraction is shown in Fig. 11. It has the anticipated behavior at the two extremes of concentration: at very low concentrations, the sound speed is roughly that in water, it increases monotonically as a function of concentration and at the maximum packing limit, the sound speed is the same as that in the packed bed case. Note that there is some scatter in the data in the solids fraction range 37–52 percent, which coincides with small but visible kinematic waves in the bed. Despite this, the sound speed increases monotonically with solids fraction. For comparison, the phenomenological model of Urick (1947) (described in the Appendix) that is based on the effective bulk modulus and density of the

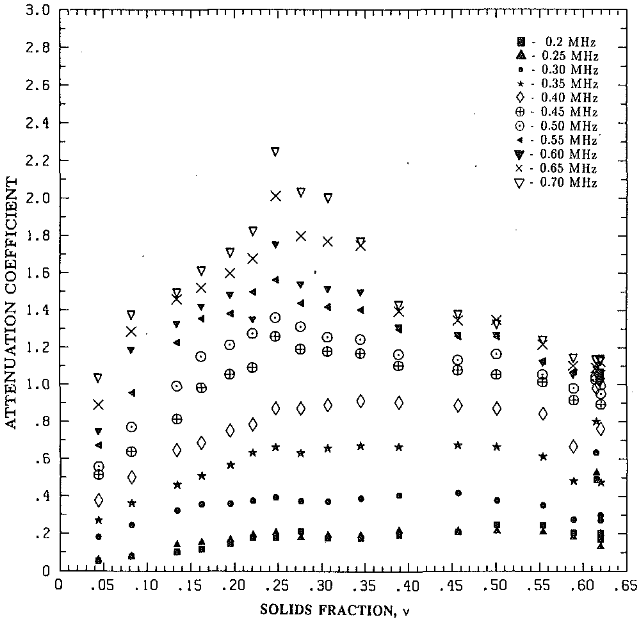

Fig. 12 Attenuation parameter, α $[m^{-1}]$, as a function of solids concentration for sound transmission in a fluidized bed. This plot shows that there is a maximum in attenuation at a solids concentration of about 30 percent, which is more pronounced at the higher frequencies.

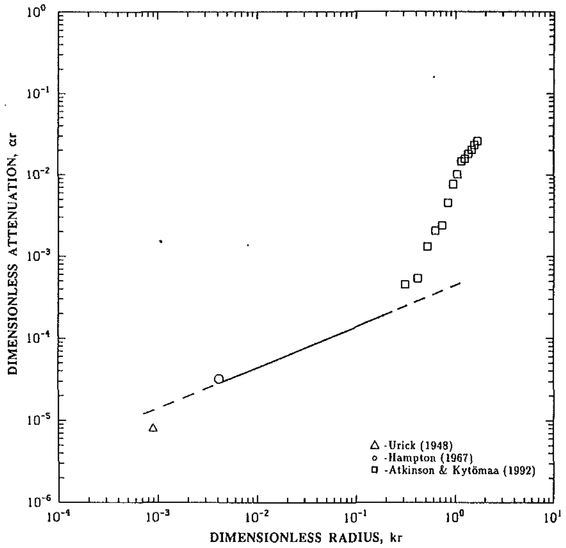

Fig. 13 Dimensionless representation of the attenuation at a solids fraction of 30 percent, showing (αr) as a function of the reduced frequency (kr) for a glass-water system. The straight line is the theory for the inertial regime (Atkinson and Kytömaa, 1992). Above $kr \sim 0.1$ the present results (□) show an elevated attenuation due to geometrical scattering, while below Re ~ 1, which corresponds $kr \sim 3 \times 10^{-3}$, viscous effects become important and actually decrease the attenuation.

mixture is also shown in this figure. In contrast to the experimental results, the theory predicts that the sound speed has a minimum at intermediate concentrations of the order of 20 percent by volume. It should be noted, however, that the nonmonotonic theory corresponds to the long wavelength limit, namely $kr \to 0$, while the experimental results are for $kr \sim 1$. The theory developed by Atkinson and Kytömaa (1992) shows that this discrepancy is the result of an interplay between viscous and inertial effects. The Urick model holds for very low frequencies where viscosity is important, while the dependence becomes monotonic at a sufficiently high frequency where inertia dominates.

6.2 Variation of Attenuation With Concentration. The variation to α with respect of frequency, described in Section 5.5, showed a monotonic increase and two distinct regions of dependence. At low frequencies, $kr < 0.75$, the attenuation grows approximately linearly with frequency, while the relationship apparently becomes quadratic for $kr > 0.75$. As an extension of this, the dependence of the attenuation parameter on frequency was evaluated for various values of the solids fraction. The picture that emerges is complex and to help its interpretation, the attenuation parameter is plotted as a function of concentration with frequency as a parameter in Fig. 12 from which the following traits can be distinguished. At low concentrations (< 20 percent) the attenuation increases with both frequency and concentration such that the slope of attenuation versus ν increases with the frequency. Indeed, by linear superposition of losses due to individual scatterers, one would expect that the increase would be monotonic with concentration. In practice this signifies that penetration becomes poor with higher solids loading, particularly at higher frequencies. This has long been known, for example, as the reason why commercially available ultrasonic Doppler velocimeters fail at higher solids contents. As the concentration is increased above 20 percent while maintaining a constant frequency, the attenuation behaves in a dramatic fashion by first leveling off and then decreasing at higher concentrations, resulting in better penetration at higher solids fractions. This phenomenon is particularly marked at high frequencies of operation. For example, at an operating frequency of 0.8 MHz ($kr = 1.5$), the attenuation in 62 percent solids (1 mm) is the same as in a mixture with 6 percent solids, while the peak attenuation coefficient α assumes twice the 62 percent value at a concentration of 25 percent. For the present system of 1 mm glass beads and water, the nonmonotonic character of the attenuation parameter is most prominent at frequencies above 0.4 MHz (kr = 0.75). This behavior has previously been observed by Urick (1947, 1948) and Hampton (1967) in their experiments with kaolinite suspensions (mean diameter of 2.26 and 0.83 μm, respectively, according to Gibson and Toksöz, 1989), and their data are included in Fig. 13 for comparison. It can be noted that the attenuation in these colloidal suspensions is high relative to the present results for the same range of frequencies. But when these attenuation data are rendered dimensionless with particle radius (αr), they are indeed found to scale with reduced frequency (kr) to a constant power. The two frequency related independent dimensionless variables are the reduced frequency (kr) and the oscillatory Reynolds number (Re $= r\sqrt{\omega/2\nu}$). Physically the parameter kr represents the ratio of the particle size to the acoustic wavelength. If $kr \ll 1$, sound travels in the "long wave" regime, while if the opposite is true, sound will refract and geometrical scattering will be important. The Reynolds number based on frequency of excitation is the ratio of the particle radius to the Stokes viscous boundary layer thickness. Re $= r/\delta$, where $\delta = \sqrt{2\nu/\omega}$. If Re $\gg 1$, the boundary layer is very thin and the dynamics are essentially governed by inviscid interactions. Conversely, if Re $\ll 1$, viscous interactions dominate. As viscosity is the source of attenuation, it can also be presented in terms of the Reynolds number (Re $= \sqrt{(rc/2\nu)kr}$). Thus for a given system, if the attenuation scales with the nth power of kr, it will scale with the $2n$th power of Reynolds number.

7 The Design of Ultrasonic Instrumentation and Limitations of the Technique

It is clear from the results of the attenuation at high concentration presented above that it is possible to design an instrument to interrogate such mixtures. The parameters that must be taken into consideration in the design of an ultrasonic instrument are

(i) the solids fraction, ν, in the mixture

(ii) the particle size, or more particularly the parameter, kr,

(iii) the particle properties (density and compressibility),

(iv) the fluid properties (density, compressibility and viscosity), and

(v) the physical dimensions of the system to be interrogated.

The sound speed, c, in a particular solid-liquid mixture is determined by the solid and liquid densities and compressibilities, as well as the solids fraction, ν. The sound speed fixes the wavelength of the transmitted sound which in turn, with the dimensions of the transmitting transducer, determines the shape and size of the beam used for the ultrasonic measurement. The depth of penetration of the ultrasound is dictated by the attenuation, which varies with the frequency of sound and the dispersed phase concentration, as well as the fluid viscosity (an effect not considered here).

We have shown that the solids fraction of the mixture does not represent a significant limitation to the use of ultrasound as a diagnostic technique (particularly as the attenuation at maximum packing is far from its maximum value, which has been shown to occur at around $\nu \sim 30$ percent), while the frequency of operation may well be a limiting factor, due to the quadratic increase in attenuation with frequency for $kr > 0.75$. The most significant limiting consideration in the use of ultrasound for the nonintrusive measurement of highly concentrated suspensions lies in the tradeoff between the spatial resolution of the transmitting transducer and the depth of penetration of the signal, L. Lateral spatial resolution depends on the beam width at the measuring location. This scales with ka. On the other hand the axial resolution is controlled by wavelength. Good spatial resolution implies a relatively short wavelength, or alternatively a large value of ka (and hence kr). This, in turn, implies high attenuation and a relatively short depth of penetration, L. It should be noted that as the shape of the ultrasonic beam does have an impact on the lateral resolution of the system good spatial resolution may be compromised when the size of the natural focal region of typical piston transducers is too large. One manner in which this problem can be circumvented is in the use of focussed transducers. The addition of an external focussing lens on a piston transducer has the effect of reducing the extent of the focal region and increasing the maximum intensity at the focus.

For the system and the range of parameters studied, an expression was derived (Atkinson and Kytömaa, 1992) to represent the attenuation parameter α for values of $kr < 1$, and in the thin Stokes layer limit:

$$\lim_{\omega \to \infty} \alpha = \frac{9}{4r}\sqrt{\frac{\mu\omega}{2}}\,\frac{\left[\dfrac{\nu}{\kappa_s} + \dfrac{(1-\nu)}{\kappa_l}\right]^{1/2}(1-\nu)(D-\rho^*\hat{\rho})}{[D(1-\nu)+C(\nu)\rho^*]^{1/2}[C(\nu)+(1-\nu)\hat{\rho}]^{3/2}} \tag{7}$$

where

$D = \rho_s/\rho_f$

$\hat{\rho} = 1 + \nu(D-1)$

$\rho^* = D - \nu(D-1)$

and (ν) is the added mass coefficient.

$$(\nu) = \frac{1+3.2\nu}{2}.$$

This leads to the result that the attenuation is proportional to $\mu^{1/2}\omega^{1/2}$, which is consistent with the Biot theory. For a system of two specific materials of given densities and bulk moduli, it is convenient to present the attenuation data in terms of the quantity $\alpha r/\sqrt{\mu\omega}$. In this manner the attenuation at different frequencies and particle sizes can be directly compared, and should only be a function of solids fraction. Our present results for 0.5 mm radius glass spheres and a frequency range of 0.1-1 MHz are presented in Fig. 14 with other data due to Urick (1948) (0.5 μm radius, 1 MHz), Hampton (1967) (1 μm radius, 100 KHz) which together represent a broad range of frequency and particle size. This figure also shows the theoretical curve for the inertial regime. The comparison reveals significant and informative differences. The present attenuation data are much larger than the theoretical curve as a consequence of the high value of ka (0.5–1.5) which introduces appreciable geometrical and multiple scattering effects which are not addressed here.

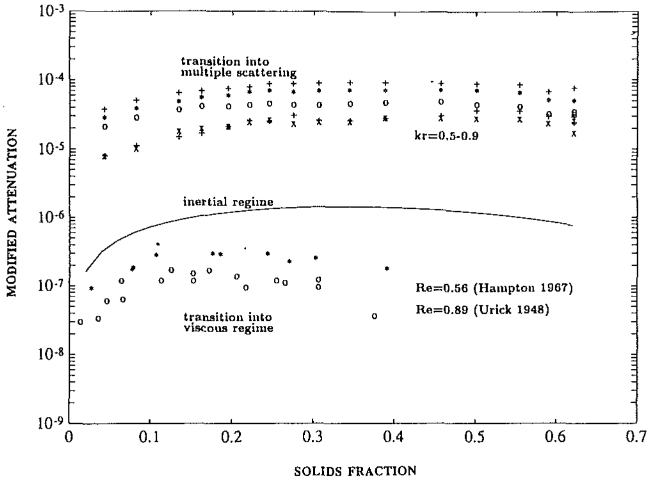

Fig. 14 Modified attenuation ($= \alpha r/\sqrt{\mu\omega}$) as a function of solids fraction. Three data sets are shown. From the top, the present attenuation measurements for $kr = 0.9 - 0.5$, the continuous curve is the theoretical prediction for the inertial regime, and below it are the transitional Reynolds number data due to Urick (1948) (Re = 0.89) and Hampton (1967) (Re = 0.56).

In addition, the small particle data correspond to low values of Reynolds number as defined in section 6.2, namely 0.56 and 0.89 for Hampton and Urick, respectively. These values correspond to the transitional regime between viscous and inertial domination, while the model is only valid in the inertial regime which is characterized by very high Reynolds numbers. In the viscous regime, viscosity effects are seen to appreciably reduce the attenuation. This is further discussed by Atkinson and Kytömaa (1992).

8 The Ultrasonic Doppler Velocimeter

Based on the results obtained in the packed bed and fluidized bed experiments, it was clear that an ultrasonic transducer operating at or near $kr = 1$ could provide information on a flowing mixture of 1.0 mm particles in a 100 mm tube at concentrations up to the maximum packing fraction, where the attenuation factor, $e^{-\alpha L} \simeq 0.10$. To confirm this supposition, the prototypical ultrasonic Doppler velocimeter shown schematically in Fig. 15 was constructed and tested. The device operates in the following manner; an unfocussed broadband transducer (Massa corp. Model TR-1283E), inclined at an angle to the vertically flowing solid-liquid mixture, insonifies the mixture in a tone-burst at a frequency in the range 200-500 KHz ($0.5 < kr < 1.0$). The waveform is created with a Wavetek (Model 166) waveform generator which is fed to an RF power amplifier (Amplifier Research AR15). A receiving transducer (Massa corp. Model TR-1283E) is connected to an ultrasonic amplifier (Panametrics 5052PR). The natural focus of this transducer is aligned with that of the transmitter, and it detects a signal that is shifted in frequency due to the velocity of the scattering particles with respect to the incident ultrasound. The frequency shift, f_d, is given by

$$f_d = \frac{2 f_i v_p \cos(\theta_T + \theta_R)}{c_{\text{eff}}} \tag{8}$$

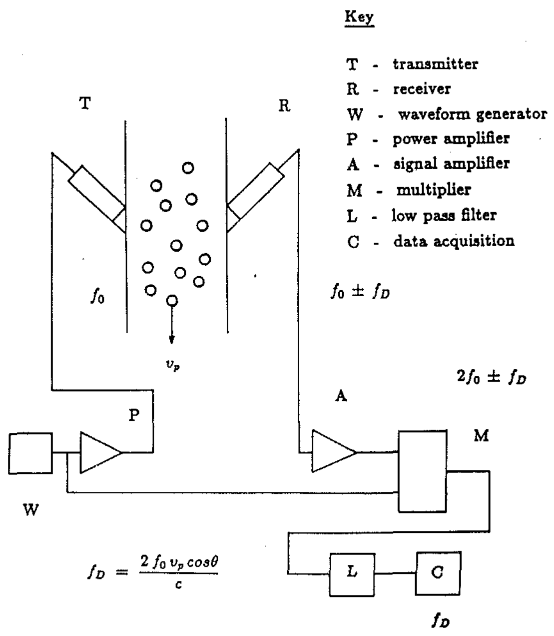

Fig. 15 Schematic of prototype ultrasonic Doppler velocimeter. The scattered signal is measured at an angle to the incident beam and it is demodulated electronically with a double balance mixer to determine the Doppler shift.

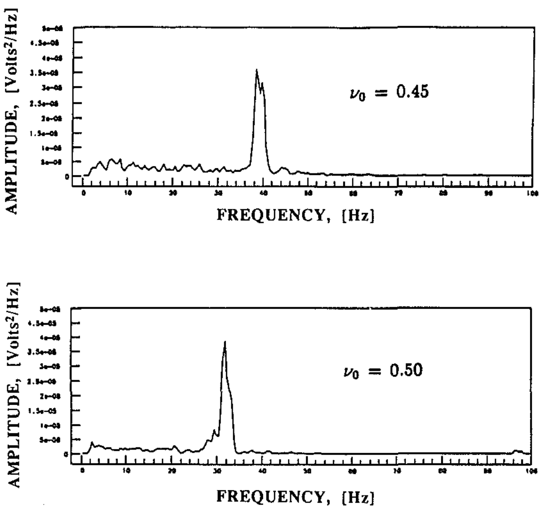

Fig. 16 Typical spectra of the demodulated scattered signal showing distinct peaks corresponding to the Doppler shift caused by particles sedimenting at concentrations up to 50 percent by volume

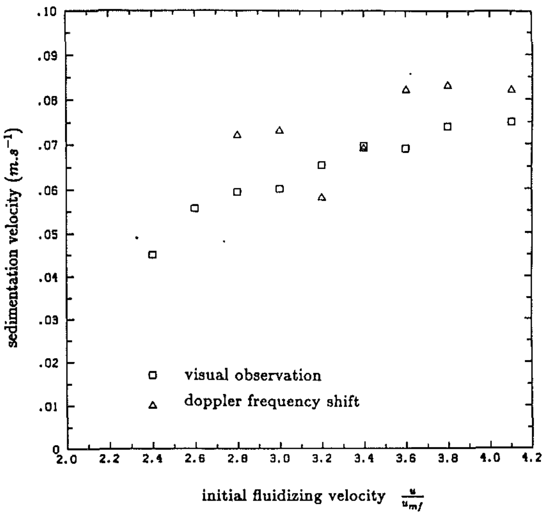

Fig. 17 Comparison of particle velocities measured visually and using the ultrasonic Doppler technique. The data show some scatter due to error in the visual technique and the short duration of the tone bursts that were used in the ultrasonic method. Longer time records would introduce averaging, and the statistics of velocity fluctuations could also be derived from these.

where v_p is the velocity of the scatterers, c_{eff} is the sound speed in the mixture and $\theta_{T(R)}$ is the angle the incident (reflected) ultrasonic beam makes with the direction of motion of the particles.

The Doppler shifted frequency is obtained by demodulating the received signal with the driving signal using a double balance mixer (Mini-Circuits SBL-3). This yields a signal that has components at the sum and the difference of the frequencies of the two waveforms. The frequency difference is proportional to the speed of the scatterers. To measure it, the high frequency component is filtered out with a low pass filter (Krohn-Hite 3320). The remaining low frequency signal (in these experiments in the range 0 to 1000 Hz) was first digitized with a data acquisition system (Masscomp 5450) and its spectrum was analyzed by determining its Fast Fourier Transform. The device was tested by measuring the settling velocity of 1 mm glass beads at a range of concentrations in a 100 mm diameter vertical column; the frequency spectra of the velocity corresponding to settling at two different initial volume fractions, namely $\nu_o = 0.45$ and $\nu_o = 0.50$, are shown in Fig. 16. The particle settling speed was independently verified by visual measurement of the downward velocity of the mixture-water interface, which for a monodispersion settles at the same speed as the particles. A comparison between the measured settling velocities and the visually observed values corresponding to a range of initial concentrations is shown in Fig. 17. This graph shows that the settling velocity, as deduced from the Doppler shifted frequency, is a good measure of the actual velocity.

By carefully choosing the frequency of excitation according to particle size, it is demonstrated that the internal speed of very high solids fractions can be measured, and furthermore, an algorithm is presented to help choose this frequency. This surpasses commercial units which are openly advertised to be unable to operate at solids fractions greater than 20 percent. The present work provides an ultrasonic method that replaces the otherwise ubiquitous Laser Doppler Velocimetry, that is rendered ineffective in opaque mixtures as the ones considered here.

9 JFE Data Bank Contribution

Data obtained in this effort have been deposited to the JFE Data Bank.

The reader can find data corresponding to Figs. 11 and 12 in the files named soundnu.m and attnu.m. In addition to the Atkinson and Kytömaa data, these also contain the data due to Urick (1948) and Hampton (1967). The files are in the form of ASCII readable MATLAB programs which can be run to give the indicated plots.

To access the file for this paper, see instructions on p. 794 of this issue.

10 Conclusions

The propagation of ultrasound in solid-liquid mixtures was investigated experimentally for a range of frequencies at concentrations spanning the range from infinite dilution to maximum packing. The measured attenuation has been shown to depend approximately linearly on kr for $0.1 < kr < 0.75$ and quadratically for $kr > 0.75$. As a consequence, because the attenuation coefficient, α, becomes prohibitively large for $kr > 1$, it is appropriate to operate at $kr \leq 1$ for most applications. This ensures an optimum wavelength, $\lambda \simeq 2\pi r$, for the operation of acoustic instrumentation. In contrast, the attenuation at a fixed frequency for $kr < 0.75$ displayed a maximum at a solids fraction of about 30 percent for 1 mm silica beads in water, with the attenuation at very high concentrations considerably less than the maximum. The attenuation results are qualitatively consistent with the data of Urick (1947) and Hampton (1967), although their measurements were conducted at much lower Reynolds number ($\simeq 1$) which corresponds to the transitional regime. Furthermore, the experiments conducted with silica beads in water reflect the range of kr and the materials encountered in sediment transport, slurry handling and many other mining and engineering applications. The intensity field produced by a circular disc transducer in a two phase medium at $kr \simeq 1$ shows excellent agreement with the Rayleigh integral with the substitution of a modified wavenumber and attenuation parameter, which allows for the prediction of the transducer beam geometry even in dense two-component mixtures for a wide range of frequencies and solids fractions. This agreement is best in the transducer far field, although the near field was also well captured and characterized. Errors in the measurement of acoustic attenuation in these experiments are typically related to the reproducibility of experiments; that is to say that experimental uncertainty is dominated by variations between successive experiments. In these experiments, the variation in α was of the order of 5–10 percent.

The limitations of the use of ultrasound for nonintrusive diagnostics were discussed, and based on the resulting guidelines, an ultrasonic instrument was built to measure the velocity of moving particles at or near maximum packing. The preliminary results from this Doppler velocimeter show good agreement with observations of the settling velocity of 1.0 mm glass spheres at high concentrations.

Acknowledgment

The authors gratefully acknowledge the support of the National Science Foundation under grant number CTS 9107449.

References

Adach, J., and Chivers, R., 1990, "A Detailed Investigation of Effective Geometrical Parameters for Weakly Focussed Ultrasonic Transducers. Part I: Optimisation of Experimental Procedures," *Acustica*, Vol. 70, pp. 12–22.

Adach, J., and Chivers, R., 1990, "A Detailed Investigation of Effective Geometrical Parameters for Weakly Focussed Ultrasonic Transducers. Part II: A Systematic Study Including an Absorbing Medium," *Acustica*, Vol. 70, pp. 135–145.

Aindow, J., Markiewicz, A., and Chivers, R., 1985, "Quantitative Investigation of Disk Ultrasonic Sources," *Journal of the Acoustical Society of America*, Vol. 78, pp. 1519–1529.

Allegra, J. R., and Hawley, S. A., 1971, "Attenuation of Sound in Suspensions and Emulsions: Theory and Experiments," *Journal of the Acoustical Society of America*, Vol. 51, pp. 1545–1564.

Anson, L., and Chivers, R., 1989, "Ultrasonic Propagation in Suspensions—A Comparison of an Multiple Scattering and an Effective Medium Approach," *Journal of the Acoustical Society of America*, Vol. 85, No. 2, pp. 535–540.

Atkinson, C. M., 1991, "Acoustic Wave Propagation and Non-Intrusive Velocity Measurements in Suspensions," Ph.D. thesis, Massachusetts Institute of Technology.

Atkinson, C. M., and Kytömaa, H. K., 1992, "Acoustic Wave Speed and Attenuation in Suspensions," accepted for publication in *Int. J. Multiphase Flow*, Vol. 18, No. 4, 1992, pp. 577–592.

Biot, M., 1956, "Theory of Propagation of Elastic Waves in a Fluid Saturated Porous Solid. II: Higher Frequency Range," *Journal of the Acoustical Society of America*, Vol. 28, pp. 179–191.

Chivers, R., and Aindow, J., 1983, "Ultrasonic Propagation Studies in Suspension Systems," *Journal of Physics D: Applied Physics*, Vol. 16, pp. 2093–2102.

Del Grosso, V., and Mader, C., 1972, "Speed of Sound in Pure Water," *Journal of the Acoustical Society of America*, Vol. 52, pp. 1442–1446.

Foscolo, P., and Gibilaro, L., 1985, "Fluid Dynamic Stability of Fluidised Suspensions: The Particle Bed Model," *Chemical Engineering Science*, Vol. 42, pp. 1489–1500.

Gibson, R. L., and Toksöz, M., 1989, "Viscous Attenuation of Acoustic Waves in Suspensions," *Journal of the Acoustical Society of America*, Vol. 85, pp. 1925–1934.

Goodsitt, M., Madsen, E., and Zagzebski, J., 1982, "Field Patterns of Pulsed Focussed Radiators in Attenuating and Nonattenuating Media," *Journal of the Acoustical Society of America*, Vol. 71, pp. 318–329.

Hampton, L., 1967, "Acoustic Properties of Sediments," *Journal of the Acoustical Society of America*, Vol. 42, pp. 882–890.

Harker, A., and Temple, J., 1988, "Velocity and Attenuation of Ultrasound in Suspensions of Particles in Fluids," *Journal of Physics D: Applied Physics*, Vol. 21, pp. 1576–1588.

Harris, G., 1981, "Review of Transient Theory for a Baffled Planar Piston," *Journal of the Acoustical Society of America*, Vol. 70, pp. 10–20.

Hilgert, W., and Hofmann, H., 1986, "Characterization of Gas Phase Flow in Bubble Columns at Low Superficial Gas Velocities with the Aid of the Ultrasonic Doppler Technique," *German Chemical Engineering*, Vol. 9, pp. 180–190.

Hsu, F., Turian, R., and Ma, T., 1989, "Flow of Non-Colloidal Slurries in Pipelines," *American Institute of Chemical Engineers Journal*, Vol. 35, pp. 429–442.

Kuster, G., and Toksoz, M., 1986, "Velocity and Attenuation of Seismic Waves in Two Phase Media: Part II. Experimental Results," *Geophysics*, Vol. 39, pp. 607–618.

Kytömaa, H. K., and Atkinson, C. M., 1992, "Sound Propagation in Suspensions and Acoustic Imaging of their Microstructure," accepted for publication in 1992 *Mechanics of Materials*, Vol. 16, pp. 189–197.

Machado, J., Sigelmann, R., and Ishimaru, A., 1983, "Acoustic Wave Propagation in Randomly Distributed Spherical Particles," *Journal of the Acoustical Society of America*, Vol. 74, No. 5, pp. 1529–1534.

McLeod, F., 1967, "A Directional Doppler Flowmeter," *International Conference of Medical Biological Engineering*, Stockholm, p. 213.

Morse, P., and Ingard, K., 1978, *Theoretical Acoustics*, McGraw-Hill, New York, NY.

O'Neil, H., 1949, "Theory of Focussing Radiators," *Journal of the Acoustical Society of America*, Vol. 21, pp. 516–526.

Plona, T. J., 1980, "Observation of a Second Bulk Compressional Wave in a Porous Medium at Ultrasonic Frequencies," *Appl. Phys. Lett.*, Vol. 36, pp. 259–261.

Shook, C., Gillies, R., Haas, D., Husband, W., and Small, M., 1982, "Flow of Coarse and Fine Slurries in Pipelines," *Journal of Pipelines*, Vol. 3, pp. 13–21.

Temkin, S., 1981, *Elements of Acoustics*, Wiley, New York, NY.

Urick, R. J., 1947, "A Sound Velocity Method for Determining the Compressibility of Finely Divided Substances," *Journal of the Acoustical Society of America*, Vol. 18, pp. 983–987.

Urick, R. J., 1948, "The Absorption of Sound in Suspensions of Irregular Particles," *Journal of the Acoustical Society of America*, Vol. 20, pp. 283–289.

Waterman, P., and Truell, R., 1961, "Multiple Scattering of Waves," *Journal of Mathematical Physics*, Vol. 2, pp. 512–540.

Yianneskis, M., and Whitelaw, J., 1984, "Velocity Characteristics of Pipe and Jet Flows With High Particle Concentration," *Liquid-Solid Flows and Erosion Wear in Industrial Equipment*, M. C. Roco, ed., ASME, New York, pp. 12–15.

APPENDIX

The velocity of sound in a two phase mixture is very accurately approximated by the phenomenological theory that models the medium as an effective single phase medium in which the speed of sound is given by

$$c_{(\text{single phase})} = \frac{1}{\sqrt{\rho\kappa}}.$$

The simplest approach is to model the medium with an effective density, ρ_{eff}, and compressibility, κ_{eff}, (Urick, 1947) where

$$\rho_{\text{eff}} = \nu\rho_s + (1-\nu)\rho_f$$

$$\kappa_{\text{eff}} = \nu\kappa_s + (1-\nu)\kappa_f$$

and to calculate the sound speed as

$$c_{\text{eff}} = \frac{1}{\sqrt{\rho_{\text{eff}}\kappa_{\text{eff}}}}.$$

This relatively simple approximation is valid in the limit that $kr \rightarrow 0$, but the experimental results deviate somewhat from this for higher kr (see Fig. 11).

Rand N. Conger
John Graham Associates,
Seattle, WA 98101

B. R. Ramaprian
Professor,
Department of Mechanical
and Materials Engineering,
Washington State University,
Pullman, WA 99164-2920

Correcting for Response Lag in Unsteady Pressure Measurements in Water

There is not much information available on the use of diaphragm-type pressure transducers for the measurement of unsteady pressures in liquids. A procedure for measuring the dynamic response of a pressure transducer in such applications and correcting for its inadequate response is discussed in this report. An example of the successful use of this method to determine unsteady surface pressures on a pitching airfoil in a water channel is presented.

Introduction

Diaphragm-type pressure transducers are most often used for pressure measurements in fluid flow research. The authors are currently involved in the measurement of the instantaneous surface pressure in the unsteady flow over an airfoil pitching at a constant angular velocity. These experiments are being conducted in a water channel. In this setup, the pressure transducer communicates with a surface pressure tap via a scanning valve and a short length of tubing. It is therefore important to know the dynamic response characteristics of this measurement system, and correct, if necessary for any inadequate response. It is possible, in principle, to obtain the dynamic response characteristics of this pressure measurement system by treating it as an unsteady fluid mechanical system. In practice, however, it is difficult to do so due to the lack of sufficient information on the characteristics of flow through the various components of this system.

An easier alternative to the above approach is to assume that the entire pressure-measurement system can be approximated by a linear dynamical system of appropriate order. It is well known that such systems are fully described by a set of parameters known as the "system parameters." Hence, the response of the system to any input can be determined if the system parameters are known. Conversely, the system parameters can be evaluated from a calibration experiment in which the system output corresponding to a known input is measured. One can then use these parameters to estimate the input (i.e., the true pressure) from the measured output (i.e., the indicated pressure) in any subsequent application.

The success of the above approach depends on how well the pressure measurement system approximates to a hypothetical linear dynamical system. It has been shown that a simple pressure measuring system such as the present one can be closely approximated by a second-order (mass-spring damper) dynamical system (Batill and Nebres, 1991). One can, therefore, determine the system parameters by giving the system a known input and comparing the transducer's response to the calculated response of a second-order system. The known input is usually either a periodic function or an impulse function. For measurements in air, in which the frequencies of interest lie in the audio range, it is easy to input a sinusoidal pressure fluctuation of known amplitude to the transducer over a range of frequencies, by using a small loudspeaker (Batill and Nebres, 1991). This procedure, however, is not suitable for pressure measurements in water, since the frequencies of interest are usually well below the audio range. On the other hand, the step-input approach can be used to determine the system parameters in this case. Such a procedure was used in the present experiments. Since there do not appear to be any earlier reports of similar dynamic response studies of pressure transducers in liquid flows, this short paper which outlines the present procedure and results should be of interest to researchers in this area.

Theoretical Framework

Let a tube of length L and cross-sectional area A be assumed to simulate the pressure tubing between the point of pressure measurement and the pressure transducer port. Under dynamic conditions, the instantaneous pressure P_t sensed by the transducer will differ from the instantaneous pressure at the measurement point P_s, due to the inertia of the fluid contained in the tube and the pressure loss ΔP_L in the system due to friction and other reasons. If this loss is assumed to be proportional to the average velocity of fluid in the tube (say, $\Delta P_L = CV$), which is reasonable for laminar flow, one arrives at the following equations:

$$\rho AL \frac{dV}{dt} = [(P_s - P_t) - CV]A. \qquad (1)$$

If A_d is the area of cross-section of the transducer and S_t the displacement of the diaphragm (assumed to be proportional to P_t), we have, from continuity,

$$AV = A_d \frac{dS_t}{dt}. \qquad (2)$$

Contributed by the Fluids Engineering Division for publication in the JOURNAL OF FLUIDS ENGINEERING. Manuscript received by the Fluids Engineering Division October 23, 1992; revised manuscript received January 19, 1993. Associate Technical Editor: D. P. Telionis.

From Eqs. (1) and (2), one gets the system response equation in the form

$$\frac{d^2P_t}{dt^2}+C_1\frac{dP_t}{dt}+C_2P_t=C_2P_s \tag{3}$$

where, again, S_s is the steady-state displacement of the diaphragm assumed to be proportional to the pressure P_s. The constants C_1 and C_2 depend on the geometry of the tubing and the fluid properties.

In practice, the tubing may consist of multiple lengths of different diameters and the pressure loss may include losses due to sudden contraction, sudden expansions and bends in the tubing. We assume that even in that case, the system response can still be described by Eq. (3). It is, however, very difficult to estimate the values of these constants from the tubing geometry and fluid properties.

Equation (3) is of the same form as the standard response equation for a second-order linear dynamical system, namely, the spring-mass-damper system

$$\frac{d^2y}{dt^2}+2C_c\omega_n\frac{dy}{dt}+\omega_n^2y=\frac{F(t)}{m}=\omega_n^2y_s \tag{4}$$

where the forcing function $F(t)$ on the right-hand side has been expressed in terms of the steady-state spring displacement y_s. For details, the reader may refer to Beckwith and Buck (1973). The parameters ω_n and C_c, usually known as the natural frequency and the damping constant of the dynamical system, can be obtained from an actual measurement of the system response to a known forcing function. Comparison of Eqs. (3) and (4) suggests that the pressure measurement system can be characterized by a natural frequency $\omega_n=C_2^{1/2}$ and a damping constant $C_c=C_1/(2\omega_n)$, which can be regarded as the system parameters.

To determine the system parameters, consider the transient response of the system to a step input function described by:

$$\begin{aligned}P_s&=0 \quad t<0\\ P_s&=P_\infty \quad t\geq 0.\end{aligned} \tag{5}$$

The solution of Eq. (3) in this case depends on the value of C_c. The ratio R_n of the indicated pressure to the true pressure is given by

$$R_n=\frac{P_t}{P_\infty}=1-e^{-C_c\omega_nt}\left[\frac{C_c}{\sqrt{1-C_c^2}}\sin\sqrt{1-C_c^2}\,\omega_nt-\cos\sqrt{1-C_c^2}\,\omega_nt\right] \tag{6}$$

for $C_c<1.0$, (under damped), and

$$R_n=\frac{-C_c-\sqrt{C_c^2-1}}{2\sqrt{C_c^2-1}}e^{(-C_c+\sqrt{C_c^2-1})\omega_nt}+\frac{C_c-\sqrt{C_c^2-1}}{2\sqrt{C_c^2-1}}e^{(-C_c-\sqrt{C_c^2-1})\omega_nt}+1 \tag{7}$$

for $C_c\geq 1$ (over damped). If the transient response $P_t(t)$, can be measured in this case, the system parameters ω_n and C_c can then be obtained from Eq. (6) or (7) as appropriate. The constants C_1 and C_2 can then be obtained from

$$C_1=2\omega_nC_c \tag{8}$$

and

$$C_2=\omega_n^2 \tag{9}$$

When the transducer is used in an actual experiment, the unknown true pressure $P_s(t)$ can be recovered from the measured pressure $P_t(t)$ from Eq. (3) by substituting the values of C_1 and C_2. If $P_t(t)$ is measured as a discrete time series, then the derivatives in Eq. (3) are estimated using an appropriate finite difference approximation. The experimental procedure therefore consists of two steps. The first step is the determination of the system parameters. The next step is the application of the known characteristics to correct the actual measurements obtained from the airfoil. These steps are described below.

Determination of System Parameters

Since the system parameters depend on the configuration of the entire measurement system and not just the pressure transducer alone, care was taken to design the test set up so that it closely mimicked the measurement system, including the pressure tubing, used in the actual airfoil experiments. The experiment consisted of subjecting this test system to an instantaneous pressure change and analyzing the result obtained during the transient process. A scanning valve was used in this test to produce the step change in pressure. This was a logical choice as the same scanning valve was to be used in the actual measurement system for switching the transducer from one pressure tap to the next. The scanivalve has a switching time of about 0.01 second, which is about two orders of magnitude smaller than the typical response time of the measuring system being studied. It is hence reasonable to assume that the scanivalve switches "instantaneously," for the purpose of the present experiments.

Figure 1 is a schematic of the experimental configuration used to perform the step-input test. Two 500-ml plastic bottles were used as the pressure reservoirs to mimic the surface port and the reference freestream static pressure port used in the actual experiments. The difference in piezometric head h between the two reservoirs was approximately 3/4 of the full scale range of the transducer being tested. The reservoirs were set up such that the 48-channel scanning valve could switch the transducer between the two reservoirs, thereby changing the pressure difference across the transducer instantaneously from 0 (channel 0) to ρgh (channel 1). The operation of the scanning valve as well as the collection of data were performed by a personal computer equipped with an analog-to-digital converter.

The test proceeded as follows: First, the scanning valve channel was set to zero. The PC was set up to take 10 seconds of transducer output voltage data at a sampling rate of 200 Hz. Approximately two seconds after initiating the data collection routine, the scanning valve was switched to channel 1, subjecting the transducer to an almost instantaneous pressure rise. The data collection continued till the end of the 10 second period. The experiment was repeated and the final results averaged.

Results

Three different transducers were tested in these experiments. These were: (i) Validyne model DP45-14, (ii) Validyne model DP15-20, and (iii) Celesco model LCVR 0-2 cm range. Typical results of the experiments are shown in Figs. 2(*a*) and 2(*b*). In these figures the instantaneous transducer output voltage v is normalized using the initial and final steady-state outputs v_i and v_0, respectively, as

$$v^*=\frac{(v-v_i)}{(v_0-v_i)} \tag{10}$$

Figure 2(*a*) shows the response of the transducer DP45-14 system. It exhibits a monotonic increase toward the final steady state and is therefore an example of an over damped system. On the other hand, the response of transducer DP15-20 system, shown in Fig. 2(*b*) exhibits an overshoot and is representative of an under damped system. A nonlinear least squares program, taken from Press et al. (1989), was used to fit the ap-

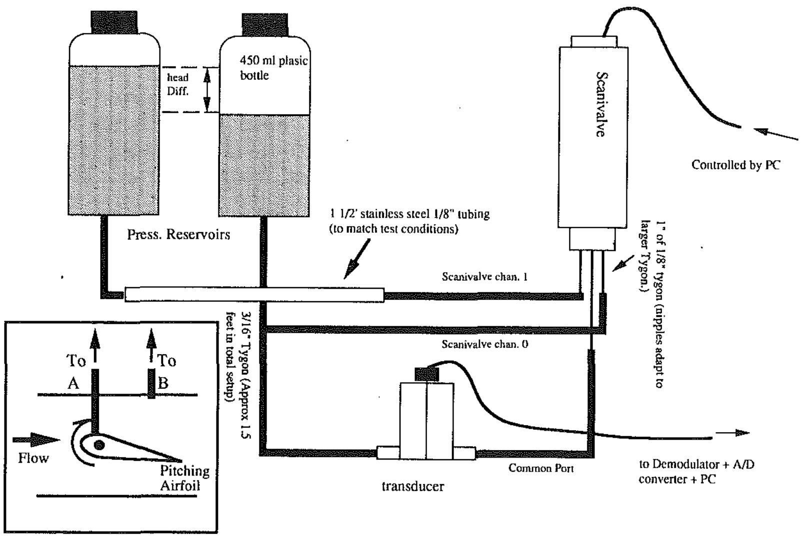

Fig. 1 Schematic of the setup for the step-response test. The schematic for the airfoil pressure measurement is shown in the inset.

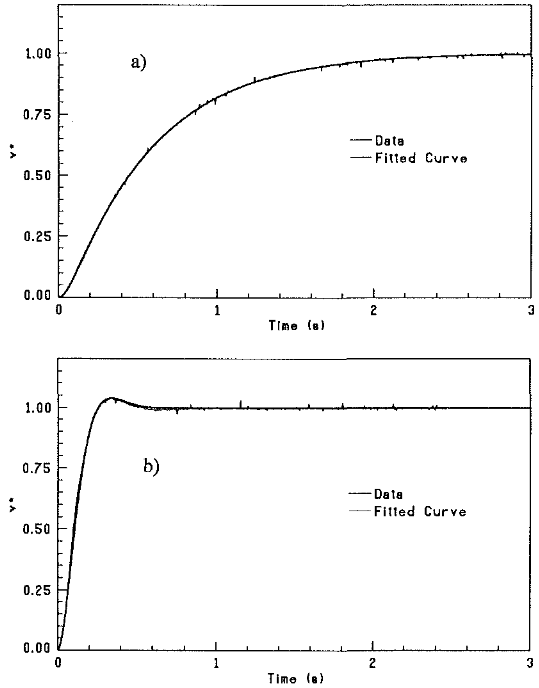

Fig. 2 Typical step response of the transducers: (*a*) Validyne DP 45-14, (*b*) Validyne DP15-20

propriate theoretical solution Eq. (6) or Eq. (7) to the experimental data in each case. The fitted curves are also shown in Figs. 2(*a*) and 2(*b*), although it is not easy to distinguish the actual data from the fitted curve. This, in effect, confirms that the transducer system can indeed by closely approximated by a second order system.

The values of ω_n and C_c corresponding to the fitted curves for the three transducer systems are listed in Table 1.

Application of Procedure

The above transducer systems were used to determine surface pressures at 80 positions along the chord of the airfoil undergoing a pitch-up maneuver from 0 to 40-degree angle of incidence (α) in steady-flow in an open-surface water channel. This maneuver was completed in times ranging from 8–20 seconds.

Table 1 System parameters for the transducer systems

Transducer	ω_n s^{-1}	C_c
Validyne DP45-15	5.86±0.05	1.600+0.005
Validyne DP15-20	16.27±0.15	0.701±0.005
Celesco LCVR	11.54±0.10	1.015±0.01

The pressure data were acquired at 3000 equal angular intervals of incidence during the pitching motion. The resulting pressure versus time data (raw data) were then smoothed by averaging over every successive 25 data points and assigning the averaged values to the average angular position of these points. This procedure provided smoothed data at intervals of approximately one-third of a degree, in the 0–40 degree incidence range. This corresponds to an effective sampling frequency of 6 Hz at the lowest pitching rate, and 15 Hz at the highest pitching rate studied. These values were quite adequate to resolve the temporal variation of pressure with acceptable accuracy. Finally, these smoothed pressure versus angle (time) data were corrected for the measurement system response using Eq. (3). The derivatives in the equation were evaluated from the pressure-time data using finite difference approximation. As an example, results are shown in Figs. 3(*a*) and 3(*b*) for the highest pitching rate of about 5 degrees per second.

Figure 3(*a*) shows smoothed pressure versus angle data from a pressure tap, obtained using each of the three different pressure transducers in separate but identical pitching realizations. The time information is also provided in each figure. The pressures are plotted in terms of the nondimensional pressure coefficient C_p which is defined, in the usual manner, as

$$C_p=\frac{p-p_\infty}{\frac{1}{2}\rho U_\infty^2} \qquad (11)$$

where p is the surface pressure, p_∞ is the reference static pressure in the free stream, ρ is density, and U_∞ is the freestream velocity. Figure 3(*b*) shows the results after applying the correction for dynamic response. The success of the reconstruction procedure can be judged from a comparison of the two figures. The three uncorrected traces show significant variation in their shape and magnitude. It is seen that the corrected trace in each case shows a small increase in amplitude and a slight lead relative to the uncorrected trace. The actual corrections are different for the three transducers. Also, the corrections in all cases are small in the present application. This was not un-

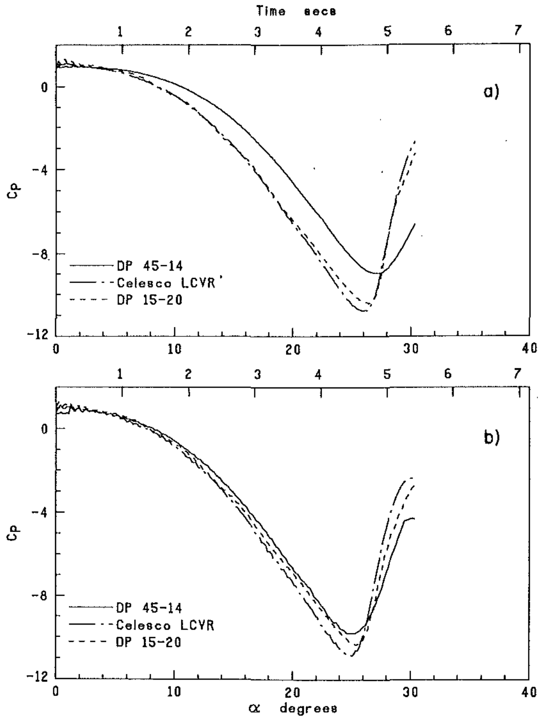

Fig. 3 Pressure versus angle/time traces from the airfoil experiment: (*a*) original transducer output, (*b*) after correcting for response lag. Experimental uncertainties: α: ±0.07 degree; time: ±0.001 s; C_p: ±6 percent.

expected since the pressure transducers had been carefully selected for these experiments and the tube lengths were kept small. It is also important to note that correction moves all the three results closer together. While the collapse is not perfect, the variation amongst the three corrected results is of the same order as the experimental uncertainties. The most divergent of the three corrected traces is that of the DP45-14 transducer system. This should be expected as its very slow response characteristics made it the least suitable arrangement for the pitching rate used in the experiment.

Conclusions

The procedure described in this report provides an effective way to correct for the phase and amplitude distortion of pressure measurements associated with the use of a diaphragm-type transducer in unsteady liquid flow. The procedure can be used in all cases where a digital data acquisition system is used to collect the data. It is suggested that for best results, one should first optimize, to the extent possible, the transducer and measurement configuration used for the task at hand. If the system selected is too sluggish, the heavily attenuated output data can become buried in noise, making reconstruction of the original signal difficult and unreliable.

Acknowledgments

This work was supported by the U.S. Airforce Office of Scientific Research grant no. AFOSR-90-0131 with first, Capt. H. Helin and subsequently Maj. D. Fant as program managers. This support is gratefully acknowledged. The authors wish to express their thanks to Validyne Inc. for loaning two of the transuducers used in these tests.

References

Beckwith, T. G., and Buck, N. L., 1973, *Mechanical Measurements*, Addison-Wesley Publishing Company, pp. 16–32.

Batill, S. M., and Nebres, J. V., 1991, "Application of Digital Filtering Techniques to Unsteady Pressure Measurements," AIAA Paper 91-0061, pp. 1–8.

Press, W. H., Flannery, B. P., Teukolsky, S. A., and Vetterling, W. T., 1989, *Numerical Recipes: The Art of Scientific Computing*, Cambridge University Press, Cambridge, pp. 521–528.

Numerical Simulations of Three-Dimensional Flows in a Cubic Cavity With an Oscillating Lid

Reima Iwatsu[1]
Institute of Computational Fluid Dynamics,
1-22-3 Haramachi, Meguro-ku,
Tokyo 152, Japan

Jae Min Hyun
Korea Advanced Institute of Science
and Technology,
Seoul, Korea

Kunio Kuwahara
The Institute of Space and
Astronautical Science,
Kanagawa, Japan

Numerical studies are made of three-dimensional flow of a viscous fluid in a cubical container. The flow is driven by the top sliding wall, which executes sinusoidal oscillations. Numerical solutions are acquired by solving the time-dependent, three-dimensional incompressible Navier-Stokes equations by employing very fine meshes. Results are presented for wide ranges of two principal physical parameters, i.e., the Reynolds number, Re $\leq$ 2000 and the frequency parameter of the lid oscillation, $\omega' \leq 10.0$. Comprehensive details of the flow structure are analyzed. Attention is focused on the three-dimensionality of the flow field. Extensive numerical flow visualizations have been performed. These yield sequential plots of the main flows as well as the secondary flow patterns. It is found that the previous two-dimensional computational results are adequate in describing the main flow characteristics in the bulk of interior when ω' is reasonably high. For the cases of high-Re flows, however, the three-dimensional motions exhibit additional complexities especially when ω' is low. It is asserted that, thanks to the recent development of the supercomputers, calculation of three-dimensional, time-dependent flow problems appears to be feasible at least over limited ranges of Re.

Introduction

Numerous studies have been made on the flow of a viscous fluid in a square cavity with its upper lid sliding at a constant speed (e.g., Tuann and Olson, 1978; Ghia et al., 1982; Schreiber and Keller, 1983; Koseff and Street, 1984a–c, Freitas et al., 1985; Ku et al., 1987; Perng and Street, 1989; Prasad and Koseff, 1989; Iwatsu et al., 1989, 1990). However, the problem of unsteady flows, induced by unsteady motion of a sliding wall, has received less attention in the literature. The unsteady motion in the infinite expanse of a viscous fluid, generated by an infinite flat plate undergoing sinusoidal oscillation in its own plane, poses a classical problem. This flow, referred to as the Stokes' second problem, admits a well-known analytical solution (Schlichting, 1979).

The flow within a two-dimensional closed finite square cavity, driven by a sliding wall which executes sinusoidal oscillation, was first treated by Soh and Goodrich (1988). This two-dimensional flow represents an extension of the Stokes' second problem to finite geometry. The primal objective of this account, however, was to inquire into the capability of certain numerical algorithms in tackling unsteady confined flows. Therefore, explicit analyses of flow characteristics were not attempted in this report.

Recently, comprehensive and systematically-organized numerical investigations were carried out by Iwatsu et al. (1992). The prominent features of unsteady confined flows in a square cavity were illuminated by scrutinizing the numerical solutions to the time-dependent, two-dimensional Navier-Stokes equations. The principal parameters are the Reynolds number, Re $= U_0L/\nu$ and the frequency parameter, $\omega' = \omega L/U_0$, where, U_0 is the maximum speed of the sliding lid, ω the frequency of the lid motion, $U \equiv U_0 \cos \omega t$, L the depth (width) of the cavity, and ν the kinematic viscosity of the fluid (see Fig. 1). The results of these two-dimensional calculations indicate that the flow exhibits characteristic changes as two parameters, Re and ω', vary over wide ranges. When ω' is high, the fluid motion is confined within the vicinity of the oscillating boundary wall; much of the cavity interior remains nearly stagnant. On the contrary, when ω' is low, the motion of the top lid penetrates deep into the cavity interior, and the global flow pattern bears similarity to the conventional driven-cavity flow with a constant-speed moving boundary. For intermediate ranges of the above two extreme cases, i.e., $\omega' \sim O(1)$, the flow characteristics vary greatly as Re is altered: at low Re, a primary vortex fills in the bulk of the cavity in the first half cycle of the lid motion and this vortex is quickly replaced by a counter rotating primary vortex in the latter half cycle. When Re is high, a multi-cell structure appears: the primary vortex of the first half cycle persists over the latter half cycle. The entire cavity region is divided into four counter rotating vortices of comparable sizes.

In the present article, three-dimensional flows driven by a sinusoidal oscillation of the top lid within a square cubical

---

[1] Presently, Obayashi Corporation, Technical Research Institute, 4-640 Simokiyoto, Kiyose-shi, Tokyo 204, Japan.

Contributed by the Fluids Engineering Division for publication in the JOURNAL OF FLUIDS ENGINEERING. Manuscript received by the Fluids Engineering Division February 28, 1992; revised manuscript received May 4, 1993. Associate Technical Editor: S. A. Ragab.

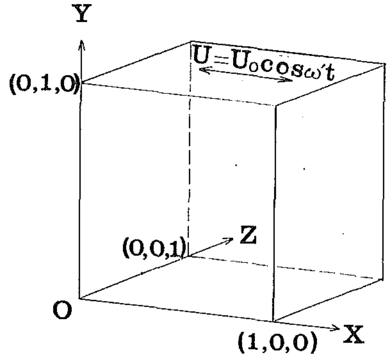

Fig. 1 Sketch of flow configuration and coordinates

container will be addressed. The problem constitutes a direct sequel to the prior two-dimensional computations (Iwatsu et al., 1992). As can easily be appreciated, the present efforts embody a formidable undertaking of numerical experimentations. Both the three-dimensionality and unsteadiness present enormous difficulties in numerical computations and data-processing. Perusal of the pertinent literature reveals that, to date, no systematic efforts have been expended on obtaining numerical solutions to three-dimensional, unsteady cavity flows. Admittedly, the progress in this field has been hampered by the prohibitive computing cost and inadequate computing capabilities.

Even in the case of the conventional cavity flow driven by the top lid sliding at a constant speed, two-dimensional calculations were shown to be insufficient in describing the experimental results for a cubical cavity (Koseff and Street, 1984a-c; Freitas et al., 1985; Iwatsu et al., 1989, 1990). Extensive numerical simulations documented in these treatises disclosed the qualitative discrepancies between the two-dimensional and three-dimensional flow fields. The major elements of three-dimensional driven cavity flows may be depicted as a primary circulation and secondary vortices. The existence of the end-walls acts to retard the main flow especially at low Re. At high Re, i.e., Re ~ 2000, the three-dimensionality of flow is pronounced, and the formation of the Taylor-Görtler-like vortices near the bottom rigid wall is discernible (see, e.g., Kim and Moin, 1985). At still higher Re, i.e., Re ~ 3000, a considerable amount of flow unsteadiness is observed, particularly in the form of meridional vortices. These eminent three-dimensional flow characteristics cannot be captured by two-dimensional calculations.

The objective of the present endeavor is to secure more realistic computational results of three-dimensional flows by solving the Navier-Stokes equations. Computation was implemented on a supercomputer using extremely high resolutions, employing as many as nearly a half million grid points. Thanks to the recent advancement in speed and capacity of computational resources, it appears that meaningful three-dimensional, unsteady calculations are feasible at least over limited ranges of physical parameters. It is expected that the present numerical solutions produce a baseline to grasp the essentials of unsteady three-dimensional flows in a confined cavity. The emphasis will be placed on illustrating the salient three-dimensional features of the flow.

The Model

Consider an incompressible viscous fluid of density ρ, inside a square cubical cavity of length L in three directions. The flow configuration and coordinates are displayed in Fig. 1. The velocity components are (u, v, w) in the (x, y, z) directions. At $t = 0$, the upper lid at $y = L$ starts sinusoidal oscillation in its own plane, described as $U = U_0 \cos \omega t$. The reference scales for length, time, velocity, and pressure are, respectively, L, L/U_0, U_0, ρU_0^2. The principal parameters are $\mathrm{Re} = U_0 L/\nu$ and $\omega' = \omega L/U_0$ (see Iwatsu et al., 1992).

The finite difference procedure adopted here is based on the MAC method (Harlow and Welch, 1965), with an upwind modulated third-order scheme (Kawamura and Kuwahara, 1986) applied to the nonlinear terms. The rest of the spatial derivatives are approximated by the second-order central differencing scheme. A nonuniform, nonstaggered mesh is adopted. The clustering of the grid points is accomplished by introducing hyperbolic tangent functions in the three directions (see page 176 of Iwatsu et al., 1989).

The number of typical grid points is 81•81•81. The grids were stretched to cluster the grid points near the walls. Prior to the full-dress calculations, tentative runs were made using three different resolutions, i.e., grid 1 (41•41•41), grid 2 (81•81•81), and grid 3 (101•101•101). The time increment Δt was set at $2\pi/8000\omega'$ for all three runs.

The outcome of these sensitivity tests indicated successful grid convergence. For instance, the values of the skin friction experienced by the moving top wall, C_f, were monitored to demonstrate grid sensitivity. Here, C_f is defined as

$$C_f(t) = \int_0^1 \int_0^1 \left. \frac{\partial u}{\partial y} \right|_{y=1} dxdz. \tag{1}$$

By undergoing Fourier series representations, the first harmonic of $C_f(t)$ can be expressed as

$$C_f = \overline{C}_f \cos[\omega' t - \delta]. \tag{2}$$

The amplitudes of the higher harmonics were extremely small, and $C_f(t)$ may now be approximated, with a high degree of accuracy, by (2). The results of the test calculations using $\mathrm{Re} = 400$, $\omega' = 1.0$ yielded $(\overline{C}_f, \delta)$ as (26.86, 16.20°) for grid 1, (31.04, 14.40°) for grid 2, and (32.34, 14.40°) for grid 3, respectively. Additional exemplary runs were conducted; these exercises convincingly point to the observations that $\overline{C}_f$ and δ are far less sensitive to the variations in Δt. The time increment Δt was $2\pi/1000\omega'$, $2\pi/8000\omega'$ and $2\pi/12000\omega'$ for the cases of $\omega' = 10.0$, 1.0 and 0.4, respectively. The sequence of calculations followed the original model development of the MAC method. The Poisson equation for the pressure was solved at the time step n. Secondly, the velocity at the next time step was obtained by solving the momentum equations. The convergence tolerance was 10^{-5} for $\Sigma(\delta p)^2$. The exemplary sensitivity tests of the time increments adopted in this study indicated that the discrepancies in the computed velocity and pressure fields was less than one percent. Summarizing these results, it was concluded that grid 2 was sufficient to delineate the salient flow characteristics of the present problem. The typical cpu time per one case ranged from 7 to 14 hours (approximately 7.73×10^{-7} sec per time step per grid point) on a FUJITSU VP-400 (1.3GFLOPS), depending on the set of physical parameters.

Results and Discussion

Full numerical solutions are obtained for a total of 12 cases. Time-marching calculations were continued from the initial state to the time instant which contained approximately 10 cycles of the lid oscillation. In most cases, a quasi-periodic state was reached within the first 4 cycles. As can be readily appreciated, the volume of data generated for time-dependent, three-dimensional flows is exceedingly large. In view of the clarity of presentation and the severe limitation of space, only the global flow characteristics will be displayed in this paper.

First, we shall consider the flows at low Re. The numerical data for Re = 100 were processed for this purpose. The numerically-constructed visualizations are useful to show the character of the main flow on the symmetry plane ($z = 0.5$). The sequential plots of (u-v) components of the velocity field

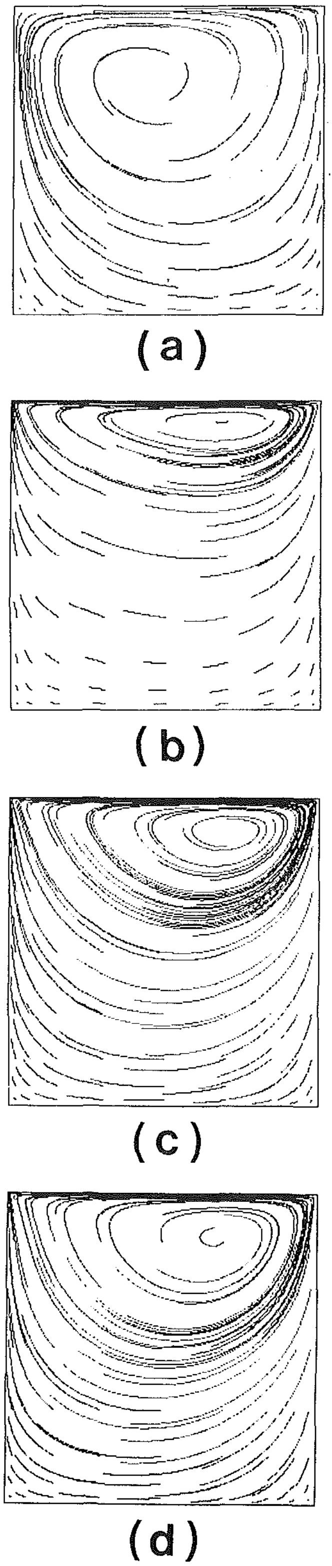
(a)

(b)

(c)

(d)

Fig. 2 Numerically constructed flow visualizations, showing u-v components in the symmetry plane ($z = 0.5$). Conditions are Re = 100, $\omega' = 0.4$. Times are (*a*) $t = 0$, (*b*) $t = T/8$, (*c*) $t = T/4$, (*d*) $t = 3T/8$, where T is the period of lid-oscillation $T = 2\pi/\omega'$. The initial instant of these plotted data is at $t = 8T + 3/4T$.

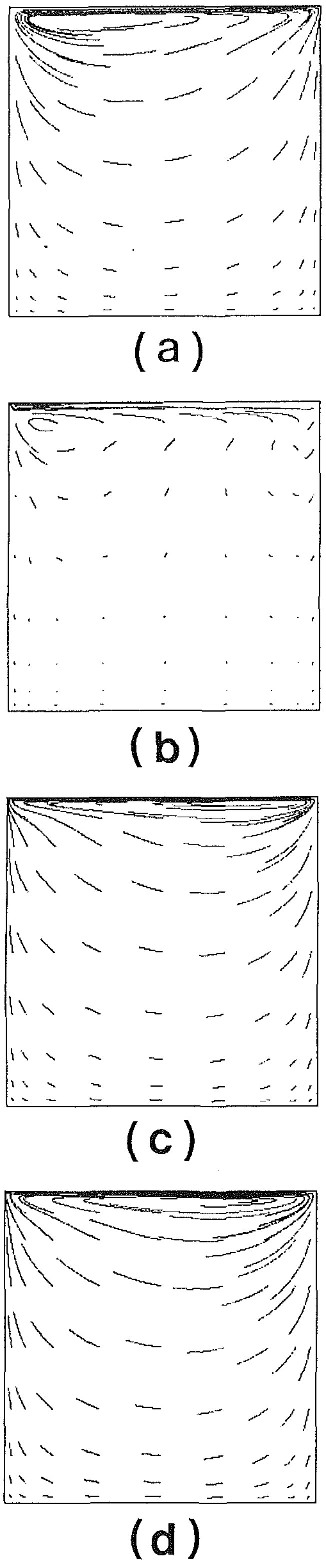
(a)

(b)

(c)

(d)

Fig. 3 Same as in Fig. 2, except for Re = 100, $\omega' = 10.0$

are displayed for the first half cycle, $0 \leq t \leq \pi/\omega'$. Figure 2 [$\omega' = 0.4$] is typical of a low ω', and Fig. 3 [$\omega' = 10.0$] is representative of a high ω' flow. The effect of the frequency is manifest in the penetration depth. This can be defined as the vertical distance, measured downward from the top wall, over which the motion of the top wall has direct influence on the global flow field. When ω' is low, the impact of the lid motion penetrates a long distance into much of the whole domain of the cavity. However, if ω' is high, the direct influence of the lid motion penetrates into only a small vertical length of the cavity near the top wall. As stressed by Iwatsu et al. (1992), if ω' is high, the profiles of u-velocity versus y,

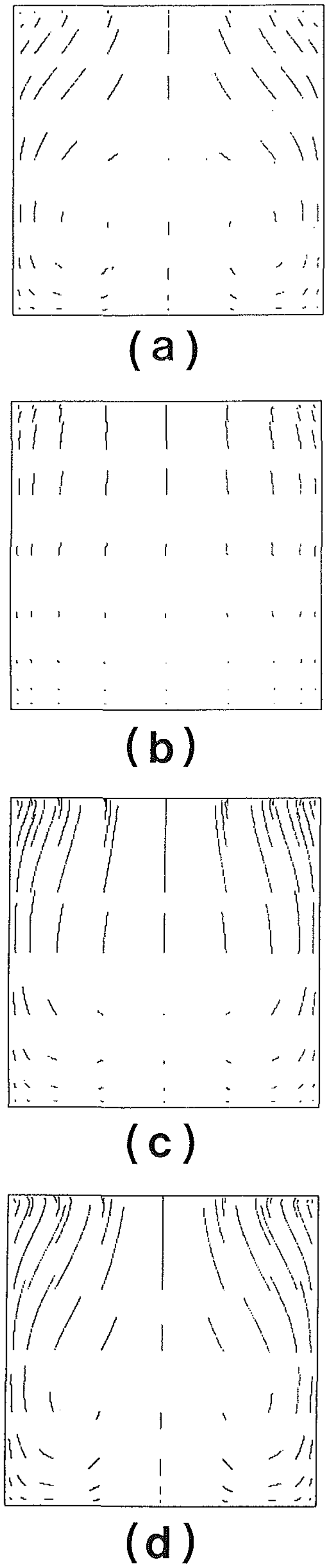

Fig. 4 Numerically constructed flow visualizations, showing *v-w* components in the transverse plane $x = 0.5$. Conditions are Re = 100, $\omega' = 0.4$.

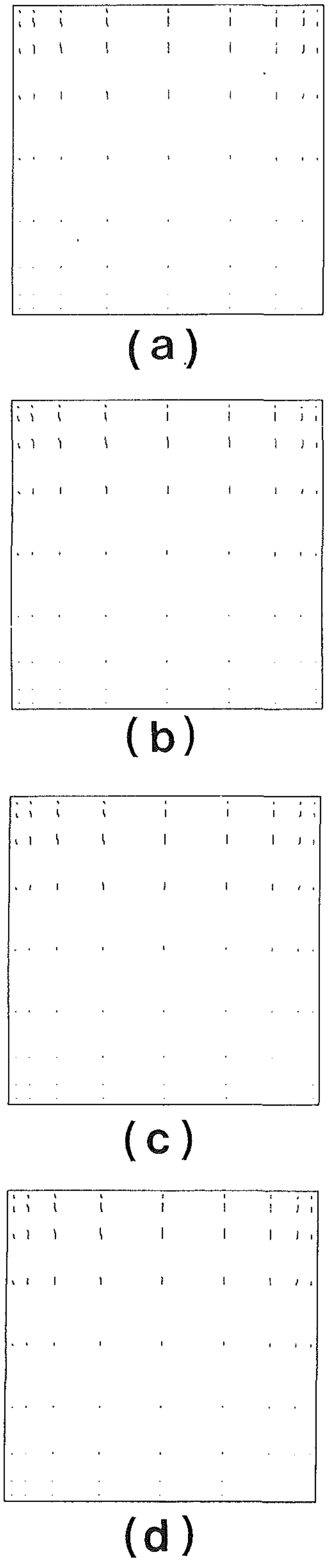

Fig. 5 Same as in Fig. 4, except for Re = 100, $\omega' = 10.0$

when scaled by using the factor $(\mathrm{Re}\omega')^{-1/2}$, bear strong qualitative resemblance to the classical solution of the Stokes' second problem (see Figs. 2(*c*), 3(*c*), 4(*c*) of Iwatsu et al., 1992). When ω' is moderate, $\omega' \sim O(1)$, a hybrid nature of the above two flows is evident. Thorough comparisons of the present three-dimensional data against the preceding two-dimensional computations (Iwatsu et al., 1992) establish that the major qualitative features of the main flow (u-v components) in much of the three-dimensional cavity interior are consistent with the descriptions of two-dimensional computations.

Next, the secondary flows, consisting of (v-w) components, are visualized in the y-z transverse plane ($x = 0.5$). These will serve to illuminate the eminent features underscoring the three-dimensional nature of realistic flow systems. Figure 4 exemplifies the case of a low ω' ($\omega' = 0.4$), and Fig. 5 for a high

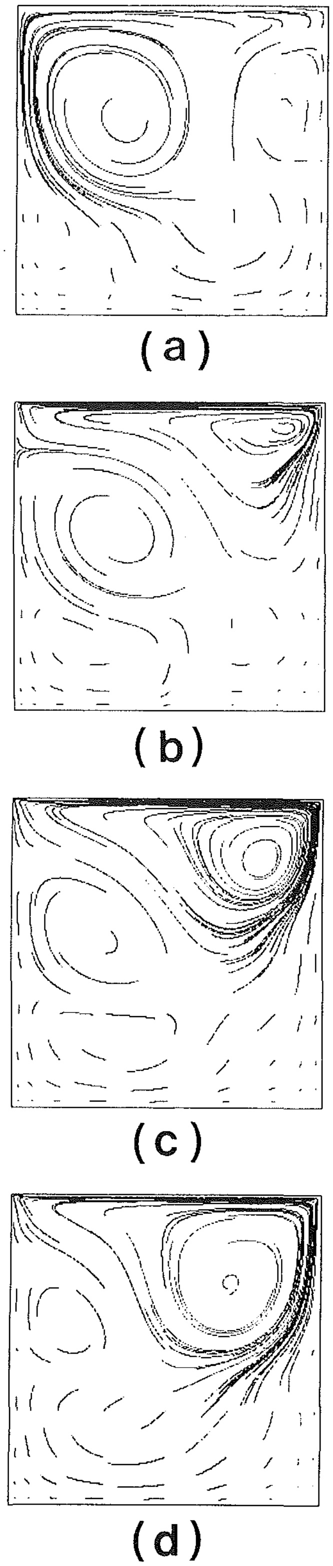

Fig. 6 Same as in Fig. 2, except for Re = 1000, $\omega' = 0.4$

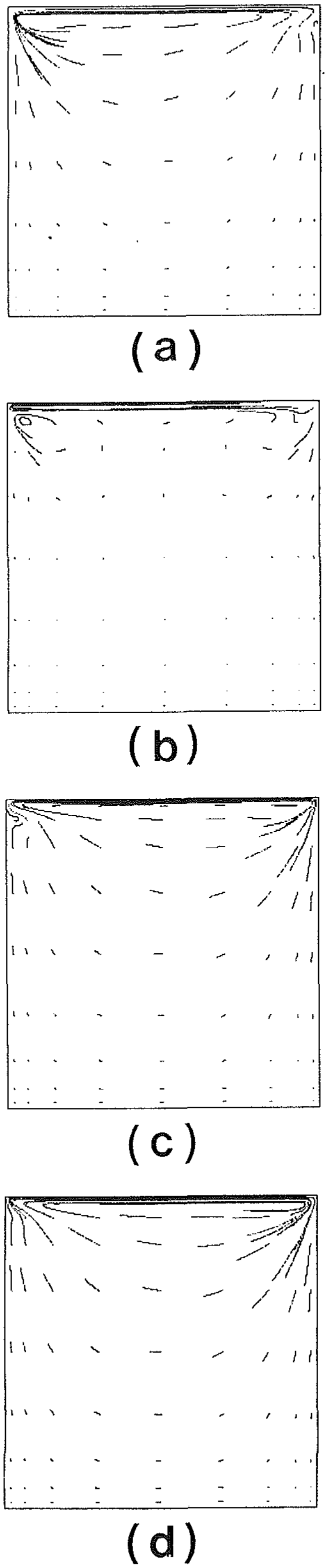

Fig. 7 Same as in Fig. 2, except for Re = 1000, $\omega' = 10.0$

ω' ($\omega' = 10.0$). When ω' is small, the presence of the secondary flows is discernible and this clearly illustrates appreciable three-dimensionalities of the global flow patterns. In particular, the three-dimensionality is notable in the regions close to the end-walls ($z = 0$ and $z = 1$). However, when ω' is large, as shown in Fig. 3, the main flow itself is weak in the bulk of the interior. Accordingly, as demonstrated in Fig. 5, the strengths of the secondary flows in the interior are vanishingly small. The results in Figs. 3 and 5 for low Re indicate that, when ω' is high, the overall flow structure may be approximated as two-dimensional in large portions of the cavity interior. It is also ascertained that, as exhibited in Fig. 3, the principal structure of the main flow, e.g., the plots of u versus y, as well as of v versus y, in the bulk of the three-dimensional cavity interior can be depicted reasonably well by two-dimensional calculations (see Iwatsu et al., 1992).

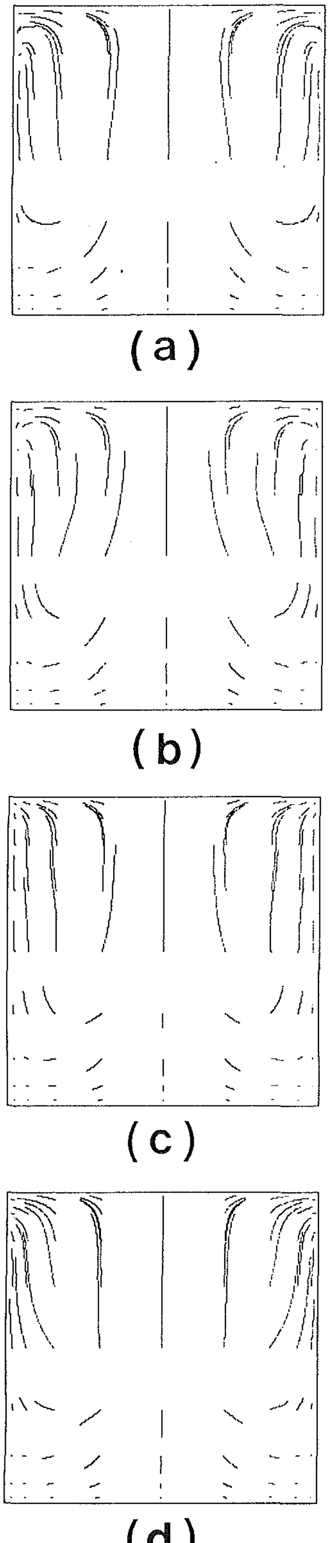

Fig. 8 *Same as in Fig. 4, except for Re = 1000, $\omega' = 0.4$*

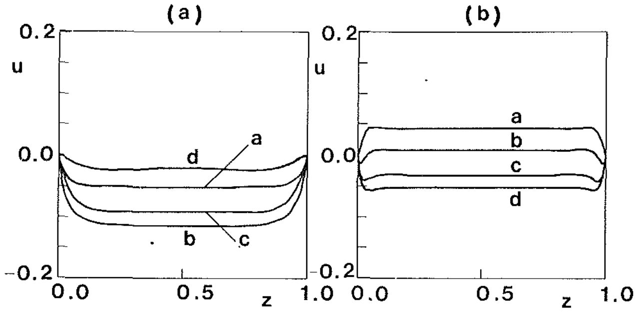

Fig. 9 The transverse (z) variations of u along the line $x = 0.5$, $y = 0.75$. Re = 100. Times are: a, $t = 0$; b, $t = T/8$; c, $t = T/4$; d, $t = 3T/8$; where T is the period of lid-oscillation $T = 2\pi/\omega'$. The initial instant of these plotted data is at $t = 17T + 3/4T$. (a) $\omega' = 0.4$, (b) $\omega' = 10.0$.

In the next stage, situations of high Re are considered. Before proceeding to examine the flow details, it is worth mentioning the time-dependence of the global flow at high Re. As examples, the velocity profiles at a high Reynolds number, e.g., Re = 2000, are scrutinized. The flow demonstrates characteristic changes as ω' encompasses a broad range. First of all, a completely quasi-periodic state was not realized for the case of low ω', e.g., $\omega' = 0.4$, in the present investigation. For this case, computation was continued from the initial state to the time instant which contained 20 cycles of lid-oscillation. The time histories of velocity components at fixed points were recorded and analyzed. These data exhibit that the time variations of velocity components are contaminated by the higher harmonics of the imposed basic frequency and they did not approach a strictly quasi-steady, regular wave profiles. However, it should be added that the contributions of the higher harmonics to the overall velocity amplitudes were minor. Also, it is noted that the results of runs at $\omega' = 1.0$ and 10.0 were far more cyclic. The visual information of the time histories confirms this assertion. These plots are similar to the figures presented earlier (see Fig. 9 of Iwatsu et al., 1992).

In a manner similar to the previous discussions for low Re, the patterns of main flow for Re = 1000 (u-v components) on the symmetry plane ($z = 0.5$) are depicted in Fig. 6 (for $\omega' = 0.4$) and in Fig. 7 (for $\omega' = 10.0$). When ω' is small, the main flow is vigorous and it fills in much of the cavity interior, as illustrated in Fig. 6. On the contrary, when ω' is large, substantial fluid motions are confined to narrow regions adjacent to the moving boundary wall. This is suggestive of the fact that the main flow in the bulk of the interior is approximately one-dimensional at high ω'. The above characterizations of the main flow in the symmetry plane are qualitatively similar to the results of two-dimensional calculations. The u-y plots and v-x plots in the plane of $z = 0.5$ are in broad qualitative consistency with Figs. 2–7 of Iwatsu et al. (1992).

However, at large Re, the general flow properties entail considerable three-dimensionalities, and these are best illuminated by inspecting the secondary flows, especially at low ω'. The numerical flow visualizations render the plots of (v-w) components in the plane $x = 0.5$. When ω' is small (see Fig. 8 for $\omega' = 0.4$), the existence of substantial secondary flows is apparent in bulk of the cavity interior. However, when ω' is large, the secondary flows are very weak in much of the interior region. The v-w plots at $x = 0.5$ for this case are almost blank, and this picture is not presented here. A thin-layer-like flow is realized when ω' is very high. It should be remarked that the Stokes' second problem provides the (dimensional) penetration depth $(\omega/2\nu)^{-1/2}$ for a semi-infinite oscillating plate. The ratio of penetration depth to the cavity depth L, $(\omega/2\nu)^{-1/2}/L = (1/2 \cdot \omega L/U_0 \cdot U_0L/\nu)^{-1/2} = \sqrt{2}(\omega' \cdot \mathrm{Re})^{-1/2} \ll O(1)$ for a high Re, high ω case, e.g., Re = 1000 and $\omega' = 10.0$. This argument is supportive of the realization of nearly one-dimensional flow in the interior core, as demonstrated in the present three-dimensional results.

Exploiting the wealth of numerical data, we shall now illustrate the explicit transverse (z) variations of the principal velocity component u. Figure 9 is for a low Re. The three-dimensionality, as denoted by the z-variations, tends to be

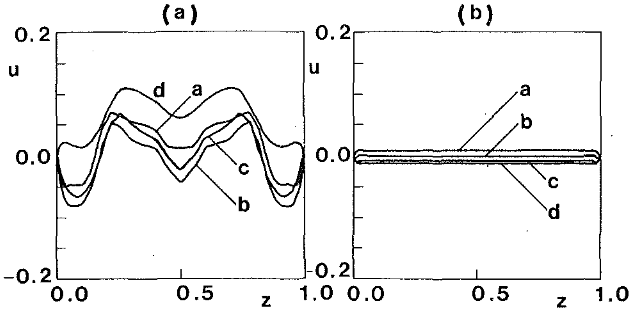

Fig. 10 Same as in Fig. 9, except for Re = 2000

appreciable near the endwalls when ω' is small. However, in much of the central interior, the u-velocities are fairly uniform in z, implying considerable degrees of two-dimensionality.

At high Re, the z-variations in u are profound when ω' is small. As seen in Fig. 10(a), prominent z-variations of u in the interior are evident. When ω' is large (see Fig. 10(b)), the u-velocities themselves tend to be rather small, and two-dimensional approximations are largely valid in the interior.

Conclusion

Numerical investigations are carried out of the three-dimensional flows within a cubic cavity driven by the top lid which executes harmonic oscillation. Comprehensive and detailed results are presented over wide ranges of physical parameters, i.e., $\mathrm{Re} \leq 2000$, $\omega' \leq 10.0$. It is clearly shown that for low Re, the overall characteristics of the main flow can be approximated by two-dimensional flow predictions. When Re is high, the flow features depend greatly on the value of ω'. When ω' is high, the main flow in the interior core bears similarity to the classical analytic solution of the Stokes' problem. When ω' is low, three-dimensionality is pronounced and the secondary flows are appreciable. On balance, the present numerical simulations are encouraging in that straightforward three-dimensional flow calculations are shown to be feasible at least over limited parameter ranges.

Acknowledgment

Appreciation is extended to the referees. Their constructive opinions led to improvement in the paper.

References

Freitas, C. J., Street, R. L., Findikakis, A. N., and Koseff, J. R., 1985, "Numerical Simulation of Three-Dimensional Flow in a Cavity," *International Journal for Numerical Methods in Fluids*, Vol. 5, pp. 561-575.

Ghia, U., Ghia, K. N., and Shin, C. T., 1982, "High-Re Solutions for Incompressible Flow Using the Navier-Stokes Equations and a Multigrid Method," *Journal of Computational Physics*, Vol. 48, pp. 387-411.

Harlow, F. H., and Welch, J. E., 1965, "Numerical Calculation of Time-Dependent Viscous Incompressible Flow of Fluid with Free Surface," *Physics of Fluids*, Vol. 8, pp. 2182-2187.

Iwatsu, R., Ishii, K., Kawamura, T., Kuwahara, K., and Hyun, J. M., 1989, "Numerical Simulation of Three-Dimensional Flow Structure in a Driven-Cavity," *Fluid Dynamics Research*, Vol. 5, pp. 173-189.

Iwatsu, R,, Hyun, J. M., and Kuwahara, K., 1990, "Analyses of Three-Dimensional Flow Calculations in a Driven Cavity," *Fluid Dynamics Research*, Vol. 6, pp. 91-102.

Iwatsu, R., Hyun, J. M., and Kuwahara, K., 1992, "Numerical Simulation of Flows Driven by a Torsionally-Oscillating Lid in a Square Cavity," ASME JOURNAL OF FLUIDS ENGINEERING, Vol. 114, pp. 143-151.

Kawamura, K., and Kuwahara, K., 1986, "Computation of High Reynolds Number Flow Around a Circular Cylinder with Surface Roughness," *Fluid Dynamics Research*, Vol. 1, pp. 145-162.

Kim, J., and Moin, P., 1985, "Application of a Fractional-Step Method to Incompressible Navier-Stokes Equations," *Journal of Computational Physics*, Vol. 59, pp. 308-323.

Koseff, J. R., and Street, R. L., 1984a, "Visualization Studies of a Shear Driven Three-Dimensional Recirculation Flow," ASME JOURNAL OF FLUIDS ENGINEERING, Vol. 106, pp. 21-29.

Koseff, J. R., and Street, R. L., 1984b, "On End Wall Effects in a Lid-Driven Cavity Flow," ASME JOURNAL OF FLUIDS ENGINEERING, Vol. 106, pp. 385-389.

Koseff, J. R., and Street, R. L., 1984c, "The Lid-Driven Cavity Flow: A Synthesis of Qualitative and Quantitative Observations," ASME JOURNAL OF FLUIDS ENGINEERING, Vol. 106, pp. 390-398.

Ku, H. C., Hirsh, R. S., and Taylor, T. D., 1987, "A Pseudospectoral Method for Solution of the Three Dimensional Incompressible Navier-Stokes Equations," *Journal of Computational Physics*, Vol. 70, pp. 439-462.

Perng, C. Y., and Street, R. L., 1989, "Three-Dimensional Unsteady Flow Simulations: Alternative Strategies for a Volume-Averaged Calculation," *International Journal for Numerical Methods in Fluids*, Vol. 9, pp. 341-362.

Prasad, A. K., and Koseff, J. R., 1989, "Reynolds Number and End-Wall Effects on a Lid-Driven Cavity Flow," *Physics of Fluids*, A1 Vol. 2, pp. 208-218.

Schlichting, H., 1979, *Boundary-Layer Theory*, Seventh English Edition, Translated by Kestin, J., McGraw-Hill, New York, pp. 93-94.

Schreiber, R., and Keller, H. B., 1983, "Driven Cavity Flows by Efficient Numerical Technique," *Journal of Computational Physics*, Vol. 49, pp. 310-333.

Soh, W. H., and Goodrich, J. W., 1988, "Unsteady Solution of Incompressible Navier-Stokes Equations," *Journal of Computational Physics*, Vol. 79, pp. 113-134.

Tuann, S. Y., and Olson, M. D., 1978, "Review of Computing Methods for Recirculating Flows," *Journal of Computational Physics*, Vol. 29, pp. 1-19.

H. Ströll
Wehrtechnische Dienststelle für
Fernmeldewesen und Elektronik,
D-91171 Greding, Germany

F. Durst

M. Perić

Lehrstuhl für Strömungsmechanik,
Universität Erlangen-Nürnberg,
Cauerstr. 4,
D-91058 Erlangen, Germany

J. C. F. Pereira
Instituto Superior Tecnico,
Avenido Rovisco Pais,
1096 Lisboa, Portugal

G. Scheuerer
Advanced Scientific Computing GmbH,
Am Gangsteig 26,
D-83607 Holzkirchen, Germany

Study of Laminar, Unsteady Piston-Cylinder Flows

The present paper concerns numerical investigation of a piston-driven, axisymmetric flow in a pipe assembly containing a sudden expansion. The piston closes the larger of the two pipes. The impulsively starting intake flow is the topic of this investigation. Results of numerical calculations and laser-Doppler measurements are presented to provide an insight into the features of the flow. The calculation procedure employed in this study is based on a finite-volume method with staggered grids and SIMPLE-algorithm for pressure-velocity coupling (Patankar and Spalding, 1972). The convection and diffusion fluxes in the Navier-Stokes equations are discretized with first order upwind and second order central differences, respectively. A fully implicit Euler scheme is used to discretize the temporal derivatives. The Navier-Stokes equations were suitably transformed to allow prediction of the flow within the inlet pipe (fixed grid) and cylinder region (moving grid) simultaneously (once-through procedure). Laser-Doppler measurements of both axial and radial velocity components were performed. Refractive index matching was used to eliminate the wall curvature effects. For each measuring point 20 cycles were measured, showing high repetition rates. Comparison of measured and predicted velocity profiles shows good agreement.

1 Introduction

Among the different classes of time dependent flows, the periodic or reciprocating flow, originating through the action of a moving piston, has in the past received particular attention. However, most of the studies have concentrated on turbulent flows (e.g., Gosman and Watkins, 1977; Rast, 1979; Gosman, 1985; Bicen et al., 1985) in geometries close to those of internal combustion engines. Laminar investigations have not often been reported. This is why the basic behavior of cycling piston driven flows through pipe assemblies, yielding flow separation and spatially moving vortices, has not always been well understood. Recently, two of the present authors and a collegue described detailed experimental results of studies of the flow in a pipe with sudden expansion caused by the intake stroke of a piston moving in the larger pipe (Durst et al., 1989). In those experiments the piston was suddenly started from rest and then moved with a constant velocity. Flow visualization was the major technique employed in the investigations. Various parameters were investigated, such as initial piston clearance, stroke length, piston velocity, etc.

In some studies of piston-driven intake flows (e.g., Pereira, 1986), the calculation domain was divided into two subdomains, describing the inlet pipe and the in-cylinder region, respectively. The computations were then performed using basically two different computer codes. The unsteady flow in the inlet tube with fixed grid was calculated first using a numerical procedure for fixed grids. The results of these computations were used to specify boundary conditions along the step plane of the sudden pipe expansion for the calculation of the flow inside the larger cylinder where the grid was moving due to the driving piston. An obvious disadvantage of this two-pass calculation procedure is the neglect of the backward influence of the pressure at the sudden expansion, which leads (especially for small initial clearances) to serious deviations from the experimental results. In the present study, the flow in the whole region is calculated simultaneously, using one computer code (once-through procedure).

The measurement technique used in this study, to obtain experimental data describing the time and spatially varying flow field in the piston-cylinder assembly, is described in the next section. The numerical approach is summarized in the following section. Finally, predictions are compared with experimental data and the features of the flow are discussed.

Contributed by the Fluids Engineering Division for publication in the JOURNAL OF FLUIDS ENGINEERING. Manuscript received by the Fluids Engineering Division March 2, 1992; revised manuscript received February 11, 1993. Associate Technical Editor: J. Humphrey.

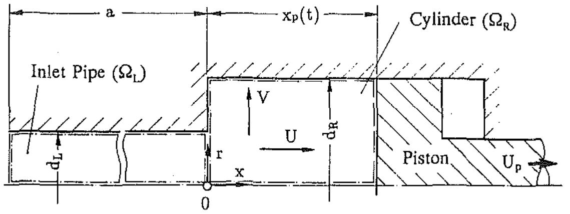

Fig. 1 Flow geometry with coordinate system and the two connected calculation domains (d_R = 45 mm, d_L = 19 mm, a = 200 mm, $x_{p,o}$ = 40 mm, $x_{p,\max}$ = 64.3 mm, U_p = 11.9 mm/s)

2 Test Section and Measurement Technique

The piston-cylinder assembly used in the measurements is shown in Fig. 1. The piston position $x_p(t)$ varied between the initial clearance $x_{p,o}$, and the maximum displacement $x_{p,\max}$ as a function of time. In the present study only linear variation (constant piston velocity) was considered.

In order to achieve refractive index matching to eliminate the wall curvature effects on near wall measurements, the piston-cylinder assembly was contained in a tank with plane walls, filled with the same liquid as that flowing fluid inside the assembly. The fluid used was a mixture of dibutylphtalate and Diesel oil that had the same refractive index ($\Delta n \pm 0.001$) as the Duran glass ($n = 1.4718$) used to build the test section.

The fluid entered and left the cylinder through a centrally located, inlet nozzle connected to a straight inlet tube. The flat head piston was driven by a very precise volumetric pump. The piston movement was electronically controlled, which allowed the setting of various piston velocities, initial clearance volumes and total piston displacements. The mode of operation, i.e., starting from rest for either an intake or an exhaust stroke, or continuous periodic operation with both intake and exhaust strokes, was also electronically controlled.

The laser-Doppler anemometer (LDA) used in the present experiments was operated in the dual beam mode. It was employed in its forward-scattering arrangement and was set up to measure the axial and radial velocity components. The beam from a 15 mW-He-Ne laser was split into two by a beam splitter prism in the integrated transmission optics. The optics included two Bragg cells that provided a shift frequency (f_{sh} = 300 kHz) between the two beams in order to allow simultaneous measurements of the magnitude of the velocity components as well as their signs. The signals from the photomultiplier output were amplified and band-pass filtered to remove the low frequency pedestal and high frequency electronic noise. The signals were then passed to a frequency-tracking demodulator for processing. From the tracker output, a constant DC-voltage corresponding to the shift frequency was subtracted to increase the resolution of the signal processing electronics. The resultant analog output yielded a "tracker output voltage" which was proportional to the instantaneous Doppler frequency. For further processing this voltage was digitized using a 12-bit analog-to-digital converter producing voltage information that could be read directly into a minicomputer.

The above described electronic signal processing and data acquisition system permitted the reliable positioning and measurement at a large number of spatial positions. The highly repetitive flow conditions assured that the entire flow field, varying in both time and space, could be mapped out in this way. For each stroke the motion of the piston was started suddenly. At the final position the piston was stopped and the measuring procedure for one test run was terminated. After this, the piston was relocated and the entire intake stroke repeated. Details on the measurement procedure are provided in Pereira (1986).

Intended was the investigation of an abruptly accelerated piston. Of course this could not be completely realized in the experiment. In fact the measured piston velocity reaches its final value in three steps, cf. Fig. 2. At $t = 0$ the fluid is at rest. Within the first phase ($0 < t < 0.2$ s) the piston is strongly accelerated and at $t = 0.2$ s it achieves about 80 percent of its final velocity. For $0.2 < t < 2.0$ s the piston velocity distribution appears almost linear and reaches maximum at $t = 2.0$ s Finally, for times $t \geqq 2.0$ s the piston moves with constant velocity U_p = 11.9 mm/s.

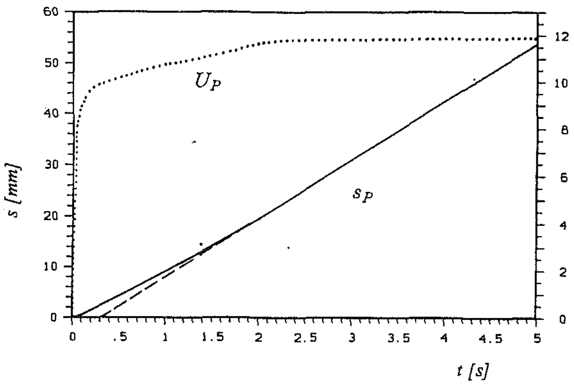

Fig. 2 Experimentally determined piston displacement and velocity as functions of time

During each measuring cycle, the measuring volume of the LDA-system was located at one measuring position defined by its x- and r-location inside the larger cylinder, where $x = 0$ is the plane of the sudden pipe expansion. Time records were taken during 20 measuring cycles showing very high repetition rates. All 20 measuring cycles were averaged yielding one final time trace of the velocity for the appropriate measuring point.

Many usual sources of small errors in LDA-measurements were negligible, such as errors in maintaining constant flow conditions, turbulence-induced velocity bias or gradient broadening of flow quantities due to the finite size of the control volume. Other errors were reduced by appropriate signal conditioning and/or calibration. For instance, subtracting the DC equivalent of the shift frequency from the tracker output, and amplifying the resultant signal by a factor of 8, allowed a substantial increase in the resolution of the analog-to-digital conversion and, hence, yielded a good resolution of the signal entering the computer. Calibration of the entire signal processing system with sine wave signals reduced small systematic errors due to voltage losses in the transfer line, so that the resulting uncertainty of the recorded velocity was estimated to be of the order of ±0.1 mm/s (0.5 percent of piston velocity). This emphasis on measurement accuracy was necessary due to very low velocities (≈ 1 mm/s) occurring in some regions of the piston induced flow.

Errors due to averaging over the control volume area were minimized by using a short focal length lens, resulting in a small control volume ($d = 110$ μm, $l = 660$ μm). Crank angle broadening, i.e., the error due to the finite length of the averaging window, was found to be negligible (≈ 1 percent) for window sizes less than 1 mm. The window was further reduced to 0.7 mm in recording the impulsive start of the piston and higher driving speeds.

The employed refractive index matching was performed to within $\Delta n = \pm 0.001$, and was maintained over one set of experiments by controlling the temperature of the liquid to within $\pm 0.15°$C. Estimates of the position uncertainty due to this temperature variation were possible by performing measurements of wall-to-wall velocity profiles and then comparing the external traversing length to the cylinder diameter. Such comparisons agreed to within approximately 0.05 mm.

3 The Governing Equations and Their Discretization

The unsteady flow in the whole domain is completely described by the mass and momentum conservation equations, best expressed in cylindrical coordinates. From the computational point of view, however, it is much more convenient to apply a coordinate transformation (see Gosman and Watkins, 1977) to allow the numerical grid to expand and contract with the piston movement. The transformed continuity and momentum equations for an incompressible fluid read then:

$$\frac{\partial(\rho x_P)}{\partial t}+\frac{\partial(\rho \tilde{U})}{\partial \xi}+\frac{x_P}{r}\frac{\partial(r\rho V)}{\partial r}=0 \tag{1}$$

$$\frac{\partial(x_P\rho U)}{\partial t}+\frac{\partial}{\partial \xi}\left(\rho\tilde{U}U-\frac{\mu}{x_P}\frac{\partial U}{\partial \xi}\right)+\frac{x_P}{r}\frac{\partial}{\partial r}\left(\rho rVU-r\mu\frac{\partial U}{\partial r}\right)=-\frac{\partial P}{\partial \xi} \tag{2}$$

$$\frac{\partial(x_P\rho V)}{\partial t}+\frac{\partial}{\partial \xi}\left(\rho\tilde{U}V-\frac{\mu}{x_P}\frac{\partial V}{\partial \xi}\right)+\frac{x_P}{r}\frac{\partial}{\partial r}\left(\rho rV^2-r\mu\frac{\partial V}{\partial r}\right)= -x_P\frac{\partial P}{\partial r}-\mu\frac{V}{r^2} \tag{3}$$

In these equations U and V represent the local velocity components in the axial and radial direction, while P is the local pressure. The fluid is characterized by its density ρ and dynamic viscosity μ. $\tilde{U} = U - U_g$ is the velocity of the fluid relative to the moving grid, x_P is the current piston position and U_g is the grid velocity, which can be expressed as a mapping defined by Eq. (4).

$$U_g(x,t):=\begin{cases}0, & -a\le x\le 0,\\ \dfrac{x}{x_P(t)}\dfrac{dx_P(t)}{dt}, & 0<x\le x_P(t).\end{cases} \tag{4}$$

The flow equations are discretized with a finite volume method. It is described in detail by Patankar (1980), so only a summary is given here. In order to avoid oscillatory pressure and velocity fields, a staggered variable arrangement is employed. Temporal derivatives are approximated by an implicit first order formula. Integrating the temporal terms of Eqs. (2) and (3) yields:

$$\frac{1}{\delta t}\int_{\delta V}\frac{1}{x_P}\left[\int_t^{t+\delta t}\frac{\partial}{\partial t}(\rho x_P\phi)dt\right]dV\approx\frac{\rho(\delta V^n\phi_P^n-\delta V^o\phi_P^o)}{\delta t} \tag{5}$$

The general variable ϕ stands for either U or V; δt is the time step, δV the cell volume, and superscripts "n" and "o" denote the new and old time levels, respectively. In the physical space the cell volume δV is equal to $x_P\delta\xi r\delta r = r\delta x\delta r$, since $\delta x = x_P\delta\xi$.

The convective fluxes are approximated by:

$$\int_{\delta V}\left[\frac{1}{x_P}\frac{\partial}{\partial \xi}(\rho\tilde{U}\phi)+\frac{1}{r}\frac{\partial}{\partial r}(r\rho V\phi)\right]dV\approx C_e\phi_e -C_w\phi_w+C_n\phi_n-C_s\phi_s, \tag{6}$$

where the Cs are the mass fluxes through the CV faces calculated as:

$$C_{e/w}=(r\delta r\rho\tilde{U})_{e/w},\quad C_{n/s}=(r\delta x\rho V)_{n/s}. \tag{7}$$

The velocities appearing in Eq. (7) are taken from the previous iteration. The CV face values of ϕ are related to nodal values by means of first order forward differences.

Finally, the diffusion fluxes are discretized as:

$$\int_{\delta V}\left[-\frac{1}{x_P}\frac{\partial}{\partial \xi}\left(\frac{\mu}{x_P}\frac{\partial\phi}{\partial \xi}\right)-\frac{1}{r}\frac{\partial}{\partial r}\left(r\mu\frac{\partial\phi}{\partial r}\right)\right]dV\approx -D_e(\phi_E-\phi_P) +D_w(\phi_P-\phi_W)-D_n(\phi_N-\phi_P)+D_s(\phi_P-\phi_S). \tag{8}$$

The gradients at the CV faces are approximated by central differences. The D-coefficients follow then as:

$$D_{e/w}=\left(\frac{\mu r\delta r}{\delta x}\right)_{e/w},\quad D_{n/s}=\left(\frac{\mu r\delta x}{\delta r}\right)_{n/s}. \tag{9}$$

Note that in the above equations $\delta x = x_p\delta\xi$, so that the coordinate transformation is not apparent in the discretized equations. Terms accounting explicitly for the grid movement are the temporal derivative, where distinction is made between the cell volumes at old and new time levels, and the convective fluxes, in which the mass fluxes are calculated with the relative velocity $\tilde{U} = U - U_g$. The fixed grid region in the inlet duct can be viewed as a special case, with the old and new cell volumes equal and with zero grid velocity.

The above analysis shows that the same discretized equations can be applied in the whole solution domain $\Omega_G = \Omega_L \cup \Omega_R$ shown in Fig. 1. In Ω_L the old and new grid line positions are kept the same, yielding automatically zero grid velocity. In Ω_R the grid line positions at the new and old time levels are calculated from the known piston position $x_p(t)$ and a prescribed distribution of the ξ-coordinate, i.e., $\delta x_i = \delta\xi_i x_p$. The cell volumes and grid velocities are then calculated from the grid coordinates.

Before proceeding to the results, the boundary conditions used in the calculations are presented. For all wall boundaries, the no slip condition was applied. In addition, the gradient of the normal velocity component in the direction normal to wall was set to zero at walls. Along the center line the normal gradient of the axial velocity, $\partial U/\partial r$ and the radial velocity V were set to zero. Along the piston surface the axial velocity component of fluid, U, was set equal to the piston velocity U_p. At the inlet plane the V-component was set to zero and the U-velocity profile was taken uniform, satisfying the global continuity requirement as determined by the piston velocity U_p.

The discretized flow equations were solved in a segregated, iterative manner following the SIMPLE algorithm of Patankar and Spalding (1972). The momentum equations were first solved using preset values of pressure and mass fluxes (predictor step), followed by the solution of a pressure-correction equation, which was derived from the continuity equation. The pressure and the velocities were then updated to satisfy the continuity requirement (corrector step). The corrected pressure and mass fluxes based on the corrected velocities were treated as new preset values and the iteration procedure is repeated until convergence is reached. Thereafter, time was incremented for another time step and the whole process repeated until prescribed time limit was reached.

The linear systems of algebraic equations resulting from discretization were relaxed with the strongly implicit method of Stone (1968), based on an incomplete LU-factorization. Only one relaxation sweep per SIMPLE iteration was performed for the momentum equations. The pressure correction equation was relaxed up to 12 times, unless its absolute residual sum had fallen by a factor of 5. In contrast to steady flow calculations, no under-relaxation was necessary for the transient cases.

Convergence was controlled by monitoring the absolute residual sums of the continuity and momentum equations, normalized by the inlet mass and momentum fluxes, respectively. The iterations were terminated after each normalized residual sum has fallen below 0.001. For the grids and time steps employed here, about 50 iterations per time step were necessary.

The spatial discretization errors were estimated by comparing solutions at the same time level calculated on two grids with grid spacings h and $2h$. For a first order discretization scheme, the error e_h was approximately equal to the difference between the two solutions (cf. Caruso et al., 1985):

$$e_h=\phi_h-\phi_{2h}$$

In order to estimate temporal discretization errors, the same

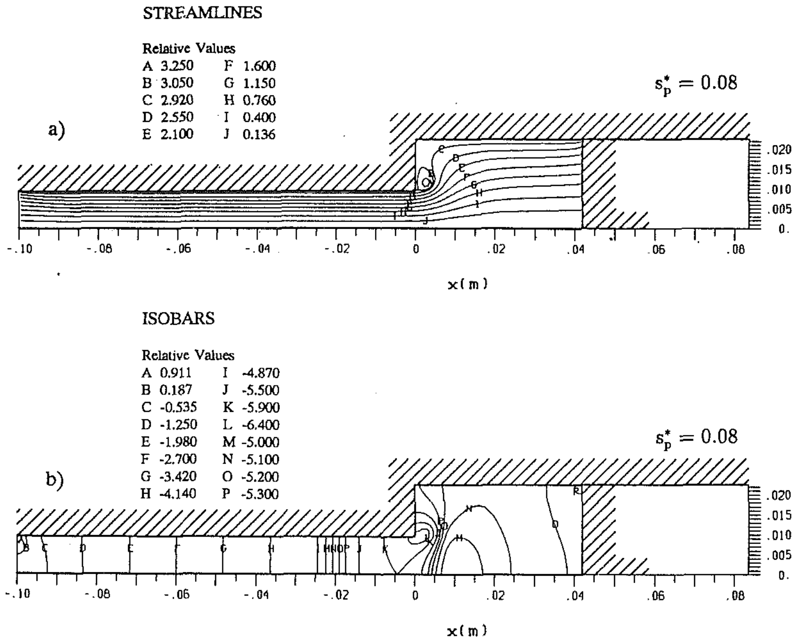

Fig. 3 Predicted streamlines (*a*) and isobars (*b*) at $s_p^* = 0.08$.

approach was used: for a given mesh spacing h, calculation was performed using time steps δt and $2\delta t$. The difference between the two solutions at a given time t represents an estimate of the temporal discretization error.

4 Results and Discussion

In this section numerical results for an impulsively started intake stroke are presented. The calculations were performed on a CDC CYBER 855. Owing to the storage restriction (131000 words per user) a compromise was made between the size of the computational grid and the considered length of the inlet pipe. The latter was taken to be 100 mm long for these predictions, whereas the actual length in the experiment was 200 mm. This is justified by the fact that the flow in the inlet pipe is almost fully developed until shortly before expansion. Thus the shortening of the inlet pipe does not affect significantly the flow in the cylinder. As already mentioned, an abruptly accelerated piston movement was intended to be investigated. Therefore, all results were obtained for a constant piston velocity $U_p = 11.9$ mm/s, equivalent to a Reynolds number Re $= \rho U_p d_L/\mu$ of 98 and thus ensuring laminar flow conditions. The piston was impulsively started at $t = 0$, i.e., within the first time step it was accelerated from rest to the velocity U_p. The initial clearance, i.e., the distance between the expansion plane ($x = 0$) and the piston surface at $t = 0$, was 40 mm. In the discussion to follow, the piston position is related to the initial position and the total stroke considered (here 24.3 mm, corresponding to the time interval of 2.04 s) and expressed as the dimensionless displacement s_p^*.

Calculations were performed on two grids (41×19 and 82×38 CV) with time step $\delta t = 0.005$ s, and for the finer grid up to $s_p^* = 0.25$ also with a halved time step size. This was necessary in order to be able to estimate the spatial and temporal discretization errors. The former were found to be on average of the order of 3 percent of the mean inlet velocity. The maximum values were higher at the beginning than at the end of the stroke, and were reaching locally (at the symmetry axis) 20 percent of the mean inlet pipe velocity. The temporal discretization errors were found to be much smaller and below 1 percent of the inlet velocity everywhere. This is attributed to the relatively small time step used.

Figures 3 to 5 show the predicted streamline patterns and the pressure contours for the dimensionless piston displacements $s_p^* = 0.08$, $s_p^* = 0.25$ and $s_p^* = 1.0$, respectively. While the numerical grid inside the inlet tube remained unchanged with time, the control volumes within the piston chamber were stretched in streamwise direction. As the piston moved to the right, fluid was sucked through the inlet pipe into the cylinder and it separates at the sudden expansion, forming a counterclockwise rotating toroidal vortex, as is shown in Figs. 3(*a*), 4(*a*), and 5 (*a*). As can be seen from these figures, after forming close to the step the vortex was convected towards the piston and is elongated with increasing piston displacement. Its axial velocity component is typically twice that of the piston speed. This was also found out by Durst et al. (1989) using flow-visualization techniques.

Nearly over the entire length of the inlet pipe, i.e., for -0.08 $m < x < -0.01$ m, the velocity profiles appear fully developed. This is also apparent from the streamline and isobar plots in Figs. 3, 4, and 5 (parallel streamlines, constant pressure in the cross-section). Moreover, the flow in that region exhibits only a very weak time dependence. Under these assumptions the momentum equations reduce to:

$$\frac{\mu}{r}\frac{d}{dr}\left(r\frac{dU}{dr}\right)=\frac{dP}{dx}. \tag{10}$$

This relationship implies that the pressure is a linear function of x. This observation is corroborated in Fig. 6, where the axial pressure distributions are plotted for the piston displacements under consideration. Shortly after the onset of the stroke ($s_p^* = 0.08$) the pressure gradient inside the tube is somewhat steeper than for the later stages $s_p^* = 0.25$ and $s_p^* = 1.0$. For $s_p^* = 0.08$, the backward influence of pressure from cylinder on the flow in the intake pipe extends for about one diameter and reduces for increasing displacements (cf. Figs. 3(*b*), 4(*b*), 5(*b*). Applying the two-pass procedure (Pereira, 1986), this elliptic pressure effect is not taken into account, leading to somewhat poorer predictions, especially for situations with small initial clearances.

As the flow structure is controlled by the balance of momentum, pressure and viscous forces, a qualitative description of the structure of the flow field can be obtained by analyzing the velocity and pressure distributions (plotted in Figs. 3 to 5) in terms of the momentum balance. Figure 4 exhibits an area "H$_1$" (shaded in Fig. 4(*b*) of high pressure, with the pressure increasing toward the symmetry line. Owing to the positive

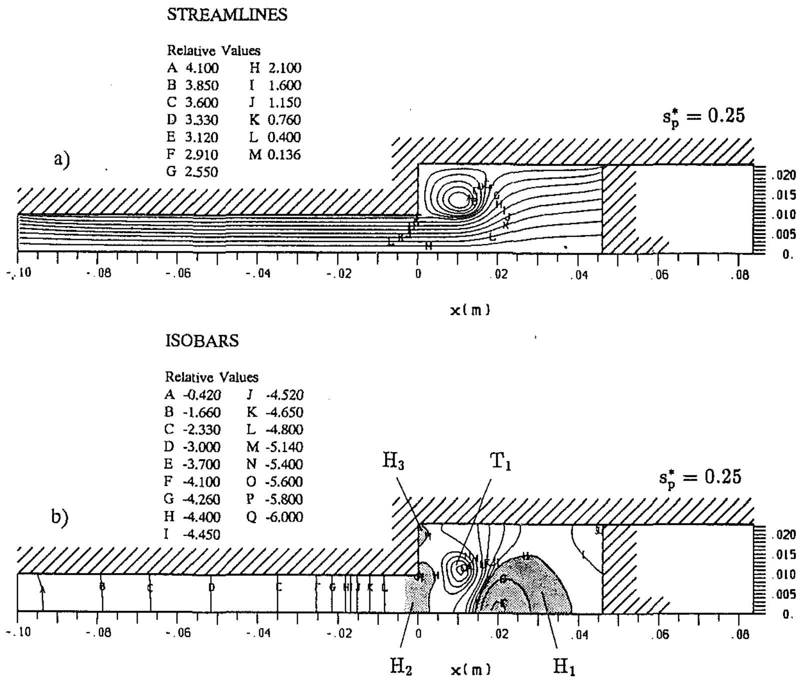

Fig. 4 As Fig. 3, at $s_p^* = 0.25$

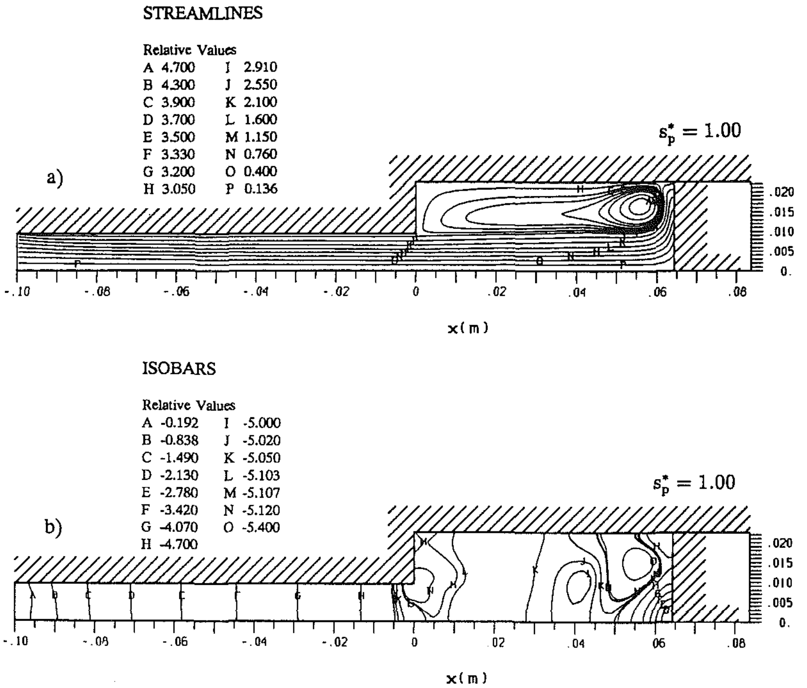

Fig. 5 As Fig. 3, at $s_p^* = 1.00$

pressure gradient acting on the incoming flow, the fluid elements become decelerated ($\partial U/\partial x < 0$). According to the continuity equation, this leads (for fixed r) to an increase of the radial velocity component ($\partial V/\partial r > 0$) and consequently to the deflection of the main jet flow in the r-direction. Due to their higher velocity, fluid elements moving along the center line overcome the pressure gradient more easily than fluid elements coming from the pipe wall region. As a consequence, near the symmetry line the streamlines are almost parallel to the cylinder axis. However, with increasing distance from the centerline, the x-momentum reduces to a form similar to that of the Hagen-Poiseuille flow. Fluid elements further away from the symmetry axis, which bear less kinetic energy, are more strongly retarded than the energy-rich elements near the tube center. Therefore, the deflection of streamlines in the radial direction becomes greater as r increases.

On the left-hand side ($0.008\ m < x < 0.01\ m$) of the intersection between the vortex structure (Fig. 4(*a*) and the low pressure area T_1 (Fig. 4(b)), streamlines and isobars are approximately mutually orthogonal (cf. Fig. 7). In this small subregion, the axial pressure drop is the driving force for the rotational flow. Due to the axial pressure increase, on the right-hand side, the streamlines and isobars are no longer normal but actually superimposed on one another (cf. streamline E and isobar K). For all fluid elements lying on both isobar K and streamline E, the x-momentum is balanced by the pressure

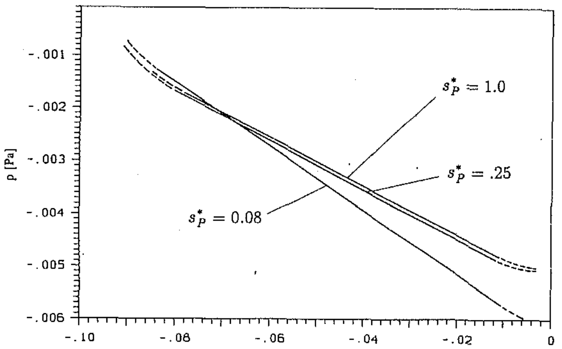

Fig. 6 Axial pressure distribution in the intake pipe for three piston displacements: $s_p^* = 0.08$, $s_p^* = 0.25$ and $s_p^* = 1.00$

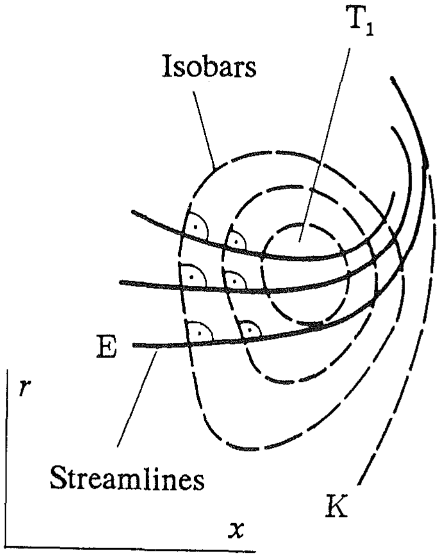

Fig. 7 Streamlines and isobars inside a vortex in the region of low pressure T_1

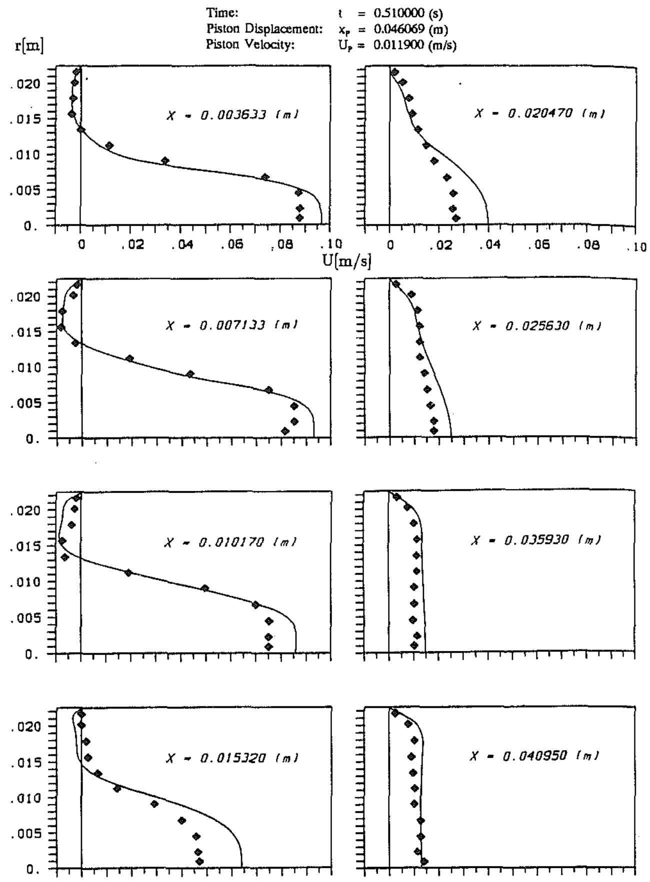

Fig. 8 Predicted and measured axial velocity profiles for $s_p^* = 0.25$

force such that the isobars effectively act as pressure barriers that cannot be crossed by fluid elements of lesser kinetic energy.

In the vicinity of the wall, the momentum and pressure balance cannot be maintained and the fluid elements are accelerated in the negative x-direction by the pressure forces established in the flow field. At some distance from the wall, where the viscous forces are of lesser importance than inertia terms, an approximation for the deflection of the fluid elements is given by the radial pressure equation which reads

$$\frac{c^2}{R} = \frac{1}{\rho}\frac{\partial P}{\partial n}, \tag{11}$$

where c is the total velocity and R the radius of curvature of the fluid element path considered. $\partial P/\partial n$ is the derivative normal to this trajectory. The inwardly directed pressure force provides the centripetal acceleration c^2/R involved in the deflected motion of the fluid element. For straight trajectories, the pressure remains constant normal to the fluid element path, as can be observed e.g., within the inlet pipe.

In the high pressure areas H_2 and H_3 (shaded areas in Fig. 4(b)) similar processes of deflection are repeated, finally leading to the vortex structure plotted in Fig. 4(a). In this fashion, continuity is globally satisfied. By marching in the streamwise coordinate, the pressure drops towards the piston surface, building a pressure minimum at the edge formed by the piston surface and cylinder wall. The locations of the high and low pressure areas within the flow field relative to the vortex center remain unchanged with time t, so that the pressure-momentum analysis made above is also applicable for later stages (cf. Fig. 5(a) and 5(b) of the flow.

The relatively high pressure gradient appearing in the corner of the piston surface and the cylinder wall is caused by the boundary singularity at this edge. While the fluid at the piston surface has to move with piston speed $U_p(t)$, along the stationary cylinder wall, the no slip condition implies $U = V = 0$.

For the dimensionless piston strokes $s_p^* = 0.25$ and $s_p^* = 1.0$, the predicted axial velocity profiles at successive x-locations inside the cylinder are compared to experimental data in Figs. 8 and 9. The predictions for $s_p^* = 0.25$ do not agree with the experimental data. Significant discrepancies occur mainly in the region around symmetry axis. The cause lies in the difference between the simulated and real piston velocity at this phase of the starting flow. As can be seen from Fig. 2, in the experiment at that position the piston had reached only 90 percent of its final velocity, whereas the profiles shown in Fig. 8 were predicted for a constant piston velocity $U_p = 11.9$ m/s. The mass flow rate (suction) is therefore higher in the computation, and since the cross-sectional area is small around the symmetry axis, the velocity differences are the largest there. The computations were performed before the experimental data was fully evaluated; although constant piston velocity was intended for both cases, it appeared difficult to achieve this goal in experiment.

For $s_p^* = 1.0$ (Fig. 9), the piston had achieved its full velocity and matched that used in the calculations. For this piston position the agreement between predicted and measured profiles is very satisfactory, which supports the former argument regarding disagreement at $s_p^* = 0.25$. The same conclusion applies to the radial velocity components (not shown).

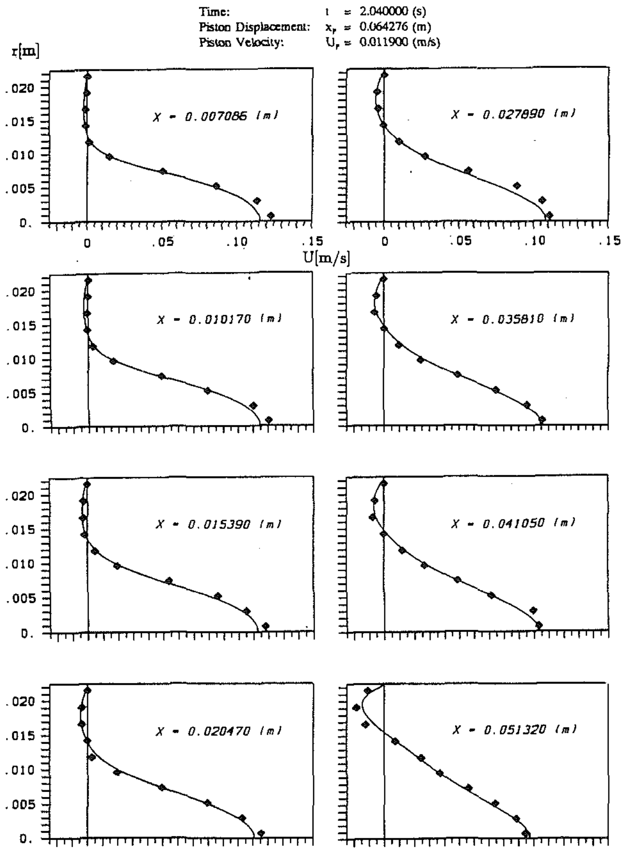

Fig. 9 Predicted and measured axial velocity profiles for $s_p^* = 1.00$

5 Conclusions and Final Remarks

The unsteady flow generated by an impulsively started piston movement in a piston/cylinder assembly was investigated experimentally and numerically. Care was taken to obtain accurate experimental data for this complex unsteady flow using LDA technique and refractive index matching. The numerical method based on SIMPLE algorithm was extended to allow computations with both moving and fixed grids. For the grid and time step used, the numerical errors were of the order of 3 percent, which was considered sufficient for the analysis of flow features. Comparison of the predicted results with the experimental data demonstrates that the incorporated coupling of the moving grid region and fixed grid region allows for accurate and efficient calculation of in-cylinder flows. The present calculation procedure is also applicable to the prediction of periodic intake/exhaust flows. Application to such flows and comparison with experimental data are reported in Stöll (1989).

Future efforts are directed to increasing the efficiency and accuracy of the method. The efficiency can be increased by performing multigrid iterations on each time level and by adapting the code to take advantage of vector and parallel processing. These efforts are under way. In future calculations the piston velocity will be taken directly from experiment, in order to allow quantitative comparisons throughout the cycle. At higher Reynolds numbers the flow will become three-dimensional; this will also be investigated in the near future.

Acknowledgments

The present work was sponsored by the Deutsche Forschungsgemeinschaft within the program "Finite Approximationen in der Strömungsmechanik." The authors gratefully acknowledge this support.

References

Bicen, A. F., Vafidis, C., and Whitelaw, J. H., 1985, "Steady and Unsteady Airflow Through the Intake Valve of a Reciprocating Engine," ASME JOURNAL OF FLUIDS ENGINEERING, Vol. 107, pp. 413–420.

Caruso, S. C., Ferziger, J. H., and Oliger, J., 1985, "Adaptive Grid Techniques for Elliptic Fluid Flow Problems," Report No. TF-23, Thermosciences Division, Department of Mechanical Engineering, Stanford University, CA.

Durst, F., Maxworthy, T., and Pereira, J. C. F., 1989, "Piston-Driven, Unsteady Separation at a Sudden Expansion in a Tube: Flow Visualization and LDA Measurements," *Physics of Fluids A*, Vol. 1, pp. 1249–1260.

Gosman, A. D., and Watkins, A. P., 1977, "A Computer Prediction Method for Turbulent Flow and Heat Transfer in Piston/Cylinder Assemblies," *Proceedings of the 1st Symposium on Turbulent Shear Flows*, Pennsylvania State University, p. 523.

Gosman, A. D., 1985, "Multidimensional Modelling of Cold Flows and Turbulence in Reciprocating Engines," SAE Paper 850344.

Patankar, S. V., and Spalding, D. B., 1972, "A Calculation Procedure for Heat, Mass and Momentum Transfer in Three-Dimensional Parabolic Flows," *International Journal of Heat and Mass Transfer*, Vol. 15, pp. 1787–1806.

Patankar, S. V., 1980, *Numerical Heat Transfer and Fluid Flow*, Hemisphere Publishing Corporation, New York, NY.

Pereira, J. C. F., 1986, "Experimentelle und numerische Untersuchungen stationärer and instationärer laminarer Strömungen mit Ablösung," Dr.-Ing.-Dissertation, University of Erlangen-Nürnberg.

Rask, R. B., 1979, "Laser Doppler Anemometer Measurements in an Internal Combustion Engine," SAE Paper 790094, Vol. 88.

Stone, H. L., 1968, "Iterative Solution of Implicit Approximation of Multidimensional Partial Differential Equations," *SIAM Journal of Numerical Analysis*, Vol. 5, pp. 530–558.

Ströll, H., 1989, "Entwicklung eines effizienten Verfahrens zur Berechnung instationärer laminarer Kolben-Zylinder-Strömungen," Dr.-Ing.-Dissertation, University of Erlangen-Nürnberg.

Effect of IC Engine Operating Conditions on Combustion and Emission Characteristics

Jiang Lu
Graduate Student.

Ashwani K. Gupta
Professor.

Department of Mechanical Engineering,
University of Maryland,
College Park, MD 20742-3035

Eugene L. Keating
Naval Surface Warfare Center,
Annapolis, MD 21402

Numerical simulation of flow, combustion, heat release rate, and pollutants emission characteristics have been obtained using a single cylinder internal combustion engine operating with propane as the fuel. The data show that for good agreement with experimental results on the peak pressure and the rate of pressure rise as a function of crank angle, spark ignition energy and local cylinder pressure must be properly modeled. The results obtained for NO and CO showed features which are qualitatively in good agreement and are similar to those reported in the literature for the chosen combustion chamber geometry. The results have shown that both the combustion chamber geometry and engine operating parameters affects the flame growth within the combustion chamber which subsequently affects the pollutants emission levels. The code employed the time marching procedure and solves the governing partial differential equations of multicomponent chemically reacting fluid flow by finite difference method. The numerical results provide a cost effective means of developing advanced internal combustion engine chamber geometry design that provides high efficiency and low pollution levels. It is expected that increased computational tools will be used in the future for enhancing our understanding of the detailed combustion process in internal combustion engines and all other energy conversion systems. Such detailed information is critical for the development of advanced methods for energy conservation and environmental pollution control.

1 Introduction

Combustion in internal combustion (IC) engines (one of the major process of energy conversion) and the release of energy is a very complex phenomenon. In recent years, the energy crisis and concern about increasing atmospheric pollution have initiated much research effort, resulting in rapid development of combustion science and its applications. In spite of the fundamental importance and practical applications, the combustion processes in internal combustion engines are far from being fully understood. This is due to, among other things, their interdisciplinary character and great complexity. In order to describe a typical combustion process one must take into account, in addition to reaction kinetics, phenomena involving heat and mass transfer, both on the molecular and on the macroscopic scales, and therefore the phenomena of phase changes, conduction, diffusion, radiation, and the dynamics of continuous media. The fuel-air mixture in the IC engine is ignited at high pressure using a spark plug and the resulting flame kernel propagates in the combustion chamber. The development of flame kernel and flame growth is a complex and not well understood process. The random nature of the turbulent compressible flow inside the cylinder and the particular state of flow near the spark gap at the time of ignition can contribute to engine cyclic variations, engine roughness and emission of pollutants (Gupta et al., 1989 and Heywood, 1988). The flame propagation in the engine cylinder depends upon local fluid mechanics, fuel oxidation chemistry and heat transfer. Previous studies have shown strong coupling between the above factors (Ramos, 1989 and Borman, 1980) and all factors have an important influence on the emission of pollutants.

Increased awareness of the environmental pollution control and energy conservation has lead to greater emphasis on the detailed understanding of the various processes that undergo during the energy conversion process. The phenomenon of air pollution involves a sequence of events: generation of pollutants and their release from the source, transport and transformation in and removal from atmosphere, and their effects on humans, materials, and other live species. In the United States, the transportation sector represent a major source of energy consumption. Internal combustion engines are a major source of power in the transportation sector. In an IC engine, fuel is introduced into the combustion chamber either in the form of fuel droplets or as a prevaporized gas. The fuel and oxidizer must then be mixed by microscopic fluid dynamic and turbulent motions before the chemical reaction, with the associated combustion, must occur. The flow and turbulence structure in internal combustion engine influences significantly the mixing and combustion processes which subsequently affects the power output, fuel economy, cold start capability,

---

Contributed by the Fluids Engineering Division for publication in the JOURNAL OF FLUIDS ENGINEERING. Manuscript received by the Fluids Engineering Division July 31, 1991; revised manuscript received November 29, 1992. Associate Technical Editor: D. G. Lilley.

and exhaust pollutants emission level. The flow and combustion processes in an IC engine are strongly dominated by the local Reynolds number during the complete cycle of its operation. The local Reynolds number is much affected by the combustion chamber geometry, location of ignition source, mixture preparation, engine speed, etc. An examination of the combustion processes in IC engine reveals that the engine operation can be characterized by complicated fluid mechanical and physical/chemical processes encompassing turbulent flow, droplet and particle motion, heat and mass transfer, and chemical reaction. The fluid mechanics and ignition process of practically all combustion engines have a profound influence on their operating characteristics since both the fluid mechanics and the ignition process controls the rate of mixing of the fuel and oxidizer, rate of combustion, and the formation of product species.

The mixing of reactants within the combustion chamber is important from both the combustion and pollutants emission point of view. Mixing occurs on a time scale which is long compared to that of the chemical reaction. Furthermore, the duration of the exothermic process is considerably shorter than that of the transport process (for example, turbulence, evaporation, diffusion, and heat transfer) which controls the combustion rate. Thus mixing rates and subsequent exothermic energy release are dependent on the local flowfields, turbulence levels, and thermal ignition source. A close examination of these processes must, therefore, be attained to meet the ever-growing demand for developing more efficient, economical fuel flexible and environmentally acceptable IC engines. In this paper, the effect of engine operating parameters from a homogeneously charged spark ignition engine are examined for their effects on combustion and emission. The flat piston geometry used here provided easy means of directly comparing the calculated results with the available experimental data. It is recognized that some of the advanced concepts in IC engine piston geometry design may involve configurations other than flat top. Our previous efforts (Gupta et al., 1991) on the piston geometry design revealed significant effects on combustion and emission characteristics.

2 Combustion in IC Engines

Historically flat head piston has been used in many IC engines. Flat heat piston geometry is relatively simple from the computational point of view and experimental data is available on this type of geometry. From the point of view of engine thermal efficiency, knock and NO_x formation, the best combustion systems are those having the shortest combustion times, the so-called "fast-burn systems." One way to shorten the combustion time is to build compact combustion chambers in either the piston or cylinder head with central or multiple ignition points, where the travel distance for flames are the shortest. Another approach is to create intense turbulence in the charge to increase burning rates. The turbulence generated by the intake process is damped appreciably before ignition, in spite of the positive effects of compression (reduction of the size of the eddies cause them to rotate faster by conservation of angular momentum) and, therefore, additional turbulence generators are added in contemporary combustion systems. The most popular of these are squish systems, which have a small clearance between part of the head and the piston when at top dead center. As the piston approaches TDC, the gases in the clearance spaces are squished violently into the chamber, thus producing the intense turbulence at the moment of fast-burn combustion. A very few examples of high-intensity turbulence generation methods that have been used exists in the literature. The system introduced by Toyota is based on an auxiliary combustion chamber (called the turbulence generating pot, TGP) connected with the main chamber by a restricted passage. Ignition is initiated close to this passage. After ignition, combustion of the mixture in the auxiliary chamber generates a strong jet of combustion gases, making the mixture in the main chamber turbulent and accelerating the combustion process.

Swirl is also utilized in many different types of stratified charge internal combustion engines (Gupta et al., 1984). The Honda CVCC system diverged somewhat from the true aims of stratification by using only a very small pre-chamber (about 10 percent of the main chamber volume) containing a rich ignition charge firing into the main chamber which is maintained under fuel lean operating conditions. The engine is normally throttled and may also be called a jet ignition engine. However that may be, it is the only current example of a mass produced stratified charge engine.

Overington and Haslett (1976) added a spark plug to a modified swirl chamber of typical diesel engine with approximately 50 percent of the chamber volume in the swirl chamber. It was claimed that this engine ran unthrottled on gasoline, as well as on kerosene and diesel fuel and gave a part load economy between that of a diesel and a homogeneously charged gasoline engine. The schematic diagram of the various prechamber turbulence promoting, jet ignition systems represented by Texaco FCCS, Ford PROCO, and MAN-FM systems are given by Groff et al., (1981). Each system has its own merits and the stratification principles of all the engines vary quite widely.

The review of previous efforts reveals that the fluid dynamics and combustion chemistry has a strong influence on the combustion behavior in IC engines which subsequently affects the pollutants emission characteristics. Any efforts to reduce the pollutants emission characteristics must therefore be directed at the basic understanding of the various ongoing processes during combustion. This paper provides a systematic examination of the engine operating parameters, using a homogeneously charged IC engine, on the combustion and pollutants emission characteristics. A flat piston geometry is used here for the results presented in this paper. Further comprehensive results on the effect of piston geometry will be provided in a subsequent publication. The numerical data are compared with experimental results, where possible. The numerical study described here provides an approach for inexpensive means of developing high efficiency and low pollution IC engine than that obtained by experimental means alone.

3 Mathematical Modeling

In the present study, the simulation of combustion and pollutants emission in a homogeneous-charge spark-ignition engine has been carried via KIVA-II (Butler et al., 1989) which was originally developed by Los Alamos National Lab. KIVA-II is a 3-D time marching code that solves the governing partial differential equations of multi-component chemically reactive fluid flow by ALE (Hirt et al., 1974 and Pracht, 1975) finite difference method. The transient solution is marched out in a sequence of time steps. The code solves problems in either rectangular or cylindrical coordinates. The homogeneous-charge spark-ignition model engine examined in the present study has conventional flat-top piston geometry with a spark plug mounted at the top of the cylinder head. Since the geometry of the model engine is axisymmetric, calculations have been performed in cylindrical coordinates with Swirl Ratio, SR = 1.0. The swirl ratio is defined as the ratio of fluid to crank angular velocity.

The code deals with turbulence by a standard version of the $k-\epsilon$ model (Launder and Spalding, 1972). Chemical reactions are grouped into slow kinetic reactions and fast equilibrium reactions. Kinetics reaction rates are evaluated by single-step global progress rate expression of the Arrhenius form. Equilibrium reactions are calculated by an iterative procedure. The wall heat transfer and wall shear stress are modeled by a log-

Table 1 Engine specifications (Groff et al., 1981)

Compression Ratio	8.56
Bore (mm)	105.0
Stroke (mm)	75.25
Connecting rod length (mm)	158.0
Piston Offset (mm)	1.52

Table 2 Text conditions (Groff et al., 1981)

Test No.	Run 3	Run 9	Run 10	Run 11
Engine speed (RPM)	1,500	1,500	1,500	1,500
Intake pressure (kPa)	59.8	59.9	59.9	60.2
Volumetric efficiency (%)	40.2	39.7	40.1	40.1
Equiv. ratio (phi)	0.87	1.395	1.12	0.98
Residual fraction (%)	0.12	0.14	0.14	0.14
Spark advance (BTDC)	27°	30°	25°	27°

arithmic law of the wall model. The NO concentration is predicted by the extended Zeldovich mechanism (Ramos, 1989 and Gupta et al., 1984). The formulation details, solution procedure, and numerical technique used in the code are described by Butler et al. (1989) and Amsden et al. (1985)

The homogeneous-charge spark-ignition engine used at GM Research Lab (Groff et al., 1981) and elsewhere is selected as a model engine for present study. The details on engine specifications and test conditions are given in Tables 1 and 2.

3.1 Kinetic Reaction Model. In practice, the oxidation of hydrocarbon fuel is a very complicated phenomena involving multi-step chain reactions. Due to the lack of understanding on the detailed chemistry of fuel oxidation mechanism and the limitation of computer capacity, it was not practical to combine the multi-step reaction model with a general multi-dimensional code to describe the detailed kinetic mechanism. The common practice is to use the simplified single- or two-step global kinetic reaction models for engineering applications.

The single-step global kinetic expression for hydrocarbon fuel oxidation is given as:

$$\text{Fuel} + \frac{n_1}{\phi}\,\text{O}_2 \rightarrow n_2\text{CO}_2 + n_3\text{H}_2\text{O} \qquad (1)$$

where n_1 is the stoichiometric coefficient for oxygen, and ϕ is fuel/air equivalence ratio of the mixture.

The single-step global kinetic reaction rate is usually expressed as:

$$k = C_f T^{\xi} \exp(-E_a/RT)[\text{Fuel}]^a\ [\text{oxidizer}]^b \qquad (2)$$

where

$[\ ]$ = molar concentration of species
R = universal gas constant
E_a = activation energy
T = gas temperature
C_f = adjustable preexponential factor
a, b = reaction orders
ξ = adjustable temp. const. (=0 in the present study)

Westbrook and Dryer (1981) summarized that for most hydrocarbon fuels the variation of E_a over the range 26 to 40 kcal/mole affects only the computed flame thickness. Their results obtained with E_a = 30 kcal/mole were quite satisfactory. Usually C_f represents kinetic collision frequency of reactant atoms. Under most IC engine operating conditions the flame is turbulent and the single-step global kinetics model does not account for the turbulence interactions. Therefore the preexponential factor C_f becomes very much an empirical constant which needs to be adjusted from case to case so that the calculated data provides good agreement with experimental measurements. Another drawback of single-step global kinetics model is that it does not account for the influence of variation of pressure in combustion rate and flame propagation speed. But experimental evidence does show that pressure has a strong effect on the flame speed (Groff and Matekunas, 1980). To overcome this problem, a modified single-step global reaction rate expression introduced by Diwakar (1984) was adopted in present studies. The modified model introduces a pressure correction term $(P_{\text{inv}}/p)^n$ into Eq. (2):

$$k = C_f T^{\xi} \exp(-E_a/RT)[\text{Fuel}]^a\ [\text{oxidizer}]^b\ (P_{\text{inv}}/p)^n \qquad (3)$$

where P_{inv} is the cylinder pressure at inlet valve closure. Typically the value of n lies in the range of $1.2 \sim 1.3$. The reason for this modification is that in the original model the flame travels very rapidly after TDC compared to the experimental observations. In other words, the computed flame speed is too high compared to the measurements, and the computed flame speed gets higher as the cylinder pressure increases. The above behavior is contrary to the nature of laminar flame speeds measured in bombs and also the nature of turbulent flame speeds measured in reciprocating engines, where the flame speed decreases with increasing pressure. Since the ratio $p_{\text{inv}}/p < 1$ during compression and expansion cycles, the pressure correction term will reduce the reactions rate and the flame speed under conditions of high cylinder pressure.

3.2 Ignition Model. In KVIA-II the ignition process is modeled as a heat source at the location of the spark. The internal energy of the computational cell at the spark location is increased by a factor of (1.0+DT*IG) on each time step DT until the combustion is self-sustained (typically when the temperature at the cell reaches 1600 K). The reciprocal time constant XIGNIT determines not only the total energy added to the cell, but also the rate at which ignition energy is added. In real spark-ignited engines, the electrical discharge produced between the spark plug electrodes create a very high-temperature (3000-6000 K) plasma kernel (Heywood, 1988) which develops into a self-sustaining and propagating flame front (a thin reaction sheet where the exothermic combustion reactions occur). Conventional ignition systems deliver 30 to 50 mJ of electrical energy to the spark source and only a fraction of the energy supplied to the spark gap is transmitted to the gas mixture. About 0.2 mJ of energy is required to ignite a quiescent stoichiometric fuel-air mixture at normal engine conditions by means of a spark (Heywood, 1988). For lean and rich mixtures the energy required may be an order of magnitude high (~3 mJ). The ignition model used in this study is rather simple and can not model the high-temperature plasma kernel because the chemical equilibrium reaction solver can only handle reactions under 5000 K. If XIGNIT is too large, the peak temperature of the cell at spark location may exceed 5000 K and the calculations will terminate. If XIGNIT is too small, the rate of ignition energy addition is slower than the rate of energy transfer between the ignition cell and adjacent cells. Under these conditions misfire will occur. The fraction of energy added to the ignition cell is so chosen that the variation of fuel fraction burned with crack angle matches with the experimental measurements.

4 Results and Discussions

Results presented here are with a flat piston top homogeneous-charge spark-ignition engine. The purpose of selecting this model engine is that the engine has been extensively studied experimentally and the available data (Groff et al., 1981) can be used to verify numerical modeling results and calibrate some key empirical parameters which must be specified in the code. The engine specifications and test conditions are given in Tables 1 and 2. The fuel used was propane. In order to evaluate the effects of pressure correction term and ignition energy on combustion rate and flame speed (which subsequently affects the variations of cylinder pressure with crack angle) calculations have been performed by the single-step global reaction model with different power of pressure correction term and different

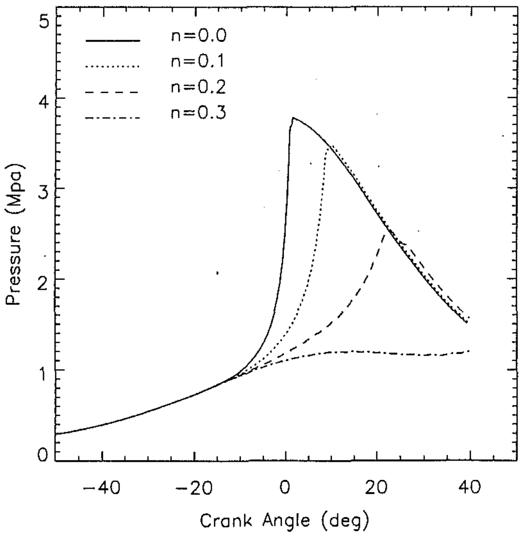

Fig. 1 Variation of cylinder pressure with crank angle for different values of cylinder pressure correction exponent (*n*) at C_f = 5.0 × 10^{11}, XIGNIT = 5.5 × 10^3, phi = 0.87, spark at 27 deg and engine speed = 1500 rpm

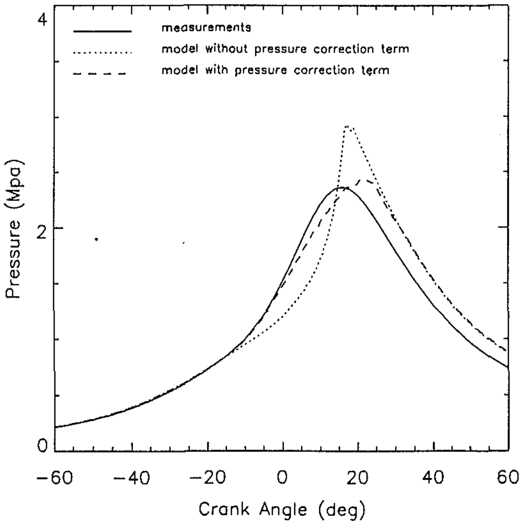

Fig. 3 Comparison of calculated results with experimental data (Groff et al., 1981 Run 3) at phi = 0.87, spark at 27 deg, engine speed of 1500 rpm and XIGNIT = 5.5 × 10^3. No pressure correction term C_f = 3.0 × 10^{11}, *n* = 0, *a* = 0.1, *b* = 1.65. With pressure correction term C_f = 1.55 × 10^{13}, *n* = 1.3, *a* = 0.1, *b* = 1.65.

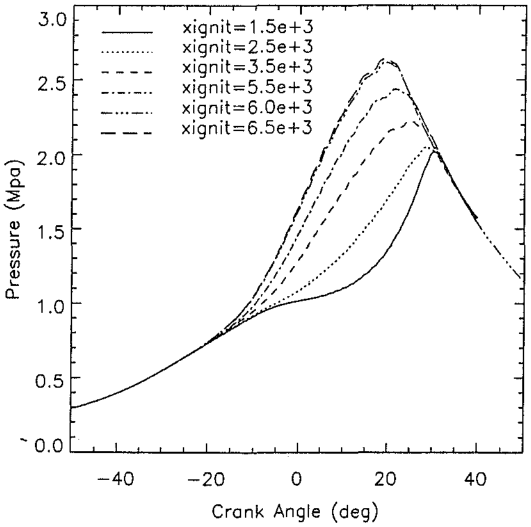

Fig. 2 Variation of cylinder pressure with crank angle for different spark ignition energy fraction (XIGNIT) at cylinder pressure correlation term exponent of *n* = 1.3, C_f = 1.55 × 10^{13} phi = 0.87, spark at 27 deg and engine speed = 1500 rpm

ignition energy addition rate. In the first instance the ignition energy fraction XIGNIT was maintained constant at 5.5×10^3 and the power of the pressure correction term varied from 0.0 to 0.3. The spark in both cases is given at a crank angle of 27 deg BTDC. The total spark energy (E_{spark}) was approximately 9 mJ. As shown in Fig. 1 for no pressure correction term to original single-step reaction rate expression (i.e., $n = 0$), the cylinder pressure increases very rapidly immediately after the development of the flame. This suggests fast development of flame and the reactants take less time to proceed to products. The calculated flame front propagates very rapidly under high pressure conditions. Any increase in *n* causes a reduction in the flame speed which subsequently decreases the peak cylinder pressure. In addition the increase in *n* results in slow rise of peak pressure. As an example, for $n = 0.3$ the peak pressure and rate of pressure rise is very slow. The decrease in the magnitude of the peak pressure is due to the larger chamber volume at which peak pressure occurs and slower flame speed which allows more time for the heat loss through the cylinder walls. In the second case the effect of changing the ignition energy addition rate on cylinder pressure variation and flame speed was examined. Figure 2 indicates that a change in ignition energy fraction (XIGNIT) can also delay the flame propagation and the subsequent rise of pressure in the combustion chamber. It is worth noticing that for a value of XIGNIT greater than 6.0×10^3 the development of cylinder pressure with crank angle is no longer affected. This is due to the fact that the spark is automatically cut off when the combustion is self-sustained.

Figure 3 shows the variation of cylinder pressure with crack angle for the engine operating under the test conditions (Groff et al., 1981) given in Table 2, with $C_f = 1.55 \times 10^{13}$, $n = 1.3$ and XIGNIT = 5.5×10^3. The calculated pressure record provides a very good agreement with the experiment data of Groff et al. (1981). The local pressure in cylinder during engine operation is not strictly uniform and the value of cylinder pressure shown in Fig. 3 is an integral of local pressure over the entire domain volume, so that it is a volume-averaged value. The average temperature is calculated assuming the ideal gas conditions, i.e.,

$$\overline{T}=\frac{\overline{P}V}{NR} \tag{4}$$

where

P = volume-averaged pressure

V = total volume of chamber

N = total number of moles in the mixture

R = universal gas constant.

Having examined the progress in pressure variation with crank angle at one equivalence ratio (i.e., at $\phi = 0.87$) and one engine speed (namely 1500 rpm) it is of interest to see how this pressure variation will change with engine speed and equivalence ratio. Both of these parameters are expected to modify the development of flame within the combustion chamber.

Figure 4 shows the variation of cylinder pressure for 1500 rpm at different equivalence ratios, with other parameters constant ($n = 1.3$, XIGNIT = 5.5×10^3 and $C_f = 1.55 \times 10^{13}$). The effect of engine speed (at 600, 1500, and 3000 rpm) on the development of cylinder pressure is shown in Fig. 5. Decrease in pressure with increase in engine speed suggests decreased burning. This may be due to the lower residence time available for the gases to burn during the power stroke of the

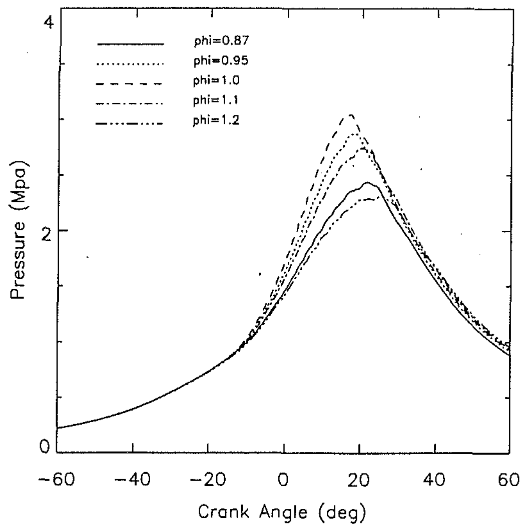

Fig. 4 The effect of equivalence ratio on cylinder pressure and engine speed of 1500 rpm. Spark at 27 deg BTDC, XIGNIT = 5.5×10^3, C_f = 1.55×10^{13}, n = 13, a = 0.1, b = 1.65.

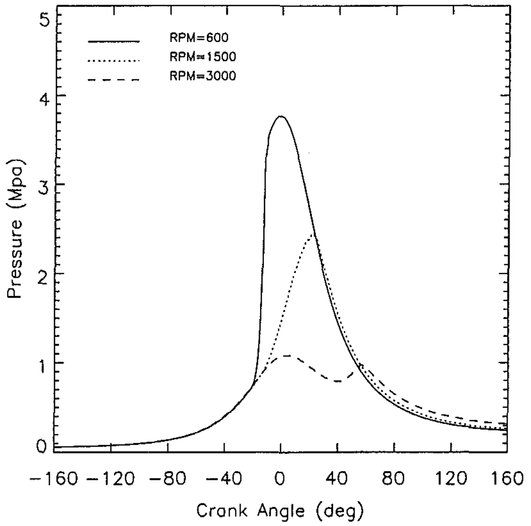

Fig. 5 The progress in pressure variation at engine speeds of 600, 1500, and 3000 rpm at phi = 0.87, spark at 27 deg BTDC, XIGNIT = 5.5×10^3, C_f = 1.55×10^{13}, a = 0.1 and b = 1.65

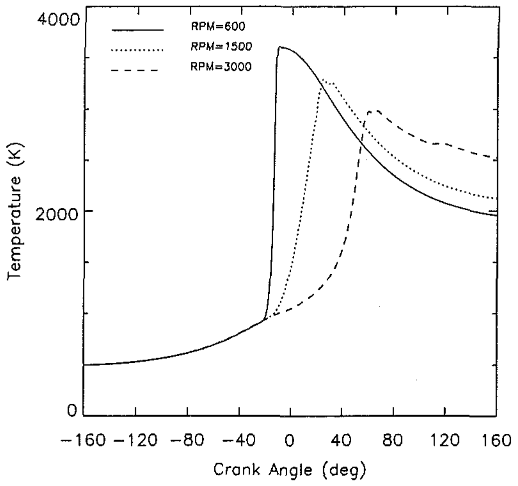

Fig. 6 The progress in temperature variation at engine speeds of 600, 2500, and 3000 rpm at phi = 0.87, spark at 27 deg BTDC, XIGNIT = 5.5×10^3, C_f = 1.55×10^{13}, a = 0.1 and b = 1.65

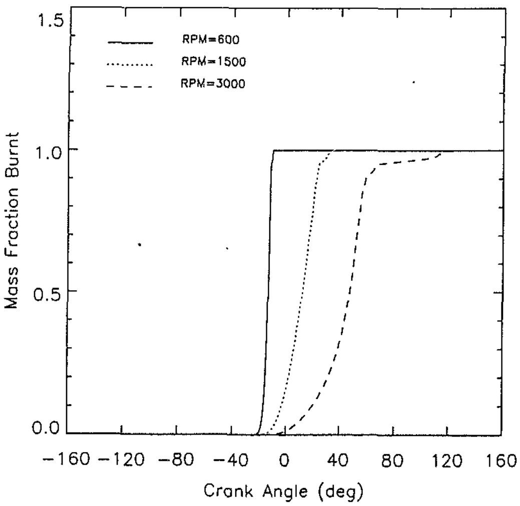

Fig. 7 The progress in mass fraction of the mixture burnt at 600, 1500, and 3000 rpm at phi = 0.87, spark at 27 deg BTDC, XIGNIT = 5.5×10^3, C_f = 1.55×10^{13}, a = 0.1 and b = 1.65

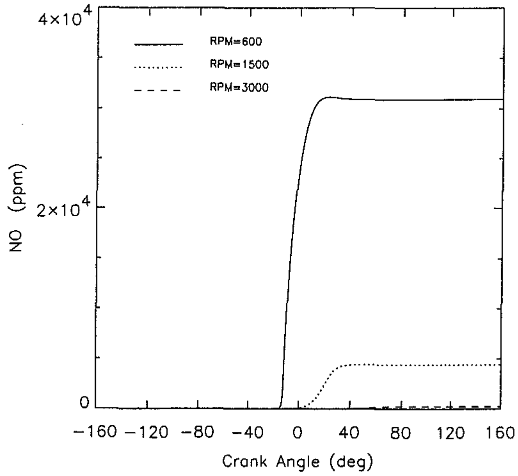

Fig. 8 The progress in NO evolution at 600, 1500 and 3000 rpm at engine operating conditions of phi = 0.87, spark at 27 deg BTDC, XIGNIT = 5.5×10^3, C_f = 1.55×10^{13}, a = 0.1 and b = 1.65

engine. In order to check that the mass fraction burnt and the subsequent mean temperature are also affected at the three engine speeds, calculations were performed under similar conditions (i.e., equivalence ratio of 0.87, spark at 27 deg BTDC, ignition energy (XIGNIT = 5.5×10^3) and swirl ratio (SR = 1). [It is to be noted that swirl ratio had a negligible effect on pressure rise, peak pressure, CO and temperature and NO_x.] The results are presented in Figs. 6 and 7 for temperature and mass fraction burnt, respectively. Although the mass fraction burnt is delayed at higher rpm the burnout is complete even for 3000 rpm (i.e., at about 60 deg ATDC). The decrease in temperature with increase in engine speed is attributed to increased heat transfer and significantly different fluid mechanics inside the engine. The results, however, do confirm the trend of increased fuel consumption and poor fuel burning at higher engine speeds. The nitric oxide emission at higher speed is lower due to lower peak temperatures and the decreased residence time of the gases at higher temperature, see Fig. 8. The results presented in Figs. 3-5 show that the pressure correction term proposed by Diwakar (1984) can effectively adjust the reaction rate and cylinder pressure, but the drawback of the modified rate expression is that the adjustable parameters, such as C_f, need to be adjusted on a case to case basis in order to provide a good agreement with the experimental data. We (a). CO (mole fraction)

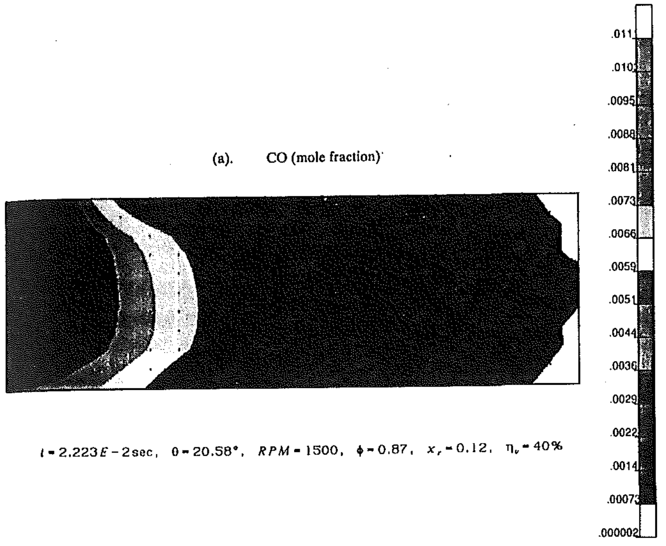

(b). TEMPERATURE (K)

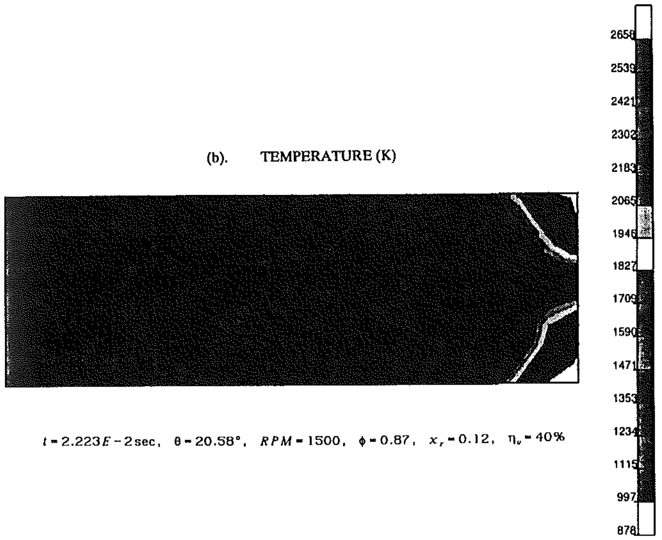

(c). NO (mole fraction)

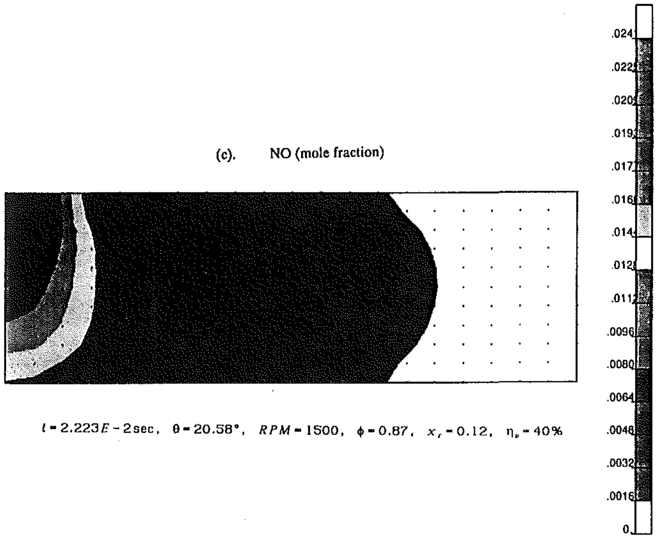

Fig. 9 Contours of CO, temperature and NO within the combustion chamber at crank angle θ = 20.02 deg ATDC, engine speed 1500 rpm, phi = 0.87, residual mass fraction (X_r) = 12 percent and volumetric efficiency of engine (η_v) = 40.1 percent

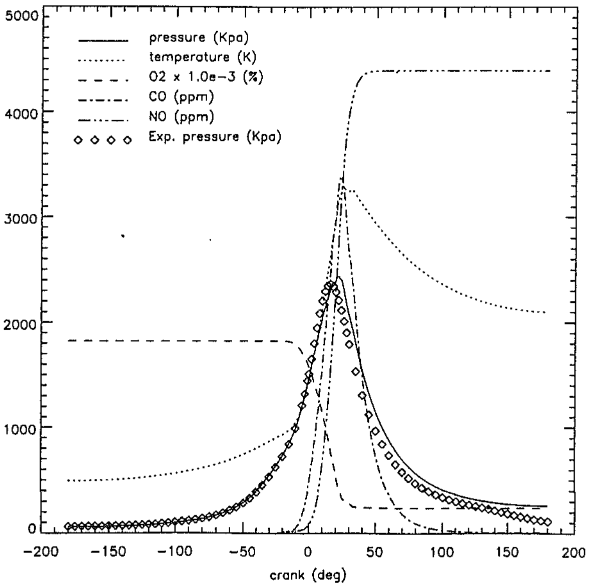

Fig. 10 The evolution of NO, CO, O_2 cylinder pressure and mean temperature with crank angle position at an equivalence ratio of 0.87 (i.e., fuel lean mixture), spark at 27 deg BTDC and engine speed of 1500 rpm, XIGNIT = 1.55×10^3, X_r = 0.12, η_v = 40.1 percent, C_f = 1.55×10^{13}, a = 0.1 and b = 1.65

have examined many values of n, XIGNIT and C_f. However, in order to keep a low number of adjustable parameters, our suggestion is to keep the value of n = 1.3 and vary the value of C_f and XIGNIT for different cases until a good agreement is achieved with the experimental data.

After obtaining the acceptable conditions that describe the history of pressure rise and decay in the cylinder with crank angle, properties of other gaseous species and mean temperature were then evaluated. Ideally one would like to learn the production (or disappearance) of intermediate species as well as the formation of all the permanent species. If this detailed information was known then one could design a system with desirable combustion product stream. In this paper information was obtained on the local variation of CO, O_2, NO, and temperature. The spatial variation of different species concentrations and local temperature in the cylinder at various position of the crank angle was obtained. The results showed that immediately after the flame onset significant variations of species concentration and temperature exists within the combustion chamber at all crack angle positions in the expansion stroke of the cycle. The NO evolution only becomes important after top dead center in the cycle. Sample results for CO, temperature and NO at a crank angle position of θ = 20.02 deg ADTC are shown in Fig. 9. In these cases the engine rpm, equivalence ratio, residual fraction left after firing from each cycle and volumetric efficiency was held constant at 1500 rpm, 0.87, 0.12, and 40.1 percent, respectively. The results clearly showed the flame growth with time and the subsequent spatial variation of CO, NO, and temperature within the combustion zone. For the conditions examined here negligible NO formation occured at θ = 20.97 BTDC despite the presence of very high temperature zone (about 2500 K) near the ignition source. This is due to the negligible residence time of gases at higher temperatures which resulted in negligible NO. Progressive increase in crank angle revealed that the NO contours always lag the temperature contours as expected. The values obtained for CO, O_2, NO, and temperature as a function of crank angle were converted to the volume-averaged values. The resultes presented in Figs. 10 and 11 are for NO, CO, O_2, cylinder pressure and mean temperature at equivalence ratios of 0.87 and 0.98 (i.e., for the fuel lean case). The results show the expected trends, i.e., maximum NO is found immediately

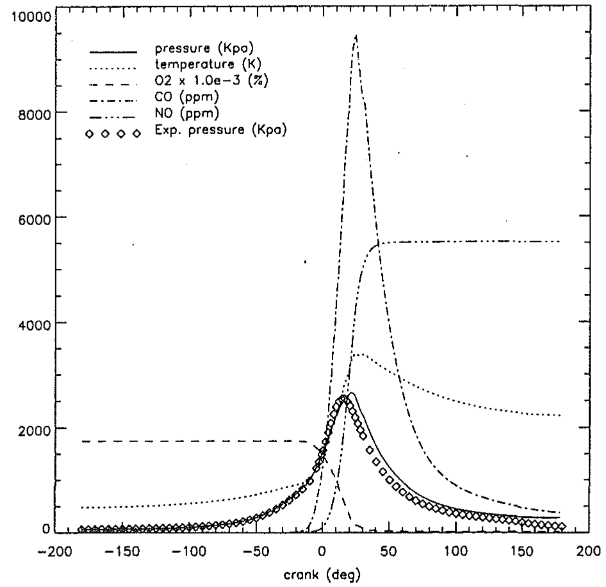

Fig. 11 The evolution of NO, CO, O_2 cylinder pressure and mean temperature with crank angle position at an equivalence ratio of 0.98 (i.e., fuel lean mixture), spark at 27 deg BTDC, X_r = 0.14, η_v = 40.1 percent and engine speed of 1500 rpm, XIGNIT = 5.5×10^3, C_f = 1.7×10^{13}, n = 1.3, a = 0.1 and b = 1.65.

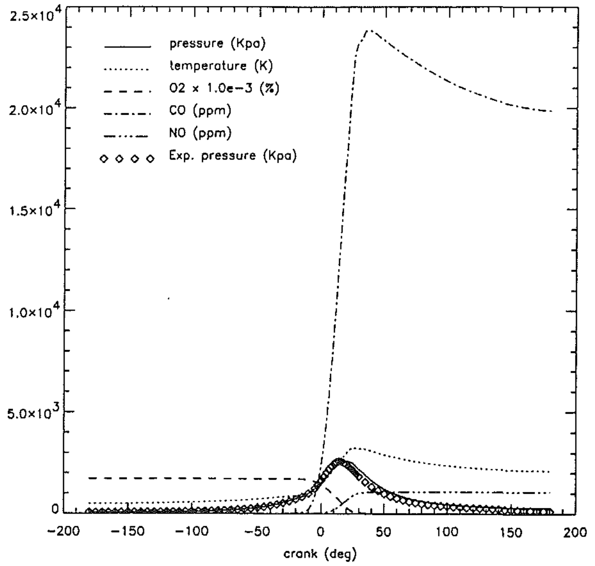

Fig. 12 The evolution of NO, CO, O_2, cylinder pressure and mean temperature with crank angle position at an equivalence ratio of 1.12 (i.e., fuel rich mixture), spark at 25 deg BTDC, engine speed of 1500 rpm, XIGNIT = 5.5×10^3, C_f = 1.8×10^{13}, n = 1.3, a = 0.1, b = 1.65 X_r = 0.14, η_v = 40.1 percent

downstream of the maximum temperature position. The consumption of oxygen yields the conversion of fuel to products with CO as the intermediate product. Increase in equivalence ratio to 1.12 and 1.395 (see Figs. 12 and 13) results in high level of CO emission, lower mean flame temperature which results in lower NO emission levels. The NO emission contribution is only due to thermal NO_X formation since the fuel used contains no fuel bound nitrogen. The variation of NO and CO was examined at different equivalence ratios and the results shown in Fig. 14 clearly indicate the incomplete oxidation of CO as the input fuel-air mixture is progressively changed from fuel lean to fuel rich operation conditions. The decrease of NO in both the fuel rich and fuel lean conditions is due to the lower peak flame temperatures.

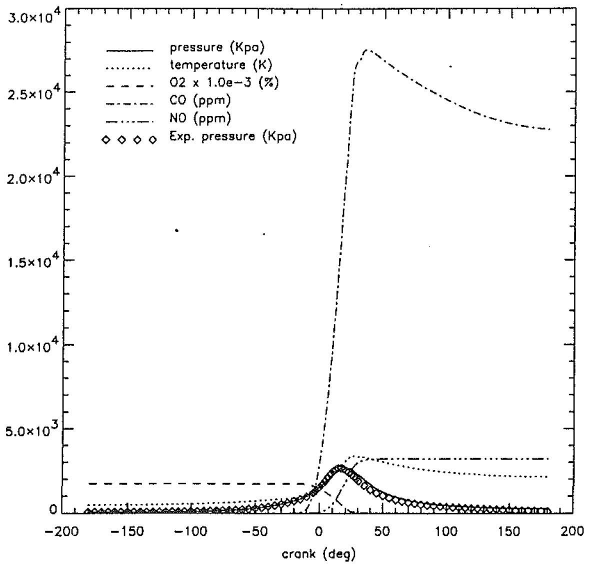

Fig. 13 The evolution of NO, CO, O_2 cylinder pressure and mean temperature with crank angle position at an equivalence ratio of 1.395 (i.e., fuel rich mixture), spark at 30 deg BTDC, engine speed of 1500 rpm, XIGNIT = 5.5×10^3, C_f = 2.4×10^{13}, n = 1.3, a = 0.1, b = 1.65, X_r = 0.14 and η_v = 39.7 percent

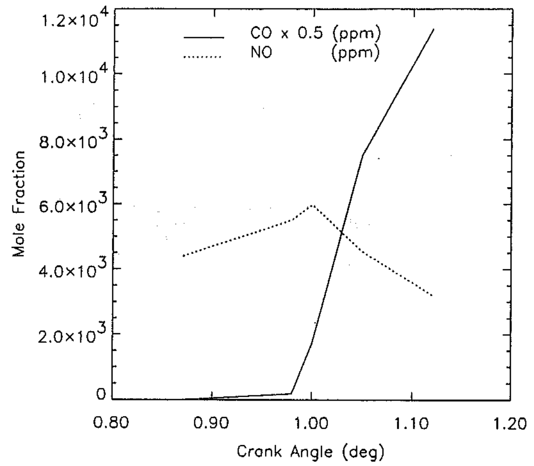

Fig. 14 The evolution of NO and CO with crank angle at 1500 rpm at phi = 1.395, spark at 30 deg BTDC, XIGNIT = 5.5×10^3, C_f = 2.4×10^{13}, n = 1.3, a = 0.1, b = 1.65 and X_r = 0.14 and η_v = 39.7 percent

5 Conclusions

The results presented here have shown the significant effect of engine operating parameters on combustion and emission characteristics. The data for volume-averaged cylinder pressure as a function of crank angle are compared with experimental data and shows a very good agreement. The peak pressure and temperature, and rates of pressure rise and temperatures are significantly affected with engine speed. The results support the general increase in fuel consumption and poor burning at higher engine speeds. The results obtained for CO, O_2, NO, and temperature have also shown the expected trends under both the fuel lean and fuel rich operation of the engine and are similar to those reported in the literature for the chosen flat top piston geometry. Proper selection of the reaction rate, ignition energy and pressure correction term are critical for obtaining the good results. Systematic examination of these values have resulted in well defined value for each of the above parameters. These parameters can now be used for further development of the desirable combustion process which yields high combustion efficiency and low pollution levels. It is, however, advisable to selectively compare the calculated results with experimental results. This approach provides cost effective means of developing advanced IC engine combustion chamber design that provides high level of fuel conversion efficiency and low pollution levels. It is believed that with the increased computational power now available, increased predictive tools will be used in the future for enhancing our understanding of the detailed combustion processes in combustion systems.

Acknowledgment

Partial support of this research by Sonex Research and USNA is gratefully acknowledged.

References

Amsden, A. A., Ramshaw, J. D., O'Rourke, P. J., and Dukowicz, J. K., 1985, "KIVA: A Computer Program for Two- and Three-Dimensional Fluid Flows with Chemical Reactions and Fuel Sprays," LA-10245-Ms, Los Alamos National Laboratory, Los Alamos, NM.

Amsden, A. A., O'Rourke, P. J., and Butler, T. D., 1989, "KIVA-II: A Computer Program for Chemically Reactive Flows with Spray," LA-11560-MS, Los Alamos National Laboratory, Los Alamos, NM.

Borman, G. L., 1980, *Modeling Flame Propagation and Heat Release in Engines, Combustion Modeling in Reciprocating Engines*, Eds., Mattavi, J.N., and Amann, C. A., Plenum Press, New York, p. 163–192.

Diwakar, R., 1984, "Assessment of the Ability of a Multi-Dimensional Computer Code to Model Combustion in a Homogeneous-Charge Engine," SAE paper No. 840230.

Groff, E. G., and Matekunas, F. A., 1980, "The Nature of Turbulent Flame Propagation in a Homogeneous Spark-Ignited Engine," SAE paper No. 800133.

Groff, E. G., Alkidas, A. C., and Myers, J. P., 1981, "Combustion Data for an Axisymmetric Homogeneous-Charge Spark-Ignition Engine," GMR-3577, GM Research Laboratory, Warren, MI.

Gupta, A. K., Lilley, D. G., and Syred, N., 1984, *Swirl Flows*, Abacus Press, U.K.

Gupta, A. K., Beshai, S., Deniz, O., and Chomiak, J., 1989, "Combustion Chamber Geometry Effects on Cycle-by-Cycle Variation of Heat Release Rate," *Proc. ASME Winter Annual Meeting Forum on Industrial Applications of Fluid Mechanics*, San Francisco, Dec. 10–15, 1989, ASME FED-Vol. 86, pp. 23–27.

Gupta, A. K., Lu, J., and Keating, E. L., 1991, "Piston Geometry Design Effects on Combustion and Emission Characteristics," *Proc. ASME Computers in Engineering Conference*, Santa Clara, CA, Aug. 19–22, 1991, Vol. 1, p. 685–695.

Heywood, J. B., 1988, *Internal Combustion Engine Fundamentals*, McGraw-Hill, New York, NY.

Hirt, C. W., Amsden, A. A., and Cook, J. L., 1974, "An Arbitrary Lagrangian-Eulerian Computing Method for All Flow Speed," *Journal of Computational Physics*, Vol. 14, pp. 227–253.

Launder, B. E., and Spalding, D. B., 1972, *Mathematical Methods of Turbulence*, Academic Press, New York.

Overington, M. T., and Haslett, R. A., 1976, "British Institute of Mechanical Engineering, Stratified Charge Conference," London, England, Nov. 1976, Paper No. C253/76.

Pracht, W. E., 1975, "Calculating Three Dimensional Fluid Flows at All Speeds with an Eulerian-Lagrangian Computing Mesh," *Journal of Computational Physics*, Vol. 17, pp. 132–159.

Ramos, J. I., 1989, *Internal Combustion Engine Modeling*, Hemisphere Publishing Co., New York.

Westbrook, C. K., and F. L. Dryer, 1981, "Simplified Reaction Mechanisms for the Oxidation of Hydrocarbon Fuels in Flame," *Combustion Science and Technology*, Vol. 27, pp. 31–43.

Flow Field in the Secondary, Seal-Containing Passages of Centrifugal Pumps[1]

E. A. Baskharone
Associate Professor.
Mem. ASME

S. J. Hensel[2]
Graduate Research Assistant.
Mem. ASME

Department of Mechanical Engineering,
Texas A&M University,
College Station, Texas 77843

This paper illustrates the impact of seal configuration on the through-flow leakage in centrifugal pumps with shrouded impellers. The flow model is based on the Petrov-Galerkin finite element method, and the computational domain permits the primary/secondary flow interaction at both ends of the clearance gap. The model is applied to a hydraulic pump with two different seal configurations for the purpose of comparison. The computed results show a strong dependency of the leakage flow percentage and swirl-velocity retention on the overall shape of the shroud-to-housing passage including, in particular, the seal geometry. The results are generally consistent with documented observations and measurements in similar pump stages. From a rotordynamic standpoint, the current computational model conceptually provides the centered-rotor "zeroth-order" flow field for existing perturbation models of fluid/rotor interaction. The flow model is applied to two different secondary passage configurations of a centrifugal pump, and the results used in interpreting existing rotordynamic data concerning the same passage configurations.

Introduction

Leakage flow in the shroud-to-housing gap of centrifugal pumps has significant performance and rotor-integrity consequences. First, it is the leakage flow rate, as determined by the through-flow velocity component, which is typically a major source of the stage losses. The swirl velocity component, on the other hand, is perhaps the single most predominant destabilizing contributor to the impeller rotordynamic behavior. Control of the through-flow velocity in the clearance gap is often achieved through utilization of a tight-clearance seal. Suppression of the flow swirl, however, requires careful design of the leakage passage and/or the use of such devices as the so-called swirl "brakes" (e.g., Childs et al., 1991) or straightening grooves/ribs in the inner housing surface (e.g., Ohashi, 1988). Unfortunately, an efficient leakage control device, such as the labyrinth seal, may itself trigger an instability problem of fluid-induced vibration (Childs and Elrod, 1988). In the current study, two seal configurations, comprising part of the shroud-to-housing passage in a centrifugal pump, are analyzed for comparison. In both cases, the impeller geometry and the pump operating conditions are identical.

The current computational tool is an expanded version of a finite-element model which was previously proposed by the authors (Baskharone and Hensel, 1989), where the mere idea of including primary-flow segments in the computational domain definition was introduced. This was a means of avoiding the need for what would otherwise be unrealistic boundary conditions at the primary/secondary flow interface. The model, initially based on a laminar flow assumption, has since been upgraded by recognizing such aspects as turbulence and inertia domination of the flow field.

The outcome of the current study is tightly linked to the rotordynamic stability analysis of shrouded pump impellers. This is true in the sense that the numerical results can essentially be utilized as the "zeroth-order" flow field in existing perturbation models (e.g., Baskharone and Hensel, 1991a) for computing the stiffness, damping and inertia coefficients of the fluid/shroud interaction forces, as the impeller axis undergoes a whirling motion around the housing centerline. Accuracy of these rotordynamic coefficients was reported by Baskharone and Hensel (1991a) to be a strong function of the centered-impeller flow solution, which is under investigation here.

Analysis

Figure 1 shows the primary and secondary flow passages in a typical pump stage, and the computational domain under consideration. The latter includes two primary-flow segments, which render the domain to a double/entry, double/departure flow region. Also shown in Fig. 1 are the major features of the finite element model in which a biquadratic curve-sided element (Fig. 2) is used as the discretization unit.

Definition of the computational domain in the manner shown in Fig. 1 is hardly traditional. Inclusion of two primary flow

---

[1] This research was funded by NASA-Marshall Space Flight Center (Huntsville, Alabama), Contract No. NAS8-37821, technical monitor: James Cannon.

[2] Currently with Westinghouse Savannah River Technology Center, Aiken, South Carolina.

Contributed by the Fluids Engineering Division for publication in the JOURNAL OF FLUIDS ENGINEERING. Manuscript received by the Fluids Engineering Division August 10, 1992; revised manuscript received December 30, 1992. Associate Technical Editor: N. A. Cumpsty.

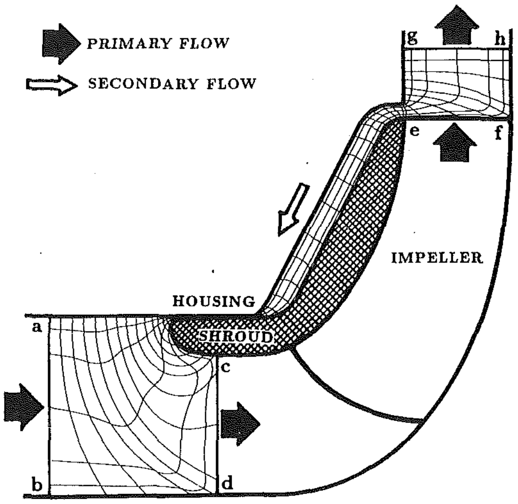

Fig. 1 Definition of the computational domain in a typical centrifugal pump

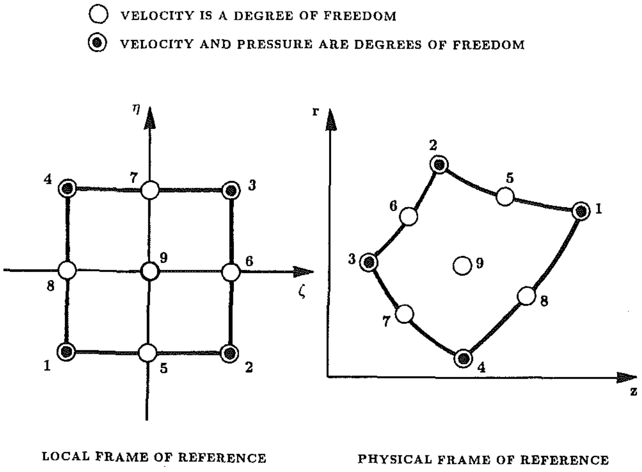

Fig. 2 Biquadratic nine-noded finite element of the Lagrangian type

segments in this domain is aimed at facilitating, to a reasonable level, the primary/secondary flow interaction effects at both ends of the secondary passage, without resorting to a much larger numerical model, had the impeller subdomain been added. Existing computational models, by comparison, treats the secondary passage as totally isolated from the primary-flow passage (e.g., Childs, 1989). As seen in Fig. 1, inclusion of the primary-flow passages (labeled a-b-d-c and e-f-h-g) clearly alleviates the need to specify what would otherwise be grossly simplified boundary conditions at the two primary/secondary flow interaction locations at both ends of the secondary-flow passage.

It might appear, at first, that the current flow problem is solvable using one of the existing commercial flow codes. However the very nature of the computational domain, as a multiple entry/departure flow region, and some of the corresponding boundary conditions (discussed later in this section) are too nontraditional for such codes.

Flow-Governing Equations. The momentum and mass conservation laws governing the swirling axisymmetric flow of the incompressible fluid in Fig. 1 can be expressed as follows:

$$V_r\frac{\partial V_r}{\partial r}+V_z\frac{\partial V_r}{\partial z}-\frac{V_\theta^2}{r}=-\frac{1}{\rho}\frac{\partial p}{\partial r}+\nabla\cdot(\nu_{\text{eff}}\nabla V_r)+\frac{\partial \nu_t}{\partial r}\frac{\partial V_r}{\partial r}-\frac{\nu_{\text{eff}}}{r^2}V_r+\frac{\partial \nu_t}{\partial z}\frac{\partial V_z}{\partial r} \quad (1)$$

$$V_r\frac{\partial V_\theta}{\partial r}+V_z\frac{\partial V_\theta}{\partial z}+\frac{V_rV_\theta}{r}=\nabla\cdot(\nu_{\text{eff}}\nabla V_\theta)-\left[\frac{1}{r}\frac{\partial \nu_t}{\partial r}+\frac{\nu_{\text{eff}}}{r^2}\right]V_\theta \quad (2)$$

$$V_r\frac{\partial V_z}{\partial r}+V_z\frac{\partial V_z}{\partial z}=-\frac{1}{\rho}\frac{\partial p}{\partial z}+\nabla\cdot(\nu_{\text{eff}}\nabla V_z)+\frac{\partial \nu_t}{\partial z}\frac{\partial V_z}{\partial z}+\frac{\partial \nu_t}{\partial r}\frac{\partial V_r}{\partial z} \quad (3)$$

$$\frac{\partial V_r}{\partial r}+\frac{\partial V_z}{\partial z}+\frac{V_r}{r}=0 \quad (4)$$

where:

V_r, V_θ, and V_z are the r, θ, and z velocity components
p = is the static pressure,
ρ = is the flow density,
ν_t and ν_{eff} = are the eddy and effective kinematic viscosity coefficients, respectively.

Turbulence Model. The turbulence closure in this study is that devised by Baldwin and Lomax (1978), together with an enhanced version of the near-wall zone treatment proposed by Benim and Zinser (1985). First, the effective kinematic viscosity ν_{eff}, in Eqs. (1) through (3), is cast in terms of the molecular and eddy components, ν_l and ν_t. In calculating the eddy component, ν_t, the procedure assumes the presence of two, inner and outer, layers. In the inner layer, the Prandtl-Van Driest formulation yields the following expression:

$$\nu_{t,i}=l^2|\omega| \quad (5)$$

where the subscript i refers to the inner layer, and the symbol ω stands for the local vorticity. The mixing length, l, in expression (5) is defined as follows:

Nomenclature

A = finite element area in the meridional plane
K, k = constants in the turbulence closure
L = length along the finite element boundary
l = mixing length
$M_i(\zeta, \eta)$ = linear shape function associated with the ith corner node of a finite element
$N_i(\zeta, \eta)$ = quadratic shape function associated with the ith corner, midside or interior node of a finite element
p = static pressure
U_t = tip speed of the pump impeller
$\mathbf{V}$ = absolute velocity vector
V_z, V_θ, V_r = absolute velocity components in the cylindrical frame of reference
$\mathbf{W}$ = relative velocity vector
W_i = weight function in the Petrov-Galerkin weighted-residual analysis
z, r = coordinates in the meridional plane
ζ, η = coordinates in the element local frame of reference
ν = kinematic viscosity
ρ = density
τ_w = wall shear stress
$\{\Phi\}$, $\{\phi\}$ = global and element vector of unknown velocity components and pressure
Ω = impeller spinning speed
ω = vorticity

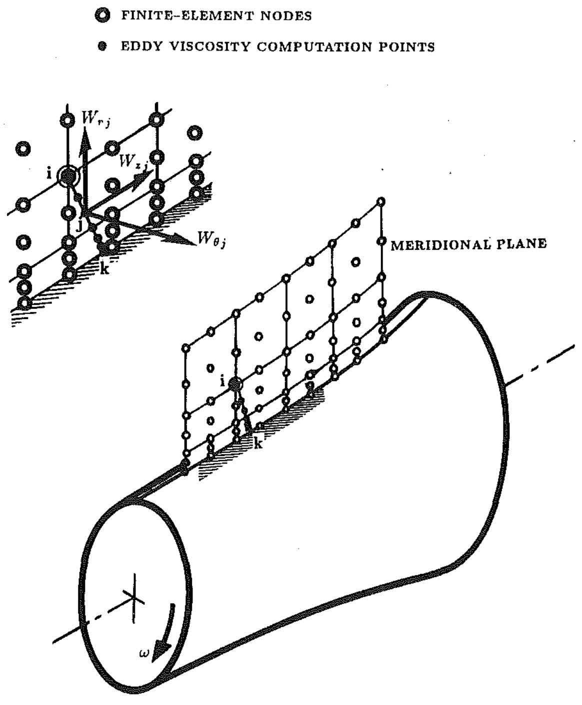

Fig. 3 Near-wall refinement for accurate prediction of the eddy viscosity

$$l=ky\left[1-\exp\left(\frac{-y^{+}}{A^{+}}\right)\right],\quad y^{+}=\frac{\sqrt{\rho_{\omega}\tau_{\omega}}}{\mu_{\omega}}y;\ \text{and} \tag{6}$$

where:

y = the distance normal to the nearest wall,
A^{+} = the sublayer thickness,
τ_{ω} = the wall shear stress

The model switches from Van Driest formulation to that of the outer region at the smallest value of y for which the inner and outer values of the eddy kinematic viscosity are equal. The formulation for the outer layer is given by:

$$\nu_{t,\,o}=KC_{cp}F_{\max}y_{\max}F_{KLEB} \tag{7}$$

where:

$$F_{\max}=y_{\max}|\omega|\left[1-\exp\left(\frac{-y^{+}}{A^{+}}\right)\right];\ \text{and}$$

$$F_{KLEB}=\left[1+5.5\left(C_{KLEB}\frac{y}{y_{\max}}\right)^{6}\right]^{-1}$$

with $y_{\max}$ referring to the value of y at which $F_{\max}$ occurs. The various constants in Baldwin-Lomax model are as follows:

$$A^{+}=26,\ k=0.4,\ K=0.0168,\ C_{cp}=1.6;\ \text{and}\ C_{KLEB}=0.3$$

A modification to the Baldwin and Lomax turbulence closure was made in the current study to accommodate the angular motion of the shroud surface (Fig. 1). Referring to the definition of the inner-layer kinematic eddy viscosity, and considering the case in which the layer is attached to this rotating surface, the vorticity and wall shear stress were both defined on the basis of the relative velocity (**W**) as opposed to the absolute velocity (**V**), where:

$$\mathbf{W}=\mathbf{V}-\Omega r\mathbf{e}_{\theta} \tag{8}$$

where:

Ω = the rotor spinning speed
r = the local radius
$\mathbf{e}_{\theta}$ = the unit vector in the positive tangential direction

In this case, the relative vorticity (ω_R) is expressible in terms of the absolute vorticity (ω) as follows:

$$\omega_R=\omega-2\Omega \tag{9}$$

Calculation of the eddy viscosity in the outer layer (Eq. (7)), as pertaining to the rotating surface, was consistently performed using the relative flow properties.

Computation of the wall shear stress, τ_w, is based on the near-wall zone treatment proposed by Benim and Zinser (1985). The assumption here is that the universal law of the wall at any wall location is extendible to an interior computational node that is closest to the wall at this location (Fig. 3). Referring to this minimum distance from the wall by $y_{\min}$, the following expression for the wall shear stress is then obtained:

$$\tau_w=\begin{cases}\dfrac{\nu_l\rho W_{\min}}{y_{\min}} & \text{for } y^{+}_{\min}<11.6\\[2ex] \dfrac{\kappa C_D^{1/4}\rho W_{\min}k_{\min}^{1/2}}{\ln\left(EC_D^{1/4}\,y_{\min}\dfrac{k_{\min}^{1/2}}{\nu_l}\right)} & \text{for } y^{+}_{\min}\geq 11.6\end{cases} \tag{10}$$

where:

$$k_{\min}=\frac{\tau_w}{\rho C_D^{1/2}},\quad C_D=0.09,\quad \kappa=0.4,\quad E=9.0$$

The symbol $W_{\min}$ in expression (10) refers to the interior-node velocity relative to the wall for a rotating wall segment, and is identical to the absolute velocity otherwise (Fig. 3). Note that the outcome of this equation in the case where $y^{+}_{\min}\geq 11.6$ is a recursive relationship since the wall shear stress τ_w now appears on both sides of the equation. An iterative procedure is executed, in this case, to compute τ_w.

Enhancement of the accuracy of the preceding turbulence closure, including the near-wall model, is achieved with the aid of an array of points that is different from the primary set of computational nodes in the finite-element model. This is in contrast to the model by Benim and Zinser, where the flow properties at the finite-element node closest to the wall were used to calculate the wall shear stress. Figure 3 shows an enlarged segment of the computational domain near a generally rotating wall, in which the primary nodes in the finite-element discretization model are identified by hollow circles, while the points used in the eddy viscosity computations at the typical node "*i*" are solid circles. The objective here was twofold; to estimate the cut-off location between the inner and outer layer with sufficient accuracy, and to capture the steep gradients of the flow variables near the solid wall.

Boundary Conditions. Referring to the flow-permeable boundary segments in Fig. 1, the boundary conditions over these segments are as follows:

(*i*) *Stage Inlet Station.* This is the boundary segment a-b in Fig. 1, which is located sufficiently far upstream from the impeller. Fully developed flow is assumed at this location, giving rise to the following boundary condition:

$$\frac{\partial V_r}{\partial z}=\frac{\partial V_\theta}{\partial z}=\frac{\partial V_z}{\partial z}=0$$

In addition, the stage-inlet static pressure is specified at the node midway between the endwalls on this station.

(*ii*) *Impeller Inlet and Exit Stations.* These are labeled c-d and e-f in Fig. 1. Fixed profiles of the velocity components, corresponding to the stage operating conditions, are imposed over these boundary segments. Note that the operating conditions here involve the primary impeller passage, and do not include the secondary mass flow rate.

(*iii*) *Stage Exit Station.* The flow behavior at this station (designated g-h in Fig. 1) is viewed as predominantly confined to satisfying the mass and angular momentum conservation equations in a global sense. In their derivative forms, these can be expressed as follows:

$$\frac{\partial V_r}{\partial r} = -\frac{V_r}{r} \text{ and } \frac{\partial V_\theta}{\partial r} = -\frac{V_\theta}{r}$$

These two boundary conditions are linear and are, therefore, introduced non-iteratively in the numerical solution process. Moreover, a zero normal derivative of V_z is imposed over this station, and the stage-exit static pressure is specified at the computational node midway between the endwalls on this station.

As for the solid boundary segments in Fig. 1, namely those of the housing and shroud as well as the hub surface segment b-d, the no-slip boundary condition applies as follows:

$$V_r = 0,\ V_z = 0 \text{ and } V_\theta = C$$

where C is equal to (Ωr) and zero for rotating and nonrotating boundary segments, respectively.

Finite-Element Formulation. A special version of the Petrov-Galerkin weighted residual method is used to derive the finite-element form of the flow-governing equations. The current approach ensures upwinding of the convection terms in the momentum equations while preserving the elliptic nature of the diffusion terms. This, for a simple orthogonal grid, would be equivalent to backward-differencing the convection terms and central-differencing the diffusion terms in the conventional finite difference analyses of inertia-dominated flows. Successful implementation of this strategy, within a finite-element context, was achieved by Hughes (1978) for only simple (linear and bi-linear) finite-element configurations by modifying the integration algorithm in the process of deriving the element equations. This effectively eliminated the "wiggles" in the streamwise pressure variation which are typically associated with the conventional Galerkin's weighted residual approach when applied to high Reynolds number flows, such as the present. Expansion of essentially the same concept to a highly accurate biquadratic element, is employed in the current model, by selecting the weight functions on a term-by-term basis.

The characteristic features of the finite element discretization model in the current study are shown in Fig. 1. The discretization unit, which is a nine-noded curve-sided finite element of the Lagrangian type (Zienkiewicz, 1971) is separately shown in Fig. 2 in both the local and physical frames of reference. Within a typical element (e), let the spatial coordinates be interpolated as follows:

$$z^{(e)} = \sum_{i=1}^{9} N_i(\zeta, \eta) z_i, \quad r^{(e)} = \sum_{i=1}^{9} N_i(\zeta, \eta) r_i$$

where N_i are quadratic "shape" functions associated with the element corner, midside and interior nodes. Next, the flow variables are interpolated throughout the element in a similar fashion. Guided by the Ladyshenskaya-babuska-brezzi compatibility requirements (Carey and Oden, 1986) for the problem at hand, the velocity components and pressure are expressed as follows:

$$V_z^{(e)} = \sum_{i=1}^{9} N_i(\zeta, \eta) V_{z,i}, \quad V_r^{(e)} = \sum_{i=1}^{9} N_i(\zeta, \eta) V_{r,i},$$

$$V_\theta^{(e)} = \sum_{i=1}^{9} N_i(\zeta, \eta) V_{\theta,i}, \quad p^{(e)} = \sum_{k=1}^{4} M_k(\zeta, \eta) p_k$$

where M_k are the linear shape functions associated with the element corner nodes.

According to the weighted residual method, the error functions produced by Eqs. (1) through (4) as a result of substituting the interpolation expressions, above, are then made orthogonal to a special set of weight functions over the finite element subdomain. In constructing the latter set of functions, the so-called error consistency criterion of Hood and Taylor (1974) was implemented, whereby the element shape functions, M_k were used in conjunction with the continuity equation. On the other hand, quadratic functions which include the element shape functions "N_i" and a set of derived functions "W_i" were used in conjunction with the momentum equations in such a way to ensure full upwinding of the convection terms. Of these, the functions "W_i" were previously defined by Heinrich and Zienkiewicz (1977) in terms of the shape functions and some upwinding constants which depend on the element geometry and local velocity direction.

With the weight functions now defined, derivation of the finite-element equivalent to Eqs. (1) through (4) is straightforward. The process requires linearization of these equations, using known values for the velocity components and eddy viscosity, and use of Gauss divergence theorem. The final form of these equations for the typical element (e) is as follows:

$$\begin{aligned}
&\left[\int_{A(e)}\int\left\{\hat{\nu}_{\text{eff}}\left(\frac{\partial N_i}{\partial r}\frac{\partial N_j}{\partial r}+\frac{\partial N_i}{\partial z}\frac{\partial N_j}{\partial z}\right)+W_i\left(\hat{V}_r\frac{\partial N_j}{\partial r}+\hat{V}_z\frac{\partial N_j}{\partial z}\right)\right.\right.\\
&\qquad\left.\left.-N_i\frac{\partial\hat{\nu}_t}{\partial r}\frac{\partial N_j}{\partial r}+\frac{\hat{\nu}_{\text{eff}}}{r^2}N_iN_j\right\} rdA\right]V_{r,j}\\
&-\left[\int_{A(e)}\int\frac{\hat{V}_\theta}{r}N_iN_j rdA\right]V_{\theta,j}-\left[\int_{A(e)}\int N_i\frac{\partial\hat{\nu}_t}{\partial z}\frac{\partial N_j}{\partial r}rdA\right]V_{z,j}\\
&+\left[\int_{A(e)}\int\frac{1}{\rho}N_i\frac{\partial M_k}{\partial r}rdA\right]p_k=\oint_{L(e)}\hat{\nu}_{\text{eff}}N_i\,(\vec{n}\cdot\nabla V_r)dL
\end{aligned}\tag{11}$$

$$\begin{aligned}
&\left[\int_{A(e)}\int\left\{\hat{\nu}_{\text{eff}}\left(\frac{\partial N_i}{\partial r}\frac{\partial N_j}{\partial r}+\frac{\partial N_i}{\partial z}\frac{\partial N_j}{\partial z}\right)+W_i\left(\hat{V}_r\frac{\partial N_j}{\partial r}+\hat{V}_z\frac{\partial N_j}{\partial z}\right)\right.\right.\\
&\qquad\left.\left.+\left(\frac{1}{r}\frac{\partial\hat{\nu}_t}{\partial r}+\frac{\hat{\nu}_{\text{eff}}}{r^2}+\frac{\hat{V}_r}{r}\right)N_iN_j\right\}rdA\right]V_{\theta,j}\\
&\qquad\qquad=\oint_{L(e)}\nu_{\text{eff}}rN_i(\vec{n}\cdot\nabla V_\theta)dL
\end{aligned}\tag{12}$$

$$\begin{aligned}
&-\left[\int_{A(e)}\int N_i\frac{\partial\hat{\nu}_t}{\partial r}\frac{\partial N_j}{\partial z}rdA\right]V_{r,j}+\left[\int_{A(e)}\int\left\{\hat{\nu}_{\text{eff}}\left(\frac{\partial N_i}{\partial r}\frac{\partial N_j}{\partial r}\right.\right.\right.\\
&\left.\left.\left.+\frac{\partial N_i}{\partial z}\frac{\partial N_j}{\partial z}\right)+W_i\left(\hat{V}_r\frac{\partial N_j}{\partial r}+\hat{V}_z\frac{\partial N_j}{\partial z}\right)+N_i\frac{\partial\hat{\nu}_t}{\partial z}\frac{\partial N_j}{\partial_z}\right\}rdA\right]V_{z,j}\\
&+\left[\int_{A(e)}\int\frac{1}{\rho}N_i\frac{\partial M_k}{\partial r}rdA\right]p_k=\oint_{L(e)}\nu_{\text{eff}}rN_i(\vec{n}\cdot\nabla V_z)dL
\end{aligned}\tag{13}$$

$$\begin{aligned}
&\left[\int_{A(e)}\int\left(M_k\frac{\partial N_j}{\partial r}+\frac{1}{r}M_kN_j\right)rdA\right]V_{r,j}\\
&\qquad+\left[\int_{A(e)}\int M_k\frac{\partial N_j}{\partial z}rdA\right]V_{z,j}=0
\end{aligned}\tag{14}$$

In these equations, the subscripts "i" and "j" vary from 1 to 9, while "k" varies from 1 to 4. Also the symbol $\hat{()}$ in these equations signifies a value that is known from a previous iteration or an initial guess. The global set of equations is achieved by assembling Eqs. (11) through (14) among all elements, for the current iterative step, and the result is a system of linear algebraic equations in the flow nodal variables.

Results and Discussion

Two secondary-flow passage configurations, corresponding to the same impeller geometry and operating conditions, were chosen for comparison. These are shown in Fig. 4, and feature a conventional wear-ring and a face seal as part of the secondary passage. The pump, which was the focus of rotordynamic testing by Sulzer Bros. (Bolleter et al., 1989), has the

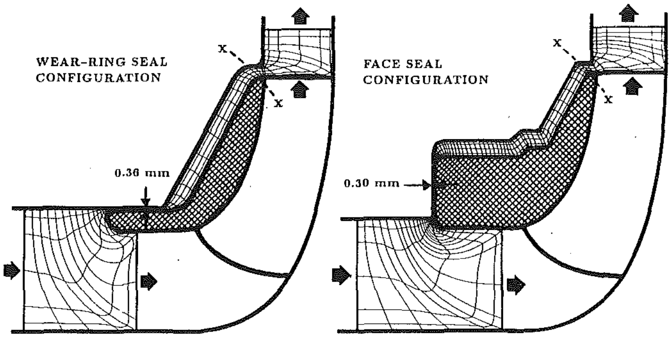

Fig. 4 Sulzer Bros.' wear ring and face-seal pump configurations (Bolleter et al., 1989)

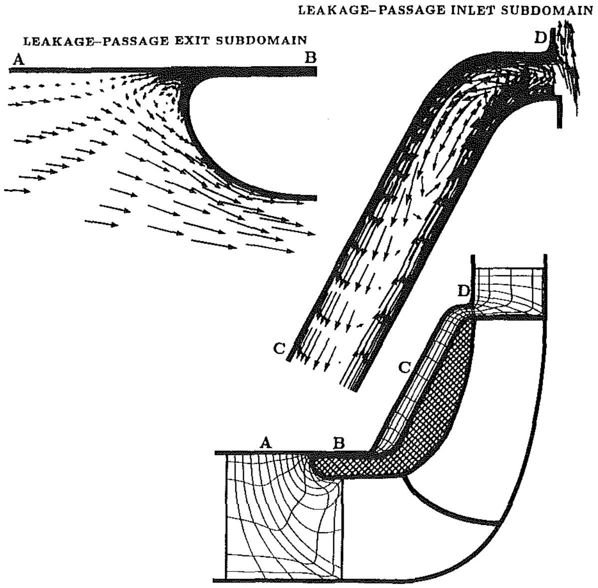

Fig. 5 Meridional velocity vector plot for the wear ring-seal pump configuration

following characteristics and design-point operating conditions.

Impeller tip radius = 17.5 cm
Impeller speed = 2000 rpm
Working medium is water at 30°C
Volumetric flow rate = 130 l/s
Total head = 68 m
Reynolds' number (based on the tip speed and radius) = 8.02×10^6

In creating the finite-element models in Fig. 4, a total of thirteen computational nodes were placed on each cross-flow grid line in the seal region. These nodes were closely spaced near the walls in anticipation of large velocity gradients there. In an early numerical experimentation phase of the study, this finite-element grid was proven to provide a good flow resolution and rule out any significant grid dependency of the computed flow field.

Figure 5 shows a plot of the computed meridional velocity component for the conventional wear-ring seal configuration. This component, together with the corresponding swirl velocity and static pressure (Figs. 6 and 7) constitute the flow solution corresponding to the current model. Examination of Fig. 5 reveals that the shroud-to-housing flow is experiencing a pronounced recirculatory motion in the secondary-passage segment leading to the wear-ring seal. This is a result of the tendency of the fluid particles adjacent to the shroud to migrate radially outwards due to the centrifugal force caused by the shroud rotation, on one hand, and the tendency of those particles near the housing to proceed radially inwards as a result of the static pressure differential across the passage, on the other.

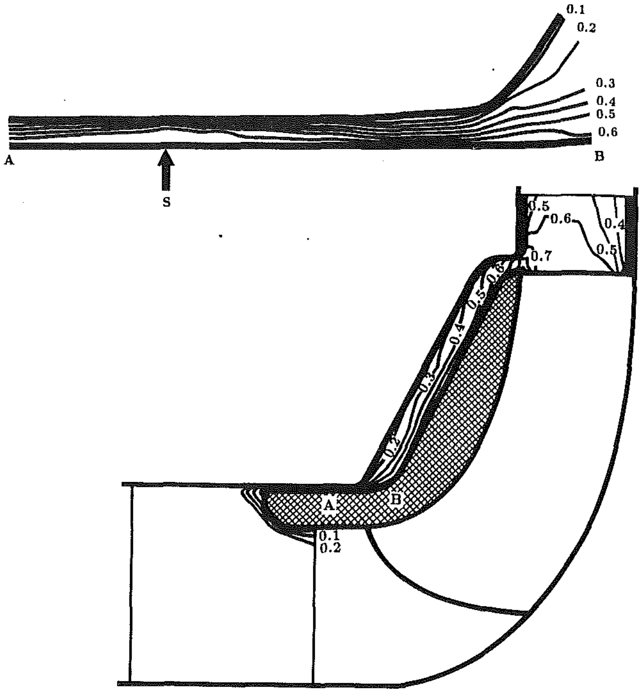

Fig. 6 Contour plot of the nondimensional swirl velocity for the wear ring-seal pump configuration

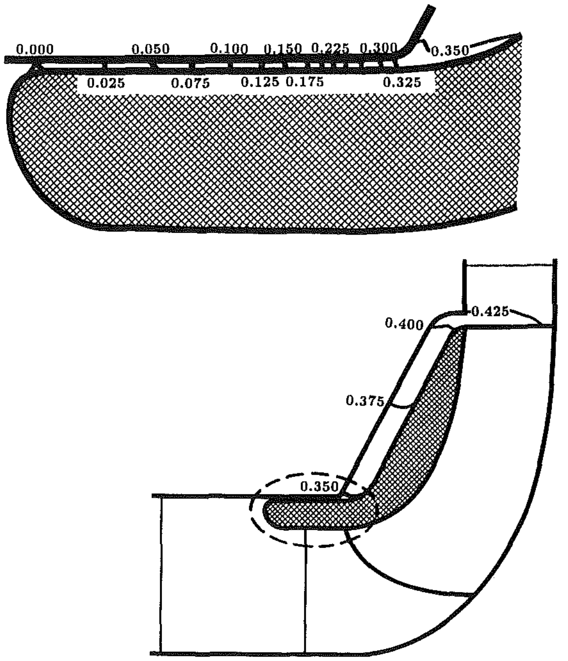

Fig. 7 Contour plot of the nondimensional static pressure for the wear ring-seal pump configuration

Contours of the swirl velocity component and static pressure associated with the secondary flow field are shown in Figs. 6 and 7, respectively. The swirl velocity values in Fig. 6 are nondimensionalized using the impeller tip speed U_t, and the nondimensional pressure ($\bar{p}$) in Fig. 7 is defined as follows:

$$\bar{p} = \frac{(p - p_i)}{\rho U_t^2}$$

with p and p_i referring to the local and stage-inlet pressures,

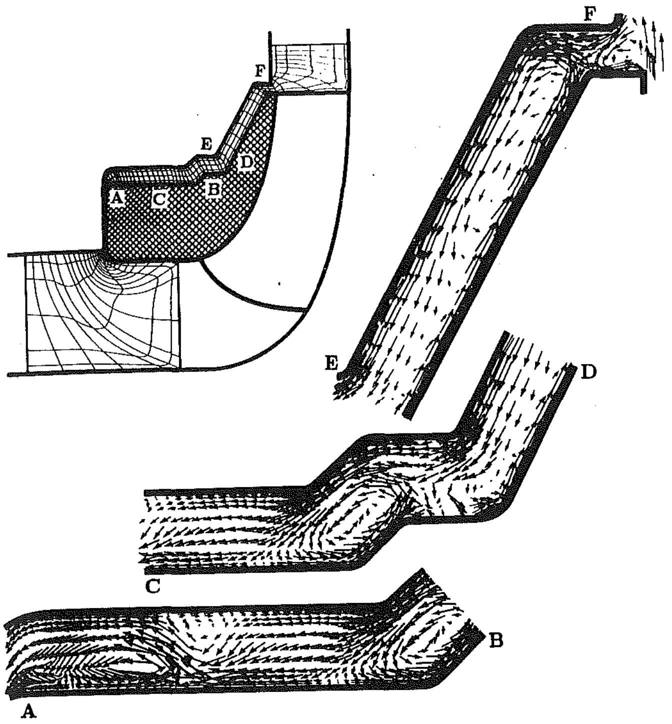

Fig. 8 Meridional velocity plot for the face-seal pump configuration

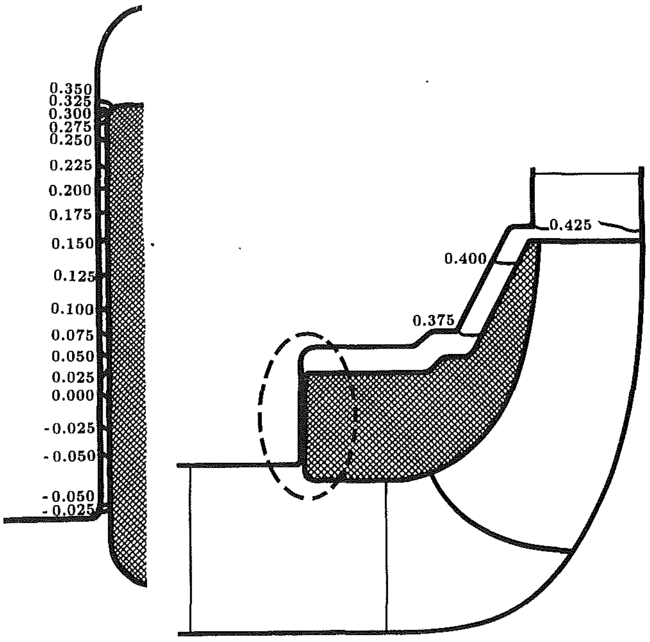

Fig. 10 Contour plot of the nondimensional static pressure for the face-seal pump configuration

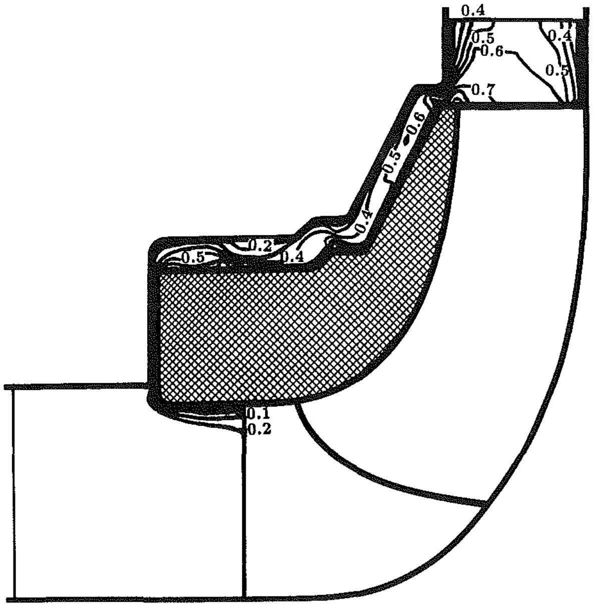

Fig. 9 Contour plot of the nondimensional swirl velocity for the face-seal pump configuration

respectively. Also shown in Fig. 7 is a magnified view of the wear-ring seal where the major part of the pressure differential, across the leakage passage, takes place.

The meridional and swirl velocity components, along with the static pressure obtained for the face-seal pump configurations are shown in Figs. 8 through 10. Again, the meridional velocity vectors, in Fig. 8, indicate a strong recirculatory motion in virtually all segments of the secondary passage. Reasoning of this flow behavior was discussed earlier. However, a unique, and perhaps peculiar, flow structure is seen to exist in the horizontal segment of the leakage passage in Fig. 8, where radial shifting of the flow trajectories and vortex breakdown takes place. It is apparent, however, that the magnitude of the pressure gradient in this low-radius region exceeds that of the centrifugal force. This seems to weaken the flow recirculation in this leakage-passage segment, confining it to the shroud side of the leakage passage.

There is a rather modest amount of experimental data to validate the computed flow field in Figs. 5 through 10. First, it was indicated by Sulzer Bros. that the average swirl velocity component at the leakage-passage inlet station was measured, for the face-seal pump configuration under the above-mentioned operating conditions, to be approximately 0.5 of the impeller tip speed (Childs, 1989). With the current finite-element model, the average value of this velocity component was computed to be 0.526 of the tip speed. Note that the shroud-to-housing swirl velocity profile, which gave rise to this average value, is not specified a priori, but is rather part of the finite-element flow solution (Fig. 9). This advantage, as indicated earlier, is a result of including primary flow segments in the computational domain definition (Fig. 4). Further experimental observations which are consistent with the computed flow field in this study concern the recirculatory pattern of the meridional flow (Fig. 8), and were qualitatively reported by Guelich et al. (1989).

Rigorous verification of the seal friction resistance was not quite attainable. This was particularly the case for the face-seal configuration, which is rather an uncommon seal type. Indeed the only "vaguely" similar problem in literature is that of a rotating disk in a stationary chamber (e.g., Daily and Nece, 1960) or in open space (e.g., Uzkan and Lipstein, 1986). Such studies were focused on the pumping of secondary, often cooling, flow over the face of what is typically a bladed-rotor disk between the shaft and the disk tip radius. The flow direction in this case would naturally be radially outwards, in contrast to that of the face seal flow (Fig. 4), which is predominantly driven by a strong inward pressure decline. Validation of the wear-ring seal results, on the other hand, may appear possible in light of such experimental correlations as those of Yamada (1962). The fact, however, is that Yamada's study did not account for the seal-inlet preswirl velocity which, by reference to Fig. 6, is hardly confined to a thin layer adjacent to the rotor, nor did the study address the complex flow pattern at the end of the shroud-to-housing gap leading to the seal segment (Fig. 4). In fact, the combination of these two real flow effects lead to an early, but localized, flow separation over the shroud surface at the point marked "S" in Fig. 6, a situation that was not encountered in Yamada's study, where only simple isolated annular seals were tested.

Fortunately, the authors were recently able to validate the current computational model, including the turbulence closure, for a straight annular seal using Yamada's experimental data (Baskharone and Hensel, 1991). The seal under consideration had a clearance/length ratio of 0.034, and a Reynolds' number (based on the clearance width and inlet through-flow velocity) of 13,280. The computed seal resistance for this seal was reported to be in excellent agreement with Yamada's experimental data. Furthermore, the agreement between the computed profiles of through-flow and tangential velocity components and those of Morrison et al. (1988) was equally favorable.

Performance assessment of the two secondary-flow passages (Fig. 4), in light of the numerical results, involves their effectiveness as leakage suppressants and swirl dissipators. In order to determine the leakage control capacity of each passage, the mass flux was integrated at the passage inlet station. The results indicated that the leakage-flow rates in the wear-ring and face-seal pump configurations were 0.0011 and 0.0038 m^3/s, respectively. These represent 0.85 and 2.92 percent of the primary flow rate, and illustrate the relative superiority of the wear-ring seal configuration, as a leakage-control device over the face-seal alternative. This, in part, is due to the highly favorable streamwise pressure gradient across the face seal as a result of the substantial radius diminishment, between the seal inlet and exit station, which lessens the boundary layer build-up over the solid walls and eliminates the likelihood of any flow separation. On the other hand, the tendency of the fluid particles to migrate radially outwards near the constant-radius shroud surface, in the case of the wear-ring seal, added to the complex flow structure in the passage leading to the seal, create an environment for an early flow separation over the shroud surface (location "S" in Fig. 6). Despite the rapid flow reattachment, in this case, the recirculation region, following the separation point, has the effect of enhancing the seal frictional resistance and, therefore, the sealing effectiveness of the wear-ring seal configuration by comparison. Another contributing factor behind the wear-ring effectiveness, as a leakage-control device, is the existence of a substantial recirculation zone at the seal-exit station (Fig. 5), with practically no comparable seal-exit flow behavior in the case of the face-seal configuration (Fig. 8). As for the swirl velocity dissipation across the secondary passage, examination of Figs. 6 and 9 reveals that the "kink" in the secondary passage of the face-seal pump configuration (Fig. 9), is causing a sudden and measurable reduction in the swirl velocity in the axial passage segment, with no equivalent swirl velocity reduction mechanism in the wear-ring seal pump configuration. More importantly, the average swirl velocity component at the secondary passage inlet station (designated x-x in Fig. 4) was found to be as low as 0.526 of the impeller tip speed for the face-seal pump configuration, as opposed to 0.812 for its counterpart. Worth noting is the fact that the choice of station x-x in Fig. 4 is consistent with that of Childs (1989), as a meaningful parameter in interpreting the rotordynamic behavior of the same pump configurations in Fig. 4. Although these swirl characteristics of the face-seal pump configuration are not quantitatively convertible into a rotordynamic stability-related factor, it is established (Childs et al., 1991) that swirl suppression at the secondary passage inlet station is among the most effective tools for shrouded-impeller rotordynamic stability enhancement. This, in view of the current results, would imply that the face-seal pump configuration provides a less destabilizing effect. The conclusion here is consistent with the experimental findings of Bolleter et al. (1989), who reported comparable direct-damping coefficients for the fluid/shroud interaction system, but a significantly lower cross-coupled stiffness coefficient for the face-seal pump configuration. Since unstable operation of the impeller (in the form of a whirling motion) is triggered by low direct damping and/or high cross-coupled stiffness, the experimental measurements suggest that the face-seal pump configuration results in a more stable impeller operation, which is what the numerical results seem to imply.

Concluding Remarks

The finite-element model of the pump secondary flow in this paper is a versatile tool for predicting the leakage-suppression and rotordynamic-stability characteristics of viable secondary-passage designs. The model accuracy stems from the manner in which the computational domain is defined to permit the typically strong primary/secondary flow interaction. Simulation of the flow turbulence and recognition of the inertia domination in formulating the problem makes the model applicable to a wide range of real-life operating conditions. The model was applied to two representative configurations of seal-containing secondary passages in an existing centrifugal pump stage for code verification and seal-performance assessment purposes. The results are consistent with experimental measurements concerning the same pump, and documented observations in similar secondary-passage configurations. The computed flow field in the current study constitutes the so-called "zeroth-order" flow solution in existing perturbation models of the fluid-induced vibration of shrouded pump impellers. This explains the desire for an accurate flow field in the secondary passage, since the output of such perturbation models would naturally be a strong function of the flow behavior prior to the impeller excitation.

Acknowledgment

This study was funded by NASA-Marshall Space Flight Center (Huntsville, AL), contract no. NAS8-37821, technical monitor: James Cannon. Partial funding was also provided by the Texas A&M Turbomachinery Research Consortium.

References

Baldwin, B. S., and Lomax, H., 1978, "Thin Layer Approximation and Algebraic Model for Separated Turbulent Flows," AIAA Paper No. 78-257.

Baskharone, E. A., and Hensel, S. J., 1989, "A New Model for Leakage Prediction in Shrouded-Impeller Turbopumps," ASME JOURNAL OF FLUIDS ENGINEERING, Vol. 111, pp. 118-123.

Baskharone, E. A., and Hensel, S. J., 1991, "A Finite-Element Perturbation Approach to Fluid/Rotor Interaction in Turbomachinery Elements. Part 1: Theory," ASME JOURNAL OF FLUIDS ENGINEERING, Vol. 113, No. 3, pp. 353-361.

Baskharone, E. A., and Hensel, S. J., 1991, "A Finite-Element Perturbation Approach to Fluid/Rotor Interaction in Turbomachinery Elements. Part 2: Application," ASME JOURNAL OF FLUIDS ENGINEERING, Vol. 113, No. 3, pp. 362-367.

Benim, A. C., and Zinser, W., 1985, "Investigation into the Finite Element Analysis of Confined Turbulent Flows Using a $k-\epsilon$ Model of Turbulence," *Computer Methods in Applied Mechanics and Engineering*, Vol. 51, pp. 507-523.

Bolleter, U., Leibundgut, E., and Sturchler, R., 1989, "Hydraulic Interaction and Excitation Forces of High Head Pump Impellers," Presented at the Third Joint ASCE/ASME Mechanics Conference, University of California, La Jolla, CA.

Carey, G. F., and Oden, J. T., 1986, "Finite Elements: Fluids Mechanics," *The Texas Finite Element Series*, Vol. IV, Prentice-Hall.

Childs, D. W., 1989, "Fluid-Structure Interaction Forces at Pump-Impeller-Shroud Surfaces for Rotordynamic Calculations," SSME *Journal of Vibration, Stress and Reliability in Design*, Vol. 111, pp. 216-225.

Childs, D. W., Baskharone, E., and Ramsey, C., 1991, "Test Results for Rotordynamic Coefficients of the SSME HPOTP Turbine Interstage Seal With Two Swirl Brakes," ASME *Journal of Tribology*, Vol. 113, No. 3.

Childs, D., and Elrod, D., 1988, "Annular Honeycomb Seals: Test Results for Leakage and Rotordynamic Coefficients, Comparisons to Labyrinth and

Smooth Configurations," NASA Conference Publication 3026, Rotordynamic Instability Problems in High-Performance Turbomachinery, pp. 143–159.

Daily, W., and Nece, R. E., 1960, "Chamber Dimension Effects on Induced Flow and Frictional Resistance of Enclosed Rotating Disks," ASME *Journal of Basic Engineering*, Vol. 82, No. 1, pp. 217–231.

Guelich, J., Florjancic, D., and Pace, S. E., 1989, "Influence of Flow Between Impeller and Casing on Part-Load Performance of Centrifugal Pumps," *Rotating Machinery Dynamics*, ASME Publication DE-Vol. 2, pp. 227–235.

Heinrich, J. C., and Zienkiewicz, O. C., 1977, "Quadratic Finite Element Schemes for Two-Dimensional Convective-Transport Problems," *Int. J. Num. Meth. Eng.*, Vol. 11, pp. 1831–1844.

Hood, P., and Taylor, C., 1974, "Navier-Stokes Equations Using Mixed Interpolation," *Proceedings of the International Symposium on Finite Element Methods in Flow Problems*, University of Wales, Swansea, United Kingdom.

Hughes, T. J. R., 1978, "A Simple Scheme for Developing 'Upwind' Finite Elements," *Int. J. Num. Meth. Engg.*, Vol. 12, pp. 1359–1365.

Morrison, G. L., Johnson, M. C., and Tatterson, G. B., 1988, "3-D Laser Anemometer Measurements in an Annular Seal," ASME Paper No. 88-GT-64.

Ohashi, H., Sakurai, A., and Nishima, J., 1988, "Influence of Impeller and Diffuser Geometries on the Lateral Fluid Forces of Whirling Centrifugal Impeller," NASA CP-3026, pp. 285–306.

Uzkan, T., and Lipstein, N. J., 1986, "Effects of Honeycomb Shaped Walls on the Flow Regime Between a Rotating Disk and a Stationary Wall," ASME Paper No. 86-GT-161.

Yamada, Y., 1962, "Resistance of Flow Through an Annulus with an Inner Rotating Surface," *Bulletin of JSME*, Vol. 5, pp. 302–310.

Zienkiewicz, O. C., 1971, *The Finite Element Method in Engineering Science*, McGraw-Hill, New York, NY.

Numerical Simulation of Laminar Flow of Yield-Power-Law Fluids in Conduits of Arbitrary Cross-Section

Idir Azouz
Graduate Research Assistant,
Mechanical Engineering Department.

Siamack A. Shirazi
Assistant Professor,
Mechanical Engineering Department.
Assoc. Mem. ASME

Ali Pilehvari*
Visiting Assistant Professor,
Petroleum Engineering Department.

J. J. Azar
Professor,
Petroleum Engineering Department.

The University of Tulsa,
Tulsa, OK 74104-3189

A numerical model has been developed to simulate laminar flow of Power-law and Yield-Power law fluids in conduits of arbitrary cross-section. The model is based on general, nonorthogonal, boundary-fitted, curvilinear coordinates, and represents a new approach to the solution of annular flow problems. The use of an effective viscosity in the governing equation of the flow allows the study of the flow behavior of any fluid for which the shear stress is a function of shear rate only. The model has been developed primarily to simulate annular flow of fluids used in drilling and completion operations of oil or gas wells. Predicted flow rates versus pressure gradient for laminar flow of Newtonian fluids in concentric and eccentric annuli, and Power-law fluids in concentric annuli compare very well with results derived from analytical expressions. Moreover, the predictions for laminar flow of Power-law and Yield-Power-law fluids in eccentric annuli are in excellent agreement with numerical and experimental data published in the literature. The model was also successfully applied to the case of laminar flow of Power-law fluids in an eccentric annulus containing a stationary bed of drilled cuttings and the results are presented herein.

Introduction

During the drilling phase of oil/gas wells, a drilling fluid, which is usually a non-Newtonian fluid, is pumped down the drill-string. This fluid returns through the annular gap between the string and the casing wall, and carries to the surface the drilled cuttings generated at the bottom of the hole. With the recent development in directional and horizontal drilling technology, there is a great deal of interest in the understanding and modeling of cuttings transport in highly inclined wellbores. In this case, the problem of cuttings transport is further complicated due to the eccentricity of the annulus and the probable presence of a cuttings bed (Fig. 1). With these additional parameters, the development of a model for cuttings transport becomes more difficult and requires a thorough understanding of the drilling mud flow behavior in the irregular annular geometry.

An early contribution to the understanding of annular flow is due to Lamb (1945) who derived an equation that relates flow rate to frictional pressure drop for the laminar flow of a Newtonian fluid in a concentric annulus. Piercy et al. (1933), on the other hand, investigated the flow of a Newtonian fluid through an eccentric annulus and derived an analytical solution to the equation of motion by using a complex variables transformation approach. According to White (1974), this important work by Piercy et al. (1933) has often been overlooked by other investigators. For instance, Redberger and Charles (1962) used bipolar coordinates together with a conformal transformation to obtain a numerical solution for the case of laminar flow of a Newtonian fluid in an eccentric annulus.

The first analytical solution to the concentric annular flow of a non-Newtonian fluid was derived by Fredrickson and Bird (1958). They presented a relationship between flow rate and

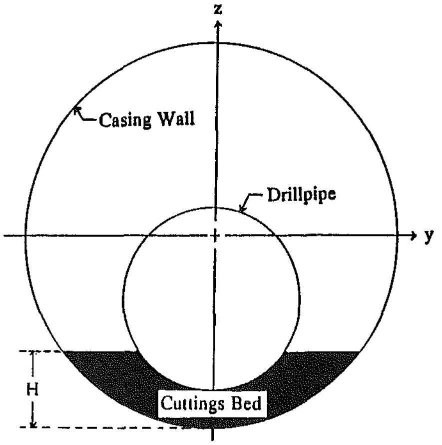

Fig. 1 Flow geometry for a partially blocked annulus

---

* Currently, Assistant Professor, Department of Chemical and Natural Gas Engineering, Texas A&M University-Kingsville.

Contributed by the Fluids Engineering Division for publication in the JOURNAL OF FLUIDS ENGINEERING. Manuscript received by the Fluids Engineering Division June 12, 1992; revised manuscript received March 3, 1993. Associate Technical Editor: R. L. Panton.

pressure drop in graphical forms for Bingham-plastic and Power-law fluids. An excellent study in the area of non-Newtonian fluids in eccentric annuli was performed by Guckes (1975). He used bipolar coordinates and a finite-difference technique to solve the equations of motion. However, his computational model is unstable at high eccentricities. The method of bipolar coordinates was also used by Haciislamoglu (1990) to investigate the flow of Yield-Power-law fluids in eccentric annuli. Tao and Donovan (1955), on the other hand, were the first to develop the so-called "narrow-slot" model. They tried to approximate the eccentric annulus by a slot of variable height. However, their mathematical expression for the slot height was incorrect. Although this expression was later corrected by Iyoho and Azar (1981), the model is still restricted to annuli with large inner to outer radius ratios.

None of the models mentioned above can be applied to cases where the annular geometry is deformed, such as the case of a partially blocked annulus due to accumulation of drilled cuttings. The purpose of the present study is to develop a numerical model which can be used to simulate the flow behavior of Power-law and Yield-Power-law fluids in conduits of arbitrary cross-section. A new approach based on general, non-orthogonal, curvilinear coordinate system is adopted in this work. This frees the computational simulation from geometry restriction which is a major drawback of all the models that have been developed in the past.

Governing Equation

The axial momentum equation for steady-state, fully developed laminar flow of incompressible fluids in an annulus of arbitrary, constant cross-sectional area (see Fig. 1) may be written as (see for instance, Haciislamoglu, 1990):

$$\frac{\partial}{\partial y}\left[\mu(\Gamma)\,\frac{\partial u}{\partial y}\right]+\frac{\partial}{\partial z}\left[\mu(\Gamma)\,\frac{\partial u}{\partial z}\right]=\frac{dP}{dx} \tag{1}$$

where u is the axial velocity (x-direction), dP/dx is the total axial pressure gradient which includes gravitational terms, x, y, and z are Cartesian coordinates, and $\mu(\Gamma)$ is the effective viscosity which is a function of the shear rate Γ whose mathematical expression depends on the type of rheological model used. The advantage of using an effective viscosity is that any fluid, for which the shear stress is a function of shear rate only and no additional normal stresses are produced by shearing, can be considered by obtaining the appropriate expression for $\mu(\Gamma)$ and substituting it into Eq. (1).

Equation (1) is to be solved subject to a no-slip condition at all solid boundaries. An integral form of the continuity equation is used to compute the flow rate for a given pressure gradient.

Rheological Models. A review of technical literature reveals that many rheological models have been developed in the past. The rheological behavior of drilling muds and cement slurries is closely matched by the Yield-Power-law model (see Zamora and Lord, 1974) and, to a lesser extent, by the Power-law model. The relationships between shear stress and shear rate for these two models are given by:

$$\tau=\tau_0+K\,\Gamma^n \quad \text{(Yield-Power-law)} \tag{2}$$

and

$$\tau=K\,\Gamma^n \quad \text{(Power-law)} \tag{3}$$

where τ is the shear stress, τ_0 is the yield-point shear stress, K is the consistency index, n is the flow behavior index, and Γ is the shear rate defined below. The constants τ_0, K, and n are commonly called "model parameters." It can be noticed from Eqs. (2) and (3) that Yield-Power-law and Power-law models involve 3 and 2 parameters, respectively. These parameters are empirically determined. Also, notice that the Power-law model is a special case of the Yield-Power-law model for $\tau_0 = 0$.

For fully developed flow of isotropic fluids where u is the only nonzero velocity component, the shear rate Γ takes the form (Bird et al., 1960):

$$\Gamma=\left[\left(\frac{\partial u}{\partial y}\right)^2+\left(\frac{\partial u}{\partial z}\right)^2\right]^{0.5} \tag{4}$$

In this study, both Yield-Power-law and Power-law models are incorporated into the numerical code, with the effective viscosity $\mu(\Gamma)$ expressed as:

$$\mu(\Gamma)=\frac{\tau_0}{\Gamma}+K\,\Gamma^{n-1} \quad \text{(Yield-Power-law)} \tag{5}$$

$$\mu(\Gamma)=K\,\Gamma^{n-1} \quad \text{(Power-law)} \tag{6}$$

Boundary-Fitted Curvilinear Coordinate System. The flow domain under consideration (see Fig. 1) is not easily described in any of the classical coordinate systems due to the irregular shape of the boundaries. The use of such systems will inevitably pose a problem both in implementing boundary conditions and in writing a general code to solve the governing equation. Therefore, an alternative system consisting of boundary-fitted curvilinear coordinates (Anderson et al., 1985) is suggested. The cardinal feature of such a system is that some coordinate line coincides with each boundary of the physical domain. This allows boundary conditions to be specified entirely along coordinate lines without need of interpolation. As shown in Fig. 2, the physical domain in the (y, z)-space is mapped to a rectangular computational region in the (ζ, η)-space, where ζ and η are the new coordinates. This technique frees the computational simulation from geometry restriction and allows a general code to be written in which the shape of the physical region is simply specified by input.

Using this approach, Eq. (1) is recast in this new coordinate system according to a transformation of the form:

$$\eta=\eta(y,\,z) \tag{7a}$$

$$\zeta=\zeta(y,\,z) \tag{7b}$$

Furthermore, partial derivatives with respect to y and z are transformed to partial derivatives in the transformed plane (ζ, η) according to the following expressions:

$$\frac{\partial}{\partial y}=\eta_y\,\frac{\partial}{\partial \eta}+\zeta_y\,\frac{\partial}{\partial \zeta} \tag{8a}$$

$$\frac{\partial}{\partial z}=\eta_z\,\frac{\partial}{\partial \eta}+\zeta_z\,\frac{\partial}{\partial \zeta} \tag{8b}$$

Nomenclature

dP/dx = axial pressure gradient (psi/in.)
e = eccentricity of the annular geometry (dimensionless)
H = thickness of the cuttings bed (in.)
J = Jacobian of the transformation (dimensionless)
K = consistency index (lb$_f$•s^n/ft^2)
n = flow behavior index (dimensionless)
Q = flow rate (gal/min)
r_0 = casing radius (in.)
r_i = dillpipe radius (in.)
u = axial velocity component (ft/s)
x, y, z = Cartesian coordinates (in.)
α, β, γ = coordinate transformation parameters (dimensionless)
Γ = total shear rate (s^{-1})
$\mu(\Gamma)$ = effective viscosity (lb$_f$•s/ft^2)
η, ζ = boundary-fitted coordinates (in.)
τ = shear stress (psi)
τ_0 = yield-point shear stress (psi)

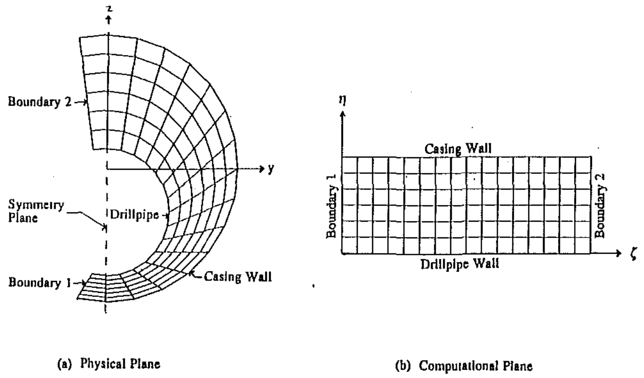

(a) Physical Plane (b) Computational Plane

Fig. 2 Mapping of physical plane to computational plane

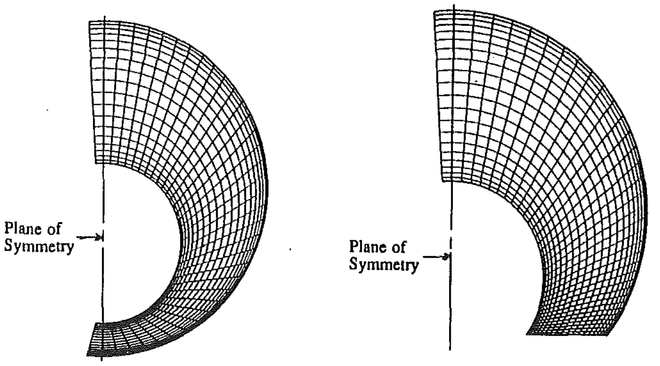

(a) Eccentric Annulus (b) Eccentric Annulus with a Bed of Cuttings

Fig. 3 Typical grid point distributions

where subscripts denote differentiation, and the metrics are given by the following identities:

$$\eta_y = -z_\zeta / \mathrm{J} \tag{9a}$$

$$\eta_z = y_\zeta / \mathrm{J} \tag{9b}$$

$$\zeta_y = -z_\eta / \mathrm{J} \tag{9c}$$

$$\zeta_z = y_\eta / \mathrm{J} \tag{9d}$$

When the above transformations are applied to Eq. (1), it takes the form:

$$\frac{\partial}{\partial \zeta}\left[\frac{\mu(\Gamma)}{\mathrm{J}}\left(\alpha \frac{\partial u}{\partial \zeta} - \gamma \frac{\partial u}{\partial \eta}\right)\right] + \frac{\partial}{\partial \eta}\left[\frac{\mu(\Gamma)}{\mathrm{J}}\left(\beta \frac{\partial u}{\partial \eta} - \gamma \frac{\partial u}{\partial \zeta}\right)\right] = \mathrm{J}\,\frac{dP}{dx} \tag{10}$$

where J is the Jacobian of the transformation and is given by:

$$\mathrm{J} = y_\zeta z_\eta - y_\eta z_\zeta \tag{11}$$

and α, β, and γ are coordinate transformation parameters given by:

$$\alpha = y_\eta^2 + z_\eta^2 \tag{12a}$$

$$\beta = y_\zeta^2 + z_\zeta^2 \tag{12b}$$

$$\gamma = y_\zeta y_\eta - z_\eta z_\zeta \tag{12c}$$

Solution Procedure

Finite-difference expressions in the computational plane are used to approximate Eq. (10), and thus a grid generation scheme is necessary to map grid points from the transformed space to the physical domain. An excellent review of grid generation techniques is given by Thompson et al. (1985). An algebraic scheme is used in this study to provide this mapping. Hyperbolic-tangent stretching functions are then used to cluster grid points in regions where the gradient of the flow variables is expected to be large. Figure 3 shows typical grids used in the computation. Notice that only half of the physical domain needs to be considered because of symmetry.

All partial derivatives are discretized using second-order central differencing at all interior points. In the case of an eccentric annulus with no blockage, second-order forward differencing is used at the boundary $\eta = 0$ (inner pipe wall), second-order backward differencing at $\eta = \eta_{\max}$ (casing wall), and reflective boundary conditions at $\zeta = 0$ and $\zeta = \zeta_{\max}$. For the case of a partially blocked eccentric annulus, second-order forward differencing is used at $\zeta = 0$, with the remaining boundaries treated in a similar manner as the previous case. Substitution of the finite-difference equivalents of the various derivatives into Eq. (10) results in a system of algebraic equations for the velocity component u which is then solved by the Gauss-Seidel method.

Equation (10) contains two unknowns: u and $\mu(\Gamma)$. However, $\mu(\Gamma)$ is a function of gradients of u as can be seen from Eqs. (4)-(6). Thus, calculations of $\mu(\Gamma)$ are lagged behind those of u by one iteration step. After each iteration step, the new values of u are used to compute Γ and then either Eq. (5) or Eq. (6) is used to update the effective viscosity $\mu(\Gamma)$. This procedure is repeated until the desired convergence of u is achieved.

The case of a Yield-Power-law fluid requires further consideration. Indeed, the occurrence of Γ in the denominator of Eq. (5) inevitably gives rise to computational difficulties if the shear rate Γ becomes vanishingly small (for instance, in plug flow region). A way around these difficulties is to impose a lower limit on the computed values of Γ. This procedure is briefly described below.

First, an arbitrary lower limit value for Γ is chosen (for example, $10^{-6}\ \mathrm{s}^{-1}$ is used in this study). Computed values of Γ are then compared to this limit and if a value of Γ is found to be smaller than this limit, it is set equal to it. Iterations are then performed until convergence of the velocity u is achieved. Typically, 50 iterations are sufficient for the cases considered in this study. The limit is then decreased and the iterative procedure is repeated. The whole process is repeated until no significant change in the velocity profile can be noticed between two consecutive values of the lower limit. The smallest value of the lower limit reached for the cases under consideration is $10^{-22}\ \mathrm{s}^{-1}$.

A computer program in Fortran 77 was written to implement the solution procedure. Either flow rate or pressure gradient can be input. If the flow rate is input, the program uses the Secant method to determine the pressure gradient.

Results and Discussion

Power-law Fluids. Convergence of the numerical solution was investigated by independently refining the grid in the radial and the circumferential directions. The procedure used to determine the rate of convergence is described by Keller (1968) and by Blottner (1975). Successive grid refinement, coupled with Richardson's extrapolation, was used to perform an "extrapolation to zero mesh width" (Keller, 1968). The truncation error with respect to grid spacing in each direction was computed by comparing the calculated value of a given quantity to the "exact" (or extrapolated) value. The quantity examined in this study is the flow rate at a fixed pressure gradient ($dP/dx = 1.78 \times 10^{-3}$ psi/in).

Figure 4 shows the result of refining the radial grid spacing for Case A, with the geometry and fluid parameters listed in Table 1. Predictions for two values of n indicate second-order accuracy. Note that the errors in the predictions are larger for $n = 0.5$ than for $n = 1.0$. This is due to the velocity gradients near solid boundaries being larger for Power-law fluids ($n <$

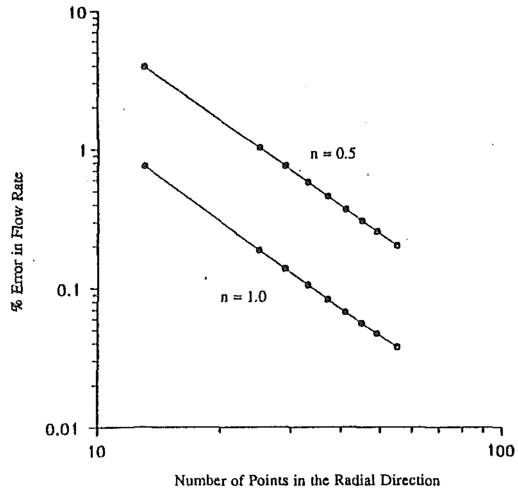

Fig. 4 Percent error in flow rate versus number of grid points in the radial direction (Case A)

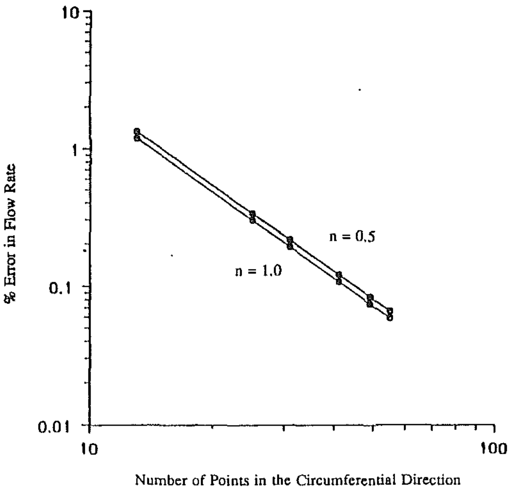

Fig. 5 Percent error in flow rate versus number of grid points in the circumferential direction (Case A)

Table 1 Geometry and fluid parameters

Case	r_o (in)	r_i (in)	e (%)	n	K ($lb_f \cdot s^n/ft^2$)	τ_0 (lb_f/ft^2)
A	2.5	1.19	62	—	0.01563	0
B	2.5	1.19	0	—	0.01563	0
C†	0.363	0.23	43	0.8	0.0337	0
D	2.5	1.19	62	—	0.01563	0
E††	0.30	0.098	65	0.91	0.10089	.141
F	5.0	2.5	—	0.7	0.00522	.5
G	2.5	1.19	62	—	0.002618	0

—Not fixed.
†With limiting viscosity $\mu(\Gamma)_{max} = 0.02526\ lb_f \cdot s/ft^2$ (1200 cp).
††With limiting viscosity $\mu(\Gamma)_{max} = 0.14929\ lb_f \cdot s/ft^2$ (7150 cp).

1.0) than for Newtonian fluids ($n = 1.0$). Figure 5 shows the results of refining the circumferential grid spacing, while holding the radial grid spacing constant. The results also indicate second-order accuracy with respect to the circumferential grid spacing. It is interesting to note that there is little difference between the errors predicted for $n = 0.5$ and $n = 1.0$. This indicates that the gradients in this direction are basically of the same magnitude for the Newtonian and non-Newtonian fluids considered in this study. A study of Figs. 4 and 5 suggests that for non-Newtonian fluids, the numerical solution is more sensitive to the grid spacing in the radial direction than it is to the grid spacing in the circumferential direction. Results such as those presented in Figs. 4 and 5 may aid the program users in deciding how many grid points should be used in each direction to achieve the desired accuracy.

The accuracy of the numerical solution was also verified by applying the numerical model to several cases where analytical solutions, numerical solutions, and experimental data are available. The analytical solution cases considered are for the laminar flow of Newtonian fluids in concentric and eccentric annuli derived by Piercy et al. (1933), and Power-law fluid in concentric annuli obtained by Fredrickson and Bird (1958). The predicted flow rates for given pressure gradients were compared with those obtained from analytical expressions. Comparison showed excellent agreement between the model predictions and the analytical solutions. For example, Fig. 6 shows the variation of the flow rate with the pressure gradient for a Power-law fluid in a concentric annulus as predicted by the present model and the analytical expressions. The geometry and fluid parameters for this case are listed in Table 1 (Case B).

The model predictions in the case of a Power-law fluid in an eccentric annulus (Table 1, Case C) were also compared to experimental data published by Mitsuishi and Ayoagi (1973).

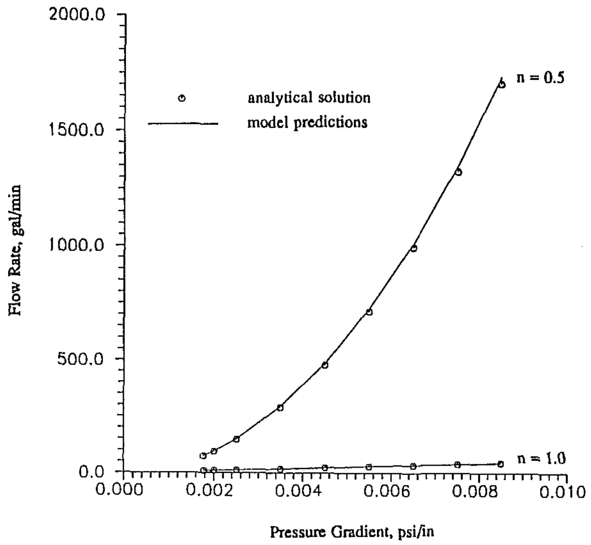

Fig. 6 Flow rate versus pressure gradient in concentric annulus (Case B)

The rheological behavior of the fluids (3.92 wt. percent HEC polymer solution) used by these authors, is a best fit by the Sutterby model (another 3-parameter fluid model, see Haciislamoglu, 1989) which approaches a constant limiting viscosity at very low shear rates. The equivalent Power-law model parameters were determined by Haciislamoglu (1989) and are used in the present work. The calculated effective viscosity was set equal to the limiting viscosity whenever its value became larger than the limit mentioned above. As shown in Fig. 7, there is a very good agreement between the experimental data and the numerical solution. It is also worth noticing that for flow rates below approximately 0.01 gal/min, the limiting viscosity causes a deviation from Power-law model behavior. (For Power-law fluids, the flow rate versus pressure gradient curve should be a straight line on a log-log plot.)

The model was also applied to Power-law fluids with n values varying from 0.5 to 1.0, and a fixed flow rate ($Q = 258$ gal/min), in a 62 percent eccentric annulus (Case D). Figures 8(*a*) and 8(*b*) show the predicted three-dimensional velocity profiles for $n = 1.0$ and $n = 0.6$, respectively. It is worth noticing that the velocity profile shown in Fig. 8(*b*) is more uniform than the one shown in Fig. 8(*a*). This is due to the slope of the velocity profile being steeper for non-Newtonian fluids than

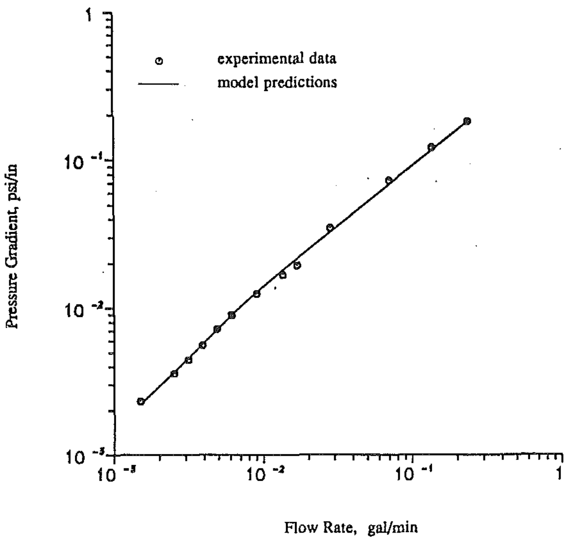

Fig. 7 Measured and computed pressure gradient versus flow rate for power-law fluid (Case C)

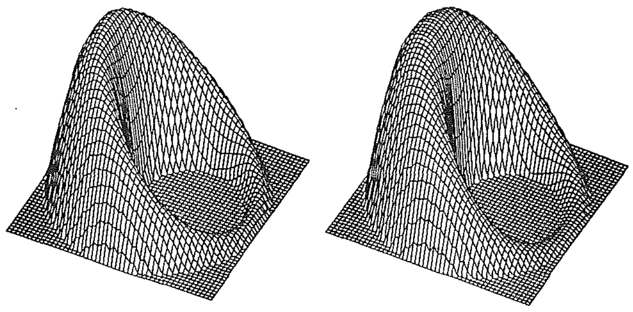
(a) n = 1.0

(b) n = 0.6

Fig. 8 Velocity profile in a 62 percent eccentric annulus, Q = 258 gal/min (Case D)

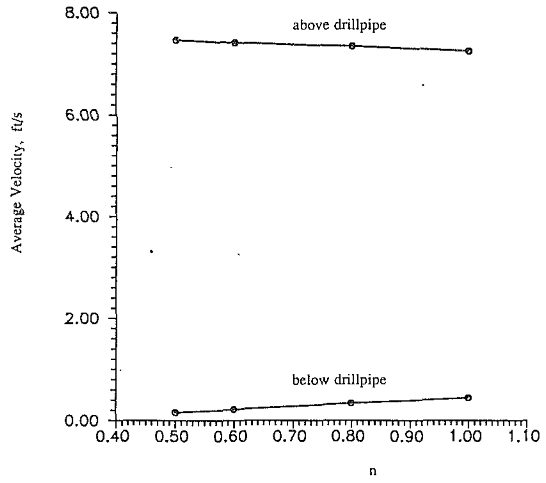

Fig. 9 Average velocity below and above the drillpipe for several values of n, Q = 213 gal/min (Case G)

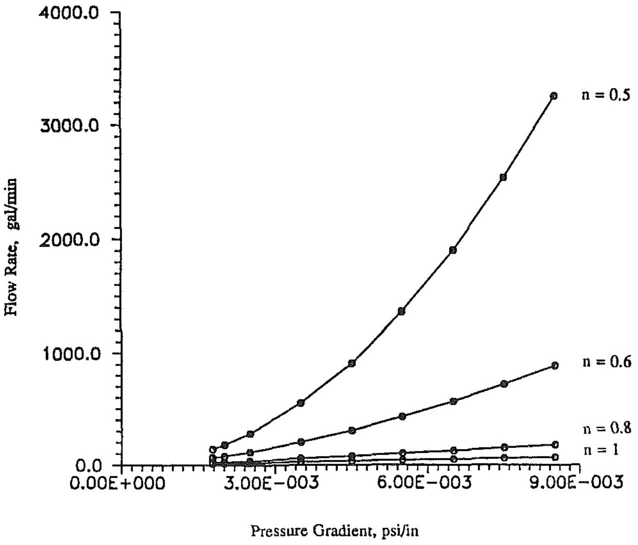

Fig. 10 Flow rate versus pressure gradient for several values of n, eccentric annulus (Case D)

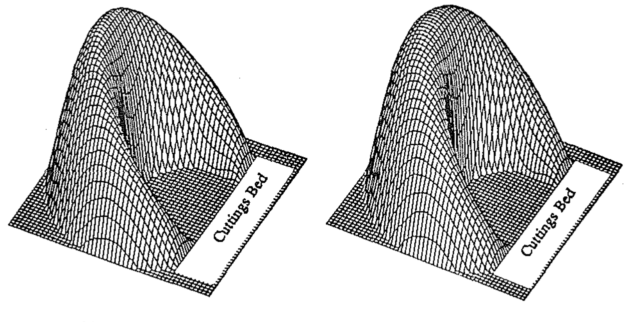

(a) n = 1.0, H = 1.0 in

(b) n = 0.6, H = 1.0 in

Fig. 11 3-D velocity profile in a 62 percent eccentric annulus, Q = 258 gal/min (Case D)

it is for Newtonian fluids. Furthermore, these figures show the difference in the velocity profiles in the widening gap (above the drillpipe) and in the narrowing gap (below the drillpipe). Figure 9 shows the computed average velocity above and below the drillpipe (at the plane of symmetry) for several values of n (Table 1, Case G). Note that the average velocity in the narrowing gap is much smaller than that in the widening gap. For instance, for $n = 1.0$, the average fluid velocity above the drillpipe is 7.22 ft/s, while the average fluid velocity below the drillpipe is only 0.43 ft/s. A study of Fig. 9 reveals that a slight increase (about 2 percent) in the average fluid velocity above the drillpipe occurs as n decreases from 1.0 to 0.5. However, a relatively significant decrease (about 60 percent) in the average fluid velocity under the drillpipe results when n decreases from 1.0 to 0.5. This is in contradiction to the common belief, based on pipe flow, that fluids having a low n-value provide a larger flow velocity under the drillpipe than Newtonian fluids do. This result has important implications in drilled cuttings transport.

The effect of the flow behavior index n on the relationship between flow rate and pressure gradient is illustrated by Fig. 10. It can be seen that for a given pressure gradient the flow rate increases significantly as n decreases. Furthermore, the relationship between pressure gradient and flow rate deviates from a straight line as n decreases. (It is assumed that the flow remains laminar for all of the flow rates shown.)

The numerical model was also applied to the case of a partially blocked annulus. This situation occurs when drilled cuttings accumulate in the narrowing gap of the annulus due to low fluid velocity in this region. For this case, no experimental data is available at the present time. However, the general behavior of the model predictions is in agreement with cases with no blockage. For instance, Figs. 11(a) and 11(b) show three-dimensional velocity profiles for the case of a partially blocked annulus (Case D, with $H = 1.0$ in, see Fig. 1) which is somewhat similar to Figs. 8(a) and 8(b) except for the lower

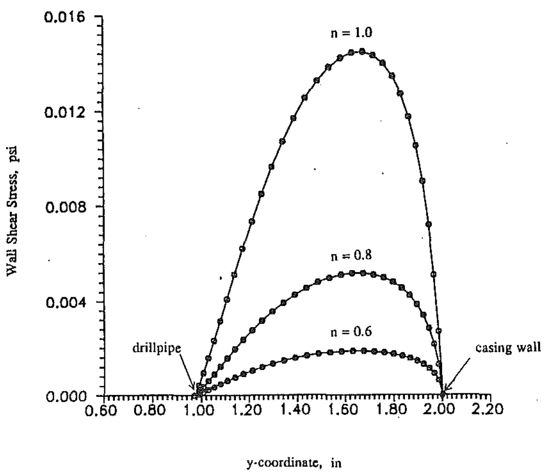

Fig. 12 Shear stress distribution on cuttings bed surface, H = 1.5 in., Q = 258 gal/min, eccentric annulus (Case D)

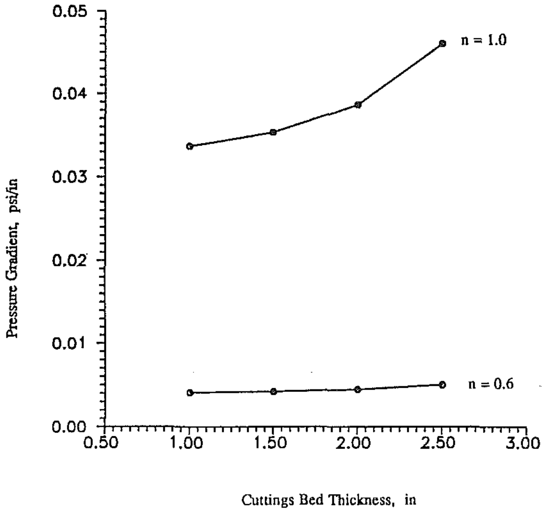

Fig. 13 Pressure gradient versus cuttings bed thickness, Q = 258 gal/min, eccentric annulus (Case D)

portion of the annular region. For this case, as in the case with no blockage, the velocity profile becomes flatter as n varies from 1.0 to 0.6 for a constant value of the flow rate (Q = 258 gal/min). It is worth mentioning that none of the models published in the literature is capable of handling this complex flow geometry. This makes the present model more attractive.

Figure 12 shows the variation of the wall shear stress on the cuttings bed surface, treated as a no-slip boundary, for several values of n, while the flow rate is held constant (Q = 258 gal/min). The distribution of the axial shear stress on the cutting bed surface may be useful for cuttings transport modeling. The figure also shows the significant influence of the flow behavior index on wall shear stress. This is consistent with the results of Fig. 10 which indicates that for a fixed flow rate, the pressure gradient decreases significantly as n decreases.

The predicted pressure gradient, for several values of the cuttings bed thickness H, is shown in Fig. 13 for different values of n and a constant flow rate (Q = 258 gal/min). Obviously, the pressure gradient increases as the flow area decreases (H increases).

Yield-Power-Law Model. To demonstrate the applicability of the numerical model to other non-Newtonian fluids, the numerical code was also applied to the case of a Yield-Power-law fluid through substitution of Eq. (4) for the effective viscosity into Eq. (10), which was then solved following the same procedure as for the Power-law case.

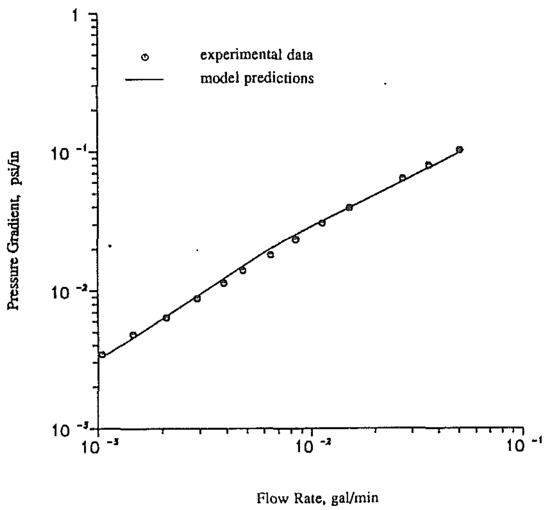

Fig. 14 Measured and computed pressure gradient versus flow rate for yield-power-law fluid (Case E)

Table 2 Maximum velocity above and below the drillpipe (at plane of symmetry) for Yield-Power-law model

Eccentricity (%)	0	25	50	75
Max. vel. above drillpipe (ft/s):				
Present method	1.32	1.91	2.06	1.93
Haciislamoglu (1989)	1.35	1.91	2.12	1.99
Max. vel. below drillpipe (ft/s):				
Present method	1.32	0.55	0.04	0
Haciislamoglu (1989)	1.35	0.56	0.04	0

To investigate the accuracy of the numerical model, the model predictions were compared to experimental data published by Mitsuishi and Ayoagi (1973). The fluid considered in this case is a 3.44 wt. percent CMC solution whose rheological behavior is again a best fit by the Sutterby model. The equivalent Yield-Power-law parameters determined by Haciislamoglu (1989) are used in this study and are listed in Table 1 (Case E). Figure 14 indicates excellent agreement between numerical results and experimental data. As in the case of the Power-law fluid discussed above, for flow rates below about 0.007 gal/min, the slope of the pressure gradient versus flow rate curve deviates from the usual Yield-Power-law behavior, due to the imposed limiting viscosity in the Sutterby model.

Predictions of the present model were also compared to corresponding results obtained by Haciislamoglu (1989) for the geometry and fluid parameters listed in Table 1 (Case F) and a flow rate of 200 gal/min. The maximum velocities above and below the drillpipe calculated by each model for several eccentricities are listed in Table 2. Strong agreement can be observed. However, it should be mentioned that while the present model can be applied to flow domains of arbitrary cross-section, the model used by Haciislamoglu (1989) is restricted to simple eccentric annuli. This reduces greatly the scope of its applicability since most of the problems of practical importance involve complex geometries.

Predicted velocity profiles for the case (Case F) considered above are presented in Fig. 15. It should be mentioned that the maximum velocities for the four values of the eccentricity are not equal. It can be noticed that for a concentric annulus (e = 0) the velocity profile is uniform throughout the annulus, with a flat portion that indicates plug flow due to the yield-point shear stress. As the eccentricity increases, the flow diverges to the widening gap of the annulus and, at e = 0.75,

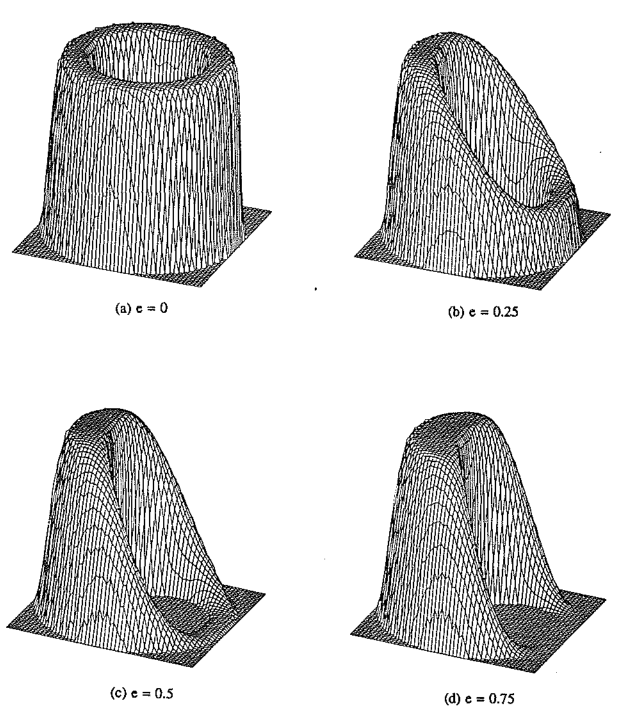
(a) $e = 0$

(b) $e = 0.25$

(c) $e = 0.5$

(d) $e = 0.75$

Fig. 15 3-D velocity profile for yield-power law fluid, Q = 200 gal/min, variable eccentricity (Case F)

no flow exists in the narrowing part of the annulus. These results can help the drilling engineer in selecting a fluid having the desired rheological behavior to achieve optimum cleaning of the borehole. For instance, the velocity profile shown in Fig. 15(d) suggests that the particular fluid which produced this profile is not recommended in highly eccentric annuli since no flow would exist in the narrowing part of the annulus.

Conclusions

A numerical model based on general, nonorthogonal, boundary-fitted, curvilinear coordinates has been developed to simulate the laminar flow of Newtonian and non-Newtonian fluids in conduits of arbitrary cross-section. The model was applied to Power-law and Yield-Power law fluids in eccentric annuli, and the predictions were shown to be in excellent agreement with published numerical and experimental results. Analysis of the flow behavior of several Power-law fluids indicates that low values of the flow behavior index n tend to produce low velocity values in the narrow part of eccentric annuli. It is also observed that eccentricity has a dramatic effect on the velocity profile of Yield-Power-law fluids. Indeed, high eccentricities can create a zone of no-flow in the narrow gap of the annulus. Other rheological models can easily be incorporated into the model through substitution of the appropriate expression for the effective viscosity into the governing equation of the flow. To demonstrate the capability of the present model to handle arbitrary geometries, the case of a Power-law fluid in a partially blocked annulus was considered. No published numerical or experimental data is available for comparison at the present time. However, the general behavior of the predictions is in agreement with cases with no blockage. This suggests that the model can reliably be used to predict the flow behavior of drilling muds or cement slurries in irregular annular geometries.

Acknowledgments

This work was supported by the Tulsa University Drilling Research Projects (TUDRP) and Oklahoma Center for the Advancement of Science and Technology (OCAST).

References

Anderson, D. A., Tannehill, J. C., and Pletcher, R. H., 1985, *Computational Fluid Mechanics and Heat Transfer*, Elsevier Science Publishing, New York.

Bird, R., Stewart, W. E., and Lightfoot, 1960, *Transport Phenomena*, John Wiley, pp. 102–103.

Blottner, F. G., 1975, "Investigation of Some Finite-Difference Techniques for Solving the Boundary Layer Equations," *Computer Methods in Applied Mechanics and Engineering*, Vol. 6, pp. 1–30.

Fredrickson, A. G., and Bird, R. B., 1958, "Non-Newtonian Flow in Annuli," *Ind. & Eng. Chem.*, Vol. 50, No. 3, pp. 347–352.

Guckes, T. L., 1975, "Laminar Flow of Non-Newtonian Fluids in an Eccentric Annulus," *Trans.* ASME, Vol. 97, Part 1, pp. 498–506.

Haciislamoglu, M., and Langlinais, J., 1990, "Non-Newtonian Fluid Flow in Eccentric Annuli," ASME *Journal of Energy Resources Technology*, Vol. 112, pp. 163–169.

Haciislamoglu, M., 1989, "Non-Newtonian Fluid Flow in Eccentric Annuli and its Application to Petroleum Engineering Problems," Ph.D. Dissertation, Louisiana State University, Baton Rouge, La.

Iyoho, A. W., and Azar, J. J., 1981, "An Accurate Slot-Flow Model for Non-Newtonian Fluid Flow Through Eccentric Annuli," *Society of Petroleum Engineers Journal*, Oct., Vol. 21, pp. 565–572.

Keller, H. B., 1968, *Numerical Methods for Two-Point Boundary Value Problems*, Blaisdell, Waltham, MA, pp. 78–81, 168–171.

Lamb, H., 1945, *Hydrodynamics*, sixth edition, Dover Publications, New York, pp. 585–587.

Mitsuishi, N., and Aoyagi, Y., 1973, "Non-Newtonian Fluid Flow in an Eccentric Annulus," *Journal of Chemical Engineering of Japan*, Vol. 6, pp. 402–408.

Piercy, N. A. V., Hooper, M. S., and Winny, H. F., 1933, "Viscous Flow Through Pipes with Cores," *Philosophical Magazine*, Vol. 15, No. 7, pp. 647–676.

Redberger, P. J., and Charles, M. E., 1962, "Axial Laminar Flow in a Circular Pipe Containing a Fixed Core," *Cdn. J. Chem. Eng.*, Vol. 40, pp. 148–151.

Tao, L. N., and Donovan, W. F., 1955, "Through-Flow in Concentric and Eccentric Annuli of Fine Clearance With and Without Relative Motion of the Boundaries," *Trans.* ASME, Vol. 77, pp. 1291–1301.

Thompson, J. F., Warsi, Z. U. A., and Mastin, C. W., 1985, *Numerical Grid Generation*, Elsevier Science Publishing, New York.

White, F. M., 1974, *Viscous Fluid Flow*, McGraw Hill, pp. 126–127.

Zamora, M., and Lord, D. L., 1974, "Practical Analysis of Drilling Mud Flow in Pipes and Annuli," SPE Paper 4976, Presented at the 1974 Annual Meeting of the Society of Petroleum Engineers of AIME, Houston, Texas, Oct. 6–9, 1974.

A Pressure-Velocity Solution Strategy for Compressible Flow and Its Application to Shock/Boundary-Layer Interaction Using Second-Moment Turbulence Closure

F.-S. Lien

M. A. Leschziner

University of Manchester,
Institute of Science and Technology,
Manchester, M60 1QD UK

A nonorthogonal, collocated finite-volume scheme, based on a pressure-correction strategy and originally devised for general-geometry incompressible turbulent recirculating flow, has been extended to compressible transonic conditions. The key elements of the extension are a solution for flux variables and the introduction of streamwise-directed density-retardation which is controlled by Mach-number-dependent monitor functions, and which is applied to all transported flow properties. Advective fluxes are approximated using the quadratic scheme QUICK or the second-order TVD scheme MUSCL, the latter applied to all transport equations, including those for turbulence properties. The procedure incorporates a number of turbulence models including a new low-Re $k-\epsilon$ eddy-viscosity variant and a Reynolds-stress-transport closure. The predictive capabilities of the algorithm are illustrated by reference to a number of inviscid and turbulent transonic applications, among them a normal shock in a Laval nozzle, combined oblique-shock reflection and shock-shock interaction over a bump in a channel and shock-induced boundary-layer separation over channel bumps. The last-named application was computed both with eddy-viscosity models and Reynolds-stress closure, leading to the conclusion that the latter yields a much greater sensitivity of the boundary layer to the shock and, arising therefrom, a more pronounced λ-shock structure, earlier separation and more extensive recirculation. On the other hand, the stress closure is found to return an insufficient rate of wake recovery following reattachment.

1 Introduction

The computational modeling of viscous transonic and supersonic flows is usually pursued with time-marching schemes that solve the set of coupled conservation laws governing the flux of mass, momentum and energy. This approach offers a number of advantages, among them the opportunity to implement accurate upwind approximations that account for the characteristics along which acoustic waves are propagated and which, at least nearly, satisfy the TVD constraint. A disadvantage of the method is, however, that it becomes increasingly "stiff" as the Mach number declines—a condition which manifests itself by a progressive deterioration in the rate of iterative convergence. In practice, difficulties begin to arise when a significant proportion of the flow being computed has a Mach number of 0.3 and below. Although convergence can be enhanced by use of artificial compressibility or preconditioning which suppresses the propagation of acoustic waves, the need for these artifacts plainly suggests that a time-marching solution of the conservation laws in their original form is ill-suited to viscous flows which contain extensive low-speed portions such as thick boundary layers and large separation bubbles.

Most flows encountered in mechanical and civil engineering are essentially incompressible. For these, the continuity equation in its basic form clearly does not offer a direct route to the pressure field, unless a coupled solution method is adopted in which the continuity and momentum equations are solved together. A coupled approach is expensive, however, and the usual practice—at least within the finite volume/finite difference framework—is to solve the flow-governing equations in a segregated fashion within an iterative sequence. To this end, the continuity equation must first be recast into a form in which the pressure becomes the principal variable—the subject of the equation. This can readily be achieved by combining

---

Contributed by the Fluids Engineering Division for publication in the JOURNAL OF FLUIDS ENGINEERING. Manuscript received by the Fluids Engineering Division August 20, 1992; revised manuscript received August 16, 1993. Associate Technical Editor: R. Arndt.

the continuity equation with those governing the momentum components. A number of related pressure-velocity algorithms, based on the above concept and identified by acronyms such as SIMPLE, SIMPLER (Patankar, 1980), SIMPLEC (Van Doormaal and Raithby, 1984) and PISO (Issa, 1986), have been formulated over the past two decades, and have been widely applied to numerous complex two- and three-dimensional viscous and turbulent flows involving, *inter alia*, separation, strong swirl, heat and mass transfer, reaction and multi-phase transport.

Because pressure-based algorithms involve an elliptic equation for the pressure (or its correction), they are not suitable, in their generic form, for supersonic or transonic flows which are described by hyperbolic or mixed systems; any attempt to apply incompressible-flow variants, without modification, to transonic flow inevitably leads to instability. Several attempts have been made to adapt pressure-based schemes to compressible conditions, some contemporaneous with the present contribution (Van Doormaal et al., 1987; Karki and Patankar, 1989; Kobayashi and Pereira, 1992; and Shyy et al., 1992). All are based, essentially on a flux-linearization strategy originally proposed by Issa and Lockwood (1977). The success of the above variants has been mixed, one recurring problem being excessive shock smearing. Essentially, the challenge is to find a mechanism for introducing just enough artificial dissipation, be it implicit or explicit, to counteract the destabilizing effect arising from the elliptic nature of the pressure equation, without undue erosion of the shock or of property variations in supersonic zones. A recent "retarded-pressure" scheme by McGuirk and Page (1989), based on concepts introduced by Wornom (1986), has shown promising shock-capturing properties in one-dimensional flow, and this has been used by Page (1990) to compute under-expanded, turbulent impinging jets. That work has given strong motivation for the efforts documented in the present paper, a major objective being to arrive at a modeling framework which is uniformly effective across the entire Mach-number range encountered in turbulent transonic flows.

The writers' experience is rooted principally in incompressible-flow modeling. In this area, the overwhelming majority of flows are turbulent, and turbulence transport contributes decisively to the balance of momentum and other flow properties. Within any Reynolds-averaged modeling framework, careful attention must therefore be paid to a realistic modeling of turbulence effects. Separated flows, in which turbulence is far from a state of equilibrium, are particularly sensitive to turbulence modeling. Here, the structure of the separated and curved shear layer bordering the recirculation zone dictates the size of the recirculation bubble, and therefore strongly influences gross flow feature such as pressure recovery, integral boundary-layer parameters, skin friction and wall heat transfer. It is now well established that a satisfactory prediction of complex turbulent flows—particularly such featuring separation, swirl and rotation—requires the use of Reynolds-stress models which account for both turbulence transport and anisotropy. Variants of Reynolds-stress closure have been used by the authors and their colleagues for several years to compute, almost invariably with pressure-based algorithms, many two- and three-dimensional attached and recirculating flows (Leschziner, 1990; Launder, 1989; Jones and Manners, 1988;

Nomenclature

a_0 = stagnation speed of sound
$\tilde{C}_{\epsilon 1}$, $\tilde{C}_{\epsilon 2}$ = coefficients in ϵ equation
$\tilde{C}_\mu$ = coefficient in Boussinesq-viscosity relation
D_{ij} = diffusion of stress $\overline{u_i'u_j'}$
DU, DV = area-related coefficients in discretized momentum equations
H = channel height
H_0 = stagnation enthalpy
J = Jacobian of transformation matrix
k = turbulence energy
l_μ, l_ϵ = length-scales in one-equation $k-l$ models
l_n, l_n^* = dimensional and dimensionless normal distance from wall
L = nozzle length
M = Mach number
M_w = isentropic wall Mach number
M ℄ = Mach number along centerline
M_{ref} = reference Mach number
M_ξ, M_η = Mach-number components in ξ- and η-directions, respectively
p = static pressure
p_0 = stagnation pressure
p' = pressure fluctuation or correction
P_{ij} = production of stress $\overline{u_i'u_j'}$
P_k = production of turbulence energy k
Re = Reynolds number
R_T = local turbulent Reynolds number, $k^2/\nu\epsilon$
R_P = mass residual in cell P
sgn = signal function
t = time
u, v = mean-velocity components in the x- and y-directions, respectively
U, V = contravariant velocity component in the ξ- and η-directions, respectively
$\overline{u_i'u_j'}$ = Reynolds-stress tensor ($\equiv \overline{u'^2}$, $\overline{v'^2}$, $\overline{u'v'}$)
x_j, $j=1, 2$ = Cartesian coordinates
y^+ = yu_τ/ν
β = angle between streamline and x-axis
γ = ratio of specific heats
δ = boundary-layer displacement thickness
δ_{ij} = Kronecker delta
δt = time step
Δx, Δs = incremental distances in x and streamwise directions, respectively
ϵ = isotropic dissipation rate of k
ϵ_{ij} = dissipation rate of $\overline{u_i'u_j'}$
κ = free-parameter in the monitor function $\overline{\mu}$
μ = dynamic viscosity
$\overline{\mu}$ = monitor function defined in Eqs. (17) and (18)
μ_T = turbulent viscosity
ξ, η = curvilinear coordinates
ρ = density
$\tilde{\rho}$ = retarded density
ρ_ξ, ρ_η = retarded-density components in ξ- and η-directions, respectively
ϕ = any conserved variable
Φ_{ij} = pressure-strain correlation

Superscripts

$'$ = numerical perturbation or turbulent fluctuation
$^{\xi,\eta}$ = pertaining to ξ and η directions, respectively
$*$ = previous iterate

Subscripts

P = center of cell
w, e, s, n = western, eastern, southern, and northern faces of cell, respectively
W, E, S, N = western, eastern, southern, and northern nodes neighboring node P
ξ, η = pertaining to ξ and η directions, respectively

Lien and Leschziner, 1992; and Ince and Leschziner, (1990), and considerable benefits in respect of predictive realism have often been derived from this level of closure.

It has been the second major objectives of the present work to identify the predictive strengths and weaknesses of Reynolds-stress closure in transonic wall-bounded flows, with particular reference to airfoil performance. Although major parts of transonic flow over airfoils are practically inviscid, the sheared regions adjacent to the airfoil's surface can play an important role in determining the airfoil's aerodynamic performance due to the rapid thickening of the boundary layers induced by the shock. This is particularly so when the shock is sufficiently strong to provoke boundary-layer separation, in which case the details of the separated (post-)interaction region largely determine the position of the shock and materially affect the lift and drag coefficients. The simultaneous presence of shear, severe adverse pressure gradient and recirculation-related curvature close to a solid boundary lead to a complex, highly anisotropic turbulence structure; it is this which justifies the application of Reynolds-stress closure in transonic conditions.

Previous studies investigating Reynolds-stress closure for predicting shock/boundary-layer interaction are rare. Efforts by Ha Minh and Vandromme (1986) and Leschziner et al. (1993)—the latter using an algebraic Reynolds-stress model with a cell-vertex scheme, both demonstrate encouraging performance in shock-induced separation over a bump examined experimentally by Delery (1983). Further as yet unpublished results by Davidson (1992), also obtained with an algebraic variant, essentially confirm Dimitriadis and Leschziner's finding that the Reynolds-stress model predicts the boundary layer to be considerably more sensitive to the shock than suggested by k-ϵ eddy-viscosity models, with separation occurring earlier and recirculation being more extensive, in broad accord with experimental data.

In what follows, the adaptation of a finite-volume pressure-velocity scheme, originally formulated for incompressible flow, to compressible conditions is considered first. The turbulence models being investigated are stated next. Initial tests for transonic and supersonic inviscid flows are then introduced, and this is followed by an application of the procedure to shock-induced separation over bumps. In the context of comparing predictions with experimental data, one issue receiving particular attention is the influence of approximating convection with schemes of different order of accuracy.

2. Computational Approach

2.1 Numerical Framework. The present solution algorithm sprang from a cell-centered, nonorthogonal, fully collocated finite-volume method developed for incompressible 3-D flow (Lien, 1992). Attention is here focused on the route taken in adapting this procedure to transonic conditions. Before embarking on this topic, however, it is appropriate to summarize the essential elements of the incompressible methodology, which all carry over to the compressible environment.

The algorithm employs a fully collocated storage arrangement for all transported properties, including the Reynolds-stress components, as shown in Fig. 1. Discretization starts from an integration of the conservation laws over the volume and application of the Gauss Divergence Theorem. Advective volume-face fluxes are approximated using either the first-order upwind scheme (UDS), Leonard's (1979) quadratic scheme QUICK or van Leer's (1979) MUSCL scheme. At all speeds, mass continuity is enforced by solving a pressure-correction equation which, as part of the iterative sequence, steers the pressure towards a state at which all mass residuals in the cells are negligibly small. In conjunction with a fully collocated approach, this method is known to provoke chequerboard oscillations, reflecting velocity-pressure decoupling. To avoid this, the widely used method of Rhie and Chow (1983) is used to interpolate for the cell-face velocities from nodal values. The interpolation essentially introduces fourth-order pressure diffusion. Within an iterative relaxation strategy, the original Rhie and Chow scheme is known to return solutions which depend (albeit weakly) on the values of the relaxation parameters used in the various conservation equations (Majumdar, 1988). This sensitivity has been carefully examined (Lien and Leschziner, 1993), and the scheme used herein is a modified variant, free from this ambiguity which arises from a dependence not only on relaxation factors but also on the Courant number.

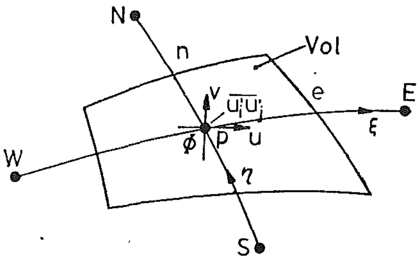

Fig. 1 Finite volume and variable-storage arrangement

Particular difficulties arise in relation to the Reynolds stresses. Their collocated storage results in stresses being decoupled from associated "driving" strains. This must be counteracted by elaborate interpolation practices not dissimilar, in principle, to those applied to pressure and velocity. These practices are given in detail in Lien (1992).

The starting point of the description of the compressible variant is the mass-conservation equation, integrated over the finite volume in Fig. 1 and over the time step δt:

$$\left[\frac{(\rho^{n+1}-\rho^{n})J}{\delta t}\right]+(\rho U_e-\rho U_w)+(\rho V_n-\rho V_s)=0 \qquad (1)$$

where J is the Jacobian of the transformation and U, V are the contravariant velocities.

$$U=u\,\frac{\partial y}{\partial \eta}-v\,\frac{\partial x}{\partial \eta} \qquad V=v\,\frac{\partial x}{\partial \xi}-u\,\frac{\partial y}{\partial \xi} \qquad (2)$$

Within the framework of a pressure-velocity scheme, the task is to reformulate the above equation in terms of pressure or a pressure correction. Such an equation, when solved in conjunction with the discretised momentum equations for the fluxes $(\rho \mathrm{U})^{n+1}$ and $(\rho V)^{n+1}$, should allow the pressure field to be determined at the advanced time level $(n+1)$.

In the present algorithm, the momentum equations are initially solved with pressures at the previous time level to yield approximate fluxes $(\rho U)^{n+1}$ and $(\rho V)^{n+1}$. These allow, together with the equation of state, the mass residual in the finite volume at level $(n+1)$ to be computed from the continuity equation. To eliminate this residual, the fluxes and density must be corrected, and this requires the introduction of pressure perturbations. Momentum-flux corrections may be related to pressure perturbations via truncated (i.e., approximated) variants of the discretised momentum equations. With attention focused, for example, on the eastern and northern faces of the cell in Fig. 1, the requisite truncated relations arise as:

$$(\rho U)_e' = \overline{DU^{\xi}}_e(p_P'-p_E')\,\frac{\partial y}{\partial \eta}-\overline{DV^{\xi}}_e(p_P'-p_E')\,\frac{\partial x}{\partial \eta} \qquad (3)$$

$$(\rho V)_n' = \overline{DV^{\eta}}_n(p_P'-p_N')\,\frac{\partial x}{\partial \xi}-\overline{DU^{\eta}}_n(p_P'-p_N')\,\frac{\partial y}{\partial \xi} \qquad (4)$$

where DU_e^{ξ} and DV_e^{ξ} are related to projections of the eastern face of the finite volume in Fig.1 on the vertical (y) and horizontal (x) directions, respectively. Density perturbations and pressure perturbations may be linked via a linearized variant of the total enthalpy-pressure relation,

$$\rho' = \frac{\gamma p'}{(\gamma-1)\left(H_0 - \frac{u^2+v^2}{2}\right)} \tag{5}$$

To satisfy mass conservation within any step, the contravariant face velocities must be corrected as follows,

$$\rho U \leftarrow \rho U(+\rho U)' \quad \rho V \leftarrow \rho V + (\rho V)' \tag{6}$$

Combining Eqs. (1)-(6) yields the pressure-correction equation,

$$A p_P' = \sum_{m=\mathrm{E,\,W,\,N,\,S}} A_m p_m' + R_P \tag{7}$$

where R_P is the mass-residual in the finite volume. In essence then, the above equation is solved in conjunction with those for momentum fluxes within an overall iterative sequence. It is appropriate to stress here that Eq. (7) is formally identical to that used for incompressible conditions; this is in contrast with the approach of Karki and Patankar (1989), for example, in which the pressure-correction equation features explicit density-fluctuation fragments as a consequence of the use of primitive rather than flux variables in the momentum equations.

The above sequence is appropriate to subsonic flow in which the conservation equations are elliptic. In supersonic and transonic conditions, the hyperbolic character of the conservation laws must be accounted for in order to retain iterative stability and capture shocks. To this end, a proposal by Hafez et al. (1979) has been adapted. This proposal—applied by Hafez et al. to the solution of the full potential equation—is based on the definition of the retarded density, $\tilde{\rho}$. In one-dimensional conditions, $\tilde{\rho}$ is:

$$\tilde{\rho} \equiv \rho - \overline{\mu}\, \frac{\partial \rho}{\partial x}\, \Delta x \tag{8}$$

in which $\overline{\mu}$ is a "weighting factor," to be defined later, controlling the degree of retardation. With relation (8), an upwind-biased gradient of the convective flux of any intensive property ϕ may be expressed, implicitly, as follows:

$$\frac{\partial(\rho u \phi/\tilde{\rho})}{\partial x} = \frac{\partial(u\phi)}{\partial x} + \frac{\partial\left[\underline{\overline{\mu}\left(\frac{u\phi}{\rho}\right)\frac{\partial \rho}{\partial x}}\right]}{\partial x} + \mathrm{HOT} \tag{9}$$

where the RHS is an expanded (i.e., explicit) form of the LHS with HOT denoting higher-order terms. The underlined term in Eq. (9) represents a dissipative mechanism equivalent to upwind-biasing.

In the present scheme, upwind-biasing is applied to all flux variables. In particular, the contravariant convecting velocities multiplying flux variables are modified via:

$$U \leftarrow \frac{\rho U}{\tilde{\rho}}, \quad V \leftarrow \frac{\rho V}{\tilde{\rho}}, \tag{10}$$

This replacement, it must be stressed, is the only juncture at which the retarded density is introduced. As demonstrated by Eq. (9), its consequence is the introduction of a dissipative mechanism which stabilizes the incompressible-flow algorithm in transonic and supersonic conditions.

To account for directional influences in the upwind-biasing process in two-dimensional conditions, the retarded density is evaluated from:

$$\tilde{\rho} = \rho - \overline{\mu}\, \frac{\partial \rho}{\partial s} \Delta s = \rho - \overline{\mu}\, [\cos(\beta)\, \frac{\partial \rho}{\partial x}\, \Delta x + \sin(\beta)\, \frac{\partial \rho}{\partial y}\, \Delta y] \tag{11}$$

with Fig. 2(*a*) giving a graphical interpretation of the above relation.

In the actual algorithm, the retarded density is determined, as indicated in Fig. 2(*b*), from:

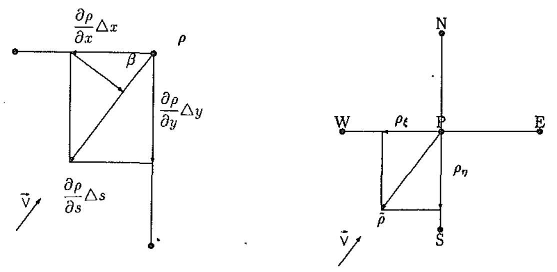

(a) (b)

Fig. 2 Schematic of density retardation in two-dimensional flow

$$\tilde{\rho} = \rho_\xi + \rho_\eta - \rho_P \tag{12}$$

where ρ_ξ and ρ_η are retarded densities in the general co-ordinate directions and are evaluated from:

$$\rho_\xi = \mathbf{M}_\xi^+ \; [(1-\overline{\mu}_w^\xi)\rho_P + \overline{\mu}\,_w^\xi \rho_W] + M_\xi^- \; [(1-\overline{\mu}\,_e^\xi)\rho_P + \overline{\mu}\,_e^\xi \rho_E] \tag{13}$$

$$\rho_\eta = \mathbf{M}_\eta^+ \; [(1-\overline{\mu}\,_s^\eta)\rho_P + \overline{\mu}\,_s^\eta \rho_S] + M_\eta^- \; [(1-\overline{\mu}\,_n^\eta)\rho_P + \overline{\mu}\,_n^\eta \rho_N] \tag{14}$$

with the Mach numbers given by:

$$\mathbf{M}_\xi = \frac{U}{a\sqrt{\left(\frac{\partial x}{\partial \eta}\right)^2 + \left(\frac{\partial y}{\partial \eta}\right)^2}} \quad \mathbf{M}_\eta = \frac{V}{a\sqrt{\left(\frac{\partial x}{\partial \xi}\right)^2 + \left(\frac{\partial y}{\partial \xi}\right)^2}} \tag{15}$$

and the superscripts +/− identify velocity directions such that,

$$\mathbf{M}_\xi^\pm = \frac{1 \pm \mathrm{sgn}(\mathbf{M}_\xi)}{2} \quad \mathbf{M}_\eta^\pm = \frac{1 \pm \mathrm{sgn}(\mathbf{M}_\eta)}{2} \tag{16}$$

The monitor functions $\overline{\mu}$ in the form given below are used to control the degree of biasing and follow from an examination of the velocity-potential equation for supersonic flow (Lien, 1992):

$$\overline{\mu}^\xi = \max\left\{0,\ \kappa\left[1 - \left(\frac{\mathbf{M}_{\mathrm{ref}}}{\mathbf{M}_\xi}\right)^2\right]\right\} \tag{17}$$

$$\overline{\mu}^\eta = \max\left\{0,\ \kappa\left[1 - \left(\frac{\mathbf{M}_{\mathrm{ref}}}{\mathbf{M}_\eta}\right)^2\right]\right\} \tag{18}$$

where the coefficient κ has been introduced to account for the physical differences arising from shock obliqueness and viscous effects, and which requires optimization on the basis of numerical experimentation. Typical values for κ are 1 for normal shock and 0.6 for highly oblique shocks, while values for $\mathbf{M}_{\mathrm{ref}}$ are in the region $0.975-1.1$.

Numerical stability during the relaxation procedure hinges on positive values for density and pressure being preserved. To this end, the density following from Eq. (12) is modified in the following form:

$$\tilde{\rho} \leftarrow \frac{\tilde{\rho}^*(\rho_\xi + \rho_\eta)}{\tilde{\rho}^* + \rho_P} \tag{19}$$

in which the density ρ, normally given by the equation of state,

$$\rho = \frac{\gamma p}{(\gamma-1)\left(H_0 - \frac{u^2+v^2}{2}\right)} \tag{20}$$

is "under-relaxed" through the relation:

$$\rho = \frac{\gamma}{(\gamma-1)H_0}\left(p + \frac{(\gamma-1)\rho^*(u^2+v^2)}{2\gamma}\right) \tag{21}$$

with ρ^* being the density in the previous iteration or time step. In summary then, the present shock-capturing algorithm is implemented in the same manner as detailed by Patankar (1980) for the staggered arrangement, except for the following variations:

- density-weighted conservation variables are adopted;
- second-order artificial dissipation is introduced, implicitly, in the transonic regime by modifying the contravariant velocity components in the convective fluxes of all transport equations according to the "retarded-density" process detailed above.

2.2 Turbulence Models. Three turbulence models feature in comparisons to be presented below. Two are eddy-viscosity models based on the solution of equations for the turbulence energy k and its rate of dissipation ϵ. The third is the Reynolds-stress-transport closure of Gibson and Launder (1978). One of the k-ϵ variants is the "standard" high-Reynolds-number model of Jones and Launder (1972), and this operates in conjunction with log-law-based wall laws of the type proposed by Chieng and Launder (1980). The other is a low-Reynolds-number variant formulated by the authors so as to conform with turbulent length-scale constraints implied by Wolfshtein's (1969) one-equation model. This model has not been published before and is thus stated below, but without the detailed derivation given in Lien (1992).

The model consists, as usual, of the constituitive equation for the eddy viscosity and two transport equations, one for the turbulence energy and the other for dissipation:

$$\mu_T = \rho \tilde{C}_\mu \frac{k^2}{\epsilon} \tag{22}$$

$$\frac{\partial \rho k}{\partial t} + \frac{\partial \rho u_j k}{\partial x_j} = \frac{\partial}{\partial x_j}\left[(\mu + \mu_T)\frac{\partial k}{\partial x_j}\right] + P_k - \rho\epsilon \tag{23}$$

$$\frac{\partial \rho\epsilon}{\partial t} + \frac{\partial \rho u_j \epsilon}{\partial x_j} = \frac{\partial}{\partial x_j}\left[\left(\mu + \frac{\mu_T}{1.3}\right)\frac{\partial \epsilon}{\partial x_j}\right] + \frac{\epsilon}{k}(\tilde{C}_{\epsilon 1} P_k - \tilde{C}_{\epsilon 2}\rho\epsilon) \tag{24}$$

where P_k is the usual turbulence-energy production. In fully-developed, high-Re turbulence, the tilded coefficients are the numerical constants of the Jones-Launder model, but in low-Re conditions, they are functions of the Reynolds numbers $\mathrm{R}_T = k^2/v\epsilon$ and $l_n{}^* = l_n k^{0.5}/\nu$, the functional dependence in the present model being,

$$\tilde{C}_\mu = 0.09\left[\frac{1 - \exp(-0.016\, l_n^*)}{1 - \exp(-0.263\, l_n^*)}\right] \tag{25}$$

$$\tilde{C}_{\epsilon 1} = 1.44\left(1 + \frac{P_k'}{P_k}\right) \tag{26}$$

$$\tilde{C}_{\epsilon 2} = 1.92[1 - 0.3\exp(-R_T^2)] \tag{27}$$

$$P_k' = \frac{\tilde{C}_{\epsilon 2} k^{3/2}}{3.53 l_n [1 - \exp(-0.263\, l_n^*)]}\exp[-0.00222\, l_n^{*2}] \tag{28}$$

The forms given above have emerged by demanding that, close to the wall, the dissipation length scale $l_\epsilon = k^{3/2}/\epsilon$ and the turbulent length scale $l_\mu = C_\mu k^{3/2}/\epsilon$, the latter implicit in the turbulent viscosity relation, should adhere to corresponding algebraic prescriptions proposed by Wolfshtein (1969). This approach has been motivated by the observation that, while these length scales are insensitive to any adverse pressure gradient acting on the near-wall boundary layer, current low-Re turbulence models tend to predict rising levels with increasing pressure gradient, leading to excessive turbulent viscosity near the wall. Additional advantages of the present model are good stability properties and relatively low sensitivity to grid density in the viscous sublayer. Another model variant which accords with length-scale constraints implied by the one-equation model of Norris and Reynolds (1975) has also been investigated, but is not given herein.

The Reynolds-stress model of Gibson and Launder (1978) consists of coupled transport equations for the individual Reynolds-stress-tensor components, and may be written in symbolic form as:

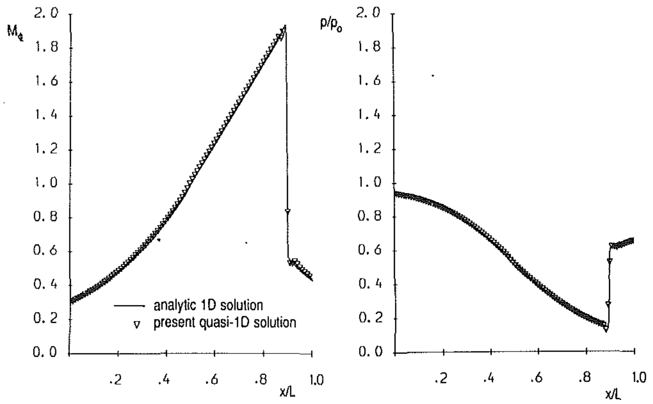

Fig. 3 Transonic inviscid flow in Laval nozzle: Mach-number and pressure distributions from 1-D solution

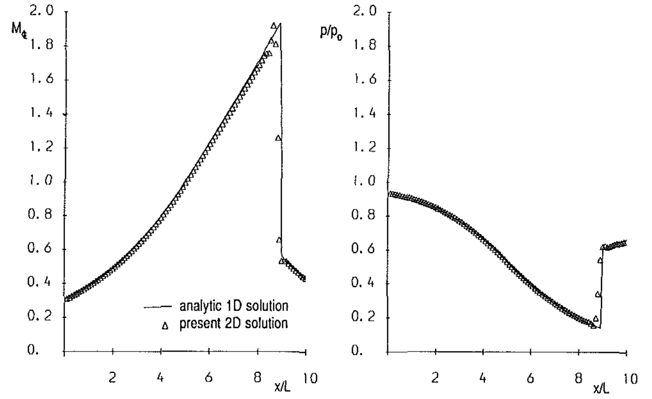

Fig. 4 Transonic inviscid flow in Laval nozzle: area-averaged Mach-number and pressure distributions from 2-D solution

$$\frac{\partial \rho \overline{u_i' u_j'}}{\partial t} + \frac{\partial u_k \rho \overline{u_i' u_j'}}{\partial x_k} = D_{ij} + P_{ij} + \Phi_{ij} - \epsilon_{ij} \tag{29}$$

where D_{ij}, P_{ij}, Φ_{ij}, and ϵ_{ij} represent, respectively, stress diffusion, production, redistribution (by pressure-strain interaction) and dissipation, the last evaluated from a related equation which is similar to that in the high-Re k-ϵ model. The principal advantage of this closure methodology is its ability to account for curvature- and wall-induced anisotropy and augmentation or attenuation of turbulence transport.

The tensorial nature of the Reynolds-stress model makes its incorporation into a nonorthogonal framework a nontrivial task. Particularly careful consideration must be given to wall-boundary conditions and the correct implementation of wall-reflection influences on the redistributive pressure-strain term Φ_{ij}. These issues are addressed separately in Lien (1992).

3 Results

In a preliminary validation stage, the present scheme was applied to inviscid transonic and supersonic flows, after which turbulent shock/boundary-layer interaction was modeled.

A simple but important inviscid test case is a transonic flow with normal shock in a Laval nozzle. The case chosen here was a nozzle of area ratio 2:1:2 subjected to an exit pressure 65 percent of the stagnation value. The quasi-one-dimensional solution was obtained with 100 nodes, while a 100×15 mesh was used to cover one half of the nozzle for the two-dimensional computation. In both cases, the nodal distributions were uniform. Predicted variations of Mach number and pressure (area-averaged in the 2-D case) are given in Figs. 3 and 4, pertaining to the quasi-1-D and 2-D solutions, respectively.

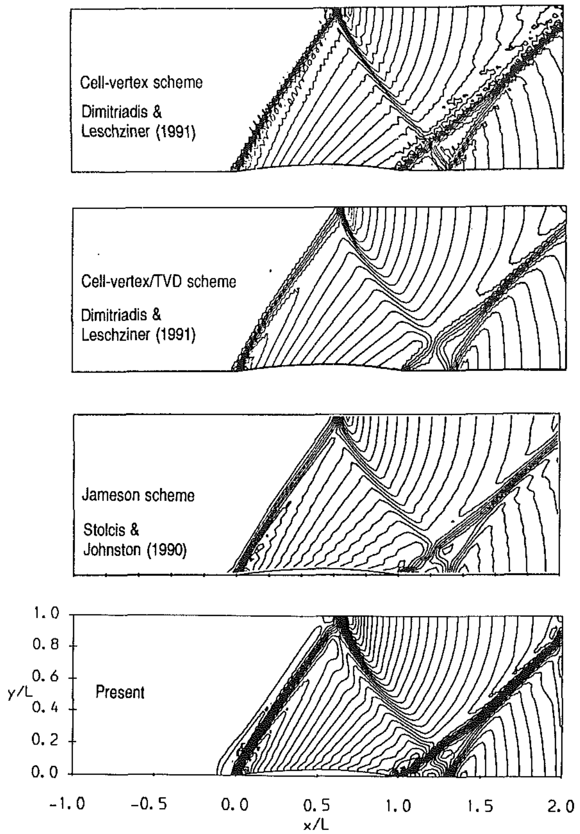

Fig. 5 Supersonic inviscid flow over 4 percent bump: Mach-number contours

Both figures also contain the analytic 1-D solution. As seen, the shock is essentially resolved within two internodal distances, with minor overshoots occurring at the shock edges.

A second inviscid case investigated was a supersonic flow at **M** = 1.4 over a 4 percent circular bump, first considered by Ni (1982). Results were obtained over a grid of 90 × 30 nodes, of which 80 × 20 were uniformly distributed in the region downstream of the bump's leading corner. Resulting Mach contours are compared in Fig. 5 with three other solutions: two obtained by Dimitriadis and Leschziner (1991) using a second-order cell-vertex/Lax-Wendroff scheme, either in conjunction with explicit second-order dissipation or with a Roe/Yee-type TVD scheme, and the third obtained by Stolcis and Johnston (1990) with Jameson's scheme including second- and fourth-order dissipation. Dimitriadis and Leschziner's grid was identical to that used herein, while Stolcis' grid was unstructured but of similar density. Figure 5 demonstrates that the present pressure-based algorithm returns a credible representation of the shock reflection and interaction processes, broadly on a par with those arising from the other formations. The contour plot arising from the present scheme indicates the existence of oscillations in some regions around the shock waves, but it must be pointed out that these can readily be removed by increasing dissipation via adjustments to the monitor functions (17) and (18). Figure 6 brings to the fore the magnitude of the oscillations implicit in the contour plot. It contrasts present variations of pressure on the lower and upper walls with corresponding results produced by the rather diffusive scheme of Ni (1982). While pressure oscillations are evident, particularly at the trailing edge of the bump, the shocks are more crisply resolved, and the weak pressure peak downstream of the trailing edge, provoked by the second reflection of the leading-edge shock on the lower surface, is captured. It should be evident that the quality with which the shocks are captured could be improved by increasing the grid density in the shock region. With the real shocks here being infinitesimally thin, no grid-independence can strictly be achieved and grid refinement is thus not sensible in the present test. The purpose of the test is merely to demonstrate that the quality of the present method is essentially equivalent to that of the more traditional time-marching schemes.

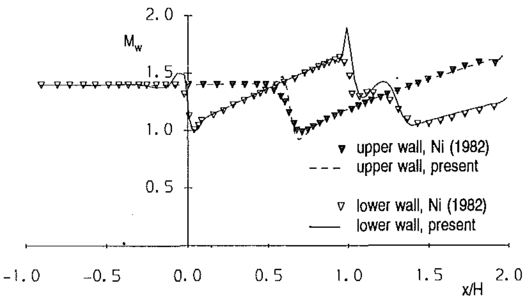

Fig. 6 Supersonic inviscid flow over 4 percent bump: pressure distributions along lower and upper walls

The main area of interest in the present study has been the modeling of shock/boundary-layer interaction. Calculations were made for three cases of shock-affected boundary layers over plane bumps for which detailed LDA measurements were performed by Delery and his associates (1983) at ONERA. The more challenging cases are the "strong-interaction" flows 'B' and 'C' in which the turbulent boundary layer separates due to a strong shock with upstream Mach number being of order M = 1.4 in both cases. The former flow is bounded by a symmetric arrangement of two bumps in a channel (i.e., the geometry is a convergent-divergent nozzle), while in the latter a single bump is opposed by a flat wall. Unfortunately, both cases are contaminated to some degree by three-dimensional features arising from the boundary layers developing on the plane walls bounding the flow in the spanwise direction; this will become apparent shortly. Contamination appears to be lower in case 'C', however, and attention has, therefore, focused principally on this flow. The quadratic QUICK scheme was used for most calculations, following a comparison of the QUICK, MUSCL and UDS schemes undertaken for case 'B'. Some facets of this comparison are conveyed in Figs. 7 and 8 which show results obtained with grids of up to 130 × 50 nodes. Typical CPU requirements for the bump calculations, performed on an Amdahl VP1100 computer, were 460 s and 1300 s for the k-ϵ and Reynolds-stress-model calculations, respectively. These figures correspond, roughly, to 1 min and 3 mins on a single-processor Cray-YMP.

Figure 7 gives variations of the isentropic Mach number along the bump wall and actual Mach number along the symmetry plane, obtained with the Reynolds-stress model (RSTM) and the three convection schemes mentioned above, while Fig. 8 contrasts, for the same quantities, the performance of the high-Re k-ϵ and Reynolds-stress-models. Features deserved to be highlighted are: the under-estimation of the downstream Mach number, reflecting three-dimensional features in the experiment, the poor performance of the k-ϵ model in respect of resolving the separation-related pressure plateau on the bump wall, and the insensitivity of the Reynolds-stress solutions to grid and numerical approximation, provided the order of accuracy of the latter is 2 and above. The level of grid-independence demonstrated explicitly in Fig. 8 and indirectly in Fig. 7 (via the comparison of solutions arising from second-order and third-order schemes for convection) has been found to extend to all quantities, including Reynolds stresses, and justifies the assertion that the predicted level of sensitivity to the adopted turbulence-modeling practices is not affected by numerical errors. Extensive comparisons between predicted and measured velocity and stress profiles, given in Lien (1992), confirm that the Reynolds-stress model returns a higher sensitivity of the boundary layer to the shock and predicts a more

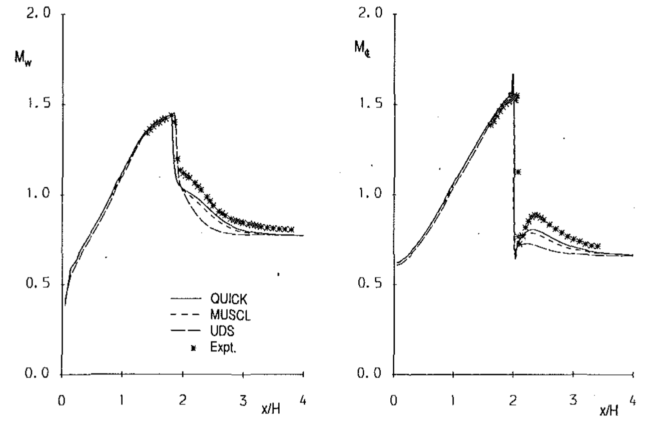

Fig. 7 Turbulent transonic flow over bump; Delery Case B: sensitivity of isentropic wall and centerline Mach number to convection approximation scheme

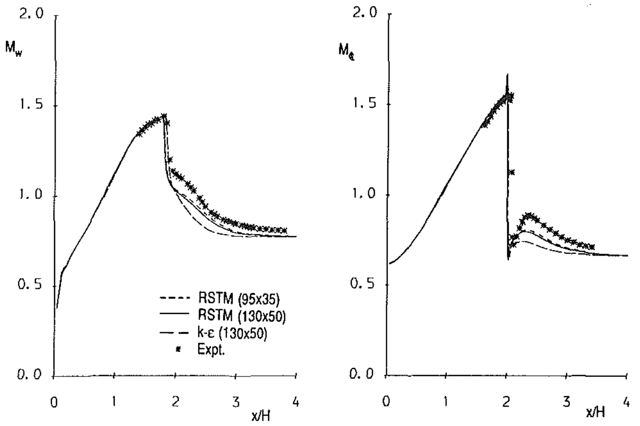

Fig. 8 Turbulent transonic flow over bump; Delery Case B: sensitivity of isentropic wall and centerline Mach number to turbulence model and grid density

extensive recirculation region, both in terms of height and length. We refrain from presenting those comparisons in this paper because very similar characteristics are observed in case 'C' which is considered next in greater detail.

Calculations reported below have all been performed with QUICK approximating mean-flow convection and MUSCL applied to the convection of turbulence quantities over grids containing 110×50 nodes for high-Re and 110×80 nodes for low-Re-model computations. As in case 'B' above, the choice of grids was, here too, made on the basis of grid-independence tests. For the low-Re model, the near-wall grid was arranged so as to give y^+-values of the order 1 along the grid line closest to the wall.

Figure 9 provides a general view of the predicted shock/boundary-layer-interaction region. All models return similar shock structures, but the RSTM yields the strongest interaction, as identified by the more pronounced λ-shock structure and the more extensive post-shock recirculation zone. In common with case 'B', separation is, here too, reflected by a characteristic bump pressure plateau following the shock, as shown in Fig. 10. It is evident that both k-ϵ variants fail to capture the separation process properly. Moreover, the near-wall treatment evidently exerts little influence on the gross flow features—a conclusion also reached by Leschziner et al. (1993) who examined four different practices for resolving the semi-viscous near-wall region. The RSTM clearly predicts a more sensitive response of the boundary layer to the shock, resulting in a larger recirculation zone and hence a much more pronounced pressure plateau. Here again, this observation concurs with earlier computations by Leschziner et al. (1993) and Ha Minh and Vandromme (1986), though these applied variants

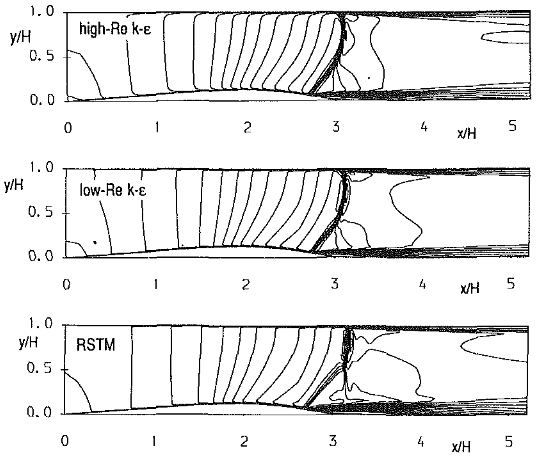

Fig. 9 Turbulent transonic flow over bump; Delery Case C: Mach-number contours

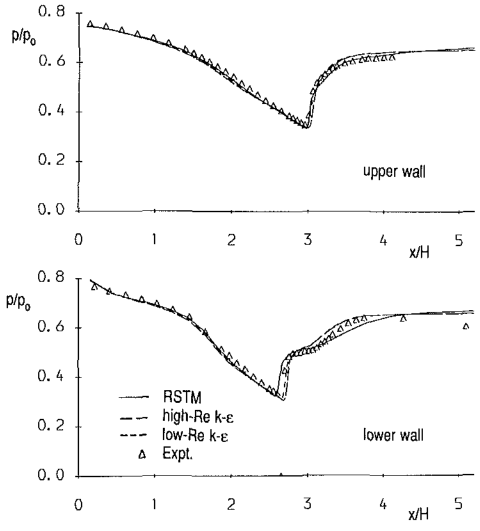

Fig. 10 Turbulent transonic flow over bump; Delery Case C: pressure distribution over bump wall

of the present model implemented within traditional time-marching schemes.

Reference to Fig. 11, which contrasts variations of displacement thickness,[1] confirms the aforementioned drastic differences in predicted sensitivity. These presumably reflects, at least to some extent, the tendency of the RSTM to attenuate the level of turbulence due to flow curvature in the boundary layer approaching the shock and in the separated shear layer bordering the recirculation bubble. On the other hand, the RSTM returns an insufficient rate of recovery following reattachment—as is evident from both Figs. 10 and 11. This weakness is rooted in two sources: first, due to the high level of sensitivity of the boundary layer to the oblique shock, displacement is exceptionally rapid—as seen from Fig. 11—and the oblique shock is so strong that the very weak normal leg of the λ-shock is hardly resolved, the consequence being an insufficient pressure recovery beyond $x/H = 3$; second, the wall-reflection fragment of the pressure-strain term in the Reynolds-stress model has an excessively attenuating influence on the wall-normal turbulence intensity and hence on the shear stress. This latter weakness has been observed in other flows too, notably in separated incompressible flow behind backward-facing steps. It is important to point out, however, that the k-ϵ variants share this defect with the RSTM to some degree,

---

[1] Even minor shock-induced oscillations at the edge of the predicted boundary layer cause difficulties in the evaluation of the displacement thickness. Hence, the results on Fig. 11 must be viewed with some caution in relation to accuracy.

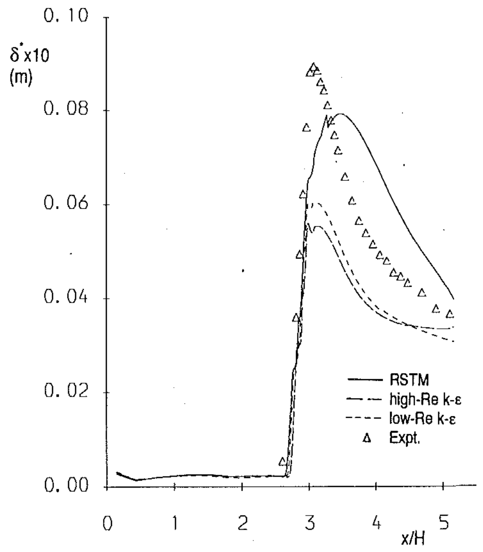

Fig. 11 Turbulent transonic flow over bump; Delery Case C: displacement thickness of boundary layer

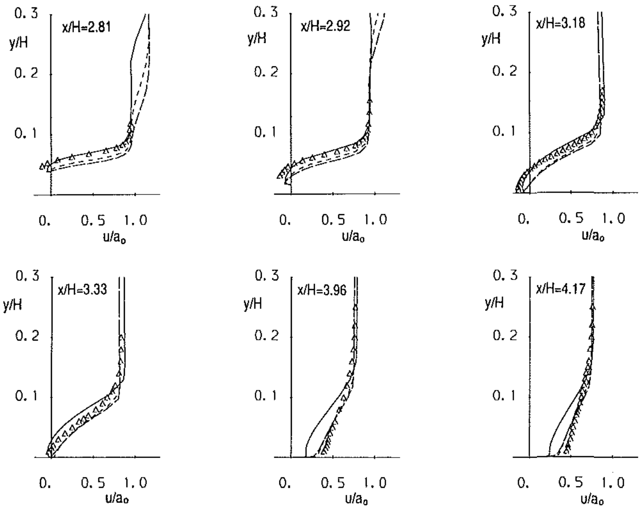

Fig. 12 Turbulent transonic flow over bump; Delery Case C: mean-velocity profiles

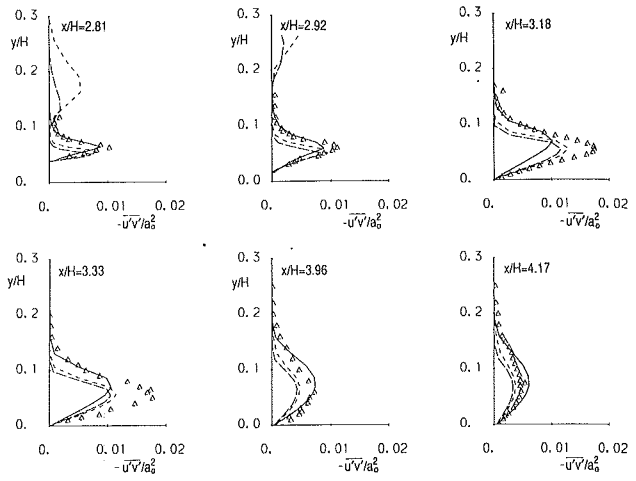

Fig. 13 Turbulent transonic flow over bump; Delery Case C: Reynolds shear-stress profiles

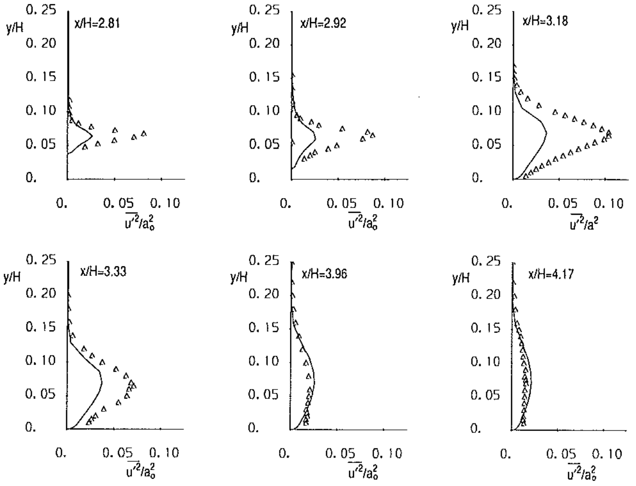

Fig. 14 Turbulent transonic flow over bump; Delery Case C: profiles of stream-wise Reynolds normal stress

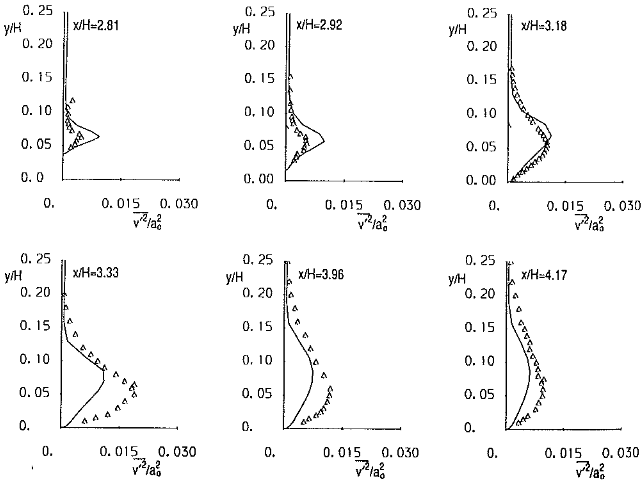

Fig. 15 Turbulent transonic flows over bump; Delery Case C: profiles of cross-flow Reynolds normal stress

the probable link being an erroneous behavior of the ϵ-equation in the presence of low P_k/ϵ values—a condition typically prevailing in wake regions. In the case of the former model type, insufficient recovery is partially obscured by the fact that a smaller recirculation zone arises, which obviously shortens and diminishes the recovery process.

A selection of velocity profiles are given in Fig. 12, and these serve to reinforce earlier comments. Thus, the k-ϵ variants return virtually identical results which identify insufficient sensitivity to the shock, weak recirculation and hence seemingly superior recovery. In contrast, the RSTM captures separation correctly, but clearly fails to give the correct recovery behavior. The somewhat erratic variation of velocity at $x/H=2.81$ and, to a lesser extent, at 2.92 is a consequence of the flow crossing the λ-shock region.

Profiles of shear and normal Reynolds stresses, corresponding to the above velocity variations, are shown in Figs. 13-15. The shear-stress profiles do not reveal drastic model-related differences. It is noted, however, that the RSTM predicts lower shear-stress levels close to the wall, which favors early separation. Once separation has occurred, the highly strained shear layer is displaced upwards, and the shear-stress maximum moves with it. In this shear layer, curvature provokes a reduction in shear stress, as is clearly seen at the location $x/H=3.18$, and this delays reattachment. Paradoxically, at least at first sight, the shear stress returned by the RSTM is especially high in the recovery region, while the velocity profiles suggest a particularly slow recovery rate. This apparent inconsistency is resolved, however, by noting that the recovery, rather than being *slow* is, in fact, *delayed* by the late reattachment predicted by the RSTM. There is, of course, no inconsistency in steeper strain being accompanied by higher shear stress. Figure 14 reveals some startling discrepancies between the predicted and the experimental streamwise normal stresses closer to the shock. Experimental levels of anisotropy reach values of 15 and above, which seems wholly unrealistic and suggests the existence of longitudinal shock oscillations, falsely interpreted as stress contributions. Such oscillations are unlikely to influence the cross-flow intensity, and Fig. 15 does, indeed, show the expected correspondence between v'^2 and $u'v'$ which interact intimately via the latter's generation rate. In contrast to the massive under-estimation of anisotropy in the vicinity of the shock, the predicted anisotropy level in the recovery region is excessive, and this provides the only clear-cut evidence of a defect in the pressure-strain component of the RSTM. Here again, this behavior has previously been observed in incompressible flows recovering from separation.

4 Conclusions

Two principal objectives have been pursued in this study: (i) the formulation of an accurate all-speed calculation procedure based on a pressure-velocity formulation, which can be applied with equal effectiveness to compressible and incompressible flow; (ii) the evaluation of advanced transport closures of turbulence in predicting shock-induced boundary-layer separation.

The paper has demonstrated that a carefully formulated pressure-based scheme can be successfully applied to transonic flow. The key to this success is a density-retardation methodology which is firmly based on and interpreted in terms of fundamental properties of the potential equation in subsonic and supersonic regions.

Variants of the k-ϵ model and a Reynolds-stress-transport closure have been applied to the problem of shock-induced separation over a channel bump, and an important conclusion to emerge is that the latter type of model returns a considerably greater sensitivity to shocks: it gives, among other benefits, a larger recirculation zone and a clearly improved representation of the influence of recirculation on the wall pressure. On the other hand, the stress closure returns an insufficient rate of wake recovery following reattachment, and this can be traced to a combination of excessive strength of the oblique leg of the λ-shock inducing separation and the excessive attenuation of turbulence close to the wall by the wall-reflection component of the pressure-strain model. The conclusions reached herein are in line with those previously derived from a parallel study using a radically different numerical framework in combination with an algebraic approximation of the Reynolds-stress closure used herein. This inspires confidence in the essential validity of the results derived from the present study.

References

Chieng, C. C., and Launder, B. E., 1980, "On the Calculation of Turbulent Heat Transfer Downstream from an Abrupt Pipe Expansion," *Numerical Heat Transfer*, Vol. 3, pp. 189–207.

Davidson, L., 1993, CERFACS' contribution to "EUROVAL-A European Initiative on Validation of CFD Codes," W. Haase, F. Brandsma, E. Elsholz, M. Leschziner and D. Schwamborn, Eds., *Notes on Numerical Fluid Mechanics*, Vieweg Verlag, Vol. 42.

Delery, J., 1983, "Experimental Investigation of Turbulence Properties in Transonic Shock-wave/Boundary-Layer Interactions," *AIAA Journal*, Vol. 21, pp. 180–185.

Dimitriadis, K. P., and Leschziner, M. A., 1991, "A Cell-Vertex TVD Scheme for Transonic Viscous Flow," *Numerical Methods in Laminar and Turbulent Flow*, Vol. 7, C. Taylor, J. H. Chin and G. M. Homsy, eds, pp. 874–885.

Gibson, M. M., and Launder, B. E., 1978, "Ground Effects on Pressure Fluctuations in the Atmospheric Boundary Layer," *Journal Fluid Mechanics*, Vol. 86, pp. 491–511.

Ha Minh, H., and Vandromme, D. D., 1986, "Modelling of Compressible Turbulent Flows: Present Possibilities and Perspectives," *Proceedings Shear Layer/Shock Wave Interactions*, IUTAM Symposium, Palaiseau, Springer-Verlag, pp. 13–24.

Hafez, M., South, J., and Murman, E., 1979, "Artifical Compressibility Methods for Numerical Solutions of Transonic Full Potential Equation," *AIAA Journal*, Vol. 17, pp. 838–844.

Ince, N. Z., and Leschziner, M. A., 1990, "Computation of Three-Dimensional Jets in Crossflow With and Without Impingement Using Second-Moment Closure," *Engineering Turbulence Modelling and Experiments*, W. Rodi, E. N. Ganić, eds., Elsever, pp. 143–153.

Issa, R. I., 1986, "Solution of Implicit Discretised Fluid Flow Equations by Operator Splitting," *J. Comput. Phys.*, Vol. 62, pp. 40–65.

Issa, R. I., and Lockwood, F. C., 1977, "On the Prediction of Two-Dimensional Supersonic Viscous Interactions Near Walls," *AIAA Journal*, Vol. 15, No. 2, p. 182–188.

Jones, W. P., and Launder, B. E., 1972, "The Prediction of Laminarisation With a Two-Equation Model of Turbulence," *International Journal of Heat Mass Transfer*, Vol. 15, pp. 301–314.

Jones, W. P., and Manners, A., 1988, "The Calculation of the Flow Through a Two-Dimensional Faired Diffuser, " *Proceedings of 6th Symposium on Turbulent Shear Flows*, Toulouse, pp. 17.7.1 – 17.7.5.

Karki, K. C., and Patankar, S. V., 1989, "A Pressure Based Calculation Procedure for Viscous Flows at all Speed in Arbitrary Configurations," *AIAA Journal*, Vol. 27, pp. 1167–1174.

Kobayashi, M. H., and Pereira, J. C. F., 1992, "Predictions of Compressible Viscous Flows at all Mach Number Using Pressure Correction, Collocated Primitive Variables and Non-Orthogonal Meshes," Paper AIAA-92-0548.

Launder, B. E., 1989, "Second-Moment Closure: Present and Future?" *International Journal of Heat and Fluid Flow*, Vol. 10, pp. 282–300.

Leonard, B. P., 1979, "A Stable and Accurate Convective Modelling Procedure Based on Quadratic Upstream Interpolation," *Computer Methods in Applied Mechanics and Engineering*, Vol. 19, pp. 59–98.

Leschziner, M. A., Dimitriadis, K. P., and Page, G., 1993, "Modelling Shock/Boundary Layer Interaction with a Cell-Vertex Scheme and Transport Models of Turbulence," *The Aeronautical Journal*, Vol. 97, pp. 43–61.

Leschziner, M.A., 1990, "Modelling Engineering Flows with Reynolds Stress Turbulence Closure," *Journal of Wind Engineering and Industrial Aerodynamics*, Vol. 35, pp. 21–47.

Lien, F. S., and Leschziner, M. A., 1992, "Second-Moment Modelling of Recirculating Flow With a Non-Orthogonal Collocated Finite-Volume Algorithm," *Turbulent Shear Flows 8*, Springer-Verlag, pp. 205–222.

Lien, F. S., 1992, "Computational Modelling of 3D Flow in Complex Ducts and Passages," Ph.D. thesis, University of Manchester.

Lien, F. S., and Leschziner, M. A., 1993, "A General Non-Orthogonal Collocated FV Algorithm for Turbulent Flow at all Speeds Incorporating Second-Moment Closure. Part 1: Computational Implementation," *Computer Methods in Applied Mechanics and Engineering*, (in press).

Majumdar, S., 1988, "Role of Under-Relaxation in Momentum Interpolation for Calculation of Flow with Non-Staggered Grids," *Numerical Heat Transfer*, Vol. 13, pp. 125–132.

McGuirk, J. J., and Page, G. J., 1989, "Shock Capturing Using a Pressure-Correction Method," *AIAA 27th Aerospace Sciences Meeting*, Jan. 9–12, Reno, Nevada.

Ni, R. H., 1982, "A Multiple Grid Scheme for Solving the Euler Equation," *AIAA Journal*, Vol. 20, pp. 1565–1571.

Norris, L. J., and Reynolds, W. C., 1975, "Turbulent Channel Flow With a Moving Wavy Boundary," Stanford Univ. Dept. Mech. Eng. Rep. FM-10.

Page, G. J., 1990, "A Computational Study of Transonic Impinging Jets," Ph.D. thesis, University of London.

Patankar, S. V., 1980, *Numerical Heat Transfer and Fluid Flow*, McGraw-Hill, New York.

Rhie, C. M., and Chow, W. L., 1983, "Numerical Study of the Turbulent Flow Past an Airfoil with Trailing Edge Separation," *AIAA Journal*, Vol. 21, pp. 1525–1532.

Stolcis, L., and Johnston, L. J., 1990, "Solution of the Euler Equation on Unstructured Grid for Two-Dimensional Compressible Flow," *The Aeronautical Journal*, Vol. 94, pp. 181–195.

Shyy, W., Chen, M-H., and Sun, C-S., 1992, "A Pressure-Based FMG/FAS Algorithm for Flow at All Speeds," Paper AIAA-92-0426.

van Leer, B., 1979, "Towards the Ultimate Conservation Difference Scheme V, A. Second-Order Sequal to Godunov's Method," *J. Comput. Phys.*, Vol. 32, pp. 101–136.

Van Doormal, J. P., and Raithby, G. D., 1984, "Enhancement of the SIMPLE Method for Predicting Incompressible Fluid Flows," *Numer. Heat Transfer*, Vol. 7, pp. 147–163.

Van Doormaal, J. P., Raithby, G. D., and McDonald, B. H., 1987, "The Segregated Approach to Predicting Viscous Compressible Fluid Flows," ASME *Journal of Turbomachinery*, Vol. 109, p. 268.

Wolfshtein, M. W., 1969, "The Velocity and Temperature Distribution in One-Dimensional Flow With Turbulence Augmentation and Pressure Gradient," *International Journal of Heat Mass Transfer*, Vol. 12, pp. 301–318.

Wornom, S. F., and Hafez, M. M., 1986, "Calculation of Quasi-One-Dimensional Flows with Shocks," *Computers and Fluids*, Vol. 14, pp. 131–140.

Analysis of an Electromagnetic Boundary Layer Probe for Low Magnetic Reynolds Number Flows

L. S. Langston
Mechanical Engineering Department,
University of Connecticut,
Storrs, CT 06269

R. G. Kasper
Naval Undersea Warfare Center,
Detachment New London,
New London, CT 06320

Electromagnetic (EM) flow meters are used to measure volume flow rates of electrically conductive fluids (e.g., low magnetic Reynolds number flows of seawater, milk, etc.) in pipe flows. The possibility of using a modified form of EM flow meter to nonobtrusively measure boundary-layer flow characteristics is analytically investigated in this paper. The device, named an electromagnetic boundary layer (EBL) probe, would have a velocity integral-dependent voltage induced between parallel wall-mounted electrodes, as a conductive fluid flows over a dielectric wall and through the probe's magnetic field. The Shercliff-Bevir integral equation, taken from EM flow meter theory and design, is used as the basis of the analytical model for predicting EBL probe voltage outputs, given a specified probe geometry and boundary layer flow conditions. Predictions are made of the effective range of the nonobtrusive EBL probe in terms of electrode dimensions, the magnetic field size and strength, and boundary layer velocity profile and thickness. The analysis gives expected voltage calibration curves and shows that an array of paired electrodes would be a beneficial feature for probe design. A key result is that the EBL probe becomes a displacement thickness meter, if operated under certain conditions. That is, the output voltage was found to be directly proportional to the boundary layer displacement thickness, δ_1, for a given free stream velocity.

Introduction

As an electrically conductive fluid flows over a dielectric wall and through an imposed magnetic field, voltages are induced in the fluid and on the dielectric surface. This phenomenon is a consequence of Faraday's law of electromagnetic induction. The voltage field is directly dependent (among other things) on the velocity distribution in the fluid.

This velocity distribution dependency has led to the very successful development of commercial electromagnetic pipe flow rate meters. For conventional pipe flows, such a meter usually consists of two wall-mounted diametrically opposed electrodes which are used to measure the induced voltage produced as a conductive fluid with an axisymmetric velocity profile flows through an imposed magnetic field in an insulated section of pipe. The induced voltage is directly proportional to volume flow rate. A linear calibration curve can be made which is dependent on the magnetic field and the electric conductivity of the fluid. Electromagnetic (EM) flow meters are discussed in detail by Shercliff (1962) and in literature available from manufacturers (e.g., Foxboro Co., Foxboro, MA, USA).

The possibility of using a modified form of the efficacious EM flow meter to measure characteristics of a boundary layer flow, is examined in this paper. A sketch of the modified EM flow meter is shown in Fig. 1. It is not clear at this point what boundary layer flow characteristic (e.g., velocity) such a device would measure, so that it will simply be called an electromagnetic boundary layer (EBL) probe, here. As shown in Fig. 1, the EBL probe consists of a single pair of line electrodes aligned with the nominal flow direction and mounted on a dielectric solid plane surface. An electrically conductive moving fluid (e.g., sea water) forms a boundary layer as the fluid moves parallel to the electrode pair, 1 and 2, through a magnetic field of flux density **B**. The magnetic field is produced by a magnet (or a current carrying coil) embedded in the dielectric surface. For the most part, the flow field considered in this paper will be the two-dimensional boundary layer over the flat plate shown in Fig. 1, and it is assumed that there is no variation of the boundary layer thickness in the region surrounding the electrodes of the EBL probe. Only steady state or time-averaged velocities will be considered.

An electrical current is induced in the fluid as it moves through the magnetic field, and the resulting current density **j** is given by Ohm's law in the form,

$$\mathbf{j} = \sigma(\mathbf{E} + \mathbf{V} \times \mathbf{B}) \tag{1}$$

where σ is the fluid conductivity, **E** is the electric field vector, **V** is the fluid velocity and **B** is the magnetic flux density produced by the magnet (or an electromagnetic coil). The induced voltage between electrodes 1 and 2, $\Delta\Phi = \Phi_1 - \Phi_2$, is related to **E** by

$$\mathbf{E} = -\nabla\phi \tag{2}$$

The crucial step here is to obtain the vector velocity **V** in (1)

Contributed by the Fluids Engineering Division for publication in the JOURNAL OF FLUIDS ENGINEERING. Manuscript received by the Fluids Engineering Division January 9, 1992; revised manuscript received April 22, 1993. Associate Technical Editor: Ho, Chih-Ming.

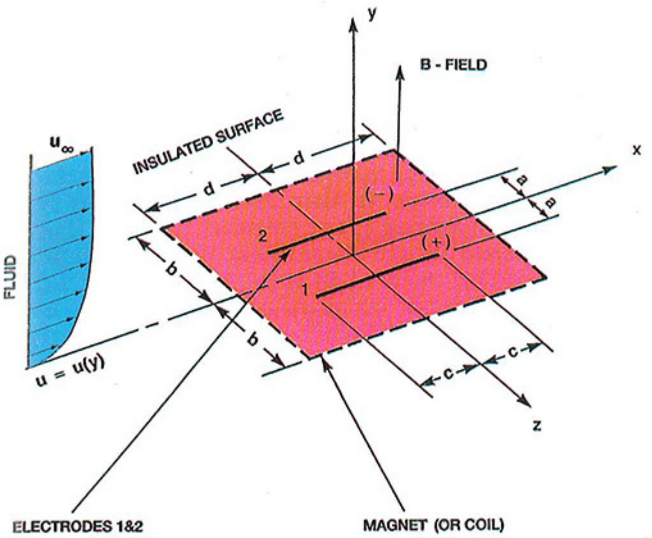

Fig. 1 Electromagnetic boundary-layer probe. As shown, a boundary-layer flow of an electrically conducting fluid in a magnetic field is in the x direction, which generates an induced current in the flow (normal to the electrodes at $x=0$), and a voltage difference $\Delta\Phi$ between the two electrodes.

from the scalar electrode voltage $\Delta\Phi$. An analytical model for doing this is presented in the section that follows this one.

Each particle of moving fluid in the magnetic field is acted upon by a Lorentz force given by

$$\mathbf{F}_L = \mathbf{j} \times \mathbf{B} \tag{3}$$

where $\mathbf{F}_L$ is the Lorentz force per unit volume of fluid. As discussed by Shercliff (1965) (and also Hemp (1988)) the magnetic Reynolds number is given by

$$\mathrm{Re}_m = \sigma \mu_m u_\infty x = \sigma \mu_m \nu \, \mathrm{Re}_x \tag{4}$$

where μ_m is the magnetic permeability of the fluid, ν is the kinematic viscosity, u_∞ is the free-stream velocity (Fig. 1), and Re_x is the conventional Reynolds number based (in this case) on the streamwise coordinate x. If the magnetic Reynolds number is much less than unity, the Lorentz force will be small and the fluid flow field will not be effected by the magnetic field (and conversely the $\mathbf{B}$ field will not be effected by the induced current density $\mathbf{j}$). At a flat plate Reynolds number of $\mathrm{Re}_x = 5 \times 10^5$, Re_m for sea water ($\sigma = 4$ (ohm m)$^{-1}$) is of the order 10^{-6}. (Re_m for liquid sodium (300°C) would be very much higher, on the order 10.) Thus the fluid flows considered in this paper (tap water, sea water and conducting fluids at conventional temperatures) will all be at a very low magnetic Reynolds number, where the Lorentz forces (Eq. (3)) can be neglected.

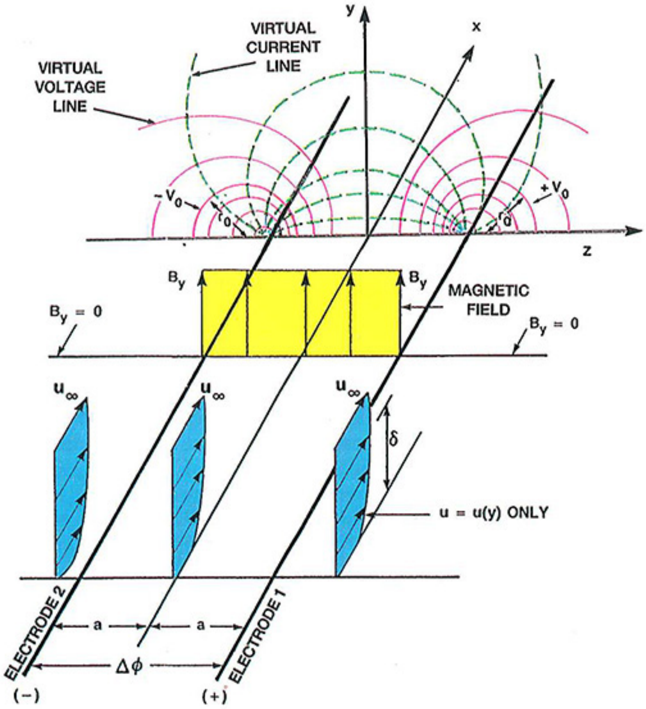

Fig. 2 Two-dimensional model of the EBL probe. Note that virtual current and voltage lines shown are for a no-flow condition.

Devices similar to the EBL probe shown in Fig. 1 have been discussed briefly by Shercliff (1962) (wall velometers) and have been proposed by Smith and Slepian (1917), and Bruno and

Nomenclature

a = electrode half-spacing (Fig. 1)
$\mathbf{B}$, B = magnetic flux density (vector, scalar)
b = magnetic field (or magnet) half-width (Fig. 1)
c = electrode half-length (Fig. 1)
d = magnetic field (or magnet) half-length (Fig. 1)
$\mathbf{E}$ = electric field
EBL = electromagnetic boundary layer
EM = electromagnetic
$\mathbf{F}_L$ = Lorentz force
G = function defined by Eq. (20)
I_v = virtual current
i_v = virtual current per unit length of electrode
$\mathbf{j}$ = current density
$\mathbf{J}_v$, J_v = virtual current density per unit of virtual current
K = constant value of weight function
n = exponent for turbulent boundary layer velocity profile
Re_m = magnetic Reynolds number (Eq. (4))
Re_x = conventional Reynolds number based on x, xu_∞/ν
SB = Shercliff-Bevir
$u = u(y)$ = velocity in x-direction as a function of y
u_∞ = free-stream velocity
V = volume of fluid
$\mathbf{V}$ = fluid velocity
$\mathbf{W}$ = weight vector (Eq. (6))
x = streamwise coordinate (Fig. 1)
y = coordinate normal to surface (Fig. 1)
z = coordinate in z (spanwise) direction (Fig. 1)
α = constant in Eq. (21)
β = constant in Eq. (21)
Δ = difference
δ = boundary layer thickness
δ_1 = boundary layer displacement thickness defined in Eq. (9)
ϵ = location and size of velocity deficit or excess (Fig. 4)
μ_m = fluid magnetic permeability
ν = kinematic viscosity
π = 3.14159····
σ = fluid electric conductivity
Φ = electrode voltage

Subscripts

1, 2, 3, 4, 5 = electrode pairs
I, II = boundary layers I and II
y = y-component
z = z-component

Kasper (1989). The Smith-Slepian device (patented well before the 1950's development of the EM flow meter) was to be mounted below the water line on a ship's hull to act as a ship's log. However, the effects of induced currents and three dimensionality were erroneously neglected, so that the device would not have given a correct measure of the ship's velocity. The more recent Bruno-Kasper device is designed to produce a voltage signal that is indicative of the velocity fluctuations in the turbulent boundary layer on the hull of a submarine or surface ship. It is not apparent how the signal could be used to obtain steady state or time-averaged boundary layer properties.

The scalar voltage output of the EBL probe shown in Fig. 1 is a function of many independent variables. They are the free stream velocity, u_∞, the boundary layer thickness, shape factor and state (laminar or turbulent), the electrode spacing ($2a$) and length ($2c$), the magnetic field size ($2b \times 2d$) and flux density (**B**) and the electric conductivity of the fluid, σ. (Use of finite width electrodes rather than line electrodes, would add another independent variable.)

One need only look at the large number of these independent variables to see that a simple analytical model of the EBL probe is called for. The purpose of this paper is to develop such a model to predict the voltage characteristics for given boundary-layer conditions. The goal will be to see what boundary-layer flow property is measured by the scalar voltage output. Results of the analysis will also provide guidance for the actual design of an EBL probe and for an experimental program to evaluate and calibrate it.

Analysis and Results

The goal in this section is to derive an expression for the open-circuit voltage $\Delta\Phi = \Phi_1 - \Phi_2$ between the electrodes (Fig. 1) in terms of the fluid velocity and geometric and magnetic terms that characterize the EBL probe. First the Shercliff-Bevir equation which is basic to the analysis will be discussed. Then a two-dimensional model (infinitely long electrodes and magnet) will be derived to show important features. Finally a three-dimensional model (finite electrodes and magnet) will be formulated and used to show that an array of paired electrodes would be a key feature in making boundary layer measurements.

(a) The Shercliff-Bevir Equation. In the study and design of electromagnetic volume flow meters, Shercliff (1962) introduced the concept of a weight function which was later made more general by Bevir (1970) as the weight vector. Their work resulted in a much-used, well-documented equation (see Bevir (1970) for the derivation, and also an alternate derivation given by Hemp (1988)) that is widely used for the design of EM volume flow rate meters. It will be referred to here as the Shercliff-Bevir (SB) equation. The equation is valid for small magnetic Reynolds numbers only. It is given by

$$\Delta\phi = \phi_1 - \phi_2 = \int_V \mathbf{V} \cdot \mathbf{W} \, dV \tag{5}$$

where $\Delta\Phi$ is the voltage measured between the parallel electrodes (see Fig. 1) (volts), V is the volume in the conducting fluid over which the EBL probe acts (m^3) (all of the fluid above the insulated surface in Fig. 1), $\mathbf{V}$ is the velocity vector at a point in the volume V of the fluid (m/s), and $\mathbf{W}$ is defined as:

$$\mathbf{W} = \mathbf{B} \times \mathbf{J}_v \tag{6}$$

where $\mathbf{B}$ is the magnetic flux density of the EBL probe (Fig. 1) (Webers/m^2, or volt s/m^2) and $\mathbf{J}_v$ is the virtual current density per unit of virtual current, (amps/amp m^2). The virtual current is a "calibration" (EBL probe geometry and magnetic field dependent) quantity. It is an electrical current that is caused to flow between the two electrodes, when there is no ($\mathbf{V} = 0$) fluid motion. It is not the actual induced current (which causes the measured voltage, $\Delta\Phi$). The induced current is produced when the conducting fluid is in motion through the magnetic field (see Fig. 1).

The weight vector, **W**, is a very useful concept that is used by volume flow rate meter designers to "correct" (usually by means of the magnetic field) for nonsymmetrical velocity profiles in pipe flows (e.g., when a flow meter is mounted close to an upstream elbow). To more clearly see what the probe voltage (Eq. (5)) represents for a boundary layer flow (Fig. 1), let it be assumed for the moment that **W** can be controlled (say by a suitable choice of **B**) in the following way. Let **W** be a constant K in the boundary layer ($y < \delta$ where δ is the boundary layer thickness) and between the electrodes (1, 2) $|x| < a$, $|z| < c$. Everywhere outside of this region, **W** is assumed to be zero (or very small). Also, it is assumed that $|\mathbf{V}| = u_\infty$ (a constant) for $y \geq \delta$ and $|\mathbf{V}| = u(y)$ and $y < \delta$. From (5) the EBL probe voltage will be

$$\Delta\phi = 4acK \int_0^\delta u(y) \, dy \tag{7}$$

Now consider a uniform flow ($u = u_\infty$ for $y > 0$ in Fig. 1) over the same EBL probe. Equation (5) yields

$$\Delta\phi_{\text{uniform}} = 4acK u_\infty \int_0^\delta dy \tag{8}$$

Subtracting (7) from (8) and using the definition of δ_1, the boundary-layer displacement thickness, one gets

$$\delta_1 = \int_0^\infty \left(1 - \frac{u}{u_\infty}\right) dy = \frac{\Delta\phi_{\text{uniform}} - \Delta\phi}{4ac\, u_\infty K} \tag{9}$$

Thus in this particular case where **W** has been specified to be a constant K, it is seen that with knowledge of $\Delta\Phi_{\text{uniform}}$, the EBL probe voltage provides a direct measure of a boundary layer integral quantity, the displacement thickness, δ_1. (Recall that δ_1 is defined as the distance by which the solid surface would have to be displaced to maintain the same mass flow rate in a uniform frictionless flow ($\Delta\Phi_{\text{uniform}}$).)

(b) Two-Dimensional Model. It is not readily apparent how one would achieve the "square-wave" weight vector distribution that was used in (5) to obtain the displacement thickness result of (9). A more plausible weight vector can be derived using the EBL probe in Fig. 2. It consists of two parallel infinite line electrodes (these eliminate end effects) with an infinitely long magnetic field between the electrodes. (Here infinite means that both c and d in Fig. 1 are much greater than a.) As before, it is assumed that there is a steady two-dimensional boundary layer flow (thickness δ) occurring in the x-direction, given as $u = u(y)$ for $y < \delta$ and $u = u_\infty$ (a constant) for $y > \delta$, with no (or small) change of δ in the x-direction.

It is assumed for the purpose of this analysis that the magnetic field has component B_y (a constant) only, as shown in Fig. 2. The magnetic field will eventually arch over and curve back to the south pole of the magnet (or coil), but it is assumed here that this will occur far from the electrodes and contribute little to **W**. Equation (5) then becomes

$$\Delta\phi = \int_{-\infty}^{\infty} \int_0^\infty \int_{-a}^{a} u(y) B_y J_{v_z} \, dz\, dy\, dx \tag{10}$$

The virtual current component in the z-direction, J_{vz}, can be obtained from a classic solution for the voltage field around a line sink and a line source pair. This is given by Skitek and Marshall (1982)

$$\phi_v(y, z) = \frac{i_v}{4\pi\sigma} \ln \left[\frac{y^2 + (z+a)^2}{y^2 + (z-a)^2} \right] \tag{11}$$

where Φ_v is the voltage due the virtual current (as defined by Bevir, 1970) I_y, and i_v is the virtual current per unit length of electrode, (amps/m). Lines of constant Φ_y and constant virtual

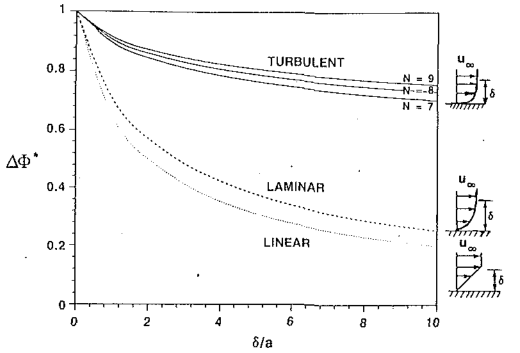

Fig. 3 Nondimensional voltage output ($\Delta\Phi^* = \Delta\Phi/(-u_\infty)\ B_y\ a$) as a function of boundary layer thickness divided by half electrode spacing, δ/a, for various boundary layer velocity profile shapes.

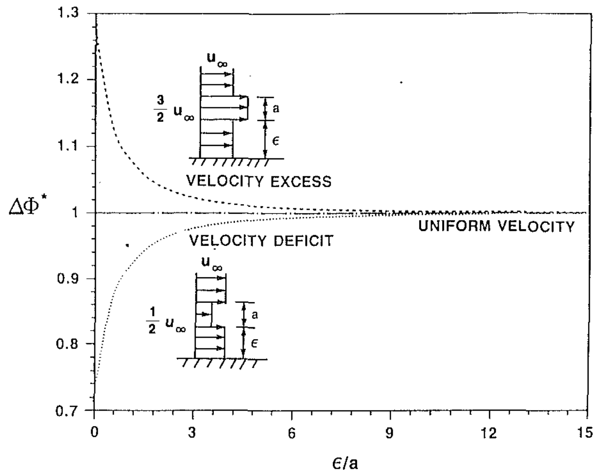

Fig. 4 Nondimensional voltage response of the two-dimensional model of the EBL probe to the position of imposed velocity discontinuities. Note that each curve represents a constant volume flow rate.

current are shown in Fig. 2. From Ohm's law and the definition of virtual current, J_{vz} in (10) is given by

$$J_{v_z} = -\frac{\sigma}{I_v}\frac{\partial \phi_v}{\partial z}, \tag{12}$$

having the units of amperes per ampere of virtual current per unit area normal to the virtual current.

Using (11) and (12) in the SB equation as given in (10), the EBL probe voltage for this two dimensional model is

$$\Delta\phi = -\frac{B_y}{2\pi}\int_0^\infty u(y)\ln\left(\frac{4a^2+y^2}{y^2}\right)dy \tag{13}$$

where B_y is the magnetic flux density (a constant as shown in Fig. 2), and $2a$ is the electrode spacing.

Using Eq. (13), various forms of the velocity $u(y)$ can be assumed to calculate the voltage output $\Delta\Phi$. For a uniform flow, $u(y) = u_\infty$, (13) yields

$$\Delta\phi_{\text{uniform}} = -u_\infty B_y a \tag{14}$$

which shows very simply that the voltage output of this two-dimensional EBL probe depends on the flow velocity, the magnetic flux strength and the electrode spacing.

For boundary flow, as shown in Fig. 2, consider three boundary layer profiles as given by

$$\left.\begin{aligned} \text{linear}\quad & u = u_\infty\left(\frac{y}{\delta}\right) \\ \text{laminar}\quad & u = u_\infty\left(\frac{3}{2}\frac{y}{\delta} - \frac{1}{2}\left(\frac{y}{\delta}\right)^3\right) \\ \text{turbulent}\quad & u = u_\infty\left(\frac{y}{\delta}\right)^{1/n} \end{aligned}\right\}\ 0 \le y \le \delta \tag{15}$$

all with $u = u_\infty$ for $y > \delta$. Equation (13) was evaluated using (15) for various boundary-layer thicknesses. The linear case and laminar case (cubic laminar flow velocity profile) can each be integrated directly. The turbulent cases were integrated numerically for a range of values of n. The results are shown in Fig. 3, which is a plot of nondimensional $\Delta\Phi^*$ (Eq. (13) divided by (14)) as a function of boundary layer thickness, δ, divided by the electrode half-spacing, a (Fig. 2).

In Fig. 3, a uniform velocity profile ($\delta = 0$) yields a probe voltage output of $\Delta\Phi^* = 1$ as a standard of comparison. All profiles in Fig. 3 start at $\Delta\Phi^* = 1$ for $\delta = 0$, but then the voltage output decreases as δ/a is increased, compared to the uniform velocity ($\delta = 0$) case. Most important, given a δ/a value, the output voltage values show that the EBL probe should be able to discriminate between a linear, laminar and turbulent boundary layer with the same free stream velocity, u_∞. In fact, with the latter, discrimination between turbulent (time-averaged) velocity profiles at different Reynolds numbers (different values of n) is possible as shown by the voltage curves calculated for $n = 7$, 8, and 9.

All of the curves in Fig. 3 show that as the volume flow rate across a yz plane decreases (i.e., with increasing δ/a) the output voltage decreases. The same is true for different velocity profiles at the same δ/a, with the linear profile having the lowest mass flow rate and lowest $\Delta\Phi^*$.

To show that the EBL probe is not just a volume flow measuring device (such as commercial units that measure volume flow in a pipe) consider the results of an analysis using the probe model of Fig. 2 and Eq. (11) at a constant flow rate. A uniform velocity profile that has a moveable "notch" (velocity deficit or wake) in it was analyzed. This velocity profile is given by,

$$\left.\begin{aligned} & u = u_\infty, \quad 0 \le y \le \epsilon \\ & u = \frac{1}{2}u_\infty, \quad \epsilon \le y \le a+\epsilon \\ & u = u_\infty, \quad a+\epsilon \le y \le \infty \end{aligned}\right\} \tag{16}$$

where a is the electrode half spacing and ϵ is the location of the notch. Putting Eq. (16) into Eq. (13) yields a closed-form solution

$$\Delta\phi^* = \frac{\Delta\phi}{-u_\infty B_y a} = 2\pi a + a\left[\frac{\epsilon}{2a}\ln\left[1+4\left(\frac{a}{\epsilon}\right)^2\right] + 2\tan^{-1}\left(\frac{\epsilon}{2a}\right)\right.$$
$$\left. -\frac{1}{2}\left(\frac{\epsilon}{a}+1\right)\ln\left[1+4\left(\frac{a}{\epsilon+a}\right)^2\right] - 2\tan^{-1}\left(1+\frac{\epsilon/a}{2}\right)\right] \tag{17}$$

and the evaluation of this is shown in Fig. 4.

The lower curve in Fig. 4 is a plot of the nondimensional voltage output as a function of ϵ, the location in the y-direction of the notch in the velocity distribution. This curve shows that, at a constant flow rate, the relatively simple two-dimensional EBL probe model is able to detect the position of the notch up to a value of ϵ/a of about 10. If the notch is above 10, the probe in effect senses a uniform flow.

The major finding here is that the EBL probe can detect details in a velocity profile within about five electrode spacings. The upper curve in Fig. 4 shows the case of a velocity overshoot (a jet or velocity notch excess of 3/2 u_∞), a distance ϵ away from the wall and a in extent. The probe output voltage is now higher than the uniform flow case (since some of the flow field is moving at a higher velocity than u_∞). Again, when the velocity discontinuity position is below an ϵ/a value of 10 the probe output voltage is sensitive to its position.

In summary, the model of Fig. 2 gives results that are shown in Figs. 3 and 4, and demonstrates what the EBL probe is measuring in terms of fluid flow velocities over a range of parameters. Also, all of the above analysis was based on steady-state or time-averaged fluid flows. What needs to be done now is to extend the analysis to a three-dimensional sensor (i.e., finite length electrodes) such as the one shown in Fig. 1.

(c) Three-Dimensional Model. By using a two-dimensional model (Fig. 2) the complicating end effects of the magnet and the electrodes (electrode half length c and $\mathbf{B}$ field half length d in Fig. 1) were eliminated. These can be taken into account by using a three-dimensional line source and sink pair in place of the two-dimensional virtual voltage field of Eq. (11). Using an expression for a finite line source (or sink) and a sink image, this virtual voltage field Φ_v for the electrode pair shown in Fig. 1 is given by (e.g., see Weber (1950))

$$\phi_v(x, y, z) = \frac{i_v}{4\pi\sigma}\left[\ln\frac{[(x+c)^2+(z-a)^2+y^2]^{1/2}+(x+c)}{[(x-c)^2+(z-a)^2+y^2]^{1/2}+(x-c)}\right.$$
$$\left.-\ln\frac{[(x+c)^2+(z+a)^2+y^2]^{1/2}+(x+c)}{[(x-c)^2+(z+a)^2+y^2]^{1/2}+(x-c)}\right] \qquad (18)$$

where $i_v = I_v/2c$, I_v is the virtual current (amps) and a and c are the electrode pair dimensions as shown in Fig. 1.

As in the two-dimensional case, a simple form is assumed for the magnetic field, given by $B_y(x, z) = B_y = \text{constant}$ for $-d \leq x \leq d$ and $-b \leq z \leq b$, and $B_y = 0$ for $|x| > d$ and $|z| > b$. As before the $\mathbf{B}$ field has been simplified with a y-component ($B_y = \text{const}$) only, assuming that the other components of $\mathbf{B}$ necessary to form closed flux lines occur far enough away from the magnet so that their contribution to $\mathbf{W}$ is small. Using B_y as defined and Eq. (18), the SB equation, (5), can be normalized by the two-dimensional uniform flow result (14), to get

$$\Delta\phi^* = \frac{\Delta\phi}{-u_\infty B_y a} = \frac{1}{4\pi ac}\int_0^\infty \frac{u(y)}{u_\infty}\int_{-d}^{d} G(x, y)dxdy \qquad (19)$$

where $u(y)$ has the same restrictions that were placed on the boundary layer for the two-dimensional probe case, and $G(x, y)$ (from the source-sink model, (18)) is

$$G(x, y) = \ln[[(x+c)^2+(b-a)^2+y^2]^{1/2}+(x+c)][[(x-c)^2$$
$$+(b+a)^2+y^2]^{1/2}+(x-c)] - \ln[[(x+c)^2+(b+a)^2+y^2]^{1/2}$$
$$+(x+c)][[(x-c)^2+(b-a)^2+y^2]^{1/2}+(x-c)] \qquad (20)$$

Equation (19) was evaluated analytically for the case of $u(y)$ as a linear profile boundary layer given in (15). The results for the nondimensional output voltage $\Delta\Phi^*$, are shown in Fig. 5 as a function of b/a for a magnet length and electrode length equal to electrode spacing ($d = c = a$). Each curve in Fig. 5 represents a linear profile boundary layer thickness, δ/a, ranging from uniform flow ($\delta/a = 0$) to $\delta/a = 3$. The electrode half spacing, a, has been chosen as the normalizing length dimension since it would be an easily measured or specified quantity.

The analytical results (from (19)) in Fig. 5 show key features of the EBL probe. The $\Delta\Phi^*$ curve for uniform flow ($\delta/a = 0$) has the largest values of output voltage, with a very pronounced maximum of $\Delta\Phi^* = 0.5$ occurring at $b/a = 1.0$, where the magnetic field width is equal to the electrode spacing. This maximum is half that of the equivalent two-dimensional model (Eq. (14)), which shows that end effects and a finite length magnet induce a smaller voltage. For this $\delta/a = 0$ curve, the output voltage rises steeply in a linear fashion as b/a values are increased from 0 to 1.0. The voltage then falls off in an exponential fashion for b/a values greater than 1.0.

The voltage output curves for each $\delta/a > 0$ linear profile boundary layer thickness in Fig. 5 have similar shapes, but each falls below the uniform flow ($\delta/a = 0$) curve (the latter is a limiting case for any boundary layer shape) as the boundary layer thickness increases and less of the flow is within the "effective range" of the EBL probe (see Fig. 4). The maximum $\Delta\Phi^*$ value for each δ/a curve is slightly shifted to the right (e.g., the maximum $\Delta\Phi^*$ (0.5) for $\delta/a = 0$ occurs at $b/a = 1.0$ while the maximum $\Delta\Phi^*$ (0.14) for $\delta/a = 3$, occurs at $b/a = 1.5$).

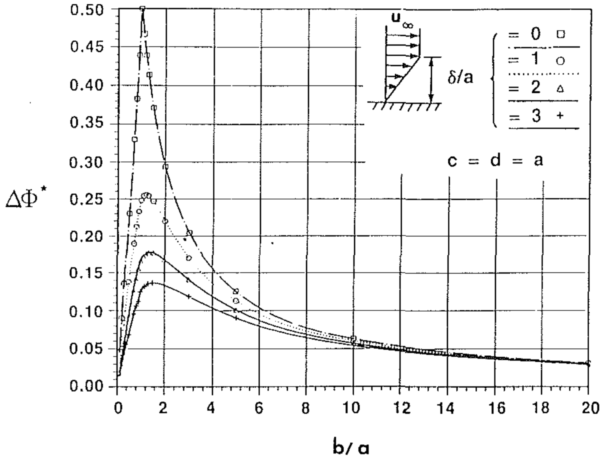

Fig. 5 Nondimensional voltage response of the three-dimensional model of the EBL probe as a function of magnetic field width divided by electrode spacing for four linear profile boundary layer thicknesses

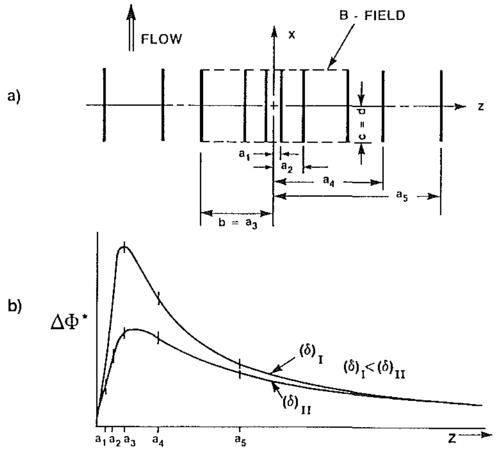

Fig. 6 Multiple paired electrode EBL probe. (*a*) Top view of array of five pairs of electrodes, for $b = a$ and $d = c$. (*b*) Voltage output of (*a*) for two boundary layer thicknesses, corresponding to results of Fig. 5.

What is striking about the family of curves in Fig. 5 is how clearly the effect of boundary layer thickness is demonstrated. It shows that at the very least, the EBL probe could be used to identify an unknown boundary layer if it were calibrated with a known boundary layer family. Similar curves (with higher $\Delta\Phi^*$ values) will result when laminar and turbulent boundary layer profiles (Eq. (15)) are used in (19). They will fall between the linear profile curves and the uniform flow curve of Fig. 5, as shown by the results of Fig. 3 for the two-dimensional model.

In Fig. 5, suppose that b/a is varied by holding the magnetic field width b constant and varying the electrode spacing, a (see (19) and (20)). Then, for a given δ/a, the voltage output curve can be thought of as being traced out by discrete voltages measured from an array of paired, parallel electrodes, for a fixed magnetic field.

An example of such a multiple paired electrode arrangement is shown in Fig. 6(a) as a sketch of a top view of an EBL probe with five pairs of electrodes, where the magnetic field is equal in width to the spacing of the third pair of electrodes and a_3 is taken to be equal to b. Based on Fig. 5 results, the voltage outputs from the five pairs of electrodes would produce a $\Delta\Phi^*$ versus z curve as sketched in Fig. 6(b) for two boundary layer thicknesses, δ_I and δ_{II}, where $\delta_{II} > \delta_I$. The inner two electrode pairs (a_1 and a_2, mounted well within the magnetic field) define the linear part of each curve. The electrode pair mounted at half spacing a_3 at the edge of the field, yields a voltage that is at or near the maximum $\Delta\Phi^*$ for each boundary layer flow.

Thus, an EBL probe with an array of parallel paired electrodes (such as in Fig. 6(a)) could be used to unobtrusively measure the entire boundary-layer flow by recording the voltages for each pair of electrodes.

The three-dimensional model given by Eq. (19) can further be used as a "design tool" to investigate the variation of other parameters. Voltage characteristics curves can be fairly easily generated for other combinations of u_∞, B_y, δ, electrode length c, and magnetic field length d and width b.

Summary and Conclusions

The goal of this paper has been to gain better understanding of what the proposed electromagnetic boundary layer probe (Fig. 1) actually measures in the boundary-layer flow of an electrically conducting fluid over a solid insulated surface. To this end the following was found:

1. The Shercliff-Bevir equation, (5), much used in the design and understanding of electromagnetic volume flow rate meters, was applied to the EBL probe. It was shown that the voltage output of a probe results in a boundary layer integral quantity, which under restricted weight vector conditions, can be used as a direct measure of the boundary-layer displacement thickness, δ_1 (Eq. (9)).
2. Using a two-dimensional line source-sink model for the virtual current part of the Shercliff-Bevir equation, some operating characteristics of the EBL probe were determined. One key result showed the range of sensitivity of the EBL probe to a parametric change in the location of a wake (or jet) embedded in an otherwise uniform two dimensional flow (about five electrode spacings from the wall for the case considered in Fig. 4). It was also shown that under controlled conditions, laminar and turbulent boundary layers could be differentiated (Fig. 3).
3. A three-dimensional line source-sink analysis used for calculating the virtual current provided a more comprehensive prediction of what an actual EBL probe would measure in a boundary layer flow. This analysis provided the means (Fig. 5) to reason that a multiple paired electrode design (Fig. 6) would be a very beneficial feature. The analysis also provides the means to predict the influence of any one of the ten independent variables that determine the output voltage of the EBL probe.

In conclusion, the analysis presented in this paper shows that the electromagnetic boundary layer probe holds promise for the nonobtrusive measurement of boundary-layer flows at low magnetic Reynolds numbers. The characterization it would provide is independent of such fluid properties as density and viscosity. The only fluid property of importance is the fluid electric conductivity, σ (Eq. (1)).

Results from the three-dimensional model (shown in Fig. 5) demonstrate that it should be possible to experimentally calibrate a multiple paired electrode EBL probe (with a nonidealized magnetic field) in a known boundary layer flow. The shape of voltage curves from such a calibration should be the same as those shown in Fig. 5 and 6(b). These curves are approximately fitted by equation

$$\Delta\phi = \frac{\alpha}{z}(1 - e^{-\beta z^2}) \tag{21}$$

where α and β are constants that depend on the linear slope and the location and value of the maximum value of $\Delta\Phi$. This equation could serve as a basis of a calibration curve for an EBL probe.

The electrode pairs have been treated as being parallel to the two-dimensional flow considered in this paper, so that the voltage output is maximized (Eq. (1)). The electrodes could also be mounted in a nonparallel position to get other voltage components of a given three-dimensional flow.

All of the analysis presented here was for steady-state or time-averaged flow velocities. Further work needs to be done on extending the EBL probe analysis to the measurement of time-dependent (e.g., turbulent) fluid flows.

Finally, the analysis presented here has answered the question of what the EBL probe actually measures in a boundary layer flow. The answer is the integral given on the right-hand side of the Shercliff-Bevir equation in (5). The EBL probe measures a voltage that is given by an integral or velocity over space, but not by the velocity itself. If the weight vector **W** (Eq. (6)) is chosen correctly, the voltage measured is directly proportional to the displacement thickness of the boundary layer (Eq. (9)), δ_1.

Thus, future work on the EBL probe might not only include experiments to verify that it can be calibrated as reasoned here, but also could include analytical efforts to find an electrode geometry and magnetic field combination that will yield a weight vector **W** which is independent of y. (This will satisfy the conditions that were used to arrive at Eq. (9)). The resulting EBL probe would then be a very effective boundary-layer displacement thickness meter.

Acknowledgments

The first author was supported as an ASEE-Navy Fellow while working on the study. Both authors express their appreciation to Dr. Kenneth M. Lima of the Naval Undersea Warfare Center for his support, and to Jeffrey Borggaad for his help in evaluating the integrals presented in the paper.

References

Bevir, M. K., 1970, "The Theory of Induced Voltage Electromagnetic Flow Meters," *Journal of Fluid Mechanics*, Vol. 43, pp. 577–590.

Bruno, A. B., and Kasper, R. G., 1989, "Underwater Electromagnetic Turbulent Velocimeter," United States Patent No. 4,848,146.

Hemp, J., 1988, "Flowmeters and Reciprocity," *Quarterly Journal of Mechanical Applied Mathematics*, Vol. 41, pp. 503–520.

Shercliff, J. A., 1962, *The Theory of Electromagnetic Flow-Measurement*, Cambridge University Press, pp. 27–31.

Shercliff, J. A., 1965, *A Textbook of Magnetohydrodynamics*, Pergamon Press, pp. 43–45.

Skitek, G. G., and Marshall, S. V., 1982, *Electromagnetic Concepts and Applications*, Prentice-Hall, pp. 203–209.

Smith, C. G., and Slepian, J., 1917, "Electromagnetic Ship's Log," United States Patent No. 1,249,530.

Weber, E., 1950, *Electromagnetic Fields, Vol. I—Mapping of Fields*, Wiley, p. 114.

S. Venkateswaran
Research Associate.

D. A. Schwer
Graduate Student.

C. L. Merkle
Distinguished Alumni Professor.

Propulsion Engineering Research Center,
Department of Mechanical Engineering,
The Pennsylvania State University,
University Park, PA 16802

Numerical Modeling of Waveguide Heated Microwave Plasmas

Waveguide-heated microwave plasmas for space propulsion applications are analyzed by a two-dimensional numerical solution of the combined Navier-Stokes and Maxwell equations. Two waveguide configurations—one purely transmitting and the other with a reflecting end wall—are considered. Plasma stability and absorption characteristics are studied and contrasted with the characteristics of resonant cavity heated plasmas. In addition, preliminary estimates of the overall efficiency and the thrust and specific impulse of the propulsion system are also made. The computational results are used to explain experimental trends and to better understand the working of these devices.

Introduction

Several experimental programs (e.g., Micci, 1984; Hawley et al., 1989; Herlan et al., 1987) are currently investigating the feasibility of microwave propulsion for future space applications such as orbit transfer and maneuvering. This new propulsion scheme belongs to a larger class of advanced propulsion systems generally referred to as electrothermal propulsion (Sovey et al., 1986). Electrothermal concepts employ electromagnetic radiation to heat a propellant gas before expanding it in a rocket nozzle to generate thrust. They are different from chemical propulsion in that the energy is obtained by electric heating and not from chemical reactions. Electrothermal concepts are also different from electromagnetic (such as MHD) and electrostatic (such as ion thrusters) concepts in that electric means are employed solely to heat the gas and not to accelerate it; the acceleration of the heated gas is accomplished in a converging-diverging nozzle similar to chemical systems.

Various electromagnetic radiation sources such as arcjets, lasers, and microwaves are being considered. In the area of arcjets and lasers, considerable research work has been accomplished over the last decade (e.g., Deininger et al., 1990, Welle, et al., 1987). Both experimental and theoretical analyses have enhanced the understanding of these systems. Results from these studies have demonstrated the potential of these concepts although there are still some issues remaining. On the other hand, microwave propulsion has received a lower level of attention with work being started more recently. The microwave concept is attractive because it possesses several advantages over other sources of radiation; in particular, microwave generation is very efficient and gas absorptivities are very high at microwave wavelengths. Recent experiments in microwave propulsion have been targeted (Balaam and Micci, 1990, Mueller and Micci, 1990) toward understanding the physics of these plasmas and evaluating the conceptual feasibility of the propulsion system.

Two kinds of microwave configurations have been proposed for heating the propellant gas—resonant cavity plasmas and waveguide heated plasmas. Figure 1 shows these concepts schematically. In the resonant cavity concept (Balaam and Micci, 1989, 1990), shown in Fig. 1(*a*), the microwaves are introduced into a cylindrical cavity that is tuned so that a standing wave pattern is maintained within the cavity. A plasma discharge is initiated at a flowfield location where the electric field intensity

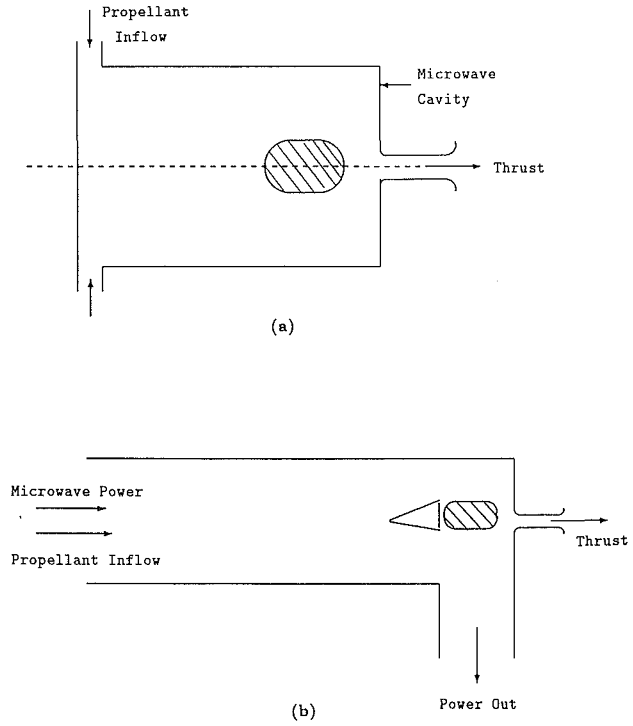

Fig. 1 Schematic diagram showing two types of microwave configurations: (*a*) resonant cavity and (*b*) waveguide heated

---

Contributed by the Fluids Engineering Division for publication in the Journal of Fluids Engineering. Manuscript received by the Fluids Engineering Division March 16, 1992; revised manuscript received June 7, 1993. Associate Technical Editor: R. A. Agarwal.

is a maximum. The propellant gas is heated by the plasma and then expanded in a nozzle. By choosing an appropriate standing wave mode in the microwave cavity, the plasma location may be controlled. In addition, plasma stabilization using a bluff-body in the flow has also been studied to provide additional control of its location. Both experiments and computations (Venkateswaran and Merkle, 1991) have shown that both free-floating and bluff-body stabilized plasmas may be stably maintained in these devices.

The second scheme, the waveguide concept, is the subject of this paper. In this concept (see Fig. 1(*b*)), the microwaves are absorbed in the travelling (or propagating) wave mode rather than in the standing wave mode (as in the resonant cavity). To accomplish this, the propellant gas is caused to flow through a tube that is located inside a standard microwave waveguide. The plasma is initiated in the gas and maintained by absorption of the microwaves in the waveguide. Such a plasma is, however, inherently unstable and tends to move toward the source of the microwave power (i.e., the end of the tube where the microwaves are introduced). In the experiments of Mueller and Micci (1989, 1990), microwaves are introduced into the waveguide at the same end as the gas flow. The plasma then propagates toward the inlet of the device. By maintaining the gas flow rate at exactly the plasma propagation speed, the plasma may in principle be stabilized. This is however a very difficult condition to ensure, and in practice, a bluff body is introduced into the flow to stabilize the plasma. Experiments with such configurations have demonstrated that the plasma may be stably maintained in the wake of the bluff body over a range of powers; recently, measurements of gas temperatures and efficiencies of the device have been carried out (Mueller, 1991).

Theoretical analysis of the microwave heating of gases has received limited attention. A one-dimensional model (Mueller and Micci, 1989) was used to study the propagating microwave plasma heated in a waveguide setup. The analysis is similar to the one-dimensional model developed by Raizer (1977) for propagating laser plasmas. The pressure is assumed to be constant, enabling the energy equation to be decoupled from the momentum equations. The mass flux then emerges as an eigenvalue of the problem and corresponds to the propagation speed of the plasma. The predicted propagation speeds do not agree well with experimentally observed values. The authors attribute this to radiation losses that were not properly accounted for in their model; however, it is also likely that the constant pressure assumption, which gives rise to the eigenvalue, is responsible for the discrepancies.

The present analysis represents the first attempt at a detailed two-dimensional modeling of waveguide-heated plasmas. Recently, resonant cavity plasmas were studied by means of a two-dimensional model which involved the coupled solution of the Navier-Stokes equations for the propellant gas and the Maxwell equations for the microwaves (Venkateswaran and Merkle, 1991). Both free-floating and bluff-body stabilized plasmas were investigated and the computational results agreed quite well with experimental observations and trends. In the present paper, the coupled Navier-Stokes and Maxwell equation analysis is adapted to study waveguide-heated plasmas. There are some important differences between the waveguide configuration and the resonant cavity configuration. One of the objectives of this paper is to identify these differences and determine the impact that they have on the characteristics of the plasma. The geometry used in the computations is similar to that used in the afore-mentioned experiments with waveguide plasmas, and bluff-body stabilization is used to keep the plasma stationary. The characteristics of the microwave discharge are studied under different operating conditions and parametric trends are identified. The results are compared with experimental measurements to strengthen our physical understanding of these devices.

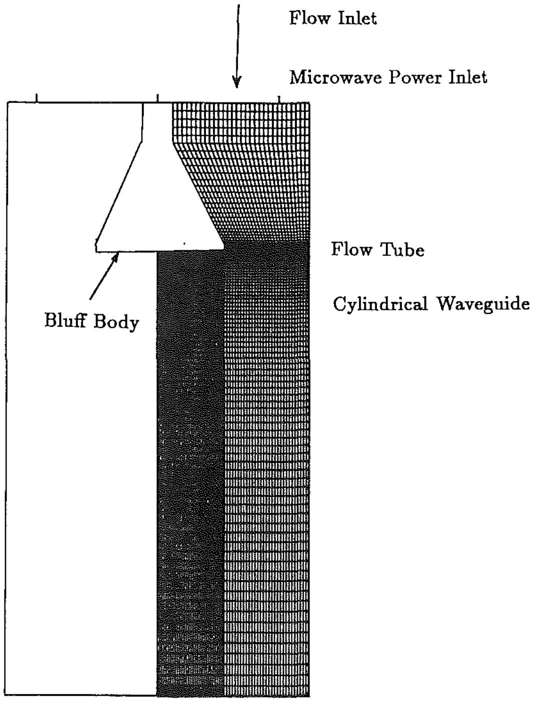

Fig. 2 Geometry used in the waveguide plasma computations showing typical finite difference grid

Description of the Waveguide Configuration

The geometry employed in the present analysis of waveguide-heated plasmas is shown in Fig. 2 along with the computational grid. The gas flows from top to bottom within the cylindrical tube while the microwaves are introduced at the top of a circular waveguide that surrounds the flow tube. Once gas break-

Nomenclature

E, F = dependent inviscid flux vectors
E_v, F_v = dependent viscous flux vectors
$\tilde{E}, \tilde{F}$ = electromagnetic flux vectors
$\mathbf{E}$ = electric field intensity
g = acceleration due to gravity
$H, \tilde{H}$ = source term vector
$\mathbf{H}$ = magnetic field intensity
Isp = specific impulse
$\mathbf{J}$ = electric current density
K_c = thermal conductivity of gas
P = preconditioning matrix
Q = independent flux vectors for fluid flow field
$\tilde{Q}$ = independent flux vectors for electromagnetic field
t = time
T = gas temperature
T_e = electron temperature
Th = thrust
u, v = velocity in x and y direction
x = axial direction
y = radial direction
Z_0 = characteristic impedance of waveguide
Δt = time step
ϵ = perturbation quantity, electric permittivity
μ = coefficient of viscosity
μ' = magnetic permeability
ρ = density
σ_{dc} = electrical conductivity for a direct current field

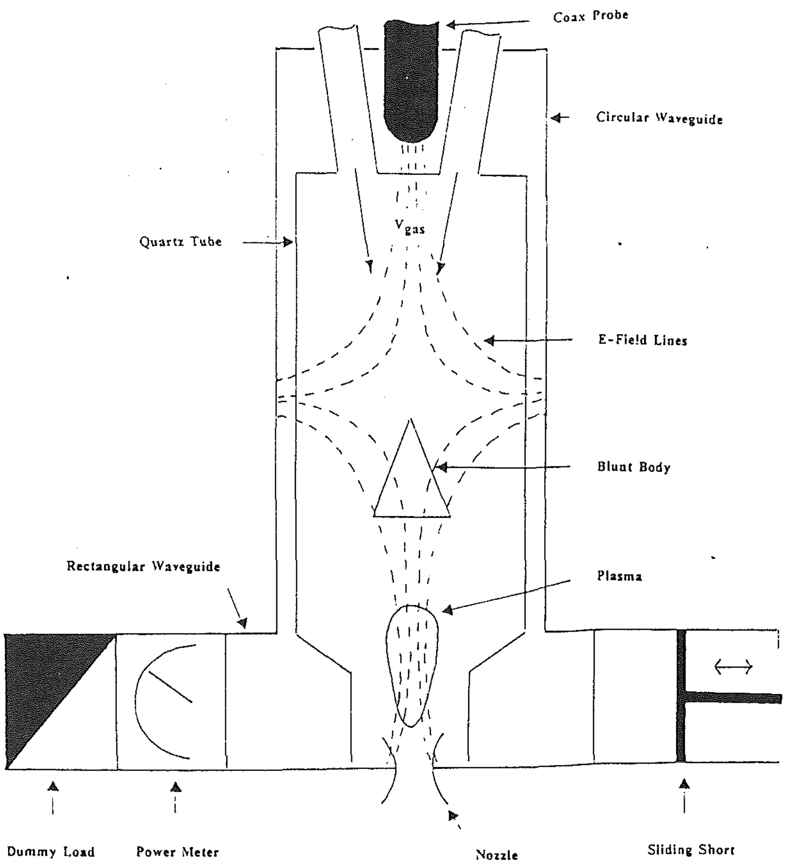

Fig. 3 Schematic of experimental setup for plasmas generated in a circular waveguide (Mueller and Micci, 1990)

down is induced, the free electrons in the gas absorb the incident microwave energy and form a plasma discharge. To provide a stable location for the plasma, a bluff body is introduced into the flow so that the plasma remains anchored in its wake. The hot plasma absorbs energy from the microwave field and, in turn, heats up the surrounding cold gas by convection, diffusion and radiation. In a propulsion system, the heated gas is subsequently exhausted through a nozzle that is located near the bottom of the plasma discharge zone.

It should be noted that not all of the incident energy is absorbed by the plasma. Part of the incident radiation is reflected by the plasma back toward the source and a fraction is transmitted through it. In an ideal waveguide, the reflected and transmitted energies are generally transmitted through the inlet and outlet ends of the waveguide and are, hence, lost from the system. (In practice, these energy components are absorbed by dummy loads.) Clearly, it is important to reduce the reflected and transmitted power losses and maximize the percent of the incident power that is absorbed by the plasma. This quantity is customarily referred to as the coupling efficiency ($\eta_c = P_{\text{abs}}/P_{\text{inc}}$).

In contrast to the waveguide setup, in a resonant cavity configuration, the top and bottom walls of the cavity repeatedly reflect the transmitted and reflected power components back toward the plasma. Therefore, the microwaves make multiple passes through the plasma. Both experiments and analyses have shown that coupling efficiencies approaching 100 percent are possible with such a setup. Further, the standing wave mode of the cavity also ensures the location of the plasma at a region of maximum electric field intensity contributing to excellent plasma stability over a wide range of conditions.

Despite the advantages of the resonant cavity configuration, the waveguide configuration remains attractive because of its simplicity. Therefore, it is desirable to determine ways of maximizing the coupling efficiency in waveguide configurations. One way of reducing the transmission power loss in the waveguide set-up is to reflect the transmitted power component at the exit end of the waveguide back toward the plasma. This would enable a second pass of this energy through the plasma and possibly increase the coupling efficiency. Secondly, the reflected component would also set up a weak standing wave pattern in the waveguide. By proper dimensioning of the geometric set-up, the standing wave mode can be established so that a node of maximum field intensity occurs inside the plasma. As we will show later, such an arrangement contributes to increased stability of the plasma.

In the experiments of Mueller and Micci (1989, 1990), two different geometric configurations have been used. In the earlier experiments, they used a long rectangular waveguide and characterized plasma propagation speeds. Further, they used a bluff body in the flow to hold the plasma and made measurements of coupling efficiencies and plasma temperatures. In the more recent experiments, they have employed a circular waveguide section, as shown in Fig. 3, with the microwaves being introduced at the top by means of an axisymmetric coupling probe. Both the circular waveguide and the axisymmetric coupling were adopted to prevent three-dimensional heating effects which were thought to cause the plasma to arc to the tube wall. At the downstream end of the waveguide, they used a rectangular flange section that was fitted with a dummy load on one end and a sliding short on the other end. This arrangement partly reflects the transmitted power back toward the plasma and causes a weak standing wave pattern to be formed in the waveguide. The experiments also included a choked orifice at the bottom of the flow tube. Measurements were made of the plasma coupling efficiency, plasma temperature as well as the overall thermal efficiency, thrust and specific impulse of the device (Mueller, 1991). These results showed that this waveguide configuration behaves quite differently from the rectangular waveguide section employed earlier, the reasons for which are discussed later.

Description of the Computational Model

Geometric Configuration. The geometric configuration used for the computational analysis (Fig. 2) was selected to match the global characteristics of the circular waveguide experiments (Fig. 3). The diameter of the flow tube and the waveguide (100 mm) are the approximately the same as the experiment while the details of the gas inlet and the choked exit have been omitted. In addition, the waveguide is modelled as axisymmetric thereby omitting the details of the rectangular end-section. This geometry retains the essential features of the microwave plasma and the fluid dynamic interation. In all the calculations, the frequency of the microwaves is 2.45 GHz and the working fluid is gaseous helium. The computational grid size used is 101 × 121 for both the fluid dynamics and the microwaves.

The boundary conditions on the microwave waveguide are extremely important. The waveguide inlet is taken to be a purely transmitting surface and TM_{01} waves are specified as incident at this end. This is representative of the experimental conditions since only TM_{01} waves can propagate through the circular waveguide section. At the exit section, we consider two alternative boundary conditions—transmitting and reflecting. The transmitting condition ensures that the microwaves that are incident on the exit section are transmitted down the waveguide without reflection back toward the plasma. This corresponds to the case when all the energy transmitted through the plasma is absorbed by a dummy load. The reflecting condition, on the other hand, reflects all waves incident on the exit section back toward the plasma. This corresponds to an end-wall condition. In practice, dummy loads tend to reflect a part of the radiation incident on them. Furthermore, in the experiments, we noted earlier that the rectangular waveguide section at the bottom end causes some reflection of radiation incident on that end. Thus, our two exit conditions represent the extreme cases, and in practice, the situation would lie somewhere in between.

Fluid Dynamic Model. The equations of motion that govern the flow of gaseous helium are the compressible Navier-Stokes equations. Because of the low Mach numbers encountered in the flow, we use the low Mach number formulation described by Merkle and Choi (1987). The low Mach number version of the equations possesses well-conditioned eigenvalues at arbitrarily low Mach numbers and thus ensures robust convergence of the time-marching algorithm. For purposes of the numerical algorithm, the equations are written in the coupled vector form including the unsteady terms:

$$P\frac{\partial Q}{\partial t}+\frac{\partial E}{\partial x}+\frac{\partial F}{\partial y}=\frac{\partial E_v}{\partial x}+\frac{\partial F_v}{\partial y}+H_1+H_2, \qquad (1)$$

where

$$P=\begin{pmatrix}1 & 0 & 0 & 0\\ u & \rho & 0 & 0\\ v & 0 & \rho & 0\\ T & 0 & 0 & \rho\end{pmatrix},\quad Q=\begin{pmatrix}p_1 y/\beta\\ uy\\ vy\\ Ty\end{pmatrix},$$

$$E=\begin{pmatrix}\rho uy\\ (\rho u^2+\epsilon p_1)y\\ \rho uvy\\ \rho uTy\end{pmatrix},\quad F=\begin{pmatrix}\rho vy\\ \rho uvy\\ (\rho v^2+\epsilon p_1)y\\ \rho vTy\end{pmatrix},$$

$$E_v=\begin{pmatrix}0\\ \frac{4}{3}\mu y\frac{\partial u}{\partial x}-\frac{2}{3}\mu y\frac{\partial v}{\partial y}\\ \mu y\frac{\partial v}{\partial x}+\mu y\frac{\partial u}{\partial y}\\ K_c y\frac{\partial T}{\partial x}\end{pmatrix},\quad F_v=\begin{pmatrix}0\\ \mu y\frac{\partial v}{\partial x}+\mu y\frac{\partial u}{\partial y}\\ -\frac{2}{3}\mu y\frac{\partial u}{\partial x}+\frac{4}{3}\mu y\frac{\partial v}{\partial y}\\ K_c y\frac{\partial T}{\partial y}\end{pmatrix},$$

$$H_1=\begin{pmatrix}0\\ -\frac{2}{3}\frac{\partial}{\partial x}(\mu v)\\ \epsilon p_1-\frac{4}{3}\frac{\mu v}{y}+\frac{2}{3}\mu\frac{\partial u}{\partial x}-\frac{2}{3}v\frac{\partial \mu}{\partial y}\\ 0\end{pmatrix},$$

$$H_2=\begin{pmatrix}0\\ -\rho g y-\mu'\overline{J}_y\overline{H}_\theta\\ +\mu'\overline{J}_x\overline{H}_\theta\\ \mathbf{J}\bullet\mathbf{E}y\end{pmatrix}.$$

Here, ρ, u, v, p, and T represent the density, x and y velocity components, the pressure and temperature, respectively. The source terms are written as two vectors H_1 and H_2. The vector H_1 contains the standard fluid dynamic source terms that arise because of the axisymmetric co-ordinates. The vector H_2 contains the source terms that arise from interactions with the electromagnetic radiation. These interaction terms are composed of the RMS values of the electric (**E**) and magnetic (**H**) fields and the electric current density (**J**). The energy equation contains the heat source from electromagnetic radiation given by **J** • **E**. In the momentum equations, the source terms arising from buoyancy and the Lorentz forces (**J** × **B**) are included. Radiation losses from the plasma are not accounted for since they do not affect the overall energy balance significantly (Venkateswaran and Merkle, 1991).

The numerical solution of Eq. (1) is obtained by using Euler implicit discretization (Warming and Beam, 1978) in time along with central differences in space for both the inviscid and viscous fluxes. Approximate factorization as described by Douglas and Gunn (1964) is used for the efficient solution of the resulting matrix operator. The details of this solution procedure which involves block tridiagonal inversions for each coordinate direction are described by Venkateswaran and Merkle (1991).

Maxwell Equation Solutions. The Maxwell equations for TM waves may be written in vector form analogous to the fluid dynamic equations:

$$\frac{\partial \tilde{Q}}{\partial t}+\frac{\partial \tilde{E}}{\partial x}+\frac{\partial \tilde{F}}{\partial y}=\tilde{H}_1+\tilde{H}_2, \qquad (3)$$

$$\tilde{Q}=\begin{pmatrix}H_\theta y\\ E_y y\\ E_x y\\ J_y y\\ J_x y\end{pmatrix},\quad \tilde{E}=\begin{pmatrix}(1/\mu')E_y y\\ (1/\epsilon)H_\theta y\\ 0\\ 0\\ 0\end{pmatrix},\quad \tilde{F}=\begin{pmatrix}-(1/\mu')E_x y\\ 0\\ -(1/\epsilon)H_\theta y\\ 0\\ 0\end{pmatrix}$$

$$\tilde{H}_1=\begin{pmatrix}-(1/\mu')E_x\\ 0\\ 0\\ 0\\ 0\end{pmatrix},\quad \tilde{H}_2=\begin{pmatrix}0\\ -(1/\epsilon)J_y y\\ -(1/\epsilon)J_x y\\ (\sigma_{dc}E_y-J_y)\nu_c y\\ (\sigma_{dc}E_x-J_x)\nu_c y\end{pmatrix}.$$

In Eq. (3), the first three rows represent the standard Maxwell's curl equations relating the magnetic field (H_θ) to the electric field (E_x and E_y). The last two equations are equations for the electric current density derived from momentum considerations for the conducting electrons in the plasma. The electrical properties of the medium, namely the electrical conductivity σ_{dc}, the collision frequency ν_c, the electrical permittivity ϵ and the magnetic permeability μ', are calculated as described by Venkateswaran and Merkle (1991).

The Maxwell equations are solved in the time domain by adopting an explicit time-marching procedure that is second-order accurate in time and space. The details of the solution algorithm are once again described by Venkateswaran and Merkle (1991). The Maxwell solutions yield an unsteady electromagnetic field. However, in terms of fluid time scales, the field is steady and is represented by the RMS values of the time varying components. In the coupled solution procedure, for each NS (Navier-Stokes) time step, we calculate the EM field over several cycles (between 1 and 10 cycles) and then time-average it to obtain the RMS field. Typically, more cycles were required per NS iteration step toward the start of the calculation. After about 100 iterations, it was generally sufficient to compute a single EM cycle per NS step. Because of the explicit nature of the Maxwell algorithm, the procedure was found to be fairly efficient.

Boundary Conditions for the Waveguide. The boundary conditions on the Maxwell equations for the EM field in the waveguide are particularly important. Previous research in the area of radio frequency plasmas (Rhodes and Keefer, 1989) specified the tangential component of the electric field at the boundaries. While this is the physically correct boundary condition for a reflecting wall (where the tangential electric field is zero), it is not proper for the power inlet and outlet sections of the waveguide. This is because the value of the electric field at these boundaries depends on the amount of power dissipated in the plasma and cannot be known *a priori*. The correct quantities to keep fixed at these boundaries are the Riemann variable (or characteristic). At the inlet section, the forward running characteristic represents the incident power and is specified as a boundary condition while the backward running characteristic represents the reflected power component and is calculated from the solution. At the exit section, the outgoing characteristic represents the power transmitted through the waveguide while the inward running characteristic represents any power that is incident at this end. Earlier, we discussed two kinds of conditions that may be applied at the exit of the waveguide—transmitting and reflecting. For the waveguide with a transmitting exit condition, the inward running characteristic is zero. For the waveguide with a reflecting end wall at the exit, the inward running characteristic is equal to the negative of the outgoing characteristic (i.e., the transmitted power is reflected back toward the plasma).

The application of the locally one-dimensional method of characteristics yields the following expressions for the forward (+) and backward (−) running characteristics:

$$\hat{q}^{+}=\frac{1}{2}\,(E_y+Z_0H_\theta),\quad \hat{q}^{-}=\frac{1}{2}\,(E_y-Z_0H_\theta) \tag{5}$$

where Z_0 is the characteristic impedance given by $\sqrt{\mu'/\epsilon}$.

As a check of our boundary procedure and to demonstrate the differences between the two undistorted electric fields, we plot the Maxwell solutions for a lossless waveguide in Fig. 4 for both transmitting and reflecting exit conditions. Figure 4(*a*) shows the RMS value of the axial electric field for the waveguide with a reflecting end wall. The characteristic equations yield the obvious condition $E_y = 0$ for this case. The reuslt clearly shows a standing wave pattern in the waveguide. Since no power is dissipated in the waveguide, all the incident power is transmitted through to the end wall, where it is reflected back toward the microwave source. It is also evident that the exit wall acts as a node of maximum intensity. One-half wavelength upstream of the end wall is a second node of maximum intensity. As mentioned earlier, this node would serve as an ideal location for the plasma. (In a later section of the paper, we will show that this location ensures excellent plasma stability.) In addition, the location of the waveguide end wall may be adjusted in order to control the location of the plasma.

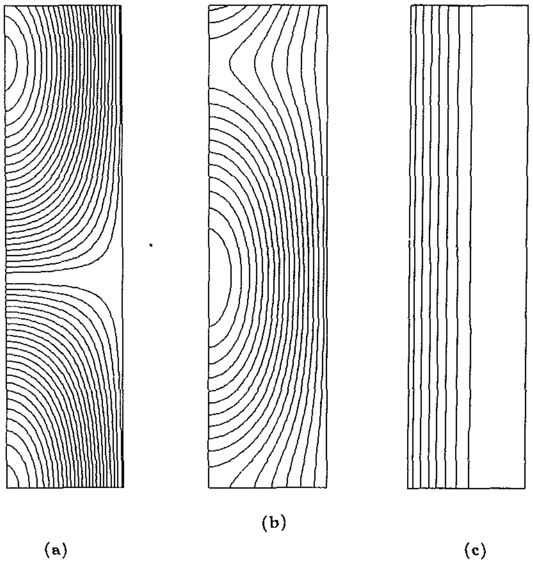

$\Delta E_r = 3000$ V/m

Fig. 4 Undistorted axial electric field in a waveguide. (*a*) Waveguide with reflecting end wall, (*b*) transmitting waveguide with one-dimensional method of characteristics, and (*c*) transmitting waveguide with proper characteristic boundary condition.

The corresponding result for the waveguide with the transmitting end condition is shown in Fig. 4(*b*). Surprisingly, this plot of the axial electric field again shows a standing wave pattern, although it is weaker than the standing wave in Fig. 4(*a*). This means that not all of the incident power is transmitted through the exit section; rather, a percent of the power is reflected at this boundary (22 percent in this case). The reason for this is the use of locally one-dimensional method of characteristics at this (two-dimensional) boundary. For the axisymmetric waveguide, the one-dimensional boundary procedure cannot eliminate reflection completely. To specify this boundary condition correctly, it is necessary to employ the two-dimensional method of characteristics. In fact, this is a familiar problem in computational fluid dynamics and a formidable one. Fortunately, however, for microwaves travelling in a lossless waveguide, there is an exact solution (e.g., Gandhi, 1981). Using this exact solution, it becomes evident that the correct characteristic quantities are given by:

$$\hat{q}^{+}=\frac{1}{2}\,(E_y+Z_{\mathrm{TM}}H_\theta),\quad \hat{q}^{-}=\frac{1}{2}\,(E_y-Z_{\mathrm{TM}}H_\theta) \tag{6}$$

where Z_{TM} is the characteristic impedance for TM waves in a waveguide and is given by $\sqrt{\frac{\mu'}{\epsilon}-\frac{k_c^2}{\omega^2\epsilon^2}}$. Here, ω is the frequency of the microwaves and k_c is the wave number in the radial direction.

Figure 4(*c*) shows the result for the transmitting waveguide using Eq. (6). Now the field pattern is completely changed. The standing wave solution is no longer evident; instead, the field lines run parallel to the waveguide axis with the maximum

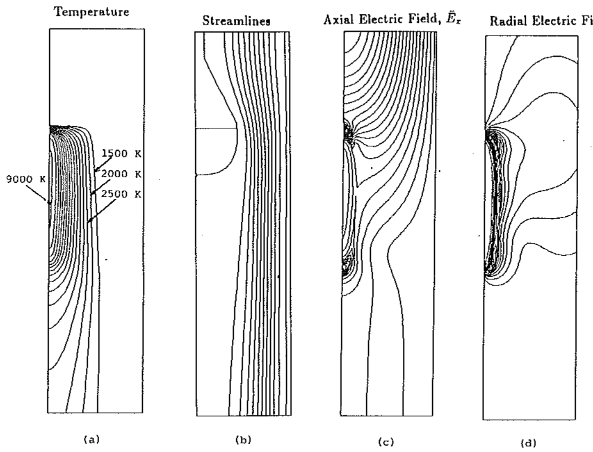

Fig. 5 Solution field for plasma generated in a transmitting waveguide. Power 3.5 kW, pressure 1 atm, gas velocity 3 m/s, mass flow 1.1 g/s, D_b = 4.5 cm. (*a*) Flowfield solution showing temperature and streamline contours and (*b*) electric field lines.

occuring at the centerline. This is the correct solution for travelling waves in the waveguide. The power fluxes of the calculation also show that all the incident power is transmitted through the exit and none is reflected. It should also be noted that for this traveling wave solution there is no preferred axial location for the plasma; hence, the need for a stabilization device such as a bluff body is evident.

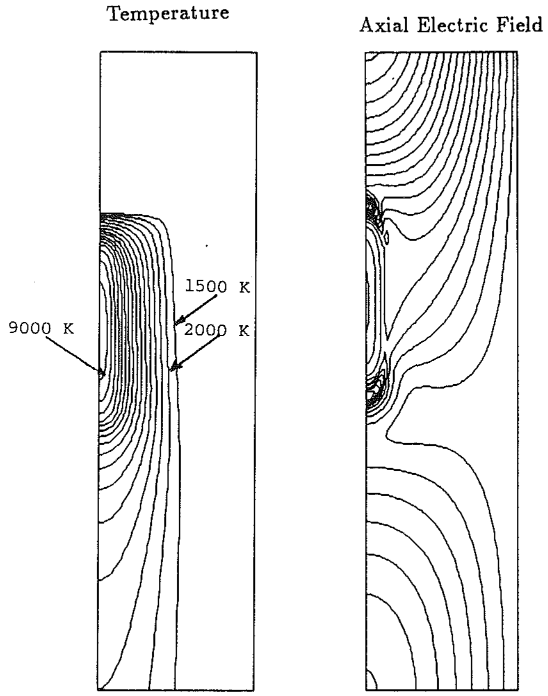

Fig. 6 Temperature contours and axial electric field for reflecting waveguide configuration. Same conditions as Fig. 5.

Characteristics of Waveguide Plasmas

In the following sections, we present the computational results for waveguide plasmas. We consider both transmitting and reflecting waveguide configurations and contrast their characteristics with resonant cavity plasmas. First, we present representative plasma solutions for the two waveguide configurations followed by an investigation of the stability characteristics of these plasmas over a wide range of microwave powers. We then study the energy coupling (or absorption) efficiencies of these devices. Finally, estimates of the performance of the device are presented in terms of thrust and specific impulse. Further, in these sections, available experimental data are presented alongside the computational results and the observed trends are discussed in order to obtain a better understanding of these devices.

Representative Plasma Solution. To provide a physical picture of waveguide heated plasmas, a typical solution for a transmitting waveguide is shown in Fig. 5. The flowfield solution is given in Fig. 5(*a*) and (*b*) while the electric field solution is in Fig. 5(*c*) and (*d*). For this case, the inlet gas velocity is 3 m/s and the gas pressure is 1 atm. The corresponding mass flow rate is 1.1 g/s. The incident microwave power is 3.5 kW.

The temperature contours in Fig. 5(*a*) show that the plasma discharge is maintained in the wake of the bluff body. As shown in Fig. 4, the electric field in the transmitting waveguide does not offer any preferred location for the plasma; consequently, its location is determined purely by the dynamics of the flow. The fluid dynamics tend to push the plasma downstream while the microwave radiation pulls it upstream. The plasma is stable in a region where these two forces balance out. The plasma is long and slender with its outer diameter being roughly defined by the edge of the bluff body. The peak plasma temperature occurs on the central axis and is about 9150 K which is typical of helium plasmas of this size (Balaam and Micci, 1989). The streamline contours in Fig. 5(*b*) show evidence of a recirculating region in the wake of the bluff body; however, the recirculating region is quite weak relative to its cold flow counterpart under similar conditions (Venkateswaran and Merkle, 1991). This is because the strong heat addition in the plasma tends to suppress the recirculation zone. In fact, in some cases, the recirculation is totally eliminated.

The axial and radial electric field contours are shown in Fig. 5(*c*) and (*d*). The electric field lines are seen to be strongly distorted in the presence of the plasma (compare with Fig. 4). Because of the skin effect, the absorption of the energy occurs at the surface (or skin) of the plasma; consequently, the electric field is nearly zero inside the plasma. Upstream of the plasma, the electric field lines show a standing wave pattern that is setup by the energy that is reflected by the plasma, while downstream of the plasma, the electric field lines run parallel to the waveguide axis, representing the transmitted component. For the transmitting waveguide configuration, both the reflected and transmitted powers are lost from the system. For this case, 3.5 kW is incident on the plasma, 2.4 kW (68.5 percent) is absorbed by the plasma, 1 kW (28.5 percent) is reflected back toward the inlet and 0.1 kW (3 percent) is transmitted through the waveguide exit. The coupling efficiency, which is defined as the ratio of absorbed to incident power, is therefore 68.5 percent for this case. This energy budget is typical of the results obtained experimentally with the rectangular waveguide configuration (Mueller and Micci, 1989)—a large fraction of the input power is reflected back by the plasma while a relatively smaller fraction is transmitted through it. (The results of the circular waveguide experiments indicate lower amounts of power reflection and, consequently, higher coupling efficiencies. The reasons for this somewhat different behavior are discussed later along with detailed comparisons.)

Figure 6 shows the results for the same conditions used in Fig. 5 except that the transmitting downstream end of the waveguide is replaced by a reflecting end-wall. For the reflecting waveguide configuration, the power transmitted to the exit section is reflected back toward the plasma and thus gets a second chance to be absorbed. It is interesting to check if this alternate configuration gives better energy coupling than the transmitting waveguide.

In all respects, the reflecting waveguide solution in Fig. 6 is remarkably similar to the transmitting waveguide solution. The electric field solution now shows evidence of a standing wave

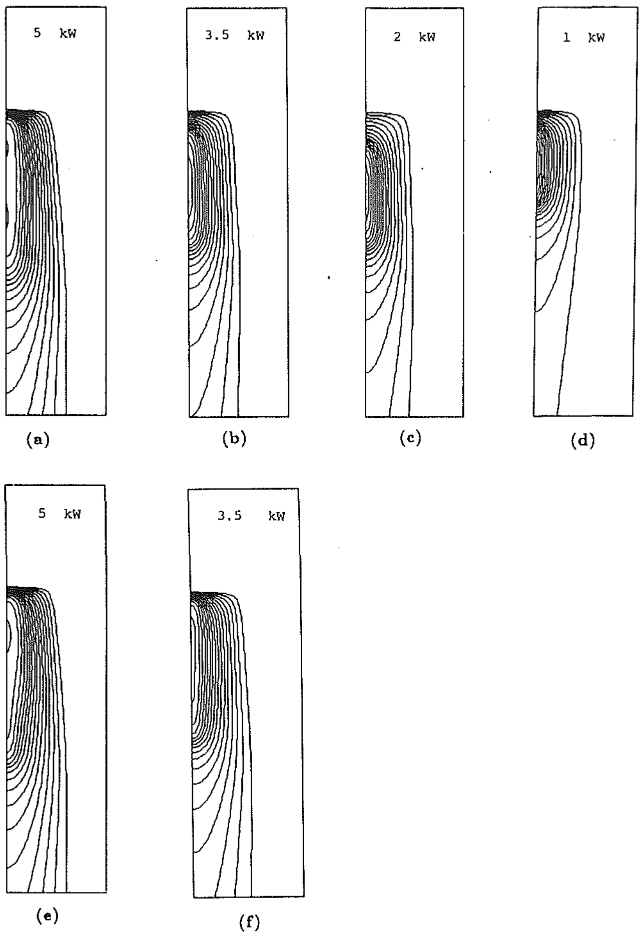

Fig. 7 Effect of power variation on (*a*)-(*d*) reflecting, and (*e*)-(*f*) transmitting configurations. Other conditions same as Fig. 5.

pattern downstream of the plasma as well indicating power reflection at the exit. The peak temperature is now 9310 K while the coupling efficiency is 68 percent (the reflected power loss is now 32 percent while there is no transmission power loss). Therefore, the reflecting condition has made very little impact on the nature of the plasma. The reason for this is the relatively small percent of the power that is transmitted through the plasma. However, the reflecting condition has a great impact on the stability of the plasma as we will see in the following section.

The Effect of Microwaver Power. Figure 7 compares the performance of the reflecting and transmitting waveguides over a wide range of microwave powers. The reflecting waveguide results are shown on the top (Figs. 7(*a*) to 7(*d*)) while the transmitting waveguide results are shown on the bottom (Figs. 7(*e*) and 7(*f*)). The flow conditions are once again the same as before (1 atm and 3 m/s inlet velocity). For the reflecting waveguide (Figs. 7(*a*) to 7(*d*)), the plasma is maintained stably in the wake of the bluff body over a wide range of powers, while for the transmitting waveguide (Figs. 7(*e*) and 7(*f*)), it is impossible to maintain the plasma at powers lower than about 3 kW.

For the reflecting waveguide, as the power is reduced from 5 kW to 1 kW, the plasma shrinks in size. This effect is more noticeable in the plasma length than in its radius since the bluff body size defines the nominal radial size of the plasma. The peak plasma temperature, however, stays constant at about 9300 K. Of particular interest is the double plasma that starts to form at the 5 kW condition. Such double plasmas have also been observed experimentally (Mueller, 1991). When the power is reduced below 1 kW, the plasma is eventually extinguished. Such a power threshold exists because, at low powers, the electrons start recombining more rapidly than they are created by ionization. In our predictions, the minimum power was about 800 W, which is similar to experimental values.

For the transmitting waveguide, in Figs. 7(*e*) and 7(*f*), at the higher powers (5 kW and 3.5 kW), the plasma discharge is qualitatively similar to the reflecting waveguide plasma. At lower powers, it is impossible to hold the plasma stably behind the bluff body. Consequently, the transmitting waveguide exhibits a power threshold (about 3 kW) that is much higher than that for the reflecting waveguide (about 800 W). Of course, this threshold would probably depend on the discharge pressure and flow rate; but, for the flow rates of interest here, the threshold power for the transmitting waveguide was consistently around 3 kW.

The improved performance of the reflecting waveguide arises because the reflecting end sets up a standing wave mode; as described earlier, the standing wave mode creates a node of maximum electric field intensity one-half wavelength upstream of the exit, which serves as an excellent location for the plasma. (In fact, computations performed with different waveguide lengths show the plasma forming at a fixed location relative to the end-wall irrespective of the location of the bluff body. This shows the plasma location is dictated strongly by the electric field and not by the fluid dynamics of the bluff body wake. In such cases, it should be possible to sustain the plasma stably even in the absence of the bluff body.) In contrast, the transmitting waveguide absorbs in the propagating wave mode which provides no preferred location for the plasma. Thus, the stability of the plasma is dictated by the interaction of the fluid dynamics with the electromagnetic field. At lower powers, the convection dynamics of the flow dominates over the microwave power and blows the plasma away from the wake of the bluff body.

For the case in Fig. 5, only 3 percent of the power is incident on the exit end. It might seem surprising that the small amount of power reflection at the exit end makes such a big difference in terms of plasma stability. However, it should be noted that in the limit of the plasma getting extinguished all the power is transmitted through the plasma and is incident on the exit end. Thus, a dynamic balance exists between the amount of power transmitted through the plasma and the maximum electric field intensity at the plasma location. At this juncture, we point out that reflecting waveguide plasmas behave very much like resonant cavity plasmas with regard to their stability. However, there is a big difference with regard to the coupling efficiency because, in the waveguide, the power that is reflected by the plasma is lost through the inlet end. We turn our attention to this aspect in the following section.

Coupling Efficiency. The coupling efficiency of the plasma is the percent of the incident power that is absorbed by the plasma. Figure 8 shows the coupling efficiency from both the computations and the experiments plotted for different powers and pressures. Here, as well as in all following figures, the computational results are represented by darkened symbols while the experiments are shown with open symbols. Figure 8(*a*) shows the coupling efficiency results from the computations using the reflecting waveguide configuration. We note that at low powers, high coupling efficiencies (between 90 and 100 percent for 1 kW) are indicated. As power is increased, coupling efficiency drops almost linearly, and at 2 kW, it is down to about 75 to 80 percent. (Recall that for the case in Fig. 6, where the incident power was 3.5 kW, the coupling efficiency was 68 percent.) The energy budgets show that as the power is increased, the fraction of the power that is reflected back by the plasma increases. The exact reason for this kind of behavior is not clear but the behavior appears to be characteristic of waveguide-heated plasmas and has been observed experimentally as well. Some representative experimental data

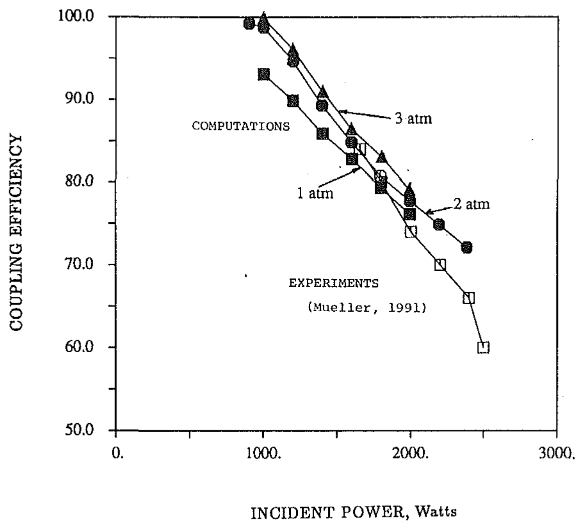

Fig. 8(a) Variation of coupling efficiency with incident microwave power. Darkened markings show present computational results, open markings show experimental data for a rectangular waveguide from Mueller (1991).

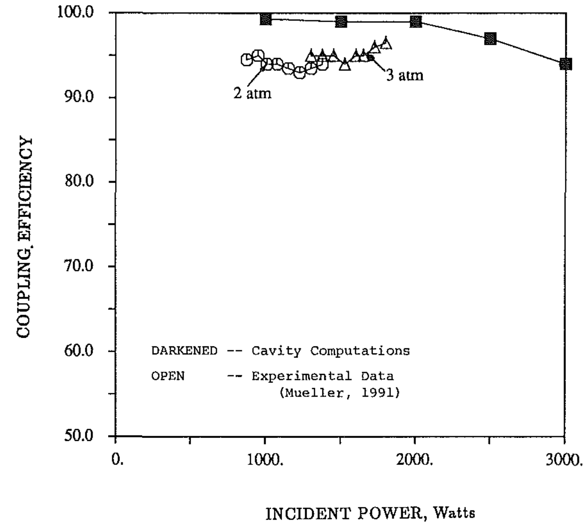

Fig. 8(b) Variation of coupling efficiency with incident microwave power. Darkened markings show computational results when the circular waveguide is modelled as a cavity. Open markings show experimental results for the circular waveguide from Mueller (1991).

from the rectangular waveguide experiments of Mueller and Micci (1989) are shown on the same figure (Fig. 8(*a*)). Even though these results are for a different geometric configuration, it is encouraging to see that the trends are qualitatively the same.

In Fig. 8(*b*), the experimental results with the circular waveguide are shown. Here, the coupling efficiency is nearly independent of the power level and is between 90 and 100 percent between 1 and 2 kW. This trend is completely different from those evidenced in Fig. 8(*a*). In fact, the circular waveguide appears to behave more like a resonant cavity than a waveguide. A close look at the experimental set-up in Fig. 4 reveals why this is the case. At the top of the waveguide, the microwaves are introduced through a coaxial probe which covers only a portion of the waveguide inlet. The rest of the inlet surface is covered by conducting material which causes power reflection at the surface. Consequently, the power that is reflected upward by the plasma is partly reflected back toward the plasma. Such reflections may take place continually until the radiation is absorbed by the plasma. In other words, the microwaves in the circular waveguide of Fig. 3 make multiple passes through the plasma much like in a resonant cavity.

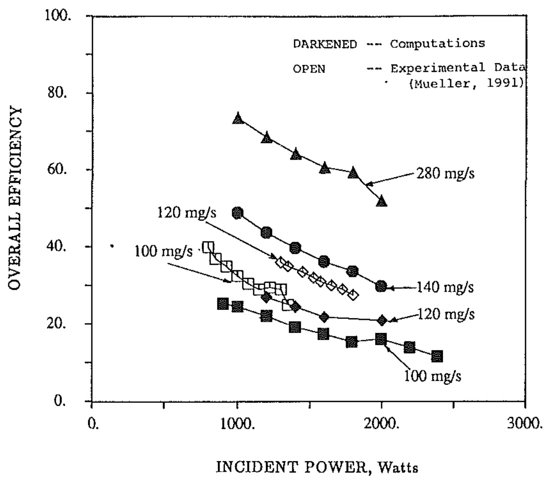

Fig. 9 Variation of overall efficiency with incident microwave power. Darkened markings are computational results. Open markings are experimental data from Mueller (1991).

In order to test the above hypothesis, the computations were repeated by changing the inlet boundary condition of the waveguide to accommodate a coaxial inlet probe. The results of these computations are also plotted on Fig. 8(*b*) and are fairly similar to the experimental results. The coupling efficiencies at powers of 1 to 2 kW are as high as 98 percent but decrease slightly at powers higher than 2.5 kW. This behavior is typical of cavity plasmas because as the power increases, the microwave plasma grows larger—after a point, the geometry of the configuration prevents further growth and the plasma starts reflecting more power (Venkateswaran and Merkle, 1991). It should be pointed out here that the results in Fig. 8(*b*) were obtained by tuning the length of the waveguide for maximum absorption (which is the resonant cavity length). In the experiments, similar tuning was achieved by adjusting the axial location of the inlet coupling probe. Therefore, while the present configuration possesses attractive absorption characteristics, it lacks the simplicity of a pure waveguide set-up (with no moving parts). Since the objective of the research is to study the feasibility of using waveguide plasmas for a propulsive device, we go back to our original configuration in the remainder of the paper and carry out estimates of the overall performance of the device.

Overall Thermal Efficiency. Once the plasma absorbs the radiation, it loses energy to the surroundings by conduction and radiation. It is, therefore, important to check how much of the energy is actually retained by the gas. The overall thermal efficiency is defined as the total energy in the gas at the exit section of the flow tube divided by the incident power. By definition, it will be less than the coupling efficiency by exactly the amount of energy that is lost to the side walls and the bluff body. Figure 9 presents experimental and computational estimates of the overall thermal efficiency versus incident power at various representative flow rates. Increasing mass flow rate (either by increasing pressure or flow velocity) increases Reynolds number, decreases thermal diffusion, reduces plasma size and thereby increases the thermal efficiency. The overall efficiency is also seen to decrease as we go to higher powers. This is because, at higher powers, the plasma grows larger which results in greater heat losses to the surroundings. Both experiments and computations reveal these trends although the computations underpredict the efficiencies somewhat. This is probably due to the differences in the two geometries that have been discussed earlier. We will see in the next section that 140 mg/s represents an optimum mass flow rate for the device. At this condition, the overall thermal efficiency is predicted to be about 40 to 50 percent.

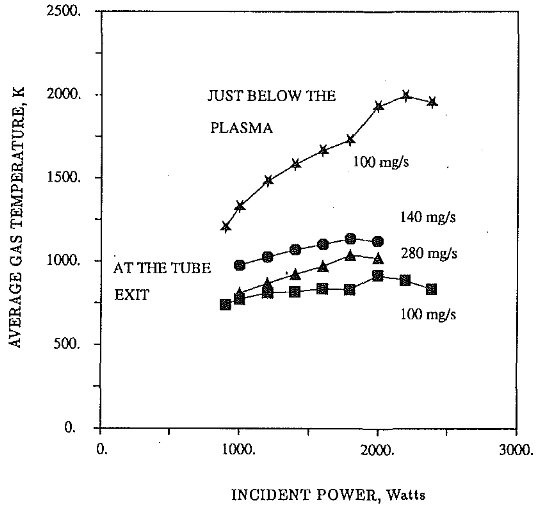

Fig. 10 Average gas temperature versus incident microwave power

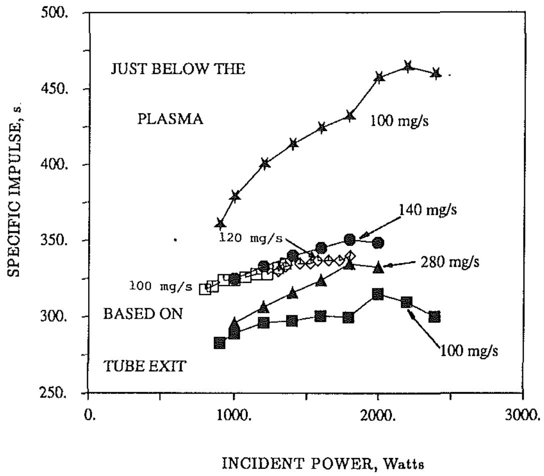

Fig. 11 Specific impulse versus incident microwave power. Darkened markings are present computational results. Open markings are experimental data from Mueller (1991).

Average Gas Temperatures. It is important to ensure that the incident radiation is absorbed efficiently and retained by the gas. It is also important to check how much the gas is heated by the radiation—in other words, the temperature to which the gas is heated. We have already seen that the peak gas temperature that occurs within the plasma core is typically between 900 and 10000K and is generally invariant to changes in operating conditions. The peak gas temperature is a useful parameter for characterizing plasmas, however, the average temperature is more important since it determines the performance of the thruster. The higher the average gas temperature the higher the specific impulse (which is the thrust per unit weight flow rate of propellant) of the thruster. Because of the highly two-dimensional nature of the plasma, the peak gas temperature is not very indicative of the average gas temperature. Figure 10 shows the average gas temperatures obtained from the computations as a function of power and mass flow rate. In all but one of the curves, the average temperatures were estimated at the exit of the flow tube. At the tube exit, the average temperatures are only about 700 to 1000 K, which are much lower than the peak plasma temperatures. At low flow rates (100 mg/s), the thermal diffusion losses from the plasma are quite large causing the gas to cool down considerably. Moderate increases in flow rate reduces these diffusion losses and the average temperature increases until it reaches an optimum (at 140 mg/s). Further increases in mass flow rate result in cooling down of the gas because the reduction in heat losses is now more than offset by the larger mass that is being heated by the plasma.

The average gas temperature is only about 1000 K even at the optimum mass flow rate and it is unlikely to provide very good performance in practice. The reason for the low gas temperatures is the location of the plasma relative to the tube exit. The plasma is located too high up in the tube and the gas cools down considerably by the time it reaches the exit section. To show this effect, a representative curve showing the average gas temperature obtained immediately below the plasma is also shown in Fig. 10. Now, the gas temperature is higher ranging from 1500 to 2200 K. Clearly, it is desirable to locate the nozzle throat as close to the plasma as possible to get the best performance of the device. As mentioned earlier, it is possible to control the location of the plasma by proper positioning of the reflecting end-wall of the waveguide. Unfortunately, in the experimental configuration shown in Fig. 3, such a flexibility was not provided. Consequently, as discussed in the next section, the experimental estimates of specific impulse were very low. Current experiments are concentrated on adapting the circular waveguide configuration to maximize the performance of the device.

Specific Impulse and Thrust. Finally, to get an idea of the performance that the waveguide plasma device is capable of delivering, we carry out simplified estimates of the specific impulse and thrust. We calculate these quantities based on the average gas temperatures given earlier and assuming isentropic expansion to vacuum. Accordingly, the specific impulse varies as the square-root of the average gas temperature while the thrust is the mass flow rate times the exhaust velocity. Figure 11 shows computed specific impulse as well as the experimental estimates. There is fairly good agreement between the two with the computations slightly underpredicting the magnitudes. The results show that the specific impulse is only about 350 s when the average temperatures are taken at the tube exit. When the calculations are based on the average temperatures obtained just below the plasma, the Isp increases to about 480 s. While this is an improvement, current chemical combustion systems can also provide Isp's in that range. In contrast, the results from the study of resonant cavity plasma devices (Balaam and Micci, 1991, Venkateswaran and Merkle, 1991) showed that Isp's up to about 600 s may be attained with that configuration. Clearly, the feasibility of waveguide heated propulsion and of microwave propulsion, in general, depends on whether higher performance can be attained. Operating efficiently at high microwave power levels and the proper optimization of the flow rate in the device are key to achieving this. The design and development of new microwave configurations with high performance capability will be an important aspect of microwave propulsion research in the following years.

In Fig. 12, similar results are shown for the thrust of the device. Again, there is fairly good agreement between the computations and the experiments pointing to the applicability of the computational model to the analysis of these propulsion systems.

Conclusions

A two-dimensional model involving the coupled solution of the Navier-Stokes equations and the Maxwell equations has been developed to model microwave plasmas heated in a waveguide setup. An implicit time-marching technique is used to solve the Navier-Stokes equations while the Maxwell equations are solved in an explicit fashion. The geometry used in the computations is similar to that used in experiments. The boundary conditions on the waveguide are extremely important; the specification of the proper method of characteristics

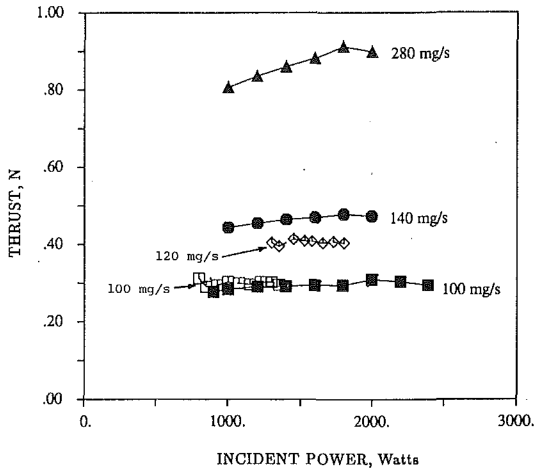

Fig. 12 Thrust versus incident microwave power. Darkened markings are computational results. Open markings are experimental data from Mueller (1991).

boundary condition enables us to treat the waveguide inlet and exit with physically meaningful conditions. For a waveguide, the inlet is generally a purely transmitting surface. Two kinds of exit boundary conditions are imposed on the waveguide—transmitting and reflecting. The transmitting condition sets up a purely propagating mode in the waveguide while the reflecting condition sets up a standing wave mode. Along with this reflecting exit condition, when the inlet end is also treated with a reflecting condition (with provision for coupling in the microwave power with a coupling probe), then the configuration becomes identical to a resonant cavity set-up.

In our computations, all three configurations—the transmitting waveguide, the reflecting waveguide and the resonant cavity—are studied and contrasted in terms of plasma stability and energy coupling efficiencies. Our results show that the transmitting waveguide cannot maintain plasmas stably at powers less than about 3 kW; on the other hand, both the reflecting waveguide and the resonant cavity indicate good plasma stability over a wide power range (down to about 800 W). This improved stability characteristic is because the standing wave mode provides a preferential location for the plasma while a purely transmitting wave does not. However, when it comes to coupling efficiency, the reflecting waveguide configuration does not perform as well as the cavity configuration. The reflecting waveguide gives high coupling efficiencies at low powers (99 percent at 1 kW) with the efficiency dropping as power is increased (68 percent at 3.5 kW). At the higher powers, the plasma reflects a greater fraction of the incident power back toward the inlet through which it is transmitted out and lost from the system. In contrast, in a resonant cavity, the reflected power is incident on a reflecting surface and directed back toward the plasma multiple times. Because of these multiple passes, the cavity plasma shows high coupling efficiencies (up to 98 percent) over a wider range of powers provided the length of the cavity is properly tuned. Both the stability and absorption characteristics mentioned above have been observed in experiments with waveguides and resonant cavities.

Performance estimates of the waveguide plasma device show that the gas is cooled considerably by the time it reaches the exit of the flow tube. Average temperatures at the exit section range from 700 to 1000 K. Corresponding specific impulses are about 300 to 350 s. Experimental estimates yield similar results. Better performance is indicated when performance estimates are based on the conditions just below the plasma. The average gas temperatures now go up to about 2200 K and the corresponding specific impulses go up to about 500 s. These numbers are competetive with existing chemical systems but better performance is necessary to justify the development of a new technology for propulsion. Typically, the target with electrothermal systems is in the range of 800 to 1200 s. Evidently, there is need for further research to study configurations that are designed to maximize performance. In particular, it is necessary to achieve high power to mass flow ratios in the device and to locate the plasma proximate to the nozzle throat. Both these factors will contribute toward higher average gas temperatures and, thus, yield better performance.

Acknowledgment

This work was sponsored by the Air Force Office of Scientific Research under Contract Number 89-0312.

References

Balaam, P., and Micci, M. M., 1989, "Investigation of Free-Floating Nitrogen and Helium Plasmas Generated in a Microwave Resonant Cavity," AIAA Paper 89-2380, 25th AIAA/ASME Joint Propulsion Conference, Monterey, CA, July.

Balaam, P., and Micci, M. M., 1990, "The Stabilization and Spectroscopic Study of Microwave Generated Resonant Cavity Plasmas," AIAA Paper 90-2635, 21st AIAA/DGLR/JSASS International Electric Propulsion Conference, Orlando, FL, July.

Deininger, W. D., et al., 1990, "30-kW Ammonia Arcjet Technology," Final Report, July 1986–Dec. 1989, JPL Publication 90-4, Feb.

Douglas, J., and Gunn, J. E., 1964, "A General Formulation of Alternating Direction Method—Part I—Parabolic and Hyperbolic Problem," *Numerische Mathematik*, Vol. 82, pp. 428–453.

Gandhi, Om. P., 1981, *Microwave Engineering and Applications*, Pergamon Press.

Hawley, M. C., Asmussen, J., Filpus, J. W., Whitehair, S., Hoekstra, C., Morin, T. J., and Chapman, R., 1989, "Review of Research and Development on the Microwave Electrothermal Thruster," *Journal of Propulsion*, Vol. 5, No. 6, Nov.–Dec., pp. 703–712.

Herlan, W. A., and Jassowski, D. M., 1987, "Microwave Thruster Development," AIAA Paper 87-2123, 23rd AIAA/SAE/ASME Joint Propulsion Conference, San Diego, CA, June.

Merkle, C. L., and Choi, Y-H., 1987, "Computation of Low-Speed Flow with Heat Addition," *AIAA Journal*, Vol. 25, Jun, pp. 831–838.

Micci, M. M., 1984, "Prospects of Microwave Heated Propulsion," AIAA Paper 84-1390, 20th AIAA/SAE/ASME Joint Propulsion Conference, Cincinnati, OH, June.

Mueller, J., and Micci, M. M., 1989, "Investigation of Propagation Mechanism and Stabilization of a Microwave Heated Plasma," AIAA Paper 89-2377, 25th AIAA/ASME Joint Propulsion Conference, Monterey, CA, July.

Mueller, J., and Micci, M. M., 1990, "Microwave Electrothermal Thrusters Using Waveguide Heated Plasmas," AIAA Paper 90-2562, 21st AIAA/DGLR/JSASS International Electric Propulsion Conference, Orlando, FL, July.

Mueller, J., 1991, "Proof of Concept Study and Performance Evaluation of a Microwave Electrothermal Thruster Using Waveguide Modes," Ph.D. dissertation, Dept. of Aerospace Engineering, Penn State, Aug.

Raizer, Yu. P., 1977, *Laser Induced Discharge Phenomena*, Vases, G. C., and Pietrzyk, Z. A., eds., Consultants Bureau, NY.

Rhodes, R., and Keefer, D. R., 1989, "Numerical Modelling of a Radio Frequency Plasma in Argon," *AIAA Journal*, Vol. 27, No. 12, Dec., pp. 1779–1784.

Sovey, J. S., Hardy, T. L., and Englehart, M. A., 1986, "A Bibliography of Electrothermal Thruster Technology 1984," NASA Technical Memorandum 86998.

Venkateswaran, S., and Merkle, C. L., 1991, "Numerical Investigations of Bluff Body Stabilized Microwave Plasmas," AIAA Paper 91-1503, 22nd Fluid Dynamics, Plasma Dynamics and Lasers Conference, Honolulu, Hawaii, June.

Warming, R. F., and Beam, R. M., 1978, "On the Construction and Application of Implicit Factored Schemes for Conservation Law," *SIAM-AMS Proceedings*, Vol. 11, pp. 85–129.

Welle, R., Keefer, D. R., and Peters, C. E., 1987, "Laser Sustained Plasmas in Forced Convective Argon Flow, Part I: Experimental Studies," *AIAA Journal*, Vol. 25, Aug., pp. 1093–1099.

Yee, K. S., 1966, "Numerical Solution of Initial Boundary Value Problems Involving Maxwell's Equations in Isotropic Media," *IEEE Transactions on Antennas and Propagation*, AP-14, May, pp. 302–307.

V. M. Fthenakis
Research Chemical Engineer,
Brookhaven National Laboratory,
Bldg. 490D,
Upton, NY 11973

K. W. Schatz
Engineering Consultant,
Mobil Research and Development Corp.,
Princeton, NJ 08540

U. S. Rohatgi
Scientist,
Brookhaven National Laboratory,
Upton, NY 11973

V. Zakkay
Professor,
Department of Applied Science,
New York University, NY 10003

Computation of Flow Fields Induced by Water Spraying of an Unconfined Gaseous Plume

Flow fields induced by the interaction of water sprays and a gaseous plume have been studied in the context of absorbing and dispersing an accidental release of toxic gas in the air. The effectiveness of water sprays in absorbing highly water soluble gases was recently demonstrated in extended laboratory and field tests. In this paper, computer simulations are presented of the Hawk, Nevada Test Site, series of water spray/HF mitigation field tests. The model used, HFSPRAY, is a Eulerean/Lagrangian model which simulates the momentum, mass and energy interactions between a water spray and a turbulent plume of HF in air; the model can predict the flow velocities, temperature, water vapor, and HF concentration fields in two-dimensional large-geometries for spraying in any direction, (i.e., down-flow, inclined-down-flow, up-flow, and co-current horizontal flow). The model was validated against recent data on spraying of water on large releases of HF. It can provide a direct input to the design of water spray systems for HF mitigation.

1 Introduction

Releases of hydrofluoric acid (HF) can be effectively controlled in the field by absorption using water sprays (Blewitt et al., 1987; Schatz and Koopman, 1989). The feasibility of this control option also was studied theoretically (Fthenakis, 1989; Fthenakis and Zakkay, 1990). In this paper, we discuss the results of modeling the Hawk field tests, which were conducted at the DOE Nevada Test Site in 1988, under the auspices of the Industry Cooperative HF Mitigation/Assessment Program (Schatz and Koopman, 1989). The model used in these simulations, HSPRAY, is based on the PSI-Cell Computer code (Crowe et al., 1977), which is an extension of the TEACH code (Gosman and Pun, 1973).

2 Description of Model

The HFSPRAY model comprises two sets of equations, one describing the gas-phase, and the other describing the drop-phase. The gas-phase is modeled, by an Eulerean approach, as a continuous fluid with properties changing with distance, in two-dimensional coordinates. The gas-phase equations include the continuity and Navier-Stokes equations, species conservation equations for hydrogen fluoride and water, and the energy conservation equation. Turbulent flow is approximated by the equation of laminar flow with effective properties (i.e., viscosity, thermal conductivity, and diffusivity) which vary from place to place. The effective viscosity, and implicitly the other effective properties, are calculated from the equations of turbulence kinetic energy (κ), and rate of dissipation (ϵ), of the kinetic energy, using the standard κ-ϵ sub-model of Launder and Spalding (1972). The κ-ϵ approach has been selected over the simpler mixing length approach, because the first is not limited by length scale and has been successfully applied to recirculating flows.

The liquid-phase is modeled according to a Lagragian approach by considering a finite number of particles of varying size and trajectory (Crowe et al., 1977). The Lagrangian approach is a convenient and accurate method of computing interfacial mass, momentum and energy transfer at the droplet surface as the droplets transverse the continuous phase. With this approach the change of drop size and direction of movement is described.

2.1 Gas-Phase Equations

Conservation of Mass

$$\frac{\partial}{\partial x}(\rho u)+\frac{\partial}{\partial y}(\rho v)=\Gamma$$

where Γ is the change in the mass of the drops per unit volume and unit time.

Conservation of Momentum

x-component

$$u\frac{\partial}{\partial x}(\rho u)+v\frac{\partial}{\partial y}(\rho u)=-\frac{\partial P}{\partial x}+2\frac{\partial}{\partial x}\left(\mu_e\frac{\partial u}{\partial x}\right)+\frac{\partial}{\partial y}\left(\mu_e\left(\frac{\partial u}{\partial y}+\frac{\partial v}{\partial x}\right)\right)-\frac{2}{3}\frac{\partial}{\partial x}\mu_e\left(\frac{\partial u}{\partial x}+\frac{\partial v}{\partial y}\right)+F_x$$

Contributed by the Fluids Engineering Division of THE AMERICAN SOCIETY OF MECHANICAL ENGINEERS and presented at the Winter Annual Meeting, Symposium on Fluids Mechanics of Sprays, Atlanta, GA, December 5, 1991. Manuscript received by the Fluids Engineering Division April 27, 1992; revised manuscript received December 28, 1993. Associate Technical Editor: O. C. Jones.

y-component

$$u\,\frac{\partial}{\partial x}(\rho v)+v\,\frac{\partial}{\partial y}(\rho v)=-\frac{\partial P}{\partial y}+2\,\frac{\partial}{\partial y}\left(\mu_e\,\frac{\partial v}{\partial y}\right)$$

$$+\frac{\partial}{\partial x}\left(\mu_e\left(\frac{\partial u}{\partial y}+\frac{\partial v}{\partial x}\right)\right)-\frac{2}{3}\,\frac{\partial}{\partial y}\,\mu_e\left(\frac{\partial u}{\partial x}+\frac{\partial v}{\partial y}\right)+\rho g+F_y$$

The 2/3 ∇u terms are included in the Navier–Stokes equations to describe the mixing of HF with air. F_x and F_y are the components of the total force from the drops, per unit volume. These forces consist of interfacial drag only; the momentum transfer due to fast mass transfer through the interface, is taken into account by correcting the drag coefficient according to the film theory outlined in Bird et al. (1960). The spatial distribution of these force components is obtained from the solution of the drop-phase equations.

κ-ϵ *turbulence model*

$$\frac{\partial}{\partial x}(\rho u\kappa)+\frac{\partial}{\partial y}(\rho v\kappa)=\frac{\partial}{\partial x}\left(\frac{\mu_e}{\sigma_\kappa}\,\frac{\partial\kappa}{\partial x}\right)+\frac{\partial}{\partial y}\left(\frac{\mu_e}{\sigma_\kappa}\,\frac{\partial\kappa}{\partial y}\right)+G-\rho_e$$

$$\frac{\partial}{\partial x}(\rho u\epsilon)+\frac{\partial}{\partial y}(\rho v\epsilon)=\frac{\partial}{\partial x}\left(\frac{\mu_e}{\sigma_\epsilon}\,\frac{\partial\epsilon}{\partial x}\right)+\frac{\partial}{\partial y}\left(\frac{\mu_e}{\sigma_\epsilon}\,\frac{\partial\epsilon}{\partial y}\right)+\frac{C_1\epsilon G}{\kappa}-\frac{C_2\rho\epsilon^2}{\kappa}$$

From κ and ϵ, the effective viscosity is determined from the Prandtl-Kolmogorov formula.

$$\mu_e=C\mu\,\frac{\rho\kappa^2}{\epsilon}$$

$$G=2\mu_e\left[\left(\frac{\partial u}{\partial x}\right)^2+\left(\frac{\partial v}{\partial y}\right)^2\right]+\mu_e\left(\frac{\partial u}{\partial y}+\frac{\partial v}{\partial x}\right)^2$$

G is the rate of generation of κ due to Reynolds stresses, $\rho\epsilon$ is the rate of dissipation of κ, and σ_κ, σ_ϵ, C_1, C_2, and $C\mu$ are empirical constants.

Conservation of Species

$$\frac{\partial}{\partial x}(\rho uY_i)+\frac{\partial}{\partial y}(\rho vY_i)=\frac{\partial}{\partial x}\left(\rho D_{ei}\,\frac{\partial Y_i}{\partial x}\right)+\frac{\partial}{\partial y}\left(\rho D_{ei}\,\frac{\partial Y_i}{\partial y}\right)-W_i$$

The sum of W_i terms in the species equations is equal to the source term, Γ, of the continuity equation.

Conservation of Energy

$$\frac{\partial}{\partial x}(\rho uT)+\frac{\partial}{\partial y}(\rho vT)=\frac{\partial}{\partial x}\left(\frac{k}{c_{pg}}\,\frac{\partial T}{\partial x}\right)+\frac{\partial}{\partial y}\left(\frac{k}{c_{pg}}\,\frac{\partial T}{\partial y}\right)+Q$$

where k is the thermal conductivity and Q is the term representing rate of heat exchange with drops in a unit volume.

Equation of State. Substitution of expressions for mixture molecular weight in the ideal gas law results in:

$$\frac{\rho}{\rho_0}=\frac{T}{T_0}\,\frac{18\,M_{\mathrm{HF}}}{(18+11\,y_w)\,(M_{\mathrm{HF}}+(29-M_{\mathrm{HF}})y_{\mathrm{HF}})}$$

The above equations are solved with wall, no-slip conditions on the floor, and either wall or free-stream conditions at the top boundary.

2.2 Droplet-Phase Equations

Momentum Transfer. Drop trajectories are considered explicitly from the equations of motion (Crowe et al., 1977). The drag coefficients in these equations are calculated by the following relationships (Beard and Pruppacher, 1971):

$$C_{Ds}=(24/\mathrm{Re})(1+0.11\ \mathrm{Re}^{0.81})\qquad\text{for Re}<21$$

$$C_{Ds}=(24/\mathrm{Re})(1+0.189\ \mathrm{Re}^{0.632})\qquad\text{for }21<\text{Re}<400$$

For Re numbers greater than 400, Buzzard's and Nedderman's (1967) experimental data are used. These coefficients were adjusted for multiple drops, as described below.

Mass Transfer. The mass sink terms in the gas-phase equations are determined from calculations based on an individual drop. The molar flux of a gas A passing through the surface of a drop is denoted by N_A where

$$N_A=K_g(Y-Y^*)$$

and the amount of gas A absorbed by a drop of diameter d during its time of passage (Δt) through the reference volume is

$$w=\pi d^2\int_0^{\Delta t}K_g(Y-Y^*)dt$$

where the superscript * indicates phase equilibrium conditions. K_g is the overall mass transfer coefficient based on the gas-phase, which is related to the individual gas and liquid mass-transfer coefficients, k_g and k_1, by:

$$K_g=1/k_g+H^*/k_1$$

where H^* is a pseudo-Henry's law coefficient accounting for the totality of dissolved species (Fthenakis, 1989); k_g is estimated from the Ranz-Marshall relationship for the Sherwood number, and k_1 from Angelo et al.'s model (1966).

Nomenclature

C_D = drop drag coefficient
C_{Ds} = single drop drag coefficient
c_{pg} = gas-phase specific heat
d = drop diameter
D_{ei} = effective diffusivity of species i
F = interfacial momentum transfer per unit volume
HF = hydrogen fluoride
H_2O = water
h_g = latent heat for water evaporation
h_{HF} = heat of solution for HF(g) + H_2O mixing
K_g = overall mass transfer coefficient based on the gas-phase
k = thermal conductivity
m = drop mass
m_{HF} = drop absorption rate of HF
m_w = drop evaporation rate
M = molecular weight
Nu = Nusselt number
Pr = Prandtl number
Re = Reynolds number
Sc = Schmidt number
T = drop temperature
T_g = gas-phase temperature
u = horizontal velocity
v = vertical velocity
V = drop volume
W_i = sink term representing absorption or evaporation per unit volume
y = mass fraction
Y = molar fraction
κ = turbulent kinetic energy
μ_e = effective viscosity
ϵ = rate of dissipation of κ
ρ = density
θ = gas-phase void fraction (volume fraction occupied by drops)

Subscripts

d = droplet phase
i = species H_2O, HF
HF = hydrogen fluoride
H2O = water vapor
x = horizontal direction
y = vertical direction
w = water vapor
0 = denotes reference conditions for dry air

The term W is the total absorption by all drops in the reference volume and is estimated from the double sum over trajectory segments and drops in each segment.

$$W = \sum_{i}^{nt} \sum_{j}^{np} w_{i,j}$$

The build-up of average concentration of the dissolved fluorides into the drop is determined from

$$C_A \bigg|_0^{\Delta t} = \frac{w}{V} \Delta t$$

where $V = \pi d^3/6$

Energy Transfer. The energy equation for a single drop can be written as:

$$mC_p \frac{dT}{dt} = \mathrm{Nu} k \pi d (T_g - T) - m_w h_g - m_{\mathrm{HF}} h_{\mathrm{HF}}$$

where

m	is the drop, mass, m_w the drop evaporation rate,
m_{HF}	the drop absorption rate of HF
h_g	latent heat for water evaporation
h_{HF}	heat of solution for $\mathrm{HF(g)} + \mathrm{H_2O}$ mixing
T	is the drop temperature, and
T_g	is the gas-phase temperature

The equations describing the HF-$\mathrm{H_2O}$ thermodynamics and chemical association are described elsewhere (Fthenakis, 1991)

2.3 Multiple Drop Analysis. Analysis at a micro-scale level (i.e., one drop) gave us relationships that can be used in the aggregated macro-level system. However, single-drop relationships, cannot be used a priori. These relationships assume that the drops do not perturb the flow velocity field, which is a reasonable assumption for studies of gas scavenging by rain, but not for spray systems.

Two separate regions of flow were considered, where drop-gas-drop interactions can change the momentum, mass, and energy transfer coefficients predicted by single-drop relationships. These regions are (*i*) near the nozzle at high flow rates of water, (dense spray) when the drops occupy a significant fraction, θ, of the volume of the gas-phase (e.g., $\theta > 0.05$) and the trajectories are close to each other, and (*ii*) farther away from the nozzle where drop trajectories are separated and we need only to consider the effect of drops following each other in a line. In the first region the following relationships (O'Rourke, 1981) are used to adjust the transport coefficients; these equations lead to the standard single drop equations as θ goes to zero.

$$\frac{C_D}{C_{DS}} = 1 + 3.5\,\theta$$

$$\mathrm{Sh} = 2(1-\theta)^{-1.75} + 0.6 \left(\frac{\mathrm{Re}}{1-\theta}\right)^{1/2} \mathrm{Sc}^{1/3}$$

$$\mathrm{Nu} = 2\,(1-\theta)^{-1.75} + 0.6 \left(\frac{\mathrm{Re}}{1-\theta}\right)^{1/2} \mathrm{Pr}^{1/3}$$

Such adjustments have been found to be significant in regions near the nozzle, for the highest flow rates of water used in these simulations.

In the rest of the region the population of the drops is small and the drops follow each other on trajectories. Then the motion of the gas induced by the preceding drops can reduce the resistance to the movement of the following drops. Ramachandran (1985) proposed relationships correlating a decline in C_{Ds} with the size of the drop and with drop-to-drop distance. According to his relationships a maximum decline of 30 percent can occur for drops of 300 μm. As the sprays considered in this study generate drops mostly in the 100–200 μm range, we adopt a 15 percent reduction in the drag coefficient due to this effect.

3 Model Verification With the Data From Hawk Field Tests

An ad hoc Industry Cooperative HF Mitigation/Assessment Program, sponsored and funded by 20 U.S. companies produced, in June 1989, a series of laboratory and field data on the mitigation of HF releases by water sprays. The field series, called the Hawk HF Test series, included 87 tests carried out in a flow chamber at the Nevada Test Site outside Mercury, Nevada. The chamber was 8 ft wide, 16 ft high, and 140 ft long and had a wind screen, inlet funnel, flow straightener and turbulence grid to achieve even flow and turbulence. Tests were done by releasing the acid horizontally, typically at a rate of 2 to 5 gpm for 10 minutes, through an orifice in the front section of the chamber. A water curtain with 8 nozzles sprayed water perpendicularly on the acid jet. In other tests, the interaction was counter-current with a single monitor downwind of the HF release. Acidic water, formed by the interaction of HF and water spray, was collected in containers below the chamber. The efficiency of removal of HF was calculated from concentration and volume measurements of the acidic water, and from air samples.

The model estimates were compared with data from the 87 field tests covering down-flow, upflow and counter-current horizontal flows, and variations of the following parameters: 1) water flow, 2) drop size, 3) distance of spray header, 4) elevation of spray, 5) wind speed, 6) humidity, 7) pressure in HF storage, and 8) angle of spray (narrow vs wide). The model predictions agree within ±6 percent with most of the field data and they also match the visual observations in the field (Schatz and Koopman, Vol I, 1989, pp. 155–163).

The Hawk field tests were simulated by a two-dimensional configuration, in a plane that represents the downwind and height dimensions (Fig. 1). The grids of the numerical solution were sufficiently fine to result in (*i*) solutions which are insensitive to further reductions of the grid size, and (*ii*) small mass errors (typically <3 percent based on the continuity). To simulate counter-current monitor flow, a 60×60 grid was sufficient, whereas in down-flow simulations at high rates of water flow, the strong turbulence induced close to the floor necessitated finer grids (e.g., 80×90) (see Section 4. on sensitivity analysis). Convergence was easier to obtain by iterating for the velocity fields and energy fields decoupled from mass transfer, before going into the complete iteration cycle.

3.1 Inlet Boundary Conditions. In the simulations described herein, the heavy gas atmospheric dispersion model HFPLUME (McFarlane et al., 1990) was used to estimate the thickness and velocity of an HF jet released from a pressurized container; these values were used as inlet boundary conditions to HFSPRAY. Plume velocities between 3.6 and 7 m/s and wind velocities of 3 m/s and 6 m/s were used. The HF plume is assumed to initially spread across the whole width of the chamber, while maintaining its thickness and relative position in respect to the floor and the nozzles. In other words, the circular plume is represented two-dimensionally by a rectangular slab of height equal to the diameter of the plume and width equal to the chamber width; the initial HF concentration is then adjusted to match the actual inlet flow rate.

3.2 Drop Size Distribution. In a spray, drops can collide and either coalesce, break-up, or shatter into smaller drops. In the present application, coalescence is the most influential of these phenomena, as shown by an analysis of drop size distribution data (Fthenakis, 1991). From this analysis we con-

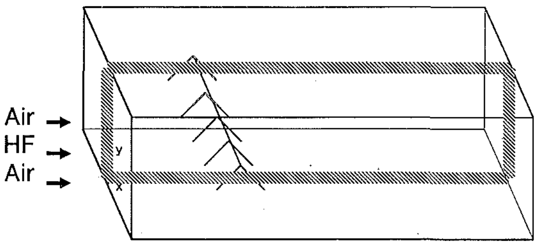

Fig. 1 Two-dimensional representation of the three-dimensional problem on a vertical slice

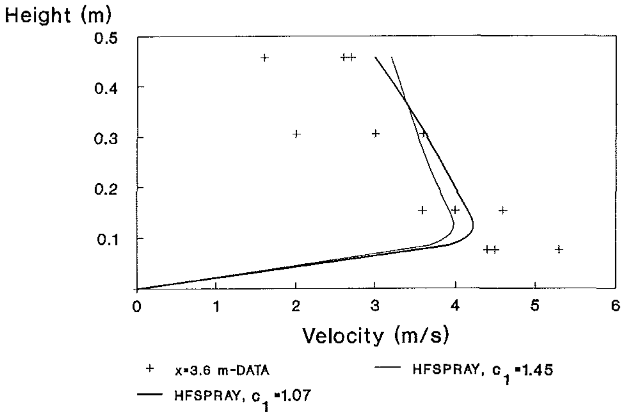

Fig. 2 Air entrainment velocities; comparison of data and values predicted for c_1 = 1.45 and $c_1 = 1.07$; down pointing TF16FCN nozzles at 3.25 m elevation

cluded that data on single nozzle drop-size, taken at a cross section 1 m away from the nozzle, closely represent the distribution of drop-size in the region where most of the interaction between drops and HF take place. In many of the simulations we present herein, the Sauter mean drop diameter was constant, although the drop size distributions were slightly different from one nozzle to another. It was important to use accurate drop-size distributions for each nozzle; using a mean drop size value instead of a drop distribution produced differences of up to 5 percent in the estimates of HF removal.

3.3 Air Entrainment. The rate of air entrainment into an 8-nozzle water curtain was estimated in the laboratory by measuring the velocity of air flowing out of the curtain at floor level. Velocity profiles for two sets of nozzles, at elevations of 3.25 m and 5.7 m from the floor, are given in Table E5-1 of volume III of Schatz and Koopman (1989). Comparisons of these data with values of velocities predicted by the model, are reported by Fthenakis (1991); a sample comparison is shown in Fig. 2.

The formulation described in Section 2, requires values of several empirical parameters. The standard values for these parameters are: $C_1 = 1.45$, $C_2 = 1.92$, $C_\mu = 0.09$, $\sigma_k = 1.0$, and $\sigma_\epsilon = 1.3$. However, this standard set does not always produce accurate results, specially for flows with adverse pressure gradients, wall curvature, recirculation and swirl as shown by Nallasamy (1987). There is some experimental evidence (Gore and Crowe, 1989) that drops in the spray also affect the turbulent intensity of the flow field. The flow regime expected in our application is complicated due to the interaction of the wall, HF jet and sprays with drops of different sizes, and it is difficult to assess the effect of these interaction on the turbulent stresses. The most common approach is to modify the source term in the equation for the dissipation rate (Leschziner and Rodi, 1981; Takemitsu, 1990; De Henau et al., 1990; Djilali et al., 1991). Our approach is also to modify the source term in the dissipation equation by selecting a value of C_1 which provides the best prediction of the air velocity profile. After numerical experimentation the value of C_1 chosen for this model was 1.07. Figure 2 shows a comparison of the predicted (for C_1 = 1.45 and $C_1 = 1.07$) and measured air velocities. Setting C_1 = 1.07 not only improved the fit to the air entrainment data but it also produced predictions of drop trajectories and plume lift which were closer to the field observations than the prediction of C_1 = 1.45. Setting C_1 equal to 1.07 leads to a reduction in the source term for the dissipation equation which follows the trend of the above reported studies. The value of the dissipation constant (σ_ϵ), was also changed since it is correlated to C_1 by $\sigma_\epsilon = \kappa^2/(C_2 - C_1)C_\mu^{0.5}$.

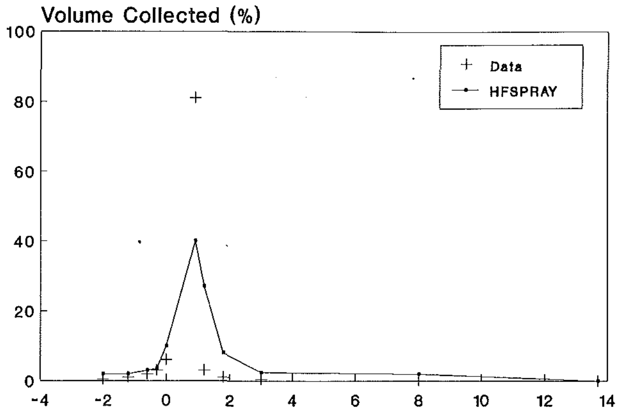

Fig. 3 Spray distribution from water collection; down pointing TF20FCN nozzles

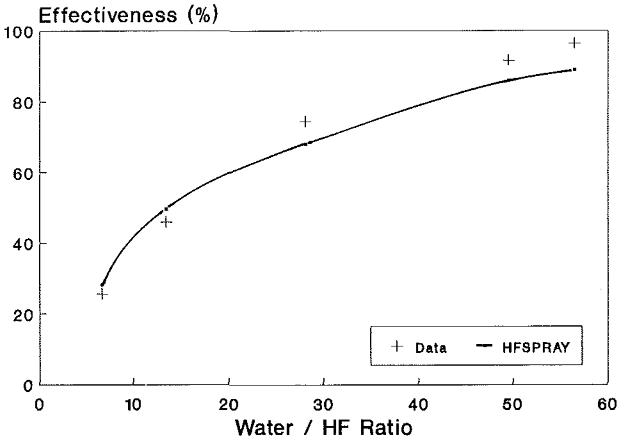

Fig. 4 Comparison of predicted effectiveness and measurements on the Hawk field tests (base case)

3.4 Estimates of Water Collection. The predicted distances and heights that drops travel within the chamber match the visual observations in the field. Also, the estimated quantities of water that drop out on the floor compare reasonably well with the field data on water collection; an example of these comparisons is shown in Fig. 3.

3.5 Base Case: Down-Flow of Sprays. The base case simulations refer to down-pointing sprays with a varying water/HF mass ratio; the HF flow rate was essentially constant here, while the water flow rate varied. Figure 4 shows the estimates of HF removal predicted by the model together with the corresponding experimental data; the estimates fit the data within 6 percent.

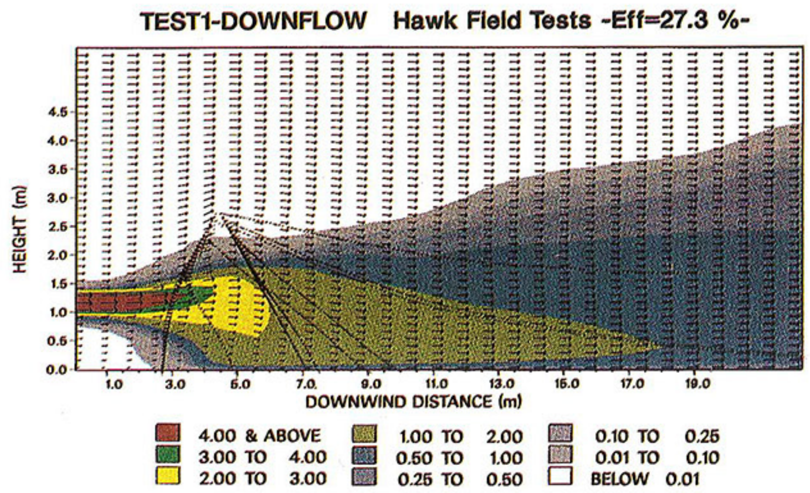

Fig. 5 Simulation of Hawk Field Test #1; shown are velocity vector fields, HF concentration (wt%) in color, and outer drop trajectories

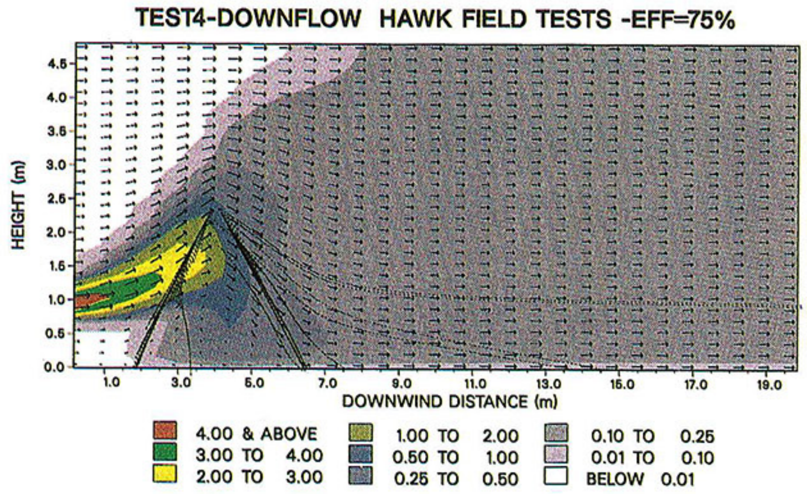

Fig. 6 Simulation of Hawk Field Test #4; shown are velocity vector fields, HF concentration (wt%) in color, and outer drop trajectories

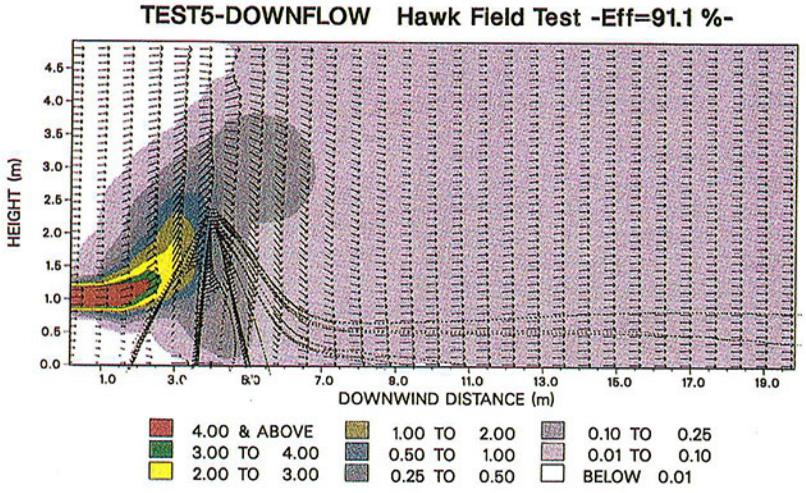

Fig. 7 Simulation of Hawk Field Test #5; shown are velocity vector fields, HF concentration (wt%) in color, and outer drop trajectories

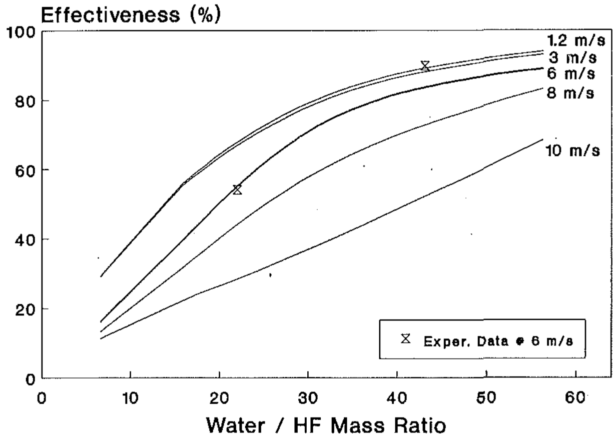

Fig. 8 The effect of wind speed variation on the effectiveness of HF removal

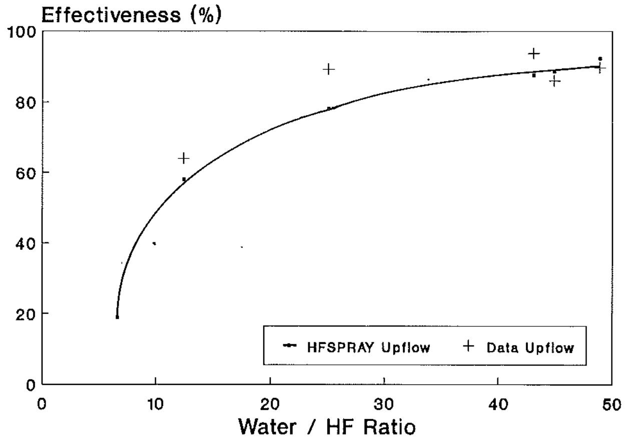

Fig. 9 Predicted effectivenss of HF removal in up pointing and down pointing nozzle configurations

Figures 5–7 display the predicted velocity vectors, the HF concentration contours, and the spray outer trajectories, for three different H_2O/HF ratios. The initial air velocity is 3 m/s, and the velocity of the HF plume varies from 3.6 to 5 m/s, depending on the HF flow rate. The zones between specific concentration contours (weight percent) are displayed in different shades. The plume enters at a uniform initial concentration of about 4 wt percent; the plots show its dilution down to 0.01 wt percent (approximately 100 ppm). The outer trajectories of all drop sizes are shown by dotted lines originating at height = 2.45 m and downwind distance = 4 m.

The model predicted a lifting of the plume in the upwind side of the spray, caused by pressure increase near the floor. On the downwind side of the spray, the droplets accelerate the flow in the horizontal direction along with transferring momentum towards the floor. This influence of the liquid spray on the gas phase is proportional to the liquid flow rate. Figures 5 to 7 display such interactions as the water flow rate increases. Figure 5 (Test 1) shows spraying at the lowest water flow used in the field (1.57 kg/s); in this simulation, very little lift is predicted at the spray region and a long plume is formed downwind of the spray. In the intermediate and high water flows (Tests 4 and 5), the HF plume encounters a recirculation zone just upstream of the spray, which enhances HF-air mixing. As the water flow increases, this recirculation becomes more intense and covers a larger region. In Test 4, (shown in Fig. 6) a higher water flow-rate (6.35 kg/s) lifts the plume upwind of the spray; a recirculation zone is induced within the spray region, which brings the plume down again and effectively mixes it with water. The higher the water flow, the more the HF plume is deflected upwards at the upwind side of the spray, and subsequently pulled down at the downwind side of the spray as more air is drawn in the spray. At the highest flow rates (Test 5: 12.5 kg/s; Fig. 7), increased recirculation induces a stronger floor jet and turbulence. The plume is lifted higher before it is trapped in the recirculation zone for effective scrubbing.

The fit of the model estimates at low and intermediate water flows (i.e., ratios) is better than the fit of the high ratio estimates (Fig. 4). For H_2O/HF Ratio = 64 the model predicts a 91 percent HF removal versus 96 percent measured in the field. According to field observations, in the high ratio tests (e.g., test #5) there was a dynamic effect above the spray nozzle, with the plume periodically being lifted to the ceiling and then collapsing down in to the spray region. This effect cannot be described by a steady-state model, such as HFSPRAY.

3.6 Wind Speed. As shown in Fig. 8, the model predicts a significant decline in the effectiveness of HF absorption with increasing wind speeds from 3 m/s to 10 m/s, whereas increases from 1.2 m/s to 3 m/s had a negligible effect. This decline of effectiveness with increasing wind speed is much more profound in low water-flow rates than in high ones. This effect happens because, at high water flows, the spray carries sufficient momentum to deflect and stop the HF plume, whereas in low flows the HF plume penetrates through the spray region.

3.7 Up-Flow of Sprays. The model estimates that more HF will be removed in upflow-spraying than in downflow at the same ratios and configurations (e.g., nozzle elevation, plume elevation) as in the field. The predicted trajectories, velocities, and concentration fields match very well with the visual field observations. The model fits well the low- and high-ratio data, but it underestimates the effectiveness by about 13 percent of the single data point at the intermediate ratio (Fig. 9). Figures 10 and 11 show the predicted velocity vectors, outer drop trajectories and concentration contours for different water flows (ratios 12.4 and 48.9, correspondingly). The spray nozzle is at 0.1 m off the floor. The outer trajectories of drops of 55, 110, 225, 450, and 700 microns are shown in this plot. The biggest drops reach a height of 2.5 m, penetrating through the plume, whereas the smaller ones start falling earlier. The HF plume flows horizontally and is lifted further downwind by thermal buoyancy and mixing.

In Test 23 (see Fig. 11), the highest water flows (12.5 kg/s) were used and more drops with a higher momentum are produced. The drops reach a height of about 4 m, and induce a strong recirculation zone near the spray's nozzle. The HF plume hits the spray and is reflected slightly downwards, inducing a lot of mixing in the spray region, with strong turbulence at the bottom of the plume; then, the HF plume flows higher, filling the chamber to the ceiling.

These results confirm that upflow is more effective (about 13 percent more) than downflow at the same flow rates and plume elevation. However, more parametric studies are required to determine the limits of the effectiveness of upflow. The effectiveness of upflow spraying is expected to be reduced with increasing nozzle-to-plume distance, to a greater extent than in downflow.

3.8 Counter-Current Flow of Sprays. In these simulations (Fig. 12), a narrow monitor sprays from 15 m downwind and is directed toward the point of release at 20 deg from the horizontal. An initial spray angle of 3 deg, and drop diameters of 1.2, 0.8, and 0.5 mm (mean size = 1 mm) were assumed. The drops travel up to a height of 3.8 m and then fall down on the plume close to the point of release; their spread at the top of the cloud is about 1 m. The 1.2 mm drops are not carried downwind, and practically all the absorption occurs in a narrow zone within 1 m from the point of release.

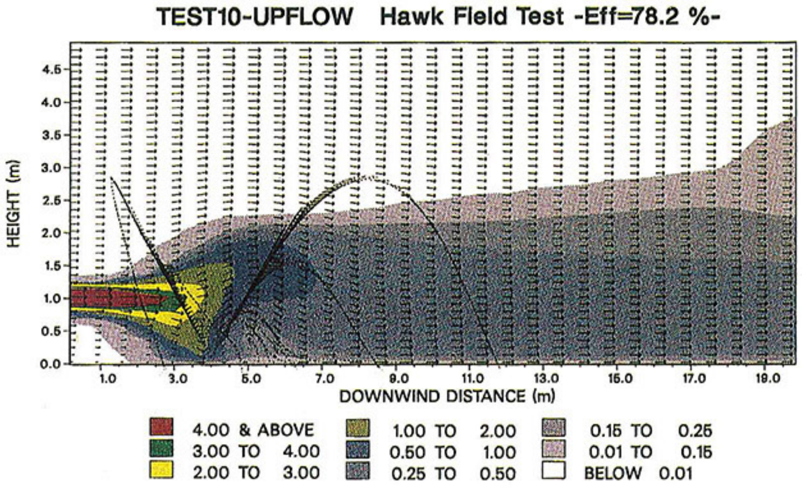
TEST10-UPFLOW Hawk Field Test -Eff=78.2 %-

Fig. 10 Simulation of Hawk test #10; spray nozzles on ground level pointing upward; shown are velocity vector fields, HF concentration (wt%) in color, and outer drop trajectories

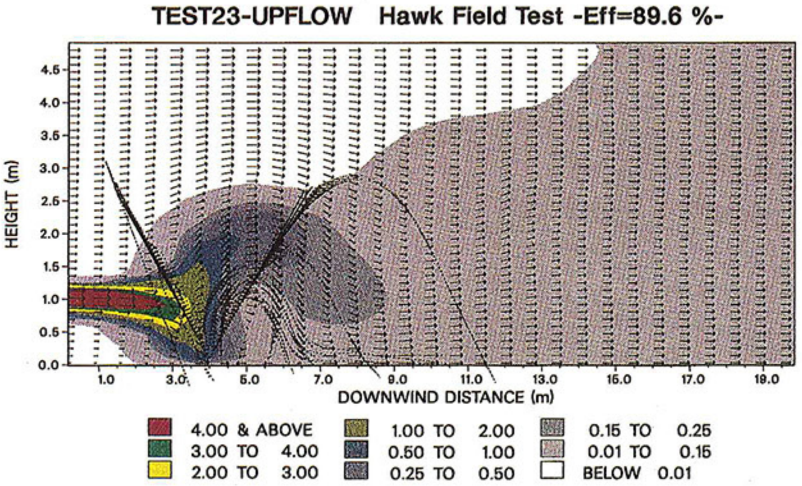
TEST23-UPFLOW Hawk Field Test -Eff=89.6 %-

Fig. 11 Simulation of Hawk test #23; spray nozzles on ground level pointing upward; shown are velocity vector fields, HF concentration (wt%) in color, and outer drop trajectories

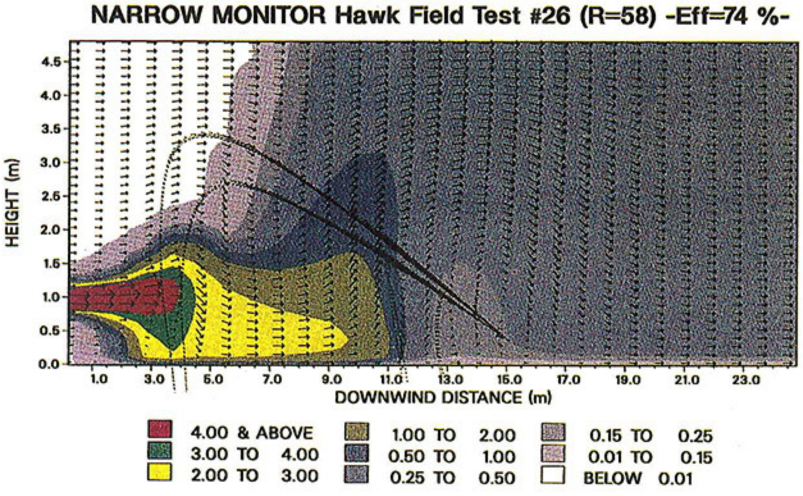
NARROW MONITOR Hawk Field Test #26 (R=58) -Eff=74 %-

Fig. 12 Simulation of Hawk test #26; monitor nozzle at $x = 15$ m, $y = 0.5$, spraying toward the incoming plume; shown are velocity vector fields, HF concentration (wt%) in color, and outer drop trajectories

Table 1 Sensitivity of predicted effectiveness (percent) to changes of grid size and number of trajectories

Grid Size:	20×20			40×40		40×60		60×90	
Trajectories #:	2	10	30	30	60	30	60	30	60
Upflow test #10:	56.	45.3	46.5	71.4	71.8	74.4	75.2	78.2	78.4
Monitor test #24:	18.	43.5	42.8			48.8	46.4	48.8	47.1

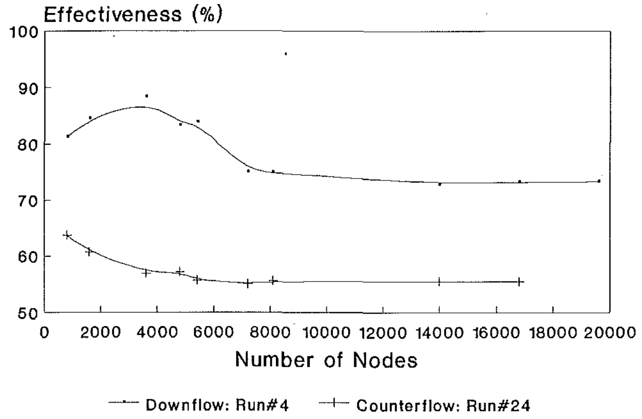

Fig. 13 Sensitivity analysis; effect of grid size on HF removal estimates

4 Sensitivity Studies

The effects of changing the values of several numerical parameters are described elsewhere (Fthenakis, 1991). These parameters included (*i*) the size of the simulation regime, (*ii*) the resolution of the grid, and (*iii*) the number of computational trajectories. In the simulations reported herein the length and height of the computational domain were set equal to the actual dimensions of the chamber used in the Hawk experiments. For unconfined flows, the size of the computational domain had to be sufficiently large so that air entrainment and drop trajectories were unrestricted. Extending the size of the domain beyond that point did not have any significant effect on the model predictions as long as the number of nodes was increased proportionally.

Increasing the number of nodes, had a significant effect on the results up to a point beyond which the solution became insensitive to further increase. A 20×40 grid qualitatively described most of the effects we have discussed, but a finer grid was used for accurate estimates. Figure 13 shows the effectiveness obtained from grids of different size: for the largest water flow rates in downward spraying, 7200 nodes (80×90 grid) were required, although for most downflow and upflow simulations a 60×90 grid was sufficient. For counter-current flows (monitor), approximately 3600 nodes (60×60 grid) were sufficient. The number of trajectories required for an insensitive solution was 30 for the 60×90 and finer grids, whereas for screening runs using a coarse (20×40) grid, 10 trajectories were sufficient (see Table 1). The iterative converge criterion in these simulations was 0.03 based on the continuity equation.

The effect of the number of drop sizes used to represent the drop size distributions associated with a given nozzle at certain water pressure, was also studied. For the nozzles we considered in this study with droplets in the range of 50-700 μm, five sizes were sufficient to obtain a solution insensitive to this parameter. Using a single mean size instead of a size distribution, produced deviations in the range of 2-5 percent.

5 Conclusions

The model HFSPRAY describes the momentum, mass, and energy interchange between drops generated by sprays and an unconfined plume of gas. This model was verified with all the existing field data involving HF releases. The estimates of HF removal fit reasonably well with these experimental data, and the predicted flow fields match the air entrainment data and the visual observations in the field.

Modeling of the water spray-HF-air interactions sheds more light on different patterns of HF flow, configurations of water spraying, and nozzle parameters. The spray's effectiveness increases with increasing water flow, and decreasing drop size, as shown by both the field data and the model estimates. Other influential parameters include the distances from nozzle-to-plume, and nozzle-to-ground distances which are pivotal in deciding if upflow is more effective than downflow, or vice versa.

The model provides a tool to assess the effectiveness of proposed spray designs for toxic gas mitigation.

Acknowledgments

The authors are especially thankful to Prof. C. T. Crowe for providing the PSI-Cell program. This research was supported, in part, from the Industry Cooperative HF Mitigation/Assessment Program, and the Photovoltaic Energy Technology Division, Conservation and Renewable Energy, U. S. Department of Energy.

References

Angelo, J. B., Lightfoot, E. N., and Howard, D. W., 1966, "Generalization of the Penetration Theory for Surface Stretch: Application to Forming and Oscillating Drops," *AIChE Journal*, Vol. 12, No. 4, pp. 751-760.

Beard, K. V., and Pruppacher, H. R., 1971, "A Wind Tunnel Investigation of the Rate of Evaporation of Water Drops Falling at Terminal Velocity in Air," *Journal of Atmospheric Science*, Vol. 28, pp. 1455-1464.

Bird, R. B., Stewart, W. E., and Lightfoot, E. N., 1960, *Transport Phenomena*, Wiley, New York, pp. 656-668.

Blewitt, D. N., Yohn, J. F., Koopman, R. P., Brown, T. C., and Hague, W. J., 1987, "Effectiveness of Water Sprays on Mitigating Anhydrous Hydrofluoric Acid Releases," *Proceedings of the International Conference on Vapor Cloud Modeling*, published by the American Institute of Chemical Engineers, J. Woodward, ed., pp. 155-171.

Buzzard, J. L., and Nedderman, R. M., 1967, *Chemical Engineering Science*, Vol. 22, p. 1577.

Crowe, C. T., Sharma, M. P., and Stock, D. E., 1977, "The Particle-Source-In Cell (PSI-Cell) Model for Gas-Droplet Flows," ASME JOURNAL OF FLUIDS ENGINEERING, Vol. 99, No. 2, pp. 325-332.

De Heanu, V., Raithby, G. D., and Thompson, B. E., 1990, "Prediction of Flows with Strong Curvature and Pressure Gradient Using the κ-ϵ Turbulence Model," ASME JOURNAL OF FLUIDS ENGINEERING, Vol. 112, pp. 40-47.

Djilali, N., Gartshore, I. S., and Salcudean, M., 1991, "Turbulent Flow Around a Bluff Rectangular Plate. Part II: Numerical Predictions," ASME JOURNAL OF FLUIDS ENGINEERING, Vol. 113, Mar., pp. 60-66.

Fthenakis, V. K., and Zakkay, V., 1990, "A Theoretical Study of Absorption of Toxic Gases by Spraying," *Journal of Loss Prevention*, Vol. 3, pp. 197-206.

Fthenakis, V. M., 1989, "The Feasibility of Controlling Unconfined Releases of Toxic Gases by Liquid Spraying," *Chemical Engineering Communications*, Vol. 83, pp. 173-189.

Fthenakis, V. M., 1991, "Modeling of Water Spraying of Toxic Gas Releases," Ph.D. thesis, Dept. of Applied Science, New York University, New York.

Gore, R. A., and Crowe, C. T., 1989, "Effect of Particle Sizes on Modulating Turbulent Intensity: Influence of Radial Location," *Symposium on Turbulence Modification in Dispersed Multiphase Flows*, FED-Vol. 80, The Third Joint ASCE/ASME Mechanics Conference, pp. 31-36.

Gosman, A. D., and Pun, W. M., 1973, Lecture notes for Calculation of Recirculating Flows, Imperial College of Science and Technology.

Launder, B. E., and Spalding, D. B., 1972, *Lectures in Mathematical Models of Turbulence*, Academic Press.

Leschziner, M. A., and Rodi, W., 1981, "Calculation of Annular and Twin Parallel Jets Using Various Discretization Schemes and Turbulence-Model Variations," ASME JOURNAL OF FLUIDS ENGINEERING, Vol. 103, pp. 352-360.

McFarlane, K., Prothero, A., Puttock, J. S., Roberts, P. T., and Witlox, H.

W. M., 1990, "Development and Validation of Atmospheric Dispersion Models for Hydrogen Fluoride," Technical Report TNER.90.015, Shell Research Limited, Chester, England.

Nallasamy, M., 1987, "Turbulence Models and Their Applications to the Prediction of Internal Flows: A Review," *Computer & Fluids*, Vol. 15, No. 2, pp. 151-194.

O'Rourke, P. J., 1981, "Collective Drop Effects on Vaporizing Liquid Sprays," Ph.D. thesis, Mechanical & Aerospace Engineering Dept., Princeton University, Princeton, NJ, pp. 67-70 and 94-97.

Ramachandran, S., 1985, "Mathematical Modeling and Computer Simulation of Mass Transfer in Simple Multiple Drop Systems," Ph.D. thesis, Rensselaer Polytech. Inst., Troy, NY, pp. 166-185.

Schatz, K. W., and Koopman, R. P., 1989, "Effectiveness of Water Spray Mitigation Systems for Accidental Releases of Hydrogen Fluoride; Industry Cooperative HF Mitigation/Assessment Program," Final Draft, Vol. I.

Takemitsu, N., 1990, "An Analytical Study of The Standard κ-ϵ Model," ASME JOURNAL OF FLUIDS ENGINEERING, Vol. 112, pp. 192-198.

Tsuneaki Ishima

Koichi Hishida
Associate Professor.

Masanobu Maeda
Professor.

Department of Mechanical Engineering,
Keio University,
3-14-1 Hiyoshi, Kouhoku-ku,
Yokohama, 223 Japan

Effect of Particle Residence Time on Particle Dispersion in a Plane Mixing Layer

A particle dispersion has been experimentally investigated in a two-dimensional mixing layer with a large relative velocity between particle and gas-phase in order to clarify the effect of particle residence time on particle dispersion. Spherical glass particles 42, 72, and 135 μm in diameter were loaded directly into the origin of the shear layer. Particle number density and the velocities of both particle and gas phase were measured by a laser Doppler velocimeter with modified signal processing for two-phase flow. The results confirmed that the characteristic time scale of the coherent eddy apparently became equivalent to a shorter characteristic time scale due to a less residence time. The particle dispersion coefficients were well correlated to the extended Stokes number defined as the ratio of the particle relaxation time to the substantial eddy characteristic time scale which was evaluated by taking account of the particle residence time.

Introduction

The dispersion of particles in the shear flow can be found in many industrial processes. The knowledge of the dispersion of particles is of great interest in improving the basic understanding on the two-phase flows, for example, the combustion of pulverized coal, the sand blasting, the pneumatic conveying, and the removal of fly ash from a power plant effluent. The present investigation was performed to reveal the flow characteristics of particles and the diffusivities of the particle in a fundamental turbulent flow.

In such two-phase flows, several investigators have experimentally obtained direct information on flow fields for both phases by laser Doppler velocimetry (Hishida et al., 1984; Modaress and Elghobashi, 1984; and Parthasaraty and Faeth, 1987). These studies have presented local information on mean velocities, turbulent properties and particle number density. They also pointed out the modification of continuous phase turbulence due to the presence of particles (Maeda et al., 1982; Hishida et al., 1986, 1987; and Fleckhaus et al., 1987).

On the other hand, numerical studies have also been performed on this subject. The attempt of numerical studies can be mainly divided into two types of approaches, namely Eularian approach and Lagrangian approach. The Eularian approach, in which particulate phase is treated as continuous phase, provides the turbulent properties of dispersed phase in an Eularian coordinate, and this approach requires less computing time (Melville and Bray, 1979; Elghobashi et al., 1984; Chen and Wood, 1986; Picart et al., 1986; and Lee and Chung, 1987). The Lagrangian approach, in which each trajectory of particles is directly simulated by solving the equation of particle motion, provides the mechanism of particle motion, but this approach requires a lot of calculating time (Shuen et al., 1985; Parthasaraty and Faeth, 1987; Berlemont et al., 1990). Both numerical studies need basically physical models and a reasonable expression of the models must be considered on the basis of experimental data. Recently, DNS (Direct Navier-Stokes Simulation) has also been carried out by several investigators (Squires and Eaton, 1990; Truesdell and Elghobashi, 1991). This simulation has succeeded in providing the local number density in each plane and the spatial spectra of kinetic energy of turbulence. For verification of turbulent modeling in two-phase flow, detailed experimental data in a fundamental flow field are still needed. The present experiment has been carried out in one of the fundamental turbulent flows, that is, a plane shear layer which has been well studied for single phase flow by many investigators (Brown and Roshko, 1974; Winant and Browand, 1974; and Hussain and Zaman, 1985). Brown and Roshko (1974) demonstrated the existence of large scale eddies in the shear layer. Winant and Browand (1974) pointed out that the development of shear layer was related by the pairing process of these large scale eddies. They also indicated that these large scale eddies play a dominant role in the momentum transport of fluid.

In particulate flow, it is likely that these large scale eddies affect the particle dispersion. Numerical studies on particle dispersion in which the effect of large scale eddies was taken into account were carried out by Chein and Chung (1987, 1988) and Tang et al. (1989). They reported that the phenomenon of the particle dispersion correlates with Stokes number ($=S_t$), which was defined as the ratio of the particle relaxation time to the characteristic time scale of large scale eddy, and this phenomenon indicated that the particles could disperse more than the fluid over a certain range of Stokes numbers.

Contributed by the Fluids Engineering Division for publication in the JOURNAL OF FLUIDS ENGINEERING. Manuscript received by the Fluids Engineering Division February 23, 1992; revised manuscript received February 3, 1993. Associate Technical Editor: M. W. Reeks.

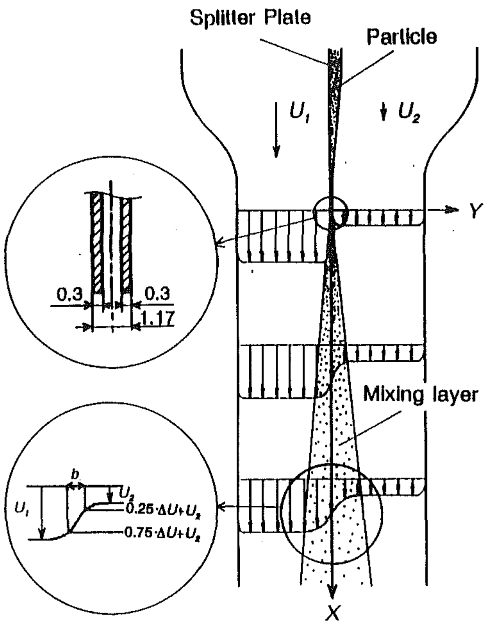

Fig. 1 Experimental flow configuration

Table 1 Flow conditions

Condition	U_1[m/s]	U_2[m/s]
(I)	21	13
(II)	13	4
(III)	15	3

Table 2 Particle properties

Mean Diameter d_p[μm]	Standard Deviation σ[μm]	Density ρ [kg/m³]	Relaxation Time[sec]
42	5.4	2590	0.014
72	7.5		0.041
135	7.9		0.144

Kobayashi et al. (1987) visualized the two phase flows in a plane shear layer and pointed out that the particles can follow the entrainment of the shear layer after a certain distance downstream of the initial mixing point since particles are hardly affected by the small vortical structure at the initial mixing region. The authors' group has experimentally investigated the particle dispersion, and found that the particle dispersion was well correlated with the Stokes number. For $S_t > 4.0$, particles could not be affected by the large scale eddy, and for $0.5 < S_t < 2.5$ particles disperse more than fluid (which is called "overshoot phenomena") (Hishida et al., 1992).

The previous studies were carried out in the flow field where particles had time enough to catch up with the eddy motion of gas-phase. In order to clarify the effect of the particle residence time in the eddy motion of gas phase on the particle dispersion, the present experiment of the particle dispersion has been carried out in a flow field with a high bulk velocity, where a high relative velocity between particle and gas-phase can be set to give a shorter interaction time in a turbulent flow.

Experimental Apparatus

The present experiment was performed in a two-dimensional, vertical turbulent shear layer wind tunnel. Figure 1 shows the experimental flow configuration. The flow was divided into two streams and passed through a setting nozzle and merged at the point of the trailed edge of the splitter plate. The splitter plate was made of two thin aluminum plates, which were 0.3 mm thin, and had a constant space, which was 0.57 mm. The test section was 75 mm in cross-stream direction, 100 mm in spanwise direction and 450 mm in length. The Cartesian coordinate and origin were located at the higher velocity side of the trailing edge. The streamwise direction was the X-axis and the cross-stream direction was the Y-axis.

In the present paper, three kinds of flow conditions are employed and are presented in Table 1. Under condition (I), gas-phase velocities U_1 and U_2 were set at 21 m/s and 13 m/s, respectively, and the bulk velocity defined as the average of the mean air flow velocities $U_b (= (U_1 + U_2)/2)$ was equal to 17 m/s. In order to clarify the effect of the particle residence time on particle dispersion, condition (II) has a similar velocity gradient to condition (I) and the bulk velocity of condition (II), which is equal to 8.5 m/s, is smaller than that of condition (I). Thus, the present data were always collated with the data on particles in condition (II) which had been obtained in the previous work by Hishida et al. (1992). For general discussion of the particle dispersion, condition (III) was also presented in the discussion on the dispersion of the particle. Condition (III) has almost the same bulk velocity of condition (II), but the velocity difference between U_1 and U_2 is higher than that of the condition (II), that is, the velocity gradient is larger than those of the other flow conditions.

Three kinds of glass particles were loaded at the initial point of the shear layer. The mean diameters of particles were 42, 72, and 135 μm and their mass flow rates for each particle were 7.5, 20.9 and 20.4 g/s. Table 2 indicates the mean diameter, the standard deviation in diameter and the particle

Nomenclature

d_p = particle diameter
f_m = most probable frequency in turbulence
N_d = particle number density
S_t = Stokes number ($= \tau_p/\tau_f$)
U = streamwise mean velocity
U_1 = air velocity of higher velocity stream
U_2 = air velocity of lower velocity stream
U_b = bulk velocity ($= (U_1 + U_2)/2$)
ΔU = $(U_1 - U_2)$
X = streamwise distance
Y = lateral distance
$Y_{0.5}$ = location at the half of ΔU
$\overline{y^2}$ = mean square displacement
u' = streamwise velocity fluctuation
v' = lateral velocity fluctuation
ϵ_f = eddy diffusivity of gas-phase
ϵ_p = particle dispersion coefficient
λ = length scale of coherent vortex
ρ_p = density of glass particle
τ_r = residence time
τ_f = characteristic time scale of turbulence
τ_p = particle relaxation time ($\rho_p d_p^2/(18\mu)$)

Subscripts

f = fluid phase
p = particle phase
L = Lagrangian scale

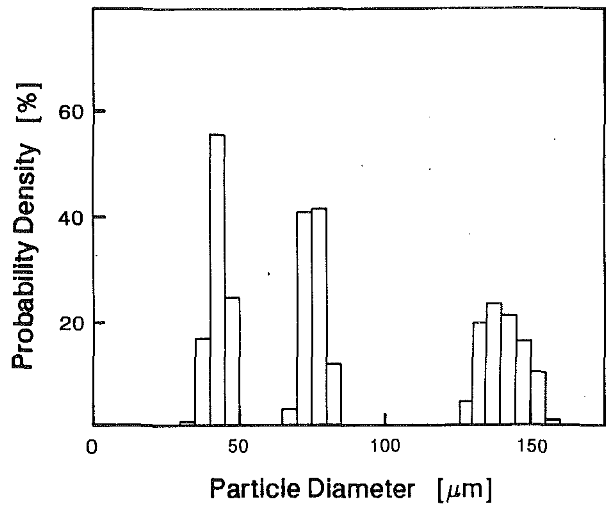

Fig. 2 Distribution of particle diameters

relaxation time for each particle. The size distribution of particle diameters obtained by microscopic measurement are shown in Fig. 2.

A three-beam laser Doppler velocimeter, which was employed in the previous work (Fleckhaus et al., 1987), was used for measurements of two-component velocities for both particle and gas phase and particle number density. Two-counter type signal processors were employed and the coincidence of each channel signal was rigorously checked by the existence of both burst envelopes of signals which indicate the presence of a particle in the measuring volume. Mean velocities, velocity fluctuations in the two components and the correlation between velocity fluctuations were evaluated from over 3000 data.

Measuring uncertainties within 95 percent confidence interval of mean velocity and velocity fluctuations are obtained as follows: for the mean velocity $(U-U_2)/\Delta U$ the uncertainties were ±0.054 at $X=150$ mm and $Y=0$ mm, and ±0.042 at $X=250$ mm and $Y=0$ mm; for the velocity fluctuation $u'/\Delta U$ the uncertainties were ±0.085 at $X=150$ mm and $Y=0$ mm, and ±0.084 at $X=250$ mm and $Y=0$ mm. The uncertainties of half width b and length scale of characteristic eddy λ were less than ±0.06 as indicated in each figure.

The turbulence characteristics of the air phase in a two-phase flow might be modified by the presence of particles. In the present experimental conditions, the maximum difference between the two velocity profiles in a single-phase and in two phases was so small that it might be neglected for the low concentration of particles. The maximum difference of $(U-U_2)/\Delta U$ are 3 percent at $X=150$ mm and $Y=0$ mm for 72 μm particle, 1 percent at $X=150$ mm and $Y=0$ mm for 42 μm particle and 0.5 percent at $X=150$ mm and $Y=0$ mm for 135 μm. Thus, single phase results could be compared with particle phase.

Results and Discussions

Single Phase Flow. Distributions of mean velocities and velocity fluctuations for the flow condition (I) are shown in Figs. 3 and 4, respectively. A slight velocity defect would be present due to the splitter plate thickness of 1.1 mm downstream, but, the distribution of the mean velocities approaches a hyperbolic tangent curve for the whole experimental region of X over 50 mm, and the distribution of the velocity fluctuations approaches a Gaussian curve downstream of $X=100$ mm. Similar features were confirmed for the other flow conditions. Figure 5 shows the streamwise distribution of half widths b. The half width is defined as the lateral distance from the point of $U_f=0.75\Delta U+U_2$ to that of $U_f=0.25\Delta U+U_2$, as mentioned in Fig. 1. It is surmised from these results that an approximately linear growth of the shear layer occurs downstream over $X=100$ mm.

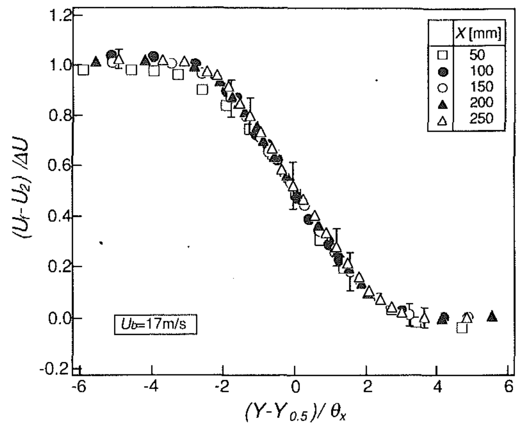

Fig. 3 Distributions of mean velocities in single-phase flow for condition (I)

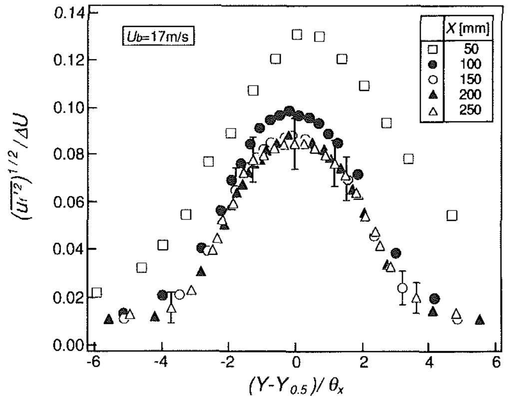

Fig. 4 Distributions of velocity fluctuations in single-phase flow for condition (I)

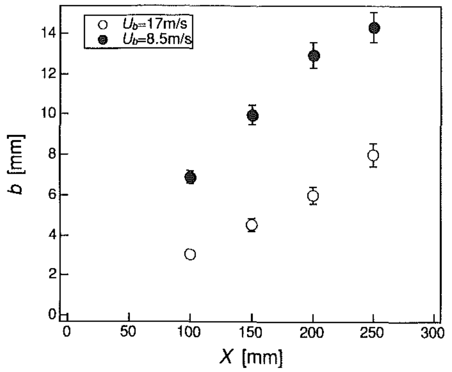

Fig. 5 Streamwise distributions of the half widths b

According to the previous studies of plane shear layer in single phase flow (Brown and Roshko (1974) and Hussain and Zaman (1985)), there are coherent structures in the shear layer and they are related to the development of the shear layer width. Figure 6 shows the streamwise distribution of the length scales of the coherent eddies λ, obtained from the same treatment by Hussain and Zaman (1985)

$$\lambda=\frac{1}{f_m}\cdot\frac{(U_1+U_2)}{2} \tag{1}$$

where f_m is the most probable frequency in turbulent flow at

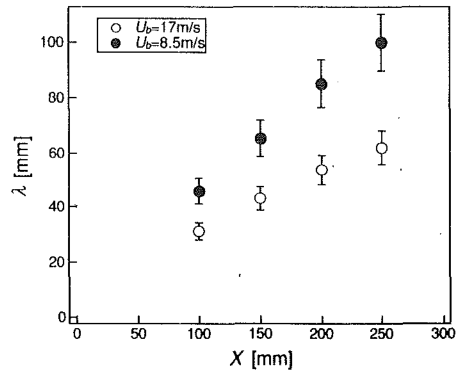

Fig. 6 Streamwise distributions of the length scales of the coherent eddies λ

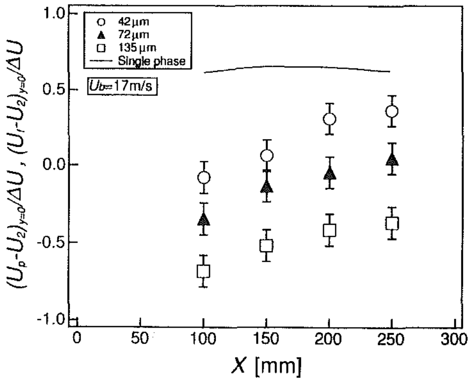

Fig. 7(*a*) Particle mean velocity at center line $Y=0$ mm for $U_b=17$ m/s

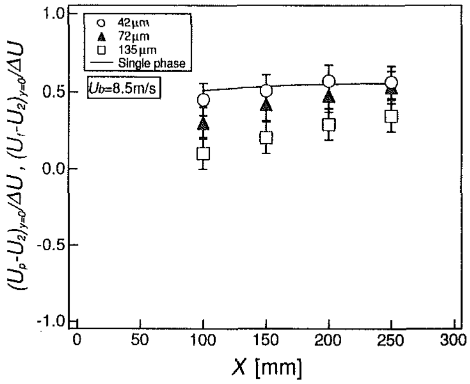

Fig. 7(*b*) Particle mean velocity at center line $Y=0$ mm for $U_b=8.5$ m/s

the outer edge of the shear layer. In the present study, the f_m is given from the results of frequency analysis of velocity fluctuation measured by a hot wire velocimeter at edges of the higher velocity side in the single-phase flow. This figure confirms that the length scale increases linearly from $X=100$ mm downstream and thereby the shear layer is fully developed in this flow field.

Two Phase Flow

Particle Mean Velocity. The streamwise distributions of particle mean velocities along the center line $Y=0$ mm are given in Figs. 7(*a*) and (*b*). The solid line in each figure indicates the result for the single-phase flow. The velocities of particles approach those of gas-phase for a particle of a smaller relaxation time with an increasing downstream distance. The particle velocities at the exit of the splitter plate are almost the same value for all three types of particles and are equal to approximately 1.1 m/s for $U_b=17$ m/s and 0.9 m/s for $U_b=8.5$ m/s. For a higher bulk velocity, particles maintain a large relative velocity for whole experimental region due to shorter traveling time than the particle relaxation time.

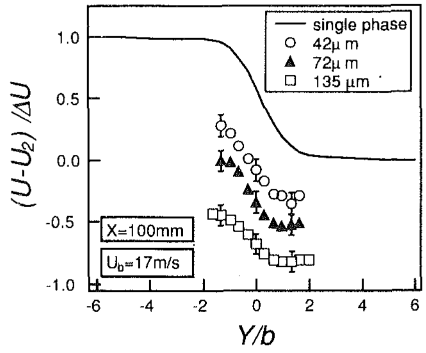

Fig. 8(*a*) Cross-sectional distributions of particle mean velocities at $X=100$ mm for $U_b=17$ m/s

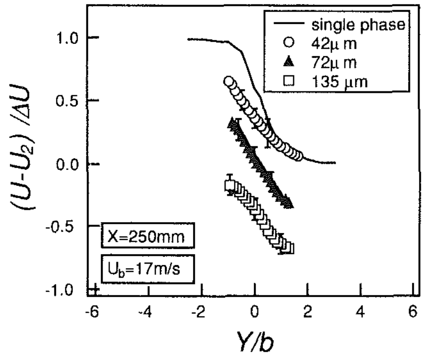

Fig. 8(*b*) Cross-sectional distributions of particle mean velocities at $X=250$ mm for $U_b=17$ m/s

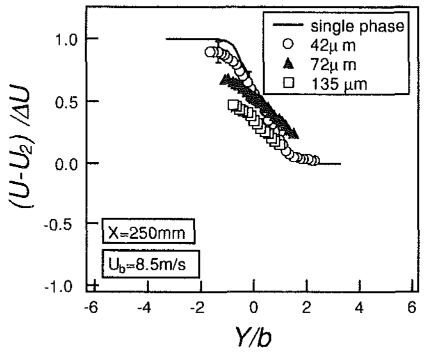

Fig. 8(*c*) Cross-sectional distributions of particle mean velocities at $X=250$ mm for $U_b=8.5$ m/s

The distributions over the cross-section at $X=100$ mm and $X=250$ mm are presented in Figs. 8(*a*)-(*c*). At $X=100$ mm for the higher bulk velocity, the relative velocity increases with an increasing particle diameter. At $X=250$ mm for the higher bulk velocity, the particle of 42 μm diameter has a small slip velocity at the lower velocity side of the shear layer, while the slip velocity remains large at the higher velocity side of the shear layer. For the lower bulk velocity, the cross-sectional distribution of particle velocities is close to that of the single-phase.

For the particle of 72 μm diameter with $U_b=8.5$ m/s as shown in Fig. 8(*c*), the velocities exceed the fluid velocity in the lower velocity side. This feature is explained as follows; when particles disperse in lateral direction, they keep their longitudinal velocity due to their inertia, that is, particles can not instantly follow the mean velocity of the gas-phase since

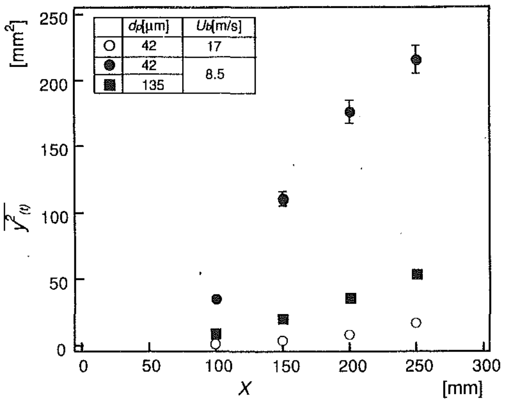

Fig. 9 Variations of particle mean square displacement

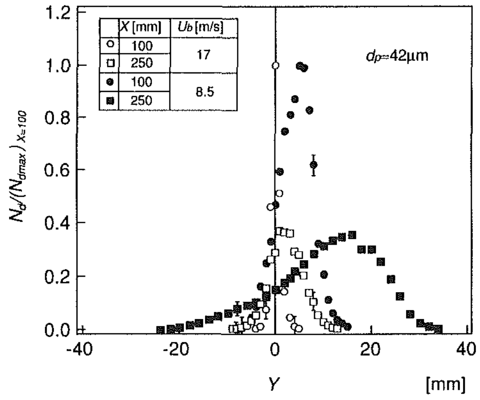

Fig. 10 Particle number density distributions

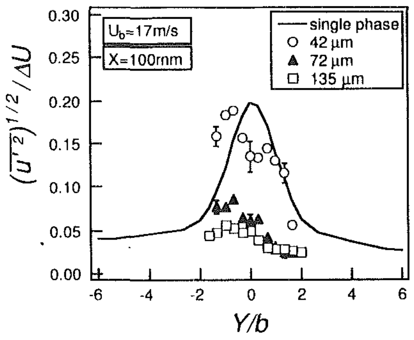

Fig. 11(*a*) Particle streamwise velocity fluctuation at $X=100$ mm for $U_b=17$ m/s

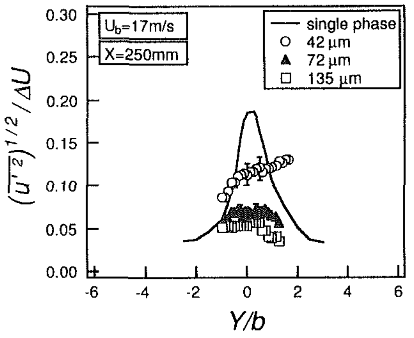

Fig. 11(*b*) Particle streamwise velocity fluctuation at $X=250$ mm for $U_b=17$ m/s

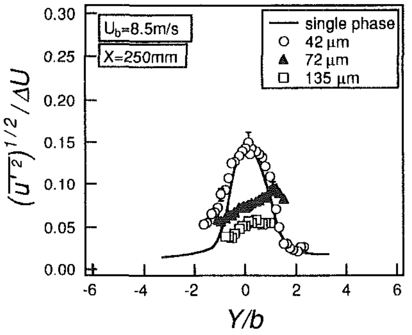

Fig. 11(*c*) Particle streamwise velocity fluctuation at $X=250$ mm for $U_b=8.5$ m/s

the particles have a large relaxation time. Therefore, the velocity of 72 μm particle is larger than that of the gas-phase in the lower velocity side and the velocity distribution of this particle has a flatter shape than that of gas phase.

Particle Number Density Distribution. To evaluate the particle dispersion from the particle number density profile, the particle mean square displacement $\overline{y^2}$ is obtained as

$$\overline{y^2}=\frac{\int N_d \cdot y^2 dy}{\int N_d dy} \tag{2}$$

where N_d is the local particle number density. Particle number density was measured by counting the number of Doppler burst signals of a particle passing through the measuring volume of the LDV. Due to the ambiguity, depending on its path of distributed particle size, the absolute value can hardly be obtained. However, a proportional number density distribution was statistically evaluated for every level. The unknown factor is evaluated by integrating the distribution for each level. The variations of $\overline{y^2}$ with X are shown in Fig. 9. For $U_b=17$ m/s, the mean square displacements for the particle of 42 μm diameter are much smaller than those for $U_b=8.5$ m/s. In order to discuss on the decrease in the mean square displacement of the particle of 42 μm diameter, cross-sectional distributions of the particle number densities are indicated in Fig. 10. For the higher bulk velocity, the peak values of number density are located around the centerline $Y=0$ mm, the distributions keep a sharp profile and the skewness of the number density distribution is smaller than that for the lower bulk velocity. In contrast, for the lower bulk velocity, the peak value shifts to the lower velocity side. These differences in the particle number densities for both conditions are caused by the difference in particle residence time. A large relative velocity causes a shorter particle residence time and a less effect of the vortical structure motion. For the lower bulk velocity, since particles so straight over a certain distance from the inlet position, particles encounter a large scale eddy in the higher velocity side because the center line of the mixing layer shifts to the lower velocity side. The shift of the centerline of the mixing layer is caused by the difference in the spreading angles between the higher velocity side and the lower velocity side. Therefore, the particles which are affected by the large scale eddy in the higher velocity side disperse to the lower velocity side (Hishida et al., 1992).

Particle Velocity Fluctuations and $\overline{u'v'}$-Correlations. The distributions of particle velocity fluctuations in the streamwise direction are shown in Figs. 11(*a*)-(*c*). The distributions of the particle velocity fluctuations become larger with a decrease in the particle diameter and approach those of gas-phase with an increase in the distance downstream and/or with a decrease in the bulk velocity.

A comparison with the lower bulk velocity indicates that the

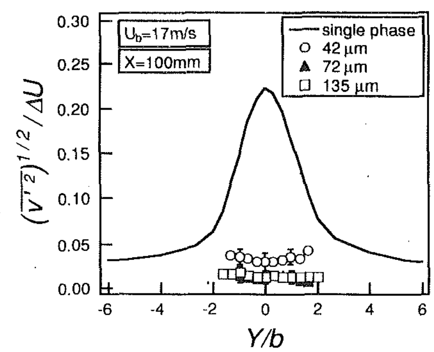

Fig. 12(*a*) Particle cross-stream velocity fluctuation at $X=100$ mm for $U_b=17$ m/s

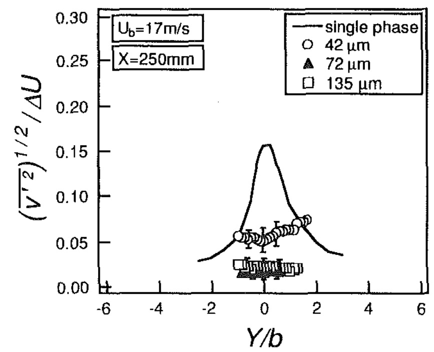

Fig. 12(*b*) Particle cross-stream velocity fluctuation at $X=250$ mm for $U_b=17$ m/s

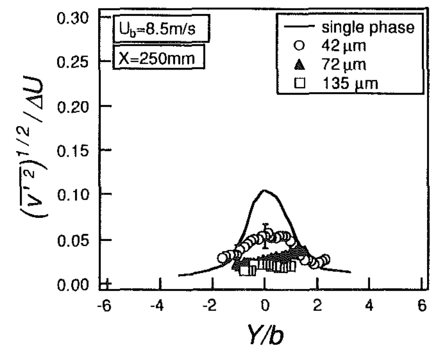

Fig. 12(*c*) Particle cross-stream velocity fluctuation at $X=250$ mm for $U_b=8.5$ m/s

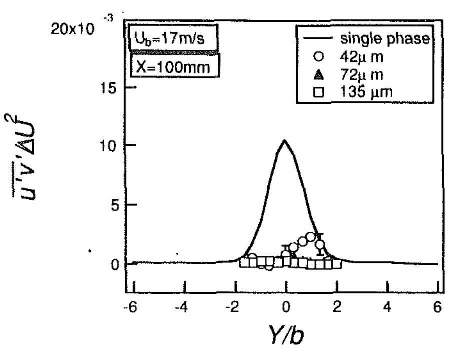

Fig. 13(*a*) Particle $\overline{u'v'}$-correlation at $X=100$ mm for $U_b=17$ m/s

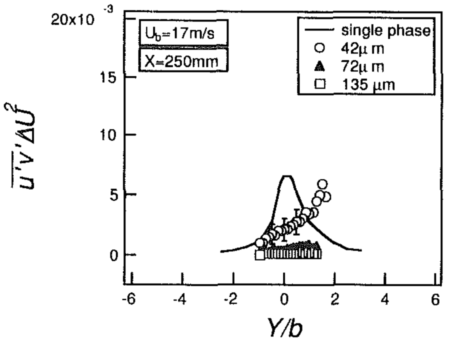

Fig. 13(*b*) Particle $\overline{u'v'}$-correlation at $X=250$ mm for $U_b=17$ m/s

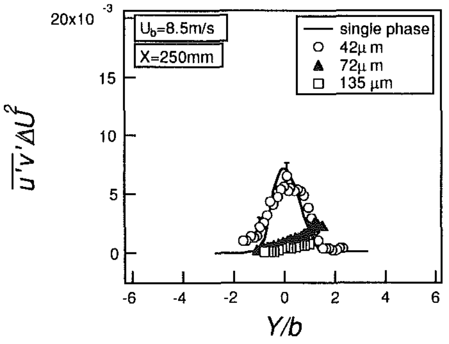

Fig. 13(*c*) Particle $\overline{u'v'}$-correlation at $X=250$ mm for $U_b=8.5$ m/s

distributions of the velocity fluctuations with large slip velocity do not have sharp peak values as indicated in Figs. 11(*a*) and (*b*). For the upstream location of $X=100$ mm as shown in Fig. 11(*a*), the particle velocity fluctuation in the streamwise direction at the higher velocity side, where Y/b is negative, is somewhat larger than that of the value at the lower velocity side. This phenomenon can be explained as follows: Upstream, where they have a large relative velocity, particles are mainly affected by the mean flow of the gas-phase because they cannot catch up with the eddy motion of the gas-phase. The magnitude of u' of the particle is generated by momentum transfer from the gas-phase to the particle. At the inlet position, as the particles have an almost uniform distribution of the mean velocities, the particle at the higher velocity side has a comparatively large slip velocity. Consequently, u' of the particle at the higher velocity side becomes large.

The distributions of particle velocity fluctuations in lateral direction are shown in Figs. 12(*a*)-(*c*). For both bulk velocities, the particle velocity fluctuations in cross-stream direction v_p' are much smaller than those in streamwise direction u_p' as shown in Figs. 11 (*a*)-(*c*). Such tendency was observed in the results of previous experiments for free jet (Fleckhaus et al., 1987; and Hardalupas et al., 1989) and for confined jet (Hishida et al., 1987). This behavior of $u_p' \gg v_p'$ for jet flow occurs due to quasi-unidirectional trajectories of solid particles from the exit of jet up to a certain downstream distance, and it is called "fan spreading." However, under flow conditions in which they are not affected by the initial condition, particles appear to have quasi-unidirectional trajectories.

The distributions of particle $u'v'$-correlation are presented in Figs. 13(*a*)-(*c*). The value of the particle $u'v'$-correlation becomes larger with downstream distance. Since the particle cannot follow the small scale eddies motion perfectly, the particle $u'v'$-correlation is mainly caused by the large scale turbulent eddy motion of the gas phase. In each figure, the particle $u'v'$-correlations become larger than those of gas-phase in the lower velocity side for 42 μm particle under both conditions and 72 μm particle with small slip velocity. This is considered to occur since particles at the higher velocity side of the shear layer have migrated towards the other side without decreasing their velocity which they have had at the higher velocity side. The behavior of the particle of 42 μm diameter with large slip

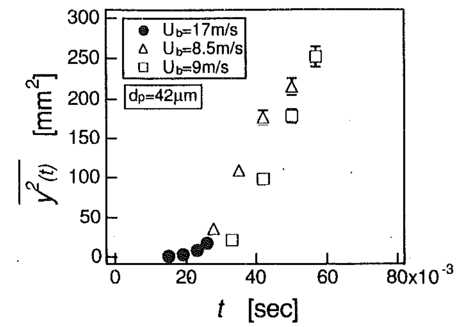

Fig. 14(*a*) Particle mean square displacement for $d_p = 42$ μm

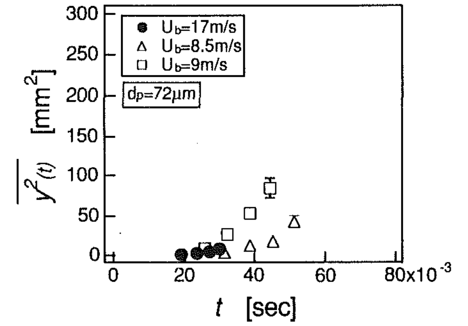

Fig. 14(*b*) Particle mean square displacement for $d_p = 72$ μm

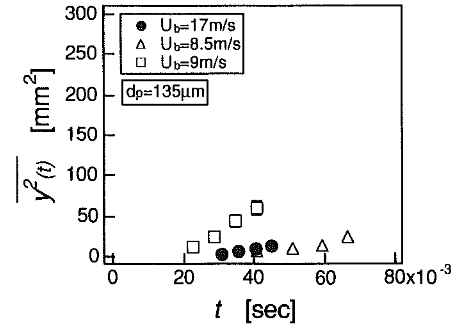

Fig. 14(*c*) Particle mean square displacement for $d_p = 135$ μm

diameter with large slip velocity is similar to that of 72 μm diameter with small slip velocity where the particles have enough residence time. Since the particle of 72 μm diameter with small slip velocity has an inertia and flies out of the vortical structures of the fluid, particles can be directly affected by the large scale eddy motions up to a certain time. For the higher bulk velocity, a large slip velocity exists as presented in Figs. 7(*a*) and 8(*a*) even for particles with a smaller relaxation time and the particles do not have enough residence time with eddy motion of gas phase. Consequently, the particle motion of a smaller inertia with less residence time is considered to be similar to that of a larger inertia with longer residence time.

Particle Dispersion Coefficient. The turbulent eddy diffusivity was defined by G.I. Taylor by extending the concept of molecular diffusion in isotropic turbulent flow (e.g., Hinze, 1975). After Taylor's study, this theory was extended to non-isotropic turbulence in the mixing layer when a dispersed particle existed (Snyder and Lumley, 1971). The time variations of the mean square displacement of particles of each diameter in the Y direction are indicated in Fig. 14. In order to generalize the relationship between particle residence time and particle dispersion, the results with the flow condition (III) $U_b = 9$ m/s are given in the figures. The mean square displacement for condition (I) is much smaller than those for the other conditions. The particle mean square displacements under conditions (II) and (III) rapidly increase with an increasing particle traveling time. However, the mean square displacement is not useful for the discussion of the particle dispersion, since the flow fields do not have just the same scale eddy, and the eddy diffusivities of gas-phase are varied for each flow condition.

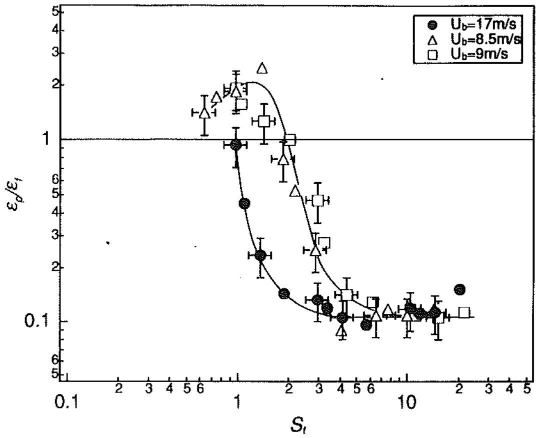

Fig. 15 Variations of ratio of particle and fluid eddy diffusivity to Stokes number

In the present study, the gas-phase eddy diffusivity was evaluated from Prandtl's mixing length theory and the particle eddy diffusivity was given by time differentiating the mean square displacement;

$$\epsilon_p = \frac{1}{2}\frac{d}{dt}\overline{y^2} \tag{3}$$

Figure 15 shows the variation of the ratio of the particle and the fluid eddy diffusivities to the Stokes number S_t. Stokes number is defined as the ratio of the particle relaxation time to the characteristic time scale number of the energy-containing eddy. The time scale of the energy-containing eddy is given by

$$\tau_f = \frac{\lambda}{\Delta U} \tag{4}$$

where λ is the length scale of the energy-containing eddy and ΔU is the velocity difference between the higher velocity and the lower velocity. The results of the eddy diffusivity ratios can be divided into two types, that is, the results for $U_b = 8.5$ m/s and for $U_b = 9$ m/s have a similar tendency to each other but the result for $U_b = 17$ m/s is different from those for the other flow conditions. The numerical calculations of Chein and Chung (1987, 1988) and Tang et al. (1989) indicated that particles can disperse more than the fluid element in a certain range of the Stokes numbers, and therefore the eddy diffusivity ratio can become larger than unity around $S_t = 1$. However, for $U_b = 17$ m/s, the eddy diffusivity ratio can not be larger than unity around $S_t = 1$. For 42 and 72 μm particles with large slip velocity, the eddy diffusivity ratio is much smaller than that under the condition with small slip velocity. This irregular behavior of the eddy diffusivity ratio is due to the neglect of the effect of the particle residence time in the eddy motion of gas-phase.

Taking account of the above discussion, the effect of the large scale eddy motion on the particle motion becomes less with a decrease in particle residence time in eddy motion of gas phase. The mean particle residence time τ_r in eddy motion is represented by

$$\tau_r = \frac{\lambda}{U_r} \tag{5}$$

where U_r is the mean slip velocity between particles and gas-phase and it is given as

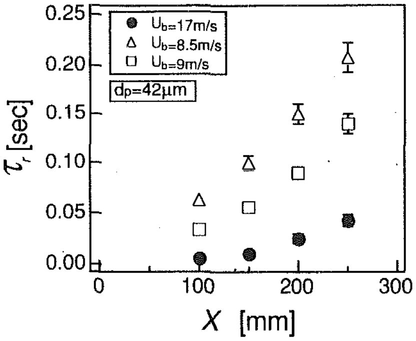

Fig. 16(*a*) **Particle residence time distributions for $d_p = 42$ μm**

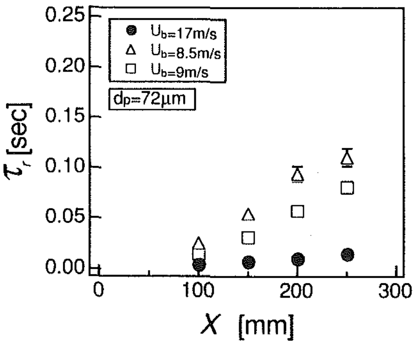

Fig. 16(*b*) **Particle residence time distributions for $d_p = 72$ μm**

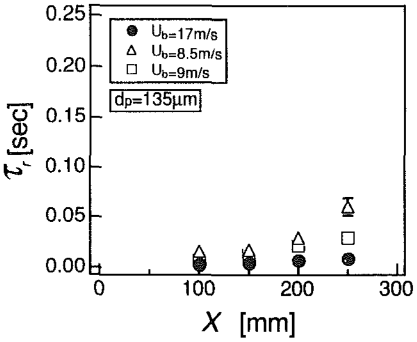

Fig. 16(*c*) **Particle residence time distributions for $d_p = 135$ μm**

$$U_r = \frac{\int |(U_f - U_p)\cdot N_d| dy}{\int N_d dy} \tag{6}$$

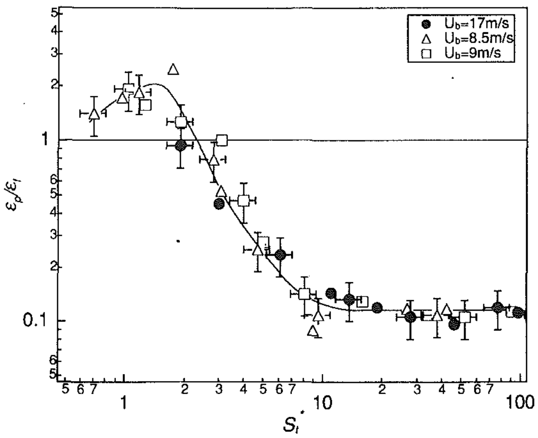

Fig. 17 **Variations of ratio of particle and fluid eddy diffusivity to modified Stokes number**

where U_f and U_p are fluid velocity and particle velocity, respectively. In the present experiment, local velocities of gas-phase and particles are precisely measured. Consequently, mean values, U_r, are properly evaluated based on experimental results. Figure 16 shows the variations of the particle residence time with distance of X. Particle residence time increases for farther downstream. Each condition indicates a different increasing rate for each level. A variety of the particle residence time is introduced by the relative velocity at the initial position and the flow conditions. Since the particle residence time is short, particles hardly follow even for the large scale eddy. A short particle residence time causes the particle to change its neighborhood fluid eddy, that is, a very similar feature of "crossing trajectory effect." Under the flow condition with large slip velocity, the characteristic time scale of the large scale eddy is apparently equivalent to a shorter characteristic time scale. Therefore, it is considered that the particle Stokes number under the condition with a large velocity difference between the particle and the fluid is substantially estimated smaller. The substantial characteristic time scale is evaluated based on the studies by Csanady (1963) and Picart et al. (1986):

$$\tau_f^* = (1 - \exp(-A(\tau_r/\tau_f)^B))\cdot\tau_f \tag{7}$$

In the present study, the constants A and B are determined from the experimental data and given as $A = 0.25$ and $B = 1.0$. Stokes number can be replaced by a new nondimensional number using τ_p and τ_f^*. The variations of the extended Stokes number S_t^* $(= \tau_p/\tau_f^*)$ and the ratio of the eddy diffusivity ϵ_p/ϵ_f are presented in Fig. 17. It is confirmed from this result that the particle dispersion is well correlated with S_t^* regardless of flow condition.

Concluding Remarks

The particle dispersion in the turbulent shear layer has been experimentally investigated to clarify the effect of particle residence time in eddy motion of gas-phase. Three kinds of spherical particles of 42, 72, and 135 μm in mean diameter were loaded into the origin of a plane shear layer. Laser Doppler velocimetry was used for the measurement of two velocity components of both particles and gas-phase and particle number density. The conclusions reached from the study are as follows:

Under flow conditions where particles have a large relative velocity, the particle eddy diffusivities for $S_t < 5$ are much smaller than those for the lower bulk velocity. And for $S_t > 3$ the particle eddy diffusivities are equal to a constant value 0.1, that is, particles with $S_t > 3$ were hardly affected by the large scale eddies due to large relative velocity.

These features of the higher bulk velocity are caused by a decrease in the particle residence time between particles and coherent eddies of the gas-phase. That is, the characteristic time scale of large scale eddy is apparently equivalent to a smaller characteristic time scale. In this case where the flow field has a large relative velocity between particle and gas phase, the modified Stokes numbers, which are evaluated by taking account of the particle residence time, are well correlated with the particle eddy diffusivity ratios for both higher and lower bulk velocities. A series of experiments on particle dispersion in a plane shear layer were carried out and the governing factor of the particle dispersion was experimentally quantified independently of flow condition.

Acknowledgments

This work subsidized by the Grant in Aid for Scientific Research of Ministry of Education of Japan under grant no. 03452125. The authors would like to acknowledge Mr.N. Ohsawa, Mr. K. Yokomori, and Mr. K. Fukuda for performing this experiment. They would also like to express their thanks to Mr. A. Ando for useful discussions on this study.

References

Berlemont, A., Desjonqueres, P., and Gouesbet, G., 1990, "Particle Lagrangian Simulation in Turbulent Flows," *International Journal of Multiphase Flow*, Vol. 16, pp. 19–34.

Brown, G. L., and Roshko, A., 1974, "On Density Effect and Large Structure in Turbulent Mixing Layer," *Journal of Fluid Mechanics*, Vol. 64, Part 4, pp. 775–816.

Chein, R., and Chung, J. N., 1987, "Effect of Vortex Pairing on Particle Dispersion in Turbulent Shear Flows," *International Journal of Multiphase Flow*, Vol. 13, No. 6, pp. 785–802.

Chein, R., and Chung, J. N., 1988, "Simulation of Particle Dispersion in a Two-Dimensional Mixing Layer," *AIChE Journal*, Vol. 34, No. 6, pp. 946–954.

Chen, C. P., and Wood, P. E., 1986, "Turbulence Closure Modelling of the Dilute Gas-Particle Axisymmetric Jet," *AIChE Journal*, Vol. 32, pp. 163–166.

Csanady, G. T., 1963, "Turbulent Diffusion of Heavy Particles in the Atmosphere," *Journal of the Atmosphere Sciences*, Vol. 20, pp. 201–208.

Elghobashi, S., Abou-Arab, T., Rizk, M., and Mostafa, A., 1984, "Prediction of the Particle-Laden Jet with a Two-Equation Turbulence Model," *International Journal of Multiphase Flow*, Vol. 10, pp. 697–710.

Fleckhaus, D., Hishida, K., and Maeda, M., 1987, "Effect of Laden Solid Particles of the Turbulent Flow Structure of a Round Free Jet," *Experiments in Fluids*, Vol. 5, pp. 323–333.

Hardalupas, Y., Taylor, A. M. K. P., and Whitelaw, J. H., 1989, "Velocity and Particle-Flux Characteristics of Turbulent Particle Laden Jets," *Proceedings of Royal Society of London*, Series A426, pp. 31–78.

Hinze, J. O., 1975, *Turbulence*, 2nd edition, McGraw-Hill, New York, NY.

Hishida, K., Maeda, M., Imaru, J., Hironaga, K., and Kano, H., 1984, "Measurement of Size and Velocity of Particle in Two-Phase Flow by a Three Beam LDA System," *Proceedings of Laser Anemometry in Fluid Mechanics*, LADOAN-Instituto Superior Tecnico, Portugal, pp. 121–136.

Hishida, K., Umemura, K., and Maeda, M., 1986, "Heat Transfer to a Plane Wall Jet in Gas-Solids Two-Phase Flow," *Proceedings of 8th International Heat Transfer Conference*, San Francisco, CA, Vol. 5, pp. 2385–2390.

Hishida, K., Ando, A., and Maeda, M., 1992, "Experiments on Particle Dispersion in a Turbulent Mixing Layer," *International Journal of Multiphase Flow*, Vol. 18, No. 2, pp. 181–194.

Hishida, K., Takemoto, K., and Maeda, M., 1987, "Turbulence Characteristics of Gas-Solids Two-Phase Confined Jet (in Japanese)," *Japanese Journal of Multiphase Flow*, Vol. 1, pp. 56–69.

Hussain, A. K. M. F., and Zaman, K. B. M. Q., 1985, "An Experimental Study of Organized Motions in the Turbulent Plane Mixing Layer," *Journal of Fluid Mechanics*, Vol. 159, pp. 85–104.

Kobayashi, H., Masutani, S. M., Azuhata, S., Arashi, N., and Hishinuma, Y., 1987, "Dispersed Phase Transport in a Plane Mixing Layer," *2nd International Symposium on Transport Phenomena in Turbulent Flows*, Tokyo, Oct. 25–29, pp. 693–706.

Lee, K. B., and Chung, M. K., 1987, "Refinement of the Mixing Length Model for Prediction of Gas-Particle Flow in a Pipe," *International Journal of Multiphase Flow*, Vol. 13, pp. 275–282.

Maeda, M., Kiyota, H., and Hishida, K., 1982, "Heat Transfer to Gas-Solid Two-Phase Flow in Separated, Reattached and Redevelopment Regions," *Proceedings of 7th International Heat Transfer Conference*, Munich, Germany, Vol. 5, pp. 249–254.

Melville, W. K., and Bray, K. N. C., 1979, "A Model of the Two-Phase Turbulent jet," *International Journal of Heat Mass Transfer*, Vol. 22, pp. 647–656.

Modaress, D., Tan, H., and Elghobashi, S., 1984, "Two-Component LDA Measurement in a Two-Phase Turbulent Jet," *AIAA Journal*, Vol. 22, pp. 624–630.

Parthasarathy, R. N., and Faeth, G. M., 1987, "Structure of Particle-Laden Turbulent Water Jets in Still Water," *International Journal of Multiphase Flow*, Vol. 13, pp. 699–716.

Picart, A., Berlemont, A., and Gousbet, G., 1986, "Modeling and Predicting Turbulence Fields and the Dispersion of Discrete Particles Transported by Turbulence Flows," *International Journal of Multiphase Flow*, Vol. 12, No. 2, pp. 237–261.

Sheun, J. S., Solomon, A. S. P., Zhang, Q. F., and Faeth, G. M., 1985, "Structure of Particle-Laden Jets: Measurements and Prediction," *AIAA Journal*, Vol. 23, pp. 396–404.

Snyder, W. H., and Lumley, J. L., 1971, 'Some Measurements of Particle Velocity Autocorrelation Functions in a Turbulent Flow," *Journal of Fluid Mechanics*, Vol. 48, Part 1, pp. 40–71.

Squires, K. D., and Eaton, J. K., 1990, "Particle Response and Turbulence Modification in Isotropic Turbulence," *Physics of Fluids*, A2, pp. 1191–1203.

Tang, I., Crowe, C. T., Chung, J. N., and Troutt, T. R., 1989, "Effect of Momentum Coupling on the Development of Shear Layer in Gas-Particle Mixture," *Proceedings of International Conference on Mechanics of Two-Phase Flows*, June 12–15, Taipei, pp. 387–391.

Truesdell, G. C., and Elghobashi, S. E., 1991, "Direct Numerical Simulation of a Particle-Laden Homogeneous Turbulent Flow," *Proceedings of FED-Vol. 121, Gas-Solid Flows ASME 1991*, Portland, pp. 11–17.

Winant, C. D., and Browand, F. K., 1974, "Vortex Paring: The Mechanism of Turbulent Mixing-Layer Growth at Moderate Reynolds Number," *Journal of Fluid Mechanics*, Vol. 63, pp. 237–255.

S. A. Kinnas
Principal Research Engineer and Lecturer.

C. H. Mazel
Research Engineer.

Department of Ocean Engineering,
Massachusetts Institute of Technology,
Cambridge, MA 02139

Numerical Versus Experimental Cavitation Tunnel
(A Supercavitating Hydrofoil Experiment)

A supercavitating hydrofoil experiment is performed at the MIT Variable Pressure water tunnel, at several angles of attack and cavitation numbers. The velocity is measured on a rectangular contour surrounding the foil and cavity as well as in the vicinity of the cavity surface. The measurements are compared to the predicted results from a nonlinear cavity analysis method in which the effects of the tunnel walls are included via images. Forces are inferred from momentum integrations of the measured velocities and compared to those predicted from the analysis.

1 Introduction

Numerous experiments have been performed on different bodies in cavitating flow and in particular on hydrofoils (e.g., Parkin, 1956; Silberman, 1959; Wade and Acosta, 1966; Leehey and Stellinger, 1975). The majority of these experiments have focused on visualizing the cavity shapes, measuring forces and making comparisons with the predictions of different analysis methods for the same flow conditions (cavitation number).

In the present experiment we have mainly been concerned with measuring the velocity flow field around a supercavitating hydrofoil. The measured velocities are compared to those predicted from an existing nonlinear cavity analysis method. In order to account for the blockage effects exactly (in an numerical sense) the cavity boundary value problem is solved by imaging the singularities representing the cavity and the foil with respect to the walls. A one to one comparison between experiment and analysis is thus being made, where identical geometry and flow conditions have been considered in both. In the past, analyses have usually assumed unbounded flow and the blockage effects were either approximated (by modifying the foil geometry and/or angle of attack) or ignored. Another objective of this experiment was to measure the velocity in the vicinity of the cavity surface and validate the basic assumption of constant velocity (i.e., pressure) on the cavity. Finally, the forces acting on the cavitating hydrofoil have been deduced from momentum integrations of the measured velocity flow field, and compared against those computed by the analysis method.

2 Experiment

2.1 The Foil and Mounting Mechanism. The anodized aluminum test foil had a supercavitating section with high loading at the trailing edge.[1] The chord length was 203.2 mm, with a 508 mm span to traverse the 508 × 508 mm test section of the MIT water tunnel. A description of the MIT water tunnel was recently presented by Kerwin (1992). The maximum foil thickness was 17.5 mm. The foil was attached to the acrylic windows of the water tunnel at two points on either end. The foil was free to pivot about the upstream attachment points, while the downstream attachments (pins) were fixed but adjustable. This arrangement, shown schematically in Fig. 1, facilitated changing the angle of attack.

A narrow slot was milled into each end of the foil and a length of rubber O-ring gasket material was fitted into this slot. When the foil was mounted in the water tunnel the gasket was squeezed between the foil and the window, preventing cross-flow from the pressure to the suction side.

2.3 Experimental Observations. The cavities were approximately two-dimensional (cavity length constant across the span) under all test conditions. By making small adjustments to the tunnel pressure it was possible to maintain the cavity length at the desired value. In a few cases the system was more sensitive, and the cavity length would spontaneously shrink or

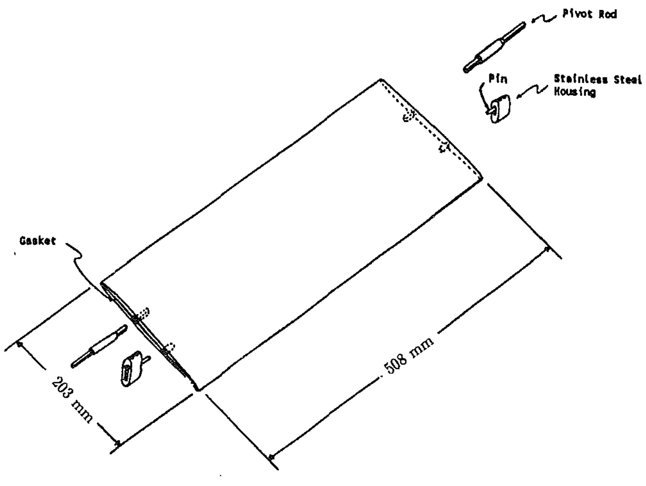

Fig. 1 A perspective view of the foil and its supports

---

[1] Its complete geometry is given in Kinnas and Mazel (1991).

Contributed by the Fluids Engineering Division for publication in the JOURNAL OF FLUIDS ENGINEERING. Manuscript received by the Fluids Engineering Division June 26, 1992; revised manuscript received April 2, 1993. Associate Technical Editor: A. Prosperetti.

grow. This seemed to be related to the amount of bubbles in the water. In these cases data runs along a leg were repeated after the cavity length had stabilized.

For each condition the extent of cavitation on the pressure side (face cavitation), and the location of cavity detachment on the suction side, were determined visually. At $\alpha = 1.85$ deg the cavitation on the suction side started at about mid-chord for all cavity lengths. There was some face cavitation in all cases, starting at the leading edge. The face cavitation was barely visible at $l = 1.5$, and extended downstream approximately 25 mm of $l = 2$, and approximately 50–75 mm for $l = 2.5$ and $l = 3$.

At $\alpha = 3.1$ deg the cavity on the suction side started approximately 50 mm from the leading edge for all cavity lengths. There was no established face cavitation for any cavity length. At $l = 3$ there were occasional, short-lived cavities on the pressure side, starting at isolated points along the leading edge.

At $\alpha = 4.85$ deg the cavity on the suction side started at the leading edge for all cavity lengths. There was no face cavitation.

2.4 Experimental Procedures. Fluid velocity measurements were made with a two-component laser doppler velocimetry system (Kerwin, 1992), permitting simultaneous acquisition of streamwise and vertical velocity components. Velocities were measured at points in a rectangular box pattern surrounding the foil and cavity. The sampling rectangle was 680 mm in the horizontal direction and 200 mm in the vertical direction. The sample spacing along the horizontal portions of the rectangle, above and below the foil, was 10 mm. The spacing along the vertical portions of the rectangle was 5 mm, except in the wake region, where the sample spacing was reduced to 2 mm.

The laser system was programmed to acquire 750 velocity readings at each sample location. Under optimal conditions these samples could be acquired within a few seconds, but in the presence of a large number of bubbles it took 20 seconds or more. Within the data acquisition program the array of 750 velocity values was processed to determine the mean and standard deviation for each velocity component. The program then discarded any points which fell more than three standard deviations from the mean, and recomputed the means and standard deviations from the reduced data set.

Two elements contribute to the variations in the velocity data, as indicated by the standard deviations: actual variations in the flow at that point as a function of time (turbulence), and variations due to errors in the flow measurement equipment. Under the conditions of this experiment the former contribution was dominant. Standard deviations for the streamwise component ranged from approximately 3 percent of the mean at points outside the wake region, to 10 percent at points directly behind the foil and cavity. The magnitudes of the standard deviations for the vertical velocity component were similar to those for the streamwise component. The values of the mean and the standard deviation were unaffected in a test case where twice as many velocity readings (1500) were used.

It was necessary to add an additional data quality check for this experiment. Due to large numbers of cavitation bubbles the laser system sometimes produced anomalously high velocity readings. A software filter that discarded any points with a velocity greater than 11 m/s, well above the range of real values, was added to the data processing software.

At one set of operating conditions ($\alpha = 5.21$ deg, $l = 1.75$, $l_0 = 0.05$, $\sigma = 0.43$, $U_\infty = 6.0$ m/s), in an attempt to measure the fluid velocity on the cavity surface for comparison with numerical prediction, the horizontal velocity component was measured at points along a vertical path approaching the cavity. This was done at two locations above the cavity, and one location below.

2.5 Evaluation of Foil Forces in the Experiment. The lift was determined by applying conservation of momentum through the sides of the rectangle surrounding the foil and cavity. The final expression for the lift involves only integrals of the velocities at the sides of the rectangle, as described in Kinnas (1991). The experimental drag was determined by using the formula:

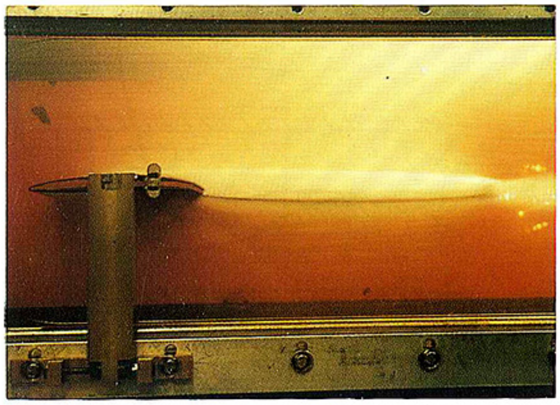

Fig. 2 Photographs from the experiment. Top: the foil section with its main and its secondary support. Middle: the foil at α = 1.85 deg with l = 1.5 supercavity. Bottom at α = 1.85 deg with l = 30 supercavity.

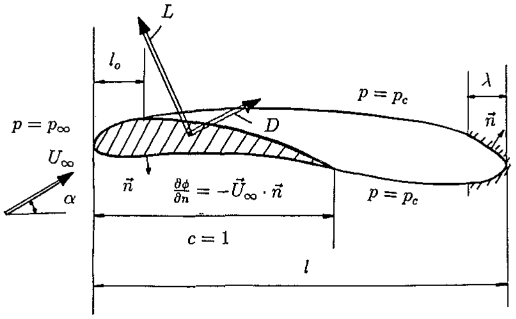

Fig. 3 Supercavitating foil

$$D = \rho U_\infty \int_{z_L}^{z_U} \Delta u dz - \rho \int_{z_L}^{z_U} (\Delta u)^2 dz \tag{1}$$

where Δu is the measured horizontal velocity defect at the downstream side of the rectangle. The velocity defect is defined as the difference between the measured velocity profile in the wake, and a hypothetical profile determined by interpolating between the velocities on either side of the wake region. z_L and z_U are the vertical coordinates of the lower and upper tips of the wake region, respectively. Equation (1) has been derived by applying conservation of momentum in a fluid domain surrounded by a rectangle whose the top and bottom sides coincide with the tunnel walls. The detailed derivation and the numerical treatment of the involved integrals are described in Kinnas (1991). The related analysis is similar to that developed by Betz (1925) and later improved by Maskell (1973). It can be shown that Eq. (1) reduces to Betz's formula in the case of uniform wake profiles outside the wake region.

3 Numerical Method

3.1 Cavitating Hydrofoil in Unbounded Flow. The fundamentals of the numerical method are described in detail by Kinnas and Fine (1991). A supercavitating hydrofoil is depicted in Fig. 3 (for convenience we take the inflow $U_\infty = 1$ and the foil chord length $c = 1$). The main characteristics of the method may be summarized as follows:

- It is a completely *nonlinear* perturbation potential based panel method. The foil and cavity are modeled with constant strength source and dipole panels. The method solves for the unknown perturbation potentials ϕ (dipole strengths) on the

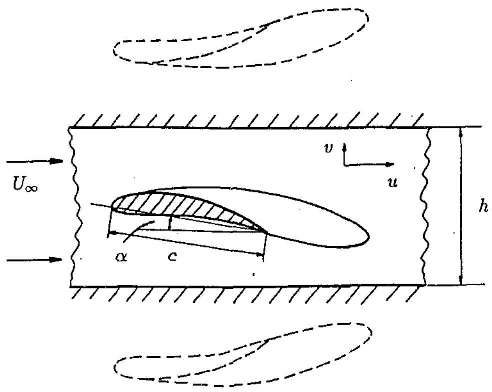

Fig. 4 Supercavitating foil inside of a tunnel. The wall is represented with images of the foil and cavity singularities. The case with number of reflections NIMAGE = 1 is shown.

fully wetted hydrofoil and for the unknown source strengths, $\partial\phi/\partial n$, on the cavity surface. The source strengths are known on the wetted foil via the kinematic boundary condition and the potentials are known on the cavity via the dynamic boundary condition. The dynamic boundary condition requires the pressure on the cavity to be constant, $p = p_c$.

- The *input* (also shown in Fig. 3):

1. The foil section geometry and the angle of attack, α.
2. The cavity length, l.
3. The cavity detachment point on the upper surface, l_0.
4. The length of the cavity termination model, λ. We have the options to apply a "curved plate model", as shown in Fig. 3, or a prescribed pressure law model (the same on both sides of the cavity) followed by an open cavity wake. In the case of the "curved plate model" (essentially an outgrow of Riabouchinsky's (1921) model) the plate is allowed to change the distance between its tips and to move up and down but is restricted from rotating. The models are described in more detail in Fine (1992).

- The *output*:

1. The cavitation number, σ, defined as usual:

$$\sigma = \frac{p_\infty - p_c}{\frac{\rho}{2U_\infty^2}} \qquad (2)$$

2. The cavity shape. This is determined in an iterative manner with the first iteration being the cavity shape from linearized cavity theory.
3. The pressure distribution on the surface of the foil.
4. The forces (lift L and drag D) acting on the foil. The lift is determined by integrating the pressure forces in the direction normal to the inflow. The drag consists of two components: (*a*) the ideal flow cavity drag which is determined by integrating the pressure forces in the direction of the inflow and, (*b*) the viscous drag which is determined by applying a uniform friction coefficient, c_f, over the wetted part of the foil. The values of the lift and inviscid cavity drag have been found to be very insensitive to the kind or extent, λ, of the cavity termination model (Kinnas and Mazel, 1991; Fine, 1992).
5. The velocity field at any point in the flow field. It is computed as the sum of the contributions of all dipoles and sources on the foil and cavity, as well as those of their images in the case of a foil inside a tunnel, addressed in the next section.

The numerics of the method have been validated extensively in Kinnas and Fine (1991) and Fine (1992). 100 panels around the cavity and foil seem to be adequate in producing convergent results. In general, for supercavitating foils at moderate angles of attack, linear theory, compared against the panel method, predicts the cavity shape and the forces with acceptable accuracy (Kinnas, 1992; Fine and Kinnas, 1992). However, the velocity flow field, especially close to the cavity or foil, is computed more accurately by the panel method than by linear theory. This is due to the fact that in linear cavity theory the upper and lower surfaces of the foil or cavity are assumed to collapse in one segment (the branch cut in the complex plane), as opposed to the panel method in which the singularities lie on the exact foil and cavity surface. Since one of the objectives of the present work was to compare the velocities from experiment and analysis, it was decided to use the panel method.

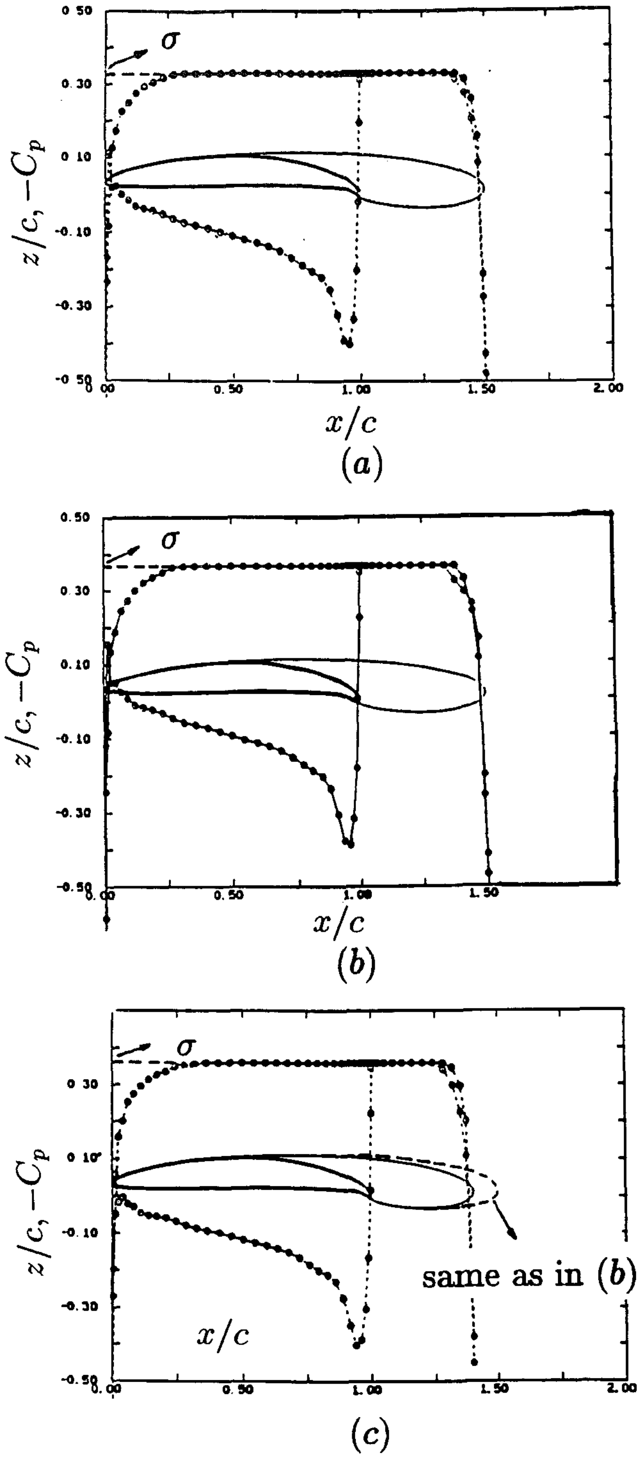

Fig. 5 Effect of walls (represented with images) on the predicted cavity shapes: (*a*) unbounded flow, $l = 1.5$ (*b*) with images, $l = 1.5$ (*c*) unbounded flow at the same cavitation number as in *b*. In all cases $\alpha = 1.85$ deg and $l_0 = 0.3$. The height of the tunnel is $h/c = 2.5$.

Table 1 Dependence of forces on the number of images; $\alpha = 1.85$ deg, $l = 1.5$, $h/c = 2.5$. NIMAGE = 0 corresponds to unbounded flow

NIMAGE	C_L	C_D
0	0.429	0.038
10	0.445	0.040

In the case of supercavitation, the forces as well as the cavity shapes have been found to depend very little on λ (Fine, 1992). Even though we could determine λ from LDV measurements at the end of the cavity, it is a fortunate result that its value does not affect the solution substantially. In all the computations we used $\lambda = 0.1$.

3.2 Cavitating Hydrofoil Inside of a Tunnel. Consider a supercavitating hydrofoil inside of a tunnel, as shown in Fig. 4. The height of the tunnel is h. The effect of the tunnel walls can be accounted for in the previously described method by including in the formulation the influence of the infinite set of images of all the singularities representing the foil and cavity with respect to both walls. In practice, a set of ten images (i.e., number of reflections NIMAGE = 10) is enough in order for the zero normal velocity condition on the walls to be satisfied within acceptable accuracy (0.5 percent of the inflow). The effect of the tunnel walls on the cavity solution can be seen in Fig. 5. The cavity shapes and pressure distributions are shown as predicted by the present method: (*a*) in unbounded flow, (*b*) when the images are included and for the same cavity length as in (*a*) and, (*c*) in unbounded flow with the cavity length corresponding to the same cavitation number as in (*b*). Comparing (*a*) with (*b*) notice that the cavity shapes do not differ substantially from each other. However, the corresponding cavitation number[2] is higher when the tunnel walls are included. Thus, for the same cavitation number the cavity length and volume will be smaller in unbounded flow, as can be seen by comparing parts (*b*) and (*c*) of Fig. 5. Therefore, the tunnel wall effects must be included when making comparisons between analysis and experiment. The effect of walls on the forces is shown in Table 1.

4 Numerical Versus Experimental Results

The foil section was analyzed using the nonlinear panel method at the same angles of attack and cavity lengths as those in the experiment. Comparisons of the velocities and forces are given next. The cavity length of $l = 2.5$ was found to be the most unstable during the experiment and thus, the corresponding results are not shown.

4.1 Velocities Around the Foil and Cavity. A representative comparison between the numerical versus experimental velocities is shown in Figs. 7 and 8 for $\alpha = 3.1$ deg and $l = 1.5$ and $l = 3.0$. The absolute value of the inflow velocity U_∞ was determined by scaling the numerical velocities through the upstream side of the rectangle until their mean value was the same as the mean value of the corresponding experimental velocities. In the calculations, the location of the cavity detachment point, l_o, was taken equal to the one measured in the experiment. An alternative would have been to use a predictive cavity detachment criterion, such as the one suggested by Franc and Michel (1985). However, using different values of l_o in the computations did not affect the results substantially, as long as the detachment point was not in the vicinity of the leading edge. The complete set of comparisons for all tested angles and cavity lengths may be found in Kinnas and Mazel (1991). From these figures we may notice the following:

- The overall agreement is very good.
- The analysis, which only models the potential flow, is not able to capture the velocity defect in the wake of the cavity. However, it predicts the flow outside the boundary layer in the wake quite accurately.
- The agreement seems to deteriorate with increasing cavity length. In particular, for $l = 3$ an appreciable shift (on the order of 10 percent of the inflow) between the numerical and the measured velocities is observed at the downstream side of the rectangle, as seen in Fig. 8. In an attempt to reduce this shift we applied an open cavity model in our analysis. The ultimate openness of the cavity was determined from the computed cavity drag by applying momentum theory. A main parameter in this model is the length of a transition region in which the cavity wake thickness reduces gradually from its value at the cavity end to its ultimate wake value. By applying this model and by changing the mentioned parameter, we were able to improve the comparison in the vicinity of the cavity end without, however, reducing the shift at the downstream end of the rectangle substantially. A possible explanation for this shift may be the reduced effective density of the fluid due to the presence of dispersed cavity bubbles, especially behind the cavity end. We did not pursue this issue further.

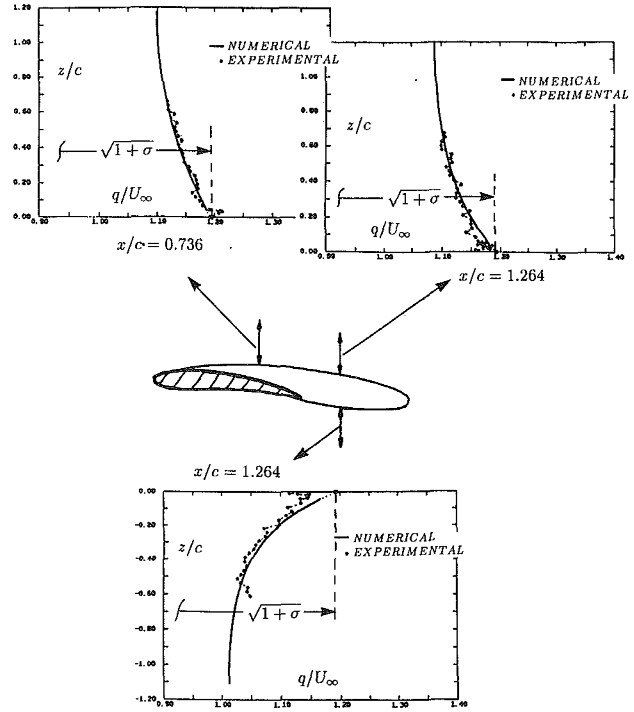

Fig. 6 Numerical versus experimental velocities as a function of the vertical distance from the cavity boundary at different chordwise locations; $\alpha = 5.21$ deg, $l = 1.75$, $l_0 = 0.05$, $\sigma = 0.43$.

4.2 Velocities Near the Cavity Surface. At one set of conditions we measured horizontal velocities at several points on a vertical path approaching the cavity. The measured velocities are shown against those predicted from the described analysis in Fig. 6. The overall comparison is very good. The basic assumption of constant velocity (i.e., pressure) on the cavity appears to be valid within acceptable accuracy. Notice that the computed velocities smoothly extrapolate to the cavity velocity q_c which has been computed from the formula $q_c/U_\infty = \sqrt{1+\sigma}$, where σ is the cavitation number predicted from the analysis. This provides a very strong test of the validity of the numerical computations. On the other hand, the quality of the measurements deteriorates as the laser beams get very close to the cavity. This may be attributed to the unsteadiness

---

[2] Remember that $\sigma = -C_p$ on the cavity.

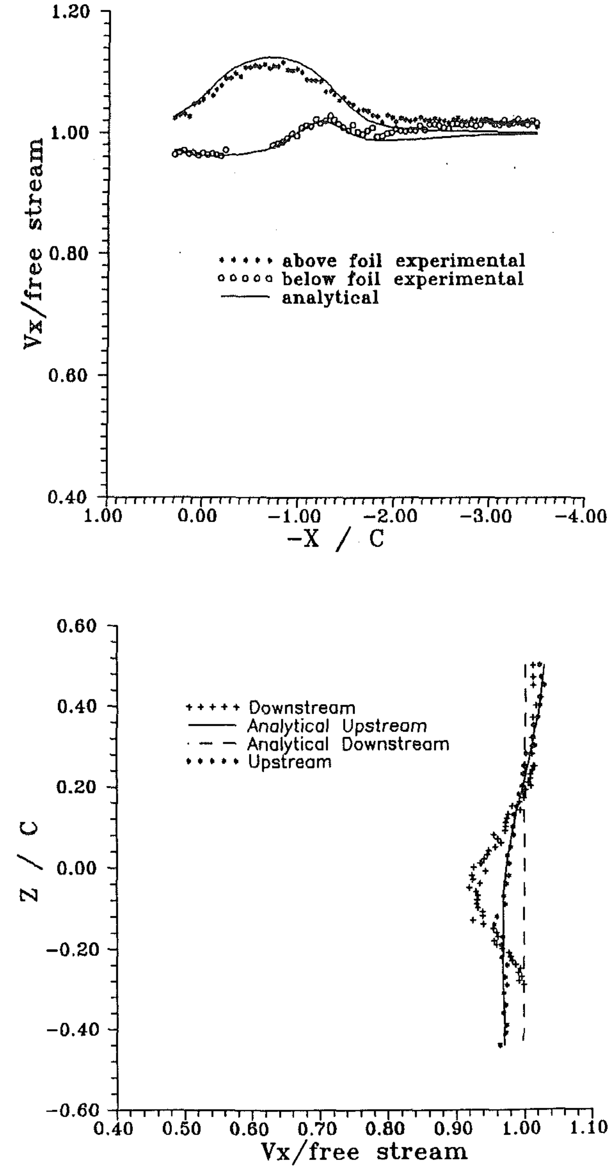

Fig. 7 **Numerical versus experimental horizontal velocities at each side of the rectangle; $\alpha = 3.1$ deg, $l = 1.5$**

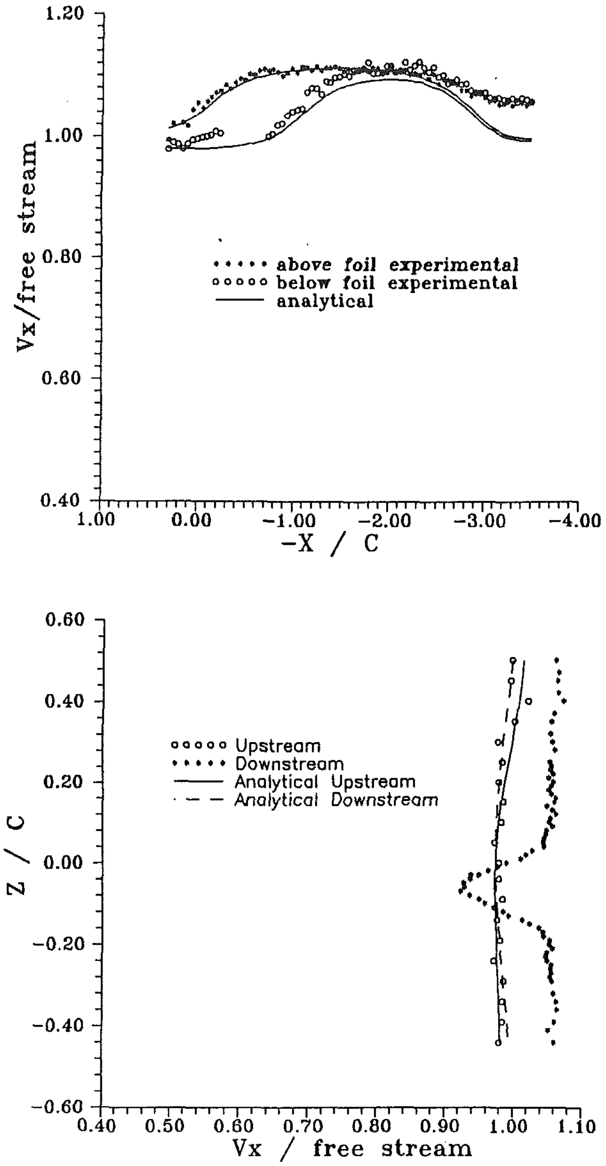

Fig. 8 **Numerical versus experimental horizontal velocities at each side of the rectangle; $\alpha = 3.1$, deg $l = 3.0$**

as well as variations in the spanwise direction[3] of the cavity surface. Figure 6 suggests that in order to find the cavity velocity, the measurements should be extrapolated to the location of cavity surface (determined visually with the help of the laser) from the measurements away from the cavity. Since the measurements do not vary smoothly with vertical distance, the computational results (scaled by a constant factor which is determined from minimizing the error between the computations and the measurements in a least squares sense) may be used in the extrapolation. This extrapolation will be more successful the smaller the slope of the velocity with distance (du/dz) is. It can be proven that the slope du/dz is proportional to q_c/R where R is the radius of curvature of the cavity. For example, the curvature of the cavity shown in Fig. 6 is largest at the bottom, where the magnitude of du/dz is larger than those corresponding to the other two locations.

4.3 Forces. A representative comparison between the forces from experiment and analysis is shown in Fig. 9 for $\alpha = 3.1$ deg. The complete set of comparisons for the other angles and cavity lengths may be found in Kinnas and Mazel (1991). The lift and drag coefficients are defined as usual from $C_L = L/[(\rho/2)U_\infty^2 c]$ and $C_D = D/[(\rho/2U_\infty^2 c)]$. In estimating the viscous drag in the analysis, a uniform surface friction coefficient $c_f = 0.002$ has been used. Even though the analysis seems to predict the correct trends (especially for the lift), the comparisons are not as favorable as those of the velocities. For the lift this may be attributed to the fact that its value is essentially proportional to the *difference* between the horizontal velocities at the top and bottom sides of the rectangle. The error in predicting the lift is of the same order as the error in predicting the mentioned difference. The relatively small error between the numerical and measured velocities, however, is magnified when expressed in terms of the difference between the velocities at the top and the bottom of the rectangle.

5 Conclusions

A systematic comparison between experiment and analysis has been performed for a supercavitating hydrofoil. The effects of the tunnel walls were modeled completely in the analysis method. The velocities were found to be in very good agreement, especially for cavities extending no more than one chord

---

[3] The cavity velocity is measured with the set of horizontal beams which are in effect "grazing" the cavity surface.

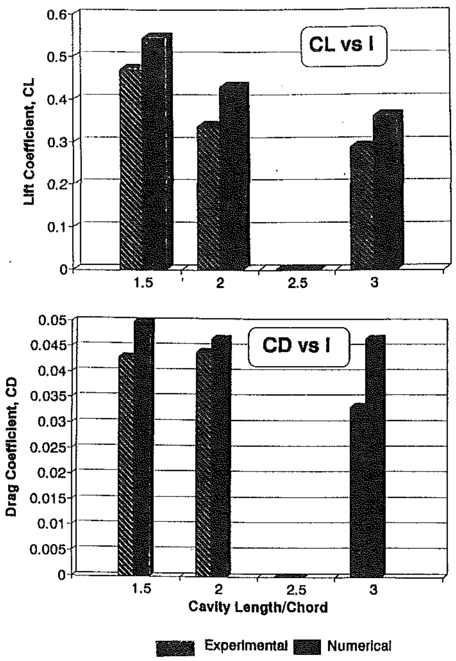

Fig. 9 Numerical versus experimental lift and drag; $\alpha = 3.1$ deg

length behind the trailing edge of the foil. However, the forces seemed to be in larger disagreement than the velocities, simply because of the magnified error in the difference between the velocities above and below the foil and cavity. Finally, the basic assumption of constant velocity on the cavity surface appeared to be valid in the experiment.

Acknowledgments

The experimental part of this work was sponsored by the Propulsion Group at Volvo-Penta of Sweden. The analytical part was sponsored by the Applied Hydromechanics Research Program administered by the Office of Naval Research (Contract: N00014-90-J-1086). The authors would like to thank Thor Hendrickson and Matt Knapp, both undergraduate students at MIT, and Dr. Neal E. Fine, currently a postdoctoral associate at MIT, for their help with the experimental and numerical aspects of this work.

References

Betz, A., 1925, "Ein Verfahren zur direkten Ermittlung des Profilwiderstandes," *ZFM*, Vol. 16, pp. 42–44.

Fine, N. E., 1992, "Nonlinear Analysis of Cavitating Propellers in Nonuniform Flow," PhD thesis, Department of Ocean Engineering, MIT, Cambridge, MA.

Fine, N. E., and Kinnas, S. A., 1992, "A Boundary Element Method for the Analysis of the Flow Around 3-D Cavitating Hydrofoils," *Journal of Ship Research* (to appear).

Franc, J. P., and Michel, J. M., 1985, "Attached Cavitation and the Boundary Layer: Experimental Investigation and Numerical Treatment," *Journal of Fluid Mechanics*, Vol. 154, pp. 63–90.

Kerwin, J. E., 1992, "The MIT Marine Hydrodynamics Water Tunnel—A 53rd Anniversary Celebration," The New England Section SNAME Meeting, MIT, Cambridge, MA, May 21.

Kinnas, S. A., 1991, "Hydrofoil Lift and Drag from Momentum Integrations," Technical Report No. 91-4, Department of Ocean Engineering, MIT.

Kinnas, S. A., 1992, "Inversion of the Source and Vorticity Equations for Supercavitating Hydrofoils," *Journal of Engineering Mathematics*, Vol. 26, pp. 349–361.

Kannas, S. A., and Fine, N. E., 1991, "Non-Linear Analysis of the Flow Around Partially or Super-Cavitating Hydrofoils by a Potential Based Panel Method," *Boundary Integral Methods—Theory and Applications*; *Proceedings of the International Association of Boundary Element Methods* (*IABEM-90*) *Symposium*, Springer-Verlag, Heidelberg, pp. 289–300.

Kinnas, S. A., and Mazel, C. H., 1991, "Numerical vs. Experimental Cavitation Tunnel," Technical Report No. 91-6, Department of Ocean Engineering, MIT.

Leehey, P., and Stellinger, T. S., 1975, "Force and Moment Measurements of Supercavitating Hydrofoils of Finite Span With Comparison to Theory," ASME JOURNAL OF FLUIDS ENGINEERING, Vol. 97, pp. 453–464.

Maskell, E. C., 1973, "Progress Towards a Method of Measurement of the Components of the Drag of a Wing of Finite Span," Technical Report No. 72232, Royal Aircraft Establishment.

Parkin, B. R., 1956, "Experiments on Circular Arc and Flat Plate Hydrofoils in Non-Cavitating and Fully Cavity Flow," Technical Report No. 47-6, Hydrodynamics Laboratory, California Institute of Technology.

Riabouchinsky, D., 1921, "On Steady Fluid Motions with Free Surfaces," *Proceedings of London Math. Soc.*, Vol. 19, pp. 206–215.

Silberman, E., 1959, "Experimental Studies of Supercavitating Flow About Simple Two-Dimensional Bodies in a Jet," *Journal of Fluid Mechanics*, Vol. 5, pp. 337–354.

Wade, R. B., and Acosta, A. J., 1966, "Experimental Observations on the Flow Past a Planoconvex Hydrofoil," ASME JOURNAL OF FLUIDS ENGINEERING, Vol. 88, pp. 273–283.

Three-Dimensional Calculation of Air-Water Two-Phase Flow in Centrifugal Pump Impeller Based on a Bubbly Flow Model

Kiyoshi Minemura
Professor.

Tomomi Uchiyama
Research Associate.

School of Informatics and Sciences,
Nagoya University,
Nagoya 464-01, Japan

To predict the behavior of gas-liquid two-phase flows in a centrifugal pump impeller, a three-dimensional numerical method is proposed on the basis of a bubbly flow model. Under the assumption of homogeneous bubbly flow entraining fine bubbles, the equation of motion of the mixture is represented by that of liquid-phase and the liquid velocity is expressed as a potential for a quasi-harmonic equation. This equation is solved with a finite element method to obtain the velocities, and the equation of motion of an air bubble is integrated numerically in the flow field to obtain the void fraction. These calculations are iterated to obtain a converged solution. The method has been applied to a radial-flow pump, and the results obtained have been confirmed by experiments within the range of bubbly flow regime.

Introduction

Related to accidents involving loss of coolant in nuclear reactors, the accurate prediction of the flow characteristics in centrifugal pumps operating under gas-liquid two-phase flow conditions is imperative. Various methods that attempt to estimate the performance change of the pumps have been proposed. Correlating methods based on the ratio of the hydraulic loss in two-phase flow to that in single-phase one (Mikielewicz et al., 1978); Minemura et al., 1985), the use of experimental homologous curves expressed in a polar coordinate (Kennedy et al., 1982); (Minato and Tominaga, 1988), and a numerical method based on one-dimensional two-phase flow equations in an impeller channel by Furuya (1985) are such examples.

Since the characteristics of the pumps under two-phase flow conditions are closely related to the states of the mixture, many researchers have been investigating the flow entrained noncondensable air bubbles. The influence of the compressibility of the mixture on the characteristics of cascade flows was investigated based on a homogeneous bubbly flow model with no-slip velocity between two phases by Nishiyama (1978), and the effect of viscosity on the behavior of shock waves around a hydrofoil was analyzed with the same model, using both Euler's and Navier-Stokes equations by Shida et al. (1986). By employing the homogeneous bubbly flow model and the Navier-Stokes equations, cavitating unsteady flow around a hydrofoil was also calculated by Kubota et al. (1989). Matsumoto and his co-workers (1988) solved a two-dimensional cascade flow by taking into account the changes in the local density and the slip velocity between the two phases. They showed that the characteristics are greatly affected by the existence of the slip.

As the two-phase flows in pump impellers do behave three-dimensionally due to the curved channel and rotation of the impeller, it is suspected that these methods, whether one or two dimensional, might obscure the true nature of the flows. If the mixture flow is assumed to be the homogeneous bubble one with fine bubbles, the equations of motion of the mixture can be represented by those of the liquid phase. This model, employed by Matsumoto, has been extended in this paper so as to analyze the three-dimensional flow in centrifugal pump impellers by examining the conservation of circulation in this flow field. The liquid velocity has a potential and is expressed by a quasi-harmonic equation, if the absolute flow in the pump inlet is assumed to be irrotational. The quasi-harmonic equation can be solved numerically with a finite-element method to obtain the velocities of the liquid phase. The equation of motion of a single bubble is numerically integrated to obtain distributions of void fraction and pressure. This three-dimensional numerical method has been used to analyze the mixture in a radial-flow pump. The distributions of the pressure and void fraction obtained are in agreement with the experimental results.

Theoretical Relations

When formulating the governing equations for two-phase flow, the following assumptions are made.

(1) The mixture is a homogeneous bubbly flow entraining fine bubbles. The bubble size is small compared to a characteristic length of the impeller channel.

(2) The bubble movements are represented by Basset-Boussinesque-Oseen's formula.

Contributed by the Fluid Engineering Division for publication in the JOURNAL OF FLUIDS ENGINEERING. Manuscript received by the Fluids Engineering Division February 16, 1992; revised manuscript received February 23, 1993. Associate Technical Editor: T. T. Huang.

(3) The mixture flow is steady in a relative frame or reference, which rotates around an axis with a constant velocity, and inviscid except for the drag force between two phases.

(4) The change of void fractions in an absolute frame of reference is quasi-steady.

(5) Neither fragmentation nor coalescence of bubble occurs.

(6) The bubbles maintain their spherical shape and change adiabatically in volume according to the pressure that surrounds them. The liquid phase is incompressible.

(7) The drag coefficient of a bubble is the same as that of a solid particle. The influence of interactions between bubbles on their movements is identical to that in a crowd of solid particles.

(8) Neither mass nor heat transfer takes place between the two phases.

(9) The mass and momentum of the gas-phase are very small and neglible compared with those of the liquid-phase. However, the effects of bubble slip are accounted for. Gravity effects on the bubble movement are also ignored.

Governing Equations of Two-Phase Mixture

The equation of motion of a bubble (mass M), moving with the velocity $\mathbf{V}_a$ in a water flow field, $\mathbf{W}_a$, can be given by the following equation (Minemura and Murakami, 1980) under the assumptions (1), (2), (6), and (9).

$$d_a(M\mathbf{V}_a)/\mathrm{dt} = \mathbf{f}_P + \mathbf{f}_D + \mathbf{f}_V \tag{1}$$

In Eq. (1), the term $\mathbf{f}_P$ is the force due to the pressure gradient, $\mathbf{f}_D$ the drag force, and $\mathbf{f}_V$ the force due to virtual mass. These terms are given by the following equations, respectively,

$$\begin{gathered}\mathbf{f}_P = -(4/3)\pi R_b^3 \nabla_a p \\ \mathbf{f}_D = (1/2)\rho_l(\pi R_b^2) C_{DTP} |\mathbf{W}_a - \mathbf{V}_a| (\mathbf{W}_a - \mathbf{V}_a) \\ \mathbf{f}_V = \rho_l C_V (4/3)\pi [D_a(R_b^3 \mathbf{W}_a)/Dt - d_a(R_b^3 \mathbf{V}_a)/dt] \\ D_a/Dt = \partial_a/\partial t + \mathbf{W}_a \bullet \nabla_a,\ d_a/dt = \partial_a/\partial t \end{gathered} \tag{2}$$

where the virtual mass coefficient C_V is assumed to be constant ($C_V = 0.5$).

In a system rotating with a constant angular velocity (Fig. 1), the acceleration terms, velocities and differential operators in Eqs. (1) and (2) are rewritten as follows,

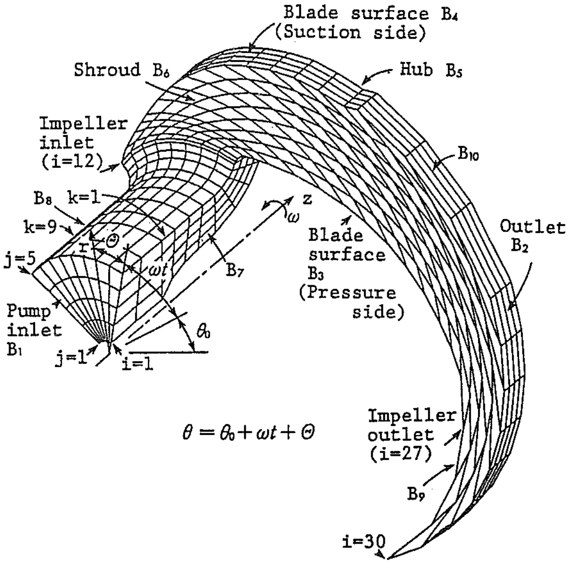

Fig. 1 Calculated flow region

$$\begin{gathered} d_a\mathbf{V}_a/dt = d\mathbf{V}/\mathrm{dt} + 2\omega \times \mathbf{V} + \omega \times (\omega \times \mathbf{r}) \\ D_a\mathbf{W}_a/Dt = D\mathbf{W}/Dt + 2\omega \times \mathbf{W} + \omega \times (\omega \times \mathbf{r}) \\ \mathbf{W}_a = \mathbf{W} + \omega \times \mathbf{r},\ \mathbf{V}_a = \mathbf{V} + \omega \times \mathbf{r} \\ D/Dt = \partial/\partial t + \mathbf{W} \bullet \nabla,\ d/dt = \partial/\partial t,\ \nabla_a = \nabla \end{gathered} \tag{3}$$

From the assumption (7), the drag coefficient of a bubble C_{DTP} in a multi-bubble systems with void fraction α can be formulated in terms of an experimental relationship (Richardson and Meikle, 1961) between the velocity of solid particles relative to liquid and voidage $(1-\alpha)$ as,

$$C_{DTP} = (1-\alpha)^{-q} \bullet C_D \tag{4}$$

where C_D is the drag coefficient of a single bubble, and q is a function of bubble Reynolds number Re:

$$q = \begin{cases} 8.9\ \mathrm{Re}^{-0.1} & (1 < \mathrm{Re} < 500) \\ 4.78 & (500 \leqq \mathrm{Re} < 7000) \end{cases}$$

Nomenclature

C_D = drag coefficient of a single bubble
C_{DTP} = drag coefficient of a bubble in a multi-bubble system
C_V = virtual mass coefficient
$\mathbf{f}$ = force acting on a bubble
g = acceleration of gravity
i = nodal number in flow direction
j = nodal number in radial direction
k = nodal number in circumferential direction
l = line segment
M = mass of a bubble
N = number of blades
n = number of bubbles in unit volume or unit vector perpendicular to boundary surface
p = absolute pressure without gravity effect
R_b = radius of bubble
Re = Reynolds number of bubble $= 2R_b|\mathbf{W} - \mathbf{V}|/\nu$
r = radial coordinate
S = surface area
t = time
u = peripheral speed of impeller
$\mathbf{V}$ = velocity vector of bubble
$\mathbf{W}$ = velocity vector of water
z = axial coordinate
α = void fraction
β = relaxation factor
Γ = circulation $= \oint \mathbf{W}_a \bullet dl$
θ = angular coordinate of bubble $= \theta_0 + \omega t + \Theta$
$\Delta\theta$ = pitch angle of impeller
Θ = angular coordinate of bubble in a rotating frame
ν = kinematic viscosity of water
ρ = density
ϕ = velocity potential or dimensionless expression of pump flow rate
$\Delta\psi_r$ = dimensionless pressure coefficient $= (p - p_0)/(\rho_l u_2^2)$
ω = angular velocity of impeller

Subscripts

0 = pump inlet or initial condition
1 = impeller inlet
2 = impeller outlet
3 = pump outlet
a = condition in an absolute frame of reference
g = gas phase
l = liquid phase
r = radial component
z = axial component
u = circumferential component

The equation of continuity for air-water two-phase flows in a relative frame of reference is written by the following equation under the assumption (3).

$$\nabla \cdot [(1-\alpha)\rho_l \mathbf{W} + \alpha \rho_g \mathbf{V}] = 0 \tag{5}$$

By using assumptions (1) and (9), Eq. (5) can be reduced to the equation of continuity for the bubbly flow, namely

$$\nabla \cdot [(1-\alpha)\rho_l \mathbf{W}] = 0 \tag{6}$$

The conservation of momentum of the mixture for a unit volume in relative frame of reference is expressed by the following equation under the assumption (3).

$$\begin{aligned}\nabla \cdot [(1-\alpha)\rho_l \mathbf{WW} + \alpha \rho_g \mathbf{VV}] + (1-\alpha)\rho_l \omega \times (2\mathbf{W} + \omega \times \mathbf{r}) \\ + \alpha \rho_g \omega \times (2\mathbf{V} + \omega \times \mathbf{r}) = -\nabla p\end{aligned} \tag{7}$$

The equation of motion for each phase is written

$$\begin{aligned}\nabla \cdot [(1-\alpha)\rho_l \mathbf{WW}] + (1-\alpha)\rho_l \omega \times (2\mathbf{W} \\ + \omega \times \mathbf{r}) = -(1-\alpha)\nabla p - \mathbf{F}\end{aligned} \tag{8}$$

$$\nabla \cdot (\alpha \rho_g \mathbf{VV}) + \alpha \rho_g \omega \times (2\mathbf{V} + \omega \times \mathbf{r}) = -\alpha \nabla p + \mathbf{F} \tag{9}$$

where $\mathbf{F}$ is the summation of drag forces on bubbles in a unit volume.

Rewriting Eq. (7) with the assumptions (1) and (9) gives the equation of momentum conservation for the bubbly flow,

$$\nabla \cdot [(1-\alpha)\rho_l \mathbf{WW}] + (1-\alpha)\rho_l \omega \times (2\mathbf{W} + \omega \times \mathbf{r}) = -\nabla p \tag{10}$$

By using Eq. (6) and constant ρ_l based on the assumption (6), Eq. (10) is transformed into Euler's equation for the bubbly flow in relative frame or reference, that is,

$$(1-\alpha)\mathbf{W} \cdot \nabla \mathbf{W} + (1-\alpha)\omega \times (2\mathbf{W} + \omega \times \mathbf{r}) = -\nabla p/\rho_l \tag{11}$$

When Eq. (11) is expressed in an absolute frame of reference by using Eq. (3), it becomes

$$\partial_a [(1-\alpha)\mathbf{W}_a]/\partial t + (1-\alpha)\mathbf{W}_a \cdot \nabla_a \mathbf{W}_a = -\nabla_a p/\rho_l \tag{12}$$

Rewriting Eq. (12) with the relation $\partial_a \alpha/\partial t = 0$ derived from the assumption (4) gives the following equation.

$$D_a \mathbf{W}_a/Dt = -\nabla_a p/[\rho_l(1-\alpha)] \tag{13}$$

To obtain liquid flow velocities, a three-dimensional finite element method which will be described later is employed. The domain of integration is divided into finite elements. If the volume of a given element is sufficiently larger than that of bubble, a void fraction α may be defined as the volumetric ratio of the volume of all the bubbles existing in an element to the volume of the element itself. Since the bubble volume is $(4/3)\pi \overline{R}_b^3$, where $\overline{R}_b$ is the mean radius of bubbles in the element, α is expressed as,

$$\alpha = (4/3)\pi \overline{R}_b^3 \cdot n \tag{14}$$

where n is the number density of bubbles.

As the value $\overline{R}_b$ is determined by the pressure p surrounding each bubble under the assumption (6), α can be considered to be a function of of p and n.

Thus,

$$\alpha = \alpha(p, n) \tag{15}$$

If we assume that the absolute liquid flow in the pump inlet region upstream of the impeller is irrotational, the flow in the impeller would also be irrotational and the velocity would have a potential. It should, however, be investigated whether the liquid velocity in this bubbly flow model has a potential.

The time rate of the change in the circulation along any closed curve (line element $d\mathbf{l}$, surface element $d\mathbf{S}$) in an absolute flow field is given with the Stokes' formula as,

$$D_a \Gamma/Dt = D_a (\oint \mathbf{W}_a \cdot d\mathbf{l})/Dt = \int [\nabla_a \times (D_a \mathbf{W}_a/Dt)] \cdot d\mathbf{S} \tag{16}$$

Using Eq. (13) for the bubbly flow, Eq. (16) reduces to

$$D_a \Gamma/Dt = -\int \nabla_a \times [\nabla_a p/\rho_l(1-\alpha)] \cdot d\mathbf{S} \tag{17}$$

Since α is a function only of p and n, Eq. (17) can be expressed in dimensionless form with the identities $\nabla_a \times \nabla_a p = 0$ and

$$\nabla_a p \times \nabla_a p = 0,$$

$$D_a \Gamma^*/Dt^* = \int (\partial \alpha/\partial n^*)(\nabla_a^* p \times \nabla_a^* n^*) \cdot d\mathbf{S}^* \tag{18}$$

where

$\Gamma^* = \Gamma/(r_1 u_1)$, $t^* = t/(1/\omega)$, $n^* = n/(1/r_1^3)$, $p^* = p/(\rho_l u_1^2)$, $\nabla_a^* = \nabla_a/(1/r_1)$, and $d\mathbf{S}^* = d\mathbf{S}/r_1^2$.

The order of the integrand in the right-hand side of Eq. (18) can be estimated as follows: The term $\partial \alpha/\partial n^*$ is rewritten via Eq. (14), for a bubbly flow, as,

$$\partial \alpha/\partial n^* = (4/3)\pi (R_{b0}/r_1)^3 \; (p_0/p)/(1-\alpha)^2 \doteqdot O(10^{-8})$$

The mass of a bubble is so small that the bubble moves in the direction of the pressure gradient with a relative velocity to water (Minemura and Murakami, 1980). Thus the gradient of the number density of bubbles n^* arise in this direction. Consequently, the relations of $\nabla_a^* p^* \parallel \nabla_a^* n^*$ and $\nabla_a^* p^* \times \nabla_a^* n^* \ll O(1)$ do hold for the steady flow, and the order of the left-hand side of Eq. (18) is estimated, for a bubbly flow, as,

$$D_a \Gamma^*/Dt^* < O(10^{-8})$$

From the above discussion, the time rate of change in the circulation Γ^* for the bubbly flow is extremely small and can be considered as constant. Thus, the absolute velocity vector W_a has a potential ϕ and is rewritten with the relative velocity vector W as,

$$\mathbf{W}_a = \mathbf{W} + \omega \times \mathbf{r} = -\nabla_a \phi \tag{19}$$

When the equation of continuity (6) in a relative frame of reference is expressed in an absolute frame of reference using the assumption (4), it becomes

$$\nabla_a \cdot [(1-\alpha)\rho_l \mathbf{W}_a] = 0 \tag{20}$$

Substituting Eq. (19) into Eq. (20) under the assumption of constant ρ_l yields a quasi-harmonic equation, governing the bubbly flow in the absolute frame of reference:

$$\nabla_a \cdot [(1-\alpha)\nabla_a \phi] = 0 \tag{21}$$

Numerical Analysis Method

In this paper, the two-phase flow equations obtained are solved for a special case of a flow in a radial-flow impeller pump of low specific-speed [specific speed: 180 (m, m^3/min, rpm); flow rate: 0.9 m^3/min; head: 19 m; rotating speed: 1750 rpm]. The geometry of the pump is almost the same as that employed in our previous experiment (Minemura et al., 1985)[1].

The calculated regions of the flow consist of a blade-to-blade flow space and the passages before and after the space, as shown in Fig. 1. The region of the pump inlet is an annular passage between concentric cylinders, and that of the pump outlet is a passage between parallel planes. Internal flows of the pump, which is operated at the optimum discharge point ($\phi = 0.08$) of the rated speed 1750 rpm, are analyzed for various inlet void fraction α_0, in which the mass flow rate is kept constant under any value of α_0. At the pump inlet, it is assumed that the bubbles have an initial diameter $2R_{b0} = 0.3$ mm, a value which is observed most frequently in the impeller under the same operating conditions (Minemura et al., 1985) as this pump. It is also assumed that the initial velocity of the bubbles is the same as those of the water and that the distribution of void fraction is uniform at the initial section.

---

[1] The pump has two-dimensional impeller blades, and the blade's trailing edge is too thick to obtain a numerical solution satisfying the Kutta condition. Thus in this calculation, the blade thickness was made constant (= 6 mm), and the depth of the impeller channel was modified so that averaged meridional velocities in a radial direction could change in the same way as the existing impeller.

When Eq. (21) is applied to radial flow pumps, it should satisfy the boundary conditions:

$$(1-\alpha)\mathbf{n}\cdot\nabla_a\phi=\begin{cases} W_z, & \text{on } B_1 \\ -W_r, & \text{on } B_2 \\ \pm\mathbf{n}\cdot\omega\times r, & \text{on } B_3 \text{ and } B_4 \\ 0, & \text{on } B_5 \text{ and } B_6 \end{cases} \tag{22}$$

where B_1 and B_2 are the inlet and outlet sections, B_3 and B_4 are the surfaces of the neighboring blades, B_5 and B_6 the hub and shroud surfaces, and $\mathbf{n}$ a unit vector perpendicular to the boundary surface. On the remainder of the boundary, $B_7 \sim B_{10}$, periodic conditions should be met as follows:

$$\begin{gathered} \phi(z,\,\theta+2\pi/N,\,r)=\phi(z,\,\theta,\,r)-\Gamma/N \\ \frac{\partial\phi(z,\,\theta+2\pi/N,\,r)}{\partial\mathbf{n}}=-\frac{\partial\phi(z,\,\theta,\,r)}{\partial\mathbf{n}} \end{gathered} \tag{23}$$

where the circulation Γ is determined so as to satisfy the Kutta condition, that is, the flows from both sides of the trailing edge join smoothly. This condition can be realized iteratively by making the pressures at the trailing edge coincide on the pressure and suction sides of the blade (Minemura and Uchiyama, 1991).

If we assume that the liquid flow velocity into the inlet section B_1 is uniform and without swirl and that the void fraction is also uniform, then $W_{az}=$ constant on B_1. On the other hand, the velocity W_{ar} on section B_2 is determined so as to conserve the mass flow rate of the mixture as well as to satisfy the radial-equilibrium equation, namely,

$$dW_{ar}^2/dz=(\omega/\pi)d\Gamma/dz-1/(2\pi r)^2 d\Gamma^2/dz \tag{24}$$

which is derived under the assumptions of circumferentially uniform distributions of the velocity and void fraction on B_2.

To obtain the uniform distribution of void fraction on B_1, bubbles are arrayed homogeneously on the initial section,[2] and their movement is traced by solving the equation of motion of a bubble. The void fraction α in the flow field is obtained as follows. The solutions of the equations of motion of a bubble produce detailed information on bubble trajectories (i.e., the time Δt and averaged radius $\overline{R}_b$ of the bubbles which pass through each control volume). The inlet void fraction α_0, on one hand, sets the volumetric flow rate of the gas phase through the initial section and determines the number of bubbles released on every bubble trajectory per unit time $\dot{n}$[3]. As the sum of the product of Δt and $\dot{n}$ for each control volume divided by its volume yields the number density of bubbles n, the void fraction α in each control volume is thus evaluated via Eq. (14).

Liquid velocities for the mixture are given by solving Eq. (21) with a finite element method. In this calculation, simplex tetrahedron elements were employed. Although the variable obtained is constant in each element, owing to the simplex method, the value at a node can be uniquely determined with a least-squares method, by using the element values related to all the elements adjacent to the node. The same method is also applied to obtain nodal void fraction.

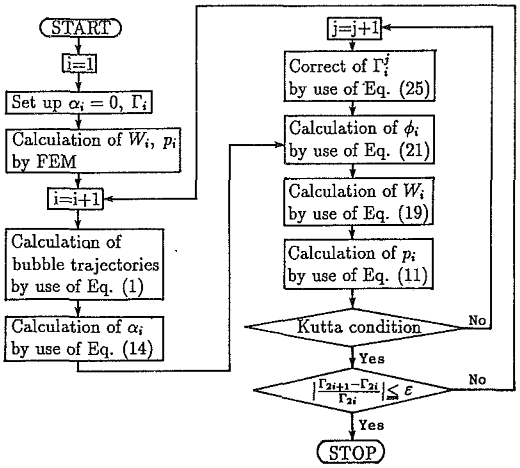

Fig. 2 Flow chart of calculation

After both the velocity W and void fraction α are determined at all the nodes, pressure gradients at every node can be evaluated with Eq. (11). Thus the pressure distribution in the field is decided by integrating the gradients numerically; [i.e., by using a least-squares method with FEM shape functions under the restriction of the pressure imposed on the inlet boundary section (Uchiyama and Minemura, 1992)].

Equations governing the two-phase mixture are reduced to Eq. (14) for void fraction, Eq. (11) for pressure, and Eq. (21) for velocity potential of liquid phase. These equations are iteratively solved as shown in Fig. 2, obtaining the flow properties of the mixture: void fraction α, velocity of water $\mathbf{W}$, and pressure p. The numerical procedure is as follows.

(i) As an initial step ($i=0$), solve Eq. (21) for the flow field wherever the void fraction is zero, $\alpha=0$, to obtain $\mathbf{W}_i$ and p_i. The solution can be given by a three-dimensional finite-element method (Minemura et al., 1988).

(ii) Numerically integrate the equation of motion of bubble, Eq. (1), in the flow field (α_i, $\mathbf{W}_i$, p_i) for the bubbles which are released from various initial positions, before evaluating the void fraction α_{i+1} in every control volume with Eq. (14).

(iii) Solve Eq. (21) in the field of α_{i+1} with FEM to obtain ϕ_{i+1}. To promote the convergence of the solution, modify α_{i+1} with the relation $\alpha_{i+1}=\alpha_i+\beta(\alpha_{i+1}-\alpha_i)$, where β is a relaxation factor and the relation $\beta=0.5$ is used in this calculation.

(iv) Differentiate ϕ_{i+1} to obtain velocity $\mathbf{W}_{i+1}$ with Eq. (19) (Minemura et al., 1988).

(v) Calculate pressure gradients ∇p_{i+1} with Eq. (11) for the field of α_{i+1} and $\mathbf{W}_{i+1}$, before numerically integrating the gradients to obtain pressure p_{i+1}.

(vi) If the pressures on the trailing edge do not satisfy the Kutta condition, modify circulation Γ_{2i+1}^j with the following equation and return to step (iii).

$$\Gamma_{2i+1}^{j+1}=\Gamma_{2i+1}^j+\beta(1-p_P/p_S)\cdot\Gamma_{2i+1}^j \tag{25}$$

where the relaxation factor β and the criterion of convergence for the Kutta condition are taken to be unity and $|1-p_P/p_S|\leqq 0.3\times10^{-2}$, respectively.

(vii) Repeat the calculations from step (ii) to (vi) until the distribution of the void fraction converges, i.e., until Γ_{2i} converges, where the criterion for convergence is taken as $|(\Gamma_{2i+1}-\Gamma_{2i})/\Gamma_{2i}|\leqq 0.3\times10^{-2}$.

Results of Calculation and Discussions

Distribution of the void fraction obtained for $\alpha_0=0.05$ is shown in Fig. 3, where the local void fraction α divided by the inlet void fraction α_0 is plotted. The results on the suction-surface of the blade (section $k=9$ in Fig. 1), on the mid-section between the suction- and pressure-surface (section $k=5$) and on the pressure-surface (section $k=1$) are shown in Fig. (a), (b) and (c), respectively. The void fraction is seen to be locally

---

[2] In this calculation, the initial bubble positions were placed in 16 rows arranged in the circumferential direction and 8 rows in the radial at a total of 128 points. The resultant radial distance Δr_0 ($\Delta r_0/r_1=0.088$) and circumferential angle $\Delta\theta_0$ between bubbles ($\Delta\Theta_0/\Delta\theta=0.063$) were kept constant for all α_0.

[3] The number $\dot{n}$ is equivalent to the axial distance between subsequent bubbles on a trajectory z_0. For example, when $\alpha_0=0.01$, then $\Delta z_0/r_1=0.012$ at the initial position nearest the wall of the suction pipe. Irrespective of the different distances between the bubbles in the radial, circumferential and axial directions, almost the same values of α were obtained in each element among the initial sections (sections $i=1\sim3$ in Fig. 1), in which the water flows axially with a uniform velocity.

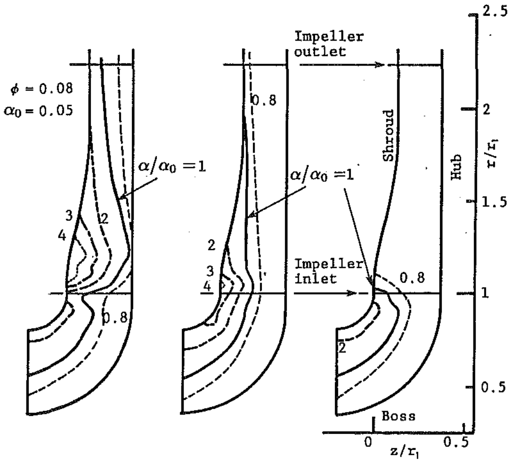

(a) Suction-surface (b) Mid-channel (c) Pressure-surface

Fig. 3 Distributions of void fraction on meridional sections ($\alpha_0 = 0.05$)

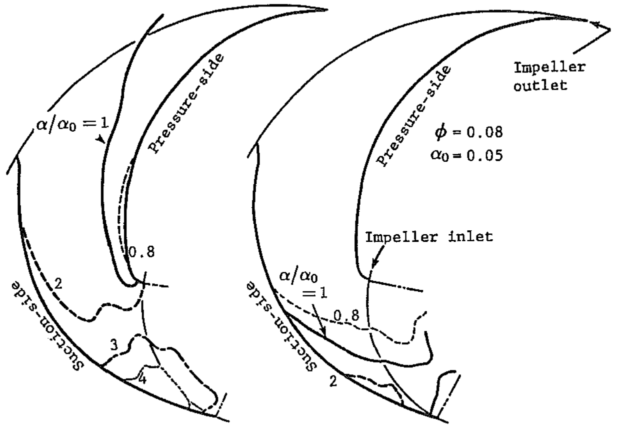

(a) Result on shroud (b) Result on mid-channel

Fig. 4 Distributions of void fraction on blade-to-blade sections ($\alpha_0 = 0.05$)

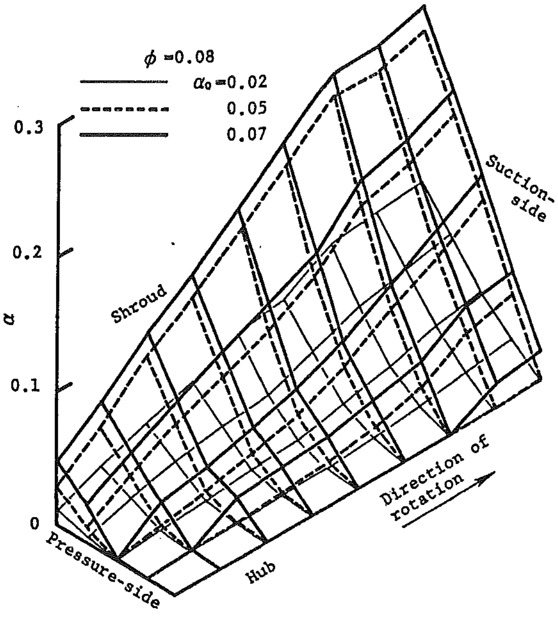

Fig. 5(*a*) Calculated distributions

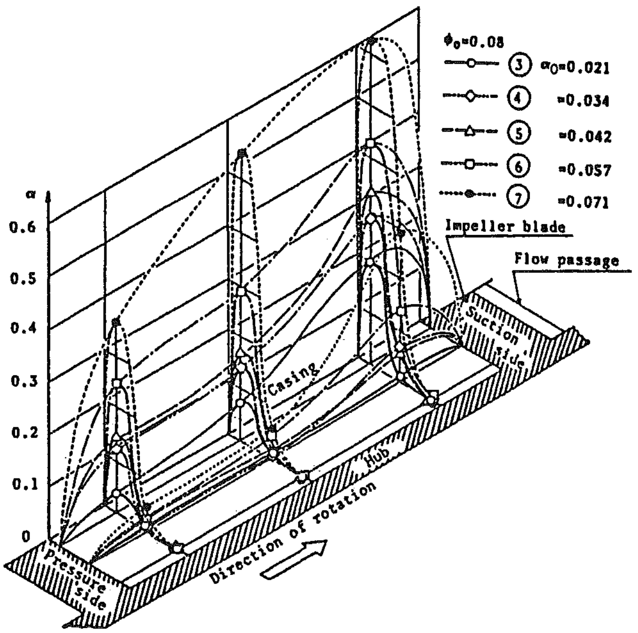

Fig. 5(*b*) Measured distributions (Uncertainty in α is ±7 percent of α and in α_0 ± 3 percent of α_0)

Fig. 5 Distributions of void fraction on the section just after impeller inlet ($r/r_1 = 1.1$)

high in the impeller inlet region, especially on the suction surface, and to increase toward the shroud from the hub, where the value of α is almost zero. The maximum value of α is more than four times α_0. This high void fraction on the suction surface is due to the fact that the bubbles entrained from the pump inlet shift toward the lower pressure zones inside the inlet curvature upstream of the impeller entrance and flow down along the shroud surface (Minemura and Murakami, 1980).

Distributions of the void fraction on blade-to-blade sections are plotted for $\alpha_0 = 0.05$ in Fig. 4. The result on the shroud (section $j = 5$ in Fig. 1) shows a higher void fraction than on the mid-channel between the shroud and hub (section $j = 3$). A region of high void fraction is observed near the suction side of the blade in the impeller inlet. The void fraction increases toward the suction side of the blade from the pressure-side. In this region, the pressure gradient along the bubble trajectory changes its sign, and the bubbles are apt to accumulate there (Minemura and Murakami, 1980).

Calculated distributions of void fraction on a section just after the impeller inlet ($r/r_1 = 1.1$) for fixed mass flow rate and different values of inlet void fraction α_0 are plotted in Fig. 5(*a*), and the results for $\alpha_0 = 0.02$, 0.05, and 0.07 are superimposed. The distributions are seen to be remarkably uneven and shift upward with the shape similar when α_0 is increased. These trends are in agreement with the experimental results (Minemura and Murakami, 1986), as seen in Fig. 5(*b*). The maximum value is, however, about half of that obtained in the experiments. This difference may be attributed to neglect of fluid viscosity.

Dimensionless iso-baric lines $\Delta\psi_r$ on meridional sections are shown for various inlet void fractions α_0 in Fig. 6 for constant mass flow rate of the mixture. The results on the suction-surface of the blade (section $k = 9$ in Fig. 1), those on the mid-section between the suction- and pressure-surface (section $k = 5$), and those of the pressure-surface (section $k = 1$) are plotted in Fig. (*a*), (*b*) and (*c*), respectively. Though the iso-baric lines for $\alpha_0 = 0$, shown by chain lines, are parallel to the pump axis on all sections within the impeller passage, the lines for $\alpha_0 > 0$ incline downward to the right and their gradient increases with an increase in α_0. This inclination, due to the

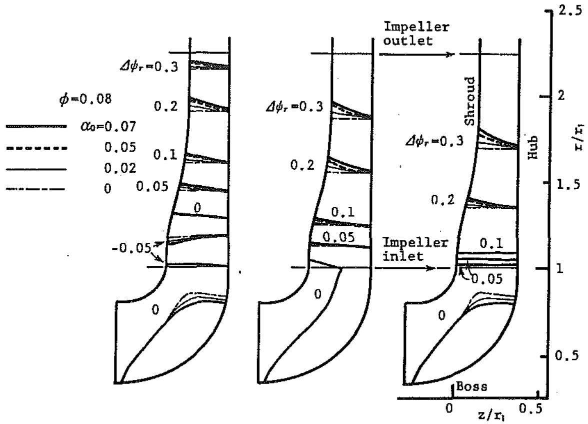

(a) Suction-surface (b) Mid-channel (c) Pressure-surface

Fig. 6 Distributions of pressure on meridional sections

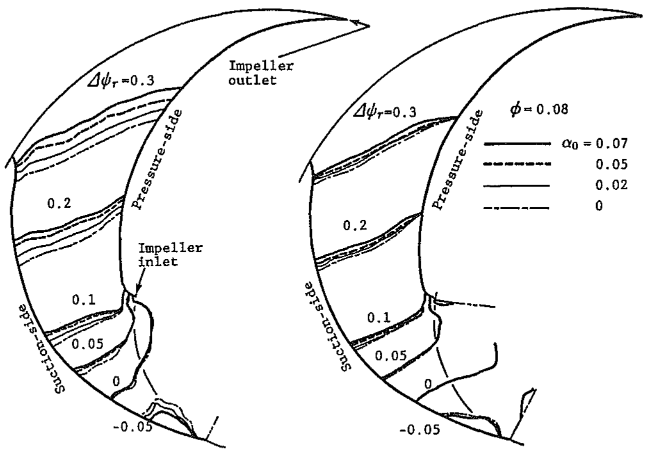

(a) Result on shroud (b) Result on mid-channel

Fig. 7 Distributions of pressure on blade-to-blade sections

higher void fraction toward the shroud, becomes more pronounced downstream of the impeller, especially on the pressure-surface (Fig. 6(*c*)).

Pressure distributions on blade-to-blade sections are shown for different α_0 in Fig. 7, where the results on the shroud and those on the mid-section between the shroud and hub are plotted in Fig. (*a*) and (*b*), respectively. In Fig. 7(*a*), a low pressure region of $\Delta\psi_r \leqq -0.05$ exists near the suction-side of the impeller inlet. When α_0 increases, this low pressure region reduces its area toward the impeller inlet, and the iso-baric lines for $\alpha_0 \geqq 0.05$ shift greatly toward the impeller outlet, except for the region near the leading edge of the pressure-side. These trends are in agreement with the experiment performed with this pump (Minemura et al., 1983) except for the region near the impeller outlet, where the secondary flow due to the fluid viscosity dominates. The results in Fig. 7(*b*) show similar change for α_0, but the change is less than on the shroud.

Conclusions

Based on a bubbly flow model, a three-dimensional numerical method has been proposed, and was employed to calculate the flow of a two-phase mixture through a radial-flow pump. The results obtained are summarized as follows:

(1) The homogeneous bubbly flow with fine bubbles, i.e., bubbles much smaller than the characteristic length of the impeller channel, can be expressed by a quasi-harmonic equation for a potential field with a void fraction distribution given.

(2) Distributions of the void fraction obtained are considerably higher and uneven in the impeller inlet region, where the maximum value of α is more than four times its corresponding value at the pump inlet.

(3) Though the pressure distributions in the radial-flow impeller are even in an axial direction under the single-phase flow condition, the pressure under the two-phase conditions decreases near the shroud, where high void fractions prevail. This reduction becomes evident toward the impeller outlet.

(4) The distributions of the void fraction and pressure which were numerically obtained are in agreement with the experimental results. Therefore, in the bubbly flow regime, the proposed model and method are appropriate for the analysis of three-dimensional two-phase flows in impellers with arbitrary geometry.

Acknowledgement

The authors express their sincere thanks to Professor Telionis for his editorial improvements in this paper.

References

Furuya, O., 1985, "An Analytical Model for Prediction of Two-Phase (Non-condensable) Flow Pump Performance," ASME JOURNAL OF FLUIDS ENGINEERING, Vol. 107, No. 1, pp. 139-147.

Kennedy, W. G., et al., 1982, "Two-Phase Flow Behavior of Axial Pumps," *Proceedings of International Meeting on Thermal Nuclear Reactor Safety.*

Kubota, A., Kato, H., and Yamaguchi, H., 1989, "Finite Difference Analysis of Unsteady Cavitation on a Two-Dimensional Hydrofoil," *Proceedings of 5th International Conference on Numerical Ship Hydrodynamics*, pp. 667-683.

Matsumoto, Y., Nishikawa, H., and Ohashi, H., 1988, "Performance of Cascade of Blades in Two-Phase Flow (Modeling and Numerical Calculation)," *JSME International Journal*, Series II, Vol. 31, No. 4, pp. 652-658.

Mikielewicz, J., Wilson, D. G., Chan, T., and Goldfinch, A. L., 1978, "A Method for Correlating the Characteristics of Centrifugal Pumps in Two-Phase Flow," ASME JOURNAL OF FLUIDS ENGINEERING, Vol. 100, No. 4, pp. 395-409.

Minato, A., and Tominaga, K., 1988, "Experiments of Steady State Head and Torque of Centrifugal Pumps in Two-Phase Flow," *Journal of Atomic Energy Society of Japan*, (in Japanese), Vol. 30, No. 3, pp. 247-256.

Minemura, K., and Murakami, M., 1980, "A Theoretical Study on Air Bubble Motion in a Centrifugal Pump Impeller," ASME JOURNAL OF FLUIDS ENGINEERING, Vol. 102, No. 4, pp. 446-455.

Minemura, K., Murakami, M., and Kataoka, T., 1983, "Pressure Distribution in a Centrifugal Impeller Handling Air-Water Mixtures," *Bulletin of JSME*, Vol. 26, No. 220, pp. 1727-1734.

Minemura, K., Murakami, M., and Katagiri, H., 1985, "Characteristics of Centrifugal Pumps Handling Air-Water Mixtures and Size of Air Bubbles in Pump Impellers," *Bulletin of JSME*, Vol. 28, No. 244, pp. 2310-2318.

Minemura, K., and Murakami, M., 1986, "Distributions of Velocities and Void Fractions in a Radial-Flow Pump Impeller Handling Air-Water Two-Phase Mixtures," *Proceedings of Cavitation and Multiphase Flow Forum*, ASME, pp. 35-38.

Minemura, K., Kikuyama, K., Murakami, M., and Uchiyama, T., 1988, "Flow of Cavitation Bubbles in a Centrifugal Pump Impeller," *JSME International Journal*, Series II, Vol. 31, No. 1, pp. 30-38.

Minemura, K., and Uchiyama, T., 1991, "Simplex Finite Element Analysis for Cascade Flows Satisfying the Kutta Condition," *Proceedings of Fluid Machinery Forum*, ASME, pp. 65-69.

Nishiyama, T., 1978, "Characteristics of Super-Cavitating Cascade with Linear Axis in High Speed Water Entrained Air Bubbles," *Transactions of JSME*, (in Japanese), Vol. 44, No. 381, B, pp. 1571-1580.

Richardson, J. F., and Meikle, R. A., 1961, "Sedimentation and Fluidization-Part IV; Drag Force on Individual Particles in an Assemblage," *Transaction of Institute of Chemical Engineers*, Vol. 39, pp. 357-362.

Shida, Y., Kuwahara, K., and Takami, H., 1986, "New Computational Method for a Flow of a Bubbly Liquid," *Proceedings of Cavitation and Multiphase Flow Forum*, ASME, pp. 46-49.

Uchiyama, T., and Minemura, K., 1992, "Numerical Quadratures of First-order Partial Derivatives Given on Discrete Points (Least Squares Methods Utilizing FEM Shape Function or Finite Difference Approximation)," *Transaction of JSME* (in Japanese), Vol. 58, No. 550, B, pp. 1747-1752.

Mach Number Scaling of Single-Component, Two-Phase Flow

D. E. Nikitopoulos
Mechanical Engineering Department,
Louisiana State University,
Baton Rouge, LA 70803

A simple two-fluid formulation is used to investigate compressibility effects and Mach number scaling for equilibrium, evaporating two-phase flow. The definition of the local two-phase Mach number emerges from a critical flow analysis. Comparisons of the theoretical critical mass flux with existing experimental data obtained in steam-water flows show very good agreement for moderate and high qualities over a wide critical pressure range. Within this quality range the predicted critical mass flux is quite insensitive to the velocity ratio. The analysis confirms previous observations, based on homogeneous flow models, indicating that in variable area ducts the critical state does not occur at a geometrical throat. Results of existing critical flow experiments in slowly diverging ducts are discussed in the light of this conclusion. Away from the neighborhood of the flash horizon, pressure-drop and kinetic energy changes are shown to scale with similar local Mach functions as those of single-phase compressible flow. Existing experimental data from vertical-upwards and horizontal two-phase flows in pipes indicate that the Mach number calculated on the basis of the local homogeneous state provides the optimum scaling performance. Scaling of the same experimental data using a Mach number based on the local nonhomogeneous state provides results that are in reasonably good agreement with the theoretical scaling guidelines and predictions, but is handicapped by considerable scatter in the scaled experimental variables.

Introduction

In single-substance, two-phase flow where mass transfer is possible between the phases one of the important physical characteristics, which may be examined independently from the flow topology, is the high compressibility which is largely caused by phase change. Most of the recent work considering two-phase flow compressibility has addressed the problem of critical flow and the associated critical flow conditions. Studies by Giot and Fritte (1972), Bouré et al. (1976), Trapp and Ransom (1982), and more recently Bilicki et al. (1987, 1988a, 1988b) have contributed to the understanding of critical flow phenomena, the methodology for the determination of critical flow conditions, as well as the definition of a critical flow parameter. Giot and Fritte (1972) derived expressions for the critical mass flux using various combinations of two-fluid governing equations for one- and two-component, equilibrium and nonequilibrium annular flows, by setting the determinant of the system of governing equations equal to zero. Bilicki et al. (1987) pointed out that the vanishing of the determinant is a necessary condition for critical flow but not a sufficient one. The vanishing of the determinant establishes a relationship between the critical mass flux and the critical state variables (Giot and Fritte, 1972) while the sufficient condition, which always involves the closure relations, determines the location of the critical state and the critical state variables themselves. On this basis, and using a homogeneous, nonequilibrium relaxation model, Bilicki et al. (1988b) have indicated that the critical state may not be attained at the immediate neighborhood of a geometrical throat.

In the present study we will use a highly simplified two-fluid formulation (Maeder et al., 1983; Nikitopoulos and Maeder, 1986) to examine the compressibility aspects of the single-component, two-phase flow process, and explore the scaling of quantities of practical interest with an appropriately defined compressibility parameter. To this end, a critical flow analysis is carried out using the formalism of Bilicki et al. (1987). The analysis does not involve flow-regime-specific closures to obtain predictions of the critical state and its location. The model used here is far too simplified to provide such predictions accurately. Instead, we have focused on the derivation of a rational definition of the critical flow parameter, examining the possibly closure-independent features of the flow, and relating these features to existing experimental results.

Formulation

The two-fluid formulation that we have utilized here is fairly standard (see Giot and Fritte, 1972; Nikitopoulos and Maeder, 1986) and the simplest one possible. It is a steady-state, one-dimensional model neglecting surface tension and "transient" forces such as virtual-mass and Basset forces. For our purposes here we have considered adiabatic flow where the two phases are in thermal equilibrium. Thus, in the interest of consistency, the gained insights will be relevant for comparisons with experimental data that have indicated existence of thermal equilibrium.

According to all the assumptions the two-fluid governing differential equations for adiabatic, single-substance, two-

---

Contributed by the Fluids Engineering Division for publication the JOURNAL OF FLUIDS ENGINEERING. Manuscript received by the Fluids Engineering Division January 20, 1992; revised manuscript received March 3, 1993. Associate Technical Editor: A. Prosperetti.

phase duct flow in thermal equilibrium are summarized in the following "mixture" form:

Momentum:

$$\Psi \frac{dW_{cm}}{dz}+\frac{dP}{dz}=-\left\{\frac{1}{R_h}\,(\bar{\tau}_{wg}+\bar{\tau}_{wf})+\rho_m\, g \sin\theta\right\}, \tag{1}$$

Energy:

$$\frac{dh}{dz}+W_{ke}\frac{dW_{ke}}{dz}+g\sin\theta=0, \tag{2}$$

Dissipation:

$$\Psi T\frac{ds}{dz}=\frac{1}{R_h}\,\{\bar{\tau}_{wg}\, w_g+\bar{\tau}_{wf}\, w_f+\bar{\tau}_i\,(w_g-w_f)\}. \tag{3}$$

These are supplemented by the mass conservation equations for each phase [$\Psi(1-x)=\rho_f w_f\,(1-\alpha)$ for the liquid and $\Psi x=\rho_g w_g\alpha$ for the vapor]. The quantities w_f and w_g are the velocities of the liquid and vapor phases, h and s are the enthalpy and entropy of the two-phase mixture defined in the usual way, $\Psi(=\dot{m}/A)$ is the mass flux, and R_h is the hydraulic radius of the duct. The quantities W_{cm}, W_{ke} and ρ_m, which manifest the "two-fluid" nature of the model, are defined as:

$$\Psi W_{cm}=\rho_f\, w_f^2(1-\alpha)+\rho_g\, w_g^{\,2}\,\alpha, \tag{4}$$

$$W_{ke}^2=w_f^2(1-x)+w_g^{\,2}x, \tag{5}$$

$$\rho_m=\rho_f(1-\alpha)+\rho_g\,\alpha, \tag{6}$$

in terms of the phase velocities, void fraction, α, and quality, x; the latter being the ratio of vapor mass flowrate to the total mass flowrate. They represent the dynamic pressure, kinetic energy and in-place density of the mixture, respectively. The quantities $\bar{\tau}_{wg}$, $\bar{\tau}_{wf}$, and $\bar{\tau}_i$ are weighted wall and net interfacial shear stresses, given by:

$$\bar{\tau}_{wg}=\tau_{wg}\frac{L_{wg}}{C}, \tag{7a}$$

$$\bar{\tau}_{wf}=\tau_{wf}\frac{L_{wf}}{C}, \tag{7b}$$

$$\bar{\tau}_i=\tau_i\frac{L_i}{C}+\Psi\frac{dx}{dz}\left(\frac{w_f+w_g}{2}-w_i\right)R_h, \tag{7c}$$

where C, L_{wg}, L_{wf}, L_i and w_i are the perimeter of the duct, its vapor and liquid wetted portions, the average interfacial length per crossection and the interfacial velocity, respectively. The second term in the expression for $\bar{\tau}_i$ represents an additional interfacial stress resulting from the mass-transfer-induced momentum exchange across the interface. Giot and Fritte (1972) in their formulation for annular flow accounted for interfacial entropy production related to mass transfer through a term that corresponds to setting $w_i=0$. For the rest of our discussion we will adopt the assumption that the interfacial velocity is equal to the average of the liquid and vapor velocities as did Levy (1982) and Dickinson and Maeder (1984). This is equivalent to explictly neglecting the dissipation resulting from the mass transfer across the interface. Implicitly this effect can be taken into account by applying an adjustment on τ_i. Consequently, $\bar{\tau}_i$, which is subject to closure, is assumed to be independent of gradients of the state variables of the flow and thus the critical mass flux derived in the next section cannot account for more elaborate closures.

Critical Flow Conditions and Critical Mass Flux

The thermodynamic and dynamic state of the flowing two-phase mixture is uniquely defined when two thermodynamic variables and one dynamic variable are known at any position in the duct, according to our one-dimensional formulation and for fluids that are simple compressible substances. The solution of the governing Eqs. (1)-(3) would yield the state of the flow at any point, provided that the appropriate closures were introduced. For our purposes we have chosen the entropy, s, pressure, P, and velocity ratio, $\sigma(=w_g/w_f)$, as the dependent flow-state variables. The governing equations can then be written as

$$A_{ji}\frac{d}{dz}\,[s,P,\sigma]=B_j, \tag{8}$$

and their formal solution is given by

$$\frac{d}{dz}\,[s,P,\sigma]=\frac{1}{\Delta}\,[N^s,N^p,N^\sigma], \tag{9}$$

where $\Delta\equiv\det(A_{ji})$, and N^s, N^p, and N^σ are determinants corresponding to each dependent variable. The index i corresponds to the dependent variables while j corresponds to Eqs. (1)-(3). For the model under consideration the vector B_j contains all the quantities that are subject to closure while A_{ji} is independent of them. The matrix coefficient A_{ji} and the vector B_j can be found in the Appendix.

The necessary condition for critical flow ($\Delta=0$, as in Bouré et al., 1976; Trapp and Ransom, 1982) leads to the following expression for the critical mass flux:

$$\psi_c^2=-\frac{[\sigma^3+x(\gamma^2-\sigma^3)]_c}{[\sigma+x(\gamma-\sigma)]_c^2}\times\left[\sigma(1-x)\frac{dv_f}{dP}+x\frac{dv_g}{dP}+\left(\frac{\partial x}{\partial P}\right)_s v_{fg}\sigma\phi\right]_c^{-1}, \tag{10}$$

where, $\gamma=\rho_f/\rho_g$, is the liquid to vapor density ratio, ϕ is a function of γ and σ given in the appendix, and the subscript c denotes that all variables and parameters are evaluated at the critical state which corresponds to a singular point (Bilicki et al., 1987). The above expression is valid for all values of the velocity ratio except when it is equal to unity (no-slip). The case of $\sigma=1$ is one where the singular point is degenerate and the necessary condition for critical flow also requires that three independent 2×2 sub-determinants of A_{ji} be equal to zero. This means that the original set of equations reduces to those for the homogeneous flow model at the critical state, and that the necessary condition for critical flow is the vanishing of the determinant of the reduced system. As a result the critical mass flux becomes:

$$\Psi_{co}^2=-\left[(1-x)\frac{dv_f}{dP}+x\frac{dv_g}{dP}+\left(\frac{\partial x}{\partial P}\right)_s v_{fg}\right]_c^{-1}. \tag{11}$$

It is unlikely that any duct flow will go into a critical condition where the critical velocity ratio is exactly unity through a sequence of flow states with $\sigma>1$. A possible situation is when the flow becomes critical at the point of homogeneous nucleation (flash horizon). Equation (11) also gives the critical mass flux if we were to assume that the velocity ratio is unity throughout the flow (homogeneous model), in which case the reduced system would govern the entire flow. The first two terms with pressure derivatives in (10) and (11) represent the contribution of the compressibility of the individual phases and the third one the contribution of the phase change, which dominates the flow at low and moderate qualities. The Mach number for two-phase flow is defined in the usual way as $\mathrm{Ma}=\Psi/\Psi_c$, and the necessary critical flow condition becomes $\mathrm{Ma}=1$. A Mach number, Ma_0, based on a critical mass flux of a corresponding homogeneous flow state can also be similarly defined using the result of (11).

Discussion

The equilibrium process corresponding to the two-phase flow in the duct can be represented on the enthalpy-entropy space by a line similar to the Fanno line (as did Michaelides and Parikh (1982) for flow in straight pipes). The "two-phase

Fanno'' line begins on the saturated liquid line where flashing first occurs and extends into the two-phase region until the critical flow point. It is useful to look at the expression for the slope of the ''Fanno'' line and the pressure gradient, the latter being a quantity that is usually measured directly in experimental studies. These expressions are easily derived from (9), yielding:

$$-(1-\mathrm{Ma}^2)\,\frac{dh}{Tds}=\frac{1}{f_d}\left[\frac{\sin\theta}{Fr}\phi_2-\frac{dA}{dz}\,\frac{D_h}{A}\,\phi_3\right]+\mathrm{Ma}^2$$

$$+\left(\frac{W_{ke}^2}{h_{fg}}\right)\phi_1+\left(1-\frac{W_v(\overline{\tau}_{wg}+\overline{\tau}_{wf})}{R_h\Theta}\right)\phi_4, \quad (12)$$

and

$$-(1-\mathrm{Ma}^2)\,\frac{v\,D_h}{W_{ke}^2}\,\frac{dP}{dz}=\frac{\sin\theta}{\mathrm{Fr}}\,\phi_2-\frac{dA}{dz}\,\frac{D_h}{A}\,\phi_3$$

$$+f_d\left[1+\frac{W_{ke}^2}{h_{fg}}\,\phi_1+\left(1-\frac{W_v(\overline{\tau}_{wg}+\overline{\tau}_{wf})}{R_h\Theta}\right)\phi_4\right], \quad (13)$$

where ϕ_1, ϕ_2, ϕ_3, and ϕ_4 are known functions of γ, α, and σ, and can be found in the Appendix; Θ is the energy dissipated per unit volume and is equal to the right-hand side of Eq. (3). A two-phase Froude number and dissipation factor have been defined as $\mathrm{Fr}=W_{ke}^2/gD_h$ and $f_d=R_h\Theta/\Psi/(W_{ke}^2/2)$, respectively. The last term of (13) can be easily shown to be always positive.

Equations (12) and (13) indicate that the important global dimensionless parameters relevant to the equilibrium, adiabatic two-phase flow process are the Froude and Mach numbers as defined above, and an appropriately defined Reynolds number whose influence is implicit. The kinetic energy to latent heat of evaporation ratio, W_{ke}^2/h_{fg}, which also appears as a parameter, is of secondary importance due to its small magnitude (of order 10^{-3} to 10^{-5} usually). Here we are mostly interested in the effects of the Mach number. Equation (13) indicates the appropriate dimensionless form of the pressure gradient and that $(1-\mathrm{Ma}^2)$ is a good candidate as a scaling factor. The equation for the kinetic energy gradient, which can be easily derived from (2), (3), and (12), indicates that $(1-\mathrm{Ma}^2)/\mathrm{Ma}^2$ should be the appropriate scaling factor for this quantity. Accordingly one expects that pressure and kinetic energy gradients from flows of the same fluid and the same orientation should follow a common trend when such scaling has been applied.

The sufficient critical flow condition $N_p=0$ which requires the, always positive, right-hand side of (13) to vanish, indicates that $dA/dz > 0$, at the critical point. Consequently, in chanels with a slowly-diverging section (e.g., Henry, 1968; Réocreux, 1974) this simple model indicates that the critical point cannot occur at the throat (point of smallest cross section). This is in agreement with Bilicki et al. (1987, 1988b) who have used homogeneous equilibrium and nonequilibrium relaxation models and reinterpreted the Moby Dick critical flow experiments (Réocreux, 1974). Bilicki et al. (1987) have also shown that the critical state may occur only at the abrupt exit (end) of the channel for constant area ducts and variable area channels whose geometry does not allow critical flow to occur at an interior point (e.g., truncated converging nozzles, flow through orifices).

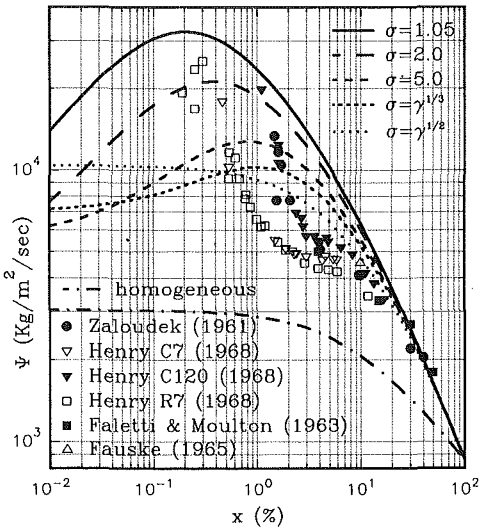

Fig. 1 Critical mass flux of water-steam, two-phase flow as a function of quality at a pressure of 0.343 MPa. Experimental data (pressures within a range of ±6 percent of nominal) and predictions of the present analysis.

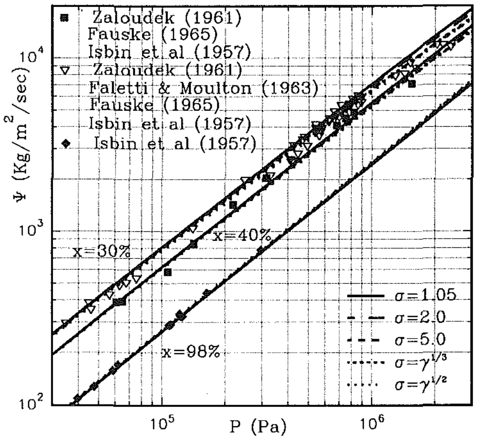

Fig. 2 Critical mass flux as a function of pressure for three different qualities. Experimental data and predictions of the present analysis. The value of the quality for all the experimental points presented is within 5 percent of the value shown by the corresponding label.

Experimental results for the critical mass flux from abruptly diverging channels (exit of a constant area duct, orifices, etc.) and from slowly diverging ones (Henry, 1968; test sections C7 and R7) at an average critical pressure of 0.343 MPa are shown in Fig. 1 as a function of critical-state quality. Predictions from Eq. (10) are included in the same figure for various velocity ratios, since no experimental information on the critical velocity ratio is available. The model shows a high sensitivity to the velocity ratio at low quality ($x<15$ percent approximately). The experiments indicate separate trends depending on the type of duct. In the past this discrepancy has been attributed exclusively to thermal nonequilibrium effects. However, Henry's data for test sections R7 and C7 were reported under the assumption that the critical state occurs at the throat and, on the basis of the previous discussion regarding the location of the critical state, it is probable that the critical mass fluxes have been assigned to the incorrect critical state variables. The sensitivity of the critical mass flux to the velocity ratio, which may be different at the critical state between different geometries while x and P are the same, could also be contributing to the discrepancy. The theoretical trends show the critical mass flux has a maximum at very low qualities, a feature not predicted by other models because they diverge as $x\rightarrow 0$ (Delhaye et al., 1982). Experiments in the range of extremely low qualities are rare, but there is one indication of such behavior in the data of Campbell and Overcamp (1966) at 0.17 MPa for N_2. The above conclusions are of course subject to the serious limitations (one dimensionality, closures assumed free of streamwise gradients of the flow variables, assumption of thermal equilibrum etc.) of the simple flow model used, which is not expected to yield accurate predictions, particularly at low qualities. Included in Fig. 1 are the predictions of the homogeneous flow model which is known to seriously under-predict the critical mass flux.

Table 1 Experimental Conditions

#	T^* (°C)	Ma^*	Fr^*	$\mathrm{Re}^* \times 10^{-3}$	Ψ(kg/m$_2$s)	x%	α%	P (KPa)
1	21	0.5	2.63	238	1681	1 – 8	24 – 80	128 – 187
2	36	0.33	2.56	269	1605	3 – 18	54 – 89	141 – 265
3	18.2	0.33	0.98	142	1033	3 – 11	53 – 86	97 – 148
4	34.2 – 35.7	.51 – .68	5.4 – 8.7	380 – 490	2342 – 2970	3 – 10	–	202 – 256
5	26.0 – 27.8	.31 – .37	1.1 – 1.3	163 – 174	1067 – 1155	12 – 20	–	88 – 133
6	–	–	–	–	88 – 354	10 – 80	35 – 97	567 – 1219
7	–	–	–	–	88 – 354	10 – 80	40 – 89	910 – 1942
Uncertainties for Experiments #1 – #5								
	±.1	±.01	±.03	±2.9	±20	±.15	±8	–

1, 2, 3 Vertical-upwards adiabatic flow, refrigerant 114, 2 in. (5.08 cm) – ID pipe (Nikitopoulos and Maeder, 1986)
4, 5 Horizontal adiabatic flow, refrigerant 114, 2 in. (5.08 cm) – ID pipe (Dickinson and Maeder, 1984)
6 Horizontal adiabatic flow, refrigerant 12, 1cm – ID Pipe (Hashizume, 1983)
7 Horizontal adiabatic flow, refrigerant 22, 1cm – ID Pipe (Hashizume, 1983)

At higher qualities ($x > 20$ percent) the critical mass flux predicted by the present model is quite insensitive to the velocity ratio (Fig. 1). This is also illustrated in Fig. 2 comparing the theoretical predictions with data from four different investigations of water-steam critical flows over a wide pressure range (0.03-3 MPa) and for three different qualities (30, 40, and 98 percent). For $x > 20$ percent the maximum variation in critical mass flux with velocity ratio is within the scatter and uncertainty of the experimental data and thus the predicitions from Eq. (10) seem to be in good agreement with the measurements.

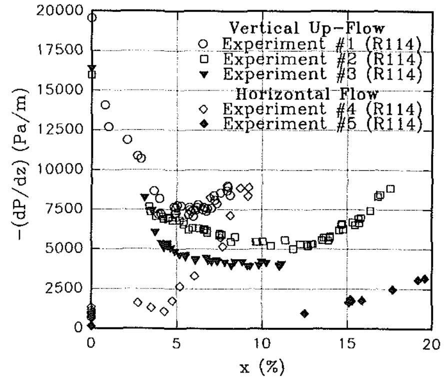

Fig. 3(*a*) **Pressure gradient from experiments #1-#5. Estimated uncertainties for −(*dP/dz*) and *x* are ±560 Pa/m and 0.15 in percent, respectively (Nikitopoulos and Maeder, 1986) and ±200 Pa/m and 0.15 in percent, respectively (Dickinson and Maeder, 1984)**

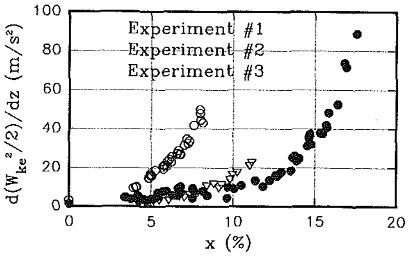

Fig. 3(*b*) **Kinetic energy gradient from experiments #1-#3. Estimated uncertainties for $d(W_{ke}^2/2)/dz$ and *x* are 0.9 m/s^2 and 0.15 in percent, respectively (Nikitopoulos and Maeder, 1986)**

Mach Number Scaling: Comparison With Experiments

In order to test the appropriateness of the Mach-number-dependent scaling factors suggested by this analysis, we have considered results obtained from experiments conducted in adiabatic, vertical-upwards (Nikitopoulos and Maeder, 1986) and horizontal (Dickinson and Maeder, 1984; Hashizume, 1983) two-phase flows in pipes. Experimental conditions together with ranges of the significant flow variables covered during these experiments are shown in Table 1. Each one of the three experimental sets (#1, #2, and #3) of Nikitopoulos and Maeder (1986) represents a sequence of states in a straight pipe corresponding to a common state at flashing (point where evaporation starts). Therefore, values of the temperature and the significant dimensionless parameters evaluated at flashing conditions (indicated by the asterisk) are included in Table 1. The same is true for the experiments of Dickinson and Maeder (1984) which we are presenting in two groups (#4 and #5). Flashing conditions were not available for the experiments of Hashizume (1983) (labeled #6 and #7). It should be pointed out that, during the experiments #1-#5, the measured pressure was always in agreement with the saturation pressure corresponding to the measured temperature to within 5%. Therefore, the flow-equilibrium assumption is good at least to within the experimental accuracy and the comparisons made here are consistent with what was postulated in theory. The quantities measured directly during these experiments (#1-#5) were the net mass flow rate, $\dot{m}$, pressure drop, Δp, temperature, T, and the average void fraction, α. The void fraction was measured by using the quick-closing valve technique. The quality of the flow was calculated from the energy equation (including the kinetic energy) by using the measured temperature, the measured average void fraction, and the elevation of the corresponding measuring station (in the case of vertical flow). Details on the experimental facilities and procedures used to obtain these measurements (experiments #1-#5) can be found in Maeder et al. (1985) and Nikitopoulos and Maeder (1986).

Measured pressure gradients from experiments #1-#5 and kinetic energy gradients from #1-#3 are presented in Figs. 3(*a*) and 3(*b*), respectively, as functions of quality. Kinetic energy gradients were calculated from the energy equation. The pressure gradient data for #6 and #7 can be found in tabular form in Hashizume (1983) and are therefore not shown here. The gradients presented are widely different, both for the vertical and horizontal flows, depending on the prevailing conditions at flashing.

We have reduced the experimental data according to the scaling guidelines and dimensionless variables suggested by our analysis, examining two possible scaling methods. One method utilizes as the principal scaling parameter the local Mach number, Ma, based on the critical mass flux calculated from (10) for each nonhomogeneous flow state described by the state variables (P, α, x). The other method uses Ma_0, based on the critical mass flux calculated from (11) and corresponding to a hypothetical state which shares the thermodynamic state of the flow but is otherwise homogeneous ($\sigma = 1$). Although we have shown in the previous section that the "homogeneous" Eq. (11) is not the appropriate one for obtaining critical mass flux predictions, it is worthwhile to examine if the Mach number, Ma_0, of the corresponding homogeneous state can be successfully used for scaling purposes because of its simplicity and velocity-ratio independence.

Using this latter method we have reduced the pressure gra-

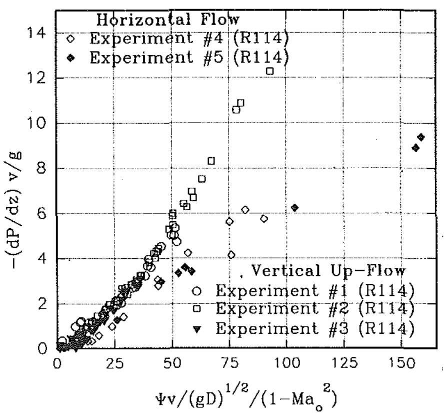

Fig. 4 Pressure gradient measurements from experiments #1-#3 (Nikitopoulos and Maeder, 1986) and #4-#5 (Dickinson and Maeder, 1984) scaled according to present analysis using the corresponding homogeneous state Mach number

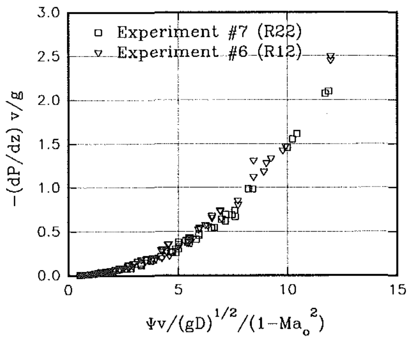

Fig. 5 Pressure gradient measurements from experiments #6 and #7 (Hashizume, 1983) scaled according to present analysis using the corresponding homogeneous state Mach number

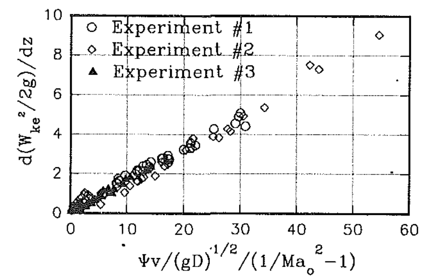

Fig. 6 Kinetic energy gradient measurements from experiments #1-#3 (Nikitopoulos and Maeder, 1986) scaled according to present analysis using the corresponding homgeneous state Mach number

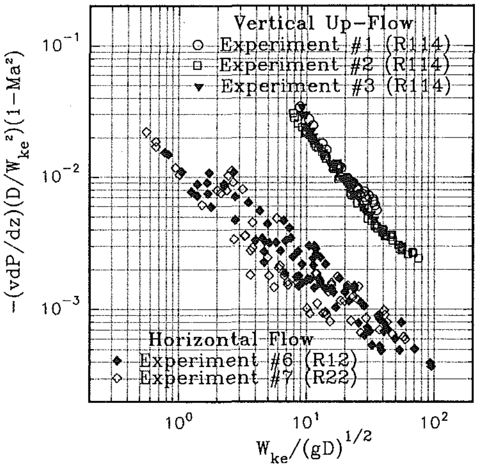

Fig. 7 Pressure gradient measurements from vertical flow experiments #1-#3 (Nikitopoulos and Maeder, 1986) and horizontal flow experiments #6 and #7 (Hashizume, 1983) scaled according to present analysis

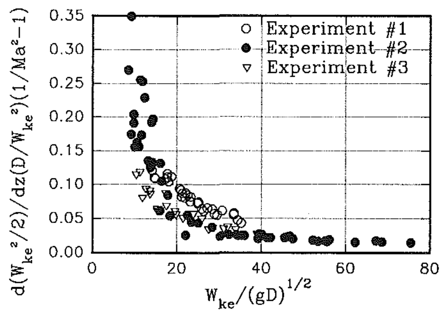

Fig. 8 Kinetic energy gradient measurements from experiments #1-#3 (Nikitopoulos and Mader, 1986) scaled according to present analysis

dient data from experiments #1-#7 as suggested by Eq. (13) utilizing $(1-\mathrm{Ma}_0^2)$ as a scaling factor and the volumetric velocity W_v (defined as Ψv) as the velocity scale, rather than W_{ke} for the sake of consistency ($W_v = W_{ke} = W_{cm}$ for a homogeneous flow). According to this scaling, Fig. 4 shows that the dimensionless pressure gradients resulting from the vertical-flow experiments #1-#3 (Nikitopoulos and Maeder, 1986) follow a single trend. The same is shown to be true for the horizontal flow cases of experiments #4 and #5 (Dickinson and Maeder, 1984) included in Fig. 4, as well as for experiments #6 and #7 (Hashizume, 1983) presented in Fig. 5. Particular trends naturally depend on the substance and orientation of the flow, since the scaling discussed here involves only the Mach number. A single trend is also indicated when the kinetic energy gradient for experiments #1-#3 is reduced according to our analysis and scaled with $(1-\mathrm{Ma}_0^2)/\mathrm{Ma}_0^2$, as shown in Fig. 6. It should be noted that the common trend is not as clear for the vertical-upwards flow experimental results with different flashing Froude numbes, Fr^*, if we magnify the region immediately after the flash horizon in Figs. 4 and 5. This does not contradict the theoretical contentions because in vertical flow the hydrostatic effect is dominant in the region following the flash horizon and therefore the Froude number is likely to be the controlling parameter in that region rather than the Mach number. The experiments clearly show that the Mach number scaling suggested by the present analysis is very successful in collapsing widely different data into single trends for vertical as well as horizontal flows. Although the two-phase flows of the experiments are nonhomogeneous the experimental evidence presented indicates that the Mach number evaluated at the corresponding homogeneous flow states is an excellent scaling parameter which encompasses the compressibility of the evaporating two-phase flow process.

The experimental data have also been scaled according to the method based on the local Mach number, Ma, which is strictly in accordance with Eq. (13) of the nonhomogeneous model used in our analysis. In such case the relevant velocity is W_{ke}. The pressure gradients form experiments #1-#3 (vertical flow), #6 and #7 (horizontal flow) scaled in this manner are presented in Fig. 7, while Fig. 8 shows the scaled kinetic energy gradients from experiments #1 to #3. It is seen from both figures that the scatter in the scaled data is considerable (more so for #6 and #7) and it reflects the relatively high uncertainty of the void fraction measurements that are used to calculate the velocity ratio. Within the bounds of this uncertainty, this scaling method is also successful in collapsing the data on common trends to a satisfactory extent, although not as well as the previous one. The scaling performance is reasonable even at low qualities where the present non-homogeneous model cannot accurately predict the critical mass flux, probably due to some form of error cancellation.

According to the experimental evidence the Mach-number-based scaling rules dictated by the present analysis have proven to be successful with a reasonably high level of confidence, because the experimental data used here (Table 1) cover a sufficiently wide range of the important two-phase flow variables (x, α, P and Ψ) and have been obtained from three different experimental facilities using three different working fluids. We have seen that both scaling methods used in this work perform reasonably well in spite of the fact that the Mach numbers used for the scaling are based on critical mass flux expressions (Eqs. (10) and (11)) that in general cannot accurately predict the actual critical mass flux for a given flow state. This allows one to view Eqs. (10) and (11) as correlations and use them successfully in combination with the proposed variables for scaling purposes.

Conclusions

A simple two-fluid formulation has been used to investigate compressibility effects and Mach number scaling for equilibrium, evaporating two-phase flow. The critical flow analysis carried out has given rise to a two-phase Mach number defined on the basis of the critical mass flux which strongly depends on the compressibility induced by phase change. The analysis supports previous observations, based on homogeneous flow models, indicating that in variable area ducts, the critical state does not occur at a geometrical throat. At qualities higher than 20 percent the predicted critical mass flux for a given critical state is insensitive to the velocity ratio and is in good agreement with critical flow experiments. Away from the neighborhood of the flash horizon pressure-drop and kinetic energy changes scale with similar local Mach functions as those of single-phase compressible flow. Existing experimental data from adiabatic, equilibrium, vertical-upwards, and horizontal two-phase flows in pipes indicate good agreement with the theoretical Mach number scaling guidelines and predictions. The same experimental data indicate that, with the appropriate choice of dimensionless variables, the Mach number based on the critical mass flux of the corresponding homogeneous-flow states can be used successfully as the scaling parameter. This result can be useful for similarity purposes and development of correlations for practical applications, especially since the complexity of evaporating two-phase flow does not permit, at present, a general and rigous treatment free of empiricism.

References

Bilicki, Z., Dafermos, C., Kestin, J., Majda, G., and Zeng, D. L., 1987, "Trajectories and Singular Points in Steady-State Models of Two-Phase Flows," *International Journal of Multiphase Flow*, Vol. 13, No.4, pp. 511-533.

Bilicki, Z., Kestin, J., and Pratt, M. M., 1988a, "The Effect of Three Closures on Critical Conditions in Two-Phase Flow with Unequal Phase Velocities," *International Journal of Multiphase Flow*, Vol. 14, No. 4, pp. 507-517.

Bilicki, Z., Kestin, J., and Pratt, M. M., 1988b, "A Reinterpretation of the Results of the Moby Dick Experiments in Terms of the Nonequilibrium Model," *Fundamentals of Gas-Liquid Flows*, E. E. Michaelides and M. P. Sharma, eds., ASME FED-Vol. 72, pp. 11-17.

Bouré, J. A., Fritte, A. A., Giot, M. M., and Réocreux, M. L., 1976, "Highlights of Two-Phase Critical Flow: On the Links Between Maximum Flow-Rates, Sonic Velocities, Propagation and Transfer Phenomena in Single and Two-Phase Flows," *International Journal of Multiphase Flow*, Vol. 3, pp. 1-22.

Campbell, H. M., and Overcamp, T. J., 1966, "Critical Flowrate of Two-Phase Nitrogen," NASA Technical Memorandum X-53492.

Chisholm, D., 1972, "An Equation for Velocity Ratio in Two-Phase Flow, NEL Report 535.

Delhaye, J. M., Giot, M., and Riethmuller, M. L., 1982, *Thermohydrualics of Two Phase Systems for Industrial Design and Nuclear Engineering*, McGraw-Hill, New York, NY.

Dickinson, D. A., and Maeder, P. F., 1984, "An Investigation of Single-Substance Horizontal Two-Phase Flow," Brown University Report GEOFLO/20, LA-UR-84-1189.

Faletti, D. W., and Moulton, R. W., 1963, "Two-Phase Critical Flow of Steam-Water Mixtures," *AIChE Journal*, Vol. 9, No. 2, pp. 247-253.

Fauske, H. K., 1965, "Two-Phase Two-and One-Component Critical Flow, Symp. on Two-Phase Flow, "University of Exeter, P. M. C. Lacey, Ed., Vol. 1, pp. 101-114.

Giot, M., and Fritte, A., 1972, "Two-Phase Two-and One-Component Critical Flows with the Variable Slip Model," *Proceedings of the International Symposium on Two-Phase Systems, Progress in Heat and Mass Transfer*, G. Hetsroni, S. Sideman and J. P. Hartnett, eds., Pergamon Press, Vol. 6, pp. 651-670.

Henry, R. E., 1968, "A Study of One-Component, Two-Phase Critical Flows at Low Qualities," Report ANL-7430, Argonne National Laboratory.

Hashizume, K., 1983, "Flow Pattern, Void Fraction and Pressure Drop of Refrigerant Two-Phase Flow in a Horizontal Pipe-I," *International Journal of Multiphase Flow*, Vol. 9, No. 4, pp. 399-410.

Isbin, H. S., Moy, J. E., and Da Cruz, A. J. R., 1957, "Two-Phase, Steam-Water Critical Flow," *AIChE Journal*, Vol. 3, No. 3, pp. 361-365.

Levy, S., 1982, "Critical Flow Data Review and Analysis," EPRI, Final Report, NP-2192.

Maeder, P. F., Dickinson, D. A., and Nikitopoulos, D. E., 1983, "One Component Two-Phase Flow in Horizontal and Vertical Ducts: Some Basic Considerations," *Proc. Ninth Workshop Geothermal Reservoir Engineering*, Stanford University Report SGP-TR-74, pp. 279-284.

Maeder, P. F., Dickinson, D. A., Nikitopoulos, D. E., and DiPippo, R., 1985, "A Facility for the Experimental Investigation of Single Substance Two-Phase Flow," ASME FED-Vol. 29, pp. 41-46.

Michaelides, E. E., and Parikh, S., 1983, "The Prediction of Critical Mass Flux by the Use of Fanno Lines," *Nuclear Engineering and Design*, Vol. 75.

Nikitopoulos, D. E., and Maeder, P. F., 1986, "Single-Substance Two-Phase Duct Flow: A Unified Theoretical and Experimental Study," Brown University Report Number TWO PHASE/3.

Réocreux, M., 1974, "Contribution a l'etude des debits critiques en encoulement diphasique eau-vapeur," Ph.D. thesis, Universite Scientifique et Medicale de Grenoble.

Trapp, J. A., and Ransom, V. H., 1982, "A Choked-Flow Calculation Criterion for Nonhomogeneous, Nonequilibrium, Two-Phase Flows," *International Journal of Multiphase Flow*, Vol. 8, No. 6, pp. 669-681.

Zaloudek, F. R., 1961, "The Low Pressure Critical Discharge of Steam-Water Mixtures from Pipes," ASME HW-68936.

APPENDIX

Elements of the Matrix Coefficient A_{ij}

$$A_{13}=\Psi\left[\frac{\partial W_{cm}}{\partial\sigma}\right]_{P,s}\quad A_{23}=\left[\frac{\partial h}{\partial\sigma}\right]_{P,s}+W_{ke}\left[\frac{\partial W_{ke}}{\partial\sigma}\right]_{P,s}\quad A_{33}=0,$$

$$A_{12}=1+\Psi\left[\frac{\partial W_{cm}}{\partial P}\right]_{s,\sigma}\quad A_{22}=\left[\frac{\partial h}{\partial P}\right]_{s,\sigma}+W_{ke}\left[\frac{\partial W_{ke}}{\partial P}\right]_{s,\sigma}\quad A_{32}=0,$$

$$A_{11}=\Psi\left[\frac{\partial W_{cm}}{\partial s}\right]_{P,\sigma}\quad A_{21}=\left[\frac{\partial h}{\partial s}\right]_{P,\sigma}+W_{ke}\left[\frac{\partial W_{ke}}{\partial S}\right]_{P,\sigma}\quad A_{31}=\Psi T.$$

Elements of the Vector $\mathbf{B}_j$

$$B_1=-\frac{1}{R_h}\left(\bar{\tau}_{wg}+\bar{\tau}_{wf}+\rho_m g R_h\sin\theta\right)+\Psi\,W_{cm}\frac{dA}{dz}\frac{1}{A},$$

$$B_2=-g\sin\theta+W_{ke}^2\frac{dA}{dz}\frac{1}{A},$$

$$B_3=\frac{1}{R_h}\left(\bar{\tau}_{wg}w_g+\tau_i(w_g-w_f)+\bar{\tau}_{wf}w_f\right)$$

Two-Phase "Fanno" Functions

$$\phi_4=\frac{(\gamma-\sigma^3)}{(\sigma-1)[\sigma^2+\alpha(\gamma-\sigma^2)]},\quad \phi_3=\frac{\gamma\sigma^2[1+\alpha(\sigma-1)]}{[\gamma+\alpha(\sigma^3-\gamma)][\sigma^2+\alpha(\gamma-\sigma^2)]},$$

$$\phi_2=\frac{\gamma[1+\alpha(\sigma-1)][\sigma^2+\alpha(1-\sigma^2)]}{[\gamma+\alpha(\sigma-\gamma)][\sigma^2+\alpha(\gamma-\sigma^2)]},\quad \phi_1=\phi_3\frac{(\gamma-1)\,[\gamma+\alpha(\sigma-\gamma)]}{\gamma[\sigma^2+\alpha(\gamma-\sigma^2)]},$$

$$\phi=1+\frac{1}{2}\frac{\sigma-1}{\gamma-1}\left[\frac{\gamma}{\sigma^2}-2\frac{\gamma}{\sigma}+1\right].$$

Journal of Fluids Engineering
Technical Briefs

Discharge Coefficient for Free Jets From Orifices at Low Reynolds Number

Tomasz Kiljański[1]

Nomenclature

A = coefficient defined by Eq. (7)
B = coefficient defined by Eq. (9)
d = diameter of the orifice
h = head
l = length of the orifice
v = discharge velocity
ϕ = discharge coefficient
μ = viscosity
ρ = density
ζ = coefficient of the local resistance

Introduction

The problem of the velocity of free jets issuing from a small orifice in a tank wall has been well investigated for low viscosity liquids, i.e., for a high Reynolds number. The internal friction phenomena do not play an important role under these conditions—almost all the potential energy of the fluid in the vessel is converted into kinetic energy of the free jet. The discharge coefficient ϕ (Eq. (1)) is then very close to the contraction coefficient β and equals about 0.6.

$$v=\phi\sqrt{2gh} \tag{1}$$

The outflow at a high Reynolds number was discussed in detail by many authors, e.g., Judd and King (1908), Medaugh and Johnson (1940), Geller (1965), Lienhard and Lienhard (1984).

It is obvious that at a Reynolds number low enough the discharge coefficient must be lower because the discharge velocity is then limited mainly by the friction phenomena. The range of low Reynolds numbers is essential for the outflow of non-Newtonian liquids which are usually highly viscous. However, even the outflow of Newtonian liquids at low Reynolds numbers has not been well examined.

Theoretical

Assume that the flow is laminar and the kinetic energy of the jet is negligible in comparison to the energy dissipated by viscous friction. The orifice in the wall induces a local resistance to flow. Thus, the pressure drop in the outlet region may be described by Eq. (2):

$$\Delta p=\zeta\frac{\rho v^2}{2} \tag{2}$$

In the laminar flow region the coefficient of local pressure drop ζ must obey Eq. (3)

$$\zeta=\frac{C}{\mathrm{Re}} \tag{3}$$

where

$$\mathrm{Re}=\frac{vd\rho}{\mu} \tag{4}$$

In the flow conditions under consideration, the pressure drop due to friction in the outlet region equals the hydrostatic pressure at the bottom

$$\Delta p=h\rho g \tag{5}$$

Combining Eqs. (1) to (5) we obtain

$$h\rho g=\frac{C\mu\phi\sqrt{2gh}}{2d} \tag{6}$$

thus,

$$\phi=\frac{\rho\sqrt{2gh}\,d}{C\mu}=A\mathrm{Re}_0 \tag{7}$$

where

$$\mathrm{Re}_0=\frac{\rho\sqrt{2gh}\,d}{\mu} \tag{8}$$

Multiply Eq. (7) by ϕ

$$\phi^2=\frac{\rho\phi\sqrt{2gh}\,d}{C\mu}=\frac{vd\rho}{C\mu}=\frac{\mathrm{Re}}{C}$$

or

$$\phi=\sqrt{\frac{\mathrm{Re}}{C}}=B\sqrt{\mathrm{Re}} \tag{9}$$

The coefficient B can be expected to depend on the orifice length.

Experimental

Most measurements of the velocity of discharge from orifices were performed using a vertical perspex cylindrical tube 38 mm in diameter with a brass replaceable bottom with circular orifices. The fluids tested flowed due to gravitational force through the orifices of diameters 2, 3, and 5 mm and l/d ratio

---

[1] Faculty of Process and Environmental Engineering, Łódź Technical University, Łódź, Poland.

Contributed by the Fluids Engineering Division of THE AMERICAN SOCIETY OF MECHANICAL ENGINEERS. Manuscript received by the Fluids Engineering Division May 22, 1992; revised manuscript received January 19, 1993. Associate Technical Editor: D. M. Bushnell.

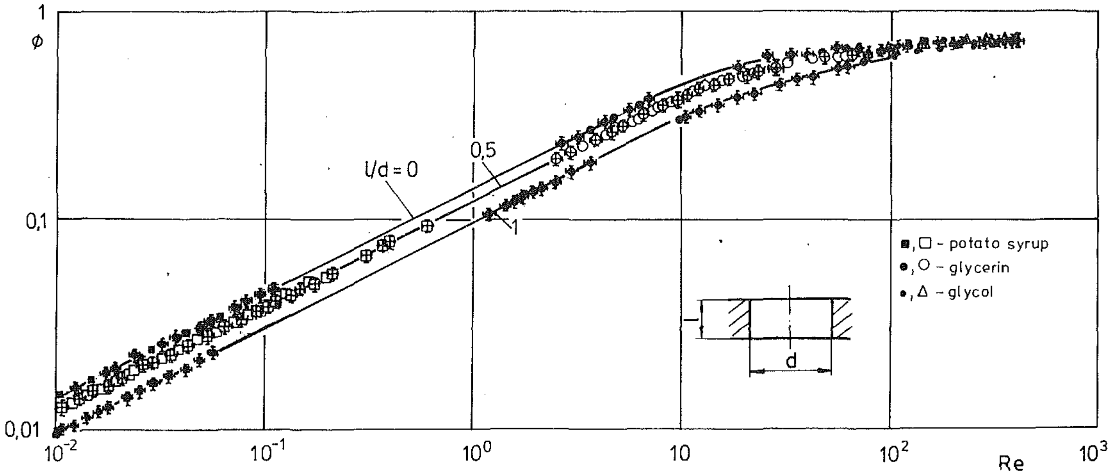

Fig. 1 Dependence of the discharge coefficient on the Reynolds number, ■ — *l/d* = 1 and 0, potato syrup; ● — *l/d* = 1 and 0, glycerin; • — *l/d* = 1 and 0, glycol; □ — *l/d* = 0.5, potato syrup; ○ — *l/d* = 0.5, glycerin, △ — *l/d* = 0.5, glycol. (Uncertainty in ϕ = 4 to 7 percent of the ϕ value, in Re 4 to 8 percent of the Re value at 20:1 odds.)

equal 0.5. Additionally, two orifices of the diameter 3 mm and *l/d* ratio equal 1 and 0 (a sharp-edged one) were used. The head of the fluid was kept constant during the measurement. Heads greater than 0.6 m were imitated by the pressure of a gas above the fluid formed in a pressure-capillary rheometer using the same brass elements with orifices. The head under pressure was calculated as

$$h = H + \frac{p}{\zeta g}$$

where H is the actual height of the fluid in the reservoir and p is the pressure of gas over the liquid.

The exit velocity was calculated by measuring the discharge volume under a constant head for a given time. In the measurements performed in the rheometer under pressure the head changed 15 mm at most during the measurement. Its average value was then taken for calculations. The coefficient of discharge was calculated from Eq. (1).

As test fluids ethylene glycol of viscosity about 0.02 Pa·s, two glycerol solutions of viscosity about 0.15 and 0.40 Pa·s, and potato syrup of viscosity about 10 Pa·s were used, all Newtonian liquids. The exact viscosity was determined for each measurement depending on the temperature.

Results

The plot in Fig. 1 presents the dependence of ϕ on the Reynolds number Re. In the range of low Re values (Re < 10) the experimental points for each *l/d* ratio lie on the straight line with the slope 0.5, which confirms the validity of Eq. (9). For $l/d = 0.5$ the regression line is described by the equation

$$\phi = 0.123\ \mathrm{Re}^{0.496}$$

Assuming the exponent is equal to the theoretical value 0.5, the equation would have the form

$$\phi = 0.124\ \mathrm{Re}^{0.5} \tag{10}$$

The standard error of log ϕ estimation equals 0.00992 which corresponds to the standard ϕ estimation error of 2.3 percent. For *d/l = 1 the regression line is described by the equation*

$$\phi = 0.0994\ \mathrm{Re}^{0.506}$$

Assuming the exponent equal 0.5, Eq. (9) would have the form

$$\phi = 0.0982\ \mathrm{Re}^{0.5} \tag{11}$$

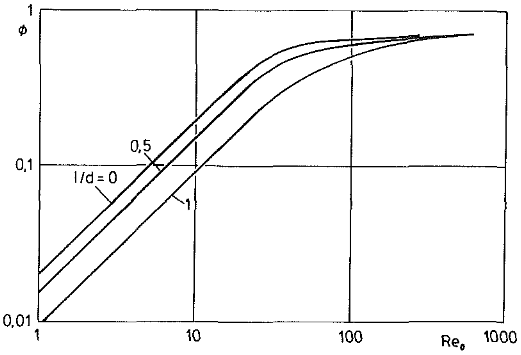

Fig. 2 Dependence of the discharge coefficient on the modified Reynolds number (8)

The standard error of log ϕ estimation equals 0.0760 which corresponds to the standard ϕ estimation error of 1.9 percent. For $l/d = 0$ the regression line is described by the equation

$$\phi = 0.142\ \mathrm{Re}^{0.5036}$$

And for the exponent equal 0.5

$$\phi = 0.141\ \mathrm{Re}^{0.5} \tag{12}$$

The standard error of log ϕ estimation equals 0.0122 which corresponds to the standard ϕ estimation error of 2.8 percent.

In the range of Re > 10 where the kinetic energy influences the velocity of discharge, the discharge coefficient assumes lower values than those predicted by Eq. (9). In this range the three curves for three *l/d* ratios converge and for Re > 300 they converge into one. In the range of Re where Eq. (9) is valid there was no contraction of the jet. The coefficient of contraction was calculated from the photos of the free jet. For Re < 10 its values were not less than 0.99.

From the practical point of view it is more convenient to present the results in the form of ϕ versus Re_0 (Eq. (7)) which allows the value ϕ to be calculated directly for given head h. The experimental results were recalculated and presented in Fig. 2 without experimental points for clarity. It is seen from the plot that Eq. (7) is valid for $\mathrm{Re}_0 < 20$. In this range the constant A (Eq. (7)) equals 0.020 for $l/d = 0$, $A = 0.0153$ for $l/d = 0.5$ and $A = 0.00964$ for $l/d = 1$.

Influence of surface tension on the jet might be expected.

Table 1

Orifice 2 mm
l/d = 0.5, glycol

Re	φ
57.9	0.640
59.1	0.605
70.5	0.640
72.5	0.625
83.9	0.625
90.0	0.632
95.8	0.638
110	0.658
120	0.670
129	0.673
130	0.689
141	0.667
147	0.682
163	0.701
169	0.684
171	0.683
190	0.705
195	0.701
204	0.705
218	0.707
231	0.708
266	0.678

Table 2

Orifice 2 mm
l/d = 0.5, glycerin

Re	φ
2.39	0.191
2.97	0.215
4.00	0.245
4.17	0.252
5.71	0.288
5.93	0.312
6.77	0.317
7.15	0.319
7.88	0.336
9.99	0.370
10.6	0.390
10.9	0.402
12.4	0.416
13.7	0.441
14.1	0.441
14.1	0.426
15.6	0.442
16.8	0.466
18.1	0.471
18.6	0.481
18.8	0.487
19.7	0.476
21.4	0.485
23.1	0.508

Table 3

Orifice 2 mm
l/d = 0.5, syrup

Re	φ
0.0375	0.024
0.0632	0.0302
0.0861	0.0339
0.118	0.0407
0.125	0.0431
0.145	0.0469
0.162	0.0481
0.188	0.0521

Table 4

Orifice 3 mm
l/d = 0.5, glycol

Re	φ
158	0.688
179	0.701
207	0.682
259	0.711
279	0.706
333	0.728
341	0.704
388	0.711
405	0.732
462	0.727

Table 5

Orifice 3 mm
l/d = 0.5, glycerin

Re	φ
4.80	0.271
7.88	0.359
12.5	0.436
16.1	0.458
16.1	0.443
19.9	0.485
23.4	0.503
23.4	0.500
29.0	0.552
31.7	0.551
33.0	0.562
41.5	0.600
48.2	0.595
54.9	0.598
61.8	0.605
71.7	0.634
79.7	0.643

Table 6

Orifice 3 mm
l/d = 0.5, syrup

Re	φ
0.0115	0.0136
0.0119	0.0135
0.0136	0.0143
0.0137	0.0146
0.0156	0.0154
0.0163	0.0159
0.0178	0.0166
0.0185	0.0168
0.0195	0.0172
0.0204	0.0174
0.0230	0.0187
0.0248	0.0200
0.0277	0.0200
0.100	0.0403
0.161	0.0507
0.209	0.0540
0.296	0.0672
0.359	0.0746
0.394	0.0758
0.487	0.0830
0.602	0.0910

Table 7

Orifice 3 mm
l/d = 0.5, glycol

Re	φ
113	0.700
149	0.722
182	0.711
223	0.720
250	0.694
285	0.699
314	0.690
346	0.688
380	0.686

Table 8

Orifice 3 mm
l/d = 0, glycerin

Re	φ
2.60	0.235
3.15	0.245
3.65	0.275
4.31	0.294
5.00	0.326
5.47	0.332
6.28	0.357
6.89	0.388
18.6	0.542
26.1	0.597
33.3	0.622
40.9	0.624
48.3	0.636
56.3	0.653
61.7	0.643
70.9	0.667
75.9	0.648

Table 9

Orifice 3 mm
ld = 0, syrup

Re	φ
0.0106	0.0140
0.0125	0.0151
0.0148	0.0166
0.0168	0.0176
0.0189	0.0188
0.0238	0.0218
0.0302	0.0256
0.0346	0.0276
0.0378	0.0286
0.0560	0.0335
0.0630	0.0357
0.0742	0.0377
0.0821	0.0413
0.0958	0.0428
0.116	0.0477

Table 10

Orifice 3 mm
ld = 1, glycol

Re	φ
104	0.621
136	0.639
175	0.662
214	0.673
250	0.676
290	0.692
323	0.690
371	0.717
396	0.695

Table 11

Orifice 3 mm
ld = 1, glycerin

Re	φ
1.20	0.112
1.46	0.120
1.59	0.123
1.75	0.133
1.95	0.140
2.13	0.146
2.48	0.153
2.91	0.172
3.72	0.186
10.5	0.298
15.4	0.387
22.2	0.401
29.9	0.448
36.3	0.468
42.5	0.485
55.7	0.524
63.5	0.533

Table 12

Orifice 3 mm
ld = 1, syrup

Re	φ
0.00987	0.0096
0.0107	0.00989
0.0102	0.0106
0.0141	0.0115
0.0152	0.0119
0.0169	0.0125
0.0222	0.0140
0.0247	0.0149
0.0295	0.0165
0.0350	0.0182
0.0428	0.0195
0.0495	0.0214
0.0503	0.0228

However, since all the experimental points for given *l/d* value lie on one curve for all fluids, the surface tension seems to have a negligible effect in these experiments.

Concluding Remarks

According to the theoretical considerations the coefficient of discharge of a Newtonian liquid from a small orifice proved

Table 13

Orifice 5 mm
$l/d = 0.5$, syrup

Re	φ
0.0138	0.0154
0.0187	0.0176
0.0245	0.0202
0.0305	0.0222
0.0372	0.0243
0.0464	0.0268
0.0542	0.0290
0.0645	0.0321
0.0698	0.0324
0.0816	0.0359
0.0866	0.0362
0.0949	0.0378
0.107	0.0408
0.115	0.0424
0.122	0.0430

to be proportional to the square root of the Reynolds number in the range of small Reynolds number. This range is limited to the Re value equal 10. The value of the discharge coefficient depends also on the length 1 of the orifice even for $l/d < 1$, but only for Re < 300.

References

Geller, Z. I., 1965, *Neft. Khoz.* (in Russian), Vol. 4, p. 60.

Judd, H., King, R. S., 1908, "Some Experiments on the Frictionless Orifice," *Engineering News*, Vol. 57, No. 13, p. 326.

Lienhard, J. H., and Lienhard, J. H., 1984, "Velocity Coefficients for Free Jets From Sharp-Edged Orifices," ASME JOURNAL OF FLUIDS ENGINEERING, Vol. 106, March, p. 13.

Medaugh, F. W., and Johnson, G. D., 1940, "Investigations of the Discharge Coefficient of Small Circular Orifices," *Civil Engineering*, Vol. 7, No. 7, p. 422.

Uncertainty Analysis

Assuming the experiments were single-point experiments, the uncertainty intervals for the results were calculated according to Kline and McKlintock (Eq. (7)). Assuming odds 20:1 the precision, bias and uncertainty limits for the variables were:

	Precision limit	Bias limit	Uncertainty limit
Height of the liquid in the reservoir	1 mm	0.1 mm	1 mm
Diameter of the reservoir	0.05 mm	0.01 mm	0.05 mm
Diameter of the orifice	0.01 mm	0.001 mm	0.01 mm
Time	0.1 s	0.01 s	0.1 s
Density	3 kg/m^3	10 kg/m^3	11 kg/m^3
Viscosity	0.5 %	4 %	4 %
glycol	0.1 mPa s	0.8 mPa s	0.8 mPa s
glycerol 1	0.8 mPa s	6 mPa s	6 mPa s
glycerol 2	2 mPa s	16 mPa s	16 mPa s
syrup	50 mPa s	0.4 Pa s	0.4 Pa s

The precision, bias, and uncertainty limits for the results were:

Velocity coefficient ϕ	4–7 % of the ϕ value	< 0.5 %	4–7 %
Reynolds number Re	2–6 % of the Re value	4–6 %	4–8 %

Prediction of Pump Performance Under Air-Water Two-Phase Flow Based on a Bubbly Flow Model

Kiyoshi Minemura[1] and Tomomi Uchiyama[1]

This paper is concerned with the determination of the performance change in centrifugal pumps operating under two-phase flow conditions using the velocities and void fractions calculated under the assumption of an inviscid bubbly flow with slippage between the two phases. The estimated changes in the theoretical head are confirmed with experiments within the range of bubbly flow regime.

Nomenclature

$\mathbf{C}$ = absolute velocity
C_D = drag coefficient of a single bubble
g = acceleration of gravity
H_{imp} = head developed by impeller
h = hydraulic loss of head
p = absolute pressure without gravity effect
R_b = radius of bubble
Re = Reynolds number of bubble = $2R_b|\mathbf{W}-\mathbf{V}|/\nu$
r = radial coordinate
t = height of blade
u = peripheral velocity of impeller
$\mathbf{V}$ = relative velocity of bubble
$\mathbf{W}$ = relative velocity of water
z = axial coordinate
α = void fraction
θ = angular coordinate
$\Delta\theta$ = pitch angle of impeller
ν = kinematic viscosity of water
ρ = density
ψ_{imp} = dimensionless expression of H_{imp}, $=H_{\mathrm{imp}}\,(u_2^2/g)$
ω = angular velocity of impeller

Subscripts

0 = pump inlet or zero value of α
1 = impeller inlet
2 = impeller outlet
3 = pump outlet
g = gas phase
l = liquid phase
u = circumferential component

Introduction

In terms of the safety analysis of nuclear reactors or new developments in off-shore crude oil pumps, it is indispensable to understand states of flow in centrifugal pumps under two-phase flow conditions and the corresponding performance of the pumps. To clarify theoretically the behavior of the gas-liquid, two-phase mixture in centrifugal pump impellers, a three-dimensional numerical method based on a bubbly flow

---

[1] Professor and Research Associate, respectively, School of Informatics and Sciences, Nagoya University, Nagoya 464-01, Japan.

Contributed by the Fluids Engineering Division of THE AMERICAN SOCIETY OF MECHANICAL ENGINEERS. Manuscript received by the Fluids Engineering Division February 16, 1992; revised manuscript received February 23, 1993. Associate Technical Editor: T. T. Huang.

Table 13

Orifice 5 mm
$ld = 0.5$, syrup

Re	φ
0.0138	0.0154
0.0187	0.0176
0.0245	0.0202
0.0305	0.0222
0.0372	0.0243
0.0464	0.0268
0.0542	0.0290
0.0645	0.0321
0.0698	0.0324
0.0816	0.0359
0.0866	0.0362
0.0949	0.0378
0.107	0.0408
0.115	0.0424
0.122	0.0430

to be proportional to the square root of the Reynolds number in the range of small Reynolds number. This range is limited to the Re value equal 10. The value of the discharge coefficient depends also on the length l of the orifice even for $l/d < 1$, but only for Re < 300.

References

Geller, Z. I., 1965, *Neft. Khoz.* (in Russian), Vol. 4, p. 60.

Judd, H., King, R. S., 1908, "Some Experiments on the Frictionless Orifice," *Engineering News*, Vol. 57, No. 13, p. 326.

Lienhard, J. H., and Lienhard, J. H., 1984, "Velocity Coefficients for Free Jets From Sharp-Edged Orifices," ASME JOURNAL OF FLUIDS ENGINEERING, Vol. 106, March, p. 13.

Medaugh, F. W., and Johnson, G. D., 1940, "Investigations of the Discharge Coefficient of Small Circular Orifices," *Civil Engineering*, Vol. 7, No. 7, p. 422.

Uncertainty Analysis

Assuming the experiments were single-point experiments, the uncertainty intervals for the results were calculated according to Kline and McKlintock (Eq. (7)). Assuming odds 20:1 the precision, bias and uncertainty limits for the variables were:

	Precision limit	Bias limit	Uncertainty limit
Height of the liquid in the reservoir	1 mm	0.1 mm	1 mm
Diameter of the reservoir	0.05 mm	0.01 mm	0.05 mm
Diameter of the orifice	0.01 mm	0.001 mm	0.01 mm
Time	0.1 s	0.01 s	0.1 s
Density	3 kg/m^3	10 kg/m^3	11 kg/m^3
Viscosity	0.5 %	4 %	4 %
glycol	0.1 mPa s	0.8 mPa s	0.8 mPa s
glycerol 1	0.8 mPa s	6 mPa s	6 mPa s
glycerol 2	2 mPa s	16 mPa s	16 mPa s
syrup	50 mPa s	0.4 Pa s	0.4 Pa s

The precision, bias, and uncertainty limits for the results were:

Velocity coefficient ϕ	4–7 % of the ϕ value	< 0.5 %	4–7 %
Reynolds number Re	2–6 % of the Re value	4–6 %	4–8 %

Prediction of Pump Performance Under Air-Water Two-Phase Flow Based on a Bubbly Flow Model

Kiyoshi Minemura[1] and Tomomi Uchiyama[1]

This paper is concerned with the determination of the performance change in centrifugal pumps operating under two-phase flow conditions using the velocities and void fractions calculated under the assumption of an inviscid bubbly flow with slippage between the two phases. The estimated changes in the theoretical head are confirmed with experiments within the range of bubbly flow regime.

Nomenclature

$\mathbf{C}$ = absolute velocity
C_D = drag coefficient of a single bubble
g = acceleration of gravity
H_{imp} = head developed by impeller
h = hydraulic loss of head
p = absolute pressure without gravity effect
R_b = radius of bubble
Re = Reynolds number of bubble = $2R_b|\mathbf{W}-\mathbf{V}|/\nu$
r = radial coordinate
t = height of blade
u = peripheral velocity of impeller
$\mathbf{V}$ = relative velocity of bubble
$\mathbf{W}$ = relative velocity of water
z = axial coordinate
α = void fraction
θ = angular coordinate
$\Delta\theta$ = pitch angle of impeller
ν = kinematic viscosity of water
ρ = density
ψ_{imp} = dimensionless expression of H_{imp}, $=H_{\mathrm{imp}}\,(u_2^2/g)$
ω = angular velocity of impeller

Subscripts

0 = pump inlet or zero value of α
1 = impeller inlet
2 = impeller outlet
3 = pump outlet
g = gas phase
l = liquid phase
u = circumferential component

Introduction

In terms of the safety analysis of nuclear reactors or new developments in off-shore crude oil pumps, it is indispensable to understand states of flow in centrifugal pumps under two-phase flow conditions and the corresponding performance of the pumps. To clarify theoretically the behavior of the gas-liquid, two-phase mixture in centrifugal pump impellers, a three-dimensional numerical method based on a bubbly flow

---

[1] Professor and Research Associate, respectively, School of Informatics and Sciences, Nagoya University, Nagoya 464-01, Japan.

Contributed by the Fluids Engineering Division of THE AMERICAN SOCIETY OF MECHANICAL ENGINEERS. Manuscript received by the Fluids Engineering Division February 16, 1992; revised manuscript received February 23, 1993. Associate Technical Editor: T. T. Huang.

model was proposed and applied to a radial-flow pump impeller in a sister paper (Minemura and Uchiyama, 1993). The calculated distributions of pressure and void fraction for various inlet void fractions showed good agreement with experiments.

In this paper, the head developed by the impeller under two-phase flow conditions is evaluated with the calculated velocities and void fractions in the pump and confirmed with experiments within the range of bubbly flow regime. It is also demonstrated that the head is scarcely affected by bubble diameter in the impeller or friction factor between the two phases.

Theoretical Relations

In our previous study (Minemura and Uchiyama, 1993), it was assumed that fine bubbles flow in a state of uniform dispersion and that the two-phase mixture is inviscid except for the viscous drag force on the bubble motion. Based on this bubbly flow model, Euler's equation for the bubbly flow in a system rotating with a constant angular velocity ω was obtained

$$(1-\alpha)\rho_l \mathbf{W}\cdot\nabla\mathbf{W}+(1-\alpha)\rho_l\omega\times(2\mathbf{W}+\omega\times\mathbf{r})+\nabla p=0 \quad (1)$$

By taking the scalar product of Eq. (1) and the element of streamline ds after dividing both sides of Eq. (1) with $(1-\alpha)\rho_l$, and integrating from the pump inlet to the outlet along the streamline s under the assumption of constant liquid density ρ_l, we obtain Bernoulli's equation for the bubbly flow in the rotating system:

$$[(\mathbf{W}_3^2-u_3^2)/2-(\mathbf{W}_0^2-u_0^2)/2] + (1/\rho_l)\int_{p0}^{p3}[1/(1-\alpha)]dp=0 \quad (2)$$

Using the relation $\mathbf{W}^2-u^2=\mathbf{C}_l^2-2u\mathbf{C}_{ul}$ from a velocity triangle, Eq. (2) is rewritten as

$$(u_3\mathbf{C}u_{3l}-u_0\mathbf{C}_{u0l})/g=(\mathbf{C}_{3l}^2-\mathbf{C}_{0l}^2)/2g + (1/\rho_l g)\int_{p0}^{p3}[1/(1-\alpha)]dp \quad (3)$$

It was found that the absolute flow inside the pump can be considered irrotational in bubble flow regime (Minemura and Uchiyama, 1993). The left-hand side of Eq. (3) can thus reduce to the head developed by the impeller H_{imp}, namely,

$$(u_3\mathbf{C}_{u3l}-u_0\mathbf{C}_{u0l})/g=(u_2\mathbf{C}_{u2l}-u_1\mathbf{C}_{u1l})/g\equiv H_{\mathrm{imp}} \quad (4)$$

and

$$H_{\mathrm{imp}}=(\mathbf{C}_{3l}^2-\mathbf{C}_{0l}^2)/2g+(1/\rho_l g)\int_{p0}^{p3}[1/(1-\alpha)]dp \quad (5)$$

If viscous effects are considered, then Eq. (5) should be modified to include hydraulic loss of head h as,

$$H'_{\mathrm{imp}}=(\mathbf{C}_{3l}'^2-\mathbf{C}_{0l}'^2)/2g+(1/\rho_l \mathrm{g})\int_{p'_0}^{p'_3}[1/(1-\alpha')]dp'+h \quad (6)$$

where prime notation is used to denote the values affected by the viscosity.

The impeller work given to a unit mass flow rate of the mixture, namely, the head developed by the impeller, is represented by difference in the angular momentum of the mixture M and the mass flow rate $\dot{m}(=\dot{m}_1=\dot{m}_2)$

$$H_{\mathrm{imp}}=(\omega/g)(M_2-M_1)/\dot{m} \quad (7)$$

where

$$M=r^2\int_0^t\int_0^{\Delta\theta}[\alpha\rho_g\mathbf{C}_{rg}\mathbf{C}_{ug}+(1-\alpha)\rho_l\mathbf{C}_{rl}\mathbf{C}_{ul}]d\theta dz \quad (8)$$

Calculations were carried out for a flow in a radial-flow impeller pump having low specific-speed [specific speed: 180 (m, m^3/min, rpm)] and for the normal operating condition of the pump as described in the previous report (Minemura and Uchiyama, 1993). The geometry and dimensions of the pump are shown in Fig. 1. It is assumed that bubbles flow homogeneously into the pump inlet with the same velocity as water having an initial diameter of 0.3 mm. This value was found to be most frequently observed in the impeller inlet region in this pump under the operating condition.

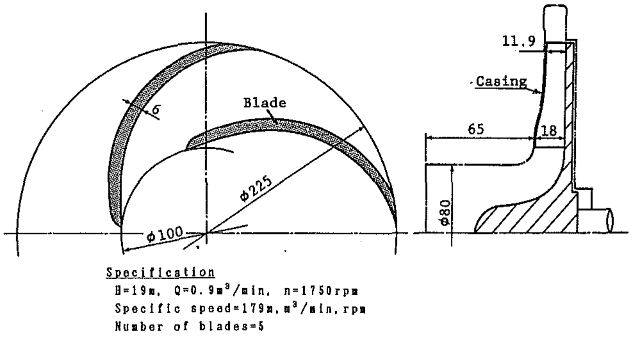

Fig. 1 Shape and dimensions of impeller

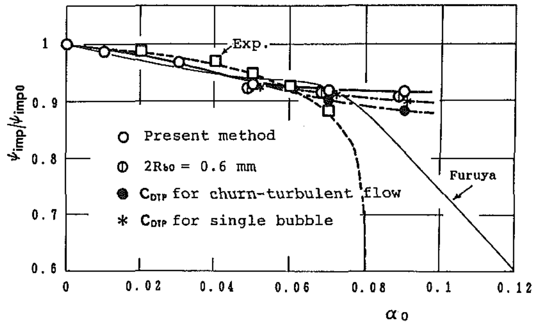

Fig. 2 The head developed by impeller as a function of α_0 (uncertainty in $\psi_{\mathrm{imp}}/\psi_{\mathrm{imp0}}$ is ±4 percent of $\psi_{\mathrm{imp}}/\psi_{\mathrm{imp0}}$ and in α_0 ±3 percent of α_0.)

The head developed by the impeller H_{imp} is evaluated by substituting velocities and void fractions calculated in the previous paper into Eq. (7). The dimensionless values ψ_{imp} obtained are shown in Fig. 2. Here the head is divided by the value corresponding to the single-phase flow with the same mass flow rate, $\psi_{\mathrm{imp}}/\psi_{\mathrm{imp0}}$. When α_0 increases, the ratio $\psi_{\mathrm{imp}}/\psi_{\mathrm{imp0}}$ decreases slightly, and becomes almost constant ($\psi_{\mathrm{imp}}/\psi_{\mathrm{imp0}}=0.92$) in the range of $\alpha_0\geq 0.07$.

Since the drag coefficient of a bubble C_{DTP} is much larger in the higher void fraction region, the bubble velocity relative to water is made lower here. When α_0 increases, therefore, increasing rate of α in the predominant region of high void fractions becomes less than that of the inlet void fraction α_0. Since the presence of this high void fraction region reduces the blade load, the higher α_0 the lower is the decreasing rate of $\psi_{\mathrm{imp}}/\psi_{\mathrm{imp0}}$.

When the drag coefficient of a single bubble C_D is tentatively used instead of C_{DTP}, the calculated results of $\psi_{\mathrm{imp}}/\psi_{\mathrm{imp0}}$, as shown by the symbol * in the same figure, deviate from those described above in the range of $\alpha\geq 0.07$, showing a slightly greater drop with increasing α.

Experimental results (Minemura et al., 1985) for a pump with almost the same geometry and dimensions as that analyzed are also plotted by the symbol □ in Fig. 2. The results change in a similar way as the calculated values for the lower range of α_0 ($\alpha_0\leq 0.06$), except for less reduction in $\psi_{\mathrm{imp}}/\psi_{\mathrm{imp0}}$. When α_0 is increased beyond the limit of $\alpha_0=0.07$, the measured values drop abruptly, and their difference becomes evident. From the observations of the bubbly flow (Murakami and Minemura, 1974), a large void is found in the impeller inlet region due to the accumulation of bubbles, showing that the bubbly flow model employed in this paper is not applicable to such a high value of α_0.

To clarify the effect of the initial bubble diameter on the impeller work, calculations with bubbles having twice the initial value employed in the foregoing, $2R_{b0}=0.6$ mm, have also been made. The results obtained are also plotted for the cases of $\alpha_0=0.05$, 0.07, and 0.09 in Fig. 2. The head ψ_{imp} for the larger bubble decreases more, but this effect is extremely small.

In the impeller inlet region near the shroud, the value α becomes locally more than four times that in the pump inlet, as mentioned in the previous paper (Minemura and Uchiyama, 1993). The drag coefficient of a bubble in such a field of void fraction C_{DTP} is determined by using $C_{\mathrm{DTP}}=(1-\alpha)^{-q}\cdot C_D$ ($q=8.9\mathrm{Re}^{-0.1}$). When the flow regime changes, the C_{DTP} value undergoes a change as well. Hench and Johnston (1972) measured the performance of a diffuser under two-phase flow conditions, and provided the drag coefficient for a churn-turbulent flow regime in the range of $\alpha\geq 0.35$, as $C_{\mathrm{DTP}}=0.11R_b(1-\alpha)^3$ [mm].

If it is assumed that the predominant region of high void fraction $\alpha\geq 0.35$ belongs to the churn-turbulent flow regime and that the drag coefficient there is given by the above equation. The head ratio then obtained decreases considerably in the range $\alpha_0\geq 0.07$ as indicated by the solid symbol in Fig. 2. But the decrease of $\psi_{\mathrm{imp}}/\psi_{\mathrm{imp0}}$ is not so large as the measured value. To predict the performance change in two-phase pumps, this coefficient was also employed by Furuya (1985), who solved two-phase flow equations in only one-dimensional. According to his results, the head shows a drastic drop when the flow changes from the bubbly flow regime to the churn-turbulent one. For a three-dimensional channel as treated in the present study, however, the usage of C_{DTP} for the churn-turbulent flow in the region having a locally high void fraction is seen not to have an effect as great as that for a one-dimensional one.

The result calculated with Furuya's method is also superimposed by a thin solid line in Fig. 2, in which the churn-turbulent flow regime corresponds to the range $\alpha\geq 0.35$. Though this one-dimensional calculation is very crude compared with the detailed analysis described in our previous paper, the predicted head by Furuya's method coincides remarkably with the experimental data except for less reduction in the range of $\alpha_0\geq 0.06$.

Conclusions

Using the velocities and void fractions calculated on the basis of a bubbly flow model, the head developed by the impeller was evaluated and the effect of friction factors on the head was discussed. The results are summarized as follows:

(1) When the inlet void fraction is as small as the flow in the impeller is in the bubbly flow regime, the head developed by the impeller can be predicted by the numerical method proposed in this paper.

(2) The effect of bubble size on the head developed by the impeller is extremely small.

(3) When the drag coefficient for bubbles in the churn-turbulent flow regime is used for the predominant region of high void fractions as $\alpha > 0.35$, the calculated head developed by the impeller is decreased, but does not drop as sharply as the measured one and the one predicted by one-dimensional calculations.

References

Furuya, O., 1985, "An Analytical Model for Prediction of Two-Phase (Non-condensable) Flow Pump Performance," ASME JOURNAL OF FLUIDS ENGINEERING, Vol. 107, No. 1, pp. 139–147.

Hench, J. E., and Johnston, J. P., 1972, "Two-Dimensional Diffuser Performance with Subsonic, Two-Phase, Air-Water Flow," ASME *Journal of Basic Engineering*, Vol. 94, No. 1, pp. 105–121.

Mikielewicz, J., Wilson, D. G., Chan, T., and Goldfinch, A. L., 1978, "A Method for Correlating the Characteristics of Centrifugal Pumps in Two-Phase Flow," ASME JOURNAL OF FLUIDS ENGINEERING, Vol. 100, No. 4, pp. 395–409.

Minemura, K., Murakami, M., and Kataoka, T., 1983, "Pressure Distribution in a Centrifugal Impeller Handling Air-Water Mixtures," *Bulletin of JSME*, Vol. 26, No. 220, pp. 1727–1734.

Minemura, K., Murakami, M., and Katagiri, H., 1985, "Characteristics of Centrifugal Pumps Handling Air-Water Mixtures and Size of Air Bubbles in Pump Impellers," *Bulletin of JSME*, Vol. 28, No. 244, pp. 2310–2318.

Minemura, K., and Uchiyama, T., 1993, "Three-Dimensional Calculation of Air-Water Two-Phase Flow in Centrifugal Pump Impeller Based on a Bubbly Flow Model," ASME JOURNAL OF FLUIDS ENGINEERING, published in this issue, pp. 766–771.

Murakami, M., and Minemura, K., 1974, "Effects of Entrained Air on the Performance of a Centrifugal Pump (1st Report, Performance and Flow Conditions)," *Bulletin of JSME*, Vol. 17, No. 110, pp. 1047–1055.

Journal of Fluids Engineering Discussion

Further Experiments on Transition to Turbulence in Constant-Acceleration Pipe Flow[1]

P. R. Bandyopadhyay.[2] The authors are to be congratulated for generating some invaluable transition data in impulsively accelerated pipe flows. On p. 225 they state that: "This further supports the conclusion that for constant-acceleration pipe startup flow, the entire flow in the test section undergoes a kind of global instability, with transition being essentially independent of axial position." This discussion is concerned with the observation of global instability.

The phenomenon of global instability has been reported earlier although in the context of deceleration, which unlike acceleration enhances transition. The authors have overlooked a relevant paper by Bandyopadhyay (1986) where also the results of a transition experiment in a suddenly applied acceleration-deceleration in a 2.54 cm diameter pipe flow of water was reported. It should also be on record that in the mid 1970s, Dr. M. R. Head in Cambridge University Engineering Department had conducted flow visualization experiments in the low-speed smoke tunnel described in Heat and Bandyopadhyay (1981) where transition took place in the entire flat plate laminar boundary layer when the whole tunnel flow was suddenly brought to a halt. In both of these experiments also, transition eventually took place simultaneously over the entire flow field.

Lefebvre and White (1991) presented information on the transition and not the instability process. It is necessary to make this distinction. It is not clear what they mean by global instability. Because in all theoretical analyses conducted so far, pipe flows have been found to be notoriously stable, the question is where do the disturbances come from in their experiments?

Flow visualization pictures from the experiments of Bandyopadhyay (1986) show a gradual, not an abrupt, development of a disorganized motion from the amplification of periodic disturbances. The pattern does not convect axially. It is the near-wall flow which is breaking down first and not the entire cross section. The disturbed layer thickness remains uniform over the entire pipe as it grows. This means that unlike flat plate boundary layer flow with a free stream, the flow can be treated as parallel. This Raleigh layer like constant thickness growth can also be observed in a duct after the passage of a shock (see the Schlieren pictures from Prof. Deckker reproduced in Head and Bandyopadhyay, 1981). In the opinion of the discusser, in the flows visualized by Bandyopadhyay (1986), a self-similar inflectional mean velocity profile is breaking down *locally*, although the name global is appealing based on observation. Inflectional velocity profiles can conceivably occur in both accelerating and decelerating pipe flows, as long as they are impulsively applied. These flow visualizations also show that the wavelength of the rollups is very close to the pipe radius and not the diameter. There does not seem to be a larger scale like the length of the pipe. However, the longitudinal direction could play a role if the rollups are not axisymmetric rings. Note that the rollups are situated diametrically across and are not staggered. So, if helical modes rather than axisymmetric ones are indeed present, they would have to appear in pairs. Because regular pipe flow transition requires disturbances to come from the inlet, the presence of helical modes in accelerating or decelerating pipe flows also is an intriguing issue (Bandyopadhyay, 1986).

Because regular pipe flow transition Reynolds numbers are known to be sensitive to the environment, are the transition Reynolds number data in Fig. 4 unique to the facility? If so, controlling the disturbances at the inlet and outlet also might provide us with a means to control the transition Reynolds number in impulsively applied accelerating or decelerating pipe flows. The role of environmental disturbances in the global instability process is unknown and clearly more work is needed to improve our understanding.

Additional References

Bandyopadhyay, P. R., 1986, "Aspects of the Equilibrium Puff in Transitional Pipe Flow," *Journal of Fluid Mechanics*, Vol. 163, pp. 439–458.

Head, M. R., and Bandyopadhyay, P., 1981, "New Aspects of Turbulent Boundry Layer Structure," *Journal of Fluid Mechanics*, Vol. 107, pp. 297–338.

Authors' Closure

Mr. Bandyopadhyay appears to be attempting to expound potential similarities in global instability between accelerating and decelerating pipe flow based on his past experimental results. Mr. Bandyopadhyay states in his paper that for this flow visualization of his Fig. 10 a fully developed state flow at a pipe Reynolds number of 2000 was first achieved. A bypass valve was then opened quickly and then shut immediately thereafter to produce an abrupt acceleration and subsequent deceleration "that nearly brought the pipe flow to a halt for a fraction of a second." It appears that the photographs were taken during deceleration at a time when the flow was essentially zero since he states "these laminar roll-ups quickly grew in size locally while exhibiting virtually no steamwise convection, and then chaos ensued as the pipe flow was re-established."

---

[1] By P. J. Lefebvre and F. M. White, published in the June 1991 issue of the *Journal of Fluids Engineering*, Vol. 112, pp. 223-227.

[2] Code 8233, Naval Undersea Warfare Center Division, Newport, R.I. 02841-5047.